

Contributors to This Volume

K. Amos
P. J. Dortmans
H. Feshbach
H. V. von Geramb
M. S. Hussein
S. Karataglidis
A. K. Kerman
R. Rapp
J. Raynal
O. K. Vorov
J. Wambach

ADVANCES IN NUCLEAR PHYSICS

Edited by
J. W. Negele
and Erich Vogt

VOLUME 25

ADVANCES IN NUCLEAR PHYSICS

VOLUME 25

CONTRIBUTORS TO THIS VOLUME

K. Amos, P. J. Dortmans

*School of Physics
University of Melbourne
Parkville, Victoria, Australia*

H. Feshbach

*Center for Theoretical Physics
Laboratory for Nuclear Science and
Department of Physics
Massachusetts Institute of Technology
Cambridge, Massachusetts*

H. V. von Geramb

*Theoretische Kernphysik
Universität Hamburg
Hamburg, Germany*

M. S. Hussein

*Instituto de Física
Universidade de São Paulo
São Paulo, SP, Brazil*

S. Karataglidis

*TRIUMF
Vancouver, British Columbia, Canada*

A. K. Kerman

*Center for Theoretical Physics
Laboratory for Nuclear Science and
Department of Physics
Massachusetts Institute of Technology
Cambridge, Massachusetts*

R. Rapp

*Department of Physics and Astronomy
State University of New York
Stony Brook, New York*

J. Raynal

*Service de Physique Théorique
C.E.-Saclay
Gif-sur-Yvette Cedex, France*

O. K. Vorov

*Instituto de Física
Universidade de São Paulo
São Paulo, SP, Brazil*

J. Wambach

*Institut für Kernphysik
Technische Universität Darmstadt
Darmstadt, Germany*

A Continuation Order Plan is available for this series. A continuation order will bring delivery of each new volume immediately upon publication. Volumes are billed only upon actual shipment. For further information please contact the publisher.

ADVANCES IN NUCLEAR PHYSICS

Edited by

J. W. Negele

*Center for Theoretical Physics
Massachusetts Institute of Technology
Cambridge, Massachusetts*

Erich Vogt

*Department of Physics
University of British Columbia
Vancouver, B.C., Canada*

VOLUME 25

KLUWER ACADEMIC PUBLISHERS
NEW YORK, BOSTON, DORDRECHT, LONDON, MOSCOW

eBook ISBN: 0-306-47101-9
Print ISBN: 0-306-46440-3

©2002 Kluwer Academic Publishers
New York, Boston, Dordrecht, London, Moscow

Print ©2000 Kluwer Academic /Plenum Publishers
New York

All rights reserved

No part of this eBook may be reproduced or transmitted in any form or by any means, electronic, mechanical, recording, or otherwise, without written consent from the Publisher

Created in the United States of America

Visit Kluwer Online at: <http://kluweronline.com>
and Kluwer's eBookstore at: <http://ebooks.kluweronline.com>

ARTICLES PUBLISHED IN EARLIER VOLUMES

Volume 1

The Reorientation Effect • *J. de Boer and J. Eicher*

The Nuclear SU_3 Model • *M. Harvey*

The Hartree-Fock Theory of Deformed Light Nuclei • *G. Ripka*

The Statistical Theory of Nuclear Reactions • *E. Vogt*

Three-Particle Scattering—A Review of Recent Work on the Nonrelativistic Theory •
I. Duck

Volume 2

The Giant Dipole Resonance • *B. M. Spicer*

Polarization Phenomena in Nuclear Reactions • *C. Glashausser and J. Thirion*

The Pairing-Plus-Quadrupole Model • *D. R. Bes and R. A. Sorensen*

The Nuclear Potential • *P. Signell*

Muonic Atoms • *S. Devons and I. Duerdorff*

Volume 3

The Nuclear Three-Body Problem • *A. N. Mitra*

The Interactions of Pions with Nuclei • *D. S. Koltun*

Complex Spectroscopy • *J. B. French, E. C. Halbert, J. B. McGrory, and S. S. M. Wong*

Single Nucleon Transfer in Deformed Nuclei • *B. Elbeck and P. O. Tjøm*

Isoscalar Transition Rates in Nuclei from the (α, α') Reaction • *A. M. Bernstein*

Volume 4

The Investigation of Hole States in Nuclei by Means of Knockout and Other Reactions •
Daphne F. Jackson

High-Energy Scattering from Nuclei • *Wieslaw Czyz*

Nucleosynthesis by Charged-Particle Reactions • *C. A. Barnes*

Nucleosynthesis and Neutron-Capture Cross Sections • *B. J. Alien, J. H. Gibbons, and
R. L. Macklin*

Nuclear Structure Studies in the $Z = 50$ Region • *Elizabeth Urey Baranger*

An $s-d$ Shell-Model Study for $A = 18 - 22$ • *E. C. Halbert, J. B. McGrory, B. H. Wildenthal,
and S. P. Panday*

Volume 5

Variational Techniques in the Nuclear Three-Body Problem • *L. M. Delves*

Nuclear Matter Calculations • *Donald W. L. Sprung*

Clustering in Light Nuclei • *Akito Arima, Hisashi Horiuchi, Kunihara Kubodera, and
Noburu Takigawa*

Volume 6

Nuclear Fission • *A. Michaudon*

The Microscopic Theory of Nuclear Effective Interactions and Operators • *Bruce R. Barrett and Michael W. Kirson*

Two-Neutron Transfer Reactions and the Pairing Model • *Ricardo Broglia, Ole Hansen, and Claus Riedel*

Volume 7

Nucleon-Nucleus Collisions and Intermediate Structure • *Aram Mekjian*

Coulomb Mixing Effects in Nuclei: A Survey Based on Sum Rules • *A. M. Lane and A. Z. Mekjian*

The Beta Strength Function • *P. G. Hansen*

Gamma-Ray Strength Functions • *G. A. Bartholemew, E. D. Earle, A. J. Ferguson, J. W. Knowles, and M. A. Lone*

Volume 8

Strong Interaction in A-Hypernuclei • *A. Gal*

Off-Shell Behavior of the Nucleon-Nucleon Interaction • *M. K. Srivastava and D. W. L. Sprung*

Theoretical and Experimental Determination of Nuclear Charge Distributions • *J. L. Friar and J. W. Negele*

Volume 9

One- and Two-Nucleon Transfer Reactions with Heavy Ions • *Sidney Kahana and A. J. Baltz*

Computational Methods for Shell-Model Calculations • *R. R. Whitehead, A. Watt, B. J. Cole, and I. Morrison*

Radiative Pion Capture in Nuclei • *Helmut W. Baer, Kenneth M. Crowe, and Peter Truöl*

Volume 10

Phenomena in Fast Rotating Heavy Nuclei • *R. M. Lieder and H. Ryde*

Valence and Doorway Mechanisms in Resonance Neutron Capture • *B. J. Allen and A. R. de L. Musgrave*

Lifetime Measurements of Excited Nuclear Levels by Doppler-Shift Methods • *T. K. Alexander and J. S. Forster*

Volume 11

Clustering Phenomena and High-Energy Reactions • *V. G Neudatchin, Yu. F. Smirnov, and N. F. Golovanova*

Pion Production in Proton-Nucleus Collisions • *B. Holstad*

Fourteen Years of Self-Consistent Field Calculations: What Has Been Learned • *J. P. Svenne*

Hartree-Fock-Bogoliubov Theory with Applications to Nuclei • *Alan L. Goodman*

Hamiltonian Field Theory for Systems of Nucleons and Mesons • *Mark Bolsterli*

Volume 12

Hypernetted-Chain Theory of Matter at Zero Temperature • *J. G. Zabolitzky*
Nuclear Transition Density Determinations from Inelastic Electron Scattering •

Jochen Heisenberg

High-Energy Proton Scattering • *Stephen J. Wallace*

Volume 13

Chiral Symmetry and the Bag Model: A New Starting Point for Nuclear Physics •

A. W. Thomas

The Interacting Boson Model • *A. Arima and F. Iachella*

High-Energy Nuclear Collisions • *S. Nagamiya and M. Gyulassy*

Volume 14

Single-Particle Properties of Nuclei Through ($e, e'p$) Reactions • *Salvatore Frullani and Jean Mougey*

Volume 15

Analytic Insights into Intermediate-Energy Hadron-Nucleus Scattering • *R. D. Amado*
Recent Developments in Quasi-Free Nucleon Scattering • *P. Kitching, W. J. McDonald,*

Th. A. J. Maris, and C. A. Z. Vasconcellos

Energetic Particle Emission in Nuclear Reactions • *David H. Boal*

Volume 16

The Relativistic Nuclear Many-Body Problem • *Brian Serot and John Dirk Walecka*

Volume 17

P -Matrix Methods in Hadronic Scattering • *B. L. G. Bakker and P. J. Mulders*

Dibaryon Resonances • *M. P. Locher, M. E. Saino, and A. Švarc*

Skyrmiions in Nuclear Physics • *Ulf-G. Meissner and Ismail Zahed*

Microscopic Descriptions of Nucleus-Nucleus Collisions • *Karlheinz Langanke and Harald Friedrich*

Volume 18

Nuclear Magnetic Properties and Gamow-Teller Transitions • *A. Arima, K. Shimizu, W. Bentz, and H. Hyuga*

Advances in Intermediate-Energy Physics with Polarized Deuterons • *J. Arvieux and J. M. Cameron*

$\bar{p}p$ Interaction and the Quest for Baryonium • *C. Amsler*

Radiative Muon Capture and the Weak Pseudoscalar Coupling in Nuclei • *M. Gmitro and P. Truöl*

Introduction to the Weak and Hypoweak Interactions • *T. Goldman*

Volume 19

Experimental Methods for Studying Nuclear Density Distributions • *C. J. Batty, H. J. Gils, and H. Rebel*

The Meson Theory of Nuclear Forces and Nuclear Structure • *R. Machleidt*

Volume 20

Single-Particle Motion in Nuclei • *C. Mahaux and R. Sartor*

Relativistic Hamiltonian Dynamics in Nuclear and Particle Physics • *B. D. Keister and W. N. Polyzou*

Volume 21

Multiquark Systems in Hadronic Physics • *B. L. G. Bakker and I. M. Narodetskii*

The Third Generation of Nuclear Physics with the Microscopic Cluster Model • *Karlheinz Langanke*

The Fermion Dynamical Symmetry Model • *Cheng-Li Wu, Da Hsuan Feng, and Mike Guidry*

Volume 22

Nucleon Models • *Dan Olof Riska*

Aspects of Electromagnetic Nuclear Physics and Electroweak Interaction • *T. W. Donnelly*

Color Transparency and Cross-Section Fluctuations in Hadronic Collisions • *Gordon Baym*

Many-Body Methods at Finite Temperature • *D. Vautherin*

Nucleosynthesis in the Big Bang and in the Stars • *K. Langanke and C. A. Barnes*

Volume 23

Light Front Quantization • *Matthias Burkardt*

Nucleon Knockout by Intermediate Energy Electrons • *James J. Kelly*

Volume 24

Nuclear Charge-Exchange Reactions at Intermediate Energy • *W. P. Alford and B. M. Spicer*

Mesonic Contributions to the Spin and Flavor Structure of the Nucleon • *J. Speth and A. W. Thomas*

Muon Catalyzed Fusion: Interplay between Nuclear and Atomic Physics •

K. Nagamine and M. Kamimura

ARTICLES PLANNED FOR FUTURE VOLUMES

The Spin Structure of the Nucleon • *Bradley Fillipone*

Rotational Phenomena in Atomic Nuclei • *David Ward and Paul Fallon*

Chiral Perturbation Theory for Mesons and Nucleons • *Stefan Scherer*

Liquid-Gas Phase Transition in Nuclear Multifragmentation • *Subal Das Gupta,*

Manyee Tsang, and Aram Mekjian

Fifty Years of the Nuclear Shell Model • *Igal Talmi*

The Deuteron • *Wallace van Orden and Michael Garcon*

PREFACE

The history of nuclear physics spans the century which is just ending. For the first half of the century low-energy nuclear physics was one of the dominant foci of all of science. Then accelerators prospered. Energies grew. Correspondingly the energies of interest for nuclear physics grew into the GeV regime and beyond. It is perhaps fitting then that this end-of-century volume of *Advances in Nuclear Physics* has three articles pertaining to the various energy regimes through which nuclear physics has developed in the past century and promises to develop in the future. One article (the second) describes new information about fundamental symmetries found with kilovolt neutrons. Another (the third) reviews our progress in understanding nucleon-nucleus (NA) scattering up to 1 GeV. The final article (the first) analyzes dilepton production as a probe for quark-gluon plasmas generated in relativistic heavy-ion collisions. This latter subject will be a major interest of nuclear physics well into the next century.

The review by Rapp and Wambach of dilepton production as a probe of hot/dense nuclear matter—including phase changes—is very timely and pertains to a subject of great scientific importance. Perhaps when future scientists and historians view the past century of science they will regard as one of its greatest intellectual accomplishments the fact that we were able to articulate scientifically the history of the universe in which we live. That history extends from the initial Big Bang to the present in which stars are continuing to evolve and finally to collapse. Hot/dense nuclear matter occurred in the early universe and now occurs in collapsing stars. In the past decade much new data has emerged about hot/dense nuclear matter from experiments at Brookhaven in the USA, CERN in Europe and GSI in Germany. The timeliness of the present review arises from the fact that it occurs just after this first generation

of relativistic heavy-ion experiments have provided an initial skirmish with the phase change and just before the advent of the second generation of experiments, with new facilities, promises to fully explore the regions of density and temperature in which the phase change is expected to occur. In fact, Brookhaven's new RHIC facility is scheduled to begin its work as this volume rushes into print. CERN's LHC will start a few years later. It is commonly accepted that dilepton production is among the best diagnostic tools for the relevant phase changes. The present review gives a very thorough analysis of dilepton production in nuclear matter.

The final article of this volume deals with one of the oldest problems in nuclear physics: nucleon-nucleus (NA) scattering. If one ignores the quark substructure of the nucleons [it remains to be shown that quantum chromodynamics (QCD) matters for NA scattering below 1 GeV] then the effect of the nucleus on the scattering depends on the nucleon-nucleon (NN) interaction and on the nuclear structure of the target. It is a complicated problem and a simple, accurate treatment of NA scattering is invaluable for the description of all nuclear reactions. For more than six decades such a simple approximation has been the optical model in which a complex mean field represents the nucleus. The imaginary part of the complex mean field represents the impact of inelastic processes on NA scattering. Usually, in the analysis of the data, the parameters of the optical potential have been entirely phenomenological. The challenge has been to relate those phenomenological parameters to a proper treatment of NA scattering using realistic interactions, or alternatively, to describe the NA scattering data using the full NN interactions of the projectile and target nucleons as well as the structure of the target. This review describes how close we have come, by the end of the century, to such a direct, microscopic, non-relativistic treatment of NA scattering below 1 GeV. The goal is in sight, Appropriate multiple scattering theories exist. Much new knowledge and data fixes the input NN data. The needed nuclear structure rests on reasonably firm ground. It is then very satisfying that so much new and old NA scattering data now conforms to description by such a direct microscopic approach. Perhaps, in the next century, the quark substructure will be found to matter for NA scattering. To determine how and why it matters will count on our also knowing how far the classical treatment of this review can carry us.

Complementing the other two massive and encyclopedic works, the second article tersely describes the evidence, accumulated over the past decade, about how nature chooses to reveal information about funda-

mental symmetries from the extreme chaos pertaining to slow neutron resonances in heavy nuclei. In hadronic interactions parity violation forces are a very tiny component added to the strong interactions. Yet one of the oldest tools in nuclear physics—slow neutrons interacting with nuclei—now provide conditions in which the tiny parity violating forces can play a role. In many cases the accidental proximity of resonances of opposite parity enhances their mixing through the parity violating force components. This article gives a full description of the reaction theory analysis needed to extract information about fundamental symmetries for the recent series of experiments at Los Alamos with polarized, epithermal neutrons.

J. W. NEGELE
E. W. VOGT

CONTENTS

Chapter 1

CHIRAL SYMMETRY RESTORATION AND DILEPTONS IN RELATIVISTIC HEAVY-ION COLLISIONS

R. Rapp and J. Wambach

1. Introduction	1
2. “Strong QCD” and Vector Mesons	11
2.1. Symmetries and Anomalies of QCD	13
2.2. Vacuum Condensates	15
2.3. In-Medium Condensates via Low-Density Expansions	18
2.4. Lattice Results	22
2.5. Dilepton Production and Vector Mesons	30
2.6. Vector-Axialvector Mixing	32
2.7. QCD Sum Rules	39
2.8. Chiral Reduction Formalism	45
3. Modeling Vector Mesons in the Medium	49
3.1. Effective Meson Lagrangians: Impact of Finite Temperature	50
3.1.1. Gauged Linear σ -Model + VDM	50
3.1.2. Massive Yang-Mills Approach	54
3.1.3. Hidden Local Symmetry	56
3.1.4. Phenomenological Meson Lagrangians	62

3.2.	Finite Baryon Density	77
3.2.1.	Mean-Field Approach: Brown-Rho Scaling	77
3.2.2.	Pion Cloud Modifications	81
3.2.3.	Direct ρ -Nucleon Resonances	94
3.2.4.	Dispersive Approaches at High Energies	97
3.2.5.	Finite Temperature Effects in Baryonic Matter	99
4.	Analysis of Dilepton Spectra: Constraints, Predictions, and Implications	101
4.1.	Constraints on Hadronic Dilepton Production	104
4.1.1.	Decay Widths and Hadronic Scattering Data	105
4.1.2.	Photoabsorption Spectra	109
4.2.	Dilepton Rates in Hot and Dense Matter	117
4.2.1.	Comparison of Hadronic Approaches	117
4.2.2.	Beyond Conventional Scenarios for Dilepton Enhancement	125
4.2.3.	Quark-Hadron Duality	131
4.3.	Photon Production Rates	137
4.4.	Space-Time Evolution of Heavy-Ion Collisions	138
4.4.1.	Hydrodynamical Approach	139
4.4.2.	Transport Simulations	142
4.4.3.	Thermal Fireball Expansion	146
4.5.	Dilepton Spectra at BEVALAC/SIS Energies	149
4.6.	Dilepton Spectra at CERN-SPS Energies	155
4.6.1.	Decays after Freezeout: Hadronic Cocktail versus Experiment	156
4.6.2.	Free $\pi^+\pi^-$ Annihilation in the Hadronic Fireball	160
4.6.3.	Medium Effects I: Invariant Mass Spectra	163
4.6.4.	Medium Effects II: Transverse Momentum Dependencies	172
4.6.5.	Time Dependence of In-Medium Signals	176
4.6.6.	Intermediate-Mass Spectra	179

Contents	xvii
4.7. Direct Photon Spectra	184
4.8. Theoretical Implications	187
5. Conclusions	193

Chapter 2

FUNDAMENTAL SYMMETRY VIOLATION IN NUCLEI

**H. Feshbach, M. S. Hussein, A. K. Kerman,
and O. K. Vorov**

1. Introduction	208
2. Summary of the Experimental Results from Triple Collaboration	210
3. Symmetry Violation within Reaction Theory	218
4. Parity Nonconservation (PNC) in the Compound Nucleus	222
5. The Sign Correlation Problem and the Role of $2p - 1h$ Doorway States	224
6. Optical Model Description of PNC	230
6.1. Optical Model Calculation of the Longitudinal Asymmetry	237
6.2. Optical Model Analysis of the TRIPLE Data	240
6.3. Optical Model Calculation of Spin Polarization and Rotation	245
7. Parity Violation in Exotic Nuclei	248
7.1. Proton and Neutron Weak Potential Strengths	249
7.2. Halo Structure Effects on the PNC Mixing	250
7.3. Halo Model and Evaluation of the PNC Mixing in the Ground State of ^{11}Be	252
8. Time Reversal Symmetry Breaking	260
9. Conclusions and Discussion	267
References	271

*Chapter 3***NUCLEON-NUCLEUS SCATTERING: A MICROSCOPIC
NONRELATIVISTIC APPROACH**

**K. Amos, P. J. Dortmans, H. V. von Geramb,
S. Karatagliidis, and J. Raynal**

1. Introduction	276
2. Formal Theory of the Nucleon–Nucleus Optical Potential	282
3. Momentum Space Optical Models	285
3.1. The Full-Folding t Matrix Approach	286
3.2. The Full Folding g Matrix Approach	290
3.3. Results of Calculations	294
4. Coordinate Space Optical Model	301
4.1. The Folding Model of the Optical Potential	302
4.2. The Helicity Formalisms	304
4.3. Multipole Expansion of the Effective Interaction	307
4.4. Particle-Hole Matrix Elements	317
4.5. The Distorted Waves	320
4.6. Amplitudes, Cross Sections and Observables	323
5. The Two-Nucleon t Matrices	328
5.1. The NN Interactions	328
5.2. The Free NN t Matrices	331
5.2.1. The Partial Wave t Matrices	333
5.3. Solution of the Lippmann-Schwinger Equation	335
5.3.1. Phase Shifts and Deuteron Properties	335
5.3.2. Off-Energy-Shell t Matrices	340
5.4. Quantum Inversion and the NN t Matrix	348
5.4.1. Case Studies	350
6. Nuclear Matter and NN g Matrices	353
6.1. Nuclear Matter g Matrices	354
6.2. g Matrices from Realistic Interactions	358
7. The Effective NN Interaction	366
7.1. Coordinate Space Representations	366
7.2. The Parameterisation Scheme	367

7.3.	Effective g Matrices in Coordinate Space	369
7.3.1.	Optimal Effective g Matrices	372
7.3.2.	Integral and Moments of the Effective Interaction	373
7.3.3.	Radial Variations of the Effective Interactions	377
8.	Nuclear Structure	380
8.1.	The Shell Model	381
8.2.	Projected HF Theory and the PHM Model	382
8.3.	Matrix Elements of Nuclear Structure Observables	386
8.4.	Spectra and Properties from the Models	387
8.4.1.	Helium Isotopes	388
8.4.2.	Lithium Isotopes	391
8.4.3.	The Spectrum of ^{12}C	398
8.4.4.	The Spectrum of ^{14}N	399
8.4.5.	The Spectrum of ^{16}O	401
9.	Electron Scattering: Operators and Observables	403
9.1.	Introduction	403
9.2.	Form Factors	403
9.2.1.	Alternative Forms of the Operator \hat{T}_{JM}^{el}	405
9.2.2.	One-Body Operators	407
9.3.	Results	411
9.3.1.	$E2$ Form Factors with sd -Shell Nuclei	411
9.3.2.	Few-Body Systems: $^{3,4}\text{He}$	416
9.3.3.	^6Li and ^7Li	419
9.3.4.	^{12}C	428
10.	Applications of the Coordinate Space Optical Model	437
10.1.	Energy and Mass Variations	438
10.1.1.	The Mass Variation with 65 and 200 MeV Protons	439
10.1.2.	Variation with Single Particle Wave Functions	443
10.1.3.	Results for 40 MeV Proton Scattering	445
10.2.	Elastic Scattering from $^{3,4}\text{He}$, $^{6,7}\text{Li}$, and ^{12}C	449
10.2.1.	Proton Scattering from $^{3,4}\text{He}$	449
10.2.2.	Proton Scattering from $^{6,7}\text{Li}$	453
10.2.3.	Scattering from ^{12}C	455
10.3.	Scattering of $^{6,8}\text{He}$ and $^{9,11}\text{Li}$ from Hydrogen	460

11.	Equivalent Local Potentials	465
11.1.	The Basic Problem and Solutions	466
11.2.	Local Equivalent Partial Wave Potentials	472
11.3.	Inverse Scattering	483
11.3.1.	The WKB Method	486
11.3.2.	Lipperheide-Fiedeldey Methods	491
11.3.3.	Newton-Sabatier Methods	495
12.	Inelastic Scattering	500
12.1.	Scattering from ^{12}C	501
12.1.1.	Scattering to Low Excitation States in ^{12}C	501
12.1.2.	Variations with Energy	508
12.1.3.	Isovector Excitations with (p, p') and (p, n) from ^{12}C	510
12.1.4.	Inelastic Scattering and Specification of States in ^{12}C	513
12.2.	Inelastic Scattering and $^{6,7}\text{Li}$	518
12.3.	Scattering of Radioactive Beams from Hydrogen	523
12.3.1.	The Scattering of ^{11}Li	523
12.3.2.	The Scattering of ^6He	526
Appendix.	Projection Operators and HF State Normalizations and Overlaps	527
A.1.	The HF State Normalization	528
A.2.	The A-1 Nucleon State Overlaps	529
References	529
<i>Index</i>	537

Chapter 1

CHIRAL SYMMETRY RESTORATION AND DILEPTONS IN RELATIVISTIC HEAVY-ION COLLISIONS

R. Rapp

*Department of Physics and Astronomy
State University of New York
Stony Brook, NY 11794-3800*

J. Wambach

*Institut für Kernphysik
Technische Universität Darmstadt
Schloßgartenstr. 9
D-64289 Darmstadt, Germany*

1. Introduction	1
2. “Strong QCD” and Vector Mesons	11
3. Modeling Vector Mesons in the Medium	49
4. Analysis of Dilepton Spectra: Constraints, Predictions, and Implications	101
5. Conclusions	193
References	197

1. INTRODUCTION

In recent years substantial experimental and theoretical efforts have been undertaken to investigate the versatile physics issues involved

in (ultra-) relativistic heavy-ion collisions, i.e. collisions of atomic nuclei in which the center-of-mass (*cms*) energy per nucleon is (much) larger than the nucleon rest mass [1, 2]. The principal goal of this initiative is to explore the phase structure of the underlying theory of strong interactions—Quantum Chromodynamics (QCD)—by creating in the laboratory new states of matter. Through varying experimental conditions such as the collision energy or impact parameter, one aims at covering as broad a regime as possible in temperature and baryon density of the excited nuclear system. In nature such new states are believed to have existed and still may be encountered on large scales in at least two astrophysical contexts: in the evolution of the early universe where a few tens of microseconds after the “big bang” a transient stage of strongly interacting matter prevailed at temperatures a few times 10^{12}K ($\sim 200\text{ MeV}$) with very small net baryon excess; in the interior of neutron stars where mass densities are likely to exceed 10^{15} g/cm^3 —about four times the central density of nuclei—while surface temperatures are as low as 10^5K or less. Experiments have been performed until recently at the Alternating Gradient Synchrotron (AGS) in Brookhaven (BNL) with *cms* energies around $\sqrt{s} \sim 5\text{ AGeV}$ and are currently underway at the CERN Super-proton-Synchrotron (SpS) at $\sqrt{s} \sim 20\text{ AGeV}$. In the near future the Relativistic Heavy-Ion Collider (RHIC) at BNL will start data-taking at $\sqrt{s} \sim 200\text{ AGeV}$, and eventually heavy ions will also be injected into the CERN Large Hadron Collider (LHC) reaching $\sqrt{s} \sim 10\text{ ATeV}$.

As nuclear matter is heated and compressed hadrons occupy more and more of the available space. Eventually they start to overlap and the initially confined quarks and gluons begin to “percolate” between the hadrons thus being “liberated”. This simple picture has originally provided the basis for models of the quark-hadron transition and has been essentially confirmed by ab-initio numerical QCD lattice calculations at finite temperature. The latter demonstrate that strongly interacting matter exhibits a rapid change in energy- and entropy-density (possibly constituting a true phase transition) within a narrow temperature interval indicating a change-over from confined hadrons to a “quark-gluon plasma” (QGP). At the same time the quarks—most notably up (*u*) and down (*d*) quarks, carrying an effective mass of a few hundred MeV in the confined phase—lose their “constituent mass” leading to the restoration of “chiral symmetry”, an approximate symmetry of QCD in the sector of “light” quarks. Once massless, left- and right-handed quarks decouple leading to a degeneracy in (hadronic) states of opposite parity. The expected phase diagram of hadronic matter is shown in Fig. 1.1. The

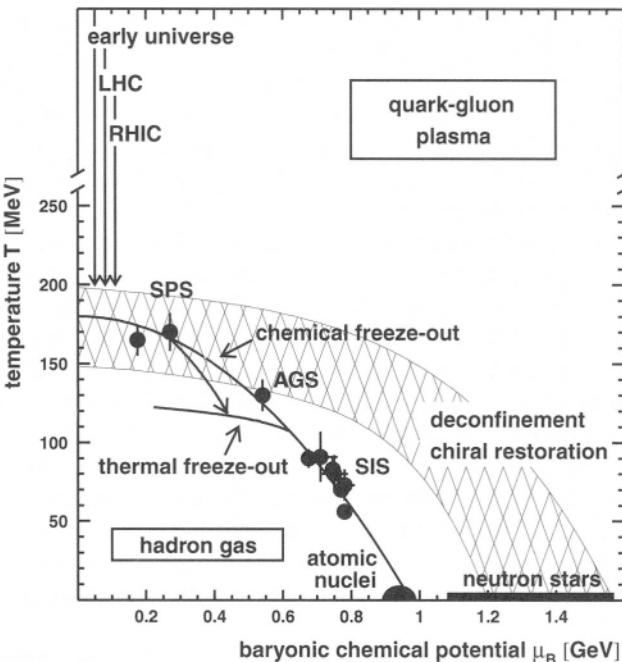


Fig. 1.1. QCD phase diagram [3, 4] in the temperature and baryon chemical potential plane with freezeout points extracted from hydrochemical analyses at SIS, AGS and SpS energies.

“confined phase” consists of an interacting gas of hadrons (a “resonance gas”) while the “deconfined phase” is comprised of a (non-ideal) gas of quarks and gluons. The hatched “phase boundary” reflects the present uncertainties from lattice QCD extrapolated to finite baryochemical potential, μ_B . Also shown are locations realized in heavy-ion systems for various laboratory bombarding energies at the point where *inelastic* collisions between the particles in the fireball cease—the so-called “chemical freezeout”—characterizing the stage where the fireball acquires its final particle composition. The “thermal freezeout” refers to the stage where *elastic* collisions are no longer supported as the mean-free paths of the hadrons exceed the size of the fireball. Their momentum distributions do no longer change and they stream freely to the detector. Based on the assumption of thermodynamic equilibrium the chemical freezeout is determined from a hydrochemical analysis of the measured abundances of particle species [5, 3] with the conclusion

that at the highest presently available energies the produced systems must be close to the phase boundary. However, subsequent rescattering still maintains local thermal equilibrium for about 10fm/c, cooling the system to appreciably lower temperatures until the thermal freezeout is reached. The latter is reconstructed from a combination of (comoving) thermal distributions and a collective transverse and longitudinal expansion of the fireball.

If the quark-hadron transition can indeed be induced in heavy-ion collisions the challenge is how to detect it in the laboratory and isolate observable signals (see, e.g., Refs. [6, 7] for recent reviews). Because of their negligible final-state interactions with the hadronic environment, dileptons (correlated lepton pairs, $l^+l^- = e^+e^-$ or $\mu^+\mu^-$) as well as photons are considered ideal probes for the high-density/-temperature regions formed in the early stages of the collision [8, 9]. However, as they are emitted continuously, they sense in fact the entire space-time history of the reaction [10, 11]. Because of an additional variable, the invariant pair mass M_{ll} , dileptons have the experimental advantage of a superior signal to background ratio as compared to real photons [12]. Consequently, dileptons provide the most promising electromagnetic data up to date.

The finally measured dilepton spectra can be chronologically divided into several phases. Before the nuclear surfaces actually touch dileptons are produced through coherent Bremsstrahlung [13] in the decelerating Coulomb field of the approaching nuclei. Their contribution seems to be negligible as compared to subsequent sources [14]. Within the first 1fm/c or so of the nuclear overlap, the excited hadronic system is far from thermal equilibrium and the corresponding “pre-equilibrium” dilepton radiation mostly consists of hard processes such as Drell-Yan annihilation leaving its trace mainly at large invariant masses $M_{ll} \gtrsim 3$ GeV. A rapid thermalization [15] is expected to subsequently establish the QGP phase, sometimes also called the “partonic phase”, where dilepton production proceeds predominantly via (perturbative) quark-antiquark annihilation. It should reflect a thermal spectrum even though, towards smaller masses, radiative corrections from gluons as well as thermal loop effects are likely to become important. At later stages when, upon expansion and cooling, the QGP has converted into a hot hadron gas, dileptons are preferentially radiated from pion and kaon annihilation processes as well as other collisions between various hadrons. The two-body annihilation processes are dynamically enhanced through the formation of (light) vector meson resonances, such as the ρ ,

ω and ϕ mesons, which directly couple to $t\bar{t}$ pairs. Thus the invariant mass of the lepton pair directly reflects the mass distribution of the vector meson at the moment of decay! This explains the distinguished role that vector mesons—in conjunction with their in-medium modifications—play for dilepton measurements in heavy-ion reactions. The situation is somewhat different for the heavy quarkonium states such as the J/Ψ or Υ : in contrast to the light vector mesons, their lifetime is substantially longer than the typical one of the hadronic fireball such that they will predominantly decay after freezeout. Therefore, as detailed further below, the importance of the corresponding dilepton signal largely resides in its magnitude and not so much in the spectral shape. Finally, when the freezeout stage is reached, the dominant sources are hadronic resonance as well as Dalitz decays, mostly from π^0 , η and ω mesons, all feeding into the low-mass region, $M_{ll} \lesssim 1 \text{ GeV}$.

A schematic view of characteristic dilepton sources in ultrarelativistic heavy-ion collisions (URHIC's) is given in Fig. 1.2. With respect to invariant mass one can roughly distinguish three regions. Let us try to draw some qualitative connections with the basic properties of strong interactions that might be addressed in the respective regimes. The

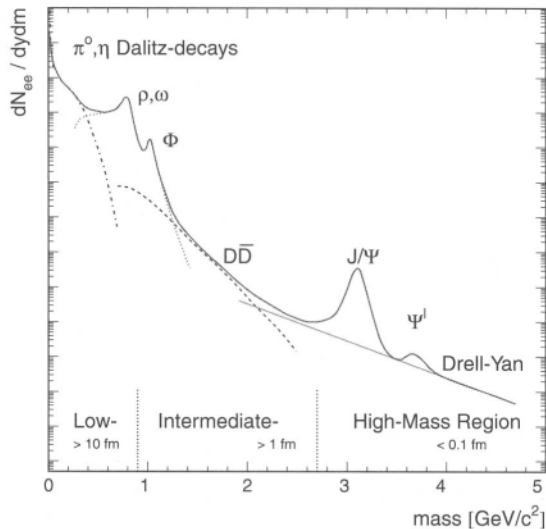


Fig. 1.2. Expected sources for dilepton production as a function of invariant mass in ultrarelativistic heavy-ion collisions [16].

low-mass region below and around the ϕ meson is governed by the light-quark sector of u , d and s quarks. In fact, it is known that in the limit of vanishing (current) quark masses the order parameter of the QCD finite-temperature phase transition is associated with chiral symmetry restoration (e.g., the quark condensate) and is most likely of first order for three flavors. Thus, in the low-mass region signals of chiral restoration should turn up, transmitted in terms of medium modifications of light hadrons. On the other hand, in the limit of very large current quark masses, the order parameter of the QCD finite- T transition is associated with deconfinement (the so-called “Wilson line”), again realized in a strong first-order transition. Thus, for heavy quarks one might hope to become sensitive to features of deconfinement. This seems indeed to be the case: the confining potential within heavy quarkonium states (J/Ψ , Υ) will be Debye-screened due to freely moving color charges in a QGP leading to a dissolution of the bound states [17]. As a consequence the final abundance of, e.g., J/Ψ mesons—and thus their contribution to the dilepton spectrum—is suppressed, signaling (the onset of) the deconfinement transition. This very important topic will not be covered in the present review, see Refs. [18] for the recent exciting developments. Finally, the intermediate-mass region (IMR) might allow insights into aspects of quark-hadron “duality”. As is evident from the saturation of the vacuum annihilation cross section $e^+e^- \rightarrow \text{hadrons}$ by perturbative QCD above ~ 1.5 GeV, the essentially structureless thermal “continuum” up to the J/Ψ can be equally well described by either hadronic or quark-gluon degrees of freedom. However, as a QGP can only be formed at higher temperatures than a hadronic gas, the intermediate mass region might be suitable to observe a thermal signal from plasma radiation [9, 19] in terms of absolute yield. The most severe “background” in this regime is arising from decays of “open-charm” mesons, i.e., pairwise produced $D\bar{D}$ mesons followed by individual semileptonic decays. Although an enhanced charm production is interesting in itself—probably related to the very early collision stages—it may easily mask a thermal plasma signal. To a somewhat lesser extent, this also holds true for the lower-mass tail of Drell-Yan production.

Until today, the measurement of dilepton spectra in URHIC’s has mainly been carried out at the CERN-SPS by three collaborations: CERES/NA45 is dedicated to dielectron measurements in the low-mass region [20,21,22,23], HELIOS-3 [24] has measured dimuon spectra from threshold up to the J/Ψ region, and NA38/NA50 [25,26,27,28] measures dimuon spectra from threshold to very high masses of about 8 GeV, with emphasis on J/Ψ suppression (for a summary of low- and intermediate-

mass dilepton measurements see Refs. [29, 30, 31]). In the near future, with RHIC coming on line pushing the collision energies to new frontiers, high resolution dilepton spectra will be measured by the PHENIX collaboration [32]. At much lower bombarding energies dilepton data have also been taken by the DLS collaboration at the BEVALAC [33, 34] and will soon become available from the high-precision detector HADES at SIS (GSI) [35]. Here only the low-mass region up to the kinematical limit of around 1 GeV is accessible and the focus is on the role of high baryon density. Unfortunately, no dilepton measurements have been performed at the AGS where presumably the highest baryon densities were attained. However, the already commissioned low-energy run at the CERN-SPS at a projectile energy of 40 AGeV is believed to close this gap penetrating into the regime of extreme baryon density.

The objective of the present article is to review the theoretical efforts in understanding the experimental results in the low-mass region which—as discussed above—is intimately connected to the question of chiral symmetry restoration. A great deal of theoretical activity has been triggered by recent observations from the CERES [20, 23] and the HELIOS-3 [24] collaborations that central nucleus-nucleus (A - A) collisions exhibit a strong enhancement of low-mass dilepton production as compared to proton-nucleus reactions¹. Whereas the p - A data can be well reproduced by final-state hadron decays with known abundances—the so-called hadronic “cocktail”—(Fig. 1.3), the latter strongly underestimate the A - A spectra. As several hundreds of pions are produced in A - A collisions, the observed increase of dilepton pairs has been attributed to $\pi^+\pi^- \rightarrow l^+l^-$ annihilation during the interacting phase of the hadronic fireball. Using vacuum meson properties many theoretical groups have included this process within different models for the space-time evolution of A - A reactions. Their results are in reasonable agreement with each other, but in disagreement with the data: the experimental spectra in the mass region from 0.3–0.6 GeV are significantly underestimated as seen from Fig. 1.4 (see also Ref. [29]). This has led to the suggestion of various medium effects that might be responsible for the observed enhancement. Among these, the “dropping” vector meson mass scenario [37, 45, 46], as will be detailed below, provides an interesting possibility since it conjectures a direct link between hadron

¹One should note that similar effects have *not* been found by NA38/50 [28], which, however, is most likely related to a rather large M_T -cut applied in their analysis. On the other hand, the DLS-data [34], taken at much lower incident energies, *do* show a very strong enhancement.

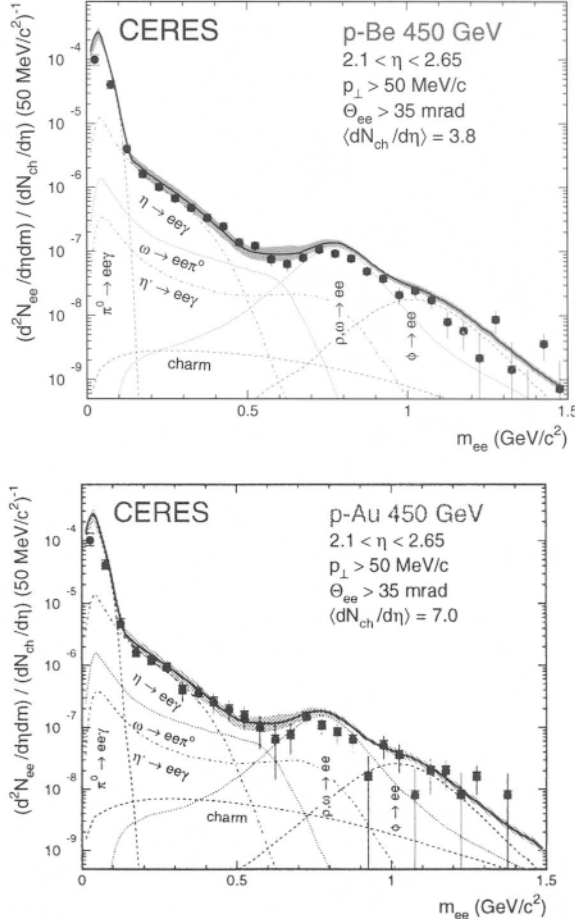


Fig. 1.3. Invariant mass spectra of dileptons as measured by the CERES collaboration [20] in 450 GeV proton-induced collisions on Beryllium (left panel) and Gold targets (right panel). The data are compared to expectations from various hadron decay channels (labeled explicitly) based on measured hadron multiplicities. The bands indicate the systematic uncertainty in the cocktail.

masses and the quark condensate and thus to the restoration of chiral symmetry towards the phase transition. When incorporated within a transport-theoretical treatment of the collision dynamics it is found to provide a unified description of both the CERES and HELIOS-3 data. Based on an interacting hadron gas many-body approaches also seem to be able to describe the observed phenomena [47, 48, 49, 50]. Here the

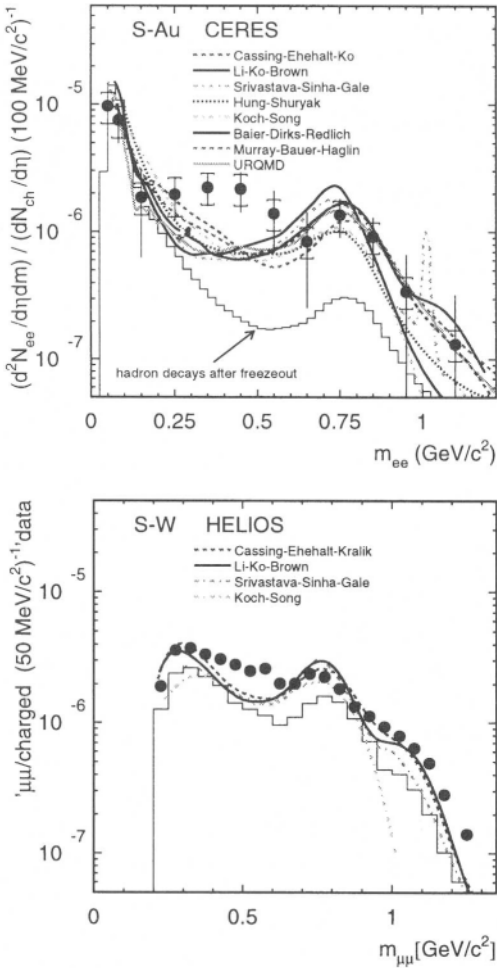


Fig. 14. Dilepton invariant mass spectra as measured in central collisions of 200 AGeV sulfur nuclei with Au targets (left panel: e^+e^- spectra from CERES/NA45 [20]) and W targets (right panel: $\mu^+\mu^-$ spectra from HELIOS-3 [24], no systematic errors included) as compared to a compilation [22] of theoretical calculations using free meson properties performed by Koch/Song [36], Li *et al.* [37], Cassing *et al.* [38, 39], Srivastava *et al.* [40], Baier *et al.* [41], the Frankfurt group [42], Hung/Shuryak [43] as well as Murray *et al.* [44]. The histograms indicate the hadron “cocktail” of final state decays which gives a good description of the $p\text{-}A$ data as shown in Fig. 1.3.

restoration of chiral symmetry manifests itself in more subtle ways which will be one of the key issues in our review.

More explicitly, the article is organized as follows: In Chapter 2 we will first recall some basic properties of strong interactions in the light-quark sector, with emphasis on the underlying symmetries of the QCD Lagrangian and their consequences in the nonperturbative regime, such as the emergence of quark and gluon condensates and the non-degeneracy of chiral partners in the hadronic spectrum. Special attention is paid to the vector and axialvector mesons as the former directly couple to dileptons. We then present model-independent methods to evaluate medium modifications of their spectral properties. Being based on virial expansions the results are in general restricted to low density and low temperature.

In Chapter 3 we move on to more specific model calculations that have been performed to assess medium modifications of vector and axialvector mesons. The presentation here concentrates on hadronic Lagrangians which can be classified into two categories, namely purely mesonic ones addressing temperature effects and those including the impact of finite baryon densities.

Chapter 4 starts out by discussing how hadronic models can be (and have been) subjected to empirical constraints that do *not* involve dilepton data in URHIC's. The philosophy here is to essentially fix the underlying model parameters to enable reliable predictions for thermal dilepton rates in hot and dense matter. In addition we will also discuss rate calculations within “non-standard” (or non-hadronic) scenarios for highly excited strong-interaction matter that cannot be reliably founded on empirical information, such as Disoriented Chiral Condensates (DCC's) or thermal quark-antiquark annihilation. The main part of Chapter 4 is then devoted to a confrontation of the various model results within a detailed analysis of recent dilepton data taken in heavy-ion experiments at the BEVALAC and CERN-SPS. An additional crucial ingredient needed to do so is the description of the space-time collision dynamics, which thermal rates have to be convoluted over. We will briefly discuss three approaches, i.e., relativistic hydrodynamics, transport simulations and more simplistic fireball expansions. Chapter 4 will end with a critical reassessment of the different mechanisms that have been invoked and outline possible theoretical implications for the nature of chiral symmetry restoration as indicative from the present status of the observed spectra.

Chapter 5 tries to summarize the major theoretical achievements in the field over the past five years or so. Based on these we will attempt

to draw conclusions on our current understanding of the QCD phase transition in hot/dense matter as evidenced from the interplay of vigorous experimental and theoretical efforts in low-mass dilepton production.

2. "STRONG QCD" AND VECTOR MESONS

In the Standard Model (SM) of particle physics strong interactions are described by Quantum Chromodynamics (QCD), a local $SU(3)$ gauge theory with quarks and gluons as elementary degrees of freedom [51]. The dynamics is governed by the QCD Lagrangian

$$\mathcal{L}_{\text{QCD}} = \bar{\psi}(i\gamma^\mu D_\mu - \mathcal{M}^o)\psi - \frac{1}{4}G_{\mu\nu}^a G_a^{\mu\nu} \quad (2.1)$$

with the non-abelian gluonic field-strength tensor given as

$$G_{\mu\nu}^a = \partial_\mu A_\nu^a - \partial_\nu A_\mu^a + igf^{abc} A_\mu^b A_\nu^c, \quad (2.2)$$

where A_μ^a represents the spin-1 gauge field with color index a ($a = 1, 8$). The gauge covariant derivative

$$D_\mu = \partial_\mu - ig(\lambda_a/2)A_\mu^a \quad (2.3)$$

induces a coupling between the spin-1/2, colored matter fields ψ of N_f flavors and the gauge fields A_μ^a (with λ_a denoting the usual $SU(3)$ Gell-Mann matrices).

In Eq. (2.1) \mathcal{M}^o represents the diagonal matrix of current quark masses,

$$\mathcal{M}^o = \begin{pmatrix} m_u & & & \\ & m_d & & \\ & & m_s & \\ & & & \ddots \end{pmatrix}, \quad (2.4)$$

which are parameters of the SM. Given their approximate values m_u , $m_d, m_s \approx 4, 7, 150$ MeV and $m_c, m_b, m_t \approx 1.5, 4.5, 175$ GeV there is an obvious separation into sectors of “light” and “heavy” quarks. For the discussion in the present article only the light-quark sector will be relevant.

To fully specify QCD we need to take account of the fact that—due to quantum-loop effects—the “fine-structure constant” $\alpha_s \equiv g^2/4\pi$

depends on the space-time distance or, equivalently, the four-momentum transfer Q of a given strong process,

$$\alpha_s(Q) = \frac{\alpha_s(\Lambda)}{1 + \alpha_s(\Lambda) \frac{33 - 2N_f}{12\pi} \ln\left(\frac{Q^2}{\Lambda^2}\right)}, \quad (2.5)$$

where Λ is a scale at which the coupling constant is to be fixed by experiment, e.g., $\alpha_s(M_Z) = 0.118$ at the Z boson mass $M_Z = 91$ GeV (see Fig. 2.1). As Q increases α_s decreases logarithmically (“asymptotic freedom”) and perturbation theory can be applied. In this regime QCD is well tested. At momentum scales of $Q \approx 1$ GeV—a typical mass scale for “light” hadrons—standard perturbation theory, however, breaks down due to a rapid increase of α_s . This is the realm of “strong QCD” where not only effective couplings but also the relevant degrees of freedom change with scale. It is this phenomenon that poses the most challenging intellectual problem in strong interaction theory and is subject to intense study via ab-initio lattice calculations and model building. At large distance scales the QCD degrees of freedom become encoded in colorless (“white”) light mesons, low-mass baryons and glueballs rather than quarks and gluons. In dealing with their mutual interactions the underlying symmetries and anomalies of QCD are of utmost importance.

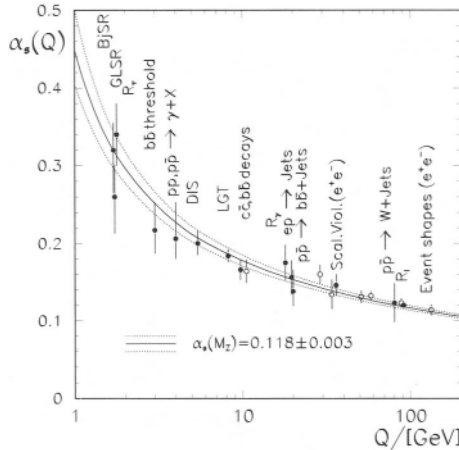


Fig. 2.1. The “running” of the strong coupling constant $\alpha_s(Q)$ from various measurements compared to theory [52].

2.1. Symmetries and Anomalies of QCD

The structure of the lowest-mass hadrons—involving the light-quark sector comprised of u, d, s quarks—is largely determined by chiral symmetry [53] and its dynamical breaking in the physical vacuum with confinement presumably playing a much lesser role. This is evidenced from the dominant role of instantons—believed to be responsible for chiral symmetry breaking and other nonperturbative phenomena—in hadronic correlators [54]. Recent lattice QCD calculations with cooling algorithms corroborate such a picture [55].

Apart from invariance under local $SU(3)_{\text{color}}$ transformations and a global $U(1)$ symmetry, i.e., multiplication of the matter fields ψ by a phase—entailing baryon number conservation—the QCD Lagrangian (2.1) has additional symmetries for vanishing quark masses. In this limit—well justified in the up- and down-quark sector and to a somewhat lesser extent in the strange-quark sector—the theory is invariant under global vector and axialvector transformations in $SU(3)$ -flavor space

$$\psi \rightarrow e^{-i\alpha_V^i \frac{\lambda^i}{2}} \psi, \quad \psi \rightarrow e^{-i\alpha_A^i \frac{\lambda^i}{2} \gamma_5} \psi \quad (2.6)$$

with conserved vector and axialvector Noether currents

$$j_{V,i}^\mu = \bar{\psi} \gamma^\mu \frac{\lambda_i}{2} \psi, \quad j_{A,i}^\mu = \bar{\psi} \gamma^\mu \gamma_5 \frac{\lambda_i}{2} \psi. \quad (2.7)$$

As a consequence, the corresponding charges

$$Q_i^V = \int d^3x \psi^\dagger \frac{\lambda_i}{2} \psi, \quad Q_i^A = \int d^3x \psi^\dagger \frac{\lambda_i}{2} \gamma_5 \psi \quad (2.8)$$

commute with the QCD Hamiltonian, $[Q_i^{V,A}, H_{\text{QCD}}] = 0$.

When decomposing the quark fields into left and right chirality components, $\psi_{L,R} = \frac{1}{2}(1 \mp \gamma_5)\psi$, the Lagrangian (2.1) takes the form

$$\mathcal{L}_{\text{QCD}} = \bar{\psi}_L i \gamma^\mu D_\mu \psi_L + \bar{\psi}_R i \gamma^\mu D_\mu \psi_R - \frac{1}{4} G_{\mu\nu}^a G_a^{\mu\nu} - (\bar{\psi}_L \mathcal{M}^o \psi_R + \bar{\psi}_R \mathcal{M}^o \psi_L) \quad (2.9)$$

and the transformations (2.6) translate to

$$\psi_L \rightarrow e^{-i\alpha_L^i \frac{\lambda^i}{2}} \psi_L, \quad \psi_R \rightarrow \psi_R \quad (2.10)$$

$$\psi_R \rightarrow e^{-i\alpha_R^i \frac{\lambda^i}{2}} \psi_R, \quad \psi_L \rightarrow \psi_L, \quad (2.11)$$

which—in the limit of vanishing quark masses—constitutes a global $SU(3)_L \times SU(3)_R$ chiral symmetry in flavor space. Left- and right-handed quarks are not mixed dynamically and thus preserve their “handedness” in strong interactions. The associated conserved charges

$$Q_i^L = \int d^3x \psi_L^\dagger \frac{\lambda_i}{2} \psi_L = \frac{1}{2}(Q_i^V - Q_i^A) \quad (2.12)$$

$$Q_i^R = \int d^3x \psi_R^\dagger \frac{\lambda_i}{2} \psi_R = \frac{1}{2}(Q_i^V + Q_i^A) \quad (2.13)$$

again commute with the QCD Hamiltonian.

For $m_q = 0$, the Lagrangian of QCD contains yet another symmetry. Under global $U_A(1)$ (axial) transformations

$$\psi \rightarrow e^{-i\alpha_5} \psi \quad (2.14)$$

(2.1) is also invariant implying a conserved (singlet) Noether current of the form

$$j_{A,0}^\mu = \bar{\psi} \gamma^\mu \gamma_5 \psi. \quad (2.15)$$

However, in the full quantum theory the divergence of $j_{A,0}^\mu$ has an anomaly

$$\partial_\mu j_{A,0}^\mu = \frac{3}{8} \alpha_s G_{\mu\nu}^a \tilde{G}_a^{\mu\nu}, \quad \tilde{G}_{\mu\nu}^a = \epsilon^{\mu\nu\alpha\beta} G_{\alpha\beta}^a, \quad (2.16)$$

—the $U(1)_A$ axial anomaly—such that finally QCD is symmetric only under the group

$$SU(3)_L \times SU(3)_R \times U(1)_V. \quad (2.17)$$

This implies the conservation of the baryonic as well as the vector and axialvector currents.

Moreover, at the classical level, massless QCD is *scale invariant*. To see this consider a scale transformation in Minkowski space,

$$x^\mu \rightarrow x'^\mu = \lambda x^\mu. \quad (2.18)$$

Quantum fields scale as

$$\phi(x) \rightarrow \phi'(x) = \lambda^d \phi(\lambda x), \quad (2.19)$$

where $d = 3/2$ for fermions and $d = 1$ for vector bosons. A field theory is called scale invariant if the action S remains invariant under scale transformations (2.18):

$$S' = \int d^4x \mathcal{L}'(x) = \int d^4x \lambda^4 \mathcal{L}(\lambda x) = S, \quad (2.20)$$

i.e., \mathcal{L} scales as λ^4 . Associated with scale invariance is another conserved current—the dilation (or scale) current—,

$$j_D^\mu = x_\nu T^{\mu\nu}, \quad \partial_\mu j_D^\mu = T_\mu^\mu = 0, \quad (2.21)$$

where $T^{\mu\nu}$ denotes the energy-momentum tensor of the theory. Considering classical quark and gluon fields and explicitly constructing $T^{\mu\nu}$ it is easily verified that the dilation current of QCD is conserved.

As in the case of the axial anomaly, scale invariance is broken in the full quantum theory. Renormalization requires the introduction of a scale Λ resulting in a running coupling constant, Eq. (2.5). As a consequence the dilation current is no longer conserved. Including finite quark masses the full expression becomes

$$\partial_\mu j_D^\mu = \frac{\beta(\alpha_s)}{4\alpha_s} G_{\mu\nu}^a G_a^{\mu\nu} + (1+\gamma)\bar{\psi}\mathcal{M}^\circ\psi, \quad (2.22)$$

where $\beta(\alpha_s) = \Lambda d\alpha_s(\Lambda)/d\Lambda$ is the Gell-Mann-Low β -function of QCD and $\gamma = d(\ln m_q(\Lambda))/d(\ln \Lambda)$ the anomalous dimension. Expanding the β -function in powers of α_s ,

$$\beta(\alpha_s) = -(33 - 2N_f) \frac{\alpha_s^2}{6\pi} + O(\alpha_s^3), \quad (2.23)$$

and keeping only the lowest term results in the operator identity [56]

$$T_\mu^\mu = -\frac{9}{8} G^2 + \bar{\psi}\mathcal{M}^\circ\psi, \quad (2.24)$$

where $G^2 \equiv \frac{\alpha_s}{\pi} G_{\mu\nu}^a G_a^{\mu\nu}$ and the (small) anomalous dimension γ has been neglected.

2.2. Vacuum Condensates

In the physical vacuum quarks and gluons condense giving rise to nonvanishing vacuum expectation values $\langle\bar{\psi}\psi\rangle$ [57, 58] and $\langle G^2 \rangle$ [59].

The physical mechanism is believed to be provided by instantons—semiclassical configurations of the gluon fields in 4-dimensional euclidean space [54]. The gluon condensate may be viewed as a strength parameter associated with nonperturbative scale breaking effects. A finite quark condensate implies that chiral symmetry is spontaneously broken. In mathematical terms the symmetry group (2.17) is broken down to

$$SU(3)_V \times U(1)_V. \quad (2.25)$$

The baryon and vector current remain conserved but the QCD vacuum is no longer symmetric under axialvector transformations (2.6). While the axial charges Q_k^A still commute with the QCD Hamiltonian the axial charge of the vacuum is nonvanishing: $\langle Q_k^A | 0 \rangle \neq 0$. The situation is analogous to a ferromagnet which consists of separate domains of aligned spins. For a given domain rotational symmetry is partially broken in the ground state, although the Hamiltonian is rotationally invariant.

For the light meson spectrum spontaneous chiral symmetry breaking manifests itself in two ways:

- (i) the appearance of eight (nearly) massless Goldstone bosons (pions, kaons, eta) which interact weakly at low energies. The ferromagnetic analogy of Goldstone particles is the occurrence of a spin wave. For large wavelengths the spin configuration begins to resemble a uniform rotation of all the spins. In the limit of infinite wavelength this does not cost any energy, thus yielding a massless Goldstone mode.
- (ii) the absence of parity doublets, i.e., the splitting of scalar and pseudoscalar, as well as vector and axialvector mesons. For massless fermions helicity eigenstates are also chirality eigenstates. Were chiral symmetry unbroken one would expect degenerate hadronic isospin multiplets of opposite parity which is clearly not observed in nature as apparent from Fig. 2.2.

As a further consequence of chiral symmetry breaking the axial-current matrix element between the vacuum and a Goldstone boson is nonvanishing. For pions one has for instance:

$$\langle 0 | j_{A,k}^\mu(x) | \pi_j(p) \rangle = -i\delta_{jk}f_\pi p^\mu e^{-ipx}, \quad (2.26)$$

and the pion decay constant $f_\pi = 93 \text{ MeV}$ serves as an order parameter which measures the strength of the symmetry breaking. A second order parameter is the quark condensate

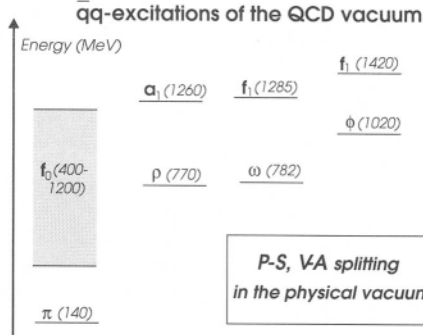


Fig. 2.2. Experimentally observed spectrum of low-mass mesons.

$$\langle \bar{\psi} \psi \rangle \equiv \langle 0 | \bar{\psi}_L \psi_R + \bar{\psi}_R \psi_L | 0 \rangle, \quad (2.27)$$

which exhibits the explicit mixing of left- and right-handed quarks in the QCD vacuum. The order parameters f_π and $\langle \bar{\psi} \psi \rangle$ are related. To see this one makes use of the operator identity

$$[Q_i^A, [Q_j^A, H_{\text{QCD}}]] = \delta_{ij} \int d^3x \bar{\psi}(x) \mathcal{M}^\circ \psi(x). \quad (2.28)$$

Taking the vacuum matrix element and inserting a complete set of excited states $|n\rangle$ one obtains the “energy-weighted sum rule” [60]

$$\sum_n 2E_n \langle n | Q_i^A | 0 \rangle^2 = -\langle m_u \bar{u} u + m_d \bar{d} d \rangle = -2\bar{m} \langle \bar{q} q \rangle \quad (2.29)$$

where \bar{m} denotes the average of m_u and m_d and $\langle \bar{q} q \rangle \equiv \langle \bar{u} u \rangle = \langle \bar{d} d \rangle$. Upon saturation of $|n\rangle$ by single-pion states the Gell-Mann-Oakes-Renner relation (GOR) [58]

$$m_\pi^2 f_\pi^2 = -2\bar{m} \langle \bar{q} q \rangle \quad (2.30)$$

is obtained. Taking $\bar{m} = 6 \text{ MeV}$ yields a value for the quark condensate, $\langle \bar{q} q \rangle = -(240 \text{ MeV})^3 = -1.8 \text{ fm}^{-3}$. Focusing on vector mesons a further order parameter can be specified as the difference between the vector and axialvector current correlators, $\langle j_{V,k}^\mu(x) j_{V,k}^\mu(0) \rangle - \langle j_{A,k}^\mu(x) j_{A,k}^\mu(0) \rangle$. It provides a direct link between chiral symmetry breaking and the spectral properties of vector and axialvector mesons and will be of most relevance in connection with dilepton production in heavy-ion experiments. Also this order parameter is related to f_π via “Weinberg sum rules” as will be discussed later.

For the medium modification of the quark condensate it will be important to consider matrix elements of the operator identity (2.28) for a given hadron h . This defines the hadronic sigma commutator, or “ σ -term”

$$\Sigma_h = \langle h | [Q_i^A, [Q_j^A, H_{\text{QCD}}]] | h \rangle = \langle h | \bar{\psi} \mathcal{M}^\circ \psi | h \rangle, \quad (2.31)$$

and the ratio Σ_h/\bar{m} has the physical interpretation of the scalar quark density inside the hadron h . By using the Feynman-Hellmann Theorem Σ_h can also be expressed in terms of the hadron mass as

$$\Sigma_h = m_q \frac{\partial m_h}{\partial m_q}. \quad (2.32)$$

From this relation and the GOR one immediately derives for the pion that $\Sigma_\pi = m_\pi/2 = 69 \text{ MeV}$, i.e., the scalar quark density inside the pion is $\Sigma_\pi/\bar{m} \approx 12$. This large value reflects the Goldstone nature of the pion in which quark-antiquark pairs are highly correlated. The sigma commutator for the nucleon can be inferred phenomenologically from low-energy pion-nucleon scattering [61] and has a value $\Sigma_N \approx 45 \pm 8 \text{ MeV}$. In models such as the “cloudy bag model” about 2/3 of this value originates from the virtual pion cloud around the nucleon [62, 63], again reflecting the collective nature of the pion.

2.3. In-Medium Condensates via Low-Density Expansions

It is to be expected that the quark and gluon condensates are modified at finite temperature, T , and quark chemical potential, μ_q . To discuss these modifications we first recall some basic thermodynamics. The equilibrium properties of a given system of 3-volume V in contact with a reservoir are specified by the grand canonical partition function

$$Z(V, T, \mu_q) = \text{Tr} \{ e^{-(\hat{H} - \mu_q \hat{N})/T} \}, \quad (2.33)$$

where \hat{H} is the Hamiltonian and \hat{N} the quark number operator. The thermal average of any operator \mathcal{O} is then given as

$$\langle \langle \mathcal{O} \rangle \rangle = Z^{-1} \sum_n \langle n | \mathcal{O} | n \rangle e^{-(E_n - \mu_q)/T}, \quad (2.34)$$

where the sum extends over a complete set of eigenstates of H and E_n are the corresponding eigenvalues. When applied to the QCD condensates one has

$$\langle\langle\bar{\psi}\psi\rangle\rangle = Z^{-1} \sum_n \langle n|\bar{\psi}\psi|n\rangle e^{-(E_n-\mu_q)/T} \quad (2.35)$$

and

$$\langle\langle G^2 \rangle\rangle = Z^{-1} \sum_n \langle n|G^2|n\rangle e^{-(E_n-\mu_q)/T}, \quad (2.36)$$

where $|n\rangle$ and E_n are now the exact QCD eigenstates and energies. The equation of state (EoS) can be directly obtained from the logarithm of Z . The free energy density is given as

$$\Omega = -\frac{T}{V} \ln Z, \quad (2.37)$$

while the energy density and pressure are derivatives of $\ln Z$ with respect to T and V ,

$$\varepsilon = \frac{T^2}{V} \left(\frac{\partial \ln Z}{\partial T} \right)_{V,N} + \mu_q \frac{N}{V} \quad (2.38)$$

$$p = T \left(\frac{\partial \ln Z}{\partial V} \right)_{T,N}. \quad (2.39)$$

In the thermodynamic limit ($V \rightarrow \infty; N/V = \text{const}$) the pressure is directly given by the free energy density as

$$p = -\Omega. \quad (2.40)$$

In fact, the state variables of the EoS determine directly the condensates. The quark condensate is obtained as the derivative of the free energy density (or pressure) with respect to the current quark mass,

$$\langle\langle\bar{\psi}\psi\rangle\rangle = \frac{\partial \Omega}{\partial m_q} = -\frac{\partial p}{\partial m_q}. \quad (2.41)$$

This is analogous to a spin system in an external magnetic field, where, in QCD, the role of the latter is played by the quark mass. To relate the gluon condensate to the thermodynamic variables one should notice that the thermal average of the trace of the energy-momentum tensor is given by

$$\langle\langle T_\mu^\mu \rangle\rangle = \varepsilon - 3p. \quad (2.42)$$

From Eq. (2.24) we then have

$$\langle\langle G^2 \rangle\rangle = -\frac{8}{9} \left[(\varepsilon - 3p) + m_q \frac{\partial p}{\partial m_q} \right]. \quad (2.43)$$

Model-independent results for the changes of the quark and gluon condensate can be obtained at low temperatures and small baryon densities. In both cases one deals with a low-density gas of confined hadrons. It is therefore appropriate to evaluate the thermal averages (2.35) and (2.36) in a hadronic basis including the vacuum as well as the lowest-mass mesons and baryons. As the temperature increases pions are thermally excited first since they represent the lightest hadrons. Considering a dilute, non-interacting pion gas, the leading correction to the vacuum condensate $\langle\bar{\psi}\psi\rangle$ is therefore given by the matrix element $\langle\pi|\bar{\psi}\psi|\pi\rangle$, and from (2.30) and (2.32) it is easily worked out that the condensate ratio becomes

$$\frac{\langle\langle\bar{\psi}\psi\rangle\rangle}{\langle\langle\bar{\psi}\psi\rangle\rangle} \simeq 1 - \frac{\sum_\pi \rho_\pi^s(T)}{f_\pi^2 m_\pi^2}, \quad (2.44)$$

where Σ_π denotes the pion σ -term and ρ_π^s the pion scalar density at given temperature. This expression is consistent with Eq. (2.41) when using the free energy density of a non-interacting Bose gas and the σ -term as the quark-mass derivative (2.32). A similar argument holds for finite baryon density and vanishing temperature. In this case nucleons give the dominant correction to $\langle\bar{\psi}\psi\rangle$ and

$$\frac{\langle\langle\bar{\psi}\psi\rangle\rangle}{\langle\langle\bar{\psi}\psi\rangle\rangle} \simeq 1 - \frac{\sum_N \rho_N^s(\mu_N)}{f_\pi^2 m_\pi^2}, \quad (2.45)$$

where Σ_N is the nucleon σ -term and ρ_N^s the nucleon scalar density at given μ_q (the nucleon chemical potential is related to the one of quarks by simply $\mu_N = 3\mu_q$). Since nucleons are heavy the scalar density is nearly equal to the number density, ρ_N . The underlying physical picture that emerges from the low-density expansion is very simple. Whenever a hadron is created in the vacuum, the condensate is changed locally since the $\bar{\psi}\psi$ -expectation value inside a hadron is different from that of the vacuum.

Let us now turn to the low-density expansion of the gluon condensate. At finite temperature the leading correction to the vacuum condensate should again be given by non-interacting pions. Since G^2 is a chiral singlet its one-pion matrix element vanishes and there is no contribution from the ideal pion gas. At finite baryon density the situation is different. First we note that the nucleon mass is determined by T_μ^μ as

$$\langle N|T_\mu^\mu|N\rangle = m_N \bar{\psi}_N \psi_N = \left[-\frac{9}{8} \langle N|G^2|N\rangle + \langle N|\bar{\psi} \mathcal{M}^o \psi|N\rangle \right], \quad (2.46)$$

where ψ_N represents the nucleon spinor and the operator identity (2.24) has been used. According to (2.32) the term proportional the quark mass, m_q , is nothing but the nucleon σ -term which is about 45 MeV. Thus the bulk of the nucleon mass is in fact generated by the gluon field. Putting things together the leading correction to the gluon condensate arises from finite baryon density such that

$$\langle\langle G^2 \rangle\rangle - \langle G^2 \rangle = -\frac{8}{9} m_N^{(0)} p_N^s(\mu_N), \quad (2.47)$$

where $m_N^{(0)}$ denotes the contribution of the nucleon mass from the G^2 matrix element.

One important conclusion which can be drawn from the above arguments is that, in spite of changing condensates, the properties of the involved hadrons by definition remain unchanged to lowest order.

At vanishing baryon density interactions in the pion gas can be included via chiral perturbation theory leading to a rigorous low-temperature expansion of the condensates [64, 65, 66]. The starting point are the thermodynamic relations (2.41) and (2.43). For simplicity we restrict ourselves to the chiral limit, $m_q \rightarrow 0$. In this case the leading contribution to p or ϵ is from the massless ideal Bose gas which is of order $O(T^4)$. The interactions among the Goldstone bosons only show up at order $O(T^8)$ such that

$$p = \frac{\pi^2}{90} (N_f^2 - 1) T^4 \left[1 + N_f^2 \left(\frac{T^2}{12 f_G^2} \right)^2 \ln \left(\frac{\Lambda_p}{T} \right) \right] + O(T^{10}), \quad (2.48)$$

where f_G denotes the weak-decay constant of the Goldstone boson in the chiral limit and Λ_p appearing in the chiral logarithm is the regularization scale. There is no T^6 -term since—in the chiral limit—the forward scattering amplitude for two Goldstone bosons vanishes. The quark-mass derivative occurring in (2.41) can be rewritten in terms of a derivative w.r.t. the mass of the Goldstone boson, m_G , and by means of the Gell-Mann-Oakes-Renner relation,

$$\frac{\langle\langle \bar{\psi} \psi \rangle\rangle}{\langle \bar{\psi} \psi \rangle} = 1 + \frac{1}{f_G^2} \frac{\partial p}{\partial m_G^2}. \quad (2.49)$$

Injecting the expression (2.48) for the pressure one arrives at

$$\begin{aligned} \frac{\langle\langle \bar{\psi} \psi \rangle\rangle}{\langle \bar{\psi} \psi \rangle} &= 1 - \frac{(N_f^2 - 1)}{N_f} \frac{T^2}{12 f_G^2} + \frac{(N_f^2 - 1)}{2 N_f} \left(\frac{T^2}{12 f_G^2} \right)^2 \\ &\quad - N_f (N_f^2 - 1) \left(\frac{T^2}{12 f_G^2} \right)^3 \ln \left(\frac{\Lambda_q}{T} \right) + O(T^8). \end{aligned} \quad (2.50)$$

While the T^2 - and T^4 -terms are model-independent, model dependence enters at order $O(T^6)$ through the regularization scale Λ_q which is related to Λ_p as [66]

$$\ln\left(\frac{\Lambda_q}{\Lambda_p}\right) = \frac{N_f^2 + 1}{6N_f^4} + 0.491. \quad (2.51)$$

The numerical value $\Lambda_q \approx 470 \text{ MeV}$ ($N_f = 2$) is determined by the isoscalar D -wave $\pi\pi$ scattering length. For two flavors the temperature scale is set by $\sqrt{8}f_\pi \approx 260 \text{ MeV}$. To derive a low-temperature expansion for the gluon condensate from (2.43) one uses the fact that

$$\langle\langle T_\mu^\mu \rangle\rangle = \epsilon - 3p = T^5 \frac{d}{dT} \left(\frac{p}{T^4} \right), \quad (2.52)$$

from which $\langle\langle G^2 \rangle\rangle$ can be expressed in terms of the Bose gas pressure alone. The use of Eq. (2.48) leads to

$$\langle\langle G^2 \rangle\rangle - \langle G^2 \rangle = -\frac{8}{9} \frac{\pi^2}{3240} N_f^2 (N_f^2 - 1) \frac{T^8}{f_G^4} \left[\ln \frac{\Lambda_p}{T} - \frac{1}{4} \right] + \dots \quad (2.53)$$

The leading $O(T^8)$ -behavior is easily understood from the observation that to order $O(T^4)$ one has a massless ideal Bose gas for which $\epsilon = 3p$ and hence $\langle\langle T_\mu^\mu \rangle\rangle = 0$. This is in agreement with the fact that a free gas of massless particles is scale invariant. The change in the gluon condensate arises solely on account of the interaction of Goldstone bosons which is not scale invariant. The high power of T implies that the gluon condensate “melts” much more slowly than the quark condensate.

2.4. Lattice Results

Obviously the low-density expansion of $\langle\langle \bar{\psi} \psi \rangle\rangle$ and $\langle\langle G^2 \rangle\rangle$ discussed in the previous section is of limited validity and cannot address the nature of the QCD phase transition. The low-temperature expansion is restricted to below $T \approx 120 \text{ MeV}$, mostly because at this point heavier mesons start to enter [65]. For finite ρ_N and vanishing T the dilute gas expression (2.45) predicts a decrease of the chiral condensate ratio which is linear in the number density. At nuclear saturation density, $\rho_0 = 0.16 \text{ fm}^{-3}$, this yields a $\sim 30\%$ drop and a naive extrapolation would indicate chiral restoration at $\rho_c \approx 3\rho_0$. This clearly cannot be trusted, since the EoS of nuclear matter greatly differs from that of a free Fermi gas at such high densities. Going beyond the dilute gas limit by using a real-

istic EoS it has been found [67] that deviations from the dilute gas set in slightly above ρ_0 .

In the vicinity of the phase boundary nonperturbative methods are needed. Even though many-body approaches [68] and renormalization-group techniques [69] are quite promising the most stringent framework is lattice QCD. Here the aim is an ab-initio understanding of the quark-hadron transition by evaluating the partition function (2.33) of QCD numerically. Because of technical difficulties this has been achieved, so far, only at vanishing baryon density.

In a theory of interacting boson fields ϕ and fermion fields ψ in contact with a heat bath the partition function Z at vanishing μ_q is given by the finite-temperature path integral

$$Z(V, T) = \int \mathcal{D}\phi \mathcal{D}\psi \mathcal{D}\bar{\psi} e^{-S^E(\phi, \psi, \bar{\psi})} \quad (2.54)$$

involving the euclidean action

$$S^E(\phi, \psi, \bar{\psi}) = \int_0^{T^{-1}} d\tau \int_V d^3x \mathcal{L}^E(x), \quad (2.55)$$

where $x = (\vec{x}, \tau)$ with $\tau = it$ and \mathcal{L}^E denotes the imaginary-time Lagrange density. The boson (fermion) fields obey periodic (antiperiodic) boundary conditions [70]. The thermal expectation value of a given operator \mathcal{O} is given as an ensemble average

$$\begin{aligned} \langle\langle \mathcal{O} \rangle\rangle &= \frac{1}{Z} \text{tr} \left\{ e^{-(\hat{H} - \mu_q \hat{N})/T} \mathcal{O} \right\} \\ &= \frac{1}{Z} \int \mathcal{D}\phi \mathcal{D}\psi \mathcal{D}\bar{\psi} \mathcal{O}(\phi, \psi, \bar{\psi}) e^{-S^E(\phi, \psi, \bar{\psi})}, \end{aligned} \quad (2.56)$$

and the field theory has been turned into a statistical mechanics problem.

For QCD the euclidean Lagrange density is given by (cf. Eq. (2.1))

$$\mathcal{L}_{\text{QCD}}^E(x) = \bar{\psi}(x)(-i\gamma_\mu D_\mu - i\mathcal{M}^0)\psi(x) + \frac{1}{4}G_{\mu\nu}^a(x)G_{\mu\nu}^a(x) \quad (2.57)$$

with the euclidean Dirac matrices obeying $\{\gamma_\mu, \gamma_\nu\} = 2\delta_{\mu\nu}$. The corresponding euclidean action is obtained as

$$S_{\text{QCD}}^E(A_\mu, \psi, \bar{\psi}) = \int_0^{T^{-1}} d\tau \int_V d^3x \mathcal{L}_{\text{QCD}}^E(x). \quad (2.58)$$

For a numerical evaluation of the partition function Z_{QCD} via the path integral a hypercubical lattice of spacing a with N_s lattice points in

each spatial direction and N_t points in the temporal direction is introduced. Temperature and volume are related to the lattice size, $N_s^3 \times N_t$, as

$$T^{-1} = N_t a, \quad V = (N_s a)^3, \quad (2.59)$$

and the temperature and volume derivatives are replaced according to

$$\begin{aligned} \frac{\partial}{\partial T} &\rightarrow \frac{1}{N_t} \frac{\partial}{\partial a} \\ \frac{\partial}{\partial V} &\rightarrow \frac{1}{3a^2 N_s^3} \frac{\partial}{\partial a}. \end{aligned} \quad (2.60)$$

Because of the scale dependence of α_s , Eq. (2.5), the lattice spacing becomes a function of the bare gauge coupling $\beta \equiv 6/g^2$ which fixes the temperature and the physical volume at a given coupling. The next step is to discretize the euclidean QCD action (2.58). Two requirements have to be met. The first is the correct continuum form of the action in the limit $a \rightarrow 0$. The second is local gauge invariance. To proceed one considers the “Schwinger line integral”

$$U^\mu(x) = e^{ig \int_x^{x+a\hat{\mu}} dy A_\mu(x+y)} \quad (2.61)$$

rather than the gauge field A_μ . In terms of U^μ the QCD partition function is expressed as

$$Z_{\text{QCD}} = \int \mathcal{D}U \mathcal{D}\psi \mathcal{D}\bar{\psi} e^{-S_{\text{QCD}}^E(U, \psi, \bar{\psi})}. \quad (2.62)$$

The discretization of the field variables $U^\mu(x) \rightarrow U_n^\mu$ and $\psi(x) \rightarrow \psi_n$ turns the line integral into a “link variable” which connects lattice site n to its neighbor $n + \hat{\mu}$. The quark fields are defined on the lattice sites n .

In the Wilson formulation [71] the gluonic part of the action, $S_G = \frac{1}{4}(G_{\mu\nu}^a)^2$, is expressed in terms of elementary plaquettes

$$U_\square \equiv U_n^\mu U_{n+\hat{\mu}}^\nu U_{n+\hat{\nu}}^{\mu^\dagger} U_{n+\hat{\nu}}^{\nu^\dagger}, \quad (2.63)$$

which constitute the smallest closed path starting from lattice site n . In terms of these plaquettes one has

$$S_G^E = \beta \sum_{\square} \left(1 - \frac{1}{3} \text{Re} \text{Tr} U_\square \right), \quad (2.64)$$

where the sum runs over all possible plaquettes. For small a

$$S_G^E = \frac{\beta g^2}{12} \sum_n a^4 (\text{Tr} G_{\mu\nu}(n) G_{\mu\nu}(n) + \mathcal{O}(a^2)), \quad (2.65)$$

which extrapolates to the proper continuum limit with $\beta = 6/g^2$ and hence satisfies both requirements of the lattice action.

To find an appropriate form for the fermionic part is more difficult. A naive discretization of the continuum Dirac action,

$$S_F^E = \int_0^{T^{-1}} d\tau \int_V d^3x \bar{\psi}(x) (\gamma_\mu D_\mu + \mathcal{M}^\circ) \psi(x), \quad (2.66)$$

leads to a lattice action

$$S_F^E = \sum_{n,m} a^4 \bar{\psi}_n K_{nm} [U] \psi_m, \quad (2.67)$$

where

$$\begin{aligned} K_{nm} &= \gamma_\mu D_{\mu,nm} + \mathcal{M}^\circ \delta_{nm} \\ D_{\mu,nm} &= \frac{1}{2a} \{ U_n^\mu \delta_{n+\hat{\mu},m} - U_{n-\hat{\mu}}^{\mu\dagger} \delta_{n-\hat{\mu},m} \}. \end{aligned} \quad (2.68)$$

In the continuum limit it describes $2^4 = 16$ fermion species rather than one. This fermion doubling per field component has its origin in the first derivative occurring in the Dirac equation. To remove the spurious degeneracy two methods have been proposed: Wilson fermions [71] in which the naive lattice action is supplemented by an extra term which ensures that in the continuum limit the extra 15 species are removed. It has the disadvantage that the numerical realization of the chiral limit $m_q \rightarrow 0$ is extremely time consuming. In studies which focus on the chiral phase transition the method of staggered fermions [72] is more suitable. Here the unwanted fermions are removed by doubling the effective lattice spacing: two separate fermion fields are introduced for even and odd lattice sites, which in the continuum limit are associated with the upper-two and lower-two components of the 4-component Dirac spinor, *i.e.*, the quark fields ψ can be reconstructed by suitable linear combination on hypercubes of length $2a$. More recently, another promising method called “domain wall fermions” has been developed to treat fermions in discretized vector gauge theories [73]. Here, a fifth dimension (in addition to 4-dimensional space-time) is introduced, and the low-lying (zero mode) fermion states are localized on “domain walls” in this

extra dimensions. This method has the attractive feature that—contrary to staggered or Wilson fermions—the full chiral symmetry of QCD is preserved to a high accuracy in its discretized version.

On a finite lattice the QCD partition function finally takes the form

$$\mathcal{Z}_{\text{QCD}} = \int \prod_{n,\mu} dU_n^\mu \prod_{n_1} d\bar{\psi}_{n_1} \prod_{n_2} d\psi_{n_2} e^{-S_{\text{QCD}}^E(U_n^\mu, \bar{\psi}_{n_1}, \psi_{n_2})}. \quad (2.69)$$

In contrast to the symbolic notation in Eq. (2.62) the measure $\mathcal{D}U\mathcal{D}\bar{\psi}\mathcal{D}\psi \equiv \prod dU d\bar{\psi} d\psi$ now has a well-defined meaning: dU_n^μ refers to the measure on the $SU(3)$ gauge group while $d\bar{\psi}, d\psi$ are the usual measures over Grassmann variables on site n .

The discretized fermion fields appear quadratic in the action and can therefore be integrated out to yield

$$\int \prod_{n_1} d\bar{\psi}_{n_1} \prod_{n_2} d\psi_{n_2} e^{S_F^E[U_n^\mu, \bar{\psi}_{n_1}, \psi_{n_2}]} = \det K[U]. \quad (2.70)$$

Thus the QCD partition function is given by a path integral solely over gauge fields U

$$\mathcal{Z}_{\text{QCD}} = \int \prod_{n,\mu} dU_n^\mu e^{-S_G^E(U_n^\mu)} \det K[U]. \quad (2.71)$$

When factorizing out the quark mass dependence in the matrix K_{nm} (2.68) as

$$K_{nm} = m_q \left(\frac{1}{m_q} \gamma_\mu D_{nm}^\mu + 1 \delta_{n,m} \right), \quad (2.72)$$

one sees that in the limit of large quark masses ($m_q \rightarrow \infty$) the term involving the covariant derivative gives a negligible contribution and the Grassmann integration (2.70) becomes a pure Gaussian integral. This results in a constant multiplicative factor in the partition function which cancels out in the expectation values of operators, $\langle\langle O \rangle\rangle$. Thus the limit of large m_q reduces to a pure gauge theory and is referred to as the “quenched approximation”. Physically it corresponds to the omission of vacuum polarization effects via quark loops.

Although in principle the condensates and the EoS can be derived from the free energy density as discussed in Sect. 2.3, in practice a direct computation of the partition function is rather difficult. Instead one calculates the expectation value of the action by taking the derivative of $\ln \mathcal{Z}_{\text{QCD}}$ with respect to the bare gauge coupling β and the bare quark masses m_q . In this way the pressure, the energy density and the

condensates are obtained by proper extrapolation to the continuum limit $a \rightarrow 0$ via a renormalization group analysis on the lattice.

Recent two-flavor results for ϵ, p and the so-called “interaction measure” $\Delta \equiv (\epsilon - 3p)/T^4 = \langle \langle T_\mu^\mu \rangle \rangle / T^4$ are shown in Fig. 2.3. One observes a rapid rise in ϵ (left panel) above a critical coupling of $\beta_c = 5.36$ roughly reaching the continuum Stephan-Boltzmann limit at the last data point. The critical coupling of $\beta_c = 5.36$ translates to a transition temperature $T_c = 140\text{ MeV}$. On the other hand, the pressure rises much more slowly

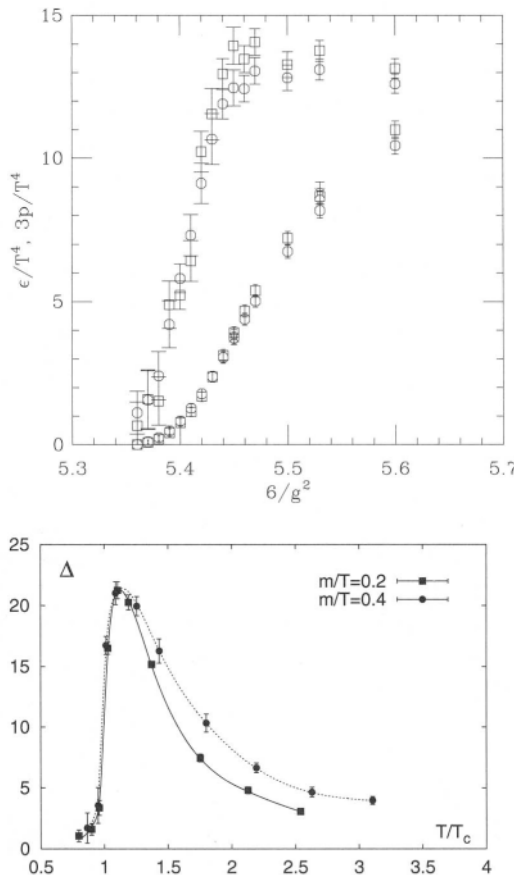


Fig. 2.3. Top: the energy density ϵ/T^4 and $3p/T^4$ as a function of $\beta = 6/g^2$ [74]. The lattice data are for $am_q = 0.0125$. Bottom: the interaction measure Δ as a function of T/T_c [75].

such that Δ remains large above the transition (right panel). This implies that above T_c the system is far from being ideal. However, the entropy density quickly approaches that of an ideal gas of quarks and gluons. A natural interpretation of this feature is that the dominant part of the non-perturbative pressure is provided by the remnant of the (vacuum) gluon condensate [76], which persists across the transition to a substantial extent (see below). Thus, above T_c one might indeed have a deconfined plasma of weakly interacting quarks and gluons in the background of a residual “bag” pressure.

Lattice results for the condensates $\langle\langle\bar{\psi}\psi\rangle\rangle$ and $\langle\langle G^2\rangle\rangle$ are shown in Fig. 2.4. The condensate ratio stays basically flat up to about 0.9 T_c after which it rapidly decreases. At first sight the relative constancy at small temperatures is at variance with the rigorous result from chiral perturbation theory which predicts a T^2 -dependence of the condensate ratio. It should, however, be realized that the lattice results are not in the chiral limit. Instead the simulations implicitly contain a rather “heavy pion” with a mass of roughly twice the physical mass. This explains the apparent differences with chiral perturbation theory. The temperature dependence of the gluon condensate can be inferred from the interaction measure Δ and the quark condensate via the relations (2.43) and (2.41). The right panel of Fig. 2.4 displays results for two flavors (solid squares) and for four flavors (open squares) while the dashed line shows the condensate in the quenched approximation rescaled by the number of degrees of freedom. While the condensate remains essentially unchanged below T_c which is consistent with the T^6 -dependence predicted from chiral perturbation theory, there is a rapid decrease slightly above T_c and the condensate eventually turns negative around $T = 200$ MeV. Asymptotic freedom implies that the effects of non-perturbative scale breaking disappear at high temperature where perturbation theory should become reliable. Intuitively one might therefore expect the gluon condensate to vanish at high temperature in accordance with the notion of an ideal quark-gluon plasma. As the lattice results (as well as chiral perturbation theory) show, this is however not the case. Scale invariance remains broken also in the high-temperature phase. This is related to the scale dependence of the running coupling constant (2.5). Identifying the scale with T introduces $1/\ln(T)$ corrections to the pressure such that at high temperatures $\langle\langle T_\mu^\mu\rangle\rangle$ is of order $T^4/(\ln T)^2 \propto g^4 T^4$ [66]. While small compared to the energy density of the plasma, $\langle\langle T_\mu^\mu\rangle\rangle$ itself grows without bounds as the temperature rises such that the gluon condensate does not disappear but becomes negative and large.

As a further result of lattice QCD we discuss the temperature dependence of “screening masses” which will become relevant for the

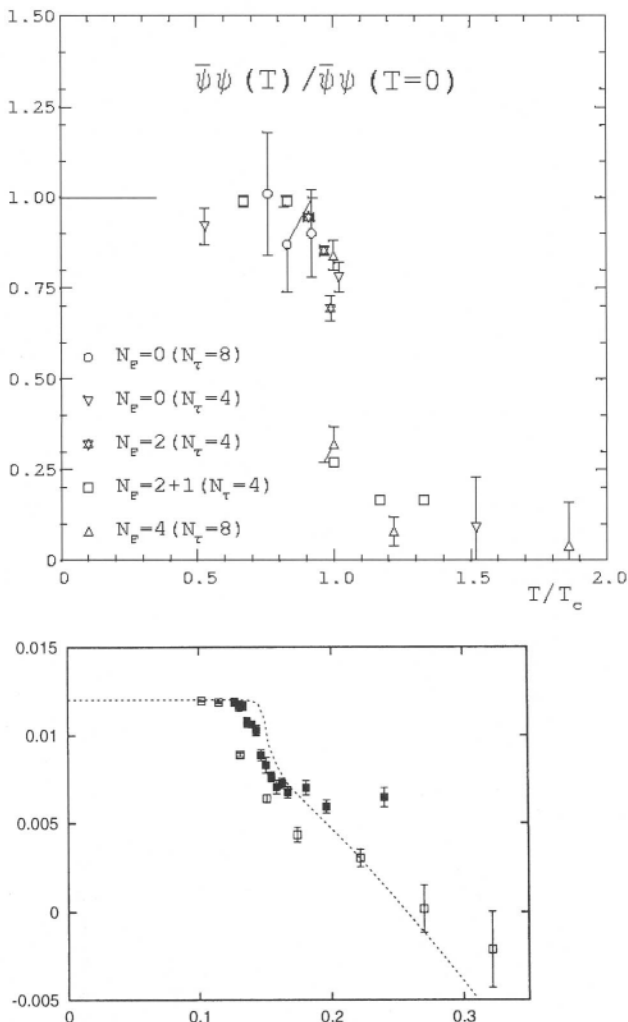


Fig. 2.4. Top: the quark condensate ratio $\langle\langle\bar{\psi}\psi\rangle\rangle/\langle\langle\bar{\psi}\psi\rangle\rangle_{T=0}$ as a function of T/T_c [77] Bottom: the temperature dependence of the gluon condensate [75].

later discussion of axial-/vector correlation functions. In general screening masses are extracted from the ensemble averaged current-current correlation functions $\langle\langle j_\mu(x)j_\mu(0)\rangle\rangle$ where the appropriate currents are denoted generically by $j_\mu(x)$. In practical calculations these correlation functions are evaluated for spatial separations r . For large r they show exponential behavior

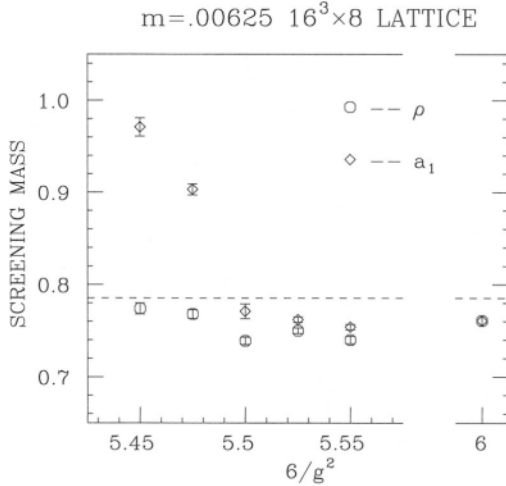


Fig. 2.5. The temperature dependence of the ρ and a_1 screening masses. The results are taken from Ref. [78].

$$\langle\langle j_\mu(x)j_\mu(0)\rangle\rangle \rightarrow e^{-m_{hr}}, \quad (2.73)$$

from which the (screening) masses of the lowest-energy hadron in the appropriate channel can be extracted numerically. Fig. 2.5 displays results for the screening masses of the ρ and a_1 meson. As dictated by spontaneous chiral symmetry breaking they are different in the physical vacuum. At the chiral transition they are found to be degenerate. The point of degeneracy coincides with the transition temperature for the melting of the condensate. The screening masses need not necessarily correspond to the “pole masses” in the propagators of the ρ and a_1 meson but rather represent the “centroids” of the in-medium vector and axialvector spectral functions. The spectral distributions themselves are likely to be quite complicated with significant reshaping, *e.g.*, a strong broadening as emerging in models of an interacting hadron gas, to be discussed later.

2.5. Dilepton Production and Vector Mesons

As mentioned in the Introduction dileptons probe all stages in the course of a heavy-ion reaction. The most interesting hot and dense phase emits low-mass dileptons predominantly from thermal annihilation processes such as quark-antiquark or pion and kaon annihilation.

The thermal rate for the production of dileptons at four-momentum q from a heat bath at temperature T is given by [8, 19]

$$\frac{d^8 N_{l+l-}}{d^4 x d^4 q} \equiv \frac{d^4 R_{l+l-}}{d^4 q} = L^{\mu\nu}(q) W_{\mu\nu}(q), \quad (2.74)$$

where to lowest order in the electromagnetic coupling, $\alpha = 1/137$, the lepton tensor is obtained as

$$\begin{aligned} L_{\mu\nu}(q) &= \frac{(4\pi\alpha)^2}{M^4} \int \frac{d^3 p_+}{(2\pi)^3 2p_{0,+}} \frac{d^3 p_-}{(2\pi)^3 2p_{0,-}} \delta^{(4)}(q - p_+ - p_-) \\ &\quad \times \text{tr}[(p_+ - m)\gamma_\mu(p_- + m)\gamma_\nu] \\ &= -\frac{\alpha^2}{6\pi^3 M^2} \left(g_{\mu\nu} - \frac{q_\mu q_\nu}{M^2} \right) \end{aligned} \quad (2.75)$$

with $p_{0,\pm} = (m_{l\pm}^2 + \vec{p}_{\pm}^2)^{1/2}$. For simplicity we will focus on the e^+e^- case and thus neglect the rest mass of the leptons as compared to their individual 3-momenta $|p_+|$, $|p_-|$. $M^2 = (p_+ + p_-)^2$ is the total four-momentum of the pair in the heat bath. The effect of the hadronic medium is encoded in the hadron tensor $W_{\mu\nu}(q)$. It is obtained from the thermal average of the electromagnetic current-current correlation function as [8, 19]

$$W_{\mu\nu}(q) = \int d^4 x e^{-iqx} \langle\langle j_\mu^{\text{em}}(x) j_\nu^{\text{em}}(0) \rangle\rangle, \quad (2.76)$$

where the average is taken in the grand canonical ensemble. For invariant masses below the charm threshold ($M < 2m_c \simeq 3 \text{ GeV}$) the current can be decomposed as

$$j_\mu^{\text{em}} = \frac{2}{3} \bar{u} \gamma_\mu u - \frac{1}{3} \bar{d} \gamma_\mu d - \frac{1}{3} \bar{s} \gamma_\mu s. \quad (2.77)$$

With the identification

$$j_\mu^{\text{em}} = j_\mu^\rho + j_\mu^\omega + j_\mu^\phi \quad (2.78)$$

$$j_\mu^\rho = \frac{1}{2} (\bar{u} \gamma_\mu u - \bar{d} \gamma_\mu d) \quad (2.79)$$

$$j_\mu^\omega = \frac{1}{6} (\bar{u} \gamma_\mu u + \bar{d} \gamma_\mu d) \quad (2.80)$$

$$j_\mu^\phi = -\frac{1}{3}(\bar{s}\gamma_\mu s), \quad (2.81)$$

its flavor content can be expressed in physical channels with the quantum numbers of the ρ , ω and ϕ meson.

For an ideal plasma of quarks and gluons at finite temperature and vanishing chemical potential the rate (2.74) is readily evaluated. Applying lowest-order perturbation theory and integrating over the three-momentum of the dilepton pair one obtains the familiar expression

$$\frac{dR^q}{dM^2} = R^q \frac{\alpha^2}{6\pi^3} M T K_1(M/T) \quad (2.82)$$

where $K_1(M/T)$ denotes a modified Bessel function and R^q involves the sum over squared quark charges and the number of colors,

$$R^q = N_c \sum_f e_f^2 = 3\left(\frac{4}{9} + \frac{1}{9} + \frac{1}{9}\right). \quad (2.83)$$

A similar expression can be derived for an ideal resonance gas at finite temperature:

$$\frac{dR^h}{dM^2} = R^h(M) \frac{\alpha^2}{6\pi^3} M T K_1(M/T), \quad (2.84)$$

where

$$R^h = \frac{\sigma(e^+e^- \rightarrow \text{hadrons})}{\sigma(e^+e^- \rightarrow \mu^+\mu^-)} \quad (2.85)$$

is accessible from experiment as indicated in the lower panel of Fig. 2.6.

From the rates (2.82) and (2.84) a simple estimate can be made for the expected dilepton signal when the hadronic fireball is close to the phase boundary (Fig. 1.1). As displayed in Fig. 2.7 for $T = 160$ MeV and $\mu_B = 0$ the predicted rates coincide above ~ 1.5 GeV but differ greatly below due to the ρ , ω and ϕ resonance structures in the electromagnetic spectral function (lower panel of Fig. 2.6).

2.6. Vector-Axialvector Mixing

As has been discussed the quark-hadron phase transition is accompanied by the restoration of chiral symmetry, *i.e.*, a “melting” of the quark condensate at the transition temperature, $T_c \approx 160$ MeV. The change of

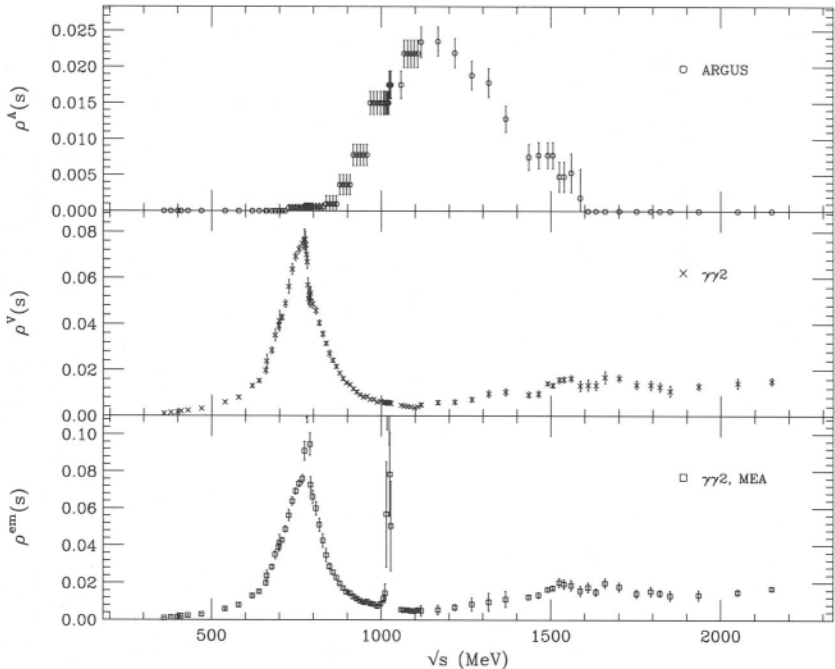


Fig. 2.6. Lower panel: experimental cross section ratio $R^h(s)/12\pi^2$ according to Eq. (2.85) from a recent data compilation [79] of various experiments on e^+e^- annihilation [80, 81, 82, 83, 84]. The middle and upper panel show the individual experimental information on vector and axialvector spectral densities, Eqs. (2.92) and (2.93), as extracted from $e^+e^- \rightarrow 2n\pi$ and τ -decay data, respectively.

$\langle\langle\bar{\psi}\psi\rangle\rangle$ is not an experimental observable, however. On the other hand it follows from chiral symmetry alone that, at the phase boundary, vector and axialvector correlators must become identical (in the chiral limit). This is evidenced by the temperature dependence of the lattice screening masses (Fig. 2.5) as will be discussed more generally in the following.

First we consider the isovector ($I = 1$) vacuum vector and axialvector correlators for two flavors. The former clearly dominates the electromagnetic spectral function (Fig. 2.6) and hence the dilepton rate. One has

$$\prod_V^{o\mu\nu}(q) = -i \int d^4x e^{iq \cdot x} \langle 0 | \mathcal{T} j_V^\mu(x) j_V^\nu(0) | 0 \rangle$$

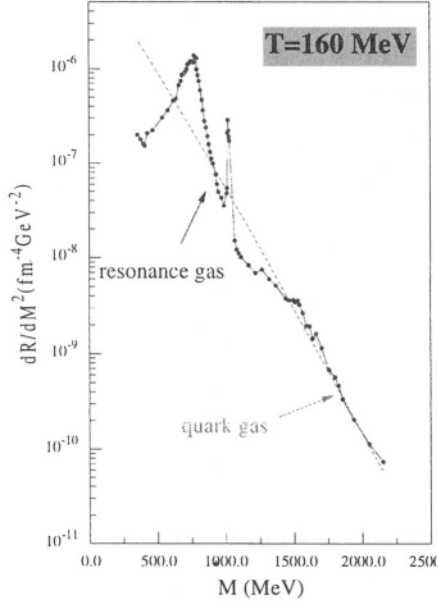


Fig. 2.7. Three-momentum integrated dilepton production rate at a temperature $T = 160$ MeV using either the resonance gas approximation, Eq. (2.84), or the perturbative $q\bar{q}$ prediction, Eq. (2.82).

$$\prod_A^{\circ\mu\nu}(q) = -i \int d^4x e^{iq \cdot x} \langle 0 | \mathcal{T} j_A^\mu(x) j_A^\nu(0) | 0 \rangle, \quad (2.86)$$

where

$$j_V^\mu = \frac{1}{2} (\bar{u} \gamma_\mu u - \bar{d} \gamma_\mu d) \quad (2.87)$$

$$j_A^\mu = \frac{1}{2} (\bar{u} \gamma_\mu \gamma_5 u - \bar{d} \gamma_\mu \gamma_5 d) \quad (2.88)$$

carry the quantum numbers of the ρ and a_1 meson, respectively. The imaginary parts of (2.86) can be expressed in terms of the vector and axialvector spectral densities, ρ_V and ρ_A , as

$$\frac{1}{\pi} \text{Im} \prod_A^{\circ\mu\nu}(q) = (q^2 g^{\mu\nu} - q^\mu q^\nu) \rho_A^\circ(q^2)$$

$$\frac{1}{\pi} \text{Im} \prod_A^{\circ\mu\nu}(q) = (q^2 g^{\mu\nu} - q^\mu q^\nu) \rho_A^\circ(q^2) - q^\mu q^\nu f_\pi^2 \delta(q^2 - m_\pi^2). \quad (2.89)$$

Due to spontaneous symmetry breaking in the physical vacuum and the resulting Goldstone nature of the pion the axialvector correlator contains an additional pion pole term. Chiral symmetry also dictates a relationship between the vector and axialvector sector which is encoded in two sum rules [85]:

$$\int ds (\rho_V^\circ(s) - \rho_A^\circ(s)) = f_\pi^2 \quad (2.90)$$

$$\int ds s (\rho_V^\circ(s) - \rho_A^\circ(s)) = 0. \quad (2.91)$$

The first one directly links the spectral functions to f_π , one of the order parameters of spontaneous symmetry breaking, while the second one is a well-known consequence of the conservation of vector and axialvector currents in the chiral limit.

The vacuum spectral functions $\rho_V^\circ(s)$ and $\rho_A^\circ(s)$ are related to physical processes. The vector spectral function can be obtained from the e^+e^- -annihilation into an even number of pions:

$$\rho_V^\circ(s) = -\frac{s}{16\pi^3 \alpha^2} \sum_{n=1} \sigma(e^+e^- \rightarrow 2n\pi), \quad (2.92)$$

while $\rho_A^\circ(s)$ can be extracted from data on τ -decay into a ν_τ -neutrino and an odd number of pions:

$$\rho_A^\circ(s) = \frac{8\pi m_\tau^3}{G_F^2 \cos\theta_c (m_\tau^2 + 2s)(m_\tau^2 - s)^2} \sum_{n=1} \frac{d\Gamma(\tau \rightarrow \nu_\tau (2n+1)\pi)}{2s}. \quad (2.93)$$

An available data compilation [79] is displayed in the upper and middle panel of Fig. 2.6. The two spectral functions are clearly different which is one of the experimental signatures that chiral symmetry is spontaneously broken. Replacing the spectral functions by a simplifying pole ansatz

$$\rho_V^\circ(s) = \frac{m_\rho^4}{g_\rho^2} \frac{1}{s} \delta(s - m_\rho^2), \quad \rho_A^\circ(s) = \frac{m_{a_1}^4}{g_{a_1}^2} \frac{1}{s} \delta(s - m_{a_1}^2), \quad (2.94)$$

one immediately derives from the Weinberg sum rules (2.91) that

$$\frac{m_\rho^4}{g_\rho^2} = \frac{m_{a_1}^4}{g_{a_1}^2}, \quad m_\rho^2 = ag_\rho^2 f_\pi^2 \quad \text{with } a = \left(1 - \frac{m_\rho^2}{m_{a_1}^2}\right)^{-1}. \quad (2.95)$$

For $m_{a_1} = \sqrt{2}m_\rho$ (*i.e.*, $a = 2$), which is not too far from reality, the KSFR relation [86] is recovered.

Turning to the hot hadronic medium the current-current correlation functions—in analogy to Eq. (2.86)—are given as the thermal averages

$$\Pi_V^{\mu\nu}(q) = -i \int d^4x e^{iq\cdot x} \langle \langle j_V^\mu(x) j_V^\nu(0) \rangle \rangle \quad (2.96)$$

$$\Pi_A^{\mu\nu}(q) = -i \int d^4x e^{iq\cdot x} \langle \langle j_A^\mu(x) j_A^\nu(0) \rangle \rangle. \quad (2.97)$$

Since the thermal medium specifies a preferred frame and thus explicitly breaks Lorentz invariance the tensor structure is now more complicated giving rise to a separate dependence on energy q_0 and three-momentum \vec{q} as well as a splitting into longitudinal and transverse components. One has

$$\Pi_{V,A}^{\mu\nu}(q_0, \vec{q}) = \Pi_{V,A}^L(q_0, \vec{q}) P_L^{\mu\nu} + \Pi_{V,A}^T(q_0, \vec{q}) P_T^{\mu\nu} \quad (2.98)$$

where P_L and P_T are the usual longitudinal and transverse projection operators:

$$P_L^{\mu\nu} = \frac{q^\mu q^\nu}{M^2} - g^{\mu\nu} - P_T^{\mu\nu}$$

$$P_T^{\mu\nu} = \begin{cases} 0, & \mu = 0 \text{ or } \nu = 0 \\ \delta^{ij} - \frac{q^i q^j}{\vec{q}^2}, & \mu, \nu \in \{1, 2, 3\} \end{cases} \quad (2.99)$$

(the space-like components of μ and ν are denoted by i and j , respectively), and $\Pi_{V,A}^{L,T}(q_0, \vec{q})$ denote the longitudinal and transverse polarization functions. In general they are different and only coincide for vanishing three-momentum $\vec{q} = 0$, *i.e.*, excitations which are at rest relative to the medium. In-medium Weinberg sum rules have been derived in Ref. [87]. Introducing the in-medium spectral distributions for vanishing three-momentum as

$$\rho_{V,A}(q_0) = -\frac{1}{q_0^2 \pi} \text{Im} \prod_{V,A}^L(q_0, 0), \quad (2.100)$$

these sum rules are given by

$$\int dq_0^2 (\rho_V(q_0) - \rho_A(q_0)) = 0 \quad (2.101)$$

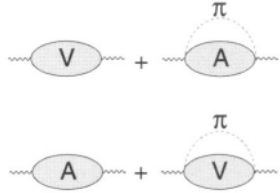


Fig. 2.8. Diagrammatic representation of the mixing of vector and axialvector correlators in a heat bath of pions.

$$\int dq_0^2 q_0^2 (\rho_V(q_0) - \rho_A(q_0)) = 0. \quad (2.102)$$

Due to the presence of pions in the thermal heat bath the vector and axialvector correlators mix (Fig. 2.8). At low temperature this mixing can be calculated in a virial expansion. To lowest order in temperature one obtains [88] the model-independent ‘‘mixing theorem’’ of vacuum correlators:

$$\begin{aligned} \Pi_V^{\mu\nu}(q) &= (1 - \epsilon) \Pi_V^{o\mu\nu}(q) + \epsilon \Pi_A^{o\mu\nu}(q) \\ \Pi_A^{\mu\nu}(q) &= (1 - \epsilon) \Pi_A^{o\mu\nu}(q) + \epsilon \Pi_V^{o\mu\nu}(q). \end{aligned} \quad (2.103)$$

The mixing coefficient ϵ is given by the thermal pion loop

$$\epsilon = \frac{2}{f_\pi^2} \int \frac{d^3 k}{(2\pi)^3} \frac{f^\pi(\omega_\pi(k))}{\omega_\pi(k)} \quad (2.104)$$

($f^\pi(\omega) = 1/(\exp[\omega/T] - 1)$: pion Bose distribution, $\omega_\pi(k)^2 = m_\pi^2 + k^2$). In the chiral limit ($m_\pi \rightarrow 0$) this reduces to

$$\epsilon = \frac{T^2}{6f_\pi^2}. \quad (2.105)$$

To lowest order there is no change in the spectral shapes themselves but rather a temperature-dependent coupling between the free vector and axialvector correlators. As is easily verified the mixing theorem fulfills the in-medium Weinberg sum rules and according to (2.103) chiral symmetry is restored for $\epsilon = 1/2$. Eq. (2.105) thus implies a transition temperature $T_c = \sqrt{3}f_\pi \approx 160\text{MeV}$ which coincides with the transition temperature $T_c = 150 \pm 20\text{MeV}$ from lattice QCD. Clearly the low-temperature expansion cannot be trusted to such high temperature. Nonetheless it is instructive to see what the consequences for the dilepton spectrum are. This is displayed in Fig. 2.9. By comparing with the results from a quark-gluon plasma one observes that both are

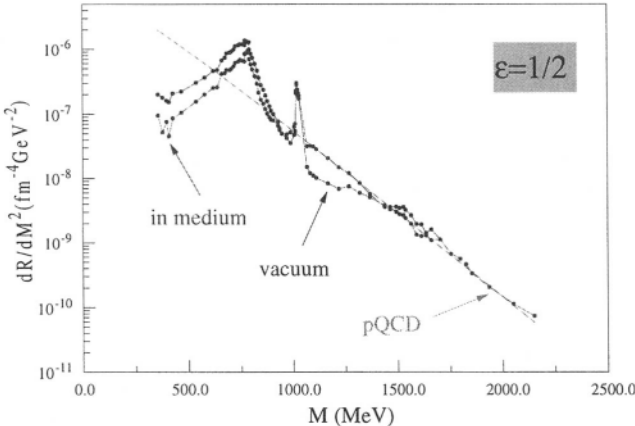


Fig. 2.9. Three-momentum integrated dilepton production rates at fixed temperature $T = 160$ MeV using the free electromagnetic correlator (labeled “vacuum”), the fully mixed one from Eq. (2.103) (“in-medium”) and the perturbative quark-gluon one according to Eq. (2.82) (“pQCD”).

indistinguishable down to invariant masses of ~ 1 GeV. This is significantly lower than without mixing in which case the two rates only coincide above ~ 1.5 GeV (the latter is conceivable from the fact that chiral symmetry breaking is a long distance phenomenon which does not impact the short-distance behavior of the correlators). In other words: the vector-axialvector mixing at finite temperature entails that the “duality threshold”—where hadronic and quark-gluon based descriptions start to agree—is reduced from its vacuum location at $M \approx 1.5$ GeV to about $M \approx 1$ GeV in the medium. At this level, the ϕ and ρ/ω resonance structures (which themselves are not affected by the simple mixing mechanism) inhibit a further penetration of the duality threshold into the low-mass region. However, let us note already at this point that it is precisely the broadening (or “melting”) of the resonances in the medium (as predicted in various hadronic model calculations) that—at the same time—flattens the (ρ) resonance structure and generates low-mass dilepton enhancement below the free ρ mass. These important issues will be reiterated in some detail throughout this article.

Further interesting conclusions about the in-medium correlators can be drawn by using a pole approximation [87] similar to (2.94):

$$\rho_V(q_0) = \frac{m_\rho^4}{g_\rho^2} Z_\rho \frac{1}{q_0^2} \delta(q_0^2 - m_\rho^{*2})$$

$$\rho_A(q_0) = \frac{m_{a_1}^4}{g_{a_1}^2} Z_{a_1} \frac{1}{q_0^2} \delta(q_0^2 - m_{a_1}^{*2}) + f_\pi^{*2} \delta(q_0^2), \quad (2.106)$$

where m_p^* , $m_{a_1}^*$ and f_π^* denote the in-medium masses and pion decay constant while Z_ρ and Z_{a_1} are the residues at the quasiparticle pole. Inserting (2.106) into the Weinberg sum rules (2.101), (2.102) yields $Z_\rho = Z_{a_1}$ from the second one, and thus from the first one

$$\frac{f_\pi^{*2}}{f_\pi^2} = a Z_\rho \left(\frac{m_\rho^2}{m_p^{*2}} - \frac{m_\rho^2}{m_{a_1}^{*2}} \right), \quad (2.107)$$

where a is given by (2.95). Since f_π^* is an order parameter of chiral symmetry the latter is restored when $m_p^* = m_{a_1}^*$. Such an approach to mass degeneracy is indeed observed in lattice QCD calculations.

In close reminiscence to the finite temperature case, Krippa [89] derived an analogous mixing theorem for a zero-temperature gas of non-interacting nucleons using soft pion theorems and current algebra,

$$\begin{aligned} \Pi_V^{\mu\nu}(q) &= (1 - \xi) \Pi_V^{\circ\mu\nu}(q) + \xi \Pi_A^{\circ\mu\nu}(q) \\ \Pi_A^{\mu\nu}(q) &= (1 - \xi) \Pi_A^{\circ\mu\nu}(q) + \xi \Pi_V^{\circ\mu\nu}(q). \end{aligned} \quad (2.108)$$

Here, the mixing parameter

$$\xi \equiv \frac{4\rho_N \bar{\sigma}_{\pi N}}{3f_\pi^2 m_\pi^2} \quad (2.109)$$

appears in terms of the leading nonanalytic term in the current quark mass ($\propto m_\pi^3$) in the chiral expansion of the nucleon **σ -term**, given by

$$\begin{aligned} \bar{\sigma}_{\pi N} &= 4\pi^3 m_\pi^2 \langle N | \pi^2 | N \rangle \\ &\simeq 20 \text{ MeV}. \end{aligned} \quad (2.110)$$

It is related to the pion mass contribution to the in-medium nucleon mass and arises from the long-distance physics encoded in the nuclear pion cloud being governed by chiral symmetry [90]. Naive extrapolation of the mixing to chiral restoration (*i.e.*, $\xi = 1/2$) yields $\rho_c \simeq 2.5\rho_0$, which again is not unreasonable.

2.7. QCD Sum Rules

The QCD sum rule approach [59] aims at an understanding of physical current-current correlation functions in terms of QCD by

relating the observed hadron spectrum to the nonperturbative QCD vacuum structure. This is achieved by a separation of short- and long-distance scales. The principal tool is the “operator product expansion” (OPE) which evaluates the time-ordered product of the light-quark QCD currents at large space-like momenta $Q^2 \equiv -q^2 > 0$. In this case the current product can be related to a series of gauge invariant local operators \mathcal{O}_n as

$$-i \int d^4x e^{iq \cdot x} \mathcal{T} j^\mu(x) j^\nu(0) = - \left(g^{\mu\nu} - \frac{q^\mu q^\nu}{q^2} \right) \sum_n c_n(Q^2, \Lambda^2) \mathcal{O}_n(\Lambda^2), \quad (2.111)$$

where Λ is the renormalization scale and c_n denote c-number functions (the Wilson coefficients) which contain the short-distance physics and can be calculated reliably. The Q^2 -independent operators \mathcal{O}_n , on the other hand, encompass the long-distance properties of QCD, manifest in the appearance of various condensates such as $\langle \bar{\psi} \psi \rangle$ or $\langle G^2 \rangle$. These operators have various dimensions, d , such that at large Q^2 (2.111) can be considered as an expansion in inverse powers of Q^2 (corrected by logarithms due to renormalization). An increase in dimension implies extra inverse powers of Q^2 such that operators of higher dimension are suppressed.

The general strategy is to take the vacuum matrix elements of (2.111) and to consider a dispersion relation (possibly subtracted) of the type

$$\begin{aligned} \Pi^\circ(Q^2 = -q^2) &= \Pi^\circ(0) - \frac{Q^2}{\pi} \int_0^\infty \frac{ds}{s} \frac{\text{Im} \prod^\circ(s)}{Q^2 + s} \\ &= \Pi^\circ(0) + Q^2 \int_0^\infty ds \frac{\rho^\circ(s)}{Q^2 + s}, \end{aligned} \quad (2.112)$$

where $\rho^\circ(s) = -(1/\pi s) \text{Im} \Pi^\circ(s)$ denotes the vacuum spectral function of the current-current correlator in question. For the electromagnetic current $\Pi^\circ(0) = 0$, since the photon is massless in the vacuum. The *l.h.s.* of Eq. (2.112) is evaluated in the OPE by determining the Wilson coefficients up to a certain dimension d while the *r.h.s.* is taken from measured cross sections (or simple parameterizations thereof) in the time-like region. For the *l.h.s.* one obtains

$$\frac{12\pi}{Q^2} \Pi^\circ(Q^2) = \frac{d}{\pi} \left[-c_0 \ln(Q^2/\Lambda^2) + \frac{c_1}{Q^2} + \frac{c_2}{Q^4} + \frac{c_3}{Q^6} + \dots \right], \quad (2.113)$$

which exhibits the power series expansion in Q^2 . In case of the ρ meson [91]

$$\begin{aligned}
c_0^\rho &= 1 + \frac{\alpha_s}{\pi} \\
c_1^\rho &= -3(m_u^2 + m_d^2) \\
c_2^\rho &= \frac{\pi^2}{3} \langle G^2 \rangle + 4\pi^2 \langle m_u \bar{u} u + m_d \bar{d} d \rangle \\
c_3^\rho &\propto \alpha_s \langle (\bar{q} q)^2 \rangle,
\end{aligned} \tag{2.114}$$

where $\alpha_s(Q^2)$ is the running QCD coupling constant given in Eq. (2.5). Explicit expressions for the coefficients c_i of other mesons can be found in Ref. [91]. While for c_2 the quark and gluon condensates enter, which are rather well known, c_3 contains the four-quark condensate, *i.e.*, $\langle(\bar{q} q)^2\rangle$, which is quite uncertain. Based on the assumption of vacuum saturation it is usually approximated in factorized form, $\langle\bar{q} q\rangle^2$, and higher meson states, especially pions, are incorporated by a phenomenological factor $\kappa > 1$ such that

$$c_3 = \kappa \alpha_s \langle \bar{q} q \rangle^2 \tag{2.115}$$

The parameter κ typically varies between 1 and 6 [46, 92, 91].

Rather than working with (2.113) the convergence of the hadronic side can be improved by observing that the physical spectrum is dominated by low-lying resonances (Fig. 2.6). To enhance their weight one employs the fact that dispersion theory implies the following relation for derivatives of Π° :

$$\frac{1}{n!} \left(-\frac{d}{dQ^2} \right)^n \prod^\circ (Q^2)|_{Q^2=Q_0^2} = \frac{1}{\pi} \int ds \frac{\text{Im} \prod^\circ(s)}{(s+Q_0^2)^{n+1}}. \tag{2.116}$$

This leads to the introduction of the “Borel transformation”

$$\hat{L}_M = \lim_{\substack{Q^2 \rightarrow \infty, n \rightarrow \infty \\ Q^2/n = M^2}} \frac{1}{(n-1)!} (Q^2)^n \left(-\frac{d}{dQ^2} \right)^n, \tag{2.117}$$

where M is the so-called Borel mass. When applied to both sides of Eq. (2.112) and by using general properties of \hat{L}_M the result of the transformation is

$$\frac{1}{\pi M^2} \int ds \rho_V^\circ(s) e^{-s/M^2} = \frac{d_V}{12\pi^2} \left[c_0 + \frac{c_1}{M^2} + \frac{c_2}{M^4} + \frac{c_3}{2M^6} + \dots \right]. \tag{2.118}$$

Note the appearance of the exponential factor in the integrand of the *l.h.s.* which suppresses the contribution from higher resonances. The *r.h.s.*

converges rapidly if M is sufficiently large such that the few lowest terms in the OPE suffice. Typically the minimum value of the Borel mass to achieve rapid convergence is around 1 GeV.

The QCD sum rule analysis in the vacuum can now be performed in two ways. Either the phenomenological side is experimentally accessible in which case values for the various condensates can be extracted, or, by using “known” values for the condensates the properties of the physical spectrum, *i.e.*, masses and coupling constants, can be inferred. The latter procedure forms the basis of QCD sum rule applications in hadronic matter. The most simple ansatz for the vacuum spectral density consists of a “delta function” parameterization of the resonance part supplemented by a “continuum step function” (cf. Fig. 2.10):

$$\rho^o(s) = \frac{Z_V}{12\pi^2} \delta(s - m_V^2) + \frac{d_V}{12\pi^2} \left(1 + \frac{\alpha_s}{\pi}\right) \Theta(s - s_V), \quad (2.119)$$

where Z_V denotes the pole strength, m_V the vector meson mass and s_V the continuum threshold. The continuum strength d_V is determined by perturbative QCD with $d_\rho = 3/2$, $d_\omega = 1/6$, $d_\phi = 1/3$. Applying this parameterization to (2.118) with $\alpha_s = 0.36$, $\langle \bar{u}u \rangle \simeq \langle \bar{d}d \rangle \simeq \langle \bar{s}s \rangle = (-250 \text{ MeV})^3$, $\left\langle \frac{\alpha_s}{\pi} G_{\mu\nu}^a G_a^{\mu\nu} \right\rangle = (330 \text{ MeV})^4$ and $\kappa = 2.36$ the *l.h.s.* and *r.h.s.* match for $Z_\rho = 9 \text{ GeV}^2$, $Z_\omega = 2.4 \text{ GeV}^2$, $Z_\phi = 0.79 \text{ GeV}^2$, $m_{\rho,\omega} = 0.77 \text{ GeV}$, $m_\phi = 1.02$

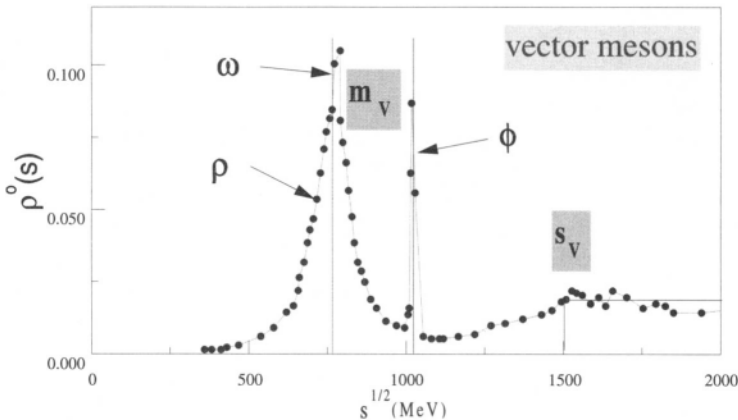


Fig. 2.10. QCD sum rule parameterization of the strength function.

GeV and $s_{\rho,\omega} = 1.5 \text{ GeV}^2$, $s_\phi = 2.2 \text{ GeV}^2$ in a ‘‘Borel window’’ of 0.8–1.5 GeV [91]. Inclusion of the vector-meson decay widths (especially for the ρ meson) does not affect these results appreciably.

The in-medium QCD sum rule analysis involves the vector current-current function in the interacting hadron gas (2.97). In the following it will be focused on the case of $\vec{q} = 0$ for which $\Pi_V^{L,T}(q_0)$ from Eq. (2.98) coincide. In analogy to the vacuum case (2.118) the in-medium sum rules at zero temperature are given by

$$\begin{aligned} & \frac{1}{\pi M^2} \left[\Pi_V(0) + \int dq_0^2 \rho_V(q_0) e^{-\frac{q_0^2}{M^2}} \right] \\ &= \frac{d_V}{12\pi^2} \left[c_0 + \frac{c_1}{M^2} + \frac{c_2(\rho)}{M^4} + \frac{c_3(\rho)}{2M^6} + \dots \right], \end{aligned} \quad (2.120)$$

where $\rho_V(q_0)$ denotes the in-medium vector spectral function (2.100). Note that, in contrast to the vacuum, $\Pi_V(0)$ no longer vanishes for the ρ and ω meson. It is related to the ρ/ω -nucleon forward-scattering amplitude [91]. On the *r.h.s.* of Eq. (2.120) the medium enters through the density-dependent Wilson coefficients $c_2(\rho)$ and $c_3(\rho)$. These in turn are chiefly determined by the density-dependent quark and gluon condensates

$$\langle\langle \bar{q}q \rangle\rangle = \langle\bar{q}q\rangle - \sum_N \frac{m_N}{2m} \rho, \quad \langle\langle G^2 \rangle\rangle = \langle G^2 \rangle - \frac{8}{9} m_N^{(0)} \rho. \quad (2.121)$$

which follow from the dilute gas expressions (2.45) and (2.47) at zero temperature. As was pointed out in Ref. [46] additional contributions to the Wilson coefficients arise from new condensates which involve mixed quark and gluon fields, the latter entering through the gauge covariant derivative D_μ (2.3). These matrix elements are proportional to moments of the quark and antiquark distribution functions

$$A_n^q = 2 \int_0^1 dx x^n [q(x) + \bar{q}(x)] \quad (2.122)$$

in the nucleon. Restricting oneself to the lowest moments and leading order in density one finally arrives for the ρ meson at [46]

$$c_2^\rho(\rho) = c_2^\rho(0) - \left(\frac{8\pi^2}{27} m_N^{(0)} - 2\pi^2 A_1^{u+d} m_N \right) \rho \quad (2.123)$$

and

$$c_3(\rho) \simeq c_3(0) + \left(\frac{896}{81} \kappa \pi^3 \alpha_s \sum_N \frac{\langle \bar{q} q \rangle}{m} - \frac{10}{3} \pi^2 A_3^{u+d} m_N^3 \right) \rho, \quad (2.124)$$

where m_N denotes the physical nucleon mass while $m_N^{(0)}$ represents the nucleon mass in the chiral limit ($m_N^{(0)} \simeq 750 \text{ MeV}$ [93]). Expressions for the density-dependent Wilson coefficient of other mesons can be found in Ref. [91].

In keeping the simple parameterization (2.119) for the in-medium spectral function,

$$\rho_V(q_0) = \frac{Z_V^*}{12\pi^2} \delta(q_0^2 - m_V^{*2}) + \frac{d_V}{12\pi^2} \left(1 + \frac{\alpha_s}{\pi} \right) \Theta(q_0^2 - s_V^*), \quad (2.125)$$

Hatsuda and Lee [46] extracted the medium dependence of the non-strange vector-meson masses as

$$\frac{m_{\rho,\omega}^*}{m_{\rho,\omega}} = 1 - (0.18 \pm 0.06) \frac{\rho}{\rho_0}. \quad (2.126)$$

The fact that these masses decrease as density increases has initially been taken as an indication of the “dropping mass scenario” of Brown and Rho [45] to which we will return below. Rather than using the parameterization (2.125), it is, however, natural to take into account the fact that the strength distributions might broaden significantly in the hadronic medium, as will be discussed in detail later. A first step in this direction was taken in Ref. [94] by including effects of the **Δ -nucleonhole** polarization in the pion cloud of the ρ meson. Its net impact on the in-medium QCD sum rule, however, turned out to be rather moderate, *i.e.*, a strong decrease of the in-medium ρ mass very similar to the Hatsuda-Lee results was still needed to satisfy the sum rule. A more general investigation of broadening effects was performed in Ref. [95] by assuming a schematic Breit-Wigner spectral function

$$A_V(q_0) = \frac{1}{\pi} \frac{q_0 \Gamma_V(q_0)}{(q_0^2 - m_V^2)^2 + q_0^2 \Gamma_V(q_0)^2} \quad (2.127)$$

with

$$\Gamma_V(q_0) = \Gamma_0 \left(\frac{1 - (\omega_V^{\text{thr}}/q_0)^2}{(1 - (\omega_V^{\text{thr}}/m_V)^2)} \right)^{\frac{1}{2}} \Theta(q_0^2 - (\omega_V^{\text{thr}})^2), \quad (2.128)$$

ω_V^{thr} denoting the appropriate in-medium threshold (for the ρ meson $\omega_\rho^{\text{thr}} = m_\pi$ was chosen which is correct to leading order in the density)

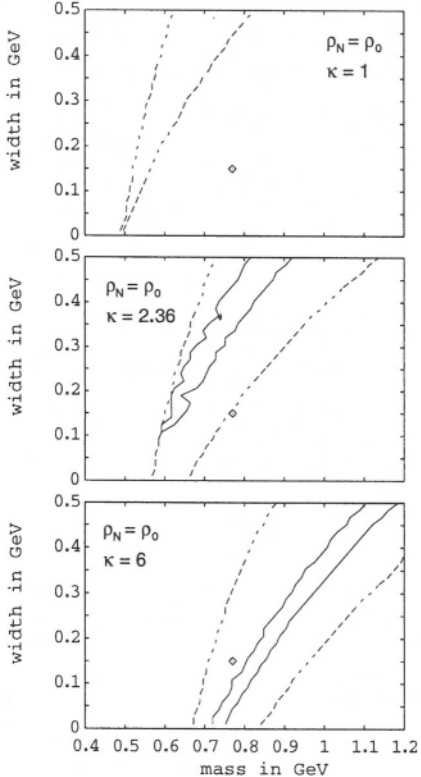


Fig. 2.11. Constraints on allowed values for the in-medium width and mass of the ρ meson from the QCD sum rule analysis of Ref. [95]. The full and dashed lines border allowed regions at 0.2% and 1% accuracy level, respectively. The diamond marks the mass and width of the free ρ meson.

and Γ_0 being a constant width parameter. One concludes from Fig. 2.11 that QCD sum rules give no stringent prediction for a dropping of vector-meson masses. This result is corroborated by the findings of Ref. [91] where a microscopic spectral function for vector mesons was used.

2.8. Chiral Reduction Formalism

Another model-independent approach that has been put forward to assess medium modifications of the vector correlation function is the so-called chiral master formula framework developed in Ref. [96]. In the general case, it starts out from gauge covariant divergence equations (Veltmann-Bell equations [97]) including explicit chiral breaking in the presence of external sources,

$$\nabla_\mu j_{V,\mu}^\mu + \epsilon_{abc} a_{\mu,b} j_{A,c}^\mu = -f_\pi \epsilon_{abc} p_b \pi_c \quad (2.129)$$

$$\nabla_\mu j_{V,a}^\mu + \epsilon_{abc} a_{\mu,b} j_{V,c}^\mu = f_\pi (m_\pi^2 + s) \pi_a - f_\pi p_a \sigma, \quad (2.130)$$

where the (axial-) vector currents

$$j_{V,a}^\mu(x) = \frac{\delta S}{\delta v_\mu^a(x)}, \quad j_{A,a}^\mu(x) = \frac{\delta S}{\delta a_\mu^a(x)} \quad (2.131)$$

and (pseudo-) scalar densities

$$\sigma = -\frac{m_q}{f_\pi m_\pi^2} \bar{q} q, \quad \pi^a = \frac{m_q}{f_\pi m_\pi^2} \bar{q} i \gamma_5 \tau^a q \quad (2.132)$$

have been defined as functional derivatives of an action S w.r.t. a pertinent set of auxiliary fields $\phi \equiv \{v_\mu^a, a_\mu^a, s, p^a\}$, respectively (here, $a,b,c = 1-3$ are isospin indices and the short-hand notation for the covariant derivative is defined as $\nabla_\mu j_a^\mu \equiv [\partial_\mu \delta_{ac} + \epsilon_{abc} v_{\mu,b}] j_c^\mu$). More specifically, the action can be thought of as the QCD action plus an external source part,

$$S = \int d^4x \{ \mathcal{L}_{\text{QCD}} + \mathcal{L}_{\text{ext}} \}$$

$$\mathcal{L}_{\text{ext}} = \bar{q} \left(\gamma^\mu [v_\mu^a + a_\mu^a \gamma_5] \frac{\tau^a}{2} - \frac{m_q}{m_\pi^2} [m_\pi^2 + s - i \gamma_5 \tau^a p^a] \right) q. \quad (2.133)$$

With the help of the Peierls-Dyson formula [98] for the S -matrix, the Veltmann-Bell equations can be rewritten as

$$\left(X_V^a + \epsilon^{abc} p^b \frac{\delta}{\delta p^c} \right) S = 0 \quad (2.134)$$

$$\left(X_A^a - (m_\pi^2 + s) \frac{\delta}{\delta p^a} + p^a \frac{\delta}{\delta s} \right) S = 0, \quad (2.135)$$

where $X_{V,A}$ are functional differential operators involving the v_μ^a and a_μ^a fields. The feature of spontaneous chiral symmetry breaking is then imposed through appropriate boundary conditions, namely that asymptotic stable states are given in terms of (massive) pion fields, *i.e.*, for $x^0 \rightarrow \pm\infty$ one requires

$$j_A^{\mu,a}(x) = -f_\pi \partial^\mu \pi_{in,out}^a(x) \quad (2.136)$$

$$\partial_\mu j_A^{\mu,a}(x) \rightarrow f_\pi m_\pi^2 \pi_{in,out}^a(x). \quad (2.137)$$

With these boundary conditions the Veltmann-Bell equations (2.134), (2.135) can be integrated to give the so-called master formula for the $SU(2)_L \times SU(2)_R$ symmetric S -matrix for massive pions, which can be

found in Ref. [96]. From the master formula one can derive expressions for pion Greens functions in terms of the (axial-) vector currents and (pseudo-) scalar densities, as well as corresponding Ward identities. Since the S -matrix plays the role of a time evolution operator (within the Heisenberg picture), the Fourier transform of the master formula takes the form of a LSZ reduction formula, incorporating the proper chiral Ward identities, and thus has been coined “chiral reduction formula”. It allows to express hadronic on-shell scattering reactions, determined by the *on-shell* S -matrix (given by the limit of vanishing external fields $\phi \rightarrow 0$), through well-defined correlation functions and form factors. The latter have to be either inferred from other experimental information (in which case the predictions for the processes under consideration are, in principle, exact, *i.e.*, compatible with unitarity, crossing symmetry and broken chiral symmetry) or evaluated in an appropriate expansion scheme.

Applications of this formalism to calculate medium modifications are readily performed using virial-type low-density approximations, as the processes have to be expressed in terms of stable final states within the hadronic matter, *i.e.*, pions and nucleons. For electromagnetic thermal production rates, this has been carried out in Refs. [99, 100]. Starting from the usual eightfold-differential rate expression,

$$\frac{d^8 N}{d^4 x d^4 q} = -\frac{\alpha^2}{6\pi^3 q^2} W(q), \quad (2.138)$$

the thermal correlator W has been related to the time-ordered (Feynman) one by

$$W(q) = \frac{2}{1 + e^{q_0/T}} \text{Im } W^F(q)$$

$$W^F(q) = i \int d^4 x e^{iqx} \frac{1}{Z} \text{tr} [e^{(\hat{H} - \mu_N \hat{N})/T} \mathcal{T} j^\mu(x) j_\mu(0)]. \quad (2.139)$$

Up to first order in the density of either pions or nucleons the imaginary parts of the latter become

$$\text{Im } W^F(q) = -3 \text{Im } \prod_V^\circ(q) + \frac{1}{f_\pi^2} \int \frac{d^3 k}{(2\pi)^3 2\omega_\pi(k)} f^\pi(\omega_\pi(k); T) \text{Im } W_\pi^F(q, k)$$

$$+ \int \frac{d^3 p}{(2\pi)^3 2E_N(p)} f^N(E_N(p); \mu_N, T) \text{Im } W_N^F(q, p) \quad (2.140)$$

(f^π : pion Bose distribution, f^N : nucleon Fermi distribution; note that our definition of the correlation functions $\Pi(q)$ differs from the one in Refs. [99, 100] by a factor of q^2). The first term on the *r.h.s.* represents the vacuum part containing the free electromagnetic current correlator, whereas the second and third terms involve the forward scattering amplitudes of (real or time-like) photons on on-shell pions and nucleons from the medium,

$$\begin{aligned} W_\pi^F(q, k) &= i \int d^4x e^{iqx} \langle \pi(k) | \mathcal{T} j^\mu(x) j_\mu(0) | \pi(k) \rangle \\ W_N^F(q, p) &= i \int d^4x e^{iqx} \langle N(p) | \mathcal{T} j^\mu(x) j_\mu(0) | N(p) \rangle. \end{aligned} \quad (2.141)$$

The relevant expansion parameters for both cases have been quoted as $\kappa_\pi = n_\pi/2m_\pi f_\pi^2$ and $\kappa_N = \rho_N g_A^2/2m_N f_\pi^2$, which should provide reasonable lowest-order results for $\kappa \leq 0.3$, corresponding to temperatures $T \leq 140$ MeV and nucleon densities $\rho_N \leq 2.5\rho_0$. However, especially for the nucleonic case, this counting scheme may be subject to large corrections if low-lying resonances or opening thresholds are present [100], see below.

Applying the chiral reduction formulae to the scattering tensors, the relevant terms of the pionic piece take the form [99]

$$\begin{aligned} \text{Im } W_\pi^F(q, k) &\approx 12 \text{Im } \prod_V^\circ(q) - 6 \text{Im } \prod_V^\circ(k+q) + 6 \text{Im } \prod_A^\circ(k-q) \\ &\quad + 8 \left[\frac{(k \cdot q)^2}{q^2} - m_\pi^2 \right] \text{Im } \prod_V^\circ(q) \text{Re}[D_\pi^R(k+q) + D_\pi^R(k-q)] \end{aligned} \quad (2.142)$$

with D_π^R denoting the retarded pion propagator and \prod_A° the free axialvector current correlator (extracted from τ -decay data as indicated in the upper part of Fig. 2.6).

The nucleonic piece is more difficult to assess; at the photon point it can be inferred via the optical theorem from the total γN cross section,

$$e^2 \text{Im } W_N^F(q, p) = -4(s - m_N) \sigma_{\gamma d}^{\text{tot}}(s) \quad (2.143)$$

(here, the deuteron cross section has been taken as representative for the isospin summed result). For time-like photons, an absorptive part starts to build up only from loop corrections for which a one-pion loop expansion was performed for non-resonant πN states (being related to on-shell πN scattering data). However, as is obvious from the experimental γN cross section, the Δ resonance has to be included. Its contribution has been evaluated as

$$\text{Im } W_{\Delta}^F(q, p) = \text{Im} \left[\frac{4m_N m_{\Delta}}{s - m_{\Delta}^2 + im_{\Delta}\Gamma_{\Delta}^0} \right] \overline{|\mathcal{M}_{N\Delta}|^2} + (s \rightarrow u) \quad (2.144)$$

with $\overline{|\mathcal{M}_{N\Delta}|^2}$ the spin-isospin summed modulus squared of the $N\Delta$ transition amplitude. The latter has been constructed compatible with current conservation and crossing symmetry, and its parameters are constrained by electric and magnetic polarizabilities as well as the electromagnetic decay width $\Gamma_{\Delta \rightarrow N\gamma} \simeq 0.7 \text{ MeV}$. In subsequent work—after the importance of the $N(1520)$ for dilepton production has been realized [101, 102, 48, 103, 49]—the $N(1520)$ contribution has been included along similar lines as the Δ in Ref. [104]. Higher order terms $\propto K_{\pi}K_{\pi}, K_{\pi}K_N, K_NK_N$ have also been estimated and claimed to be rather small in the region of interest (*i.e.*, above invariant masses of about 200MeV).

The discussion of the numerical results for the dilepton and photon production rates in the chiral reduction formalism is deferred to Sect. 4.2, where it will be put into context with other (model) approaches, most of which are elucidated in the following Chapter.

3. MODELING VECTOR MESONS IN THE MEDIUM

So far our assessment of medium effects in the current-current correlators was of a rather general nature focusing on the QCD aspects and model independence. We have repeatedly stressed the intimate relation between vector and axialvector channels, governed by chiral symmetry. The discussion now proceeds to various models that have been employed to investigate the properties of vector and axialvector mesons in hot and dense matter. On the one hand, this allows for much more specific predictions, but also implies at least a partial loss of generality. However, a careful comparison of the underlying assumptions and associated characteristic features of the results should provide valuable information on the relevant mechanisms for chiral symmetry restoration. Large efforts have been undertaken to investigate the in-medium vector meson properties, especially those of the ρ meson, due to its prominent role in heavy-ion dilepton measurements, as will be extensively addressed in Chapter 4. Much less has been done in the axialvector channel, dominated by the $a_1(1260)$ meson. This is mainly due to the fact that experimental information, in particular concerning medium effects, is and will be scarce (the hope is, of course, that ultimately QCD lattice calculations will be able to overcome this unfortunate situation). Thus, in the following, the

emphasis will inevitably be biased towards the vector channel, in particular the ρ meson.

The various approaches can be roughly divided into two categories, namely those which are based on purely mesonic Lagrangians, addressing the impact of finite temperature, and those including baryonic fields to account for finite density effects. For each model we will first briefly discuss its construction and vacuum properties, subsequently proceeding to the in-medium applications.

3.1. Effective Meson Lagrangians: Impact of Finite Temperature

3.1.1. Gauged Linear σ -Model + VDM

Based on the presumption that for the properties of the lowest-lying meson multiplets near the phase boundary chiral symmetry restoration (rather than deconfinement) should be the prevailing feature of the QCD transition Pisarski proposed [105] to study the simplest version of an effective theory which incorporates the appropriate symmetry structure, *i.e.*, the linear **σ -model**. A low-lying genuine σ meson might not be the most realistic description of the zero temperature situation, as it strongly couples to two-pion states. As a result the width is of the order of the mass such that the σ meson does not represent a well-defined degree of freedom (or quasiparticle). He argued, however, that given the fact that at chiral restoration the pion and the sigma have to become degenerate there might well arise the situation in which the phase space for $\sigma \rightarrow \pi\pi$ is locked and the σ field becomes a well-defined excitation [106].

In the linear **σ -model** the pion and sigma fields are grouped into the standard four-dimensional vector

$$\Phi = \sigma t^0 + i\vec{\pi} \cdot \vec{t}, \quad (3.1)$$

where $\vec{t} = \vec{\tau}/2$ is defined via the standard Pauli matrices and $t^0 = 11/2$ is proportional to the unit-matrix in isospin space. The (axial-) vector fields are introduced via left- and right-handed combinations as

$$\begin{aligned} A_L^\mu &= (\omega^\mu + f_1^\mu)t^0 + (\vec{\rho}^\mu + \vec{a}_1^\mu) \cdot \vec{t} \\ A_R^\mu &= (\omega^\mu - f_1^\mu)t^0 + (\vec{\rho}^\mu - \vec{a}_1^\mu) \cdot \vec{t} \end{aligned} \quad (3.2)$$

in obvious notation. The crucial step is now to assume that the $SU(2)$ chiral transformations for vector fields are *local* ones, promoting it to a gauge symmetry. The basic motivation is a natural emergence of

conventional vector dominance. Once the field-strength tensor and covariant derivative on the scalar fields are accordingly defined,

$$\begin{aligned} F_{L,R}^{\mu\nu} &= \partial^\mu A_{L,R}^\nu - \partial^\nu A_{L,R}^\mu - ig[A_{L,R}^\mu, A_{L,R}^\nu] \\ D^\mu \Phi &= \partial^\mu \Phi - ig(A_L^\mu \Phi - \Phi A_R^\mu), \end{aligned} \quad (3.3)$$

the gauged linear σ -model Lagrangian takes the form

$$\begin{aligned} \mathcal{L}_{\text{gl}\sigma} &= \text{tr}|D_\mu \Phi|^2 - 2ht^0 \text{tr}(\Phi) - \mu^2 \text{tr}|\Phi|^2 + \frac{1}{2} \lambda (\text{tr}|\Phi|^2)^2 \\ &\quad + \frac{1}{4} \text{tr}((F_L^{\mu\nu})^2 + (F_R^{\mu\nu})^2) + \frac{1}{2} m_0^2 \text{tr}((A_L^\mu)^2 + (A_R^\mu)^2). \end{aligned} \quad (3.4)$$

The corresponding vector (Noether) current is then solely determined by the mass term, resulting in

$$j_{L,R}^\mu = \frac{m_0^2}{g} A_{L,R}^\mu. \quad (3.5)$$

This is precisely the desired current-field identity of the vector dominance model [107] (VDM) where g is the universal (dimensionless) vector coupling and m_0 the (bare) vector meson mass. Furthermore, in Eq. (3.4), λ denotes the (dimensionless) scalar coupling. The “mass parameter” μ^2 is taken positive to generate the spontaneous breakdown of chiral symmetry in the physical vacuum. Explicit chiral symmetry breaking through a “magnetic background field” h ensures that the resulting vacuum state is aligned in the σ direction implying a non-vanishing expectation value $\langle \sigma \rangle \equiv \sigma_0 = \mu/\sqrt{\lambda}$ and a finite pion mass. However, after the standard shift $\sigma \rightarrow \sigma_0 + \sigma$ a “spurious” mixing term of the form $g\vec{a}_1^\mu \cdot \partial_\mu \vec{\pi}$ between the pion and the a_1 field emerges which has to be eliminated by a shift of the a_1 field,

$$\vec{a}_1^\mu \rightarrow \vec{a}_1^\mu - \frac{g\sigma_0}{m_0^2 + (g\sigma_0)} \partial^\mu \vec{\pi}. \quad (3.6)$$

As a consequence the vector and axialvector meson masses, determined by the $\text{tr}(A_{L,R})^2$ term, split according to

$$\begin{aligned} m_\rho^2 &= m_\omega^2 = m_0^2 \\ m_{a_1}^2 &= m_{f_1}^2 = m_0^2 + (g\sigma_0)^2, \end{aligned} \quad (3.7)$$

and the standard relations of the linear σ -model are modified as

$$\begin{aligned}
f_\pi &= \frac{m_\rho}{m_{a_1}} \sigma_0 \\
m_\pi^2 &= \left(\frac{m_\rho}{m_{a_1}} \right)^2 \frac{h}{\sigma_0} \\
m_\sigma^2 &= \frac{h}{\sigma_0} + 2\lambda\sigma_0^2.
\end{aligned} \tag{3.8}$$

At the mean-field level, the parameter values are fixed as $\sigma_0 = 152 \text{ MeV}$, $g = 6.55$, $h = (102 \text{ MeV})^3$ by imposing the experimental values for $f_\pi = 93 \text{ MeV}$, $m_\pi = 138 \text{ MeV}$, $m_\rho = 770 \text{ MeV}$ and $m_{a_1} = 1260 \text{ MeV}$. Some latitude arises in the choice of λ and μ due to the uncertainty in the σ mass; when identifying it as $m_\sigma = 600 \text{ MeV}$, one has $\lambda = 7.6$ and $\mu = 412 \text{ MeV}$. As emphasized in Ref. [105], the virtue of complying with VDM through the requirement of locally gauge invariant couplings greatly restricts the number of possible interaction terms (*i.e.*, the mere requirement of a global chiral symmetry would allow many more terms).

When moving to the finite-temperature modifications, Pisarski evaluated selfenergy corrections in terms of a thermal loop expansion to lowest order in g for two limiting cases. At low temperatures and in the chiral limit, one can additionally expand in small pion momenta $p \sim T \ll m_\rho, m_{a_1}$ to obtain for the on-shell thermal pole masses of the ρ and a_1 meson [105]

$$\begin{aligned}
m_\rho^2(T) &\approx m_\rho^2 - \frac{g^2 \pi^2 T^4}{45 m_\rho^2} \left(\frac{4m_{a_1}^2 (3m_\rho^2 + 4q^2)}{(m_{a_1}^2 - m_\rho^2)^2} - 3 \right) + \dots \\
m_{a_1}^2(T) &\approx m_{a_1}^2 + \frac{g^2 \pi^2 T^4}{45 m_\rho^2} \\
&\quad \times \left(\frac{4m_{a_1}^2 (3m_\rho^2 + 4q^2)}{(m_{a_1}^2 - m_\rho^2)^2} + \frac{2m_\rho^4}{m_{a_1}^2 (m_{a_1}^2 - m_\sigma^2)} - \frac{m_{a_1}^2}{m_\rho^2} \right) + \dots
\end{aligned} \tag{3.9}$$

This result is consistent with the model-independent mixing theorem (2.103) of Dey *et al.* [88] stating that there are no mass corrections to order T^2 . However, as stressed in Ref. [105], this only holds strictly on the mass shell, *i.e.*, for $q^2 = m_\rho^2$, but not away from it. Moreover, for explicitly broken chiral symmetry, *i.e.*, for $h \neq 0$, the on-shell a_1 pole mass does pick up a T^2 -term

$$m_{a_1}^2(T) \approx m_{a_1}^2 + \frac{g^2 m_\pi^2 T^2}{4 m_\sigma^2} + \dots \quad (3.10)$$

One should also note that in Ref. [108], where the $O(T^4)$ corrections have been assessed using the OPE in connection with deep-inelastic scattering amplitudes on the pion, *both* the ρ and a_1 masses have been found to decrease.

As a second limit Pisarski considered the behavior of the masses at the critical temperature for chiral restoration. For the gauged linear σ -model the latter is given in terms of the zero temperature σ expectation value by $T_c^\chi = \sqrt{2}\sigma_0 \approx 215\text{ MeV}$ (in the chiral limit). By definition, $\sigma_0 \rightarrow 0$ for $T \rightarrow T_c^\chi$, such that in the immediate vicinity of the transition several of the trilinear vertices $\propto \sigma_0$ encoded in the Lagrangian (3.4) vanish. Neglecting furthermore small terms of order T^2/m_ρ^2 , the temperature corrections to both the ρ and a_1 selfenergies turn out to be

$$\sum_{\rho, a_1}^{T_c^\chi} = \frac{1}{6} g^2 T^2 \quad (3.11)$$

resulting in $m_\rho^2(T_c^\chi) = m_{a_1}^2(T_c^\chi) = (2m_\rho^2 + m_{a_1}^2)/3 = (962\text{ MeV})^2$ (note that the $(g\sigma_0)^2$ -term in Eq. (3.7) vanishes at T_c^χ). Since the rather large value of the coupling constant g implies that a lowest-order calculation cannot be quantitatively trusted the emphasis here is not on the exact mass values but rather on the qualitative feature that ρ and a_1 masses become degenerate at a common value *in between* their vacuum masses. One should note the somewhat peculiar feature that in the low-temperature limit (3.9) the ρ and a_1 masses start out by moving *apart*. As another striking result the ω meson mass turns out not to be affected at all, $m_\omega(T_c^\chi) = m_\omega$, thus lifting the (theoretically not well-understood) zero temperature degeneracy with the ρ meson.

Pisarski also studied situations where vector meson dominance does not hold, *e.g.*, when replacing the local chiral symmetry-breaking vector mass term $\propto m_0^2$ in Eq. (3.4) by

$$\mathcal{L}_\zeta = \zeta \text{tr}(|\Phi|)^2 \text{tr}[(A_L^\mu)^2 + (A_R^\mu)^2]. \quad (3.12)$$

In this case the vacuum ρ and a_1 masses are still split by the spontaneous breaking term $(g\sigma_0)^2$, but an explicit finite-temperature calculation shows that close to the transition the masses uniformly decrease to $m_\rho(T_c^\chi) = m_{a_1}(T_c^\chi) = m_\omega(T_c^\chi) = 629\text{ MeV}$. Other possible terms outside the VDM might induce different behavior. Thus, within the gauged linear σ -model,

the fate of the (axial-) vector masses (especially for the ρ) crucially depends on whether vector meson dominance, as represented by the field-current identity Eq. (3.5), continues to hold at finite temperature.

3.1.2. Massive Yang–Mills Approach

As a second variant of the chiral Lagrangian framework to study in-medium vector meson properties we discuss the massive Yang–Mills (MYM) approach. It is very similar in spirit to the gauged linear σ -model, only that the σ degrees of freedom have been eliminated using the non-linear realization of the $SU(3)_L \times SU(3)_R$ chiral symmetry [109]. From a phenomenological point of view this might be the more appropriate effective theory at zero and low temperatures. The Lagrangian is expressed through a matrix representation

$$U = \exp(i\sqrt{2}\phi/f_\pi), \quad \phi \equiv \phi_a \frac{\tau_a}{\sqrt{2}}, \quad (3.13)$$

where, in the $SU(2)$ case, the isospin index a of the pseudoscalar fields ϕ_a runs from 1 to 3, contracted with the Pauli matrices τ_a . The vector and axialvector fields are introduced in complete analogy to the linear σ -model of the previous Section, *i.e.*, as massive gauge fields. Defining them via

$$\begin{aligned} V^\mu &\equiv V_a^\mu \tau_a / \sqrt{2}, & A^\mu &\equiv A_a^\mu \tau_a / \sqrt{2} \\ A_L^\mu &\equiv \frac{1}{2}(V^\mu + A^\mu), & A_R^\mu &\equiv \frac{1}{2}(V^\mu - A^\mu) \end{aligned} \quad (3.14)$$

leads to the Lagrangian

$$\begin{aligned} \mathcal{L}_{\text{mym}} &= \frac{1}{4} f_\pi^2 \text{tr}[D_\mu U D^\mu U^\dagger] - \frac{1}{2} \text{tr}[(F_L^{\mu\nu})^2 + (F_R^{\mu\nu})^2] \\ &+ m_0^2 \text{tr}[(A_L^\mu)^2 + (A_R^\mu)^2] - i\xi \text{tr}[D_\mu U D^\mu U^\dagger F_L^{\mu\nu} + D_\mu U D^\mu U^\dagger F_R^{\mu\nu}] \\ &+ \sigma \text{tr}[F_L^{\mu\nu} U F_{R\mu\nu} U^\dagger]. \end{aligned} \quad (3.15)$$

Note that the normalization convention chosen in Eq. (3.14) (which differs from the previous Section by a factor of $1/\sqrt{2}$), entails a factor of 2 in the terms bilinear in the (axial-) vector fields. Also, the $\rho\pi\pi$ coupling constant picks up an additional factor in its relation to the gauge coupling constant g , *i.e.*, $g = \sqrt{2}g_{\rho\pi\pi}$. This is due to the definition of the covariant derivative which in (3.15) is taken as

$$D^\mu U = \partial^\mu - ig(A_L^\mu U - UA_R^\mu). \quad (3.16)$$

The last two terms in the Lagrangian (3.15) are so-called non-minimal coupling terms (*i.e.*, of higher order in the derivatives than the other ones), which are necessary for a realistic description of the vector and axialvector meson sector in vacuum. The four free parameters (m_0, g, σ, ξ) are readily adjusted to reproduce the phenomenological masses and decay widths of ρ, ω, a_1 , etc.

At finite temperature the calculation of the vector correlator—saturated by the ρ meson in VDM—has been shown [110] to obey the general low-energy theorem of Ref. [88]. To lowest order in the “mixing parameter” $\epsilon = T^2/6f_\pi^2$, the finite-temperature ρ meson selfenergy receives two corrections from thermal one-pion loop diagrams. The relevant terms in the MYM Lagrangian (3.15),

$$\begin{aligned} \mathcal{L}_{\text{mym}} = & \frac{1}{2} m_\rho^2 \bar{\rho}_\mu^2 + [m_\rho^2 + g^2 f_\pi^2] \bar{a}_{1\mu}^2 + g^2 f_\pi \vec{\pi} \times \bar{\rho}^\mu \cdot \bar{a}_{1\mu} \\ & + \frac{1}{2} g^2 [\bar{\rho}_\mu^2 \vec{\pi}^2 - \bar{\rho}^\mu \cdot \vec{\pi} \bar{\rho}_\mu \cdot \vec{\pi}] + \dots, \end{aligned} \quad (3.17)$$

induce a $\rho\rho\pi\pi$ “tadpole” diagram (last term) as well as a πa_1 resonance loop (prelast term). The leading temperature dependence is driven by loops of pions from the heat bath. When evaluated in the chiral limit the resulting vector correlator takes the form

$$\begin{aligned} \Pi_V^{\mu\nu}(q) = & \left(g^{\mu\nu} - \frac{q^\mu q^\nu}{m_\rho^2} \right) g_\rho^2 \left(\frac{i}{m_\rho^2 - q^2} + \frac{i}{m_\rho^2 - q^2} ig^2 f_\pi^2 \epsilon \frac{i}{m_\rho^2 - q^2} \right. \\ & \left. + \frac{i}{m_\rho^2 - q^2} \frac{i^3 g^4 f_\pi^4 \epsilon}{m_{a_1}^2 - q^2} \frac{i}{m_\rho^2 - q^2} \right), \end{aligned} \quad (3.18)$$

where the second and third terms arise from the interaction vertices in Eq. (3.17) and $g_\rho = m_\rho^2/g$ is the VDM coupling constant. Making use of the Weinberg relation, $m_{a_1}^2 = m_\rho^2 + g^2 f_\pi^2$, one finally obtains

$$\Pi_V^{\mu\nu}(q) = \left(g^{\mu\nu} - \frac{q^\mu q^\nu}{m_\rho^2} \right) g_\rho^2 \left[(1 - \epsilon) \frac{i}{m_\rho^2 - q^2} + \epsilon \frac{i}{m_{a_1}^2 - q^2} \right] \quad (3.19)$$

in accordance with the model-independent mixing theorem (2.103). Deviations occur, *e.g.*, through the finite pion mass or when including the non-minimal coupling term with $\sigma \neq 0$ in the Lagrangian (3.15). As reported by Song [111] the ρ meson mass tends to increase whereas the a_1 mass decreases. Quantitatively, however, the temperature

dependencies seem to be very weak. The masses only change by a few percent even at temperatures as high as $T = 200\text{MeV}$ which already is clearly beyond the range of applicability of the low-temperature expansion. Before that chiral restoration is likely to be realized through the mixing effect.

3.1.3. Hidden Local Symmetry

The third chiral Lagrangian framework to incorporate vector mesons is the so-called “Hidden Local Symmetry” (HLS) approach proposed by Bando *et al.* [112]. It originated from the observation that the conventional $[SU(2)_L \times SU(2)_R]_{global}$ -symmetric non-linear σ -model Lagrangian,

$$\mathcal{L}_{nl\sigma} = \frac{1}{4} f_\pi^2 \text{tr}[\partial_\mu U \partial^\mu U^\dagger] \quad (3.20)$$

(U as given in Eq. (3.13)), can be recast in a form that exhibits an additional $[SU(2)_V]_{local}$ symmetry. This can be made explicit by rewriting the U -field as

$$U \equiv \xi_L^\dagger \xi_R \quad (3.21)$$

in terms of new $SU(2)$ -valued variables ξ_L and ξ_R (notice that this implies the appearance of three additional, unphysical scalar degrees of freedom). Defining the usual covariant derivative

$$\mathcal{D}^\mu = \partial^\mu - ig V^\mu \quad (3.22)$$

with an auxiliary gauge field $V^\mu = V_a^\mu \tau_a/2$ and associated gauge coupling g allows to construct two invariants under $[SU(2)_L \otimes SU(2)_R]_{global} \times [SU(2)_V]_{local}$ transformations, namely

$$\begin{aligned} \mathcal{L}_A &= -\frac{1}{4} f_\pi^2 \text{tr}[\mathcal{D}^\mu \xi_L \cdot \xi_L^\dagger + \mathcal{D}^\mu \xi_R \cdot \xi_R^\dagger] \\ \mathcal{L}_V &= -\frac{1}{4} f_\pi^2 \text{tr}[\mathcal{D}^\mu \xi_L \cdot \xi_L^\dagger - \mathcal{D}^\mu \xi_R \cdot \xi_R^\dagger]. \end{aligned} \quad (3.23)$$

When imposing the so-called unitary gauge

$$\xi_L^\dagger = \xi_R = \exp(-\pi/f_\pi) \quad (3.24)$$

(which eliminates the unphysical scalar degrees of freedom) it can be verified that, with arbitrary constant a , the combination

$$\mathcal{L} = \mathcal{L}_A + a\mathcal{L}_V \quad (3.25)$$

is indeed equivalent to Eq. (3.20). In fact, \mathcal{L}_A is in one-to-one correspondence with the starting Lagrangian $\mathcal{L}_{\text{nl}\sigma}$, whereas \mathcal{L}_V identically vanishes by virtue of the equations of motion for the gauge field. It can be assigned a physical significance by assuming that it develops its own dynamics, generating a kinetic energy term in the Lagrangian (usually attributed to the underlying QCD-dynamics or quantum effects at the composite level [112]). The physical vector field is then identified with the (isovector) ρ meson, and the HLS Lagrangian becomes

$$\begin{aligned} \mathcal{L}_{\text{hls}} &= \mathcal{L}_A + a\mathcal{L}_V - \frac{1}{4}(\vec{\rho}^{\mu\nu})^2 \\ &= \frac{1}{4}f_\pi^2 \text{tr}[\partial_\mu U \partial^\mu U^\dagger] - \frac{1}{4}\vec{\rho}^{\mu\nu} \cdot \vec{\rho}_{\mu\nu} + \frac{a}{2}g^2 f_\pi^2 \vec{\rho}_\mu^2 \\ &\quad + \frac{a}{2}g\vec{\rho}^\mu \cdot (\vec{\pi} \times \partial_\mu \vec{\pi}) + \mathcal{O}(\vec{\pi}^4) \end{aligned} \quad (3.26)$$

with the non-abelian field strength tensor

$$\vec{\rho}^{\mu\nu} = \partial^\mu \vec{\rho}^\nu - \partial^\nu \vec{\rho}^\mu + g\vec{\rho}^\mu \times \vec{\rho}^\nu. \quad (3.27)$$

The second line in Eq. (3.26) has been obtained using the weak-field expansion for the ξ -fields. One reads off that

$$g_{\rho\pi\pi} = \frac{1}{2}ag \quad (3.28)$$

$$m_\rho^2 = ag^2 f_\pi^2, \quad (3.29)$$

i.e., the gauge symmetry is spontaneously broken generating a mass for the vector field via the Higgs mechanism. This is accompanied by the disappearance of the scalar modes which have turned into the longitudinal components of now massive vectors. A particular advantage of the HLS framework is the unique way of introducing electromagnetic interactions. Since the photon couples to the charge $Q = I_3^{(L)} + I_3^{(R)}$ corresponding to the global $[SU(2)_L \otimes SU(2)_R]$ isospin symmetry, the electromagnetic field can be introduced as a global gauge symmetry. Thus the covariant derivative (3.22) can be simply extended to

$$\mathcal{D}^\mu \xi_{L,R} = (\partial^\mu - igV^\mu)\xi_{L,R} + e_0 \xi_{L,R} B^\mu \frac{\tau_3}{2} \quad (3.30)$$

with the $U(1)_Q$ gauge field B^μ and associated coupling e_0 . In addition, the corresponding kinetic term $-\frac{1}{4}B_{\mu\nu}^2 (B_{\mu\nu} = \partial_\mu B_\nu - \partial_\nu B_\mu)$ has to be added to

the HLS Lagrangian in Eq. (3.26). After rediagonalizing the fields one finds the following mass relations:

$$m_\gamma^2 = 0, \quad m_{\rho^0}^2 = a(g^2 + e_0^2)f_\pi^2, \quad m_{\rho^\pm}^2 = ag^2f_\pi^2. \quad (3.31)$$

For the special case of $a = 2$, Eqs. (3.28) and (3.29) give the universality of the ρ couplings as well as the KSFR relation [86]. Moreover, vector dominance emerges due to the vanishing of the direct $\gamma\pi\pi$ coupling and the $\rho\text{-}\gamma$ coupling is given as $g_{\rho\gamma} = m_\rho^2/g$.

Let us now turn to the finite temperature calculations performed within the HLS framework. The minimal version of the HLS Lagrangian does not involve the a_1 field. Nevertheless, the low-energy theorem, Eq. (2.103), ought to be satisfied for the vector correlator. This is indeed the case and is realized through temperature-dependent corrections to the VDM coupling constant $g_{\rho\gamma}$. As has been shown in Ref. [110], to lowest order in ϵ , the thermal pion tadpole loop on the $\rho - \gamma$ vertex, shown in Fig. 3.1, leads to correction factor $(1 - \frac{1}{2}\epsilon)$. Therefore

$$g_{\rho\gamma}^2(T) = (1 - \epsilon)g_{\rho\gamma}^2 + \mathcal{O}(\epsilon^2). \quad (3.32)$$

Moreover, in the “minimal” HLS there is no $\rho\rho\pi\pi$ contact interaction. Thus, to lowest thermal pion-loop order, the in-medium ρ mass is only modified through temperature effects in the two-pion loop which do not pick up T^2 -corrections due to the additional derivative in the $\rho\pi\pi$ coupling.

For practical purposes the HLS approach has been mainly employed to study finite-temperature modifications of the pion electromagnetic form factor, F_π , and dilepton/photon production rates. The latter will be discussed in Chap. 4. In the thermal medium, the former can be defined through the total electromagnetic vertex for the $\pi\pi \rightarrow \gamma$ transition,

$$\Gamma_\mu^{\gamma\pi\pi}(T) = (p_\mu + p'_\mu)F_\pi(q_0, \vec{q}; T). \quad (3.33)$$

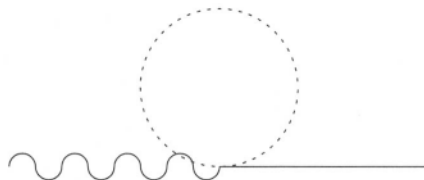


Fig. 3.1. Finite temperature correction to the $\gamma\rho$ vertex through a thermal pion tadpole loop in the HLS approach (wavy line: photon, solid line: ρ meson, dotted line: pion).

For $a = 2$ and in free space, it reduces to the well-known VDM expression,

$$F_\pi^o(M) = \frac{g_{\rho\pi\pi} g_{\rho\gamma}}{M^2 - (m_\rho^{(0)})^2 + \sum_{\rho\pi\pi}(M)}. \quad (3.34)$$

In Ref. [113], $F_\pi(T)$ has been evaluated in terms of thermal one-pion loop corrections (using $a = 2$). The total $\gamma\pi\pi$ vertex function can then be written as

$$\Gamma_\mu(T) = \Gamma_\mu^{\text{mix}} + \Gamma_\mu^{\text{vert}} + \Gamma_\mu^{\text{rho}} + \Gamma_\mu^{\text{dir}}, \quad (3.35)$$

where Γ_μ^{mix} encodes the pion-tadpole diagram (inducing $V-A$ mixing diagrammatically represented in Fig. 3.1), Γ_μ^{vert} represents thermal-loop corrections of the $\pi\pi\rho$ vertex (left panel of Fig. 3.2) and Γ_μ^{rho} accounts for the temperature dependence in the ρ selfenergy $\Sigma_{\rho\pi\pi}$ (*i.e.*, in the two-pion bubble). The appearance of a direct $\gamma\pi\pi$ vertex Γ_μ^{dir} is solely due

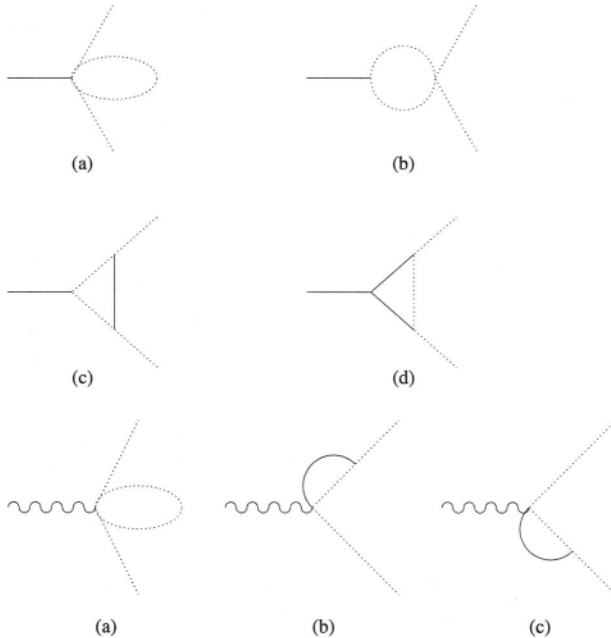


Fig. 3.2. Thermal loop corrections to the $\rho\pi\pi$ vertex (top) as well as the “direct” $\gamma\pi\pi$ vertex (bottom); the latter vanishes at zero temperature in the VDM (*i.e.*, for $a = 2$ in the HLS framework). The figures are taken from Ref. [113].

to finite-temperature vertex modifications, induced by the diagrams shown in the right panel of Fig. 3.2. In the limit of vanishing three-momentum, $\vec{q} = 0$, the in-medium form factor can be characterized by a single scalar function (see Eq. (2.100)) depending on invariant mass M only, according to

$$F_\pi(T) = Z_\pi(T) \left[\frac{g_{\rho\pi\pi}(T) g_{\rho\gamma}(T)}{M^2 - m_\rho^2 + i m_\rho \Gamma_\rho^\circ - \sum_\rho(T)} + F'_\pi(T) \right]. \quad (3.36)$$

Here, $Z_\pi(T)$ is the pion wave function renormalization constant. It can be inferred from the relevant Ward-Takahashi identity,

$$(p^\mu - p'^\mu) \Gamma_\mu(p, p') = \sum_\pi(p) - \sum_\pi(p'), \quad (3.37)$$

which ensures gauge invariance of the in-medium $\gamma\pi\pi$ transition with Σ_π denoting the in-medium pion selfenergy to be evaluated to thermal one-loop order. For on-shell pions of vanishing three momentum, as considered in Ref. [113], the simple relation

$$Z_\pi(T) = \left[1 - \frac{\partial \sum_\pi}{\partial p_0^2} (p_0 = m_\pi, \vec{p} = 0) \right]^{-1} \quad (3.38)$$

is obtained. In Eq. (3.36), the temperature-dependent $\rho\gamma$ and $\rho\pi\pi$ couplings, the temperature part of the ρ selfenergy, $\Sigma_{\rho\pi\pi}^T$, as well as the direct $\gamma\pi\pi$ piece, F'_π , arise from the various vertex terms in Eq. (3.35), respectively ($\Gamma_{\rho\pi\pi}^\circ$ denotes the free ρ decay width, and the real part of the free ρ selfenergy has been absorbed into the physical ρ meson mass, m_ρ). The resulting pion electromagnetic form factor is displayed in Fig. 3.3. One observes a strong suppression with increasing temperature over the entire invariant mass range which, to a large extent, is driven by the reduction of the vector dominance coupling $g_{\rho\gamma}(T)$, representing the vector-axial vector mixing effect. One should note, however, that the imaginary part of the vector correlator (which in VDM coincides with the imaginary part of the ρ meson propagator, *i.e.*, the spectral function), involves an additional factor from the imaginary part of the in-medium ρ selfenergy; *e.g.*, in VDM the isovector correlator is related to the pion electromagnetic form factor through

$$\text{Im} \prod_V^{I=1} = \frac{\text{Im} \sum_{\rho\pi\pi}}{g_{\rho\pi\pi}^2} |F_\pi(T)|^2. \quad (3.39)$$

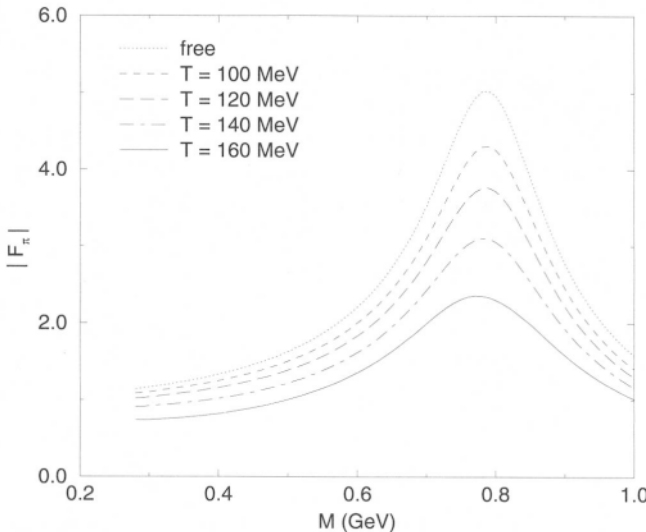


Fig. 3.3. Pion electromagnetic form factor in a finite temperature pion gas as calculated within the hidden local symmetry approach in Ref. [113].

Within the quasiparticle approximation for pions, one obtains

$$\text{Im} \sum_{\rho\pi\pi}(q_0 = M, \vec{q} = 0) \propto \frac{k^4}{\omega_\pi(k)^2} \left| \frac{\partial \omega_\pi(k)}{\partial k} \right|^{-1} \quad (3.40)$$

with the in-medium pion dispersion relation $\omega_\pi(k)$. In a pion gas, the latter is softened at small momenta due to the attractive interaction with thermal pions in the $\pi\pi \rightarrow \rho$ channel, causing a reduction of the group velocity $v_k = |\partial \omega_\pi(k)/\partial k|^{-1}$. This generates some enhancement in the vector correlator at low M , which is not captured by the electromagnetic form factor shown in Fig. 3.3 (the functional form of $\Sigma_{\rho\pi\pi}$ as quoted in Eq. (3.40) should be taken with care. It only leads to a gauge invariant vector correlator in connection with the Z_π^2 factor (3.38) which in Ref. [113] has been absorbed into the definition of $|F_\pi|^2$. In fact, one can show that $Z_\pi^2 k^2 / \omega_\pi(k)^2 = v_k^2$, which reduces the effect of the pion softening, see, e.g., Ref. [114] for a nice discussion on this point).

Qualitatively similar features for the in-medium behavior of the pion electromagnetic form factor have been found earlier within a schematic treatment in Ref. [115]. Starting from the on-shell expression for the free ρ meson decay width (ignoring any pion mass),

$$\Gamma_\rho^\circ = \frac{g_{\rho\pi\pi}^2}{4\pi} \frac{m_\rho}{12}, \quad (3.41)$$

the finite temperature corrections have been estimated assuming the validity of the in-medium KSFR relation, $2g_{\rho\pi\pi}^2 f_\pi^2 = m_\rho^2$, as well as an unmodified ρ mass (later on it has been realized that $m_\rho(T)$ does indeed not attain corrections to lowest order $O(T^2)$ [116], as said before). Then, using the lowest-order chiral perturbation theory result for the pion decay constant (for three massless flavors),

$$f_\pi(T) = f_\pi(1 - T^2/8f_\pi^2) \quad (3.42)$$

(for $N_f = 2$ the coefficient 1/8 is to be replaced by 1/12), the temperature dependence of the ρ decay width has been cast in the form

$$\Gamma_\rho(T) \simeq \frac{\Gamma_\rho^\circ}{1 - T^2/4f_\pi^2}, \quad (3.43)$$

indicating a broadening with increasing T . Vertex corrections of the $\pi\pi\rho$ coupling as required by Ward identities to ensure the conservation of the vector current have not been included in this estimate. When naively extrapolating Eq. (3.43) to high temperatures one finds the ρ width to diverge at $T = 2f_\pi \simeq 185$ MeV (230 MeV when using the two-flavor result for $f_\pi(T)$). In Refs. [117, 115] this kind of resonance melting has been qualitatively associated with the approach towards color deconfinement.

3.1.4. Phenomenological Meson Lagrangians

The chiral Lagrangian frameworks discussed in the previous Sections allow for a systematic investigation of the low-temperature chiral dynamics of the vector meson properties. The inclusion of higher resonances, however, can become a quite formidable task due to the increasing number of interaction vertices. Furthermore, chiral symmetry does not always give unique prescriptions for the latter, as we have seen above. Since the impact of certain meson resonances, which have not been incorporated via chiral Lagrangians so far, may be non-negligible more phenomenologically oriented approaches have been pursued [118, 119, 120, 47, 121, 122, 123]. They aim at including the empirically important interactions in a tractable way that also respects the relevant symmetries, such as vector current conservation or chiral symmetry. In the following, we will elaborate on two variants that have been employed in this context, namely kinetic-theory and many-body type calculations.

At low and moderate temperatures the thermal meson gas is dominated by the light pseudoscalar Goldstone bosons $P = \pi, K, \bar{K}$. A rather extensive treatment of the possible scattering processes of on-shell vector mesons V in such a system has been undertaken by Haglin [120]. He specified the following interaction Lagrangians (isospin structure suppressed)

$$\begin{aligned}\mathcal{L}_{VPP} &= G_{VPP} V^\mu P \partial_\mu P \\ \mathcal{L}_{VVP} &= G_{VVP} \epsilon_{\mu\nu\alpha\beta} \partial^\mu V^\nu \partial^\alpha V^\beta P \\ \mathcal{L}_{AVP} &= G_{AVP} A_{\mu\nu} V^{\mu\nu} P\end{aligned}\quad (3.44)$$

for the exchange of pseudoscalar, vector (V) and axialvector (A) mesons, respectively ($V^{\mu\nu}$ and $A^{\mu\nu}$ denote the usual field strength tensors). The average collision rate for the vector mesons in binary collisions with particles h from the heat bath, $Vh \rightarrow 34$ was then obtained from the kinetic theory expression

$$\begin{aligned}\bar{\Gamma}_V^{\text{coll}}(T) &= \frac{g_V g_h}{n_V(T)} \int d^3 \tilde{p}_V d^3 \tilde{p}_h d^3 \tilde{p}_3 d^3 \tilde{p}_4 (2\pi)^4 \delta^{(4)}(p_V + p_h - p_3 - p_4) \\ &\times |\overline{\mathcal{M}}_{ph \rightarrow 34}|^2 f^V(T) f^h(T) [1 + f^3(T)] [1 + f^4(T)],\end{aligned}\quad (3.45)$$

where $d^3 \tilde{p}_i \equiv d^3 p_i / 2\omega_i(p_i)(2\pi)^3$, etc., g_i are the spin-isospin degeneracy factors, $f'(T)$ thermal Bose-Einstein distribution functions, and $n_V(T)$ is the number density of the vector meson V . The coherent sum of invariant amplitudes,

$$\mathcal{M}_{pP} = \sum_R \mathcal{M}_{pPR}, \quad (3.46)$$

has been computed for both s - and t -channel exchanges of mesons R . For elastic $\rho\pi$ scattering, $R = \{\pi, \omega, \phi, a_1(1260), \omega(1390)\}$, for ρK scattering, $R = K_1(1270)$, and for $\omega\pi$ interactions, $R = \{\rho, b_1(1235)\}$ were used. For the ϕ meson the dominant processes involve kaon exchange (including inelastic channels such as $\phi\pi \rightarrow K^*K$ or $\phi K \rightarrow K^*\pi$). The final results, displayed in Fig. 3.4, reveal a moderate collisional broadening of about 40MeV for the ρ meson at $T = 150$ MeV. A similar value of ~ 30 MeV has been found for the ω meson in which case, however, it amounts to a factor of four times its natural width. The effects for the ϕ meson are smaller.

Along similar lines, Gao *et al.* [122] extended Haglin's analysis for $\rho\pi$ scattering by including isospin-exchange interactions such as $\pi^+ \rho^0 \rightarrow$

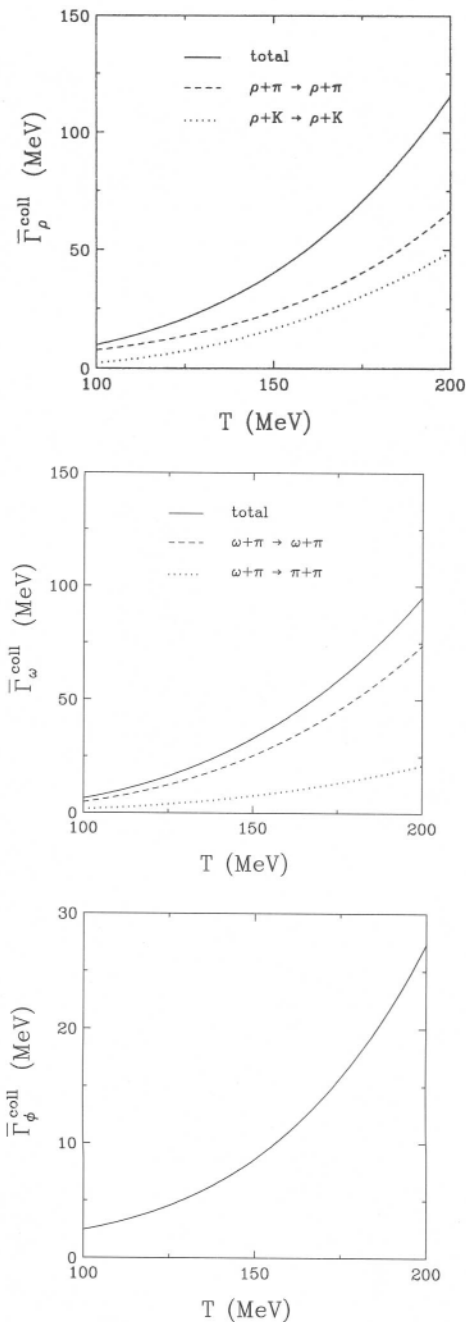


Fig. 3.4. Temperature dependence of the collisional broadening of ρ , ω and ϕ mesons (from top to bottom) as calculated in the kinetic theory approach of Ref. [120].

$\pi^0\rho^+$ and by using a different regularization method for the singularity in the t -channel pion-exchange diagram. He also employed a somewhat modified $\pi\rho a_1$ vertex which improves the phenomenology of the $a_1 \rightarrow \pi\rho$ decay [124]. In addition, the in-medium broadening of the $\rho\pi\pi$ decay width through Bose-Einstein enhancement factors of the pions (which will be discussed in more detail below) were accounted for. The resulting ρ meson spectral function,

$$A_\rho(M) = -\frac{2 \operatorname{Im} \sum_\rho(M; T)}{\left[M^2 - m_\rho^2 - \operatorname{Re} \sum_\rho(M; T)\right]^2 + [\operatorname{Im} \sum_\rho(M; T)]^2}, \quad (3.47)$$

has been obtained in terms of a total in-medium ρ selfenergy,

$$\sum_\rho(M; T) = \sum_{\rho\pi\pi}(M; T) + \sum_\rho^{\text{coll}}(T), \quad (3.48)$$

consisting of a medium-modified $\rho \rightarrow \pi\pi$ part (including the Bose enhancement) and a collisional contribution that has been approximated by its on-shell value (*i.e.*, for $M = m_\rho$). Therefore it depends on temperature only. As apparent from Fig. 3.5, the ρ meson exhibits a thermal broadening which substantially exceeds the previous estimate by Haglin: at $T = 150$ MeV, the scattering contribution from a pion gas turns out to be $\bar{\Gamma}_\rho^{\text{coll}} = 58$ MeV (see also right panel of Fig. 3.5), whereas the in-medium Bose-enhancement of the $\rho \rightarrow \pi\pi$ decay width amounts to 25 MeV. The three-momentum dependence of the spectral function is rather weak.

The evaluation of the in-medium vector meson properties in the kinetic theory treatments of Refs. [120, 122] was restricted to physical (on-shell) pole masses m_ν . On the other hand, one might expect important effects from off-shell dynamics especially for the ρ meson as it is characterized by an appreciable width already in free space (this, in turn, marks its distinguished role for low-mass dilepton yields, $M_H < m_\rho$, in heavy-ion reactions, to be discussed in Chap. 4). Off-shell dynamics are naturally accounted for within a many-body treatment of in-medium selfenergies, as we are going to discuss now.

The usual starting point is a microscopic model for the ρ meson with coupling to its “pion cloud” via two-pion states. This not only renders the correct decay width but also quantitatively describes its energy dependence over a broad range of invariant mass as encoded, *e.g.*, in $\pi\pi$ P -wave scattering phase shifts or the pion electromagnetic form factor. Given the free $\pi + \rho$ Lagrangian,

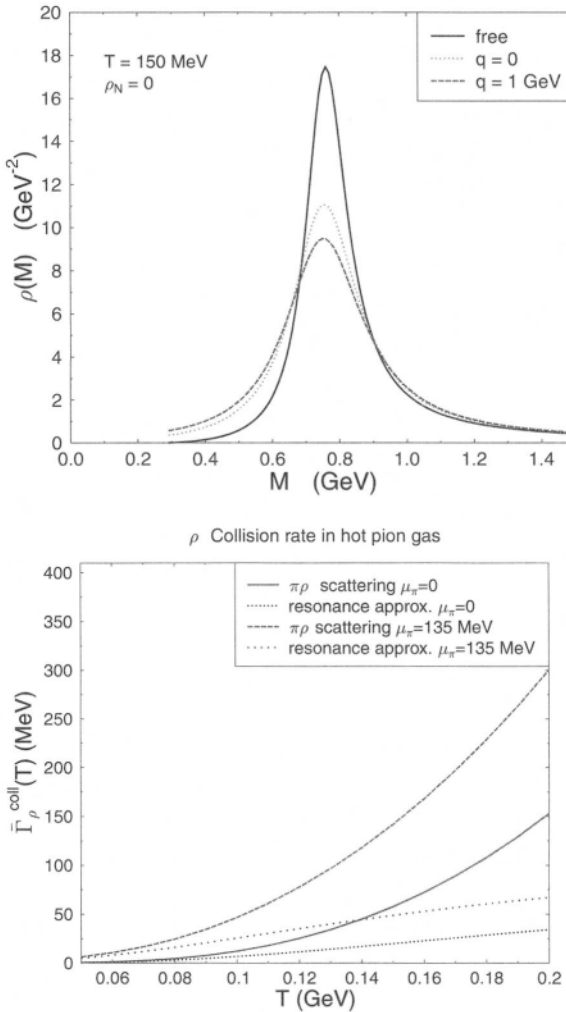


Fig. 3.5. ρ meson spectral function at $T = 150$ MeV (top) as evaluated in the kinetic theory calculations of Ref. [122] including the in-medium Bose-enhancement of the $\rho \rightarrow \pi\pi$ width. The bottom panel shows the temperature dependence of the collisional part (using two values for the pion chemical potential) for the full result including t -channel processes (full curves, labeled “ $\pi\rho$ scattering”) as well as for a calculation where only s -channel resonances have been accounted for (dotted curves, labeled “resonance approx.”).

$$\mathcal{L}_{\pi+\rho}^{\text{free}} = \frac{1}{2} \text{tr}[(\partial^\mu \pi)^2 - \phi^2] - \frac{1}{2} \text{tr}[(\rho_{\mu\nu}^2) + (m_\rho^{(0)})^2 \text{tr}[\rho_\mu^2]], \quad (3.49)$$

Sakurai proposed to adopt the ρ meson as the gauge boson of the conserved isospin [125], which can be realized by introducing the covariant derivative $\partial^\mu \rightarrow (\partial^\mu + ig_{\rho\pi\pi}\rho^\mu)$. This is rather close in spirit to the massive Yang-Mills approach discussed above. The resulting $\pi\rho$ interaction vertices are then given by

$$\mathcal{L}_{\rho\pi}^{\text{int}} = g_{\rho\pi\pi}(\vec{\pi} \times \partial^\mu \vec{\pi}) \cdot \vec{\rho}_\mu - \frac{1}{2} g_{\rho\pi\pi}^2 \vec{\rho}^\mu \cdot \vec{\pi} \vec{\rho}_\mu \cdot \vec{\pi}. \quad (3.50)$$

To lowest order in $g_{\rho\pi\pi}$ the corresponding selfenergy in vacuum reads

$$\begin{aligned} \Sigma_{\rho\pi\pi}^{\circ,\mu\nu}(M) &= ig_{\rho\pi\pi}^2 \int \frac{d^4 p}{(2\pi)^4} \frac{(2p+q)_\mu (2p+q)_\nu}{((p+q)^2 - m_\pi^2 + i\eta)(p^2 - m_\pi^2 + i\eta)} \\ &\quad - i2g_{\rho\pi\pi}^2 g^{\mu\nu} \int \frac{d^4 p}{(2\pi)^4} \frac{1}{p^2 - m_\pi^2 + i\eta}. \end{aligned} \quad (3.51)$$

The loop integrals have to be regularized. A symmetry conserving procedure is, e.g., provided by the Pauli-Villars scheme which applies subtractions to the divergent integrals according to

$$\sum^{\mu\nu}(q; m_\pi) \rightarrow \sum^{\mu\nu}(q; m_\pi) + \sum_{i=1}^2 c_i \sum^{\mu\nu}(q; M_i). \quad (3.52)$$

The required regulator masses M_i can be related to a single form factor cutoff Λ_ρ with [126]

$$\begin{aligned} c_1 &= -2, & M_1 &= \sqrt{m_\pi^2 + \Lambda_\rho^2} \\ c_2 &= 1, & M_2 &= \sqrt{m_\pi^2 + 2\Lambda_\rho^2}. \end{aligned} \quad (3.53)$$

Effectively, the same can also be achieved by writing the two-pion loop selfenergy in terms of a once-subtracted dispersion integral [114] as

$$\begin{aligned} \Sigma_{\rho\pi\pi}^{\circ}(M) &= \bar{\Sigma}_{\rho\pi\pi}^{\circ}(M) - \bar{\Sigma}_{\rho\pi\pi}^{\circ}(0) \\ \bar{\Sigma}_{\rho\pi\pi}^{\circ}(M) &= \int \frac{p^2 dp}{(2\pi)^2} v_{\rho\pi\pi}(p)^2 G_{\pi\pi}^0(M, p) \end{aligned} \quad (3.54)$$

with the vacuum two-pion propagator

$$G_{\pi\pi}^0(M, p) = \frac{1}{\omega_\pi(p)} \frac{1}{M^2 - (2\omega_\pi(p))^2 + i\eta}, \quad \omega_\tau(p) = \sqrt{m_\pi^2 + p^2} \quad (3.55)$$

and vertex functions

$$v_{\rho\pi\pi}(p) = \sqrt{\frac{2}{3}} g_{\rho\pi\pi} 2 p F_{\rho\pi\pi}(p) \quad (3.56)$$

involving a hadronic form factor $F_{\rho\pi\pi}$ [47]. From gauge invariance it follows that $q_\mu \Sigma_{\rho\pi\pi}^{\circ,\mu\nu} = 0$ and the ρ meson selfenergy can be cast in the general form

$$\sum_{\rho\pi\pi}^{\circ,\mu\nu}(q) = \left(-g^{\mu\nu} + \frac{q^\mu q^\nu}{M^2} \right) \sum_{\rho\pi\pi}^{\circ}(M). \quad (3.57)$$

Iterating it to all orders by solving the Dyson equation for the propagator, one arrives at

$$D_\rho^{\circ,\mu\nu}(q) = \left(-g^{\mu\nu} + \frac{q^\mu q^\nu}{M^2} \right) D_\rho^{\circ}(M) \quad (3.58)$$

with the scalar part

$$D_\rho^{\circ}(q) = \left[M^2 - (m_\rho^{(0)})^2 - \sum_{\rho\pi\pi}^{\circ}(M) \right]^{-1}. \quad (3.59)$$

The three free parameters (coupling constant, bare mass and cutoff) can be readily adjusted to the P -wave $\pi\pi$ phase shifts,

$$\tan(\delta_{\pi\pi}^{JI=11}(M)) = \frac{\text{Im } D_\rho^{\circ}(M)}{\text{Re } D_\rho^{\circ}(M)}, \quad (3.60)$$

and the pion electromagnetic form factor, which, imposing VDM, becomes

$$|F_\pi^{\circ}(M)|^2 = (m_\rho^{(0)})^4 |D_\rho^{\circ}(M)|^2, \quad (3.61)$$

cf. Fig. 3.6. Typical values are $g_{\rho\pi\pi}^2/4\pi = (2.7 - 2.9)$, $m_\rho^{(0)} = (0.82 - 0.85)$ GeV and $\Lambda_\rho = (1 - 3)$ GeV, depending on the regularization procedure.

Based on this standard description of the free ρ meson one can distinguish two types of in-medium effects: (i) modifications of the pion cloud, leading to a temperature-dependent $\rho\pi\pi$ selfenergy $\Sigma_{\rho\pi\pi}$, and (ii) scattering of the (bare) ρ meson on surrounding matter particles. Concerning (i) one needs to evaluate the in-medium properties of the pions. In a thermal pion gas they are only mildly affected chiefly because of their Goldstone nature. The corresponding pion “optical” potentials amount to less than 10% corrections to the free pion dispersion relation even at temperatures as large as $T = 200$ MeV [127, 128], cf. Fig. 3.7. In what follows, we shall therefore neglect the effects of a modified pion

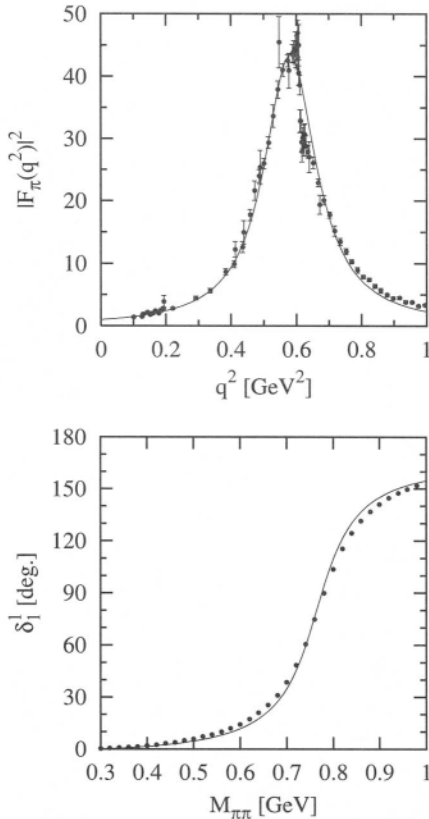


Fig. 3.6. Pion electromagnetic form factor (top) and P -wave $\pi\pi$ scattering phase shifts in free space as obtained in typical fits from phenomenological models for the ρ meson propagator.

dispersion relation on the pion cloud of the ρ meson. A more important modification of $\Sigma_{\rho\pi\pi}$ stems from the Bose-Einstein enhancement factors of the (on-shell) intermediate two-pion states, representing an enhancement of the in-medium $\rho \rightarrow \pi\pi$ width by “stimulated emission”. In the Matsubara formalism the (retarded) two-pion propagator (3.55) takes the form

$$G_{\pi\pi}(M, p; T) = \frac{1}{\omega_\pi(p)} \frac{[1 + 2f^\pi(\omega_\pi(p); T)]}{(M + i\eta)^2 - (2\omega_\pi(p))^2}, \quad (3.62)$$

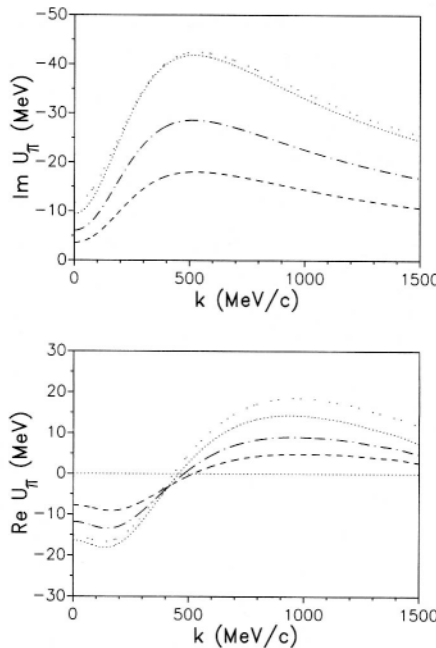


Fig. 3.7. Pion “optical” potentials (top: imaginary part, bottom: real part) in a hot pion gas as arising from a selfconsistent Brueckner calculation [128] of the pion selfenergy Σ_π and a chirally symmetric $\pi\pi$ interaction (“Jülich model” [129, 130]) within the Matsubara formalism. The on-shell potentials shown are defined as $U_\pi(k; T) = \Sigma_\pi(e_\pi(k), k; T)/2\omega_\pi(k)$, where the quasiparticle energy $e_\pi(k)$ is determined by the solution of $e_\pi(k)^2 = \omega_\pi(k)^2 + \Sigma_\pi(e_\pi(k), k; T)$. The dashed, dash-dotted and dotted lines correspond to temperatures $T = 150, 175$ and 200 MeV, respectively (the light-dotted line is obtained in first order of the selfconsistency iteration at $T = 200$ MeV).

which has been first quoted in Ref. [131]. Strictly speaking, the temperature factors are only exact for the imaginary part and the real part should be calculated from a dispersion integral. It has been shown [129], however, that the latter is well approximated by (3.62) as long as the in-medium pion dispersion relation is close to the free one. Furthermore, in Eq. (3.62) we have restricted ourselves to vanishing total three-momentum of the pion pair, the so-called “back-to-back kinematics”. It has been verified in the model of Urban *et al.* [126] that the inclusion of finite three-momentum gives virtually identical results.

Next we turn to the contributions from direct ρ scattering off thermal mesons. In the many-body treatment of Refs. [47, 123] it has

been assumed that the interactions in each spin-isospin channel are saturated by s -channel resonance formation (“leading resonance approximation”). A clue as to which meson resonances might be of importance is provided by their branching ratios into ρP states. This decay mode, however, is kinematically suppressed for resonance masses significantly below the naive kinematical threshold $m_\rho + m_P$. On the other hand, it should be emphasized that it is just these subthreshold states which potentially generate substantial strength for the in-medium ρ meson spectral function at low invariant masses (*e.g.*, in $\rho\pi \rightarrow \omega(782)$ where, given a typical thermal pion energy of 300–400 MeV, the appropriate ρ meson mass would be $M \approx 400$ –500 MeV). Using VDM the subthreshold states can be largely identified through their radiative decays $R \rightarrow P\gamma$. The various resonances R in ρP collisions can be grouped into three major categories, namely vectors V , axialvectors A and pseudoscalars P' . Following Ref. [123] we restrict our discussion to states with masses $m_R \leq 1.3$ GeV; higher ones are only relevant for invariant ρ masses beyond $M \approx 1$ GeV.

For ρPA vertices a suitable interaction Lagrangian, compatible with chiral symmetry and electromagnetic current conservation, is given by

$$\mathcal{L}_{\rho PA} = G_{\rho PA} A_\mu (g^{\mu\nu} q_\alpha p^\alpha - q^\mu p^\nu) \rho_\nu P, \quad (3.63)$$

although other choices are possible [124]. The ρP scattering via intermediate vector mesons V is determined by Wess-Zumino anomaly terms which are of unnatural parity and involve the four-dimensional antisymmetric Levi-Civita tensor $\epsilon^{\mu\nu\sigma\tau}$:

$$\mathcal{L}_{\rho PV} = G_{\rho PV} \epsilon_{\mu\nu\sigma\tau} k^\mu V^\nu q^\sigma \rho^\tau P. \quad (3.64)$$

In both Lagrangians (3.63) and (3.64), p^μ , q^μ and k^μ denote the four-momenta of the pseudoscalar, ρ and (axial-) vector mesons, respectively. As a third possibility ρP scattering can proceed via a pseudoscalar resonance. Here an obvious candidate is $\rho\pi \rightarrow \pi'(1300)$ which can be described by

$$\mathcal{L}_{\rho PP'} = G_{\rho PP'} P' (k \cdot q p_\mu - p \cdot q k_\mu) \rho^\mu P. \quad (3.65)$$

With increasing temperature the heat bath will consist of more and more heavier resonances, especially those with high spin-isospin degeneracy. After the light pseudoscalars the meson multiplet with the smallest masses are the vectors, most notably the ρ meson with nine-fold degeneracy. Motivated by the observation that the $f_1(1285)$ resonance exhibits a large $\rho\gamma$ decay width (together with a predominant 4π decay), it has

been interpreted as a “resonance” in $\rho\rho$ scattering [123]. The interaction vertex is also related to anomaly terms [132] and has been chosen in the following form,

$$\mathcal{L}_{\rho VA} = G_{\rho VA} \epsilon_{\mu\nu\sigma\tau} p^\mu V^\nu \rho^{\sigma\alpha} k_\alpha A^\tau - \frac{\lambda}{2} (k_\beta A^\beta)^2, \quad (3.66)$$

which again satisfies the appropriate conservation laws. Here, the kinetic-energy term of the axialvector field has been explicitly written to indicate a gauge freedom associated with the constant λ [133]. For practical purposes—following Ref.[123]— λ has been set to 1.

The free parameters involved, which are the coupling constants and the cutoffs for the hadronic vertex form factors, can be rather accurately determined from a simultaneous fit to both the hadronic $R \rightarrow \rho P$ and radiative $R \rightarrow \rho\gamma$ branching ratios as will be detailed in Sect. 4.1.1.

Within the imaginary time (Matsubara) formalism the ρ meson selfenergy tensor arising from binary collisions can now be calculated as

$$\Sigma_{ph}^{\mu\nu}(q) = \int \frac{d^3 p}{(2\pi)^3} \frac{1}{2\omega_h(p)} [f^h(\omega_h(p)) - f^R(k_0)] \mathcal{M}_{ph}^{\mu\nu}(p, q) \quad (3.67)$$

with the thermal Bose distribution $f^h(\omega_h(p)) = [\exp(\omega_h(p)/T) - 1]^{-1}$ of the corresponding hadron species h with on-shell energy $\omega_h(p) = \sqrt{m_h^2 + \vec{p}^2}$. $\mathcal{M}_{ph}^{\mu\nu}$ denotes the isospin-averaged forward scattering amplitude which, in the leading resonance approximation employed here, can be written as

$$\mathcal{M}_{phR}^{\mu\nu}(p, q) = IF G_{phR}^2 F_{phR}(q_{cm})^2 D_R(s) v_R^{\mu\nu}(p, q). \quad (3.68)$$

The explicit expressions for the vertex functions $v_R^{\mu\nu}(p, q)$ can be derived from the above interaction Lagrangians as has been done in Ref. [123]. IF denotes an isospin factor and the hadronic vertex form factor has been chosen of dipole type

$$F_{phR}(q_{cm}) = \left(\frac{2\Lambda_{phR}^2 + m_R^2}{2\Lambda_{phR}^2 + [\omega_p(q_{cm}) + \omega_P(q_{cm})]^2} \right)^2, \quad (3.69)$$

normalized to 1 at the resonance mass m_R . The scalar part of the intermediate resonance propagators is given by

$$D_R(s) = \frac{1}{s - m_R^2 + im_R \Gamma_R^{\text{tot}}(s)} \quad (3.70)$$

with $s = k^2 = (p + q)^2$ and the total resonance width $\Gamma_R^{\text{tot}}(s)$. Using the standard projection operators of Eq. (2.99) the selfenergy tensors (3.67)

can be conveniently decomposed into longitudinal and transverse components,

$$\sum_{\rho}^{\mu\nu}(q) = \sum_{\rho}^L(q_0, \vec{q})P_L^{\mu\nu} + \sum_{\rho}^T(q_0, \vec{q})P_T^{\mu\nu}, \quad (3.71)$$

which build up two independent modes of the in-medium ρ propagator according to

$$\begin{aligned} D_{\rho}^{\mu\nu}(q) &= \frac{P_L^{\mu\nu}}{M^2 - (m_{\rho}^{(0)})^2 - \sum_{\rho}^L(q_0, \vec{q})} + \frac{P_T^{\mu\nu}}{M^2 - (m_{\rho}^{(0)})^2 - \sum_{\rho}^T(q_0, \vec{q})} \\ &+ \frac{q^{\mu}q^{\nu}}{(m_{\rho}^{(0)})^2 M^2}. \end{aligned} \quad (3.72)$$

Fig. 3.8 shows the individual contributions to the spin-averaged selfenergy,

$$\sum_{\rho h R}(M, \vec{q}) = \frac{1}{3} [\sum_{\rho h R}^L(M, \vec{q}) + 2 \sum_{\rho h R}^T(M, \vec{q})], \quad (3.73)$$

at fixed 3-momentum modulus $|\vec{q}| = 0.3 \text{ GeV}$ and temperature $T = 150 \text{ MeV}$. Around and above the free ρ meson mass the strongest absorption is caused by $a_1(1260)$ resonance formation, which is about as large as the sum of all other channels, shared to roughly equal parts among $K_1(1270)$, $h_1(1170)$ and $\pi'(1300)$. The $K_1(1270)$ contribution acquires its maximum at lower M than the pion-resonances due to the higher thermal energies of the kaons (including their rest mass). In the low-mass region, $M \leq 0.6 \text{ GeV}$, the prevailing contribution is due to the ω meson which, however, leaves little trace in the resonance region. It is also seen that the effect of the f_1 meson is very small. In the real part of the total self-energy one observes appreciable cancellations until eventually all contributions turn repulsive (the latter feature is likely to be modified when accounting for further higher resonances). Such cancellations are typical for this kind of many-body calculations. They are the reason that one usually encounters only moderate modifications of the in-medium pole masses. On the other hand, the imaginary parts of Σ_{ρ} strictly add up, generating significant broadening. Not shown here is the in-medium Bose enhancement of the $\rho \rightarrow \pi\pi$ selfenergy. It has a very smooth behavior with a broad maximum of $\text{Im}(\Sigma_{\rho\pi\pi}(M; T) - \Sigma_{\rho\pi\pi}^0(M))/m_{\rho} \approx 25 \text{ MeV}$ at about $M \approx 0.6 \text{ GeV}$. We also note that the three-momentum dependence of the selfenergies is rather weak, being most pronounced at low M where the transverse part is responsible for the build-up of finite values. This can

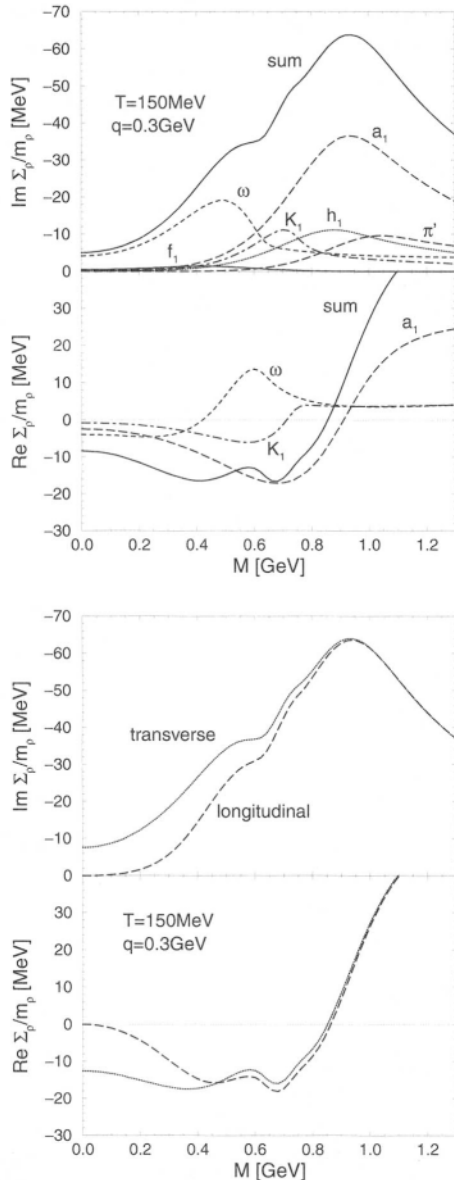


Fig. 3.8. The real and imaginary parts (lower and upper panels, respectively) of the polarization-averaged ρ selfenergy (top) from resonant scattering off thermal π , K , \bar{K} and ρ mesons in a heat bath at $T = 150 \text{ MeV}$ and $\mu_\pi = 0$; the different channels are labeled by their intermediate resonances; right panel: polarization decomposition of the combined selfenergy contributions.

be seen more explicitly from the right panel of Fig. 3.8 where the summed selfenergy contributions have been separated into the two polarization states.

In Fig. 3.9 the full spin-averaged imaginary part of the ρ meson propagator,

$$\text{Im } D_\rho(M, \vec{q}; T) = \frac{1}{3} [\text{Im } D_\rho^L(M, \vec{q}; T) + 2 \text{Im } D_\rho^T(M, \vec{q}; T)], \quad (3.74)$$

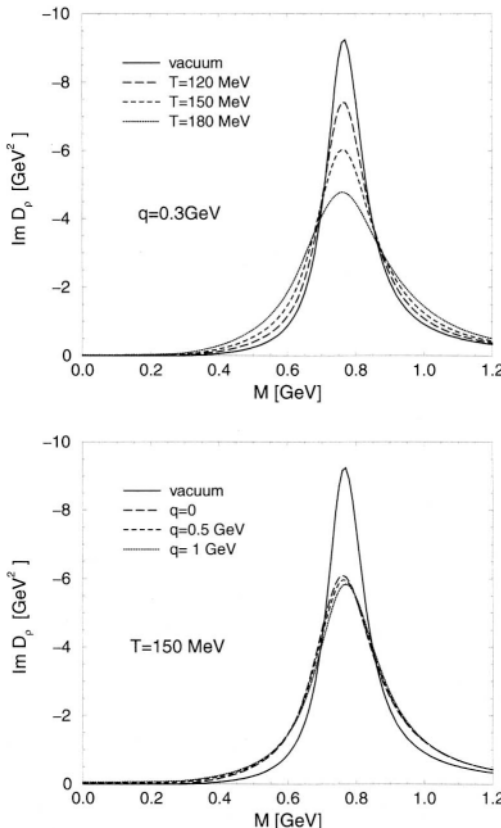


Fig. 3.9. Imaginary part of the ρ propagator (which, up to a factor of (-2) , coincides with the spectral function) in the vacuum (full curve) and in a thermal $\pi\bar{K}\bar{K}_\rho$ gas as calculated in the many-body framework of Ref. [47, 123]. Top: for fixed three-momentum $q = 0.3$ GeV at temperatures $T = 120$ MeV (long-dashed curve), $T = 150$ MeV (dashed curve) and $T = 180$ MeV (dotted curve); bottom: for fixed temperature $T = 150$ MeV at three-momenta $q = 0$ (long-dashed curve), $q = 0.5$ GeV (dashed curve) and $q = 1$ GeV (dotted curve).

in a thermal meson gas of temperatures $T = 120, 150$ and 180 MeV (left panel) as appropriate for the hadronic phase in ultrarelativistic heavy-ion collisions is shown. More explicitly, one has

$$\text{Im } D_{\rho}^{L,T}(M, \vec{q}) = \frac{\text{Im} \sum_{\rho}^{L,T}(M, \vec{q})}{\left| M^2 - (m_{\rho}^{(0)})^2 - \sum_{\rho}^{L,T}(M, \vec{q}) \right|^2} \quad (3.75)$$

with the longitudinal and transverse selfenergy parts

$$\sum_{\rho}^{L,T} = \sum_{\rho\pi\pi} + \sum_{\alpha} \sum_{\rho\alpha}^{L,T}, \quad (3.76)$$

where the summation is over the mesonic excitation channels $\alpha = \pi\omega, \pi h_1, \pi a_1, \pi\pi', KK_1, K\bar{K}_1, \rho f_1$, as discussed, and $\Sigma_{\rho\pi\pi}$ now contains the Bose-Einstein factors through Eq. (3.62). The thermal ρ meson spectral function exhibits an additional broadening (defined as the full width at half maximum) of about 80 MeV at $T = 150\text{ MeV}$ which almost doubles to $\sim 155\text{ MeV}$ at $T = 180\text{ MeV}$. On the other hand, the three-momentum dependence of the spectral function at fixed temperature is rather weak, cf. right panel of Fig. 3.9.

The results of the many-body approach are quite close to those obtained recently using kinetic theory [122] (see Fig. 3.5). The latter, however, attribute some portion of the collisional broadening to t -channel meson exchanges. Those have not been included in the many-body calculations, where the net medium effect is entirely driven by large imaginary parts from resonant s -channel interactions (including sub-threshold states). At tree level, the neglected t -channel exchanges do not generate an imaginary part. They would do so once iterated in a Lippmann-Schwinger-type equation to construct a scattering amplitude beyond tree level. In this case, however, care has to be taken in avoiding double counting when performing a combined treatment of s - and t -channel graphs (in fact, the “leading resonance approximation” implies that non-resonant interactions are, at least partially, subsumed in the resonance parameters). For the ρ meson selfenergy in a hot pion gas an unambiguous way to disentangle s - and t -channel interactions would require experimental information on $\pi\rho$ scattering phase shifts which, owing to the short lifetime of the ρ meson, can only be inferred by very indirect means.

3.2. Finite Baryon Density

The investigation of vector meson modifications in an environment of finite nucleon density via effective hadronic models has mainly been pursued within more phenomenologically oriented approaches. This is partly due to the fact that the impact of chiral symmetry on ρ -nucleon interactions is much less obvious than in the purely mesonic case (such as $\pi\rho\alpha_1$ dynamics). Also, the extension of VDM to the baryonic sector is less accurate such that electromagnetic observables provide less direct access to vector meson interactions involving baryons. Pionic interactions with nucleons and nuclei, on the other hand, are much better known: a wealth of pion-nucleus scattering data has provided a detailed understanding of the underlying physical mechanisms for their modification in cold nuclear matter [134] which are substantial. Since especially ρ mesons (and, to a lesser extent, also ω mesons) exhibit a strong coupling to two- (three-) pion states, early analyses have focused on medium effects in the virtual pion cloud. These developments will be reviewed in the second part of this Section. Subsequently it has been realized that also direct ρ - N interactions can induce substantial modifications of the ρ meson spectral function which we will discuss in the third part of this Section. The first part, however, will be devoted to recall the mean-field based analysis of effective chiral Lagrangians by Brown and Rho [45] which culminated in the famous conjecture of “Brown-Rho Scaling”. It is not exaggerated to say that, although (or just because) this conjecture is controversial, the associated hypothesis for a “dropping” of vector meson masses has been one of the main triggers for an ensuing intense theoretical (and experimental) activity.

3.2.1. Mean-Field Approach: Brown-Rho Scaling

As we have already eluded to in Sect. 2.1, in the massless limit the QCD action is scale invariant on the classical level implying that the QCD Lagrangian has scale dimension 4. Chiral meson Lagrangians, being constructed as effective low-energy theories of QCD, should in principle exhibit the same property. In the non-linear realization they are formulated in terms of the chiral field $U \equiv e^{i\pi/\pi}$ ($\pi = \vec{\pi} \cdot \vec{\tau}$) which, when including up to fourth-order derivatives (involving the quartic “Skyrme term”), read

$$\mathcal{L} = \frac{f_\pi^2}{4} \text{tr}(\partial_\mu U \partial^\mu U) + \frac{\eta^2}{4} \text{tr}[U^\dagger \partial_\mu U, U^\dagger \partial_\nu U]^2 + c \text{tr}(\mathcal{M}^0 U + \text{h.c.}) \quad (3.77)$$

Here, also the explicit symmetry breaking term being proportional to the current quark mass m_q in the quark mass matrix \mathcal{M}^o has been incorporated. As has been argued in Ref. [135] the U field carries scale dimension zero which means that the three terms on the *r.h.s.* have scale dimensions 2,4 and 0, respectively.

Following Ref. [45] the first step in the derivation of Brown-Rho scaling consists of modifying the effective Lagrangian (3.77) to reflect the appropriate scaling behavior of the QCD Lagrangian. The simplest way to restore it has been proposed by Ellis *et al.* [135] and is realized by introducing an effective “glueball” field χ with scale dimension 1 according to

$$\begin{aligned}\mathcal{L}_\chi = & \frac{f_\pi^2}{4} \left(\frac{\chi}{\chi_0} \right)^2 \text{tr}(\partial_\mu U \partial^\mu U) + \frac{\eta^2}{4} \text{tr}[U^\dagger \partial_\mu U, U^\dagger \partial_\nu U]^2 + \frac{1}{2} \partial_\mu \chi \partial^\mu \chi \\ & + c \left(\frac{\chi}{\chi_0} \right)^3 \text{tr}(\mathcal{M}^o U + \text{h.c.}) + V(\chi).\end{aligned}\quad (3.78)$$

Besides a scale invariant (i.e., dimension-4) kinetic energy term for the glueball field a potential-energy term of the form

$$V(\chi) = B \left[\frac{1}{4} \chi_0^4 + \chi^4 \ln(\chi/e^4 \chi_0) \right] \quad (3.79)$$

has also been added. Minimizing V in χ yields a nonzero ground state expectation value $\chi_0 \equiv \langle 0 | \chi | 0 \rangle$ signaling the spontaneous breakdown of scale invariance which mimics the (quantum part of the) QCD scale anomaly on the effective Lagrangian level. The divergence of the corresponding dilation current (2.21) becomes [135]

$$\partial_\mu j_\mu^B = -B\chi^4. \quad (3.80)$$

Thus, comparing to the trace anomaly of QCD (2.22) χ_0 can be related to the gluon condensate $\langle G^2 \rangle$. In addition, the QCD trace anomaly receives a contribution from explicit scale breaking through the quark mass term $(\bar{\psi} \mathcal{M}^o \psi)$ which has scale dimension 3 requiring the χ^3 factor in the corresponding term in Eq. (3.78).

As has been emphasized by Brown and Rho in subsequent work [136], the introduced χ -field is to be understood as consisting of a “soft” (mean-field) and a “hard” (fluctuation) component according to

$$\chi = \chi^* + \chi'. \quad (3.81)$$

It is the soft mean-field component χ^* that will govern the medium modifications in the chiral effective Lagrangian, whereas the hard component

χ' is to be associated with the glueball mass scale of >1 GeV, well beyond the applicability range of low-energy effective theory. Indeed, as discussed in Sect. 2.4, lattice calculations show that in the chiral transition with light quarks only about half of the gluon condensate is “melted”, corresponding to the χ^* field (an analogous feature emerges within the instanton model [54] where it has been identified as a rearrangement of the chirally broken “random” instanton liquid into a chirally restored phase with $I\text{-}A$ molecules, the latter characterizing the “hard” component of the gluon fields that survive the transition).

In their second main step Brown and Rho postulate that, as the (quark and gluon) condensates change in dense matter, the symmetries of the Lagrangian remain intact such that the variation in the condensates can be absorbed in a density-dependent change in masses and coupling constants of the effective theory. In line with the above arguments, the change in the quark condensate at a given density can be expressed as

$$\frac{\langle\langle\bar{\psi}\psi\rangle\rangle}{\langle\bar{\psi}\psi\rangle} = \left(\frac{\chi^*}{\tilde{\chi}_0}\right)^3, \quad (3.82)$$

where $\tilde{\chi}_0$ denotes the vacuum expectation value of the χ^* field. This suggests to define an in-medium pion decay constant as

$$f_\pi^* = f_\pi \frac{\chi^*}{\tilde{\chi}_0} \quad (3.83)$$

leading to the effective Lagrangian of the form

$$\begin{aligned} L^* = & \frac{f_\pi^{*2}}{4} \text{tr}(\partial_\mu U \partial^\mu U) + \frac{\eta^2}{4} \text{tr}[U^\dagger \partial_\mu U, U^\dagger \partial_\nu U]^2 \\ & + c \left(\frac{f_\pi^*}{f_\pi} \right)^3 \text{tr}(\mathcal{M}^\circ U + \text{h.c.}) + \dots, \end{aligned} \quad (3.84)$$

where the fields are now defined as ensemble averages in cold nuclear matter, i.e., $\chi^* \equiv \langle\langle\chi\rangle\rangle$ etc.. In particular, with

$$U = \exp(i\pi^*/f_\pi^*), \quad (3.85)$$

the pion field $\pi^* \equiv \pi\chi^*/\tilde{\chi}_0$ has picked up a scale dimension of one. Furthermore, it was argued that the fluctuating part of the glueball field strongly mixes with an effective low-lying σ meson (the quark-antiquark component of the scalar), and therefore the effective mass of the latter is inferred from

$$f_\pi^*/f_\pi \approx \chi^*/\tilde{\chi}_0 \approx m_\sigma^*/m_\sigma. \quad (3.86)$$

Moreover, when using the Goldberger-Treiman relation one has

$$m_N^*/m_N \approx (g_A^*/g_A)^{1/2} f_\pi^*/f_\pi. \quad (3.87)$$

Since in the Skyrme model, the (scale invariant) coefficient η^2 of the quartic Skyrme term is directly related to the axialvector coupling constant g_A , the latter is not affected at the mean-field level. (The “quenching” of g_A from 1.26 to 1, observed in Gamow-Teller and magnetic transitions in nuclei, has been argued to be due to loop effects, indicating an additional, lower scale induced in nuclei). Finally, making use of the KSFR relation [86],

$$m_V^2 = 2g^2 f_\pi^2, \quad (3.88)$$

and the fact that within the Skyrme model the hidden-gauge coupling $g^2 = \frac{1}{3}\eta^2$ is scale invariant, the vector meson masses are conjectured to complete the (approximate) Brown-Rho (BR) scaling relation:

$$\Phi(\rho) \equiv \frac{f_\pi^*}{f_\pi} = \frac{m_\sigma^*}{m_\sigma} = \frac{m_N^*}{m_N} = \frac{m_\rho^*}{m_\rho} = \frac{m_\omega^*}{m_\omega}. \quad (3.89)$$

In fact, early QCD sum rules calculations of Hatsuda and Lee [46] have given support to this relation, as discussed in Sect. 2.7, with typical values for $\Phi(\rho_0) = 0.82 \pm 0.06$ at normal nuclear matter density.

There might be, however, some problems with the BR scaling hypothesis, mainly in the finite temperature sector. On very general grounds the chiral condensate is locally altered whenever a hadron is present as discussed in Sect. 2.3. This leads to the dilute gas expressions (2.44) and (2.45) which are rigorously valid at low temperature and low density. Even though the quark condensate is decreased, by definition, nothing happens to the masses, the pion and the nucleon in this case. Secondly, when applied at low temperatures, the scaling relation (3.89) is at variance with the low-temperature expansion of the in-medium vector and axialvector correlators (2.103) and the chiral condensate ratio (2.50). While the latter is reduced already at order $O(T^2)$, the T^2 -dependence of the correlators is governed by mixing and corrections to the mass are of order $O(T^4)$ (in the chiral limit). This is implied by chiral symmetry [88] and manifest in various effective models that we have discussed in the previous Section.

3.2.2. Pion Cloud Modifications

Let us first recall some basic features of the single-pion properties in nuclear matter (for a review see, e.g., Ref. [137]). The most prominent effect on (on-shell) pions propagating through the nuclear environment is generated through resonant P -wave interactions exciting isobar-hole (ΔN^{-1}) states. As is well-known from pion nuclear physics another important pionic excitation channel is represented by P -wave nucleon-hole (NN^{-1}) states. On the other hand, S -wave πN interactions are suppressed by about an order of magnitude in symmetric nuclear matter owing to an almost exact cancellation between the isospin $1/2$ and $3/2$ partial waves [134]. The standard Lagrangians for the πNN and $\pi N\Delta$ P -wave interactions are given (in non-relativistic form) by

$$\begin{aligned}\mathcal{L}_{\pi NN} &= \frac{f_{\pi NN}}{m_\pi} \Psi_N^\dagger \vec{\sigma} \cdot \vec{k} \vec{\tau} \cdot \vec{\pi} \Psi_N \\ \mathcal{L}_{\pi N\Delta} &= \frac{f_{\pi N\Delta}}{m_\pi} \Psi_\Delta^\dagger \vec{S} \cdot \vec{k} \vec{T} \cdot \vec{\pi} \Psi_N + \text{h.c.},\end{aligned}\quad (3.90)$$

which leads to corresponding pion selfenergies in nuclear matter of the type

$$\sum_{\pi\alpha}^{(0)}(k) = -\vec{k}^2 \chi_{\pi\alpha}^{(0)}(k) \quad (3.91)$$

($k = (k_0, \vec{k})$, $\alpha = NN^{-1}, \Delta N^{-1}$). The so-called (pionic) susceptibilities are given by

$$\chi_{\pi\alpha}^{(0)}(k) = \left(\frac{f_{\pi\alpha} F_{\pi\alpha}(k)}{m_\pi} \right)^2 SI(\pi\alpha) \phi_\alpha(k) \quad (3.92)$$

in terms of spin-isospin factors $SI(\pi\alpha)$, coupling constants $f_{\pi\alpha}$ (cf. Table 3.1) and a hadronic vertex form factor usually chosen of monopole type,

TABLE 3.1
Spin-isospin transition factors and coupling constants
for pion induced (longitudinal) P -wave particle-hole
excitations in a hot $N\Delta$ gas [138].

$\pi\alpha$	πNN^{-1}	$\pi\Delta N^{-1}$	$\pi N\Delta^{-1}$	$\pi\Delta\Delta^{-1}$
$SI(\pi\alpha)$	4	16/9	16/9	400
$f_{\pi\alpha}^2/4\pi$	0.08	0.32	0.32	0.0032

$$F_{\pi\alpha}(k) = \left(\frac{\Lambda_\pi^2 - m_\pi^2}{\Lambda_\pi^2 + \vec{k}^2} \right). \quad (3.93)$$

In Eq. (3.92), ϕ_α denote the Lindhard functions which, for the more general case of a $\alpha = ab^{-1}$ particle-hole excitation, read

$$\phi_\alpha(k) = -\int \frac{p^2 dp}{(2\pi)^2} f^b[E_b(p)] \int_{-1}^{+1} dx \sum_{\pm} \frac{1 - f^a[E_a(\vec{p} + \vec{k})]}{\pm k_0 + E_b(p) - E_a(\vec{p} + \vec{k}) \pm \frac{i}{2}(\Gamma_a + \Gamma_b)} \quad (3.94)$$

including direct (sign “+”) and exchange (sign “−”) diagrams with

$$E_a(p) = (m_a^2 + p^2)^{1/2}, \\ E_b(\vec{p} + \vec{k}) = (m_b^2 + p^2 + k^2 + 2pkx)^{1/2} \quad (3.95)$$

and Fermi-Dirac distribution functions f^a, f^b . Γ_a and Γ_b are the (energy- and density-dependent) total decay widths of particle a and hole b^{-1} , respectively (notice that the holes carry the imaginary part with opposite sign). For a realistic description of the pion selfenergy short-range correlations between particle and hole have to be accounted for. These are conveniently parameterized in terms of “Migdal parameters” $g'_{\alpha\beta}$, which also induce a mixing between the channels. The resulting system of coupled equations,

$$\chi_\alpha = \chi_\alpha^{(0)} - \sum_\beta \chi_\alpha^{(0)} g'_{\alpha\beta} \chi_\beta, \quad (3.96)$$

is solved by an elementary matrix inversion yielding

$$\sum_\pi(k_0, \vec{k}) = -\vec{k}^2 \sum_\alpha \chi_\alpha(k_0, \vec{k}). \quad (3.97)$$

As an illustrative example we show in Fig. 3.10 the off-shell two-pion propagator (restricted to zero total momentum) in nuclear matter,

$$G_{\pi\pi}(E, \vec{k}) = \int \frac{idk_0}{\pi} D_\pi(k_0, \vec{k}) D_\pi(E - k_0, -\vec{k}) \\ D_\pi(k_0, \vec{k}) = [k_0^2 - \vec{k}^2 - m_\pi^2 - \sum_\pi(k_0, \vec{k})]^{-1}, \quad (3.98)$$

which directly enters into the two-pion selfenergy of the ρ meson, cf. Eq. (3.54). Clearly, the combination of ΔN^{-1} and NN^{-1} excitations entails a

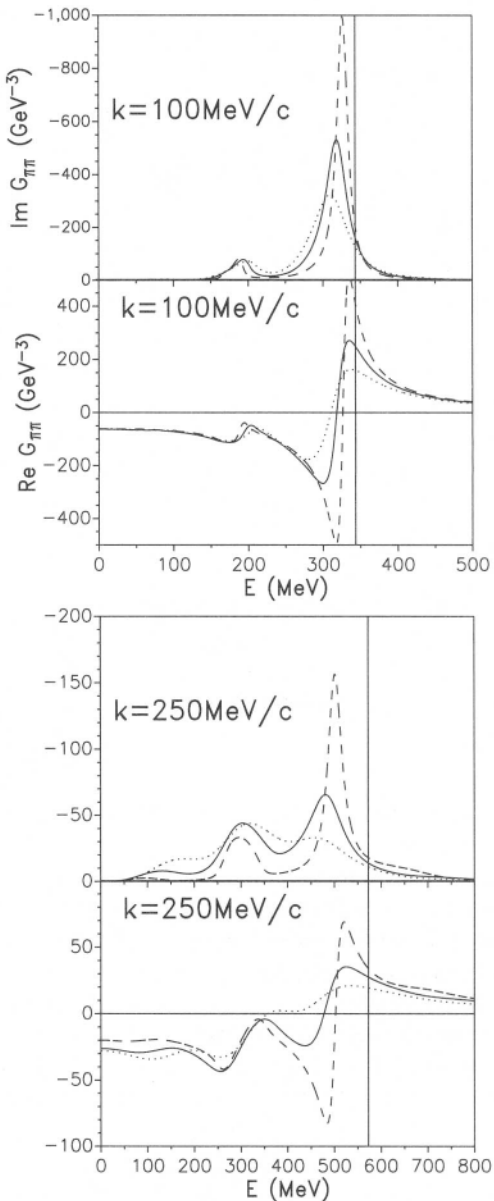


Fig. 3.10. Two-pion propagator (upper panels: imaginary part, lower panels: real part) in cold nuclear matter at densities $\rho_N/\rho_0 = 0.5, 1$, and 1.5 represented by the long-dashed, full and dotted lines, respectively (the pion selfenergies have been evaluated using the $\pi\pi$ form factor cutoff from the Bonn potential, $\Lambda_{\pi NN} = \Lambda_{\pi N\Delta} = 1.2 \text{ GeV}$, together with correspondingly large values for the Migdal parameters of $g'_{NN} = 0.8$, $g'_{N\Delta} = 0.5$). The vertical lines indicate the on-shell two-pion energy $E_{on} = 2\omega_\pi(k)$ in free space.

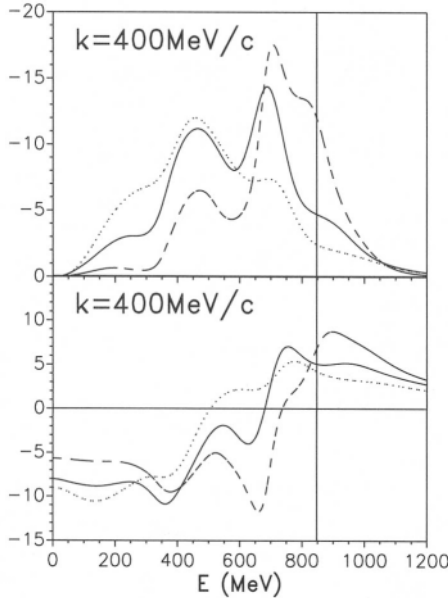


Fig. 3.10. (Continued)

rather rich structure with substantial shifts of strength towards low energies (i.e., invariant ρ masses).

Besides the modification of the intermediate pion propagators in the in-medium ρ meson selfenergy, the ΔN^{-1} - and NN^{-1} -bubbles induce a number of corresponding vertex corrections for the $\rho\pi\pi$ and $\rho\rho\pi\pi$ couplings that have to be incorporated to ensure transversality (i.e., gauge invariance) of the resulting vector propagator. They can be systematically inferred from the appropriate Ward-Takahashi identities [139], as will be detailed below. The first investigations along these lines were performed by Herrmann *et al.* [140], Chanfray and Schuck [114] as well as Asakawa *et al.* [141]. Their calculations were restricted to the effects from the ΔN^{-1} excitation and to vanishing total 3-momentum $\vec{q} = 0$ of the ρ meson. Nevertheless, appreciable modifications of the spectral function were found, in particular an in-medium broadening as well as a rather pronounced peak structure at invariant masses $M \approx 3m_\pi$ stemming from transverse ΔN^{-1} excitations (corresponding to the vertex correction represented by the left diagram in the middle panel of Fig. 3.12). In a next step, the additional effects from P-wave NN^{-1} excitations were incorpo-

rated in Refs. [142, 47]. Although the NN^{-1} channel predominantly populates the space-like momenta in the in-medium pion spectral function, it is nevertheless of significance for the ρ selfenergy, since the off-shell integration over intermediate pion states does involve space-like pion kinematics, generating additional low-mass strength in the spectral function, as we have seen above. At the same time, additional broadening at the ρ meson resonance peak emerges.

In subsequent work, Urban *et al.* [126] could overcome the restriction to back-to-back kinematics of the previous analyses. One starts from the Ward-Takahashi identities, which for the $\rho\pi\pi$ and $\rho\rho\pi\pi$ interaction vertices from Eq. (3.50) read

$$q^\mu \Gamma_{\mu ab}^{(3)}(k, q) = g_{\rho\pi\pi} \epsilon_{3ab} (D_\pi^{-1}(k+q) - D_\pi^{-1}(k)) \quad (3.99)$$

$$q^\mu \Gamma_{\mu ab}^{(4)}(k, k, q) = ig_{\rho\pi\pi} (\epsilon_{3ca} \Gamma_{vbc}^{(3)}(k, -q) - \epsilon_{3bc} \Gamma_{vca}^{(3)}(k+q, -q)), \quad (3.100)$$

respectively. The spin, isospin and momentum assignments are indicated in Fig. 3.11 (for simplicity, we only consider neutral ρ mesons characterized by the third isospin component of the isovector $\vec{\rho}$ field). In free space, where

$$\Gamma_{\mu ab}^{(3)0}(k, q) = g_{\rho\pi\pi} \epsilon_{3ab} (2k + q)_\mu$$

$$\Gamma_{\mu ab}^{(4)0}(k_1, k_2, q) = 2ig_{\rho\pi\pi}^2 (\delta_{ab} - \delta_{3a}\delta_{3b}) g_{\mu\nu}, \quad (3.101)$$

Eqs. (3.99) and (3.100) are trivially satisfied. In nuclear matter, when including NN^{-1} and ΔN^{-1} loops in the pion propagation, the required in-medium vertex corrections can be constructed by coupling the ρ meson to the lines and vertices of the pion selfenergy insertions in all possible ways, leading to the diagrams displayed in Fig. 3.12. The final result

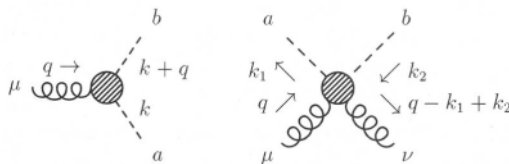


Fig. 3.11. $\rho\pi\pi$ (left) and $\rho\pi\pi$ (right) vertices involving neutral ρ mesons (curly lines). μ, ν correspond to the ρ meson polarizations, whereas a, b are isospin indices of the pions (dashed lines); all other labels refer to the in/outgoing four momenta.

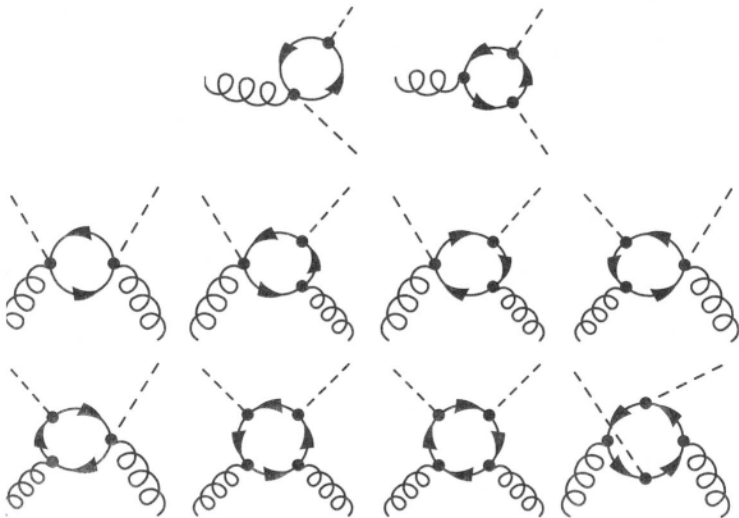


Fig. 3.12. In-medium corrections to the $\rho\pi\pi$ (upper panel) and $\rho\rho\pi\pi$ vertex (middle and lower panel) when including NN^{-1} and ΔN^{-1} excitations in the intermediate pion propagators of the ρ selfenergy. Curly lines: ρ^0 's, dashed lines: π 's, solid lines: nucleons or deltas (when forward-going) and nucleon holes (backward-going).

for the ρ meson selfenergy tensor in cold nuclear matter can then be written as

$$\begin{aligned} \sum_{\rho\pi\pi}^{\mu\nu}(q) = & i \frac{1}{2} \int \frac{d^4 k}{(2\pi)^4} i D_\pi(k) \Gamma_{ab}^{(3)\mu}(k, q) i D_\pi(k+q) \Gamma_{ba}^{(3)\nu}(k+q, -q) \\ & + i \frac{1}{2} \int \frac{d^4 k}{(2\pi)^4} i D_\pi(k) \Gamma_{aa}^{(4)\mu\nu}(k, k, q). \end{aligned} \quad (3.102)$$

The tensor can be decomposed into longitudinal and transverse components in the usual way, see Eq. (3.71). In Fig. 3.13 the spin-averaged ρ spectral function is shown for various densities (left panel) and 3-momenta (right panel). As opposed to Fig. 3.10 the underlying πNN and $\pi N\Delta$ form factor cutoffs (cf. Eq. (3.93)), which essentially determine the magnitude of the medium effects, have been fixed at $\Lambda_{\pi NN} = \Lambda_{\pi N\Delta} = 300$ MeV (together with rather small Migdal parameters of $g'_{NN} = 0.6, g'_{N\Delta} = 0.2$). These choices emerge as a consequence of model constraints imposed through the analysis of $\pi N \rightarrow \rho N$ scattering data (this will be discussed in detail in Sect. 4.1.1 where we also elaborate on the appear-

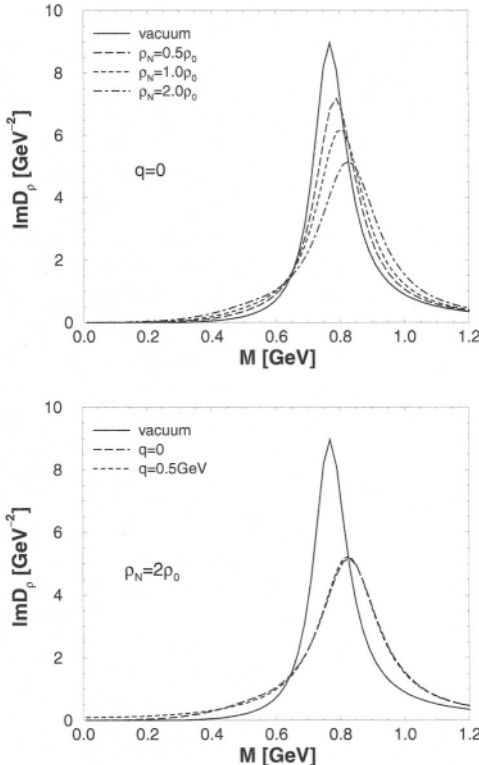


Fig. 3.13. Spin-averaged in-medium ρ propagator when accounting for P -wave NN^{-1} and ΔN^{-1} excitations in its pion cloud. Top: density dependence at fixed three momentum $q = 0$; bottom: three-momentum dependence at fixed nucleon density $\rho_N = 2\rho_0$.

ance of such “unnaturally” soft form factors). In spite of the soft form factors, the ρ meson spectral function still exhibits a significant broadening due to the pion cloud modifications, being about 55 MeV at nuclear saturation density. However, this is substantially smaller as compared to earlier calculations [140, 114, 141, 47, 126] where the $\pi\alpha$ form factors were used with the “Bonn value” (1.2 GeV) [143] for the cutoff. On the other hand, the common feature shared by all previous calculations, i.e., an upward shift of the resonance peak persists. Furthermore, the relative smallness of the medium effects does not allow for a strongly developed momentum dependence: the most significant feature of finite momenta is an enhancement of the spectral function for low invariant masses

$M \leq 0.4$ GeV (see right panel of Fig. 3.13; for the chosen momentum of $q = 0.5$ GeV the effects are largest).

On more general grounds it is important to note that the models for the in-medium ρ propagator discussed above contain a mixing of vector and axialvector correlators much in the same way as for the purely thermal case discussed in Sect. 2.6 and displayed in Fig. 2.8. This has been shown explicitly by Chanfray and collaborators [144] for the case in which the ρ meson couples to the pion-nucleon system (the conclusions remain valid when the **Δ-isobar** is included in addition). To make the argument, consider the longitudinal and transverse selfenergies of the ρ meson. According to (3.71) these can be written as

$$\begin{aligned}\sum_{\rho}^L(q_0, \vec{q}) &= \frac{\vec{q}^2}{q_0^2} \frac{\vec{q}_i \vec{q}_j}{\vec{q}^2} \sum_{\rho}^{ij}(q) \equiv g_{\rho\pi\pi}^2 \frac{\vec{q}^2}{q_0^2} \frac{\vec{q}_i \vec{q}_j}{\vec{q}^2} V^{ij}(q) \\ \sum_{\rho}^T(q_0, \vec{q}) &= \frac{1}{2} \left(\delta_{ij} - \frac{\vec{q}_i \vec{q}_j}{\vec{q}^2} \right) \sum_{\rho}^{ij}(q) \equiv g_{\rho\pi\pi}^2 \frac{1}{2} \left(\delta_{ij} - \frac{\vec{q}_i \vec{q}_j}{\vec{q}^2} \right) V^{ij}(q)\end{aligned}\quad (3.103)$$

and define (up to vertex form factors) the spatial components of the vector correlator V^{ij} ($i, j = 1, 2, 3$). When evaluated by including nucleons and pions one obtains [114]

$$\begin{aligned}V_{ij}(q) &= i \int \frac{d^4 k_1}{(2\pi)^4} \left[\left(1 + \prod^0(k_1) \right) k_{1i} - \left(1 + \prod^0(k_2) \right) k_{2i} \right] \\ &\quad \times D_{\pi}(k_1) D_{\pi}(k_2) \left[\left(1 + \prod^0(k_1) \right) k_{1j} - \left(1 + \prod^0(k_2) \right) k_{2j} \right] \\ &\quad + i \int \frac{d^4 k_1}{(2\pi)^4} \left\{ \left[\hat{k}_{1i} \hat{k}_{1j} \prod^0(k_1) + (\delta_{ij} - \hat{k}_{1i} \hat{k}_{1j}) \prod^T(k_1) \right] D_{\pi}(k_2) \right. \\ &\quad \left. + \left[\hat{k}_{2i} \hat{k}_{2j} \prod^0(k_2) + (\delta_{ij} - \hat{k}_{2i} \hat{k}_{2j}) \prod^T(k_2) \right] D_{\pi}(k_1) \right\},\end{aligned}\quad (3.104)$$

where k_1 and k_2 are the single-pion four-momenta (their sum is the incident momentum $q = k_1 + k_2$). In the above expression the dimensionless irreducible response function Π^0 is related to the pion selfenergy (including effects of short-range correlations via Migdal parameters) as $\Pi^0 = \Sigma_{\pi}/k^2$ (see Eq. (3.97)), while $D_{\pi}(k) = 1/[k_0^2 - k^2 - m_{\pi}^2 - k^2 \Pi^0(k)]$ denotes the fully dressed pion propagator with NN^{-1} insertions, cf. Eq. (3.98). Finally Π^T denotes the fully iterated spin-transverse response function, where the nucleon bubble is iterated to all orders. Expression (3.104) coincides with Eq. (3.102). The corresponding axial correlator A_{ij} can be defined in analogy to (3.103) and takes the form [144]



Fig. 3.14. The axial correlator in nuclear matter.

$$\begin{aligned} \frac{1}{f_\pi^2} A_{ij}(k) &= k_i k_j D_\pi(k) \left(1 + 2 \prod^0(k) \right) + \hat{k}_i \hat{k}_j \prod^L(k) + (\delta_{ij} - \hat{k}_i \hat{k}_j) \prod^T(k) \\ &= k_i k_j \left(1 + \prod^0(k) \right)^2 D_\pi(k) + \hat{k}_i \hat{k}_j \prod^0(k) + (\delta_{ij} - \hat{k}_i \hat{k}_j) \prod^T(k), \end{aligned} \quad (3.105)$$

where also the fully iterated spin-longitudinal response function Π^L has been introduced. The pertinent diagrams are depicted in Fig. 3.14. The crucial observation of Chanfray *et al.* is now that $V_{ij}(q)$ can be expressed in terms of the axial correlator in a form

$$V_{ij}(q) = i \int \frac{d^4 k_1}{(2\pi)^4} \left[\frac{1}{f_\pi^2} (A_{ij}(k_1) D_\pi(k_2) + A_{ij}(k_2) D_\pi(k_1)) - \left(1 + \prod^0(k_1) \right) \left(1 + \prod^0(k_2) \right) (k_{1i} k_{2j} + k_{2i} k_{1j}) D_\pi(k_1) D_\pi(k_2) \right], \quad (3.106)$$

which displays the mixing effect through the first term. This term arises from the vertex corrections displayed in Fig. 3.11. Indeed, removing a (dressed) pion one is left with the axial correlator taken at the momentum of the other pion. In contrast to the thermal case the extra pion is, however, not provided by the heat bath but rather by a nucleon from the medium. The second term in Eq. (3.106) does not reduce to the product of the axial correlator with the pion propagator. Its existence is due to the interaction of the photon with the pion via the derivative term $\vec{\pi} \times \partial^\mu \vec{\pi}$ in the interaction term of the VDM Lagrangian (3.50). The extra term does not invalidate the basic mixing concept. In fact, removing a pion the remainder is still of axial nature.

It is very pleasing to see that partial restoration of chiral symmetry through mixing of vector and axialvector correlators is also manifest in cold nuclear matter. As pointed out in Ref. [114, 126] the dominant mechanism for shifting strength to lower energies in the ρ spectral function is provided by coupling to $\pi \Delta N^{-1}$ -states through vertex corrections. These are precisely of the type $A_{ij} \Delta_\pi$ arising from the last term of the axial correlator (3.105) with a transverse ΔN^{-1} -bubble. Thus the manifestation of partial restoration of chiral symmetry is in the broadening

of the spectral function! Due to the lack of the a_1 meson as an explicit degree of freedom it is not clear at present whether the in-medium Weinberg sum rules (2.101), (2.102) are fulfilled.

A somewhat different approach for evaluating vector meson spectral distributions in cold nuclear matter has been pursued by Klingl *et al.* [91]. They start from an the $SU(3)$ chiral Lagrangian for pseudoscalar mesons and baryons [145], based on pseudovector coupling as

$$\mathcal{L}_{\Phi B} = F \text{Tr}(\bar{B} \gamma_\mu \gamma_5 [u^\mu, B]) + D \text{Tr}(\bar{B} \gamma_\mu \gamma_5 \{u^\mu, B\}_+), \quad (3.107)$$

where $\{\dots\}_+$ and $\{.,.\}$ denote anti-/commutators, respectively, and the $SU(3)$ field matrices are given by

$$B = \begin{pmatrix} \frac{\Lambda}{\sqrt{6}} + \frac{\Sigma^0}{\sqrt{2}} & \Sigma^+ & p \\ \Sigma^- & \frac{\Lambda}{\sqrt{6}} - \frac{\Sigma^0}{\sqrt{2}} & n \\ \Xi^- & \Xi^0 & \frac{-2\Lambda}{\sqrt{6}} \end{pmatrix}, \Phi = \begin{pmatrix} \frac{\pi^0}{\sqrt{2}} + \frac{\eta}{\sqrt{6}} & \pi^+ & K^+ \\ \pi^- & \frac{-\pi^0}{\sqrt{2}} + \frac{\eta}{\sqrt{6}} & K^0 \\ K^- & \bar{K}^0 & \frac{-2\eta}{\sqrt{6}} \end{pmatrix}. \quad (3.108)$$

The parameters $F \approx 0.51$ and $D \approx 0.75$ are chosen to comply with axial coupling constant $g_A = F + D = 1.26$. The four vector

$$u^\mu = -\frac{1}{2f_\pi} (\partial^\mu \Phi - ie[\mathcal{Q}, \Phi] A^\mu) \quad (3.109)$$

contains the axialvector current of the pseudoscalar fields as well as the minimal coupling term for the electromagnetic field A^μ , $\mathcal{Q} = \text{diag}(2/3, -1/3, -1/3)$ being the $SU(3)$ charge matrix. The vector meson-baryon interactions are then obtained from the minimal coupling scheme, i.e., replacing $e\mathcal{Q}A^\mu$ by $gV^\mu/2$ with

$$V^\mu = \text{diag}(\rho^\mu + \omega^\mu, -\rho^\mu + \omega^\mu, \sqrt{2}\phi^\mu), \quad (3.110)$$

and the relevant terms for V - B interactions become

$$\begin{aligned} \mathcal{L}_{V\Phi B} &= \frac{ig}{4f_\pi} \{ F \text{Tr}(\bar{B} \gamma_\mu \gamma_5 [[V^\mu, \Phi], B]) + D \text{Tr}(\bar{B} \gamma_\mu \gamma_5 \{[V^\mu, \Phi], B\}_+) \} \\ \mathcal{L}_{VB}^{(1)} &= \frac{g}{2} \{ \text{tr}(\bar{B} \gamma_\mu [V^\mu, B]) - \text{tr}(\bar{B} \gamma_\mu B) \text{tr}(V^\mu) \} \end{aligned}$$

$$\mathcal{L}_{VN}^{(2)} = \frac{g\kappa_\rho}{4M_N} \bar{N} \vec{\tau} \sigma_{\mu\nu} N \partial^\mu \vec{\rho}^\nu + \frac{g\kappa_\omega}{4M_N} \bar{N} \sigma_{\mu\nu} N \partial^\mu \omega^\nu. \quad (3.111)$$

The last part, $\mathcal{L}_{VN}^{(2)}$, has been added to include corrections due to anomalous VN tensor couplings (using $\kappa_\rho = 6$, $\kappa_\omega = 0.1$, $\kappa_\phi = 0$). Finally, the VB and (axial) ΦB vertices are supplemented by phenomenological monopole form factors

$$F_{VB}(k^2) = \frac{\Lambda_V^2 - m_V^2}{\Lambda_V^2 - k^2}, \quad F_A(k^2) = \frac{\Lambda_A^2}{\Lambda_A^2 - k^2}, \quad (3.112)$$

respectively, with rather large cutoff parameters, $\Lambda_V = 1.6 \text{ GeV}$ and $\Lambda_A = 1 \text{ GeV}$.

The in-medium vector meson selfenergies are then constructed from a low-density expansion as

$$\sum_V(q_0, \vec{q} = 0) \simeq \sum_V^\circ(q_0) - \rho_N T_{VN}(q_0), \quad (3.113)$$

which has been restricted to the case of vanishing three momentum $\vec{q} = 0$ where the longitudinal and transverse parts coincide. The $V-N$ scattering amplitudes T_{VN} are constructed from the interaction vertices, Eq. (3.111). The imaginary parts are evaluated from standard Cutkosky rules, and the real part is then obtained from a subtracted dispersion relation,

$$\text{Re } T_{VN}(q_0) = l_V + \int_0^\infty \frac{d\omega^2}{\pi} \frac{\text{Im } T_{VN}(\omega)}{(\omega^2 - q_0^2)} \frac{q_0^2}{\omega^2}, \quad (3.114)$$

the subtraction constants being fixed by the Thompson limit ($q_0 \rightarrow 0$) for Compton scattering of real photons. The set of diagrams contributing to the ρN amplitude is depicted in Fig. 3.15. Except for the last two “box” diagrams involving ω mesons, they are equivalent to the ρ selfenergy contributions obtained by Urban *et al.* [126] as encoded in the various vertex corrections displayed in Fig. 3.12.

Fig. 3.16 shows the resulting vector current correlators (divided by the energy squared) in the ρ , ω and ϕ meson channel for $\vec{q} = 0$. In the improved vector dominance scheme of Ref. [91], they are related to the vector meson selfenergies via

$$\prod_V(q_0, \vec{q} = 0) = \frac{1}{g_V^2} (\sum_V^\circ(q_0) + [a_V q_0^4 - \sum_V^\circ(q_0) q_0^2] D_V(q_0, 0)) \quad (3.115)$$

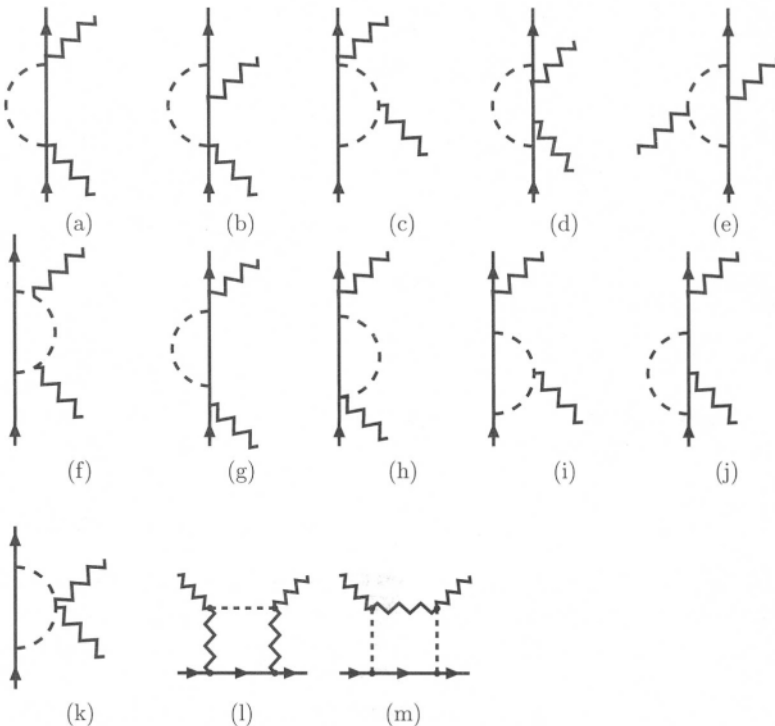


Fig. 3.15. Diagrams contributing to the ρ -N scattering amplitude in the approach of Klingl *et al.* [91]. Dashed lines: pions, wavy lines: ρ mesons (in graphs (l) and (m) the internal wavy lines represent ω mesons), solid lines: nucleons or deltas (the latter only for internal lines).

with constants $a_\rho = 1.1$, $a_\omega = a_\phi = 1$ (which give a good fit to the free $e^+e^- \rightarrow \text{hadrons}$ cross sections). As in the other approaches discussed above, the ρ (as well as the ω) spectrum exhibit a strong broadening with increasing nuclear density (note, however, that it is quantitatively overestimated, as the hard form factors employed in this calculation, Eq. (3.112), entail a large overprediction of $\pi N \rightarrow \rho N$ and $\pi N \rightarrow \omega N$ scattering data). In addition, the in-medium ω meson mass is reduced, the ρ meson mass being practically unchanged (as is revealed by inspection of the real part of the correlator (not shown); the apparent peak shift in the left panel of Fig. 3.16 is due to an additional division by ω^2 in the plot). The modifications in the ϕ channel, which are due to modifications in the kaon cloud, are rather moderate.

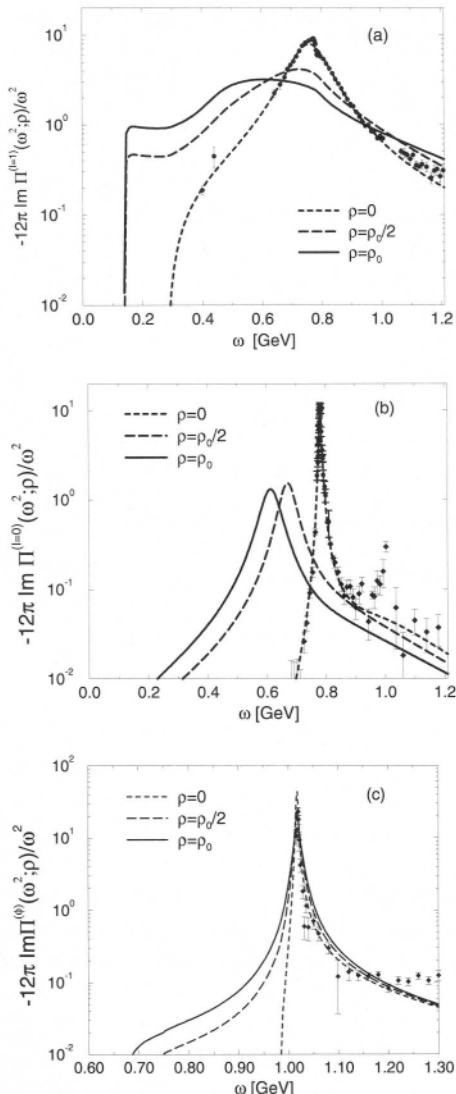


Fig. 3.16. Medium modifications of the vector correlators in nuclear matter within the approach of Klingl *et al.* [91]. Panels (a), (b) and (c) correspond to the ρ , ω and ϕ meson, respectively.

3.2.3. Direct ρ -Nucleon Resonances

Besides modifications of the pion cloud the (bare) ρ meson may couple directly to the surrounding nucleons. From meson-exchange models such as the Bonn potential [143] one knows that, e.g., the ρNN (or $\rho N\Delta$) coupling constant can be quite large, even though the correspondings-channel process $\rho N \rightarrow N \rightarrow \rho N$ is kinematically strongly disfavored. Such a kinematic suppression will be much less pronounced with increasing energy of the resonance in the intermediate state. There are indeed several baryonic resonances listed in the particle data table [146] which exhibit a significant branching fraction into the ρN channel.

Friman and Pirner [147] first suggested to calculate a ρ meson self-energy from direct ρ - N interactions in terms of $N(1720)$ and $\Delta(1905)$ resonances. The latter two have large branching ratios of well above 50% to P -wave ρ - N states. Later on it was realized [101, 102] that some lower-mass resonances – well below the naive ρN -threshold of $m_N + m_\rho$ – can have a strong coupling to predominantly S -wave ρ -nucleon states, most notably the $N(1520)$. Its decay into ρN is only possible due to the finite width of the ρ going into $\pi\pi$. However, the kinematically accessible fraction of the ρ spectral function in $N(1520) \rightarrow \rho N$ decays,

$$F = \int_{2m_N}^{M_{max}} \frac{MdM}{\pi} A_\rho(M), \quad (3.116)$$

amounts to only about $F \simeq 2\%$ (with $M_{max} = m_{N(1520)} - m_N \simeq 580 \text{ MeV}$). Yet the experimental branching ratio for this decay is $\sim 20\%$ out of the total width of $\Gamma_{N(1520)}^{tot} = 120 \text{ MeV}$. Another indication for the importance of the $N(1520)$ in its coupling to vector meson-nucleon states is found in γN cross sections, where, next to the $\Delta(1232)$, the $N(1520)$ represents the most prominent resonance structure. Besides the (not always well-known) hadronic branching ratios, the photoabsorption cross sections are an important source of information to constrain the various ρNB couplings, as will be discussed in Sect. 4.1.2.

Appropriate ρNB interaction Lagrangians can be classified according to the parity of the resonance B : negative/positive parity states are associated with S/P -waves in ρ - N , respectively, which are the dominant partial waves for moderate three-momenta. In the non-relativistic limit, gauge invariant interaction vertices can be written down as

$$\mathcal{L}_{\rho BN}^{S_wave} = \frac{f_{\rho BN}}{m_\rho} \Psi_B^\dagger (q_0 \vec{s} \cdot \vec{\rho}_a - \rho_a^0 \vec{s} \cdot \vec{q}) t_a \Psi_N + \text{h.c.} \quad (3.117)$$

$$\mathcal{L}_{\rho BN}^{P-wave} = \frac{f_{\rho BN}}{m_\rho} \Psi_B^\dagger (\vec{s} \times \vec{q}) \cdot \vec{\rho}_a t_a \Psi_N + \text{h.c..} \quad (3.118)$$

The summation over a is in isospin space with isospin matrices $\vec{t} = \vec{\tau}, \vec{T}$ depending on whether the resonance B carries $I=1/2$ or $3/2$, respectively. Analogously, the various vector/scalar products act in spin-momentum space with spin operators $\vec{s} = \vec{\sigma}, \vec{S}$ corresponding to $J=1/2$ - or $J=3/2$ -resonances (spin-5/2 resonances such as $B=\Delta(1905)$ considered in Ref. [147] require a tensor coupling of type $[R_{ij} q_i \rho_{j,a} T_a]$). From these interaction vertices one can derive in-medium selfenergy tensors for ρ -induced BN^{-1} excitations, which proceeds in close analogy to the pionic case discussed above. Due to the spin-1 character of the ρ meson one encounters both transverse and longitudinal components as

$$\sum_{\rho\alpha}^{(0),T}(q_0, q) = -\left(\frac{f_{\rho\alpha} F_{\rho\alpha}(q)}{m_\rho}\right)^2 SI(\rho\alpha) Q^2 \phi_{\rho\alpha}(q_0, q) \quad (3.119)$$

$$\sum_{\rho\alpha}^{(0),L}(q_0, q) = -\left(\frac{f_{\rho\alpha} F_{\rho\alpha}(q)}{m_\rho}\right)^2 SI(\rho\alpha) M^2 \phi_{\rho\alpha}(q_0, q) \quad (3.120)$$

with $Q^2 = q^2, q_0^2$ for the transverse P - and S -wave contributions, respectively, whereas the longitudinal part appears only for the S -wave interactions. The spin-isospin factors SI for various resonances can be found in Table 3.2, where also a typical set of coupling constants and cutoff parameters (entering the hadronic vertex form factor, taken to be of monopole form, Eq. (3.93) without the pion mass term) is quoted. The Lindhard functions ϕ coincide with the pionic case, Eq. (3.94).

An important feature when calculating the corresponding ρ meson selfenergy and spectral function has been pointed out in Ref. [101]: as a result of low-energy strength appearing in the in-medium ρ spectral function (due to broadening), the phase space for the in-medium $N(1520) \rightarrow \rho N$ decay increases substantially, i.e., the fraction F defined in Eq. (3.116) becomes much larger than the 2% in case of a free ρ meson. This induces a strong density-dependent increase of the in-medium $N(1520)$ decay width, which has to be reinserted into the expression for the $N(1520)$ width entering into the Lindhard function. This selfconsistency problem has been solved by numerical iteration in Ref. [101], where besides the $N(1520)$ eight further ρN resonances have been included (essentially coinciding with the set given in Table 3.2, although using a somewhat different parameter set: most notably, the cutoffs have been uniformly set to $\Lambda_{\rho BN} = 1500 \text{ MeV}$ with associated coupling constants to reproduce the

TABLE 3.2

Parameters of the ρBN vertices as obtained from the interaction Lagrangians, Eqs. (3.117) and (3.118), when adjusted to photoabsorption spectra and $\pi N \rightarrow \rho N$ scattering [102, 49]; table columns from left to right: baryon resonance B , relative angular momentum in the ρN decay as implicit in the interaction Lagrangians, spin-isospin factor (note that in its definition we have absorbed an additional factor of $\frac{1}{2}$ as compared to table 2 in Ref. [47]), average value for the partial decay width into ρN as extracted from Ref. [146] (including all possible partial waves), partial decay width resulting from the fit using the parameter values in the subsequent two columns, and in-medium correction to the total decay width (widths and cutoffs are quoted in [MeV]).

B	$l_{\rho N}$	$SI(\rho BN^{-1})$	$\Gamma_{\rho N}^0$	$\Gamma_{\rho N}^{0,fit}$	$\frac{f_{\rho BN}^2}{4\pi}$	$\Lambda_{\rho BN}$	Γ^{med}
$N(939)$	P	4	—	—	6.0	1500	0
$\Delta(1232)$	P	16/9	—	—	16.2	700	25
$N(1440)$	P	4	<28	0.5	1.1	600	200
$N(1520)$	S	8/3	24	23.5	6.8	600	300
$\Delta(1620)$	S	8/3	24	36	1.5	700	200
$\Delta(1700)$	S	16/9	128	111	2.5	1000	200
$N(1720)$	P	8/3	115	100	8.5	600	100
$\Delta(1905)$	P	4/5	>210	315	14.5	1200	50
$N(2000)$	P	6/5	~300	75	1.0	1500	50

ρN branching ratios). The converged results for the transverse and longitudinal parts of the ρ spectral function, A_ρ^T and A_ρ^L , at normal nuclear matter density are shown in Fig. 3.17. One observes a strong broadening of 200–300 MeV (on top of the free width) with the only visible structure being a shoulder at $M \approx 0.5$ GeV (at zero three-momentum) originating from the $N(1520)N^{-1}$ channel, which, however, is strongly washed out by a simultaneously emerging in-medium width of $\Gamma_{N(1520)}^{tot} \approx 350$ MeV. Similar results arise in the calculations of Ref. [102].

In Ref. [148] a $\pi N/\rho N/\omega N$ coupled channel approach has been pursued to assess the ρN scattering amplitude. Using the standard T - ρ approximation to calculate in-medium selfenergies again reveals a strong coupling of both ρ and ω to collective $N(1520)N^{-1}$ states with roughly equal strength. In-medium corrections to the widths have not yet been accounted for. In Ref. [103] they have been shown to somewhat reduce the strength in the low-lying $N(1520)N^{-1}$ excitation in the ρ spectral function (in addition to a strong smearing).

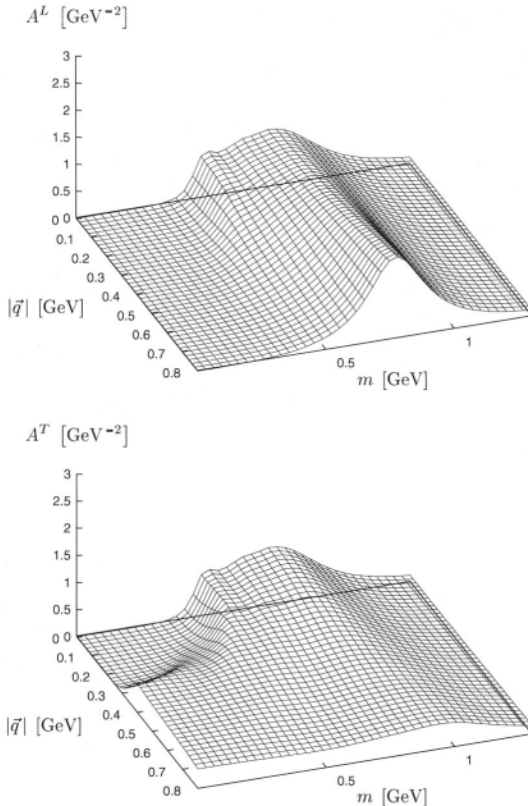


Fig. 3.17. Transverse and longitudinal parts of the ρ spectral function in cold nuclear matter when including direct ρ -induced BN^{-1} excitations according to Ref. [101]. Note that in this figure the spectral function has been defined as $A^{L,T} = (-1/\pi)\text{Im}D_\rho^{L,T}$, which differs, e.g., from Fig. 3.13 by a factor of $(-1/\pi)$.

3.2.4. Dispersive Approaches at High Energies

For ρ mesons of large energies, $q_0 \gg 1$ GeV, the resonance descriptions discussed in the previous Sections should become less reliable. On the one hand, the couplings to resonances with masses beyond 2 GeV are not very well known. On the other hand, on general grounds, one should expect that a hadronic description ceases to be the appropriate one. An alternative way to extract in-medium ρ meson properties at large energies has been suggested in Ref. [149] using high-energy γN cross sections in connection with vector dominance. Via the optical theorem the

imaginary part of the γN forward scattering amplitude can be related to the total cross section as

$$\sigma_{\gamma N}^{\text{tot}}(q_0) = -\frac{4\pi}{q} \text{Im } T_{\gamma N}(q_0), \quad (3.121)$$

where $q_0 = q$ denotes the incoming photon energy or laboratory momentum. A dispersion relation is applied to extract the real part as

$$\text{Re } T_{\gamma N}(q_0) = \int_0^\infty \frac{d\omega^2}{\pi} \frac{\text{Im } T_{\gamma N}(\omega)}{(\omega^2 - q_0^2)} \frac{q_0^2}{\omega^2}, \quad (3.122)$$

the subtraction point at zero energy being determined by the Thompson limit (cf. also eq. (3.114)). VDM then provides the link to the vector meson-nucleon scattering amplitude as

$$T_{\gamma N} = 4\pi\alpha \left(\frac{1}{g_\rho^2} f_{\rho N} + \frac{1}{g_\omega^2} f_{\omega N} + \frac{1}{g_\phi^2} f_{\phi N} \right). \quad (3.123)$$

Both naive quark model arguments (where $T_{\rho N} \approx T_{\omega N}$, while $g_\omega^2/g_\rho^2 \approx 8$) and empirical information inferred from photoproduction data of ρ , ω and ϕ mesons (see, e.g., Ref. [150]) suggest that the second and third term in eq. (3.123) are comparatively small. This allows the direct extraction of mass and width modifications for (on-shell) ρ mesons in the low-density limit (neglecting Fermi motion) according to the expressions

$$\begin{aligned} \Delta m_\rho(q_0) &\approx -2\pi \frac{\rho_N}{m_\rho} \text{Re } T_{\rho N}(q_0) \\ \Delta \Gamma_\rho(q_0) &\approx -4\pi \frac{\rho_N}{m_\rho} \text{Re } T_{\rho N}(q_0), \end{aligned} \quad (3.124)$$

which reflect a simple version of the well-known in-medium optical potentials. In the applicable energy regime of $q_0 \geq 2 \text{ GeV}$, Eletsky and Ioffe obtained $\Delta m_\rho \approx (60\text{--}80) \text{ MeV}$ and $\Delta \Gamma_\rho \approx 300 \text{ MeV}$ for transversely polarized ρ mesons at nuclear saturation density. However, the thus obtained $\Delta \Gamma$ does not directly have the meaning of a resonance broadening as at high energies it includes contributions from both elastic and diffractive scattering processes.

A similar analysis has been performed by Kondratyuk *et al.* [151] based on photoproduction (rather than Compton scattering) data to extract $T_{\gamma N \rightarrow \rho N}$, and then using $T_{\rho N} = (e/g_\rho) T_{\gamma N \rightarrow \rho N}$ to obtain the ρN scattering amplitude. The results agree within $\sim 30\%$ with those of Ref. [149]. Moreover, using a resonance model for the low-energy regime (based on

similar ρN resonances as discussed in the previous Section), they demonstrated that the $T\text{-}\rho$ approximation does not lead to reliable predictions for mass shifts due to the importance of higher-order-in-density corrections as, e.g., induced through the N^* broadening in matter. On the other hand, given the large broadening of the ρ spectral function as found in previous Sections, the quasiparticle nature of the in-medium ρ meson is lost and its in-medium mass ceases to be a well-defined quantity (note that, in general, the calculation of an in-medium spectral function does not rely on the quasiparticle concept).

3.2.5. Finite Temperature Effects in Baryonic Matter

When applying hadronic models to calculate dilepton production in (ultra-) relativistic heavy-ion collisions at present laboratory energies, ranging from 1–200 AGeV, sizable temperatures and baryon densities are encountered simultaneously. Whereas (in thermal equilibrium) the meson densities are exclusively determined by a given temperature T (with an additional possibility of meson chemical potentials), the composition of baryon matter at fixed density ρ_B changes appreciably with temperature. Apart from the appearance of finite thermal meson abundances, the heating of a cold nuclear system induces two additional features:

- (i) the nucleon Fermi-distribution functions experience a substantial smearing. Given a (kinetic) Fermi energy of $\epsilon_N^F \simeq 40 \text{ MeV}$ at nuclear saturation density, it is clear that even at BEVALAC/SIS energies of 1–2 AGeV, where the typical temperatures are in the 50–100 MeV range, thermal motion is quite significant as seen from the left panel in Fig. 3.18.
- (ii) a certain fraction of the nucleons is thermally excited into baryonic resonances; e.g., at a temperature of $T = 170 \text{ MeV}$ and in chemical equilibrium the nucleon and Δ number densities are equal owing to the larger spin-isospin degeneracy factor of the Δ ($g_\Delta = 16$) as compared to nucleons ($g_N = 4$) (right panel of Fig. 3.18).

Realistic calculations of spectral functions in a hot and dense meson/baryon mixture should include these effects. The first one is readily incorporated by using finite-temperature Fermi distribution functions in connection with thermal propagators; e.g., in the imaginary time (Matsubara) formalism, the finite- T Lindhard functions for an excitation of a baryon resonance B on a nucleon N takes the form

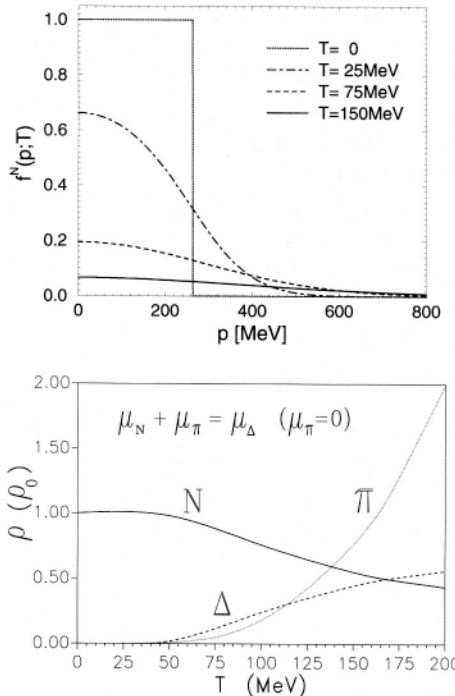


Fig. 3.18. Finite-temperature effects in baryonic matter. Top: Fermi-distribution functions for nucleons at normal nuclear matter density $\rho_0 = 0.16\text{ fm}^{-3}$ at temperatures $T = 0$ (dotted curve), $T = 25\text{ MeV}$ (dashed-dotted curve), $T = 75\text{ MeV}$ (dashed curve) and $T = 150\text{ MeV}$ (full curve). The corresponding (relativistic) nucleon chemical potentials are $\mu_N = 975, 956, 832$ and 542 MeV , respectively. Note that the nuclear (kinetic) Fermi energy at zero temperature is about $\epsilon_N^F(p_F) \approx 37\text{ MeV}$. Bottom: composition of a hot $\pi N \Delta$ gas as a function of temperature at a fixed baryon density of $\rho_B = \rho_N + \rho_\Delta = 0.16\text{ fm}^{-3}$. For comparison, the thermal pion number density is also shown. Note that the nucleon density will be further depleted when including other baryonic resonances.

$$\begin{aligned} \phi_\alpha(q_0, q; \mu_B, T) = & - \int \frac{p^2 dp}{(2\pi)^2} \int_{-1}^{+1} dx \\ & \times \sum_{\pm} \frac{f^N[E_N(p)] - f^B[E_B(\vec{p} + \vec{k})]}{\pm q_0 + E_N(p) - E_B(\vec{p} + \vec{k}) \pm \frac{i}{2}(\Gamma_B + \Gamma_N)}, \quad (3.125) \end{aligned}$$

which, in fact, not only includes the direct BN^{-1} bubble and its exchange term, but also the corresponding NB^{-1} excitation (and exchange term) occurring on the finite (thermal) abundance of the resonance species B .

Apparently, ϕ_α has the correct analytic (retarded) properties, i.e., $\phi_\alpha(q_0) = (\phi_\alpha^*(-q_0))$.

Eq. (3.125) can be directly generalized to obtain baryonic resonance excitations on thermally excited baryons. Of course, the corresponding coupling constants (and form-factor cutoff parameters) for $\rho B_1 B_2$ vertices ($B_1, B_2 \neq N$) are mostly unknown. In Ref. [103] it has been argued, however, that (in analogy to the “Brink-Axel” hypothesis for nuclear giant dipole resonances on excited states) the most important nucleonic excitation pattern, i.e., the $N(1520)N^{-1}$ should also be present on other baryonic resonances. From the particle data table one can indeed find some evidence for this conjecture: e.g., the $\Sigma(1670)$ (which is a well-established four-star resonance with spin-isospin $J^P = 1\frac{3}{2}^-$), when interpreted as a $\rho\Sigma$ (or $\rho\Lambda$) “resonance”, very much resembles the quantum numbers and excitation energy ($\Delta E = 500\text{--}700\text{ MeV}$) of the $\rho N \rightarrow N(1520)$ transition. In addition, the branching ratio of $\Sigma(1670)$ decays into “simple” final states such as $N\bar{K}$, $\Sigma\pi$ or $\Lambda\pi$ is substantially less than 100%. Similar excitations on non-strange baryonic resonances are even more difficult to identify as the latter themselves decay strongly via pion emission (i.e., the $B_1 \rightarrow B_2\rho$ decay is immediately followed by further $B_2 \rightarrow N\pi$ and $\rho \rightarrow \pi\pi$ decays). Nevertheless, from pure quantum numbers it is tempting to associate, e.g., $\Delta(1930)\Delta^{-1}$ or $N(2080)N(1440)^{-1}$ excitations with S -wave “Rhosobar” states.

To end this Chapter we show in Fig. 3.19 the final result of a many-body calculation [47, 49, 123, 50] for the ρ meson spectral function in cold nuclear matter (left panel) as well as hot hadronic matter roughly corresponding to CERN-SPS conditions (right panel) including both thermal mesonic (Sect. 3.1.4) and baryonic resonances (Sects. 3.2.3 and 3.2.5) as well as pion cloud modifications (Sect. 3.2.2), also at both finite T and μ_B . One finds a very strong broadening of the ρ in hot/dense matter, resulting in an almost entire “melting” of the resonance structure at the highest temperatures and densities. Possible consequences for experimentally measured dilepton spectra in heavy-ion collisions and theoretical interpretations will be discussed in detail in the following Chapter.

4. ANALYSIS OF DILEPTON SPECTRA: CONSTRAINTS, PREDICTIONS, AND IMPLICATIONS

As already mentioned in the Introduction, recent experimental analyses of dilepton production in fixed target heavy-ion collisions at both relativistic (1–2 AGeV, BEVALAC) and ultrarelativistic (158–200

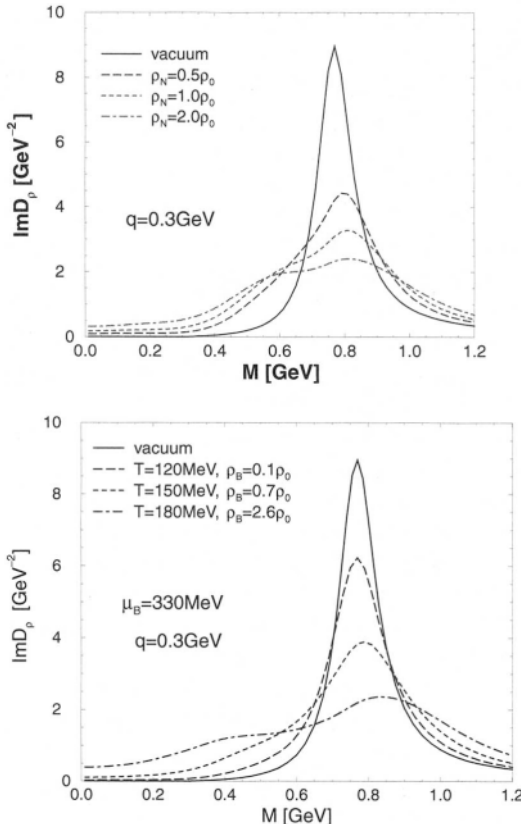


Fig. 3.19. Spin-averaged ρ meson spectral function (at fixed 3-momentum $q = 0.3\text{ GeV}$) within the many-body approach of Refs. [47, 50]. Top: in cold nuclear matter; bottom: at various temperatures and total baryon densities corresponding to a fixed baryon chemical potential of $\mu_B = 0.330\text{ GeV}$ and vanishing meson chemical potentials.

AGeV, CERN-SpS) projectile energies have exhibited a strong enhancement of low-mass pairs as compared to expectations based on free decay processes of the various hadrons in the final state (“freezeout”). Once the hadronic composition of the freezeout state is known, this so-called “hadronic cocktail” contribution to the observed spectra dilepton spectra can be quite reliably assessed without further assumptions, and has been shown to be in excellent agreement with the measurements performed under equivalent conditions in proton-induced collisions on

various nuclei. This corroborated the naive expectation that the projectile protons essentially traverse the target nuclei with the hadronization of the produced secondaries mostly taking place outside the nucleus, thus leaving no traces of significant in-medium effects in the observed dilepton decays.

As a first step further from the theoretical side, various authors have calculated the contributions from $\pi^+\pi^-$ -annihilation occurring during the lifetime of the interacting hot fireball formed in the heavy-ion induced reactions. Even without invoking any in-medium modifications, this already requires some knowledge about the dynamics within the fireball, in particular its pion abundance and momentum distributions. However, many different models for the URHIC-dynamics arrive at the same conclusion, namely that the experimentally observed enhancement at invariant masses $M_{ll} \approx (0.2\text{--}0.6)\text{GeV}$ cannot be explained when using free $\pi\pi$ annihilation (see also Fig. 1.4).

To learn about the type of medium modifications which eventually can account for the spectacular experimental results, it is most desirable to perform as “parameter-free” calculations as possible. Although at the present stage, modeling of the collision dynamics unavoidably involves some uncertainty, the underlying microscopic processes for dilepton production can and should be determined imposing as much independent experimental information as possible. This is particularly true for hadronic models involving medium effects, where the predictive power resides in the reliability of the density dependence. Such models typically comprise a large number of different processes, some of which can be subjected to consistency checks.

The outline of this Chapter is as follows: in Sect. 4.1 we discuss various constraints that the existing hadronic models have been (partially) exposed to. In Sect. 4.2 the predictions for the dilepton production rates within different hadronic approaches and more exotic ones will be confronted. Photon rates are discussed in short in Sect. 4.3. Sect. 4.4 gives a brief (by no means complete) survey of the different ways to model heavy-ion collision dynamics with focus on those that have been employed to calculate dilepton spectra. We then proceed to the analysis of low-mass dilepton spectra, starting in Sect. 4.5 from intermediate bombarding energies (1–2 AGeV) as performed at the BEVALAC (DLS collaboration) and to be remeasured in future precision measurements at SIS (HADES collaboration). The main part, presented in Sect. 4.6, reviews the extensive theoretical efforts that have been made to date in studying the experimental data on low-mass dilepton production at the full CERN-SPS energies (158–200 AGeV), where most of our current

understanding on the possible mechanisms involved is based on. Sect. 4.7 contains a much less comprehensive view at direct photon measurements, mainly to illustrate their potential for providing consistency checks on existing models for dilepton enhancement. Finally, in Sect. 4.8, we attempt to give a critical assessment of the theoretical implications that have emerged so far.

4.1. Constraints on Hadronic Dilepton Production

As with most problems in nonperturbative QCD, the calculation of low-mass dilepton radiation from interacting hot and dense hadronic matter has invariably to rely on effective approaches for the underlying production processes. To aim at quantitative predictions it is thus of essential importance to minimize the corresponding uncertainties in the calculations. In principle, two guidelines are at our disposal: (i) explicit implementation of (dynamical) symmetries shared with QCD, (ii) model constraints imposed by independent experimental information. Constraints of type (i) typically govern the interaction dynamics, (approximate) chiral symmetry in our context, whereas (ii) usually serves to narrow the range of the parameters within effective models on a quantitative level. Ideally, both aspects should be satisfied; in practice, however, the complexity of the problem enforces compromises in one or the other way.

In the previous two Chapters we have already elaborated on the chiral symmetry aspects of the various approaches in some detail, and how models for the vector-vector correlator in free space can be constructed in accordance with empirical data. Here we will address the issue of imposing constraints of type (ii) on the in-medium behavior of the vector mesons and their coupling to photons. Depending on the type of data, substantially different kinematical regimes may be probed, thus not only narrowing parameter choices but also sensing dynamical (off-shell) properties of the model under consideration. The simplest constraints on coupling constants of the interaction vertices one is interested in are provided by the partial decay widths of the corresponding resonances. These are usually not very precise and, more importantly, do not contain information on energy-momentum dependencies or combined effects of several processes. More stringent constraints are thus obtained from scattering data. We will discuss both purely hadronic reactions and photoabsorption spectra—which are more directly related to the dilepton regime—where a wealth of high-precision data on both the nucleon and various nuclei exists. The focus will again be on the ρ meson which,

as repeatedly mentioned, is the most important player in the game of low-mass dileptons from URHIC's.

4.1.1. Decay Widths and Hadronic Scattering Data

A standard approach to calculate modifications of a particle a embedded in the medium is based on the two-body scattering amplitude T_{ab} , integrated over the momentum distributions of the matter particles b . In the simplest version this represents the standard T - ρ approximation and thus captures the linear-in-density effects. However, for the ρ meson, which is a short-lived resonance (on strong interaction scales), the following complications arise: firstly, elastic ρ -hadron scattering amplitudes are not directly accessible from experiment. Secondly, the large (vacuum) width implies that in realistic calculations one cannot just use the physical pole mass, but has to account for its spectral mass distribution, $A_\rho(M)$. This, in turn, allows one to consistently incorporate processes involving off-shell ρ mesons, in particular for masses $M \leq m_\rho$, which are most relevant for low-mass dilepton spectra.

As mentioned in Chap. 3, a straightforward estimate of coupling constants for ρ -meson scattering on surrounding matter-hadrons, h , into a resonance R can be obtained from the reverse process, i.e., the decay $R \rightarrow ph$, cf. Tab. 4.1. Based on the interaction Lagrangians given in Chap. 3, one can derive the expression for the decay width $\Gamma_{R \rightarrow ph}$ and then adjust the coupling constant to reproduce the experimentally measured value.

TABLE 4.1

Mesonic resonances R with masses $m_R \leq 1300$ MeV and substantial branching ratios into final states involving either direct ρ 's (hadronic) or ρ -like photons (radiative); all widths are quoted in [MeV].

R	$I^G J^P$	Γ_{tot}	ph Decay	Γ_{ph}^0	$\Gamma_{\gamma h}^0$
$\omega(782)$	$0^- 1^-$	8.43	$\rho\pi$	~5	0.72
$h_1(1170)$	$0^- 1^+$	~360	$\rho\pi$	seen	?
$a_1(1260)$	$1^- 1^+$	~400	$\rho\pi$	dominant	0.64
$K_1(1270)$	$\frac{1}{2} 1^+$	~90	ρK	~60	?
$f_1(1285)$	$0^+ 1^+$	25	$\rho\rho$	≤8	1.65
$\pi(1300)$	$1^- 0^-$	~400	$\rho\pi$	seen	not seen
$a_2(1320)$	$1^- 2^+$	110	$\rho\pi$	78	0.31

Let us first discuss purely mesonic interactions relevant for the finite-temperature modifications of the ρ meson [123]. For the axialvector meson resonances in $P\rho$ scattering the vertex (3.63) leads to

$$\Gamma_{A \rightarrow \rho P}(s) = \frac{G_{\rho PA}^2}{8\pi s} \frac{IF(2I_\rho + 1)}{(2I_A + 1)(2J_A + 1)} \int_{2m_\pi}^{M_{\max}} \frac{MdM}{\pi} A_\rho^\circ(M) q_{cm} \times \left[\frac{1}{2} (s - M^2 - m_\pi^2)^2 + M^2 \omega_P(q_{cm})^2 \right] F_{\rho PA}(q_{cm})^2. \quad (4.1)$$

From Eq. (3.64) one obtains for vector mesons

$$\Gamma_{V \rightarrow \rho P}(s) = \frac{G_{\rho PV}^2}{8\pi} \frac{IF(2I_\rho + 1)}{(2I_V + 1)(2J_V + 1)} \int_{2m_\pi}^{M_{\max}} \frac{MdM}{\pi} A_\rho^\circ(M) \times 2q_{cm}^3 F_{\rho PV}(q_{cm})^2. \quad (4.2)$$

Besides the coupling constant, G , the cutoff parameter Λ entering the hadronic vertex form factors is a priori unknown. From principle reasoning it should be in a sensible range for hadronic processes, i.e., $\Lambda \leq 1\text{--}2\text{ GeV}$. The hadronic widths are not very sensitive to the precise value of Λ , e.g., variations in the above mentioned range entail variations in G^2 of typically 10% or less. However, as has been stressed in Ref. [123], one can do better by simultaneously adjusting the radiative decay widths of the resonances. Within the vector dominance model the radiative decay widths follow from the hadronic ones by (i) taking the $M^2 \rightarrow 0$ limit, i.e., substituting $A_\rho^\circ(M) = 2\pi\delta(M^2)$ for real photons, (ii) supplying the VDM coupling constant $(e/g)^2 \simeq 0.052^2$ and (iii) omitting the $(2I_\rho + 1)$ isospin degeneracy factor for the final state. This yields for both axialvector and vector resonances ($R = A, V$)

$$\Gamma_{R \rightarrow \gamma P} = \frac{G_{\rho PR}^2}{8\pi} \left(\frac{e}{g} \right)^2 \frac{IF}{(2I_R + 1)(2J_R + 1)} 2q_{cm}^3 F_{\rho PR}(q_{cm})^2. \quad (4.3)$$

Since the decay momentum, q_{cm} , acquires its maximum value at the photon point it is clear that the latter is more sensitive to the form-factor cutoff. With the dipole form factors of Eq. (3.69) a universal $\Lambda_{\rho PR} = 1\text{ GeV}$ yields quite satisfactory results for the decay widths of most resonances (cf. Tabs. 4.1, 4.2). If suitable data are available, an additional consistency check can be performed by comparing to the dilepton Dalitz decay spectra for $R \rightarrow Pl^+l^-$ as, e.g., done in Ref. [152] for the case of the ω meson.

A similar procedure can be applied for baryonic resonances. With the commonly employed non-relativistic ρNB Lagrangians given in Sect. 3.2.3, the decay width into ρN states becomes

TABLE 4.2

Results of a fit [123] to the decay properties of ρ - h induced mesonic resonances R with masses $m_R \leq 1300$ MeV (the $f_1(1285)$, $\pi(1300)$ and $a_2(1320)$ coupling constants are in units of GeV^{-2} , widths and formfactor cutoffs in [MeV]).

R	$IF(\rho h R)$	$G_{\rho h R}$ [GeV $^{-1}$]	$\Lambda_{\rho h R}$	$\Gamma_{\rho h}^0$	$\Gamma_{\gamma h}^0$
$\omega(782)$	1	25.8	1000	3.5	0.72
$h_1(1170)$	1	11.37	1000	300	0.60
$a_1(1260)$	2	13.27	1000	400	0.66
$K_1(1270)$	2	9.42	1000	60	0.32
$f_1(1285)$	1	35.7	800	3	1.67
$\pi(1300)$	2	9.67	1000	300	0
$a_2(1320)$	2	5.16	2000	80	0.24

$$\begin{aligned} \Gamma_{B \rightarrow \gamma N}(\sqrt{s}) = & \frac{f_{\rho NB}^2}{4\pi m_\rho^2} \frac{2m_N}{\sqrt{s}} \frac{(2I_\rho + 1)}{(2J_B + 1)(2I_B + 1)} SI(\rho NB) \\ & \times \int_{2m_\pi}^{\sqrt{s}-m_N} \frac{MdM}{\pi} A_\rho^\circ(M) q_{cm} F_{\rho NB}(q_{cm})^2 v_{\rho NB}(M) \quad (4.4) \end{aligned}$$

with the vertex function $v_{\rho NB}(M) = (M^2 + 2q_0^2)$ or $2q_{cm}^2$ for S - or P -wave resonances, respectively. However, the experimental values for $\Gamma_{B \rightarrow \rho N}$ are often beset with substantial uncertainties, especially for resonance masses below the free ρN threshold. Moreover, the simple version of VDM seems to be less accurate in the baryonic sector. As a consequence radiative decay widths, $\Gamma_{B \rightarrow \gamma N}$, can easily be overestimated [147]. But unlike the case for the mesonic resonances, much more quantitative constraints for the radiative couplings of baryonic excitations can be drawn from the analysis of photoabsorption spectra on single nucleons as well as nuclei, to be discussed in the following Section in detail. Before we come to that let us elaborate here on some further purely hadronic reactions which can provide valuable, comprehensive information on low-density nuclear effects in the vector correlator.

As first pointed out by Friman [153] the analysis of $\pi N \rightarrow \rho N$ scattering data is closely related to the modifications of the ρ -propagator in nuclear matter. Diagrammatically, any cut through the in-medium ρ -selfenergy insertions represents a pertinent scattering process. In particular, all single cuts going through NN^{-1} lines in the diagrams of Fig. 3.12 or in the dressed single-pion propagator constitute a contribution to the $\pi N \rightarrow \rho N$ reaction. Formally, this amounts to taking the imaginary part

of the relevant contributions to the in-medium **ρ -meson** selfenergy. By using the optical theorem and detailed balance one finds for the isospin-averaged cross section

$$\sigma_{\pi N \rightarrow \rho N}(s, M) = \frac{-3q_{cm}m_N}{k_{cm}^2 \sqrt{s}} \lim_{\rho_N \rightarrow 0} \frac{\text{Im} \sum_{\rho}^o(M) - \text{Im} \hat{\Sigma}_{\rho N}(M)}{\rho_N}, \quad (4.5)$$

where $\hat{\Sigma}_{\rho N}$ denotes the in-medium selfenergy containing only the diagrams with πNN^{-1} cuts. The center-of-mass 3-momenta k_{cm} and $q_{cm}(M)$ belong to the incoming pion and outgoing ρ meson with fixed mass M , respectively. For comparison with experimental data, $\sigma_{\pi N \rightarrow \rho N}(s, M)$ has to be integrated over the free ρ -meson spectral mass distribution, i.e.,

$$\sigma_{\pi N \rightarrow \rho N}(s) = \int_{2m_\pi}^{\sqrt{s}-m_N} \frac{MdM}{\pi} A_\rho^o(M) \sigma_{\pi N \rightarrow \rho N}(s, M). \quad (4.6)$$

Two types of contributions to $\hat{\Sigma}_{\rho N}$ arise: (i) from the medium modifications in the pion cloud of the ρ meson, namely pion-induced NN^{-1} excitations corresponding to t -channel pion exchange in the $\pi N \rightarrow \rho N$ reaction, and (ii) from Rhosobar-type excitations through the $B \rightarrow \pi N$ partial decay widths corresponding to the s -channel processes $\pi N \rightarrow B \rightarrow \rho N$. The surprising result [153] is that the total cross section (4.6) is very sensitive to the cutoff parameter $\Lambda_{\pi NN}$ in the πNN form factor appearing in the pion cloud. Using the standard monopole form, $\Lambda_{\pi NN}$ -values of slightly below 400 MeV already saturate the experimentally measured cross sections above the free ρN threshold. When additionally allowing for the type (ii) s -channel baryon resonance contributions which are essential for the description of the photoabsorption spectra (see next Section), this number has to be further reduced to about $\Lambda_{\pi NN} \approx 300$ MeV. Such on typical hadronic scales “unnaturally” small values are presumably related to the lack of unitarity in the resulting Born-type scattering graphs for the $\pi N \rightarrow \rho N$ process, as implicit in most models for the in-medium ρ -meson selfenergy. In fact, rather soft $\pi NN/\Delta$ form factors (with 300–500 MeV cutoffs) have been encountered in the literature, e.g., in separable models of πN scattering [154] (which resembles our model for the pion selfenergy) or pion photoproduction [155].

Other ways to extract information on the **ρ -meson** properties in nuclear matter which actually go beyond the low-density limit might be provided by two-pion production experiments on nuclei. Pion-induced experiments of the type $\pi + A \rightarrow A + \pi\pi$ have been performed at

TRIUMF for $\pi\pi$ invariant masses of up to 400 MeV. This mass regime is, however, dominated by S -wave states [156]. Alternatively, one could use proton-induced reactions as had been proposed for 2.5–2.9 GeV energy beams at SATURNE [157]. At low scattering angle one might be able to probe the in-medium ρ -meson spectral function close to the $q_0 = q$ line around $q_0 = 1$ GeV, where P -wave Rhosobars are expected to be important. Very interesting results have also been reported by the TAGX collaboration [158] for the reaction ${}^3\text{He}(\gamma, \pi^+\pi^-)ppn$ where, based on a partial wave analysis of the outgoing pions, the data have been interpreted in terms of a large downward shift of the in-medium ρ -meson mass, although no calculations using medium-modified ρ -meson spectral functions are available yet. Another possibility might be provided by extracting phase information on electro-produced ρ -mesons in $A(e, e')$ reactions at TJNAF [159].

For the ω meson a similar analysis has been performed in the $\pi N \rightarrow \omega N$ reaction [153] which also hints at a soft πNN form factor. In Refs. [153, 148] the effects of direct ωN scattering have been assessed. It seems that the $\omega N(1520)N^1$ excitation (the “Omegasobar”) plays an equally important role as in the ρN interaction, leading to strong effects for the ω -meson spectral function in nuclear matter.

A promising experiment to assess the in-medium ω properties is planned at GSI [160]. In pion-induced reactions (via the elementary process $\pi N \rightarrow \omega N$), ω mesons can be produced in nuclei almost recoil free, thus allowing sufficient time for decay in the nuclear environment. The invariant mass spectrum will then be measured through the dilepton channel. Another option is the proposed transfer reaction $d + A \rightarrow {}^3\text{He} + \omega(A - 1)$ [161].

4.1.2. Photoabsorption Spectra

A very important consistency check for any model of dilepton production can be inferred from photoabsorption spectra on both proton and nuclei [100, 162, 102, 104]. They represent the $M^2 = 0$ limit of the (time-like) dilepton kinematics and are most relevant for heavy-ion energy regimes with sizable baryon densities (on the order of normal nuclear matter density and above). These are clearly realized at BEVALAC/SIS energies but apparently also at the CERN-SPS where, as seen from rapidity spectra, significant baryonic stopping is exhibited. Whereas the absorption spectra on the proton provide low-density constraints, the various nucleus data constitute a true finite-density test ground with the additional advantage over hadronic probes that the

incoming photon suffers little absorption thus probing the inner, most dense regions of nuclei. The proton photoabsorption cross sections have been used by several groups to check their models for dilepton production.

In the microscopic BUU transport model of Effenberger *et al.* [163] the elementary γN cross sections have been calculated in terms of resonance contributions from $\Delta(1232)$, $N(1520)$, $N(1535)$ and $N(1680)$ as well as smooth background parameterizations of one- and two-pion photo-production amplitudes to reproduce the nucleon data. When moving to finite nuclei, medium effects have been accounted for through modifications in the resonance widths (explicitely treated in terms of collisional broadening and Pauli-blocking), collective potentials in Δ and nucleon propagation as well as Fermi motion. Reasonable agreement with the experimental data is obtained. However, applications for dilepton production in nucleus-nucleus colisions are not available yet.

In the “master formula approach” for the vector correlation function [99, 100] (cf. Sect. 2.8), γ absorption spectra have been calculated in Refs. [100, 104]. Fig. 4.1 shows the results for the nucleon (left panel) and nuclei (right panel). The dashed curve in the left panel represents a parameter-free prediction of the contribution from non-resonant πN states (opening at the threshold energy of about $q_0 = 140$ MeV) as extracted from πN scattering data. It corresponds to non-resonant one-pion photoproduction and essentially saturates the data beyond the Δ resonance region. This is at variance with both the BUU calculations mentioned above [163] as well as experimental phase analyses [169, 164, 170] which show that for incoming photon energies $q_0 \geq 0.6$ GeV two-pion production processes start to prevail [171]. The photoabsorption cross sections on nuclei are calculated by averaging the nucleon cross section over Fermi motion,

$$\frac{\sigma_{\gamma A}}{A} = \int \frac{d^3 p}{4\pi p_F^3/3} \Theta(p_F - |\vec{p}|) \sigma_{\gamma N}(s), \quad (4.7)$$

yielding a reasonable fit to the experimental data. The dashed curve in the right panel of Fig. 4.1 was obtained with the πN background being artificially reduced by a factor of three (compensated by larger $\Delta(1232)$ and $N(1520)$ contributions to still reproduce the nucleon data) which seems to improve the fit. Note here that a simple averaging over Fermi motion seems to give a sufficient smearing of the $N(1520)$ resonance, in contrast to previous findings in the literature [172, 173, 163, 102] where a strong in-medium resonance broadening was required.

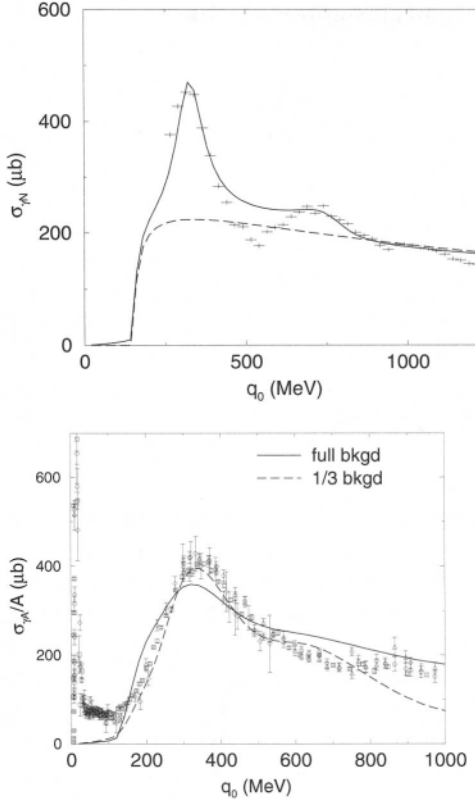


Fig. 4.1. Total photoabsorption cross section on the nucleon (top) and on nuclei (bottom) within the chiral reduction approach taken from Ref. [104]. The nucleon and nuclei data are from Ref. [164] and Refs. [165, 166, 167, 168], respectively.

In the effective Lagrangian approaches where the in-medium vector meson properties are calculated in terms of explicit interactions with surrounding matter particles, the resulting spectral functions can be related to total photoabsorption cross sections. In Refs. [162, 91] the electromagnetic current-current correlation function has been expressed to lowest order in density in terms of the Compton tensor for forward γN scattering, $T_{\gamma N}^{\mu\nu}$, as

$$\Pi_{\text{em}}^{\mu\nu}(q) = \Pi_{\text{em}}^{\circ\mu\nu}(q) + g_N \int \frac{d^3 p}{(2\pi)^3} \frac{M_N}{E_p^N} T_{\gamma N}^{\mu\nu}(q; p) \Theta(p_F - |\vec{p}|). \quad (4.8)$$

For real photons, only the transverse part of $T_{\gamma N}$ survives. Taking the low-density limit, $pF \rightarrow 0$, and using the optical theorem,

$$\sigma_{\gamma N}(q_0) = -\frac{4\pi\alpha}{q_0} \text{Im } T_{\gamma N}^T(q_0, |\vec{q}| = q_0), \quad (4.9)$$

as well as VDM,

$$\text{Im } \prod_{\text{em}}^T(q_0, \vec{q}) = \sum_{V=\rho, \omega, \phi} \frac{1}{g_V^2} \text{Im } \sum_V^T(q_0, \vec{q}), \quad (4.10)$$

one obtains the desired relation between the isospin-averaged γ -nucleon cross section and the vector meson selfenergies:

$$\sigma_{\gamma N}(q_0) = \frac{4\pi\alpha}{q_0} \lim_{\rho_N \rightarrow 0} \frac{1}{\rho_N} \sum_{V=\rho, \omega, \phi} \frac{1}{g_V^2} \text{Im } \sum_V^T(q_0, |\vec{q}| = q_0) \quad (4.11)$$

(note that $\text{Im}\Pi^0(M^2)$ vanishes below the two-pion threshold $M = 2m_\pi$). Unfortunately, no explicit results for photoabsorption spectra are available in the approach of Refs. [162, 91].

A slightly different way of deriving analogous relations has been pursued in Ref. [102]. Here, the starting point is the total cross section of a photon per unit volume element d^3x of cold nuclear matter, averaged over the incoming polarizations,

$$\begin{aligned} \frac{d\sigma}{d^3x} &= \frac{1}{2} \sum_{\lambda} \sum_f \frac{1}{v_{in}} \frac{1}{2q_0} |\mathcal{M}_f|^2 (2\pi)^4 \delta^{(4)}(p_f - q) \\ &= -\frac{4\pi\alpha}{q_0} \frac{1}{2} \sum_{\lambda} \epsilon_{\mu}(q, \lambda) \epsilon_{\nu}(q, \lambda) \text{Im } \prod_{\text{em}}^{\mu\nu}(q), \end{aligned} \quad (4.12)$$

where $\mathcal{M}_f = e \langle f | j_{\mu}^{\text{em}}(0) | i \rangle \epsilon^{\mu}(q, \lambda)$ is the transition matrix element of the electromagnetic current, taken between the initial nuclear ground state $|i\rangle = |0\rangle$ and final states $|f\rangle$ with $\epsilon_{\mu}(q, \lambda)$ being the photon polarization vector. Neglecting small contributions from isoscalar vector mesons within the VDM, the electromagnetic correlator can be saturated by the neutral ρ meson using the field-current identity

$$j_{\text{em}}^{\mu} = (m_{\rho}^{(0)})^2 / g_{\rho} \rho_3^{\mu}. \quad (4.13)$$

Using the completeness relation for photon polarization vectors,

$$\sum_{\lambda} \epsilon_{\mu}(q, \lambda) \epsilon_{\nu}(q, \lambda) = -g_{\mu\nu}, \quad (4.14)$$

the total photoabsorption cross section, normalized to the number of nucleons A , takes the form

$$\begin{aligned} \frac{\sigma_{\gamma A}^{\text{abs}}}{A} &= \frac{1}{\rho_N} \frac{d\sigma}{d^3x} \\ &= -\frac{4\pi\alpha}{q_0} \frac{(m_\rho^{(0)})^4}{g_\rho^2} \frac{1}{\rho_N} \text{Im } D_\rho^T(q_0, |\vec{q}| = q_0) \end{aligned} \quad (4.15)$$

with the transverse in-medium ρ -meson propagator

$$\text{Im } D_\rho^T = \frac{\text{Im} \sum_\rho^T}{|M^2 - (m_\rho^{(0)})^2 - \sum_\rho^T|^2} \quad (4.16)$$

(for $M^2 = 0$ the longitudinal part vanishes identically). Note that Eq. (4.15) does not involve any low-density approximations. However, for $\rho_N \rightarrow 0$ and $A = 1$ (corresponding to the absorption process on a single nucleon), one has

$$\lim_{\rho_N \rightarrow 0} \text{Im } D_\rho^T(q_0, \vec{q}) = \lim_{\rho_N \rightarrow 0} \text{Im} \sum_\rho^T(q_0, \vec{q}) / (m_\rho^{(0)})^4, \quad (4.17)$$

thus readily recovering Eq. (4.11). In the model of Ref. [102] the ρ -meson selfenergy in nuclear matter receives two contributions,

$$\sum_\rho^T = \sum_{\rho\pi\pi}^T + \sum_{\rho N}^T, \quad (4.18)$$

representing the renormalization of the pion cloud through πNN^{-1} and $\pi\Delta N^{-1}$ excitations as well as direct ρBN^{-1} interactions, respectively. However, as has been noted long ago, the most simple version of the VDM (4.13) typically results in an overestimation of the $B \rightarrow N\gamma$ branching fractions when using the hadronic coupling constants deduced from the $B \rightarrow N\rho$ partial widths. One can correct for this by employing an improved version of the VDM [174], which allows to adjust the $BN\gamma$ coupling μ_B (the transition magnetic moment) at the photon point independently [147]. It amounts to replacing the combination $(m_\rho^{(0)})^4 \text{Im} D_\rho^T(q_0, \vec{q})$ entering Eq. (4.15) by the following “transition form factor”:

$$\begin{aligned} \mathcal{F}^T(q_0, \vec{q}) &= -\text{Im} \sum_{\rho\pi\pi}^T |d_\rho - 1|^2 - \text{Im} \sum_{\rho N}^T |d_\rho - r_B|^2 \\ d_\rho(q_0, \vec{q}) &= \frac{M^2 - \sum_{\rho\pi\pi}^T -r_B \sum_{\rho N}^T}{M^2 - (m_\rho^{(0)})^2 - \sum_{\rho\pi\pi}^T - \sum_{\rho N}^T}, \end{aligned} \quad (4.19)$$

where

$$r_B = \frac{\mu_B}{f_{\rho BN}} \frac{e}{m_\rho} \frac{g}{g} \quad (4.20)$$

denotes the ratio of the photon coupling to its value in the naive VDM. In principle, each resonance state B can be assigned a separate value for r_B but, as will be seen below, reasonable fits to the photoabsorption spectra can be achieved with a single value making use of some latitude in the hadronic couplings $f_{\rho BN}$ and form-factor cutoff parameters Λ_ρ within the experimental uncertainties of the partial widths (4.4). The final expression to be used for the photoabsorption calculations then reads

$$\frac{\sigma_{\gamma A}^{\text{abs}}}{A} = \frac{4\pi\alpha}{g^2 q_0} \frac{1}{\rho_N} \mathcal{F}^T(q_0, |\vec{q}| = q_0). \quad (4.21)$$

Let us first discuss the γN spectra, in particular the role of background contributions (which in this context can be regarded as “meson exchange” processes), encoded in the low-density limit of $\Sigma_{\rho NN}$. With the coupling constants of the πNN - and $\pi \Delta N$ -vertices fixed at their standard values (cf. Tab. 3.1), the strength of the background is controlled by the cutoff $\Lambda_{\pi NN}$ in the phenomenological (hadronic) vertex form factors. In early applications to dilepton spectra [140, 114, 141, 142, 47, 91] the values were chosen around (1–1.2) GeV in reminiscence to the Bonn potential [143]. However, with the analysis of photoabsorption spectra [102] it became clear that much lower values are required, at most of around 600 MeV. Shortly thereafter, Friman pointed out [153] that this is still too large to be compatible with available $\pi N \rightarrow \rho N$ scattering data as discussed in the previous Section, enforcing even smaller values [49], thereby further suppressing the “background” contribution in the photoabsorption spectra. Using the value of $\Lambda_\pi \approx 300$ MeV deduced in Sect. 4.1.1 actually improves the description of the γN spectra in the “dip region” between the $\Delta(1232)$ and the $N(1520)$ resonances [49] as compared to the results obtained with $\Lambda_{\pi NN} = 550$ MeV in Ref. [102], see left panel of Fig. 4.2. Moreover, the non-resonant contribution in the Δ region now amounts to about $70 \mu b$, which coincides with what has been extracted from experimental phase analyses [169, 164, 170]. On the other hand, the parameter-free assessment of this background component in the “master formula approach” [100] differs by approximately a factor of 3 across the entire photon energy range under consideration (a very similar result is found when using the Bonn-value of 1.2 GeV deduced from πN data in the framework of Ref. [126]). Given the magnitude of

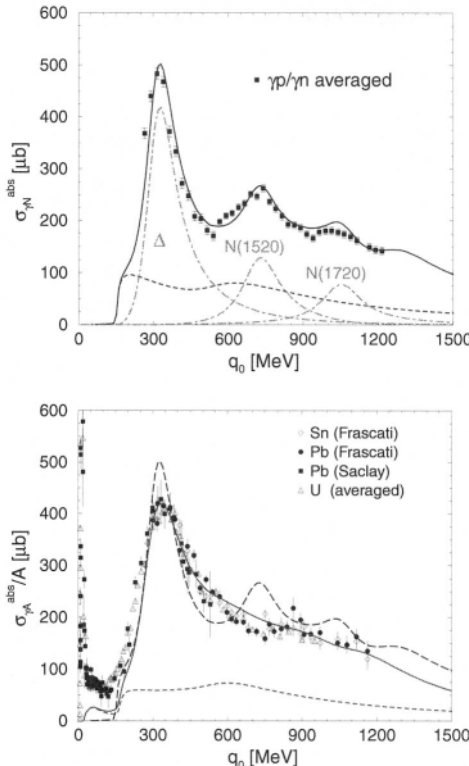


Fig. 4.2. Total photoabsorption cross section on the nucleon (top) and on nuclei (bottom) as obtained in the ρ spectral function approach [102, 50]. Top: full result of the fit using the parameters of Tab. 3.2 (solid line), $\pi\pi$ “background” (dashed line) as well as the three dominant ρN resonances $\Delta(1232)$, $N(1520)$ and $N(1720)$ (dashed-dotted lines); the data are averaged over proton [175] and neutron [176] measurements. Bottom: full result (solid line) and non-resonant background contributions (short-dashed line) for $\rho_N = 0.8\rho_0$, as well as the lowest-order-density result from the nucleon fit (long-dashed line); the data are taken from Refs. [165, 166, 167, 168].

the background, the resonance contributions encoded in $\Sigma_{\rho B}$ are readily adjusted to obtain a good fit to the γN data. The employed resonances and vertex parameters are summarized in Tab. 3.2. One should note that an unambiguous determination of coupling constants and form-factor cutoffs parameters is not possible from the total absorption cross section alone. To further disentangle them more exclusive reaction channels (e.g., one- and two-pion photoproduction) need to be analyzed. Never-

theless, for the purpose of predicting reliable dilepton production rates the constraints from the total absorption cross sections give reasonable confidence.

For absorption spectra on nuclei, one experimentally observes an almost independent scaling with the mass number A of different nuclei (cf. right panel of Fig. 4.2). This suggests that both surface and nuclear structure effects play a minor role as might be expected since the incoming photon predominantly probes the interior of the nuclei. Therefore it appears justified to perform the calculations for the idealized situation of infinite nuclear matter at an average density, which has been taken as $\bar{\rho}_N = 0.8\rho_0$ (in fact, the results for the normalized cross section, Eq. (4.21), depend only weakly on density within reasonable limits of $0.6 \leq \rho/\rho_0 \leq 1$). As compared to the free nucleon two additional features appear in the nuclear medium: short-range correlation effects in the resummation of the particle-hole bubbles and in-medium corrections to the resonance widths. Due to the rather soft form factors involved, the P -wave pion-induced excitations turn out to favor rather small Landau-Migdal parameters of $g_{NN} = 0.6$ and $g'_{\alpha\beta} = 0.2$ for all other transitions including P -wave Rhosobars. The S -wave ρBN^{-1} bubbles show only marginal evidence for short-range correlations with a slight tendency towards larger values (the results in the left panel of Fig. 4.2 have been obtained with $g'_{S\text{-wave}} = 0.6$). However, as already mentioned above, the observed disappearance of the $N(1520)$ resonance in the nuclear medium requires a large in-medium increase of its width. Such a behavior has indeed been found in a selfconsistent microscopic treatment of the ρ -meson spectral function and the $N(1520)$ width in nuclear matter [101], which is based on a very similar framework as employed here. The actual value used for $\Gamma_{N(1520)}^{\text{med}}$ in Fig. 4.2 is in accordance with Ref. [101]. On the other hand, the net in-medium correction to the $\Delta(1232)$ width is quite small. This reflects the fact that a moderate in-medium broadening is largely compensated by Pauli blocking effects on the decay nucleon. The sensitivity of the results with respect to the in-medium widths of the higher lying resonances is comparatively small. It is also noteworthy that below the pion threshold some strength appears. This is nothing but the well-known “quasi deuteron” tail above the giant dipole resonance, arising from pion-exchange currents. These are naturally included in the spectral function framework through higher orders in density in the pion cloud modifications. Also note that a linear-density approximation to Eq. (4.19), which is equivalent to the γN result, does not properly reproduce the γA data.

4.2. Dilepton Rates in Hot and Dense Matter

Having discussed the approaches that have been constructed to compute the vector correlator in hot and dense matter as well as the corresponding efforts and philosophies to constrain the underlying assumptions, we now turn our attention to the results for the dilepton production rates. To be able to draw any conclusions from the eventual analysis of dilepton spectra in heavy-ion collisions it is essential to assess the differences and similarities in the model predictions on an equal footing, i.e., without the complications arising from modeling the space-time history of the collisions or experimental acceptance cuts. In practically all microscopic approaches one calculates an eight-fold differential rate per unit four momentum and four volume. To facilitate the comparison, it has become common to focus on the 3-momentum integrated rates

$$\frac{dR_{l^+l^-}}{dM^2}(M) = \int \frac{d^3 q}{2q_0} \frac{dR_{l^+l^-}}{d^4 q}(q_0, \vec{q}) \quad (4.22)$$

at fixed temperature T and baryon density ρ_B (or, equivalently, baryon chemical potential μ_B). In the following we will first address the class of more “conventional”, hadronic calculations based on essentially known interactions, and then put these into context with results from scenarios associated with “new” physics such as QGP or DCC formation.

4.2.1. Comparison of Hadronic Approaches

As elaborated in Sect. 2.5 the general expression for the dilepton production rate in a hadronic medium of given temperature T and baryon chemical potential μ_B can be written as

$$\frac{dR_{l^+l^-}}{d^4 q} = L_{\mu\nu}(q) W^{\mu\nu}(q), \quad (4.23)$$

where $L_{\mu\nu}$ and $W_{\mu\nu}$ denote the leptonic and hadronic tensor, respectively, cf. Eqs. (2.75) and (2.76). The latter can also be written as

$$W^{\mu\nu}(q; T) = \sum_i \frac{e^{E_i/T}}{Z} \sum_f \langle i | j^\mu(0) | f \rangle \langle f | j^\nu(0) | i \rangle (2\pi)^4 \delta^{(4)}(q + p_f - p_i), \quad (4.24)$$

which is straightforwardly related to the retarded current-current correlation function according to

$$-2 \operatorname{Im} \prod_{\text{em}}^{\mu\nu}(q) = (e^{q_0/T} - 1) W^{\mu\nu}(q). \quad (4.25)$$

Inserting Eqs. (2.75) and (4.25) into (4.23), and exploiting gauge invariance, $q_\mu \Pi_{\text{em}}^{\mu\nu} = 0$, one obtains the general result

$$\frac{dR_{l^+l^-}}{d^4 q} = -\frac{\alpha^2}{\pi^3 M^2} f^B(q_0; T) \operatorname{Im} \prod_{\text{em}}(q_0, \vec{q}) \quad (4.26)$$

with the thermal Bose occupation factor $f^B(q_0; T) = (e^{q_0/T} - 1)^{-1}$ and the spin-averaged correlator

$$\operatorname{Im} \prod_{\text{em}}(q_0, \vec{q}) = \frac{1}{3} [\operatorname{Im} \prod_{\text{em}}^L(q_0, \vec{q}) + 2 \operatorname{Im} \prod_{\text{em}}^T(q_0, \vec{q})], \quad (4.27)$$

given in terms of its standard decomposition into longitudinal and transverse projections.

4.2.1a. Effects of a Hot Meson Gas. Let us start by considering a hot meson gas without any baryons. The most obvious source of dilepton radiation from such a system is the free $\pi^+\pi^- \rightarrow l^+l^-$ annihilation process with no further medium effects included. This process is reliably described within the simple VDM framework, so that very little model uncertainty is involved once the experimental data for the pion electromagnetic form factor in the time-like region are properly accounted for. Therefore we will use this process as a standard baseline for comparing medium effects within various approaches. In VDM (i.e., invoking the field-current identity (4.13)) $\pi\pi$ annihilation proceeds via the formation of an intermediate ρ meson. The corresponding hadronic tensor is then saturated by the ρ -meson propagator,

$$W^{\mu\nu}(q) = -2 f^\rho(q_0; T) \frac{(m_\rho^{(0)})^4}{g_{\rho\pi\pi}^2} \operatorname{Im} D_\rho^{\mu\nu}(q). \quad (4.28)$$

Thus the dilepton production rate for $\pi^+\pi^- \rightarrow \rho \rightarrow \gamma^* \rightarrow e^+e^-$ becomes

$$\begin{aligned} \frac{dR_{\pi\pi \rightarrow ee}}{d^4 q}(q_0, \vec{q}) &= -\frac{\alpha^2 (m_\rho^{(0)})^4}{\pi^3 g_{\rho\pi\pi}^2} \frac{f^\rho(q_0; T)}{M^2} \operatorname{Im} D_\rho(q_0, \vec{q}) \\ &= -\frac{\alpha^2}{\pi^3 g_{\rho\pi\pi}^2} \frac{f^\rho(q_0; T)}{M^2} \operatorname{Im} \sum_{\rho\pi\pi}^\circ(M) |F_\pi^\circ(M)|^2, \end{aligned} \quad (4.29)$$

where the second equality implies the use of the free ρ -meson propagator. As is well-known a thermodynamically equivalent way to describe

the *same* contribution is to consider the decay of thermal ρ mesons in the system. Accounting for both $\pi\pi$ annihilation and ρ decays clearly constitutes double counting.

In-medium modifications to the free $\pi\pi$ annihilation process in a hot meson gas have been studied by several groups, as we have already discussed in some detail in Sect. 3.1. At a fixed temperature of $T = 150 \text{ MeV}$ the three-momentum integrated rates (as given by Eq. (4.22)) are confronted in Fig. 4.3 for some of the different approaches available in the literature. One of the selected examples is of model-independent nature [99] putting the emphasis on chiral symmetry aspects of the interactions, whereas the other two [119, 123] represent the more phenomenological approaches based on effective Lagrangians.

The chiral reduction formalism employed by Steele *et al.* (which combines chiral Ward identities with experimental data on spectral functions in the vector and axialvector channels, dominated by the ρ and $a_1(1260)$ mesons, respectively, cf. Sect. 2.8) is shown as the short-dashed line in Fig. 4.3. The appearance of the a_1 (predominantly formed in resonant $\rho\pi$ scattering) in the electromagnetic rates represents the mixing effect of the vector and axialvector correlators as dictated by chiral symmetry. Most of the enhancement over the free $\pi\pi$ rate for invariant masses below $M_{ee} \approx 0.6 \text{ GeV}$ can indeed be assigned to the (Dalitz-decay) tails of the $a_1(1260)$. On the other hand, note that there is

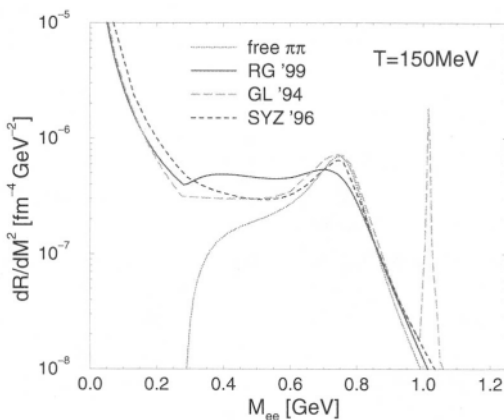


Fig. 4.3. Three-momentum integrated dilepton rates in a hot meson gas at $T = 150 \text{ MeV}$ in the hadron-based approaches of Gale/Lichard [119] (long-dashed line), Steele *et al.* [99] (short-dashed line) and Rapp *et al.* [47, 123] (solid line). The dotted line represents free $\pi\pi$ annihilation.

practically no depletion of the ρ -meson peak around $M_{ee} \simeq m_\rho$. This is a consequence of the density expansion inherent in this virial-type expansion which evades any kind of diagrammatic resummations. Such resummations naturally occur in the propagator formalism: even if the (in-medium) selfenergy correction is evaluated to lowest order, the solution of the corresponding Dyson equation automatically generates iterations to all orders which typically leads to a downward shift of strength as we will see below.

In Ref. [119] a large number of mesonic tree level scattering amplitudes involving e^+e^- final states has been computed within the VDM, employing phenomenological Lagrangians compatible with gauge invariance and inspired by the chiral properties of low-energy QCD [109]. The corresponding coupling constants have been determined along the lines discussed in Sect. 4.1.1 using the experimental branching ratios for radiative decays, etc. Within standard relativistic kinetic theory the dilepton production rate has then been obtained by suitable momentum integrations over the squared matrix elements including appropriate thermal occupation factors (for a given process, the kinetic theory expressions can be shown to be equivalent to standard finite-temperature field theoretic results to leading order in temperature). The long-dashed curve in Fig. 4.3 represents the final result of this analysis, also exhibiting substantial excess over the free $\pi\pi$ rate for low masses $M_{ee} \leq 0.6 \text{ GeV}$, which is predominantly generated by the radiative decay of the omega, $\omega \rightarrow \pi^0 e^+ e^-$. Contributions from $a_1(1260)$ mesons have not been included. The incoherent summation of the various processes does again not induce any depletion of the peak, leading to a close overall resemblance with the rate from the chiral reduction formalism [99] (short-dashed curve).

In Ref. [47] the imaginary time (Matsubara) formalism has been employed to calculate the ρ propagator in hot hadronic matter accounting for the full off-shell dynamics of the considered interactions. As far as meson gas effects are concerned, only resonant $\rho\pi \rightarrow a_1(1260)$ and $\rho K/\bar{K} \rightarrow K_1(1270)/\bar{K}_1(1270)$ contributions were included at the time, yielding very similar results as have been obtained before in an (on-shell) kinetic theory framework [120] (which is mainly due to the fact that both the a_1 and K_1 resonances are situated above the free $\rho\pi$ and ρK thresholds, respectively, resulting in little off-shell sensitivity). A more comprehensive analysis of the finite temperature ρ -meson selfenergy was performed in Ref. [123] along the same lines as in Ref. [47]. The most notable of the additionally included mesonic resonances turned out to be the $\omega(782)$ meson accessible through interactions of off-shell ρ

mesons (with mass $M \simeq 500 \text{ MeV}$, cf. Fig. 3.8) with thermal pions. The corresponding dilepton production process is $\rho\pi \rightarrow \omega \rightarrow \pi ee$, i.e., the radiative Dalitz decay of thermal ω mesons. It indeed quantitatively coincides with the equivalent contribution calculated in Ref. [119]. In addition, the most simple temperature effect in the pion cloud of the ρ meson has been included, consisting of a Bose-Einstein enhancement in the in-medium $\rho \rightarrow \pi\pi$ decay width. Schematically written it modifies the imaginary part of the $\rho\pi\pi$ selfenergy as

$$\text{Im} \sum_{\rho\pi\pi}^{\circ}(M) \rightarrow \text{Im} \sum_{\rho\pi\pi}(M; T) = \text{Im} \sum_{\rho\pi\pi}^{\circ}(M)[1 + 2f^\pi(M/2)], \quad (4.30)$$

cf. also Eq. (3.62). The full result of Ref. [123] is shown by the solid line in Fig. 4.3: in the low-mass region it exceeds the results of both the chiral reduction approach [99] and of the incoherent summation of decay/scattering processes [119]. The discrepancy to the latter can be traced back to the a_1 -meson contribution and, more importantly, to the Bose enhancement in the $\rho \rightarrow \pi\pi$ decay width [123]. Also note that the ρ -meson spectral function calculation induces a $\sim 40\%$ suppression of the signal in the vicinity of the free ρ mass. This is a characteristic feature of many-body type approaches and is not present in density-expansion schemes as implicit in the calculations of Gale/Lichard and Steele *et al.* It can be easily understood as follows [123]: the ρ spectral function (which governs the dilepton rate in the many-body framework) can be schematically written in terms of the selfenergy as

$$\text{Im } D_\rho = \frac{\text{Im} \sum_\rho}{|M^2 - m_\rho^2|^2 + |\text{Im} \sum_\rho|^2}, \quad (4.31)$$

where we have absorbed the real part of the selfenergy in the (physical) ρ mass m_ρ . In the low-mass region, where $m_\rho \gg M$ and $m_\rho^2 \gg |\text{Im} \Sigma_\rho|$, the denominator is dominated by m_ρ so that

$$\text{Im } D_\rho(M \ll m_\rho) \propto \frac{\text{Im} \sum_\rho}{m_\rho^4}. \quad (4.32)$$

Since $\text{Im} \Sigma_\rho$ basically encodes a summation of scattering amplitudes times (pion-) density, one immediately recognizes the close analogy to kinetic theory or low-density expansions. On the other hand, in the vicinity of the ρ -peak, where $M \simeq m_\rho$, the denominator in Eq. (4.31) is dominated by $\text{Im} \Sigma_\rho$ so that

$$\text{Im } D_\rho(M \simeq m_\rho) \propto \frac{1}{\text{Im} \sum_\rho}, \quad (4.33)$$

demonstrating that the consequence of an increase in density is a suppression of the maximum, which cannot be straightforwardly casted in a low-density expansion.

4.2.1b. Effects of Finite Baryon Density. The situation becomes more involved when comparing dilepton production rates in the presence of baryons. Most of the investigations so far have been restricted to the case of nucleons at zero temperature, which is particularly obvious for model constraints inferred from ρN or $\gamma N/\gamma A$ scattering data as discussed in Sect. 4.1. The first complication arises from the fact that in any finite temperature system with a net baryon density, some fraction of the nucleons will be thermally excited into baryonic resonances and therefore, in principle, should not be included in medium modifications generated by nucleons. For instance, at a temperature of $T = 150$ MeV and total baryon density $\rho_B = \rho_0$ (which, when accounting for all baryonic resonances with masses $m_B \leq 1.7$ GeV as well as the lowest-lying Λ and Σ hyperons, translates into a common baryon chemical potential of $\mu_B \simeq 385$ MeV) only about one third of the baryons are actually nucleons. On the other hand, also excited resonances will have nonzero cross sections with pions or ρ mesons which are, however, usually somewhat smaller in magnitude. The second subtlety consists of a substantial smearing of the zero temperature nucleon distribution functions (Fig. 3.18) which might further suppress any nucleon-driven medium effects in high-energy heavy-ion collisions. Nevertheless, meson-nucleon interactions are typically much stronger than meson-meson ones, such that even at full CERN-SPS energies (158–200 AGeV), where the final pion-to-nucleon ratio is about 5:1, baryons have a substantial impact on pion and ρ -meson properties as has been demonstrated by several authors.

In one class of models, medium effects in dilepton production rates are again studied by focusing on the role of the ρ -meson spectral function [140, 114, 47, 147]. As a representative we choose the most recent version of Refs. [102, 49, 123, 50], where both effects of finite temperature and finite density have been incorporated. In the baryonic sector the naive VDM, which works well for the description of purely mesonic processes (see previous Section), is improved by the Kroll-Lee-Zumino coupling [174] in the transverse part to optimally reproduce photoabsorption data (cf. Sect. 4.1.2). The dilepton rate is then given by

$$\frac{dR_{\pi\pi \rightarrow ee}}{d^4 q}(q_0, \vec{q}) = \frac{\alpha^2}{\pi^3 g_{\rho\pi\pi}^2} \frac{f^\rho(q_0; T)}{M^2} \frac{1}{3} [\mathcal{F}^L(q_0, \vec{q}) + 2\mathcal{F}^T(q_0, \vec{q})] \quad (4.34)$$

with the transverse transition form factor \mathcal{F}^T from Eq. (4.19), whereas the longitudinal part, not being constrained by photon data, is obtained in the naive VDM,

$$\mathcal{F}^L(q_0, \vec{q}) = -(m_\rho^{(0)})^4 \operatorname{Im} D_\rho^L(q_0, \vec{q}). \quad (4.35)$$

Within model-independent approaches, a simultaneous assessment of finite temperature and finite density effects has been performed by Steele *et al.* [100, 104] using the chiral reduction formalism. Here the in-medium dilepton rates are based on the in-medium vector correlator as outlined in Sect. 2.8.

The thermal rate results employing the in-medium ρ spectral function and the chiral reduction formalism are confronted in Fig. 4.4. We should stress again that both approaches have been thoroughly constrained in both their finite density and finite temperature behavior (cf. Sects. 4.1.1 and 4.1.2). However, some differences emerge in the dilepton regime. At low invariant masses $M_{ee} \leq 0.6 \text{ GeV}$ the rates qualitatively agree in that a strong additional enhancement due to the presence of nucleons is observed. Quantitatively, the spectral function results give up to a factor of ~ 2 more e^+e^- yield around $M_{ee} \approx 0.4 \text{ GeV}$ —exactly the region where the $N(1520)$ contribution figures in most importantly. This discrepancy indeed originates from the different assignment of “background” and resonance contributions in the photoabsorption spectra: in the chiral reduction formalism, the γN cross sections are dominated by the non-resonant “background” (see left panel of Fig. 4.1), whereas the most recent ρ spectral function calculations attribute the major strength to direct ρN resonances, most relevant the $N(1520)$ (see left panel of Fig. 4.2). The important point is now that when moving from the photon point to the time-like dilepton regime (at small three-momentum), the resonance contributions are much more enhanced than the more or less structureless background, which is essentially a kinematic effect¹. As we have pointed out in Sect. 4.1.2, these deviations can be resolved by analyzing more exclusive channels in the photoabsorption data. A more severe, *qualitative* difference in the rate predictions of Fig. 4.4 again

¹Similar conclusions have been reached in Ref. [104]; it has been shown there that when “artificially” reducing the πN background obtained from the chiral reduction formalism in the photoabsorption spectra by a factor of 3 and assigning the missing strength to the $N(1520)$, the resulting prediction for the dilepton rate in the $M = 0.4 \text{ GeV}$ region increases by a factor of 2–3.

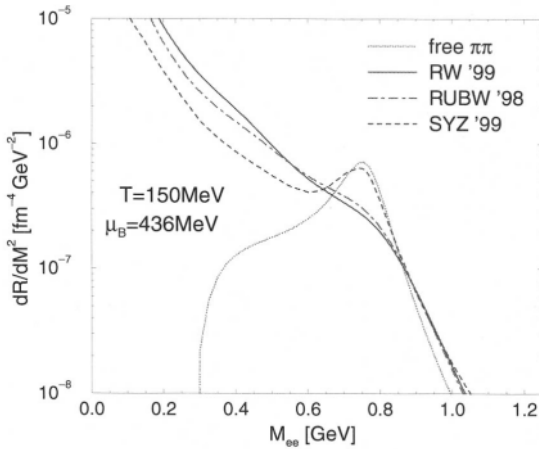


Fig. 4.4. Three-momentum integrated dilepton rates in a hot meson-nucleon gas at $T = 150 \text{ MeV}$ and a nucleon density $\rho_N = 0.5\rho_0$ (corresponding to a nucleon chemical potential $\mu_N = 436 \text{ MeV}$) in the hadronic approaches of Steele *et al.* [100] (dashed line) and Rapp *et al.* [102, 123] (dashed-dotted line). The solid line corresponds to the full results of Ref. [50], i.e., when additionally including scattering contributions off thermally excited baryonic resonances at a common baryon chemical potential $\mu_B = \mu_N$ as described in Sect. 3.2.5.

shows up around the free ρ/ω mass. Whereas the virial-type density expansion of the chiral reduction formalism leaves the dilepton yield essentially unchanged, the spectral function result exhibits a strong reduction of the resonance peak due to a large in-medium broadening of the ρ meson (see the discussion at the end of the previous Section). Thus, contrary to collective effects, which are typically driven by strong resummation effects in the *real* part of the selfenergy, higher order effects in the *imaginary* part of the vector meson propagators seem to play an important role. Finally we remark that the additional inclusion of excitations on thermally excited resonances of type $B_1B_2^{-1}$ (cf. Sect. 3.2.5) [50] further reinforces the broadening and low-mass enhancement by up to 20%, see solid curve in Fig. 4.4.

To summarize this Section about the various hadronic dilepton rate calculations one may conclude that quite different approaches pursued in the literature so far have reached a reasonable consensus in the pure mesonic sector. The corresponding enhancement over the “standard candle” of free $\pi\pi$ annihilation below the free ρ/ω masses amounts to a factor of $\sim 3\text{--}5$ at typical temperatures around $T = 150 \text{ MeV}$. At finite

baryon density, due to the stronger nature of meson-baryon interactions, a substantially stronger impact on in-medium dilepton rates has been found, entailing more pronounced discrepancies between various models, differing *quantitatively* in the low-mass region (by factors of 2–3), and, more importantly, *qualitatively* as far as the fate of the vector meson resonance peaks is concerned.

4.2.2. Beyond Conventional Scenarios for Dilepton Enhancement

In this Section we will present some more speculative mechanisms for dilepton production which conceptually deviate from the rather well established hadronic reactions discussed in the previous Section. In particular, we will address radiation from quark-antiquark annihilation, disoriented chiral condensates and a dropping ρ -meson mass as implied by BR scaling.

4.2.2a. Quark-Gluon Plasma. At sufficiently high invariant masses as well as temperatures and densities asymptotic freedom of the quark interactions implies that the rate can be described by perturbation theory. In lowest order of the strong coupling constant, $O(\alpha_s^0)$, it is determined by the free $q\bar{q} \rightarrow \gamma^* \rightarrow e^+e^-$ annihilation process through a convolution over anti-/quark three-momenta $p_{\bar{q}}, p_q$ according to

$$\frac{dR_{q\bar{q} \rightarrow ee}}{d^4 q} = \int \frac{d^3 p_q}{(2\pi)^3} \frac{d^3 p_{\bar{q}}}{(2\pi)^3} \sum_q v_{q\bar{q}} \sigma_{q\bar{q} \rightarrow ee}(M) f^q(p_q^0) f^{\bar{q}}(p_{\bar{q}}^0) \delta^{(4)}(q - p_q - p_{\bar{q}}), \quad (4.36)$$

where the total color-averaged $q\bar{q} \rightarrow ee$ cross section for each flavor $q = u, d, s, \dots$ is given by

$$\sigma_{q\bar{q} \rightarrow ee}(M) = e_q^2 \frac{4\pi\alpha^2}{9M^2} \left(1 - \frac{4m_q^2}{M^2}\right)^{-\frac{1}{2}} \left(1 + \frac{2m_q^2}{M^2}\right) \quad (4.37)$$

with current quark masses m_q and fractional quark charges $e_q = -\frac{1}{3}, -\frac{2}{3}$. In Eq. (4.36)

$$v_{q\bar{q}} = \frac{M\sqrt{M^2 - 4m_q^2}}{2\omega_{p_q}\omega_{p_{\bar{q}}}} \quad (4.38)$$

denotes the relative velocity between quark and antiquark, and

$$f^q(p_q) = \frac{N_s N_c}{\exp[u \cdot p_q - \mu_q] + 1}$$

$$f^{\bar{q}}(p_{\bar{q}}) = \frac{N_s N_c}{\exp[u \cdot p_{\bar{q}} + \mu_q] + 1} \quad (4.39)$$

their Fermi distribution functions including spin-color degeneracy factors as well as the quark chemical potential μ_q . The fluid velocity of the plasma relative to the thermal frame is denoted by u^μ . For a plasma at rest $u^\mu = (1, 0, 0, 0)$ and in the limit of vanishing quark masses the momentum integrations can be performed analytically yielding [177, 178]

$$\begin{aligned} \frac{dR_{q\bar{q} \rightarrow ee}}{d^4 q} &= \frac{\alpha^2}{4\pi^4} \frac{T}{q} f^B(q_0; T) \\ &\times \sum_q e_q^2 \ln \frac{(x_- + \exp[-(q_0 + \mu_q)/T])(x_+ + \exp[-\mu_q/T])}{(x_+ + \exp[-(q_0 + \mu_q)/T])(x_- + \exp[-\mu_q/T])} \end{aligned} \quad (4.40)$$

with $x_\pm = \exp[-(q_0 \pm q)/2T]$. For $\mu_q = 0$ Eq. (4.40) simplifies to

$$\frac{dR_{q\bar{q} \rightarrow ee}}{d^4 q} = \frac{\alpha^2}{4\pi^4} f^B(q_0; T) \left(\sum_q e_q^2 \right) \left(1 + \frac{2T}{q} \ln \left[\frac{1+x_+}{1+x_-} \right] \right). \quad (4.41)$$

Note that, apart from the overall Bose factor f^B , this result carries a temperature-dependent correction factor as compared to the widely used $O(T^0)$ approximation. The additional In-term gives in fact a negative contribution which becomes significant for invariant masses below $M_{ee} \approx 1 \text{ GeV}$, cf. Fig. 4.5. Another noteworthy feature is that with increasing net quark density ($\mu_q > 0$) the perturbative emission rate from a QGP decreases slightly at low masses due to the mismatch between the quark and antiquark Fermi spheres.

Perturbative QCD corrections to the $q\bar{q}$ rate have been studied, e.g., in Refs. [179, 180, 181] and turned out to be appreciable, especially when extrapolated to invariant masses well below 1 GeV where the results cease to be reliable. Furthermore, since in the plasma phase at moderate temperatures, $T \approx (1 - 2)T_c$, the strong coupling constant is still of order 1, nonperturbative effects might not be small either in this regime. In particular, the gluon condensate is non-vanishing as discussed in Sect. 2.4. In Ref. [182], e.g., the somewhat speculative existence of an (euclidean) A_4 condensate of type $\left\langle \frac{\alpha_s}{\pi} A_4^2 \right\rangle$ has been shown to generate

a strong enhancement in the rate at low invariant masses. More conservative approaches include instanton-induced interactions [54] (known to be of prime importance for the nonperturbative QCD vacuum structure and the low-lying hadronic spectrum) which, in somewhat modified appearance at finite temperature/density (i.e., as so-called instanton-

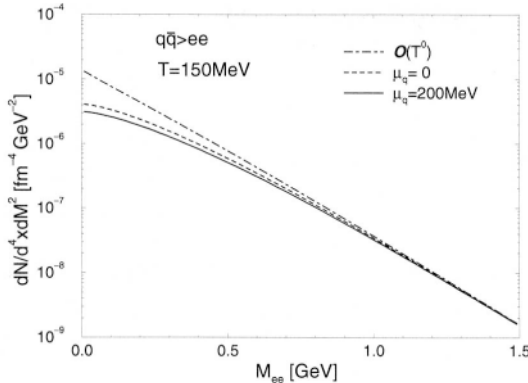


Fig. 4.5. Three-momentum integrated perturbative $q\bar{q} \rightarrow e^+e^-$ annihilation rates at temperature $T = 150\text{MeV}$: for $\mu_q = 0$ (dashed line) and $\mu_q = 200\text{MeV}$ (solid line) using Eq. (4.40), and at $\mu_q = 0$ using Eq. (4.41) to order $O(T^0)$ (dashed-dotted line). All curves have been obtained for three massless quark flavors.

antiinstanton (*I-A*) molecules) might still prevail at moderate plasma conditions [182, 184, 185]; in fact, *I-A* molecule induced $q\bar{q}$ interactions, as opposed to single instantons, lead to nonzero contributions in the vector channel, which, however, seem to be quite small [184].

A generic feature of dilepton production rates from the plasma phase are the so-called van-Hove singularities [179, 186, 187], i.e., (possibly) sharp structures as a function of the dilepton energy. They originate from a softening of the quark dispersion relation in the medium (the so-called “plasmino” branch [179]) and are typically located at rather small energies below -0.5 GeV . On the other hand, finite imaginary parts in the quark selfenergy as well as smearing effects when accounting for finite three-momenta of the virtual photon [188] will damp these peaks. Also, soft Bremsstrahlung-type processes involving gluons such as $q\bar{q} \rightarrow g\gamma^*$ or $qg \rightarrow \gamma^*q$ may easily overshine the van-Hove structures at low M [179], even after including Landau-Pomeranchuk type effects [189], i.e., destructive interferences in the coherent emission.

4.2.2b. Disoriented Chiral Condensate. Another possibility of increased (soft) dilepton radiation related to the chiral phase transition has been associated with so-called Disoriented Chiral Condensates (DCC’s), which have been suggested to develop in the cooling process of high-energy heavy-ion collisions [190, 191]. Assuming the formation of a chirally restored plasma phase in the early stages of the collision,

a sufficiently rapid transition into the chirally broken phase might not select the standard ground state characterized by a single scalar (sigma) condensate $\langle \sigma \rangle = \langle \bar{q} q \rangle \neq 0$, but rather “jump” into a chirally rotated (metastable) state carrying a nonvanishing pseudoscalar (i.e., pion-) condensate $\langle \vec{\pi} \rangle = \langle \bar{q} \gamma_5 \vec{\tau} q \rangle \neq 0$. In particular, this state carries nonzero net isospin, which provides the basis for detecting it in event-by-event analyses of heavy-ion collisions through anomalous fluctuations in, e.g., the number of π^0 s. Since the pion condensates inherent in the DCC constitute an enhanced source of predominantly soft pions, it has soon been realized that within this coherent state a copious annihilation into soft dilepton pairs might occur, similar to the standard $\pi\pi$ annihilation, only at much lower invariant masses. In fact, the dominant yield from such coherent radiation will be concentrated well below the two-pion threshold [192]. Therefore, such a signal will be very difficult to discriminate in a heavy-ion collision due to the notoriously large background from $\pi^0 \rightarrow \gamma e^+ e^-$ Dalitz decays after freezeout. However, as suggested in Ref. [193], non-coherent pions from the surrounding heat bath may annihilate on the coherent state, forming dilepton pairs of typical invariant masses in a rather narrow window around $M \approx 2m_\pi$, thus avoiding the π^0 Dalitz-decay region. Starting from the standard linear σ -model Lagrangian,

$$\mathcal{L}_{lsm} = \frac{1}{2} \partial_\mu \phi \partial^\mu \phi - \frac{1}{4} \lambda (\phi^2 v^2)^2 + H\sigma, \quad (4.42)$$

the coupling to the electromagnetic current is realized through the third component of the isovector current as

$$\begin{aligned} j_\mu^{\text{em}}(x) &= [\vec{\pi} \times \partial_\mu \vec{\pi}]_3 \\ &= \frac{i}{2} [\pi^+(x) \tilde{\partial}_\mu \pi(x) \pi(x) \tilde{\partial}_\mu \pi^+(x)], \end{aligned} \quad (4.43)$$

where the pion fields in charge basis are related to the isospin fields as

$$\begin{aligned} \pi(x) &= \frac{1}{\sqrt{2}} [\pi_1(x) - i\pi_2(x)] \\ \pi^+(x) &= \frac{1}{\sqrt{2}} [\pi_1(x) + i\pi_2(x)]. \end{aligned} \quad (4.44)$$

The electromagnetic current-current correlator entering the dilepton rate can then, employing a mean-field treatment, be expressed by pion

two-point functions as

$$\begin{aligned} W_{\mu\nu}(x, y) = & \langle \pi^\dagger(x)\pi(x) \rangle \langle \partial_\mu\pi(x)\partial_\nu\pi^\dagger(y) \rangle \\ & + \langle \partial_\mu\pi^\dagger(x)\partial_\nu\pi(x) \rangle \langle \pi(x)\pi^\dagger(y) \rangle \\ & - \langle \partial_\mu\pi(x)\pi^\dagger(x) \rangle \langle \pi^\dagger(x)\partial_\nu\pi(y) \rangle \\ & - \langle \partial\pi^\dagger(x)\pi(x) \rangle \langle \pi(x)\partial_\nu\pi^\dagger(y) \rangle. \end{aligned} \quad (4.45)$$

Further following Ref. [193], the charged pion fields are expanded in creation and annihilation operators (a_k^\dagger, a_k for positive and b_k^\dagger, b_k for negative pions) with accompanying mode functions f_k as

$$\pi(\vec{x}, t) = \int \frac{d^3 k}{(2\pi)^3} e^{i\vec{k}\cdot\vec{x}} [f_k(t)a_k + f_k^*(t)b_{-k}^\dagger]. \quad (4.46)$$

The time evolution of the pion fields, and thus of the dilepton production rate, is then determined by specifying the mode functions together with appropriate initial conditions for the σ mean-field. Results have been obtained for both a purely thermal scenario (pion gas) and a DCC (“quench”) scenario at equivalent initial energy density. A strong enhancement (factors of ~ 10 –50) of the DCC based rates over the thermal ones, Eq. (4.29), was found at invariant masses around $2m_\pi$, but restricted to rather low total three-momenta $|\vec{q}| \leq 300$ –500 MeV. The quoted ranges roughly reflect the uncertainty in the underlying approximations as estimated from a second calculation using classical equation-of-motion techniques to describe the time evolution of pion and σ fields.

4.2.2c. “Dropping” Rho-Meson Mass. The most prominent approach that has been successfully applied to explain the low-mass dilepton enhancement in the CERN-SPS experiments in connection with the chiral restoration transition is based on the BR scaling conjecture [45] for effective chiral Lagrangians. In the dilepton context, the most relevant feature is the decrease of the ρ -meson mass at finite temperature and density which, reinforced through enhanced thermal occupation factors at lower masses, leads to a strong excess of e^+e^- pairs below the free ρ mass through the $\pi\pi$ -annihilation channel. As long as no collisional broadening in the ρ width is included, the e^+e^- yield is sharply centered around the corresponding in-medium mass m_ρ^* . Unlike in the DCC scenario, where the enhancement is localized at invariant masses around $2m_\pi$, m_ρ^* will “sweep” over the entire low-mass region in the course of a heavy-ion collision due to the continuous cooling and dilution of the system from the chiral restoration point towards freezeout.

More realistically, also in the dropping mass scenario the ρ -meson spectral function will undergo a substantial broadening in the hot and dense hadronic medium. In particular, if the decrease in the ρ mass is (partially) identified with resonant S-wave ρ - $N(1520)N^{-1}$ interactions (as discussed in detail in Ref. [103]), then large in-medium widths of the $N(1520)$ resonance (as inferred from nuclear photoabsorption data) inevitably induce a large width of the low-lying $N(1520)N^{-1}$ state. Since such an increase in width affects both the denominator *and* the numerator of $\text{Im}D_\rho$, entering the dilepton rate (4.29), the broadening does in essence not reduce the total number of produced pairs.

4.2.2d. Off Equilibrium Pion Gas. Another class of non-conventional scenarios with potential impact on dilepton radiation is associated with off-equilibrium situations. Deviations from thermal equilibrium are usually addressed within kinetic theory or transport-type approaches, and the preferred method to assess dilepton yields under these conditions should be numerical simulations. Fortunately, in the case of heavy-ion collisions, thermalization of the hadronic system seems to require only a few rescatterings, so that local thermal equilibrium (in the comoving frame of collective expansion) is established on time scales which are much shorter than the typical lifetime of the hadronic fireball [194, 195]. A fast approach to thermal equilibrium is further corroborated in scenarios with initially deconfined matter as demonstrated, e.g., in QCD inspired event generators such as HIJING [196] or parton cascades [15]. Complete chemical equilibration, however, is by far less certain; in an expanding pion gas, e.g., the empirical absence of pion number changing processes in low-energy $\pi\pi$ interactions (i.e., for invariant masses below $M_{\pi\pi} \simeq 1 \text{ GeV}$) together with the assumption of isentropic expansion entails the build-up of a finite pion chemical potential $\mu_\pi > 0$ towards lower temperatures [197]. Another possibility is that early hadron formation processes do not transform into a chemically equilibrated initial hadron gas but rather follow, e.g., string dynamics [198].

The field-theoretical implementation of a finite μ_π into the thermal dilepton production rate from $\pi\pi$ annihilation has been studied by Baier *et al.* [41, 199] in the real-time formalism of finite temperature field theory. For practical purposes they worked in an approximation which amounts to introducing the chemical potential through Bose distribution functions as

$$\tilde{f}^B(k_0; \mu_\pi, T) = \begin{cases} f^B(|k_0|; \mu_\pi, T), & k_0 > 0 \\ -[1 + f^B(|k_0|; \mu_\pi, T)], & k_0 < 0 \end{cases} \quad (4.47)$$

with the standard finite- μ_π Bose factor $f^B(|k_0|; \mu_\pi, T) = [e^{(ik_0 - \mu_\pi)/T} - 1]^{-1}$. In the Boltzmann approximation and for situations not too far off equilibrium it was shown that the production rate in the standard one loop approximation (i.e., Eq. (4.29) with $\Sigma_{\rho\pi\pi}$ given by the free $\pi\pi$ bubble) simply picks up an overall enhancement factor according to

$$\frac{dR_{\pi\pi \rightarrow ee}}{d^4 q}(q_0, \vec{q}; \mu_\pi) = (1 + 2\delta\lambda) \frac{dR_{\pi\pi \rightarrow ee}}{d^4 q}(q_0, \vec{q}; \mu_\pi = 0) \quad (4.48)$$

with $\delta\lambda = \lambda - 1$ and the “fugacity” $\lambda = e^{\mu_\pi/T}$ (to lowest order in μ_π/T one recognizes $(1 + 2\delta\lambda) \simeq e^{2\mu_\pi/T}$).

The situation becomes more complicated if one includes higher thermal loop corrections in the pion propagators of the intermediate two-pion states. Without going into further details, we mention that the use of off-equilibrium distribution functions then implies the appearance of terms involving products of retarded and advanced propagators, schematically given as

$$\begin{aligned} D_\pi^R(k)D_\pi^A(k) &= \frac{1}{k^2 - m_\pi^2 + i\text{sgn}(k_0)\epsilon} \frac{1}{k^2 - m_\pi^2 - i\text{sgn}(k_0)\epsilon} \\ &= \frac{1}{(k^2 - m_\pi^2)^2 - \epsilon^2}, \end{aligned} \quad (4.49)$$

which apparently exhibit ill-defined poles, the so-called “pinch-singularities”. They have to be regularized, e.g., by accounting for thermal pion selfenergies Σ_π with finite imaginary parts $\text{Im}\Sigma_\pi \neq 0$, as was done in Refs. [41, 199]. As a somewhat surprising result, to leading order in $1/\text{Im}\Sigma_\pi$ the pinch term actually generates an overall reduction (enhancement) of the dilepton production rate for positive (negative) μ_π .

4.2.3. Quark-Hadron Duality

A key question that is at the heart of the entire heavy-ion physics program concerns discriminating signatures for the possible occurrence of a chiral restoration phase transition. In our context of low-mass dilepton observables we have already qualitatively eluded to some of them in the preceding Section, most notably DCC formation (characterized by a strong enhancement in the two-pion threshold region at low three-momenta) and the dropping ρ -meson mass (characterized by a complete extinction of the yield around the ρ peak, accompanied by a strong enhancement for lower invariant masses). However, there is also the

possibility that in the vicinity of the phase transition the dilepton radiation from the hot and dense fireball does *not* depend on whether it is in the chirally broken confined phase or the chirally restored QGP phase. In other words, in a certain temperature and density window around the transition region the dilepton rate calculations using either hadronic or quark-gluon degrees of freedom merge together, i.e., the two descriptions become *dual*. Although this would imply that there is no unique dilepton signature which could distinguish the two phases, it is a highly non-trivial scenario. In the low-mass region, say for invariant masses $M_{ll} \leq 1.5 \text{ GeV}$, it requires that the hadronic side, which at low densities/temperatures is dominated by rather narrow resonances $\rho, \omega, \phi, \rho'$, etc., develops into a supposedly more or less structureless quark-gluon world (although the latter might still involve nonperturbative interactions). To illustrate that there are indeed indications for such a scenario [50, 200], we compare in Fig. 4.6 the lowest-order perturbative QCD $q\bar{q}$ annihilation rates with the (most recent) full hadronic in-medium spectral function calculations at identical temperatures and equivalent baryon-/quark-chemical potential. Already at moderate temperature ($T = 140 \text{ MeV}$) and density ($\rho_B = 0.75\rho_0$) they are not very different from each other (left panel), especially when contrasted with the result for free $\pi\pi$ annihilation. Nevertheless, the in-medium $\pi\pi$ curve still exhibits a clear trace of the ρ peak. The latter is completely “melted” at $T = 180 \text{ MeV}$, $\rho_B = 4\rho_0$ leading to remarkably close agreement with the $q\bar{q}$ result in the invariant mass range of $M_{ee} \simeq (0.5\text{-}1.0) \text{ GeV}$ (one should note that the deviations between the partonic and the in-medium hadronic results towards low M_{ee} might be reduced once soft “Bremsstrahlung”-type graphs are accounted for in the QGP environment. On the other hand, as discussed in Sect. 4.2.2, plasmino modes can lead to additional non-trivial structures in the dilepton production rate [179, 186, 187] below $M_{ee} \simeq 0.5 \text{ GeV}$. The disagreement beyond 1 GeV is mainly caused by missing states involving more than two pions (such as the $\rho'(1450)$ in the hadronic description of the free vector correlator, most notably four-pion type πa_1 annihilation graphs, see also below). From an experimental point of view this means that, even if no *distinct* signatures for the appearance of new phases are extractable from low-mass dilepton production, the absolute yields and spectral shape are very different from free $\pi\pi$ annihilation and contain rather specific information on properties of strongly interacting matter in the vicinity of the phase boundary. We will reiterate this point within a detailed analysis of low-mass dilepton observables below.

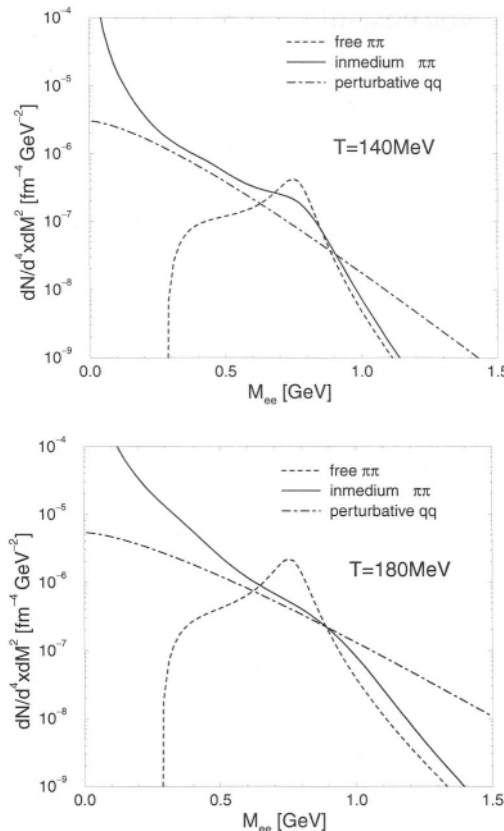


Fig. 4.6. Three-momentum integrated dilepton production rates at a baryon chemical potential $\mu_B = 408 \text{ MeV}$ and temperatures $T = 140 \text{ MeV}$ (top) and $T = 180 \text{ MeV}$ from free $\pi\pi$ annihilation (dashed curves), in-medium $\pi\pi$ annihilation within the most recent hadronic many-body approach of Refs. [47, 102, 123, 50], and from lowest order QCD $q\bar{q}$ annihilation (dashed-dotted curves); the latter two are calculated at equivalent baryon/quark chemical potentials of $\mu_q = \mu_B/3 = 136 \text{ MeV}$.

The duality arguments can be made more rigorous starting from the inter-mediate-mass region, $1.5 \text{ GeV} \lesssim M_{ll} \lesssim 3 \text{ GeV}$. Conceptually the situation there is more transparent: firstly, one might expect that at these energies the $q\bar{q}$ annihilation process is already rather well described by a perturbative treatment. In fact, there is strong empirical support for this expectation from the well-known $e^+e^- \rightarrow \text{hadrons}$ cross section, which

can be accounted for by the perturbative result for $e^+e^- \rightarrow q\bar{q}$ within a 30% accuracy in the above mentioned range, i.e.,

$$\sigma(e^+e^- \rightarrow \text{hadrons}) = \frac{4\pi\alpha^2}{3M^2} R^{\text{pert}} \quad (4.50)$$

with the famous $\sigma(e^+e^- \rightarrow \text{hadrons})/\sigma(e^+e^- \rightarrow \mu^+\mu^-)$ -ratio

$$R^{\text{pert}} = N_c \sum_q (e_q)^2. \quad (4.51)$$

Secondly, since at ~ 2 GeV one is probing space-time distances of the order of 0.1 fm, possible corrections from the surrounding heat bath should also be small. This gives some confidence that the perturbative expression for the dilepton emission rate from a quark-gluon plasma (4.36) is a reasonable approximation at intermediate masses. The challenge then is to match this result to a hadron-based calculation at temperatures in the vicinity of T_c .

In Ref. [201] this type of duality has been *enforced* in the spirit of a Hagedorn-type hadronic mass spectrum, where the complicated structure of overlapping, interacting hadronic resonances is encoded in some simple spectral density $\xi_h(M)$. Using VDM for the dilepton decays of the vector mesons,

$$\Gamma_{V \rightarrow ll}(M) = \frac{1}{g^2(M)} \frac{4\alpha^2 M}{3}, \quad (4.52)$$

the corresponding three-momentum integrated dilepton production rate at temperature T in Boltzmann approximation,

$$\frac{dR_{V \rightarrow ll}}{dM^2} = \xi_V(M) \frac{\alpha^2 M^2 T}{6\pi g^2(M)} K_1(M/T) \quad (4.53)$$

(K_1 : modified Bessel function), is then determined by the subspectrum of vector mesons, $\xi_V(M)$, and the corresponding VDM coupling $1/g(M)$. Further assuming that the $e^+e^- \rightarrow \text{hadrons}$ cross section is saturated by vector mesons,

$$\begin{aligned} \sigma(e^+e^- \rightarrow V) &= \frac{(2\pi)^3 \alpha^2}{g^2(M) M} \xi_V(M) \\ &\simeq \sigma(e^+e^- \rightarrow h) \end{aligned} \quad (4.54)$$

one can trade the dependence on $g(M)$, $\xi_V(M)$ for the experimental cross section ratio as [201]

$$\frac{dR_{V \rightarrow ll}}{dM^2} = \frac{\alpha^2 MT}{6\pi^3} K_1(M/T) R^{\text{exp}}(M), \quad (4.55)$$

where $R^{\text{exp}}(M)$ now also accommodates (moderate) deviations from the lowest-order pQCD result, Eq. (4.51). A similar procedure has been pursued by Huang [79] who additionally included lowest-order temperature effects through the vector-axialvector mixing phenomenon induced by soft pion contributions from the heat bath (cf. Sect. 2.6), leading to

$$\frac{dR_h}{dM^2} = \frac{4\alpha^2 MT}{2\pi} K_1(M/T) \left(\rho_{em}^\circ(M) - \left(\epsilon - \frac{\epsilon^2}{2} \right) [\rho_V^\circ(M) - \rho_A^\circ(M)] \right) \quad (4.56)$$

with $\epsilon = T^2/6f_\pi^2$ (in the chiral limit and for two flavors). The first term involving the full vacuum electromagnetic correlator coincides with (4.55), whereas the free vector and axialvector correlators are responsible for the soft pion corrections. Huang also extracted them from data, as delineated in Sect. 2.6, see Eqs. (2.92) and (2.93). It turns out that the finite-temperature corrections are marginal for dilepton invariant masses $1.5 \text{ GeV} \leq M_{ee} \leq 2.5 \text{ GeV}$ and, moreover, that the “empirical” results using Eq. (4.55) closely follow the perturbative results (4.51), cf. the open circles and the dotted line in Fig. 4.7. This is not surprising recalling that the “duality threshold” in vacuum is situated at $M \approx 1.5 \text{ GeV}$. On the other hand, it was pointed out in Ref. [201] that, when comparing the “empirically” inferred rate (4.55) to the phenomenological hadronic rate calculations in terms of binary collisions of Ref. [119], the latter fall short by a factor of 2–3. However, in the hadronic treatment of Ref. [119] contributions from $a_1(1260)$ mesons (in particular $\pi a_1 \rightarrow ll$), which are most relevant for the intermediate-mass region, had not been included at the time. This has been improved later on [202, 203, 204] and shown to resolve the afore mentioned discrepancy (Fig. 4.7). The yield from πa_1 processes was indeed found to dominate other sources such as $\pi\omega$, $\pi\rho$, $\pi\pi$ or $K\bar{K}$ channels for invariant masses $1.2 \text{ GeV} \leq M_{ll} \leq 2.2 \text{ GeV}$. In particular, it results in good agreement with both the perturbative $q\bar{q}$ and the “empirical” calculations including the lowest order V - A mixing effect [79], Eq. (4.56), down to invariant masses of about 1 GeV, cf. solid line, dotted line and open points, respectively, in Fig. 4.7. In fact, the $\pi a_1 \rightarrow \rho' \rightarrow e^+e^-$ contributions exactly correspond to the mixing effect since thermal pions colliding with an a_1 meson “move” strength from the axialvector to the vector channel! Also shown in Fig. 4.7 are the results obtained within the chiral reduction formalism [205]; here the free correlators have been determined from a set of 12 ρ , ω , ϕ , a_1 and K_1

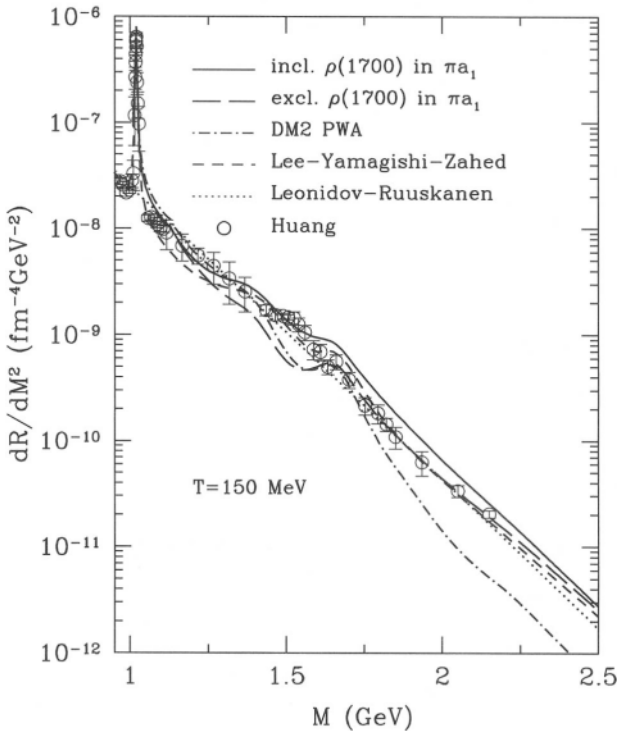


Fig. 4.7. Three-momentum integrated dilepton production rates in the intermediate-mass region at a temperature $T = 150$ MeV, as obtained in various approaches. Solid, long-dashed and dashed-dotted curve: hadronic calculations of Ref. [204] with different ways of estimating the πa_1 contribution; short-dashed curve: chiral reduction approach [205]; dotted curve: using the perturbative value $R^{\text{pert}} = 2$ in Eq. (4.55) [201]; open circles: using empirical spectral densities including lowest order temperature corrections according to Eq. (4.56) [79]. The plot is taken from Ref. [204].

resonances below $M = 2$ GeV, and by a parameterization of $R^{\text{exp}}(M)$ above. Single-meson final-state corrections have then been inferred via chiral Ward identities. Again, the agreement with the other approaches is quite satisfactory.

As we will see in Sect. 4.6.6, the intermediate-mass emission rates as deduced above provide a good description of experimental $\mu^+\mu^-$ spectra measured by the HELIOS-3 collaboration [24] at full CERN-SPS energies (200 AGeV), which show an excess of a factor of 2–3 in S+W as compared to p+W collisions. Similar observations have been made by the NA50/NA38 collaboration [25, 27], and the most natural explanation

seems to be thermal radiation. This further supports the theoretical arguments for quark-hadron “duality” in intermediate-mass dilepton production. Since the intrinsic energy scales in this region are already suggestive for a perturbative treatment within the partonic picture, the agreement with the phenomenological hadronic calculations above 1.5 GeV may be considered as the more intriguing part (it will still be worthwhile to understand the origin of the 30–40% deviations of $R_{exp}(M)$ from the lowest-order perturbative $q\bar{q}$ results). As we have argued already in Sect. 2.6, medium effects start to become visible below 1.5 GeV, where the lowest-order in temperature V-A mixing establishes a three-fold degeneracy between vector and axialvector correlators on the one hand (dictated by chiral symmetry), and the perturbatively calculated $q\bar{q}$ rates on the other hand, reaching down to about 1 GeV.

4.3. Photon Production Rates

In our analysis of electromagnetic observables in heavy-ion reactions we will also address spectra of single (real) photons. This is motivated by the observation that every process capable of creating a dilepton pair can, in principle, lead to the radiation of a (real) photon: the latter simply constitutes the $M^2 \rightarrow 0$ limit of the virtual (time-like) photon which occurs as an intermediate state in each dilepton-producing reaction. This intimate relation has already been extensively exploited for imposing model constraints on in-medium effects through photoabsorption data on the nucleon and nuclei, cf. Sect. 4.1.2. In Sect. 4.7 the reverse process, i.e., photon production in heavy-ion reactions, will be used as an additional consistency check.

Theoretical calculations for photon production rates have been performed for both the hadronic and the plasma phases. In the latter, one has mainly focused on lowest-order QCD calculations for two-body reactions of the annihilation type, $q\bar{q} \rightarrow g\gamma$, as well as the Compton type, $q(\bar{q})g \rightarrow q(\bar{q})\gamma$. The first analysis of hadronic photon rates has been performed in Ref. [206] for a heat bath of the lightest, non-strange pseudoscalar (π, η) and vector mesons (ρ, ω). The most important reactions have been attributed to the analogues of the QGP processes, $\pi\pi \rightarrow \rho\gamma$ and $\pi\rho \rightarrow \pi\gamma$, as well as the vector meson decay channels $\omega \rightarrow \pi\gamma$ and $\rho \rightarrow \pi\pi\gamma$. The conclusion of Ref. [206] was summarized as “the hadron gas shines as brightly as the quark-gluon plasma”, i.e., the photon production rates of both phases closely coincided over a large range of photon energies $E_\gamma \geq 0.5$ GeV. Later on the importance of the $a_1(1260)$ meson—not included in Ref. [206]—as an intermediate state in $\pi\rho \rightarrow a_1 \rightarrow \pi\gamma$ has

been realized, especially for photon energies above 0.5 GeV. The impact of nucleons on photon production has been explicitly discussed, e.g., in Ref. [100]. In fact, analogous information can be readily extracted from any dilepton rate calculation involving baryonic processes [47, 147, 91] by extrapolating it to the photon point. To be specific, the differential photon production rate can be obtained from the dilepton expression (4.23) by simply replacing the lepton tensor by the photon tensor

$$P_{\mu\nu} = 4\pi\alpha \int \frac{d^3 p}{(2\pi)^3 2p_0} \sum_{\lambda} \epsilon_{\mu}^{*}(\lambda, p) \epsilon_{\nu}(\lambda, p) \delta^{(4)}(p - q) \quad (4.57)$$

such that

$$\frac{dR_{\gamma}}{d^4 q} = P_{\mu\nu} W^{\mu\nu}, \quad (4.58)$$

which can be simplified to

$$q_0 \frac{dR_{\gamma}}{d^3 q} = \frac{\alpha}{4\pi^2} W(q) \quad (4.59)$$

with $q_0 = |\vec{q}|$ and $W(q) \equiv g_{\mu\nu} W^{\mu\nu}$. In the (improved) VDM, e.g., the photon rate becomes

$$q_0 \frac{dR_{\gamma}}{d^3 q} = \frac{\alpha}{\pi^2 g_{\rho}^2} f^{\rho}(q_0) \mathcal{F}^T(q_0, |\vec{q}| = q_0) \quad (4.60)$$

with the transverse transition form factor from Eq. (4.19).

4.4. Space-Time Evolution of Heavy-Ion Collisions

Dilepton spectra as measured in (ultra-) relativistic heavy-ion collision experiments might be, at least conceptually, split up into two components: the first one arises from the phase where the system is characterized by strong interactions among its constituents, as a result of which a certain amount of photons (real and virtual) is radiated. Once the hadronic system has reached a degree of diluteness where the short-range strong interactions are no longer effective (the so-called hadronic freezeout stage), all unstable resonances decay according to their vacuum lifetimes, with some probability into radiative channels. Therefore, this second component (which has become known as the “hadronic cocktail” contribution to the dilepton spectra) does not contain any information on in-medium properties of the parent particles. However,

it can be reasonably well reconstructed once the hadronic abundances at freezeout are known (this may not be that evident and we will come back to this issue in Sect. 4.6.1). On the other hand, given one's favorite dilepton production rate in hot and dense matter, the calculation of the first component requires the knowledge of the space-time history of the colliding and expanding nuclear system. This is one of the major objectives in relativistic heavy-ion physics by itself. In the following we will discuss three different approaches to simulate the reaction dynamics in their application to evaluate dilepton spectra.

4.4.1. Hydrodynamical Approach

The hydrodynamic description of heavy-ion collisions is based on the assumption that the strong interactions in the matter are able to maintain local thermal equilibrium throughout the expansion of the nuclear system until some breakup stage (the freezeout). Thus, each fluid cell in its rest frame is characterized by standard thermodynamic variables such as pressure, temperature and (energy-) density. For this reason the hydrodynamic framework is the most natural one for the implementation of equilibrium dilepton rates, as the latter are formulated in exactly the same variables. It has a long tradition in its application to high-energy reactions involving high-multiplicity hadronic final states, starting from hadron-hadron [207, 208] (or even e^+e^- [209]) collisions to the more modern field of relativistic nucleus-nucleus reactions [210, 211, 212, 213, 214]. The basic equations are the conservation of energy and momentum, which can be expressed in a Lorentz-covariant form as

$$\partial_\mu T^{\mu\nu}(x) = 0 \quad (4.61)$$

through the energy-momentum tensor $T^{\mu\nu}(x)$. For an ideal fluid, i.e., neglecting any viscosity, the latter is given by

$$T^{\mu\nu}(x) = [\varepsilon(x) + p(x)]u^\mu(x)u^\nu(x) - p(x)g^{\mu\nu} \quad (4.62)$$

with local energy-density $\varepsilon(x)$, pressure $p(x)$ and fluid 4-velocity $u^\mu(x)$. Additionally conserved currents, such as the baryon number current, $j_B^\mu = \rho_B u^\mu$, or the strangeness current are enforced by pertinent continuity equations,

$$\partial_\mu j_B^\mu = 0, \text{etc.} \quad (4.63)$$

Let us also mention here that in the later stages of heavy-ion collisions the pion number might be effectively conserved due to the empirical

absence of pion-number changing processes at small *cm* energies (see also Sect. 4.2.2). In this case, one has a further continuity equation,

$$\partial_\mu j_\pi^\mu = 0, \quad (4.64)$$

which induces a nonzero pion chemical potential.

The basic ingredient governing the hydrodynamic evolution of the system is the equation of state (EoS), i.e., the dependence of the pressure on energy- and baryon-density, $p = p(\epsilon, \rho_B)$. For heavy-ion collisions at (ultra-) relativistic energies, the early stages can be barely considered as proceeding under any kind of equilibrium conditions. In the hydrodynamic description, one therefore has to assume a so-called formation time τ_0 (typically around 1–2 fm/c) together with some initial conditions for the energy density. Given a specific EoS, these have to be determined by requiring a reasonable fit to the finally observed hadronic spectra, with some additional freedom of how and at which temperature the freezeout occurs. The differential equations for the evolution are usually solved numerically on a space-time grid using finite-differencing methods.

Many interesting issues can be addressed within the hydrodynamic framework, as, e.g., the interrelation between collective flow and freeze-out temperature [211] or properties of the EoS in connection with potential phase transitions in strongly interacting matter [215, 213, 216]. Here, we restrict ourselves to the evaluation of dilepton spectra. Given a thermal production rate, dR/d^4q , the total spectrum from in-medium radiation is straightforwardly obtained as a sum over all timesteps in the evolution and over all fluid cells of the grid of individual temperature and density above the freezeout value. The contribution of a single cell is given by

$$\left(\frac{dN_u}{d^4 q} \right)_{cell} = \left(\frac{dN_u}{d^4 q d^4 x} (q_0, \vec{q}; T_{cell}, \mu_{B,cell}) \right) V_{cell} \Delta t, \quad (4.65)$$

where the time-step width Δt and cell 3-volume V_{cell} are to be taken in the local rest frame of the cell. As there is no preferred direction in this frame, the virtual photon of invariant mass $M = (q_0^2 - \vec{q}^2)^{1/2}$ and three-momentum \vec{q} can be assumed to decay isotropically into dileptons. The resulting two lepton tracks then have to be boosted to the lab-system according to the local fluid velocity u^μ , where possible experimental acceptance cuts can be readily applied. However, in some practical applications, this procedure might be too time consuming. An approximate but more efficient way is to first integrate over the (possibly complicated)

three-momentum dependencies to obtain dR/dM^2 and then regenerate rapidity and transverse momentum distributions according to [217]

$$\frac{dR}{dM^2 dy q_i dq_i} = \frac{1}{2 M T K_1(M/T)} e^{-E/T} \frac{dR}{dM^2}(M, T) \quad (4.66)$$

with $E = q_\mu u^\mu$. This procedure has been employed, e.g., in the hydrodynamic models of Refs. [214, 43], where dilepton spectra at the full CERN-SPS energies have been analyzed. In both works the hydrodynamic equations have been solved locally in (2+1) dimensions assuming cylindrical symmetry of the collision system (which implies a restriction to central collisions).

A further simplification can be made in the limit of ultrarelativistic collision energies, as suggested by Bjorken [218]. In this case the longitudinal expansion is dominant and boost invariance can be assumed so that the longitudinal velocity scales with the distance from the central region as $v_L = z/t$. Neglecting transverse expansion, the 4-volume element simply becomes

$$d^4x = d^2r_i dz dt = \pi R_i^2 dy \tau d\tau \quad (4.67)$$

with the proper time $\tau = (t^2 - z^2)^{1/2}$ and *cms* rapidity

$$y = \frac{1}{2} \ln \frac{t+z}{t-z}. \quad (4.68)$$

The transverse extension R_i is typically taken close to the overlap radius of the colliding nuclei. From local entropy conservation,

$$\frac{\partial(su_\mu)}{\partial x_\mu} = 0, \quad (4.69)$$

one finds the entropy-density to behave as $s(\tau) = s(\tau_0)\tau_0/\tau$. Moreover, for isentropic expansion one can relate the final-state hadron multiplicity to the formation time τ_0 , initial entropy-density and transverse size as [219]

$$\frac{dN_h}{dy} \simeq \pi R_i^2 \tau_0 s(\tau_0). \quad (4.70)$$

If one further assumes an ideal gas EoS, the temperature scales as

$$T(\tau) = T_0 \left(\frac{\tau}{\tau_0} \right)^{-1/3}. \quad (4.71)$$

The dilepton rates are then easily integrated over the time history of the hot nuclear system, as has been done, e.g., in Refs. [10, 177, 115, 220] or,

specifically for CERN-SpS conditions at 158–200 AGeV in Refs. [40, 221, 41, 178].

The contribution to the dilepton spectrum from hadron decays after freezeout proceeds along similar lines as in transport calculations (see the following Section).

The discussion of the actual results for the final dilepton spectra is deferred to Sect. 4.6 where it will be put into perspective in comparison with other dynamical approaches for the heavy-ion reaction dynamics.

4.4.2. Transport Simulations

The transport-theoretical approach has been extensively used in the past in various facets to describe heavy-ion reaction dynamics over a broad range of collision energies. Among these are the Boltzmann-Uehling-Uhlenbeck (BUU) approach [222] and its relativistic extensions (RBUU) [223, 224], Quantum Molecular Dynamics [225] and its relativistic versions RQMD [226], UrQMD [227], or the Hadron-String Dynamics (HSD) [195].

In the relativistic treatments the evolution dynamics of the two colliding nuclei are governed by a coupled set of (covariant) transport equations for the phase-space distributions $f_h(x, p)$ of hadron h ,

$$\begin{aligned} & \left\{ \left(\prod_{\mu} - \prod_{\nu} \partial_{\mu}^{\rho} U_h^{\nu} - M_h^* \partial_{\mu}^{\rho} U_h^S \right) \partial_x^{\mu} + \left(\prod_{\nu} \partial_{\mu}^x U_h^{\nu} + M_h^* \partial_{\mu}^x U_h^S \right) \partial_p^{\mu} \right\} f_h(x, p) \\ &= \sum_{h_2 h_3 h_4 \dots} \int d2 d3 d4 \dots [G^* G]_{12 \rightarrow 34 \dots} \delta^{(4)}(\Pi + \prod_2 - \prod_3 - \prod_4 \dots) \\ & \quad \times \{ f_{h_3}(x, p_3) f_{h_4}(x, p_4) \bar{f}_h(x, p) \bar{f}_{h_2}(x, p_2) \\ & \quad - f_h(x, p) f_{h_2}(x, p_2) \bar{f}_{h_3}(x, p_3) \bar{f}_{h_4}(x, p_4) \} \dots \end{aligned} \quad (4.72)$$

The *lhs* describes the motion of particle 1 under consideration in momentum-dependent relativistic mean fields $U_h^S(x, p)$ and $U_h^{\mu}(x, p)$, which correspond to the real part of the scalar and vector hadron self-energies, respectively. The *rhs* represents the collision term for the process $1 + 2 \rightarrow 3 + 4 + \dots$ involving momentum integrations for incoming particle 2 as well as all outgoing particles $3, 4, \dots$. The associated “transition rate” $W \equiv [G^* G]_{12 \rightarrow 34 \dots} \delta^{(4)}(\Pi + \prod_2 - \prod_3 - \prod_4 \dots)$ is given in terms of the relativistic G-matrix (i.e., the in-medium scattering amplitude). For on-shell two-body scattering the transition rate can be expressed through the differential cross section as

$$W = s \frac{d\sigma}{d\Omega}(s, \theta) \delta^{(4)}(\Pi + \prod_2 - \prod_3 - \prod_4) \quad (4.73)$$

with *cms* energy $s = (\Pi + \Pi_2)^2$ and scattering angle θ . The hadron quasi-particle properties in Eq. (4.72) are defined via the mass-shell constraint [228], characterized by $\delta(\Pi_\mu \Pi^\mu - M_h^{*2})$, with effective masses and momenta given by

$$\begin{aligned} M_h^*(x, p) &= M_h + U_h^S(x, p) \\ \Pi^\mu(x, p) &= p^\mu - U_h^\mu(x, p), \end{aligned} \quad (4.74)$$

while the phase-space factors

$$\bar{f}_h(x, p) = 1 \pm f_h(x, p) \quad (4.75)$$

account for Pauli blocking or Bose enhancement, depending on the type of hadron in the final and initial state. The ellipsis in Eq. (4.72) indicate further contributions to the collision term with more than two hadrons in the final/initial channels. The transport approach (4.72) is fully specified by in-medium potentials $U_h^S(x, p)$ and $U_h^\mu(x, p)$ ($\mu = 0, 1, 2, 3$), which determine the mean-field propagation of the hadrons, and by the transition rates $G^\dagger G \delta^{(4)}(\dots)$ in the collision term that describe the scattering and hadron production/absorption rates. Clearly, these quantities should be in accordance with empirical information as much as possible. Therefore, a frequently used model for the underlying microscopic mean-field potentials is the $\sigma - \omega$ (Walecka) model [229] (also known as “Quantum Hadrodynamics” or QHD) which accounts for the ground-state properties of nuclear matter as well as proton-nucleus scattering, once momentum-dependent corrections are properly included. To make a more direct link to the underlying quark structure, which should become relevant at full CERN-SPS energies, the ideas of the Walecka model have been extended to couple the mean fields to the constituent quarks within the hadrons [37], without distorting the nuclear matter properties. In the HSD approach, where the (soft) hadronic dynamics are also based on (chiral) quark dynamics along the lines of NJL-models, extra care has been taken to correctly handle the “hard” processes (relevant in the collision term). This has been achieved by employing the LUND string fragmentation model [198], which correctly describes inelastic hadronic reactions over a wide energy regime. The HSD model has been successfully applied to heavy-ion reactions ranging from SIS (1 AGeV) to CERN-SPS (200 AGeV) energies, see Ref. [195] for a comprehensive presentation.

In the transport framework, dilepton observables can be calculated with relative ease by incorporating the relevant process in the collision

term using the corresponding cross sections. In the case of $\pi\pi$ annihilation, which in VDM proceeds through ρ -meson formation, one has

$$\begin{aligned}\sigma_{\pi^+\pi^-\rightarrow e^+e^-}(M) &= \sigma_{\pi^+\pi^-\rightarrow\rho^0}(M)\Gamma_{\rho^0\rightarrow e^+e^-}(M)/\Gamma_{\rho^0}^{tot} \\ &= \frac{4\pi\alpha^2}{3} \frac{p_\pi}{M^3} |F_\pi(M)|^2\end{aligned}\quad (4.76)$$

with the electromagnetic form factor F_π and the pion decay momentum $p_\pi = (M^2/4 - m_\pi^2)^{1/2}$. Since electromagnetic processes are suppressed by a factor $\alpha = 1/137$ (for dilepton production by even a factor of α^2 , i.e., four orders of magnitude), the feedback on the heavy-ion reaction dynamics can be neglected. To account for decays of ρ mesons which are not produced in the $\pi\pi$ channel but, e.g., in πN or NN collisions, one integrates their (time-dependent) abundance in the fireball over its lifetime t_{fo} according to [37, 230]

$$\frac{dN_{\rho\rightarrow ee}}{dM} = \int_0^{t_{fo}} dt \frac{dN_{\rho^0}(t)}{dM} \Gamma_{\rho^0\rightarrow ee}(M), \quad (4.77)$$

where $dN_{\rho^0}(t)/dM$ is the number of ρ mesons per invariant mass bin dM at time t . In fact, the same treatment can be applied to ρ mesons produced in the $\pi\pi$ channel, but then the latter should no longer be accounted for through Eq. (4.76) to avoid double counting. Without any further medium modifications both variants have been shown to be equivalent [231]. For ω and ϕ mesons relations analogous to Eq. (4.77) hold. Note, however, that apart from the absolute abundances of the vector mesons (which should be similar for ρ^0 and ω and somewhat suppressed for the ϕ due to its higher mass) the key quantity which determines the dilepton yield in Eq. (4.77) are the *absolute* values of the dilepton decay widths. The (on-shell) numbers are

$$\begin{aligned}\Gamma(\rho^0 \rightarrow ee) &= 6.77 \pm 0.32 \text{ keV} \\ \Gamma(\omega \rightarrow ee) &= 0.60 \pm 0.02 \text{ keV} \\ \Gamma(\phi \rightarrow ee) &= 1.37 \pm 0.05 \text{ keV},\end{aligned}\quad (4.78)$$

clearly indicating the prevailing character of the ρ meson for radiation originating from the interacting hadronic system. Three-body decays into dilepton channels are evaluated in a similar fashion, e.g., for $a_1(1260) \rightarrow \pi ee$:

$$\frac{dN_{a_1\rightarrow\pi ee}}{dM} = \int_0^{t_{fo}} dt N_{a_1}(t) \frac{d\Gamma_{a_1\rightarrow\pi ee}}{dM} \quad (4.79)$$

with $N_{a_1}(t)$ being the number of a_1 mesons present at time t . The differential Dalitz-decay width is given via the radiative decay width $\Gamma_{a_1 \rightarrow \pi\gamma} = 0.64 \text{ MeV}$ as [230]

$$\frac{d\Gamma_{a_1 \rightarrow \pi ee}}{dM} = \frac{2\alpha}{3\pi} \frac{\Gamma_{a_1 \rightarrow \pi\gamma}}{M} \frac{\left[(m_{a_1}^2 + M^2 - m_\pi^2)^2 - 4m_{a_1}^2 M^2 \right]^{3/2}}{(m_{a_1}^2 - m_\pi^2)^3} \quad (4.80)$$

(this expression is reminiscent of Eq. (4.1) after stripping off the hadronic and VDM form factors from the latter).

Due to the above argument, also transport analyses have primarily investigated in-medium effects in dilepton production by focusing on modifications of the ρ meson (or $\pi\pi$ annihilation). The most straightforward effect to incorporate is to simply change the in-medium ρ mass (as motivated by theoretical predictions such as BR scaling discussed in Sect. 3.2.1). It can be accommodated by appropriate mean-fields in the transport equations, together with replacing the free masses m_ρ by m_ρ^* in Eqs. (4.76) or (4.77), as has been done, e.g., in Refs. [38, 37, 39, 232, 230, 233]. On the other hand, medium modifications which go beyond the mean-field treatment of on-shell quasiparticles are not easily implemented. This is obvious for the case in which the in-medium widths of the propagated hadrons become so large that they lose their quasiparticle nature. Although there is no satisfactory solution to this problem yet (see Ref. [234, 235] for recent progress), some attempts have been made to account for the broadening effect of the ρ in a transport framework. In Ref. [36] the cross section approach based on Eq. (4.76) has been employed by simply multiplying $\sigma_{\pi^+\pi^- \rightarrow e^+e^-}(M)$ with a temperature-dependent “in-medium correction factor”, which is determined as the ratio

$$R_{\text{med}}(M, T) \equiv \frac{[dR/dM^2 d^3 q]_{q=0}^{\text{med}}}{[dR/dM^2 d^3 q]_{q=0}^{\text{free}}} \quad (4.81)$$

of the (equilibrium) dilepton production rate for free $\pi\pi$ annihilation over the in-medium one [113]. To assign a temperature for a given $\pi\pi$ event necessary to evaluate R_{med} , the local (invariant) pion density in the transport has been used assuming local thermal equilibrium. A possible three-momentum dependence (at fixed invariant mass M) as well as dispersion corrections to the explicit pion propagation in the transport have been neglected (the impact of a modified pion dispersion relation on the overall transport dynamics has been shown to be small in Ref. [236]). Along similar lines Refs. [48, 237] proceeded in taking the $\pi\pi$ annihilation cross section as

$$\sigma_{\pi^+\pi^-\rightarrow e^+e^-}(M) = -\frac{16\pi^2\alpha^2}{g_{\rho\pi\pi}^2} \frac{1}{p_\pi^2 M^2} (m_\rho^{(0)})^4 \operatorname{Im} D_\rho(q_0, \vec{q}) \quad (4.82)$$

with the full in-medium spectral function based on the many-body calculations of Refs. [47, 102, 126], including the non-trivial three-momentum dependence (for the vacuum spectral function Eq. (4.76) is recovered). Here the temperature has been deduced from the slope parameter associated with the pion-momentum distributions in the local rest frame (“comoving” frame). Both calculations are in principle plagued by a singularity towards the two-pion threshold $M=2m_\pi$, caused by the inherent inconsistency of how the pions are treated in the transport and in the dilepton rate. However, in practice this failure does not seem to entail severe disturbances except for very close to threshold. In Refs. [48, 237] the additional decays of ρ mesons produced in meson-baryon and baryon-baryon interactions have been accounted for by using a medium modified mass distribution according to

$$\frac{dN_\rho}{dM} = -\frac{2M}{\pi} \operatorname{Im} D_\rho(q_0, \vec{q}), \quad (4.83)$$

together with a constant branching ratio of $\Gamma_{\rho\rightarrow ee}/\Gamma_\rho^{tot} = 4.5 \cdot 10^{-5}$ for the dilepton channel. This leads to a quite different spectral shape as compared to the $\pi\pi$ component included via Eq. (4.76), and might not be realistic (see also the criticism in Ref. [235]). It has been improved in due course by introducing an additional phase space factor $(m_\rho/M)^2$ into the electromagnetic branching ratio.

To avoid double counting when using medium-modified dilepton rates, it is important to omit explicit production channels that are included in the medium effects [48]; e.g., if the ρ selfenergy in the in-medium propagator contains $\pi\rho \rightarrow a_1$ contributions, the explicit $a_1 \rightarrow \pi e^+e^-$ decays have to be switched off. This holds for any process that can be generated by cutting any selfenergy diagram of the many-body spectral function.

4.4.3. Thermal Fireball Expansion

A much simplified attempt to capture the basic features of a heavy-ion reaction relevant for dilepton production is represented by fireball models, some of which are reminiscent to the Bjorken hydrodynamical description. One class of approaches [47] is based on temperature evolutions parameterized in accordance with microscopic transport simulations [232], e.g.,

$$T(t) = (T^i - T^\infty)e^{-t/\tau} + T^\infty \quad (4.84)$$

with the initial temperature of the hadronic phase, T^i , a time constant τ and an “asymptotic” temperature T^∞ . The baryon density is determined by the number of participants supplemented with an (isotropic) volume expansion, which can be approximately described by an “average” baryon chemical potential, e.g., $\mu_B \approx 350\text{--}400\,\text{MeV}$ for lab-energies of $158\text{--}200\,\text{AGeV}$. The total dilepton yield from $\pi\pi$ annihilation is then normalized to the transport results for the case when no-medium effects are included. The pertinent normalization factor turns out to be $N_0 \approx 2\text{--}3$ and can be understood as an overpopulation of the pion phase space due to a finite chemical potential. In fact, for typical SpS freezeout temperatures of $T_{fo} \approx 120\,\text{MeV}$, the simplistic fireball model results in a total pion number which falls short by about 50% as compared to the experimentally observed pion-to-baryon ratio of 5:1 if no pion chemical potential is involved. This can be corrected for by introducing a finite value of $\mu_\pi \approx 50\,\text{MeV}$, amounting to a pion fugacity (in Boltzmann approximation) of $z_\pi = e^{\mu_\pi/T_{fo}} \approx 1.5$. On the level of dilepton production from $\pi\pi$ annihilation [238, 239] this results in an enhancement factor of $N_0 \approx z_\rho = z_\pi^2 \approx 2.3$.

A more microscopic understanding of the emergence of finite (meson) chemical potentials can be gained by noticing that the strong interactions of, e.g., pions— $\pi\pi$ scattering or πN interactions dominated by baryonic resonances—are essentially elastic, i.e., pion-number conserving. Maintaining the assumption of local thermal equilibrium pion-number and entropy conservation then enforces the build-up of a pion chemical potential in the expansion and cooling process within the hadronic phase of a heavy-ion collision, as has been first pointed out in Ref. [197]. Such a scenario fits in fact nicely into the picture of recent hadro-chemical analysis [5, 240, 3], where a large body of data for finally observed particle abundances at SpS energies ($158\,\text{AGeV}$) could be accommodated by a universal temperature and baryon chemical potential of $(T, \mu_N)_{ch} \approx (175, 270)\,\text{MeV}$, characterizing the *chemical* freezeout of the system (the same method successfully describes the AGS data as well, cf. Fig. 1.1). From here on the particle composition in terms of (w.r.t. to strong interactions) stable particles does no longer change, although the hadronic system still interacts via elastic collisions sustaining thermal equilibrium until the *thermal* freezeout is reached. The evolution proceeds along a trajectory in the $T - \mu_N$ plane which can be determined by imposing entropy and baryon-number conservation within, e.g., a hadronic resonance gas equation of state. The induced pion ($\mu_\pi(T)$) and

kaon ($\mu_K(T) \simeq \mu_{\bar{K}}(T)$) chemical potentials along this trajectory increase approximately linearly, reaching typical values of $\mu_\pi^{fo} \simeq 60\text{--}80\,\text{MeV}$ and $\mu_{K,\bar{K}}^{fo} \simeq 100\text{--}130\,\text{MeV}$ at thermal freezeout, being located around $(T, \mu_N)_{fo} \simeq (115 \pm 10, 430 \pm 30)\,\text{MeV}$. Other chemical potentials associated with strong interactions are kept in relative chemical equilibrium, e.g., $\mu_\Delta = \mu_N + \mu_\pi$ or $\mu_\rho = 2\mu_\pi$ according to elastic reactions $\pi N \rightarrow \Delta \rightarrow \pi N$ or $\pi\pi \rightarrow \rho \rightarrow \pi\pi$.

Finally one needs to introduce a time scale to obtain the volume expansion. For SpS energies the latter is realistically approximated by a cylindrical geometry as

$$V_{FC}^{(2)}(t) = 2 \left(z_0 + v_z t + \frac{1}{2} a_z t^2 \right) \pi \left(r_0 + \frac{1}{2} a_\perp t^2 \right)^2, \quad (4.85)$$

where two firecylinders expanding in the $\pm z$ direction have been employed to allow for a sufficient spread in the particle rapidity distributions. Guided by hydrodynamical simulations [43] the primordial longitudinal motion for Pb(158 AGeV)+Au reactions is taken to be $v_z = 0.5c$, and the longitudinal and transverse acceleration are fixed to give final velocities $v_z(t_{fo}) \simeq 0.75c$, $v_\perp(t_{fo}) \simeq 0.55c$ as borne out from experiment [241] (this, in turn, requires fireball lifetimes of about $t_{fo} = 10\text{--}12\,\text{fm}/c$ and implies transverse expansion by 3–4 fm, consistent with HBT analyses [242]). The parameter r_0 denotes the initial nuclear overlap radius, e.g., $r_0 = 4.6\,\text{fm}$ for collisions with impact parameter $b = 5\,\text{fm}$ and $N_B \simeq 260$ participant baryons. The parameter z_0 is equivalent to a formation time and fixes the starting point of the trajectory in the (T, μ_N) plane. Estimates for the initial baryon densities can be taken, e.g., from RQMD calculations which for CERN-SpS energies typically lie around $\rho_B^i \simeq 2\text{--}4\rho_0$ [243], corresponding to, e.g., $(T, \rho_B)_{ini} = (190\,\text{MeV}, 2.55\rho_0)$ on the above specified trajectory.

Dilepton spectra from in-medium $\pi\pi$ annihilation (or, equivalently, ρ decays) are now straightforwardly calculated by integrating the thermal rate, Eq. (4.34). Using $q_0 dq_0 = M dM$, one has

$$\begin{aligned} \frac{dN_{\pi\pi \rightarrow ee}}{dM d\eta} &= \int_0^{t_{fo}} dt V_{FC}(t) \int d^3 q \frac{M}{q_0} \frac{dR_{\pi\pi \rightarrow ee}}{d^4 q}(q_0, \vec{q}; \mu_B, \mu_\pi, T) Acc(M, \vec{q}) \\ &= \frac{\alpha^2}{\pi^3 g_{mp}^2 M} \int_0^{t_{fo}} dt V_{FC}(t) \int \frac{d^3 q}{q_0} \\ &\quad \times f^\rho(q_0; \mu_\rho, T) \mathcal{F}(M, \vec{q}; \mu_B, \mu_\pi, T) Acc(M, \vec{q}), \end{aligned} \quad (4.86)$$

where the function $Acc(M, \vec{q})$ accounts for the experimental acceptance cuts specific to the detector characteristics (e.g., in the CERES experi-

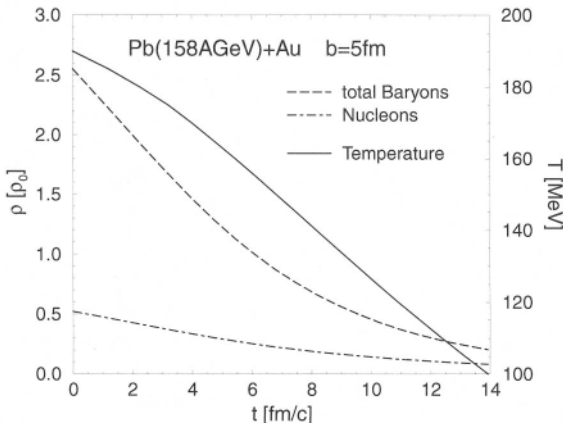


Fig. 4.8. Time evolution of temperature (full line, right scale), total baryon density (long-dashed line, left scale) and nucleon density (dashed-dotted line, left scale) as typical for 30% central $\text{Pb}(158\text{A GeV})+\text{Au}$ collisions at impact parameter $b = 5\text{fm}$ with fixed entropy per baryon and assuming effective pion- and kaon-number conservation.

ment each electron/positron track is required to have transverse momentum $p_T > 0.2 \text{ GeV}$, to fall in the (pseudo-) rapidity interval $2.1 < \eta < 2.65$, and to have a pair opening angle $\Theta_{ee} > 35 \text{ mrad}$). The meson chemical potentials have throughout been introduced in Boltzmann approximation, i.e., $f^\pi(\omega; \mu_\pi, T) \equiv f^\pi(\omega; T) e^{\mu_\pi T}$, etc.

The fireball models certainly oversimplify the dynamics present in more realistic descriptions of relativistic heavy-ion collisions. However, their relative simplicity enables more transparent comparisons between various underlying models for the microscopic rates [142, 47, 100, 205, 244, 50] at the level of experimentally observed data, potentially discriminating different temperature and density dependencies of bare rates once integrated over a common “cooling-curve”.

4.5. Dilepton Spectra at BEVALAC/SIS Energies

The first measurements of dilepton invariant mass spectra in proton and heavy-ion induced reactions at bombarding energies in the 1–5 AGeV range have been performed by the DLS collaboration for p+Be collisions at 1, 2.1 and 4.9 AGeV, for Ca+Ca at 1 and 2 AGeV and for Nb+Nb at 1.05 AGeV [33]. Although the *cms* energy available in a primary nucleon-nucleon collision at 1 GeV laboratory energy only suffices to produce dilepton pairs of invariant masses up to $M \simeq 0.45 \text{ GeV}$,

significant yields have been observed beyond this naive kinematical limit in the collisions involving heavy ions. Therefore, these first generation DLS data have been interpreted as the first evidence for the $\pi\pi \rightarrow e^+e^-$ annihilation channel, predominantly populating the invariant mass region $M_{ee} \geq 0.4 \text{ GeV}$ (up to about 1 GeV). Theoretical calculations based on BUU transport models [245, 246] have confirmed this conjecture. Also, for lower invariant masses, $M \leq 0.4 \text{ GeV}$, the major contributions to the dilepton spectra were identified as Dalitz decays of Δ 's and η 's as well as proton-neutron Bremsstrahlung processes, resulting in a fair agreement with the first generation DLS data [245, 246]. The limited statistics of the latter did not allow for any further conclusions.

From more recent publications of the DLS collaboration [34] it turns out that new measurements of dilepton yields in $p+p$, $p+d$ as well as in 1 AGeV $d+C$, $He+Ca$, $C+C$ and $Ca+Ca$ collisions have been substantially revised in comparison to the previous data set [33] due to improvements of the DLS detector and of the data analysis, correcting for dead-time losses. The $p+p$ data for 1–5 GeV incident energies are reasonably well described by standard Dalitz and vector meson decay sources (for recent transport calculations see Ref. [247] using the UrQMD and Ref. [248] using the HSD approach; both analyses essentially agree up to slight uncertainties in some meson production channels; also the role of $N(1520) \rightarrow Ne^+e^-$ decays, not included in Ref. [247], was found to be significant in Ref. [248] especially for the higher energies). This gives confidence in the elementary production channels when carrying the calculations to the more complicated systems. Nevertheless, significant discrepancies start to build up already for light projectiles such as in $d+Ca$ and $He+Ca$ systems [247]. In the 1 AGeV $C+C$ and $Ca+Ca$ reactions the experimental reanalysis [34] resulted in corrections of up to factors of 6–7 as compared to the first generation data. Consequently, the afore mentioned theoretical approaches now appreciably underestimate the dilepton yield in the invariant mass region $0.15 \text{ GeV} \leq M_{ee} \leq 0.65 \text{ GeV}$. This is apparent, e.g., from the left panels of Fig. 4.9, where a rather complete calculation of the various dilepton sources including (free) $\pi\pi$ annihilation employing the HSD model is displayed [237]. In particular, this calculation reproduces well the total yields and transverse momentum spectra of π 's and η 's as measured for the same collision systems and energies by the TAPS collaboration [249]. This imposes stringent constraints on the dilepton yields from π^0 and η Dalitz decays. Note that the former result in a satisfactory description of the mass region $M_{ee} \leq 0.15 \text{ GeV}$. On the other hand, it was noted in Ref. [34] that, assuming an isotropic dilepton emission from a thermal source, the

new DLS data could be accounted for by (arbitrarily) increasing the η contribution by a large factor close to 10. This observation could be reconciled with the TAPS data imposing a dramatic anisotropy in the η production, since the TAPS data are taken mainly at mid-rapidity, whereas the DLS data are at forward rapidities. Although the HSD calculations show some enhancement of the η distributions [237] at forward angles, this would at maximum allow for a 20% enhancement of the total η yields [249] which is nowhere close to providing an excess of the η signal as required to reproduce the DLS data.

The question thus arises whether in-medium effects can resolve the discrepancy. As an example of the conditions probed at BEVALAC energies, Fig. 4.10 shows a typical time dependence of the baryon density for inclusive Ca+Ca collisions at 1AGeV bombarding energy as extracted from the transport model of Ref. [250]. The evolution roughly proceeds in 3 stages: in the first 5fm/c the nuclei penetrate each other to form a high-density phase at about $2\rho_0$ which then quite rapidly dilutes towards freezeout. The accompanying temperatures at the highest densities are around $T \approx 80\text{--}100\,\text{MeV}$ and therefore one should expect the system to stay in the hadronic phase throughout. Since the pion densities are rather small ($n_\pi = 0.03\,\text{fm}^{-3}$ at $T = 100\,\text{MeV}$), the dominant medium effects should be driven by nucleons and baryonic resonances in the system (note that at $T = 100\,\text{MeV}$ already $\sim 25\%$ of the baryons are thermally excited into Δ 's).

In Ref. [237], the impact of many-body effects [47, 102] on the ρ -meson spectral function, generated through πN and ρN interactions (also including finite-temperature effects, which are, however, much smaller), has been investigated. The results are shown in the two right panels of Fig. 4.9. Apparently, the full results still underestimate the second generation DLS data by a factor of 2–3. Very similar results are obtained [237] when employing the finite-density/zero-temperature ρ -meson spectral function of Ref. [101], which is based on a selfconsistent calculation of resonant ρN interactions. Since present transport approaches cannot fully account for the off-shell dynamics of the pions (especially close to and below the two-pion threshold), additional calculations using the thermal fireball along the lines of Sect. 4.4.3 have been performed. Integrating the thermal dilepton emission rates over the density and temperature profile of Fig. 4.10 leads to very similar results as obtained in the HSD calculation.

Alternative theoretical attempts were made by including dropping vector meson masses in transport calculations. Ref. [233] focused on the role of the $N(1520)$ -resonance, which exhibits a strong coupling to the

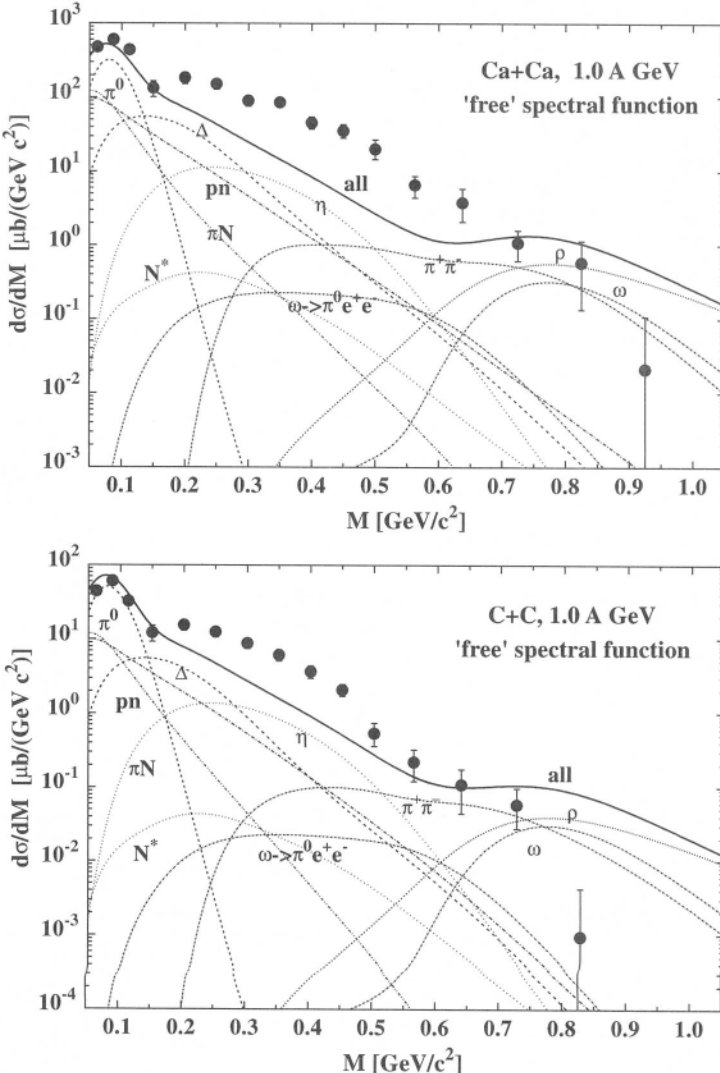


Fig. 4.9. Dilepton spectra as measured in Ca+Ca (upper panels) and C+C (lower panels) reactions at 1.0 AGeV projectile energies. The experimental data from the DLS collaboration [34] are compared to HSD transport calculations, using either a “free” ρ spectral function (left panels) or the in-medium one from Refs. [47, 102] (right panels) for both $\pi\pi$ annihilation and direct decays of ρ mesons produced in baryonic collisions. The DLS acceptance filter (version 4.1) as well as a mass resolution of $\Delta M/M = 10\%$ are included. The thick solid lines represent the total results. The thin lines in the left panels indicate the individual contributions from the different production channels, i.e., starting from low M : Dalitz decays $\pi^0 \rightarrow \gamma e^+ e^-$ (dashed line), $\eta \rightarrow \gamma e^+ e^-$ (dotted line), $\Delta \rightarrow Ne^+ e^-$ (dashed line), $\omega \rightarrow \pi^0 e^+ e^-$ (dot-dashed line), $N^* \rightarrow Ne^+ e^-$ (dotted line), proton-neutron bremsstrahlung (dot-dashed line), πN bremsstrahlung (dot-dot-dashed line); for $M \approx 0.8 \text{ GeV}$: $\omega \rightarrow e^+ e^-$ (dot-dashed line), $\rho^0 \rightarrow e^+ e^-$ (dashed line), $\pi^+ \pi^- \rightarrow \rho \rightarrow e^+ e^-$ (dot-dashed line). The plots are taken from Ref. [237].

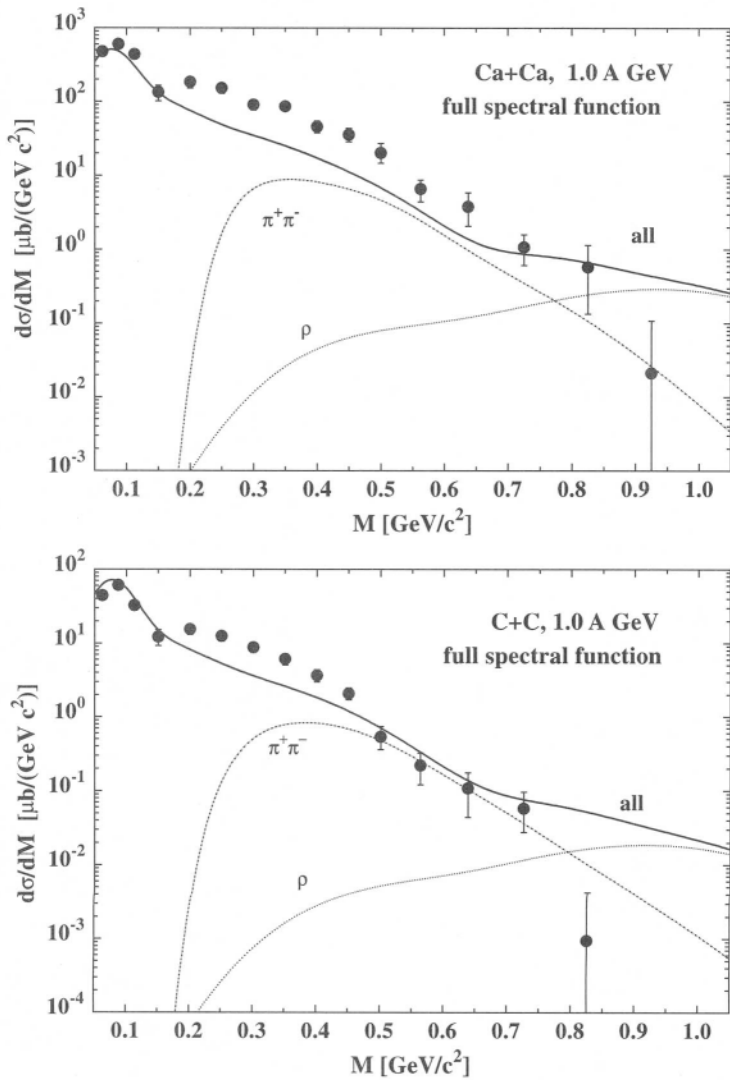


Fig. 4.9. (Continued)

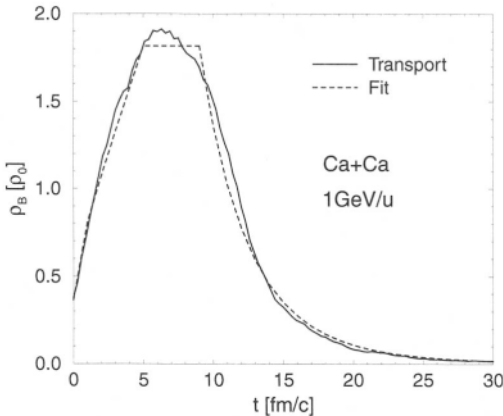


Fig. 4.10. Evolution of average baryon density as a function of time in inclusive 1 AGeV Ca+Ca collisions as extracted from the transport model of Ref. [250] (solid curve); the dashed curve is a simple parameterization thereof with a maximal temperature of $T_{max} = 100$ MeV in the high density phase and a time-independent baryon chemical potential of $\mu_B = 0.76$ GeV.

$\rho N/\gamma N$ channel, see Sects. 3.2.3 and 4.1.2. Rather than including it via the in-medium ρ -meson spectral function as was done in Ref. [237], the Dalitz decays $N(1520) \rightarrow Ne^+e^-$ were evaluated explicitly, confirming its relative importance for the low-mass dilepton spectra. However, once an additional reduction of the ρ mass is introduced (using, e.g., the QCD sum rule results, $m_V^* = m_V(1 - C\rho/\rho_0)$ with $C \approx 0.18$), the hadronic decay width of the $N(1520)$ strongly increases due to the opening of phase space in the ρN decay, which results in a net reduction of the dilepton yield from $N(1520)$ decays (note that the in-medium broadening is included in the many-body calculations of Refs. [102, 101]). Although the direct ρ decay contributions are enhanced by a factor of about 3 with a dropping ρ mass, the total spectra still underestimate the DLS data by a factor of 3–4 for invariant masses $0.15 \text{ GeV} \leq M \leq 0.5 \text{ GeV}$. Similar conclusions have been reached in Ref. [247] where the use of dropping vector meson masses has been found to give a small net increase of the spectra around $M \approx 0.4 \text{ GeV}$, together with the reduction around the free ρ/ω peak.

Concluding this Section we emphasize that there is currently no theoretical explanation of the second generation DLS data for dilepton production in 1–2 AGeV heavy-ion collisions, with the various model predictions falling short by large factors of 2–3 above the π^0 Dalitz region

and below $M \simeq 0.5$ GeV. The upcoming high-precision dilepton measurements with the HADES detector at GSI will be crucial to shed new light on this situation.

4.6. Dilepton Spectra at CERN-SpS Energies

The dilepton program at the CERN-SpS started in 1990–1992 with the ^{32}S beam at 200 AGeV, followed by a 450 GeV proton run in 1993 and ^{208}Pb nuclei accelerated to 158 AGeV in 1995, 1996 and 1998. Data have been taken by three collaborations: CERES/NA45 for e^+e^- pairs using ^{197}Au targets (as well as ^9Be in the proton run) [20, 23, 251], HELIOS-3 [24] for $\mu^+\mu^-$ pairs using ^{184}W targets, and NA38/NA50 [25, 26, 27] also for $\mu^+\mu^-$ pairs using ^{32}S , Cu and ^{238}U as well as ^{208}Pb targets for the lead runs. The major challenge in these experiments is the large background due to both charged hadrons and, more severely, combinatorial misidentification of pairs in the same event, i.e., the pairing of t^+ and t^- tracks which did not arise from the decay of the *same* virtual photon (or other *correlated* physical processes, as, e.g., the so-called “open charm” contributions, where a pairwise production of $D\bar{D}$ mesons is followed by subsequent weak decays $D \rightarrow t^+ X$ and $\bar{D} \rightarrow t^- X$). In the CERES experiment, e.g., charged hadrons are suppressed with Cerenkov detectors, whereas the combinatorial background to the “physical” e^+e^- signal is typically determined through pairing of like-sign pairs, i.e., e^+e^+ and e^-e^- .

As a result of the different ways in handling these problems, the kinematical regions covered by the three experiments are quite distinct, see Fig. 4.11. Before one can identify non-trivial signals from the highly complicated measurements in nucleus-nucleus collisions, one has to have good control over the more simple systems first. The proton-induced reactions, supposedly governed by the mere free decays of the produced hadrons involving no significant rescattering, thus serve as an important aid in understanding the detector systematics. The free hadronic decay contributions have become known as the hadronic cocktail and will be discussed in the next Section. Since at full CERN-SpS energies the pion-to-baryon ratio observed in the final state of heavy-ion induced reactions is about 5:1 (with little dependence on the impact parameter b), the dominant in-medium source is expected to stem from $\pi\pi$ annihilation. The assessment of this contribution without any medium-modifications will be addressed in sect. 4.6.2. In Sects. 4.6.3 and 4.6.4 we proceed to the analysis of the experimental data in the available kinematic projections, i.e., invariant mass and transverse pair-momentum, with emphasis on

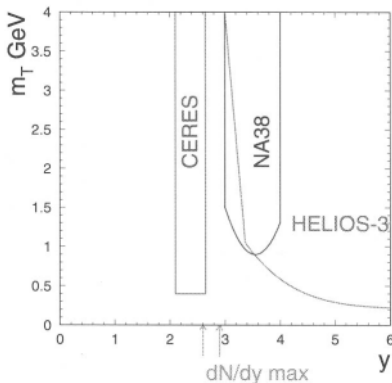


Fig. 4.11. Kinematical regions covered by the three collaborations that have measured dilepton spectra at full CERN-SPS energies of 158–200 AGeV. The plot is taken from Ref. [22].

in-medium effects that have been proposed. In Sect. 4.6.5 we discuss how the various parts of the in-medium signals relate to the time of emission within different theoretical models. In particular, the issue of quark-gluon/hadron duality, raised in Sect. 4.2.3, will be reiterated for both the low- and intermediate-mass region.

4.6.1. Decays after Freezeout: Hadronic Cocktail versus Experiment

From the experimental side, a systematic study of the cocktail contributions has been performed by the CERES/NA45 collaboration. It has been shown [20] that the e^+e^- invariant mass spectra in $p+Be$ and $p+Au$, normalized to the number of charged particles observed in the same rapidity window, can be well reproduced in terms of known hadron decays using particle production multiplicities from $p+p$ data, cf. Fig. 1.3 in the Introduction. The low-mass end of the spectrum, $M_{ee} \leq 0.15$ GeV, is completely saturated by π^0 Dalitz decays, whereas for $0.15 \text{ GeV} \leq M_{ee} \leq 0.6 \text{ GeV}$ η and ω Dalitz decays are prevailing. Beyond $M_{ee} = 0.6 \text{ GeV}$ up to about 1.5 GeV the direct decays of the light vector mesons, ρ , ω , $\phi \rightarrow e^+e^-$, are the dominant sources, substantially smeared due to the finite mass resolution of about 10% in the CERES detector (which, in fact, stems from the finite momentum resolution of the individual lepton tracks). Here one should note that, for an equal number of produced ρ^0 's and ω 's, the dilepton yield from the latter is by almost a factor of 2 larger than the former, since in free space the probability $P_{V \rightarrow ee}$ for decaying into the dilepton channel is determined by the relative branching ratio of electromagnetic over total decay width, i.e.,

$$P_{V \rightarrow ee} = \frac{\Gamma_{V \rightarrow ee}}{\Gamma_V^{tot}} = \begin{cases} 0.0045\%, & V = \rho \\ 0.0071\%, & V = \omega \\ 0.0311\%, & V = \phi \end{cases} \quad (4.87)$$

This is a quite different characteristics as compared to the signal from an interacting (thermalized) system, cf. Eq. (4.77) and the subsequent remarks. The CERES assessment of the cocktail in proton-induced reactions has been confirmed by microscopic transport calculations [38, 232]. The latter give equivalent results for the dimuon data of HELIOS-3 [24] taken in $p+W$ reactions. Thus the measured dilepton spectra in proton-induced reactions at CERN-SpS energies can be well understood by the final-state hadron decays in a consistent way.

The situation changes drastically when moving to heavy-ion projectiles. In the first measurements at the CERN-SpS, which were performed with a 200AGeV ${}^{32}\text{S}$ beam, the CERES collaboration found a total enhancement factor of measured pairs over the expectation based on the cocktail of 5.0 ± 0.7 (stat) ± 2.0 (syst) (integrated over the invariant mass range 0.2–1.5 GeV) [20] in central collisions with ${}^{197}\text{Au}$ targets. The enhancement is in fact most pronounced around $M_{ee} \approx 0.45$ GeV, reaching a factor of 10 (Fig. 4.12). Whereas the CERES data are taken close to midrapidity ($2.1 \leq \eta \leq 2.65$), the HELIOS-3 experiment [24] covered more forward rapidities $3.7 \leq \eta \leq 5.2$. Here the enhancement, when comparing to transport calculations [39, 232], is less developed but still significant (although the HELIOS-3 collaboration did not quote any systematic errors).

The '95 and '96 runs with 158 AGeV ${}^{208}\text{Pb}$ projectiles in essence confirmed the sulfur results, cf. right panel of Fig. 4.12. Here, the final state hadron decay contributions have been evaluated in an alternative way as recently developed by the CERES collaboration. It is based on hadron abundances from the thermal model of Ref. [3], where the (chemical) freezeout conditions for temperature and baryon chemical potential have been deduced from an optimal fit to a large body of hadronic observables at SpS and AGS energies (the such obtained cocktail agrees with sources scaled from $p+p$ collisions within 20–30%, with the only exception of the ϕ meson—related to strangeness enhancement—which we will not address here). The resulting enhancement of the '96 data over the “thermal-model” cocktail in the 30% most central Pb+Au collisions then amounts to 2.6 ± 0.5 (stat.) ± 0.9 (syst.) [251] in the invariant mass range 0.25–0.7 GeV. In terms of the experimental analysis, the '96 data set is the best understood with the highest statistics (a factor of 5 larger

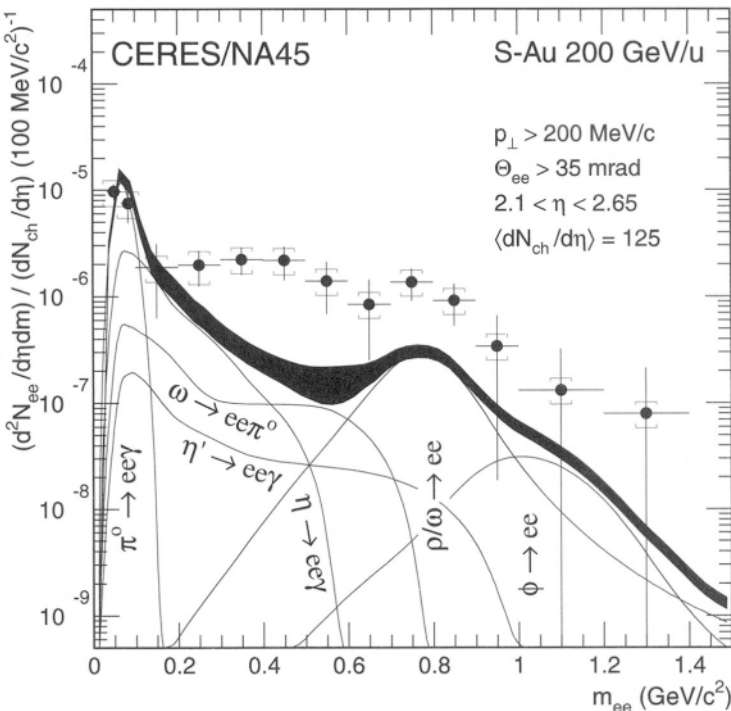


Fig. 4.12. Dilepton spectra from heavy-ion collisions as measured by the CERES/NA45 collaboration. Top: central 200 AGeV S+Au collisions, contrasted with the hadronic cocktail contributions as extrapolated from hadron multiplicities in $p+p$ data. The plot is taken from Ref. [20]. Bottom: 35% central 158 AGeV Pb+Au collisions (open squares: '95 data, full circles: '96 data), compared to a hadronic cocktail inferred from a thermal model with $T = 175 \text{ MeV}$ and $\mu_B = 270 \text{ MeV}$ [3], which reproduces the measured hadronic multiplicities in Pb+Pb collisions at identical projectile energy.

than in '95). It is consistent with both the '95 sample and the '93 sulfur results within two standard deviations (note that the S+Au data are based on a higher centrality selection). Nevertheless, the net signal in the '96 data seems to lie systematically below the '95 data, this trend being more accentuated towards higher masses. In particular, at the free vector meson masses the '96 data are basically accounted for by the hadronic cocktail. If this feature will be confirmed in future measurements, it has severe consequences for the theoretical interpretation of the spectra. A rather precise determination of the ω contribution, which is the dominant cocktail component at the ρ/ω mass, will be most important to draw

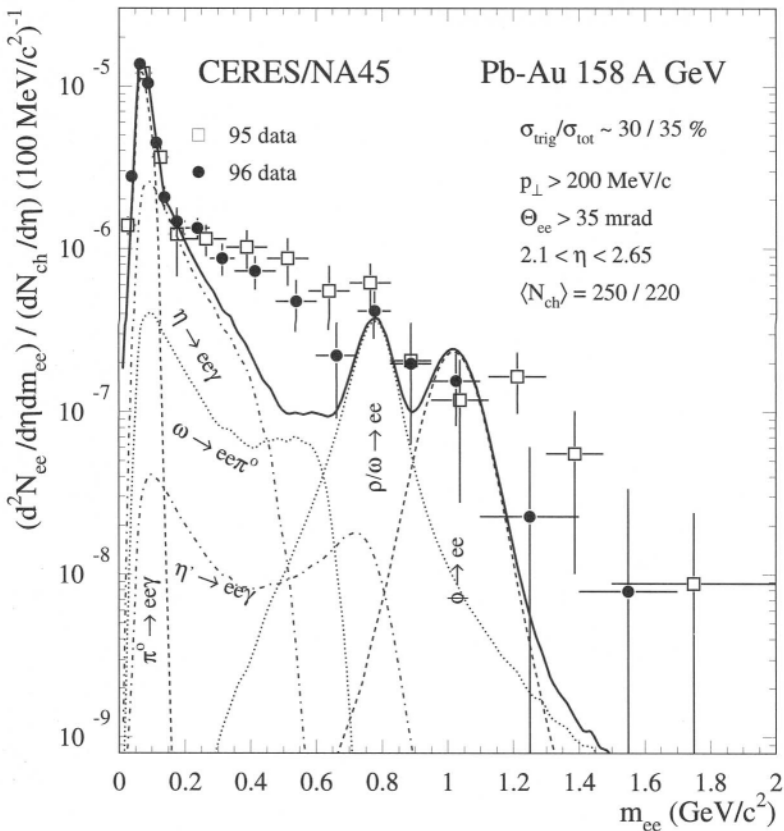


Fig. 4.12. (Continued)

firm conclusions. Unfortunately, the ω yield in heavy-ion reactions is not very well determined so far. In hydrodynamical calculations as, e.g., presented in Ref. [252], the ω -meson yield might be substantially smaller than in the CERES cocktail if its final abundance is determined by a simultaneous thermal *and* chemical freezeout temperature as low as $T_{fo} = 120 \text{ MeV}$. The most promising way to resolve this issue will be provided by an improved mass resolution in the dilepton measurements. If the latter can be reduced to about 2%, the ω peak will clearly stick out, thus putting valuable constraints on other (in-medium) sources in its vicinity. An upgrade of the CERES experiment using an additional time projection chamber (TPC) is expected to achieve the required resolu-

tion. An accordingly small mass binning will critically depend on a sufficiently large data statistics.

Once the direct $\omega \rightarrow e^+e^-$ decays are known, also the Dalitz-decay contributions $\omega \rightarrow \pi^0 e^+ e^-$ are fixed. The latter constitute an important part of the cocktail in the mass region where the experimental excess of dilepton pairs is the largest, i.e., $0.3 \text{ GeV} \leq M_{ee} \leq 0.6 \text{ GeV}$. The other important hadronic decay in this region is $\eta \rightarrow \gamma e^+ e^-$ and, to a lesser extent, $\eta' \rightarrow \gamma e^+ e^-$. Therefore, an enhanced production of η, η' mesons in heavy-ion as compared to proton-induced reactions could significantly alter the cocktail composition. Mechanisms for such a behavior have indeed been proposed in connection with the (partial) restoration of the $U_A(1)$ symmetry (see also Sect. 2.1) in high density/temperature matter, reducing the η and η' masses and thus increasing their (final) abundances [253]. However, an enhanced η, η' production also entails an increase of the direct photon yield from the two-photon decay modes $\eta, \eta' \rightarrow \gamma\gamma$. In Ref. [254] upper limits on inclusive photon measurements in heavy-ion collisions at the SpS have been converted to a maximally allowed η production. Assuming that the upper limit of the photon signal is entirely saturated by extra η decays, it has been shown that the η yield in ^{32}S induced reactions cannot be enhanced by more than a factor of 1.5 as compared to the $p+p$ case. Similar arguments have been drawn to limit the η' enhancement to a factor of 2.5. As a result, using the upper bounds on η and η' numbers, the CERES cocktail in 200 AGeV S+A collisions (displayed in the left panel of Fig. 4.12) is increased by at most 40% which is far from accounting for the observed excess in the 0.3–0.6 GeV region (this situation is reminiscent to BEVALAC/SIS energies, where an increased η yield as the source for the dilepton enhancement found by DLS in A - A collisions has also been ruled out by means of the TAPS two-photon data, see Sect. 4.5). The failure of the hadronic cocktail to describe the low-mass dilepton spectra in nucleus-nucleus collisions at the SpS thus inevitably points towards radiation originating from processes occurring during the interaction phase of the collisions, which will be discussed in the following sections.

4.6.2. Free $\pi^+\pi^-$ Annihilation in the Hadronic Fireball

One of the strongest evidences for a “non-trivial” source of dilepton pairs in heavy-ion reactions is illustrated in Fig. 4.13. The total e^+e^- pair yield, normalized to the number of charged particles in the final state, exhibits a clear increase with multiplicity, indicating two- (or more) body annihilations. Since the most abundant particles at SpS energies are

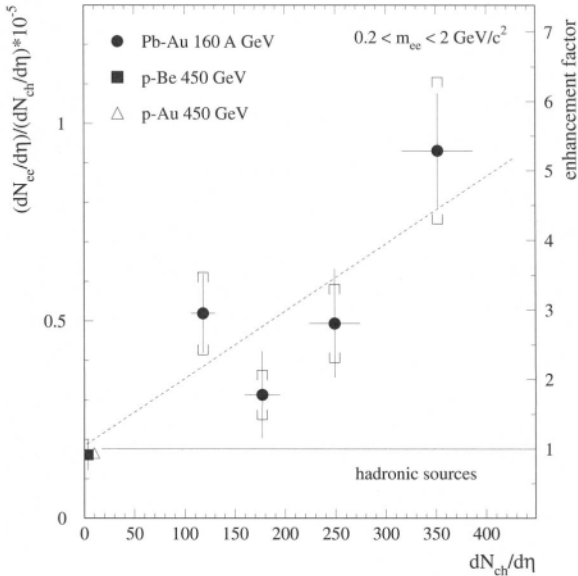


Fig. 4.13. Total dilepton pair yield, normalized to the number of observed charged particles in the corresponding rapidity interval, and resulting enhancement factor over the hadronic cocktail (right vertical scale) as a function of charged particle multiplicity as found in different collision systems. The horizontal solid line indicates the expectation from final-state hadron decays whereas the dashed line is a linear interpolation of the data which implies a quadratic dependence on the number of charged particles as expected from an additional two-body annihilation source. The plot is taken from Ref. [23].

pions, the obvious candidate for this behavior is the $\pi^+\pi^- \rightarrow \rho^0 \rightarrow e^+e^-$ process. Many authors have calculated its contribution in various approaches to model the heavy-ion reaction dynamics, leading to rather good agreement with each other as we have already eluded to in the Introduction, see Fig. 1.4 for the case of ^{32}S -induced reactions. All calculations share the common feature that, although the total yield is appreciably increased, the shape of the spectra strongly deviates from the data in that one finds too much yield around the free ρ mass and too little below, which is a trivial consequence of the free pion electromagnetic form factor peaking at the ρ resonance.

At this point it is useful to notice an important difference between transport and hydrodynamical approaches. In the latter the total yield is typically by a factor of at least 2 smaller than in the former ones if no chemical potentials for pions are involved as is the case, e.g., for the

(dotted) Hung-Shuryak curve [43] in the left panel of Fig. 1.4 (see also Ref. [214]). Although in both schemes the final hadronic spectra are usually equally well accounted for, hydrodynamic calculations involve smaller (average) pion densities n_π (due to the restriction to $\mu_\pi = 0$) and hence larger fireball volumes V_{FB} to obtain an identical final number of pions. This means that, for a given total number of pions, $N_\pi = n_\pi \times V$, larger average densities in the transport simulations lead to a larger dilepton signal from $\pi\pi$ annihilation, since the latter is basically proportional to the pion density squared, $N_{\pi\pi \rightarrow ee} \propto n_\pi^2 \times V$. On the other hand, in the Bjorken-type hydrodynamical calculations of Baier *et al.* [41] where a pion chemical potential of $\mu_\pi = 100 \text{ MeV}$ has been employed, the dilepton yield is even slightly larger than in most of the transport results, cf. solid line in the left panel of Fig. 1.4. This is understandable, as the “average” squared pion density in this calculation is increased over the $\mu_\pi = 0$ case by roughly the squared fugacity $(\exp[\mu_\pi/T])^2 \approx \exp[2 \times 100/150] \approx 4$. Another quantity which governs the amount of dileptons radiated from the hadronic fireball is its total lifetime. For Pb + Au collisions at the full SpS energy (158AGeV) the latter is around 10–15 fm/c. However, as pointed out by Shuryak and Hung [213], the upcoming low-energy run at 40AGeV may lead to initial conditions that are close to the so-called “softest” point in the EoS of the quark-hadron transition, associated with a very small initial pressure. In this case, the system expands very slowly entailing a much increased fireball lifetime which would have to leave its trace in the total dilepton yield.

The incompatibility of free $\pi\pi$ annihilation persists in the Pb + Au data. Although the excess signal in the more recent CERES measurements is somewhat reduced as compared to the early sulfur runs the inclusion of free $\pi\pi$ annihilation in theoretical models can still not resolve the discrepancy with the data. This statement is corroborated by the trend that in the Pb + Au system the cocktail is close to saturating the data in the ρ/ω region, where the free $\pi^+\pi^- \rightarrow \rho^0 \rightarrow e^+e^-$ process has its maximal contribution! Thus one is seemingly led to the following two alternatives:

- (i) $\pi\pi$ annihilation is not an important ingredient in the dilepton spectra, but rather some very different processes with flat characteristics as a function of invariant mass, e.g., $q\bar{q}$ annihilation. However, this is not easy to imagine for the SpS conditions, where one expects the excited nuclear system to spend the major part of its space-time history in a hadronic phase with a large pion component;

- (ii) $\pi\pi$ annihilation is the dominant process. In this case drastic medium modifications are inevitable to fill in the 0.3–0.6 GeV mass region without giving too much yield around the free **ρ -meson** mass.

Both possibilities will be considered in the forthcoming Sections.

4.6.3. Medium Effects I: Invariant Mass Spectra

Most of the in-medium effects proposed so far have drawn their attention to the pion-pion annihilation channel. They can be roughly divided into the following two categories

- (I) a temperature- and density-dependent reduction (“dropping”) of the ρ meson mass, m_ρ^* , according to BR scaling or the Hatsuda-Lee QCD sum rule calculations, usually applied without invoking any changes in the pion propagation. This then entails a reduction of the **ρ -meson** width due to the shrinking pion phase space at smaller m_ρ^* as well as a sharp threshold—at twice the free pion mass $2m_\pi$ —for the onset of the enhancement in the invariant mass dilepton spectra;
- (II) a modification of both π and ρ properties due to phenomenologically inferred interactions with the surrounding hadrons in the hot and dense gas which, depending on the language used, are encoded in the **ρ -meson** spectral function (e.g., Refs. [47, 147, 101]), in vector current correlation functions (e.g., in Refs. [100, 91]), in the pion electromagnetic form factor (Ref. [113]), etc. Also the rate calculations for individual processes as, e.g., performed in Refs. [119, 221], should be assigned to this category, as was discussed in Sect. 4.2.1.

4.6.3a. 200 AGeV Sulfur Beam Runs. For dilepton spectra in the 200 AGeV ^{32}S -induced reactions the consequences of a dropping ρ -meson mass have been explored in Refs. [38, 37, 39, 232]. All these analyses find good agreement with the experimental data (Fig. 4.14). The mechanism is clear: in the early phase, characterized by hadronic initial conditions of $T^i \simeq 170\,\text{MeV}$ and $\rho_B^i \simeq 2.5\rho_0$, the in-medium mass m_ρ^* is close to the two-pion threshold. As the hot fireball expands thereby diluting and cooling, m_ρ^* starts to rise and sweeps across the low-mass region thus filling the dilepton continuum between 0.3 and 0.6 GeV (at freeze-out, the **ρ -meson** has regained about 80% of its vacuum mass). At the same time, the ρ (or $\pi\pi$) contribution around the free ρ peak is strongly reduced, which is also in line with the experimental data. However,

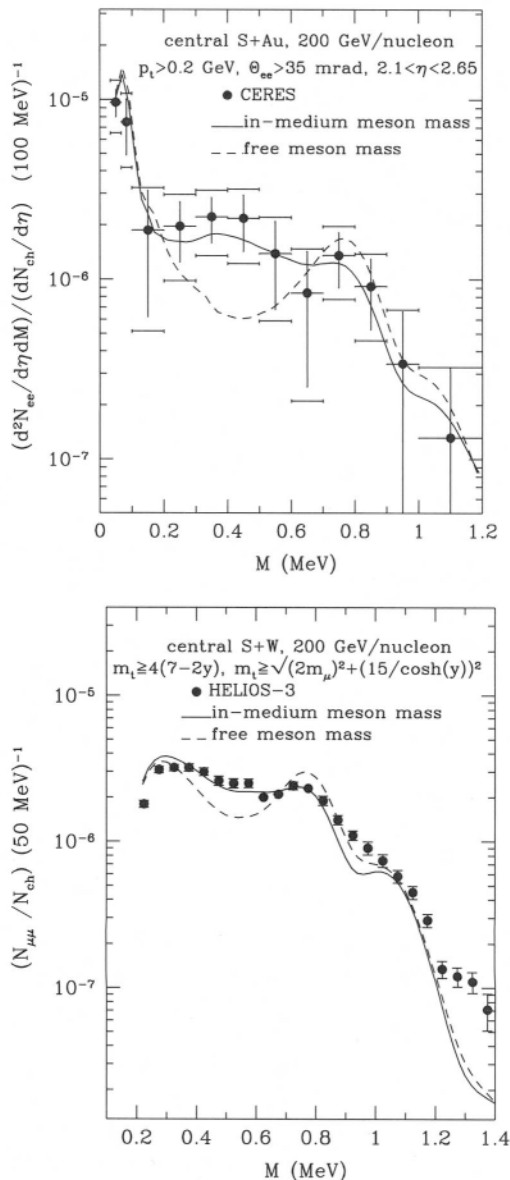


Fig. 4.14. Comparison of dilepton data from central 200 AGeV sulfur-induced reactions on heavy nuclei with transport calculations employing a dropping ρ mass (full curves) as opposed to a free ρ mass (dashed curves) [232]. Top: CERES dielectron spectra on Au targets; bottom: HELIOS-3 dimuon spectra on W targets.

between the ω and the ϕ mass the situation is less clear, mainly due to limited experimental mass resolution and statistics (the former amounting to $\sim 8\text{--}11\%$ in this mass region for the '92-'95 CERES data). The medium modifications of the ω meson itself have only little impact on the dilepton spectra, although in BR scaling the ω mass is subjected to the same reduction as the ρ mass. The reason is simply that the $\omega \rightarrow e^+e^-$ decays mostly occur after the hadronic freezeout where medium effects are absent. The final number of ω mesons is roughly equal to the case where no dropping masses are assumed. This is so because in Refs. [37, 232] rather large pion chemical potentials $\mu_\pi = 100\,\text{MeV}$ are present in the initial conditions when using the free masses to correctly reproduce the observed number of final pions. On the other hand, when using in-medium masses, much smaller μ_π are required to obtain about the same final number of pions and ρ/ω mesons. Within the Walecka-type mean-field potentials employed in the transport equations of Refs. [37, 232] the scalar field has been assumed to act on the constituent u/d -quark content of the hadrons only, thus leaving the mass of the ϕ meson, which is an almost pure $s\bar{s}$ state, unchanged. An important point to note is that the baryons (rather than pions which govern the finite-temperature effects) in the hadronic fireball are the key component in generating the large (attractive) scalar fields which are at the origin of the dilepton enhancement.

Dropping meson masses have also been implemented in hydrodynamical simulations [41, 43]. Although the total dilepton signal in the latter is typically smaller than in the transport frameworks (if $\mu_\pi \equiv 0$, see previous Section), they also give reasonable agreement with the S + Au data [41, 43].

As representatives for the analyses of the CERES S + Au data that are based on more “conventional” scenarios we have chosen the calculations within the chiral reduction approach [100] and the many-body approach for the ρ -meson spectral function [47] in its recent version (including constraints from nuclear photoabsorption [102] and $\pi N \rightarrow \rho N$ data [49], Rhosobar excitations on thermally excited baryon resonances as well as a more complete assessment of the mesonic contributions [123]. The results are confronted in Fig. 4.15 with experiment. To facilitate the direct comparison both spectra have been computed in the thermal fireball expansion of Ref. [47] (with $T^i = 170\,\text{MeV}$, $T^\infty = 110\,\text{MeV}$, $\tau = 8\,\text{fm}/c$, $t_{fo} = 10\,\text{fm}/c$ in Eq. (4.84), $N_B^{part} = 110$, a constant isotropic expansion velocity $v = 0.4c$ and $\mu_B = 0.39\,\text{GeV}$ which translates into initial/freezeout baryon densities of $\rho_B^i = 2.49\rho_0 / \rho_B^{fo} - 0.32\rho_0$ and a freeze-out temperature of $T^{fo} = 127\,\text{MeV}$; in addition an overall normalization

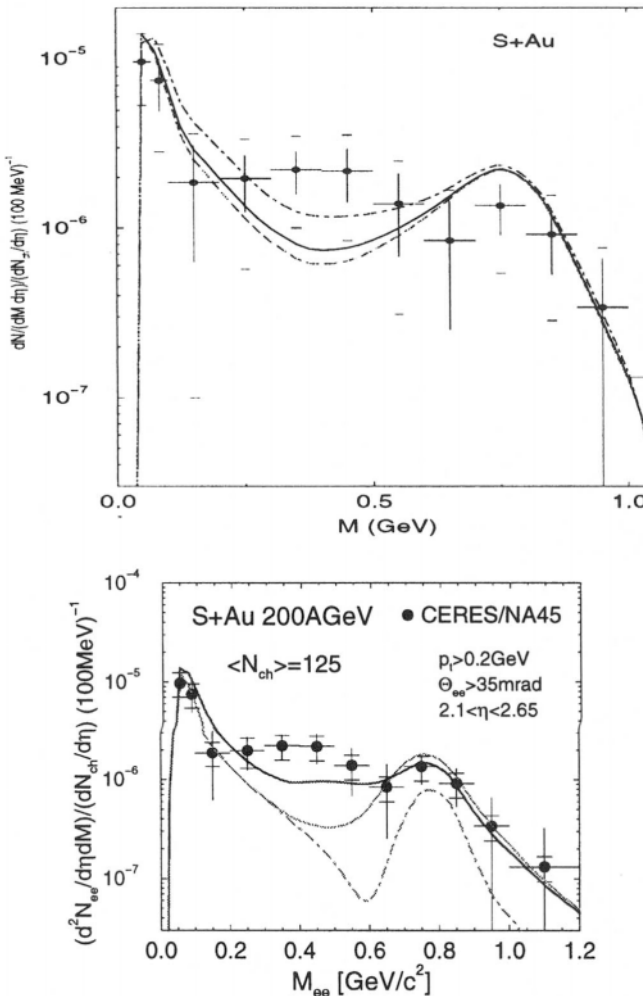


Fig. 4.15. Comparison of CERES data from central 200 AGeV S + Au reactions with thermal fireball calculations including in-medium effects according to the chiral reduction formalism [100]. (Left panel; all curves include the hadronic cocktail as given by transport results [37]; in addition, in-medium radiation is accounted for in the following ways: pure pion gas (dashed curve), pion-nucleon gas using $\rho_N^t = 0.7 \rho_0$ corresponding to the realistic case of $\mu_B = 0.39 \text{ GeV}$ (full curve), and pion-nucleon gas using the full baryon density $\rho_N^t \equiv \rho_B = 2.5 \rho_0$ (dashed-dotted curve)), and within the many-body approach for the ρ spectral function [47, 126, 49, 123] (right panel; dashed-dotted curve: hadronic cocktail; dotted curve: cocktail plus $\pi\pi$ annihilation using the free ρ spectral function; full curve: cocktail plus $\pi\pi$ annihilation using the in-medium ρ spectral function).

factor $N_0 = 3$ has been introduced in reminiscence to transport results [37], corresponding to an “average” pion chemical potential of ~ 80 MeV). Neither of the two “conventional” approaches gives as good agreement with the S + Au data as the dropping ρ mass scenarios (this is even more pronounced for other attempts [40, 221, 36, 41]), although the experimental uncertainty is not small. In the chiral reduction formalism (left panel in Fig. 4.15) the incoherent summation of individual rate contributions in a low-density expansion (for both pions and nucleons) generates some enhancement over the results based on free $\pi\pi$ annihilation (dotted curve in the right panel), but does not lead to any depletion of the free ρ peak. Consequently, the *shape* of the theoretical curves does not match the experimental data very well. This is qualitatively different in the many-body approach (right panel in Fig. 4.15). The strong broadening of the ρ -meson spectral function yields a factor of ~ 2 more enhancement below $M_{ee} \approx 0.6$ GeV together with some reduction in the ρ/ω region, which makes it somewhat more compatible with the data. A possible caveat might be given by the fact that the (experimental) systematic errors presumably have little (or at least a very smooth) dependence on invariant mass. This could mean that an agreement of the theoretical curves in the 0.3–0.5 GeV region entails a disagreement around $M_{ee} \approx 0.2$ GeV and vice versa. We will come back to this point further below. Another noteworthy feature is that, although the in-medium spectral function is larger than the free one at the high mass end for $M_{ee} \geq 0.9$ GeV (cf. Fig. 3.19), this feature does not show up in the dilepton spectrum in the right panel of Fig. 4.15, which can be traced back to the mass resolution of the CERES detector in the ’92 setup ($\delta M/M \approx 11\%$ around $M \approx 1$ GeV).

The spectral function approach has also been employed using a more realistic description of the heavy-ion reaction dynamics within the HSD transport simulations [48]. Fig. 4.16 shows the results for the HELIOS-3 data in 200 AGeV S + W collisions using the free (upper panel) and in-medium (lower panel) ρ spectral function, the latter based on the model of Refs. [102, 126]. Again, the broadening of the ρ spectral function significantly improves the agreement with experiment.

4.6.3b. 158AGeV Lead Beam Runs. Again, let us first address analyses involving dropping meson masses. Fig. 4.17 shows results of the HSD transport approach [230], which once more demonstrate that a reduced ρ -meson mass is very well in line with the experimentally observed low-mass dilepton enhancement at full CERN-SPS energies, most notably around the 0.5 GeV region. Similar conclusions have been drawn in the transport calculations of Ref. [255] for the 8% most central

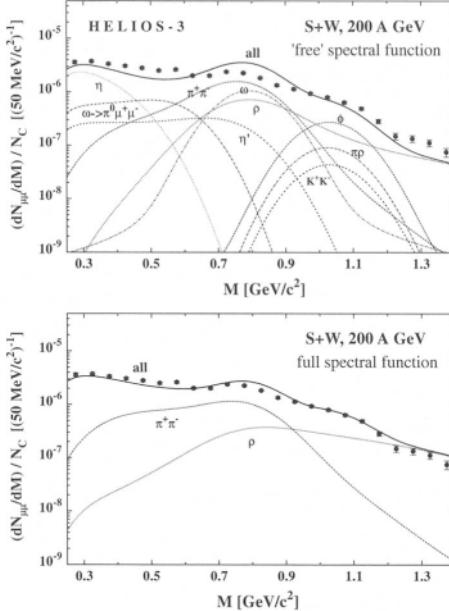


Fig. 4.16. Comparison of HELIOS-3 data from central 200 GeV S + W reactions with HSD transport calculations [48] employing free (upper panel) and in-medium (lower panel) ρ spectral functions from Refs. [47, 102]. Note that the high-mass end of the contribution labeled by “ ρ ” (which stem from meson-baryon and baryon-baryon collisions) is probably somewhat overestimated, cf. the remarks following Eq. (4.83).

sample of the '95 CERES data, as well as in the hydrodynamical description of Ref. [43].

Proceeding to category II (“conventional” medium modifications), we display in Fig. 4.18 a comparison of transport and fireball calculations. The left panel shows recent BUU transport calculations [257] along the lines of Ref. [36] where the in-medium effects entirely reside in finite temperature effects in the $\pi\pi$ annihilation channel and $\pi\rho$ -type contributions (dominated by the $a_1(1260)$). Due to collisional broadening introduced in the (denominator of) the pion electromagnetic form factor the significance of the in-medium $\pi\pi$ channel is rather moderate; the processes inducing the broadening (i.e., $\pi\rho$ collisions) are treated explicitly for dilepton production to approximately restore unitarity in the transport framework. Within 1.5 standard deviations, all data points for 30% central Pb + Au are reproduced; in the low-mass region, $M_{ee} \approx 0.3\text{--}0.6\text{ GeV}$, this is largely achieved through a strong contribution of the

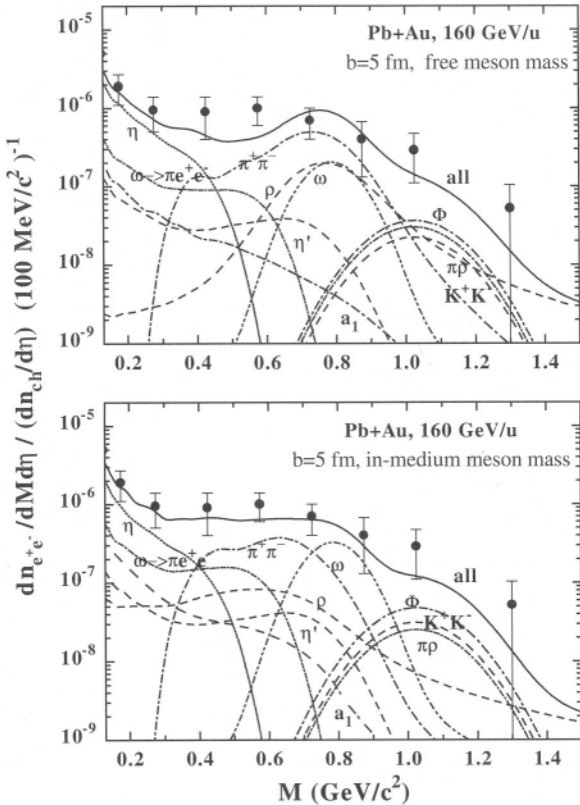


Fig. 4.17. Comparison of the (preliminary) '95 CERES data [21] from 35% central 158 AGeV Pb + Au reactions with HSD transport calculations [230] employing free (upper panel) and dropping (lower panel) meson masses.

$\omega \rightarrow \pi^0 e^+ e^-$ and $\eta \rightarrow \gamma e^+ e^-$ Dalitz decays, each about a factor of 2 larger than in the CERES cocktail. As we have mentioned earlier, especially the ω contribution is as of now not very well under control (and has been introduced through suitable initial conditions in the transport); on the other hand, one also realizes from the left panel of Fig. 4.18 that at the free ρ/ω mass the direct decays $\omega \rightarrow e^+ e^-$ tend to overestimate the experimental data, i.e., the freezeout ω abundance has been pushed to its limit. In contrast, the in-medium spectral function approach [142, 47, 47, 91, 101] assigns the major part of the low-mass enhancement to the (modified) $\pi\pi$ channel including the effects of baryons. The right panel of Fig.

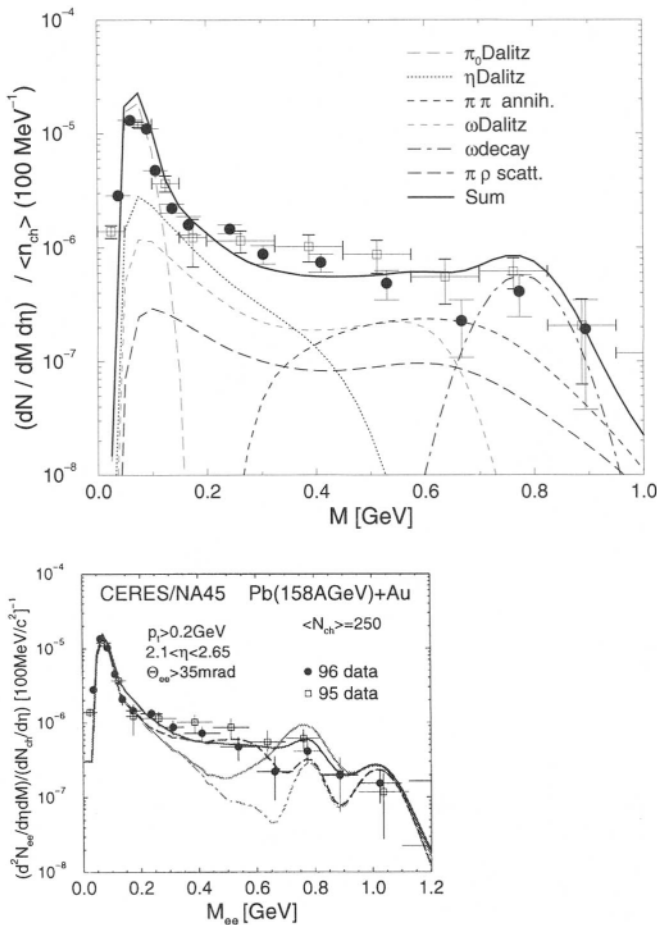


Fig. 4.18. Comparison of the CERES data from 35%/30% central 158 AGeV Pb + Au collisions with BUU transport calculations [36, 257] including finite-temperature effects in the pion electromagnetic form factor and through explicit $\pi\rho$ scattering (top). Bottom fireball calculations [47] using thermal production rates from in-medium $\pi\pi$ annihilation in three scenarios; dashed-dotted line: CERES cocktail (no in-medium contribution, no ρ decays); dotted line: cocktail plus free $\pi\pi$ annihilation; solid line: cocktail plus $\pi\pi$ annihilation employing the in-medium ρ spectral function [102, 123, 50]; long-dashed line: cocktail plus $\pi\pi$ annihilation using a dropping ρ mass.

4.18 shows the pertinent results [123, 50] employing a thermal fireball model including the experimentally determined hadro-chemical freeze-out as well as the subsequent build-up of finite pion chemical potentials (cf. Sect. 4.4.3) in 30% central Pb + Au (the time evolution is specified by initial/freezeout conditions $(T, \rho_B)_{ini} = (190\text{ MeV}, 2.55 \rho_0)$, $(T, \rho_B)_{fo} = (115\text{ MeV}, 0.33 \rho_0)$ with $N_B^{part} = 260$). The hadronic cocktail part has been taken from the CERES collaboration [256] based on an identical chemical freezeout but with the ρ -meson contribution removed, since the latter is accounted for by the in-medium $\pi\pi$ annihilation at the freeze-out stage of the fireball. Also included in Fig. 4.18 is the result obtained with a dropping ρ mass based on the same fireball evolution. The density and temperature dependence of m_ρ^* has been assumed to resemble QCD sum rule estimates,

$$m_\rho^* = m_\rho (1 - C_{\rho B/\rho_0}) \left(1 - \left(T/T_c^\chi\right)^2\right)^\alpha \quad (4.88)$$

with $C = 0.15$, $T_c^\chi = 200\text{ MeV}$ and $\alpha = 0.3$. Given the experimental uncertainties both the dropping ρ mass and the in-medium broadening give reasonable account for the dilepton enhancement in the 0.3–0.6 GeV region. Substantial differences set in beyond, where the down-shifted ρ mass does no longer contribute, as opposed to the broadening scenario. At the ρ/ω peak, the more recent data seem to favor the former, but between the ω and ϕ , the in-medium spectral function might do better, providing sufficient yield. Once again we see that an improved mass resolution of the measurements, separating ω and ϕ cocktail ingredients more distinctly, is crucial to reach definite conclusions on these issues.

Hydrodynamical calculations employing in-medium rates of category II have been performed recently in Ref. [252]. In particular, the differences between the many-body [47, 102] and the chiral reduction approach [100] and their consequences for dilepton production in central Pb + Au have been explored in some detail. On the level of the bare rates the two approaches agree reasonably well in the pion gas sector, but differ by factors of ∼2 already at finite (nucleon) densities as low as 0.5 ρ_0 , cf. Sect. 4.2.1 and Fig. 4.4². This directly translates into a similar discrepancy in the $\pi\pi$ induced dilepton signal, with the many-body rates resulting in the larger yield (left panel of Fig. 4.19), once more demonstrating that baryons play an important role at full SpS energies of

²One should note that the ρ spectral function on which the calculations in Ref. [252] are based, is not the most recent (more complete) one, although it includes constraints from photoabsorption spectra according to Ref. [102],

158–200 AGeV. These findings are very reminiscent to the naive fireball calculations in central S + Au displayed in Fig. 4.15. Note that the absolute magnitude of the $\pi\pi$ -induced signal in Fig. 4.19 is appreciably smaller than in transport calculations, owing to the vanishing pion chemical potential implicit in the hydrodynamical framework. The final results are therefore not quite able to account for the CERES data in the $M_{ee} \simeq 0.5$ GeV region. At the same time, as a consequence of the rather small thermal ω meson abundance at freezeout, the signal from direct $\omega \rightarrow e^+e^-$ decays amounts to only about 50% of the one in the CERES cocktail; thus, there is no issue of overpredicting the ρ/ω region (right panel of Fig. 4.19).

One of the most attractive features of hydrodynamic simulations is their capability of incorporating phase transitions in the time evolution in a well-defined way via the equation of state. For SpS energies at 158–200 AGeV, however, the general findings are [40, 43, 214] that the dilepton signal from a possibly formed quark-gluon plasma, as estimated by employing perturbative $q\bar{q} \rightarrow ee$ annihilation rates, is down by about an order of magnitude as compared to the $\pi\pi$ channel for invariant masses below 1 GeV (dashed-dotted curve in the left panel of Fig. 4.19). Recalling that the thermal $q\bar{q}$ production rates are not very different from the in-medium hadronic ones (cf. Fig. 4.6 in Sect. 4.2.3), one has to conclude that at SpS energies the space-time volume occupied by the QGP phase is rather small (this might not be the case for the mixed phase).

The CERES collaboration has also analyzed their data with respect to centrality dependence of the invariant mass spectra, i.e., dividing them in four distinct event classes with average charged multiplicities $\langle N_{ch} \rangle = 150, 210, 270$ and 350. Although one finds a clear increase of the enhancement with $\langle N_{ch} \rangle$, especially the low-multiplicity events do not allow for more quantitative statements. No systematic theoretical analyses are available yet.

4.6.4. Medium Effects II: Transverse Momentum Dependencies

An additional observable to help discriminate different mechanisms that lead to a similar enhancement in the invariant mass spectra is the dilepton transverse momentum q_t , i.e., the total momentum of the dilepton pair perpendicular to the beam axis of the colliding nuclei. From a theoretical point of view this possibility is provided by the fact that the specification of a preferred reference frame—that is, the thermal frame, in which the matter as a whole is at rest—breaks Lorentz invariance of

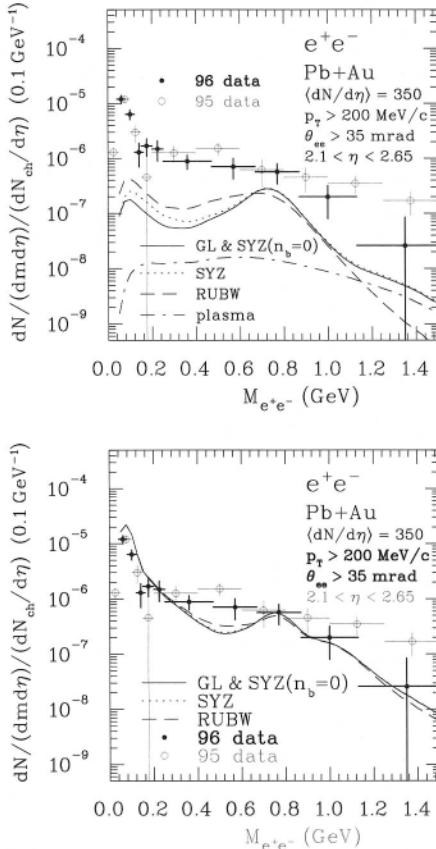


Fig. 4.19. Comparison of the '95 and '96 CERES data from 8% central 158 AGeV Pb + Au with hydrodynamical calculations [252]. Top: dielectron yields from the interaction phase using hadronic rates without baryonic effects [119, 99] (solid line) and including baryonic effects according to the chiral reduction [100] (dotted line) or the many-body framework [102] (long-dashed line), and from the QGP phase using perturbative $q\bar{q}$ annihilation (dashed-dotted line); bottom: final spectra including hadron decays after freezeout (line identification as in left panel).

space-time. It implies that the in-medium propagators of the vector mesons (or, equivalently, their spectral functions) separately depend on energy q_0 and three-momentum modulus $|\vec{q}|$ (or on invariant mass $M = (q_0^2 - \vec{q}^2)^{1/2}$ and three-momentum). Moreover, their polarization states are no longer isotropic, but split up into two completely independent modes, most conveniently described in terms of longitudinal and transverse

components, see Sect. 2.6, Eqs. (2.97), (2.98). A different behavior of the latter might induce anisotropies in the dilepton yield which are, however, extremely difficult to measure. No such attempt has been made to date. On the other hand, transverse momentum spectra in three (four) adjacent invariant mass bins have been extracted by the CERES collaboration in the '95 ('96) lead runs. Since in the CERES experiment the full kinematic information on the individual lepton tracks is recorded, their q_t -spectra are subject to the same statistical and systematic errors as the invariant mass spectra.

In the previous Section we have seen that both the dropping ρ mass and the in-medium spectral function scenarios can reproduce the invariant mass spectra at full CERN-SPS energies reasonably well. Both approaches have also been employed to calculate transverse momentum spectra [49, 103] (Figs. 4.20, 4.21). Naively one would expect that a mere

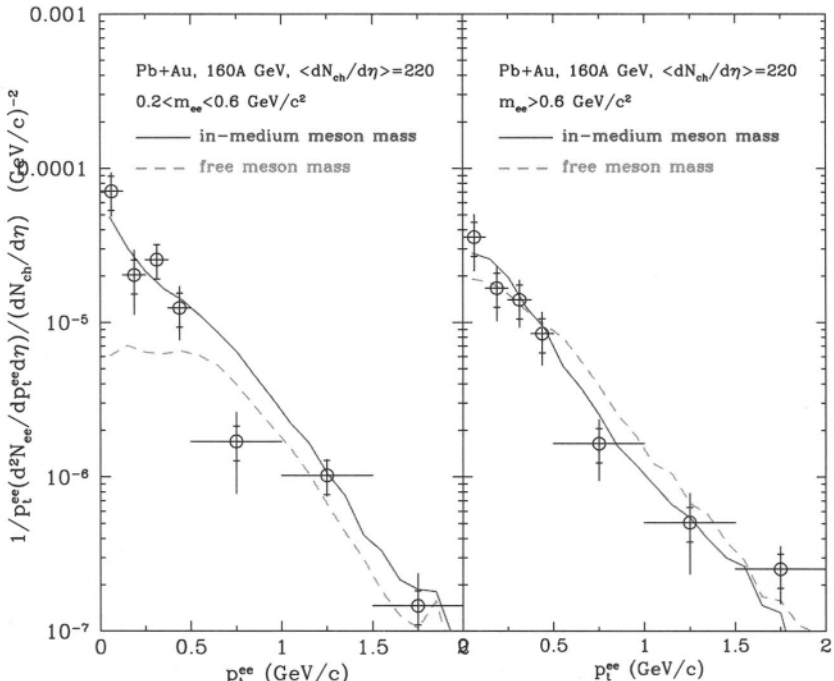


Fig. 4.20. Comparison of the CERES transverse momentum spectra in two invariant mass bins from 30% central 158 AGeV Pb + Au [23] with dropping ρ mass calculations in a transport model [103]. Dashed and full curves: using free and in-medium masses, respectively.

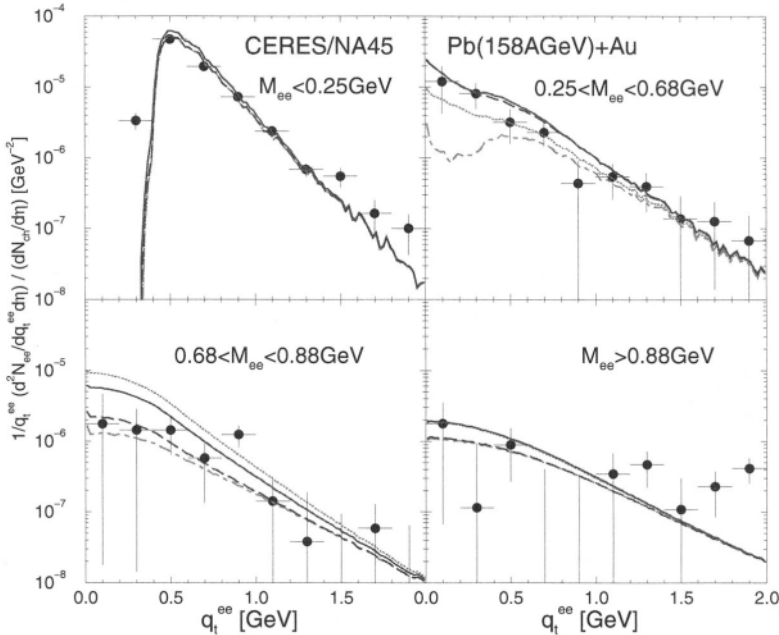


Fig. 4.21. Comparison of the CERES transverse momentum spectra in four invariant mass bins from 30% central 158 AGeV Pb + Au [251] using a thermal fireball model including finite μ_π [50]. Dashed-dotted curves: CERES cocktail; dotted curves: cocktail + free $\pi\pi$ annihilation, dashed curves: cocktail + $\pi\pi$ annihilation with a dropping ρ mass, full curves: cocktail + $\pi\pi$ annihilation using the in-medium ρ spectral function.

reduction of the ρ mass does not entail any distinct traces in the q_t -dependence; this is, however, not true due to a subtle interplay with the thermal occupation factors $f^\rho(q_0)$, which depend on energy. Thus, for a small ρ mass m_ρ^* , the three-momentum dependence of $q_0 = [(m_\rho^*)^2 + \vec{q}^2]^{1/2}$ is more pronounced, leading to a relative enhancement of ρ mesons of small three-momentum. This is nicely reflected by the left panel of Fig. 4.20, where the enhancement of the dropping ρ mass curve in the $0.2 \text{ GeV} < M < 0.6 \text{ GeV}$ invariant mass bin is predominantly concentrated at transverse momenta $q_t \lesssim 0.6 \text{ GeV}$, in good agreement with the '95 CERES data. More complicated three-momentum dependencies may arise in the spectral function approach. This was first pointed out in Ref. [147], where substantial effects with increasing three-momentum were predicted on the basis of a strong ρN P -wave coupling to the $N(1720)$ and $\Delta(1905)$ resonances. The accompanying hadronic vertex form factors,

$$F_{\rho BN}(q) = \Lambda_{\rho BN}^2 / (\Lambda_{\rho BN}^2 + \vec{q}^2), \quad (4.89)$$

which govern the suppression of large three-momenta of the ρ , were used with rather hard cutoff parameters of $\Lambda_{\rho BN} = 1.5$ GeV. However, in a subsequent analysis of photoabsorption spectra [102] it turned out that such values are not compatible with γp and γA data, requiring much softer $\Lambda_{\rho BN} \approx 0.6$ GeV. These constraints have been extracted before any data on dilepton q_T -spectra were available. A spectral function calculation of the latter [50], including these constraints, is shown in Fig. 4.21. Similar to the dropping ρ mass results, its basic features agree with the data.

In another projection of the data, the CERES collaboration generated invariant mass spectra for two distinct regions of transverse pair momentum, i.e., $q_T < 0.5$ GeV and $q_T > 0.5$ GeV [251]. Again, one clearly observes that the major part of the low-mass enhancement is concentrated in the low-momentum bin, whereas the high-momentum bin is essentially consistent with the cocktail (Fig. 4.22). This is just opposite to the rate calculations based on P -wave ρN scattering performed in Ref. [147], which confirms the necessity for rather soft form factors as predicted on the basis of photoabsorption data. The theoretical calculations shown in Fig. 4.22 contrast once more the results of a dropping ρ mass and the in-medium broadened spectral function. At the present status of the data, both explanations are viable.

4.6.5. Time Dependence of In-Medium Signals

The great hope that has been associated with dilepton observables as penetrating probes is to learn about the innermost zones of high-density and high-temperature matter formed in the early stages of nuclear collisions. Thus, after our detailed study of various models in their application to experimental low-mass dilepton spectra we would like to address the question as to what extent signals from the highest excitation phases can be disentangled, i.e., how certain features in the spectra might be related to the time (or temperature/density) of emission. Unfortunately, the answers are beset with strong model dependences, even if the “background” from the hadronic cocktail were accurately known (as we will for simplicity pretend in the following). The dropping ρ mass scenario implies an obvious correlation between invariant mass and emission time for the in-medium signal: using as a rough guideline the fireball evolution for 30% central Pb + Au collisions [50] (cf. Fig. 4.8) together with a temperature- and density-dependent mass given by the QCD sum rule-type relation (4.88), the time instances $t=1, 6$ and 11 fm/c

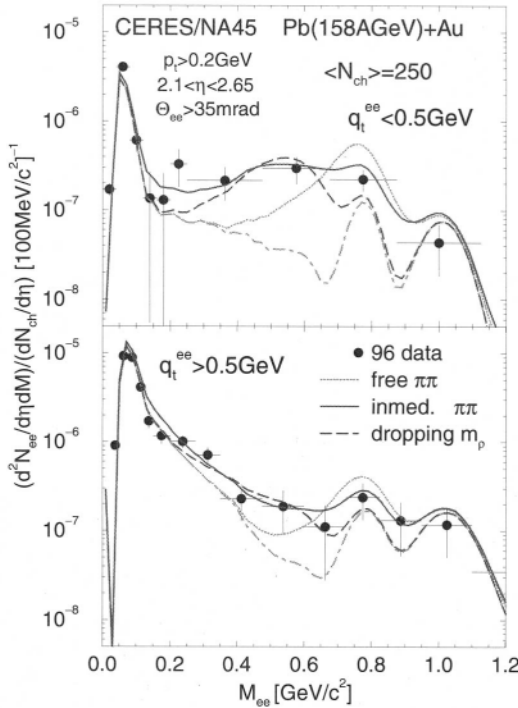


Fig. 4.22. Comparison of 30% central 158 AGeV Pb + Au CERES invariant mass spectra in two transverse momentum bins [251], $q_t < 0.5$ (upper panel) and $q_t > 0.5$ (low panel) with thermal fireball calculations [50] (including finite μ_π) employing a dropping ρ mass (dashed curves) and an in-medium spectral function (full curves); the dashed-dotted curve is the CERES cocktail (without the $\rho \rightarrow e^+e^-$ contribution), added to the respective $\pi\pi$ annihilation yields from the fireball.

correspond to masses $m_\rho^*(t) = 275, 465$ and 650 MeV, respectively, which directly reflect the populated dilepton invariant mass regions. The situation is less straightforward when an in-medium spectral function is employed. The left panel of Fig. 4.23 shows a (partial) decomposition of the total in-medium signal in three equidistant time slabs. Within a few percent the integrated yield from each of the three time intervals is essentially equal which is due to a trade-off between increasing volume and decreasing temperature during the expansion. Although lower masses are preferably populated at earlier stages, the time dependence of the spectral shape is rather smooth especially when comparing to the dropping mass scenario. The most prominent feature associated with

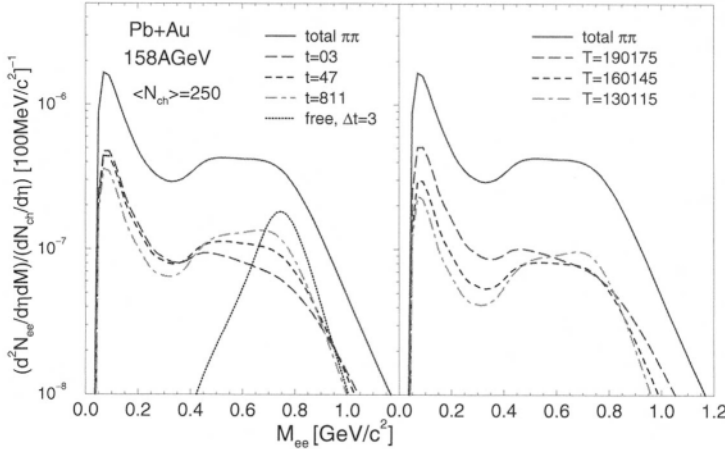


Fig. 4.23. Decomposition of the $\pi\pi \rightarrow ee$ signal employing the in-medium ρ spectral function from Refs. [102, 123, 50] in 30% central Pb + Au (including the acceptance of the CERES detector). The solid line is the total yield from a thermal fireball of lifetime $t_f = 11.5 \text{ fm}/c$. In the left panel, the long-dashed, short-dashed and dashed-dotted curves represent the contributions from the time intervals $t = 0-3 \text{ fm}/c$, $t = 4-7 \text{ fm}/c$ and $t = 8-11 \text{ fm}/c$, respectively, and the dotted curve arises for an emission via free $\pi\pi$ annihilation over a duration of $\Delta t = 3 \text{ fm}/c$ being almost independent on the evolution stage. In the right panel the yields arising during temperature intervals $T = 175-190 \text{ MeV}$ (long-dashed curve), $T = 145-160 \text{ MeV}$ (short-dashed curve) and $T = 115-130 \text{ MeV}$ (dashed-dotted curve) are displayed.

early emission times is a strong depletion of the free ρ peak around $M \approx 0.75 \text{ GeV}$. The total final spectrum (solid line in Fig. 4.23) in fact closely resembles the contribution from intermediate times ($4-7 \text{ fm}/c$, short-dashed curve) multiplied by a factor of 4. This means that the time-integrated in-medium signal actually probes a hadronic resonance gas at an average temperature and density of about $T \approx 150-160 \text{ MeV}$ and $\rho_B \approx \rho_0$, not very far from the expected phase boundary to the quark-gluon plasma. Also note that a typical emission spectrum from free $\pi\pi$ annihilation is quite different from the in-medium pattern even close to freezeout.

At low masses a more pronounced differentiation emerges when one divides the emission contributions into temperature (density) slices, cf. right panel of Fig. 4.23. The strongest fingerprint of a high temperature/density phase seems to be around the free two-pion threshold, $M_{ee} \approx 0.3 \text{ GeV}$. The difference to the time decomposition arises since the system spends somewhat longer time ($3 \text{ fm}/c$) in the high temperature

interval than in the two lower temperature bins (about 2 fm/c). This effect originates from a (slight) softening of the equation of state as borne out of hydrodynamic simulations [213]. It is expected to be much more pronounced in the low-energy (40 AGeV) run at the SpS.

4.6.6. Intermediate-Mass Spectra

In this Section we would like to investigate in how far medium effects that have been invoked to explain the low-mass enhancement are relevant for/consistent with the intermediate-mass regime (IMR). In Sect. 4.2.3 it has already been eluded to the conjecture that in vacuum, starting from invariant masses of about $M_{ee} \approx 1.5 \text{ GeV}$, one enters the “dual” regime, i.e., the thermal dilepton emission rate can be reasonably well accounted for without further medium effects by either

- (i) perturbative $q\bar{q} \rightarrow e^+e^-$ annihilation, based on the observation that the reverse process accounts for the total inclusive cross section for $e^+e^- \rightarrow \text{hadrons}$ within $\sim 30\%$, or
- (ii) binary hadronic collisions, once an appropriate set of meson states is included, being similarly constrained by $e^+e^- \rightarrow \text{hadrons}$ cross sections in the corresponding (exclusive) channels.

Then the following questions have to be asked:

- (1) Are such “dual” rates compatible with experimental spectra?
- (2) How do medium effects, which are crucial at low masses, influence the intermediate-mass region?

For the quark-gluon description it has been argued that medium effects should play a minor role as the small distance annihilation of (nearly) massless quarks and antiquarks inhibits large corrections from the surrounding heat bath. However, this is much less obvious within the hadronic picture since the interacting mesons (such as in the dominant πa_1 channel) carry substantial rest masses which already make up a large fraction of the *cm* energy so that the annihilation reactions involve fairly small momentum transfers.

At the CERN-SpS, intermediate-mass dilepton spectra have been measured by the HELIOS-3 and NA38/NA50 experiments. In analogy to the low-mass case one can divide the spectra into a (physical) background part and an in-medium signal radiated from the interaction phase of the fireball. If one again defines the background as the contributions arising in $p + p$ collisions, the higher masses probed necessitate a somewhat different composition that now mainly stems from hard processes

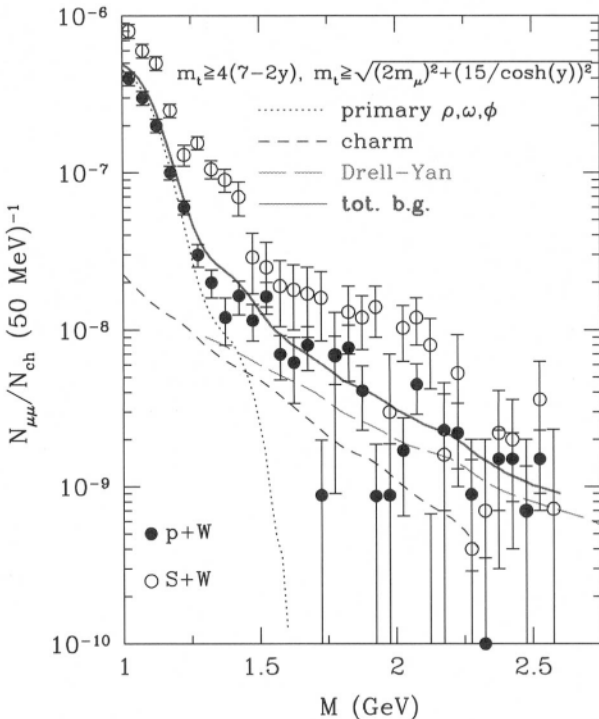


Fig. 4.24. Dimuon invariant mass spectra from the HELIOS-3 collaboration [24] taken in 450 GeV proton-induced and 200 AGeV sulfur-induced reactions on tungsten targets (full and open circles, respectively), compared to the expected background yields from light vector mesons (dotted curve), Drell-Yan processes (long-dashed curve), open charm decays (short-dashed curve) and their sum (solid curve). The plot is taken from Ref. [204].

occurring in the primordial stage of the collision. Most notably these are Drell-Yan annihilation as well as open-charm decays (i.e., an l^+l^- pair originating from the separate decay of an associatedly produced pair of D and \bar{D} mesons) which are negligible in the low-mass region [258], but start to dominate over the final-state meson decays for $M_{ll} \gtrsim 1.5 \text{ GeV}$. Contrary to the final-state meson decays, the initial hard processes are assumed to scale with the number of primary nucleon-nucleon collisions to provide their contribution in $p + A$ and $A + A$ reactions (for the open charm, e.g., this has been verified for $p + A$ collisions in Ref. [258]. Fig. 4.24 shows a comparison of the the HELIOS-3 $\mu^+\mu^-$ data from $p + W$ and $S + W$ collisions with the various background sources [29, 204]. Whereas

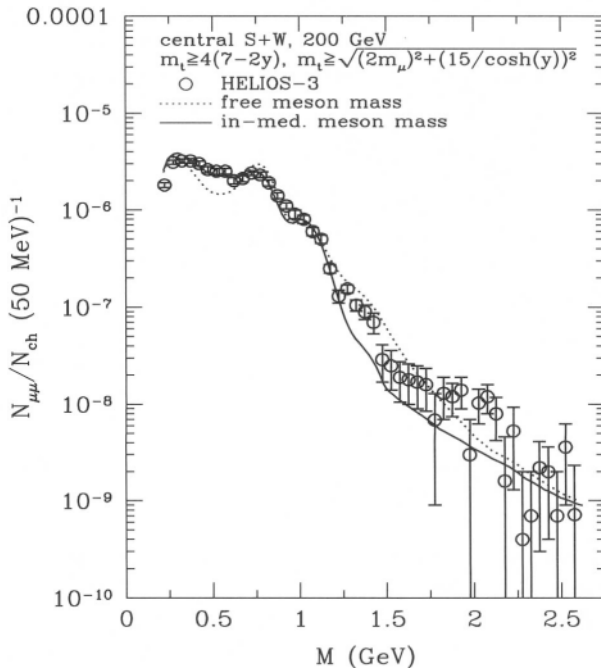


Fig. 4.25. Dimuon invariant mass spectra as measured by the HELIOS-3 collaboration [24] in 200 AGeV S + W reactions, compared to transport calculations using a purely hadronic description for the dilepton radiation from the fireball. Dotted line: employing free hadron masses; Solid line: dropping mass scenario. The plot is taken from Ref. [204].

the total background reproduces the $p + W$ spectra quite satisfactorily, the S + W data are underestimated by a factor of 2–3 throughout the entire mass range from 1–2.5 GeV (equivalent observations have been reported from the NA38/NA50 collaboration [27]).

Li and Gale have performed transport calculations including the radiation from the fireball using the mesonic production rates from binary collisions [204]. They find good agreement with the HELIOS-3 data in the intermediate-mass region if no further medium effects are included (dotted line in Fig. 4.25). In particular, this implies that both perturbative $q\bar{q}$ rates and the lowest-order in temperature mixing effect in the axia-/vector correlator are compatible with the data (as follows from the rate comparison discussed in Sect. 4.2.3). On the other hand, the low-mass end of the spectrum (below ~ 1 GeV) cannot be explained in terms of binary collisions without invoking any further medium

effects. Li and Gale therefore employed the dropping mass scenario extrapolated to include the higher mass (non-strange) vector resonances as well. The data are then nicely reproduced from the two-muon threshold up to about 1.2 GeV, but seem to be underestimated beyond (possibly also between the ω and ϕ mass).

Using the emission rates from the chiral reduction formalism, together with an expanding thermal fireball model [47], Lee *et al.* [205] have obtained similar results to the Li-Gale calculations with free meson masses.

As of now there are no intermediate-mass dilepton calculations available using in-medium many-body spectral functions. Here the question is whether a strong broadening of, e.g., the ρ resonance could lead to an over-estimation of the data in the 1–1.5 GeV mass region. However, from a theoretical point of view, if the broadening scenario indeed approaches chiral restoration by merging into the perturbative plateau-value for the vector and axialvector correlators (as we have argued in Sects. 2.6, 4.2.3), the HELIOS-3 data will be reproduced, see the above remarks. Also note that the in-medium **ρ -meson** spectral function as used for the low-mass region actually exhibits only a rather moderate enhancement (factor of ~ 2) over the vacuum one for invariant masses somewhat above the free ρ peak (Fig. 3.19). Above 1 GeV further contributions need to be included for a more complete description of the vector correlator, such as $\pi a_1 \rightarrow \rho'$ selfenergies corresponding to four-pion like processes. This will closely resemble the kinetic theory treatment in terms of the various binary scattering processes, as performed in Ref. [204]. Since coherence effects in the many-body treatment are expected to be small especially towards higher energies (already in the low-mass region they were found to be quite moderate), there should be little discrepancies to the (incoherent) kinetic approach, even on a quantitative level. Beyond $M = 1.5$ GeV the “dual” (hadronic or partonic) production rates are characterized by an essentially flat spectral shape. Here the main issue therefore is whether the space-time description used for the calculations in the low-mass region will lead to a total yield that reproduces the experimentally observed enhancement. Another possible source of this excess has been pointed out by the NA50 collaboration: they showed [27] that the excess can be accounted for by introducing an anomalously increased production of open charm mesons by a factor of ~ 3 . However, there are no theoretical indications for a suitable mechanism of this kind (the final answer will be provided by a direct measurement of produced D mesons at the CERN-SPS). Lin and Wang [259]

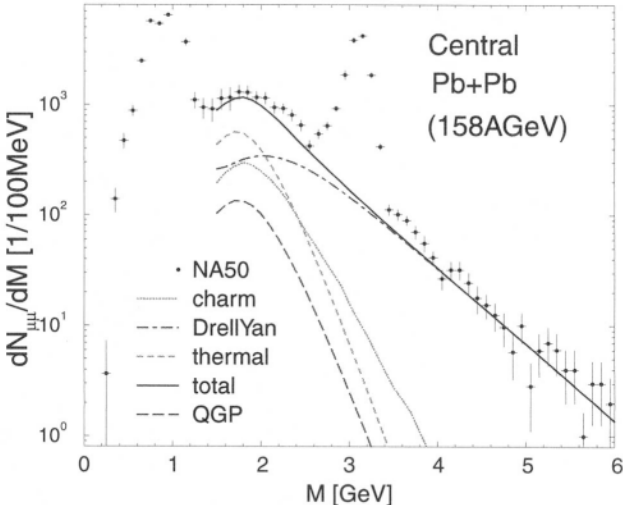


Fig. 4.26. Dimuon invariant mass spectra measured by NA50 [27] in central Pb + Pb (158 AGeV) compared to open charm contributions as inferred from p -A collisions [27] (dotted line), Drell-Yan annihilation (dashed-dotted line), thermal radiation from an expanding fireball (short-dashed line) and their sum (solid line); the long-dashed line is the part of the thermal component that is radiated from the QGP phase. J/Ψ and Ψ' decay contributions have not been included. The plot is taken from Ref. [260].

have addressed the possibility of D meson rescattering to enrich the dilepton yield in the NA50 acceptance; however, this does not constitute more than a 20% effect. On the other hand, in the recent analysis of Ref. [244] it has been shown that the use of the dual lowest-order $q\bar{q}$ annihilation rate throughout the entire mass range from 0–3 GeV folded over a schematic fireball evolution [47] leads to very similar yields in the IMR as obtained with a factor of 3 open charm enhancement; at the same time the (low-mass) CERES data are approximately accounted for (see also dashed curve in Fig. 4.30). Similar conclusions are reached in Ref. [260], cf. Fig. 4.26: the NA50 enhancement between 1.5 and 3 GeV can be explained with the dual $q\bar{q}$ rate employing the same fireball model [50] (being consistent with hadro-chemical analysis of CERN-SPS data including finite pion chemical potentials towards thermal freezeout) that leads to a satisfactory description of the CERES data once medium effects in the ρ spectral function are incorporated.

4.7. Direct Photon Spectra

As we have stressed in Sect. 4.3, real photons and dileptons can be considered as two kinematical realizations of otherwise identical electromagnetic production mechanisms. For heavy-ion reactions it follows that any model which claims success in describing the observed dilepton spectra must also be consistent with direct photon spectra. The notion “direct” has been introduced to refer to only those photons which are originating from the interaction phase of the fireball, i.e., unlike the dilepton case, the contributions from hadron decays after freezeout are considered as a background that ought to be subtracted to obtain the final spectra. This, in fact, represents the main experimental difficulty, since around 90% or more of the photons produced in heavy-ion collisions at full SpS energies stem from the $\pi^0 \rightarrow \gamma\gamma$ and $\eta \rightarrow \gamma\gamma$ decays. As a consequence direct photon observables are about two orders of magnitude less sensitive to any in-medium signals than dileptons [261]. Also note that the observed single-photon energies pick up the laboratory three-momentum of the decaying hadron and hence are not restricted by the hadron rest mass—as opposed to the invariant masses of dileptons from the Dalitz decays, where $M_{ll} \leq m_\pi$, etc. The major systematic error then arises from the uncertainty in the π^0 and η abundances. The contributions from other mesons are usually estimated from the so-called “ m_T scaling”, i.e., a $\sim \exp(-\beta m_T)$ dependence of the transverse mass spectra with a universal slope parameter β . Photon measurements at the CERN-SpS have been performed by the HELIOS-2 [262], CERES [263] and WA80/WA98 [264, 265] collaborations. In central S + Au, WA80 found a photon excess of $5\% \pm 5.8\%$ (syst) $\pm 0.8\%$ (stat) consistent with CERES and HELIOS-2 results which carry somewhat larger errors. From these measurements they extracted an upper limit for direct photons at the 90% confidence level (see below), which has been used to test theoretical models. More recently, a preliminary direct photon spectrum for central Pb + Pb has been published [265].

In hydrodynamical simulations [266, 267], it has been claimed that the upper limits set by WA80 are not compatible with purely hadronic scenarios. However, these conclusions have been drawn using a very limited number of degrees of freedom in the hadronic gas phase (π , η , ω , ρ). For equal initial energy densities this leads to much larger initial temperatures in the hadronic phase than in a quark-gluon plasma, entailing much higher photon yields. Purely hadronic models with lower initial temperatures cannot be ruled out by this reasoning. In fact, the thermal production rates of photons from a QGP are presumably not very

different from those of a hadron gas at the same temperature, as has been first noted in Ref. [206]. Hence, similar to what has been found for dileptons, one should expect that at CERN-SPS energies the rather small space-time volumes occupied by a possibly formed QGP do not generate substantial photon signals as compared to the hadronic phase. This has been explicitly demonstrated in the hydrodynamic calculations of Refs. [266, 214]. Thus one is led to focus on the multiple possibilities for hadronic photon production (Sect. 4.3).

Fig. 4.27 shows the photon transverse momentum spectra from various sources in central S + Au collisions at 200 AGeV, evaluated in the transport framework [268]. A kinematical cut in pseudorapidity of $2.1 < \eta < 2.9$ is applied to comply with the WA80 experiment. For transverse momenta $q_t \geq 0.5$ GeV the dominant processes are radiative ω and a_1 decays, the latter significantly exceeding the nonresonant $\pi\rho \rightarrow \pi\gamma$ reactions. Note that the baryonic decays seem to have little relevance here. Fig. 4.28 shows that the incoherent sum of all contributions (short-dashed curve) respects the experimental upper limits of WA80. Furthermore,

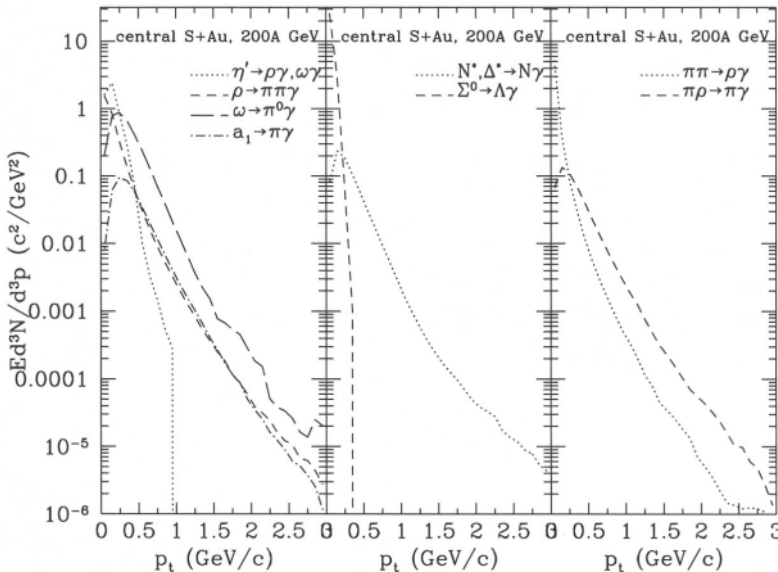


Fig. 4.27. Thermal single-photon spectra from meson decays (left panel), baryon decays (middle panel) and two-body reactions (right panel) in transport calculations for central 200 AGeV S + Au collisions [268].

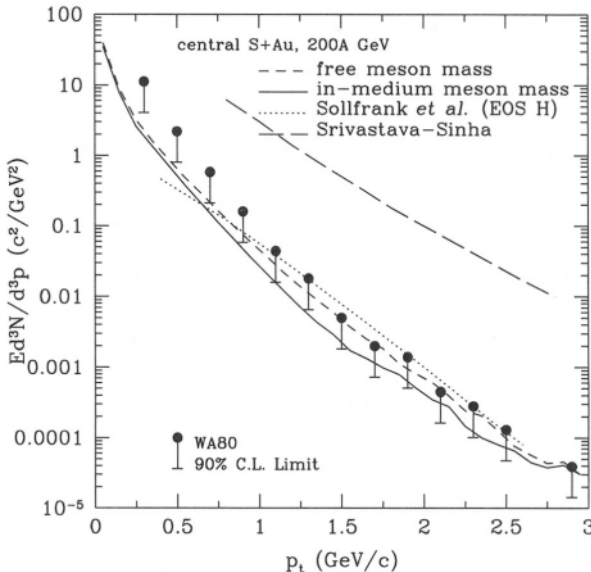


Fig. 4.28. Total direct photon spectra in central 200 AGeV S + An collisions compared to the upper limits of the WA80 collaboration [264]. Full and short-dashed curves: transport calculations of Ref. [268] with and without dropping masses, respectively; long-dashed curve: Bjorken-type hydro-calculations with a purely hadronic equation of state including π , η , ρ and ω mesons only [266]; dotted curve: 2 + 1 dimensional hydro-calculations employing a purely hadronic equation of state with a larger set of mesons as well as baryons [214]; both hydro-approaches have used the photon production rates of Ref. [206]. The compilation is taken from Ref. [268].

applying the dropping-mass scenario within the same transport approach does not induce major changes in the final spectrum (full curve in Fig. 4.28), which can be traced back to compensating mechanisms: for the radiative decays of the vector mesons ρ , ω and a_1 , their increased abundance (due to the smaller masses) is balanced by a reduced phase space for the decay products (see also Ref. [269], where similar observations have been made at the relevant temperatures of about $T \simeq 160$ MeV). Analogous features have been found for other variants of the dropping ρ -meson mass scenario when implemented in the Hidden Local Symmetry approach for π - ρ - a_1 dynamics [270]. Also shown in Fig. 4.28 are the hydrodynamical results of Ref. [266] (long-dashed curve) which, as mentioned above, strongly overshoot the WA80 bounds due to a high initial temperature in a purely hadronic description with rather few

degrees of freedom. On the other hand, using a larger set of hadronic states (including the lowest-lying pseudoscalar and vector meson nonet as well as baryon octet and decuplet), the hydrodynamical calculations of Ref. [214] are essentially compatible with the data and also not very different from the transport calculations.

Concerning the role of baryons, both the chiral reduction formalism [100] and the ρ -meson spectral function approach [47, 102, 49, 123] have reached conclusions which are at some variance with the relative assignments of the incoherent decomposition given in Fig. 4.27. Using the simple thermal fireball expansion for central S + Au collisions (where the baryon-density evolution is taken from the transport simulations) yields the photon q -spectra displayed in Fig. 4.29; for each of the two approaches, they are based on exactly the same ingredients as the corresponding dilepton spectra of Fig. 4.15. In the chiral reduction formalism the baryonic contributions are exclusively associated with the finite nucleon density in the fireball. According to the decomposition inferred from photoabsorption data (Fig. 4.1) the effects can be attributed to the $\Delta(1232)$ for $q \leq 0.4$ GeV and to the πN “background” above. In the photon production spectra for central S + Au reactions they induce an enhancement over the mesonic contributions by a sizable factor (left panel of Fig. 4.29). Very similar results follow from the ρ -meson spectral function approach, which also reproduces well the nuclear photoabsorption spectra, albeit with a somewhat different decomposition, i.e., a smaller πN “background” together with much larger contributions from direct ρN resonances. This difference is not relevant for the direct photon spectra. On the other hand, recalling the comparison to the CERES dilepton spectra in central S + Au, it has been found that the ρ -meson spectral function approach *does* lead to a larger low-mass enhancement. This can be readily gleaned from the rate comparison exhibited in Fig. 4.4: compared to the Steele *et al.*-rates, the Rapp *et al.*-rates are by a factor 2–3 larger around $M = 0.5$ GeV (but agree with the former towards the photon point).

4.8. Theoretical Implications

After the preceding rather detailed discussion of the various efforts made in exploring low-mass dilepton spectra in (ultra-) relativistic heavy-ion collisions (with additional impact from photon and intermediate-mass dilepton spectra), we have to face the question in which respects it has advanced our understanding of strongly interacting hot and dense matter. For that purpose let us try to critically review

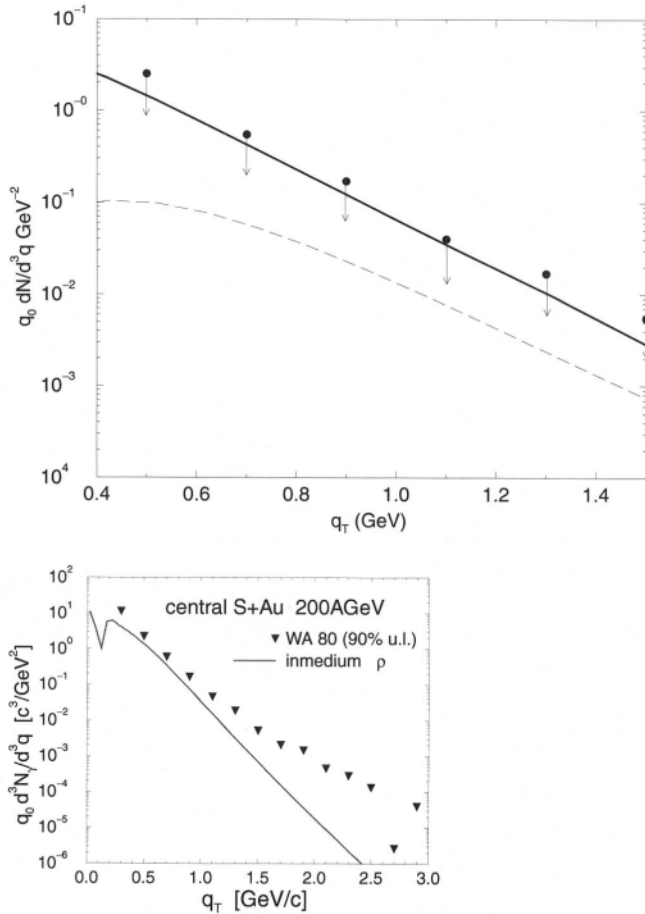


Fig. 4.29. Direct photon spectra, compared to WA80 upper limits [264], in central 200 AGeV S + Au collisions using a simple fireball evolution with thermal rates from the chiral reduction formalism [100] (top; solid and dashed curve are obtained with and without the baryonic contributions respectively) and the in-medium ρ spectral functral function [47, 102, 49, 123] (bottom).

and compare the successes and failures as well as the interrelations of the different theoretical attempts that have been pursued to describe the various experiments.

Clearly, the BR scaling conjecture has been very successful in its application to low-mass dilepton data at CERN-SPS energies of 158–200 AGeV. In its original form it predicts a very specific realization of chiral symmetry restoration, namely that all masses of the light (non-Goldstone) hadrons merge to zero. Most of the underlying arguments in its favor rely on mean-field type approximations, related to the decrease of the chiral quark condensate (via constituent quark masses) or to the presence of strong scalar fields in hot/dense hadronic matter. More recently connections have been drawn to link a reduction in the ρ and ω masses in nuclear matter to strong collective excitations in ρ - N and ω - N interactions, most notably through $N(1520)N^{-1}$ states. The ramifications of this identification are still under debate.

On the other hand, the consequences of a strong in-medium broadening of the ρ -meson spectral function, as predicted on the basis of phenomenologically well-established hadronic interactions combined with standard many-body techniques, also seem to reproduce the SPS low-mass dilepton data fairly well. If this scenario holds true close to the phase transition, it implies that the chiral partner of the ρ , the $a_1(1260)$, becomes as broad and structureless: chiral symmetry restoration manifests itself through a merging of both vector and axialvector correlators into a flat continuum (such a behavior has been conjectured to signal deconfinement in Ref. [117]). If, in addition, the height of the continuum corresponds to the perturbative $q\bar{q}$ plateau value characterized by the famous cross section ratio $R = \sigma(e^+e^- \rightarrow \text{hadrons})/\sigma(e^+e^- \rightarrow \mu^+\mu^-) = 5/3$ ($= 2$, when including strange quarks), nonperturbative effects would be marked as no longer relevant which, after all, constitutes the very essence of the quark-gluon plasma. This provokes the following theoretical exercise: we simply replace the in-medium hadronic rates in the expanding fireball model (4.86) by the perturbative $q\bar{q}$ annihilation rates, (4.40), using the same time evolution of temperature and density. The result shown in Fig. 4.30 indicates that the global use of the pQCD rate looks quite reasonable but cannot fully account for the low-mass enhancement observed in the CERES data (unless one invokes non-perturbative effects, see, e.g., Ref. [182]). More importantly, one should note that, whereas the hadronic medium effects are more sensitive to finite baryon densities, the lowest-order $q\bar{q}$ -rates exhibit a negligible dependence on a finite quark chemical potential. This obvious “duality-mismatch” clearly deserves further studies.

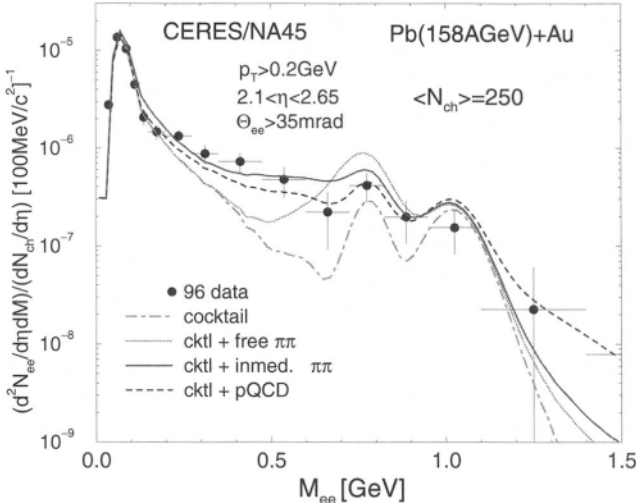


Fig. 4.30. CERES dilepton spectra in 30% central Pb + Au collisions [251] compared to a thermal fireball calculation using lowest order $q\bar{q} \rightarrow ee$ annihilation rates only (dashed line); also shown is the full in-medium ρ spectral function calculation (solid line). Both fireball yields are supplemented with the CERES cocktail.

Nevertheless, let us return to the hadronic approaches and first address the question what the discriminating features for different fates of the ρ meson could be, i.e., “dropping mass” versus “melting resonance”. Both lead to enhanced dilepton yields below the free ρ mass, but behave very differently above. Whereas the in-medium broadening implies an *enhancement* over free $\pi\pi$ annihilation between, say, the ω and the ϕ mass, the dropping mass scenario predicts a *depletion* (the possible impact from higher states, such as the $\rho'(1450)$, entering this region should be small, since (a) it is not obvious that a large fraction of their mass is due to chiral symmetry breaking, and (b) they have little significance in the pion electromagnetic form factor). As stressed above, an improved mass resolution of the currently available dilepton measurements, together with sufficient statistics, should be able to settle this issue. The mass region just above the ρ/ω resonances is also supposed to be accessible by the PHENIX experiment at RHIC, although plagued by a tremendous combinatorial background which may limit any sensitivity to resonance structures with sufficiently narrow widths. Also, both the broadening and the dropping mass are predominantly driven by finite baryon density effects, which are presumably small at RHIC. In this

respect the upcoming low-energy run at 40 AGeV at the CERN-SPS will be ideally suited, probing even lower temperatures and higher baryon densities than with the 158 AGeV beams.

The lack of “dramatic” effects in the ρ properties in a thermal gas of mesons, as found by many authors [120, 47, 121, 122, 123], seems, however, somewhat puzzling. Phenomenologically this can be traced back to the weaker meson-meson interactions (especially with “Goldstone-protected” pions), as compared to the meson-nucleon case. Thus, when carrying the calculations to higher densities it seems plausible that the ρ and the a_1 could “degenerate through broadening”. On the other hand, even at temperatures as high as $T = 200 \text{ MeV}$, quite moderate in-medium corrections to the ρ width have been deduced, reaching at most $\Gamma_{\text{med}} \simeq 200 \text{ MeV}$. Since this leaves a well-defined resonance structure, it appears unclear how the ρ and a_1 spectral distributions merge at this point. These features might either point at some shortcomings in the phenomenological approaches or indicate that the lowest-order in temperature vector-axialvector mixing is the prevailing effect in pure *meson* matter. Also note that in most model calculations the chiral condensate exhibits a strong, linear decrease with nuclear density (leading to an appreciable reduction already at normal nuclear density), whereas its temperature dependence is much less pronounced until close to the critical temperature T_c^{χ} . Again, dilepton measurements at RHIC will hopefully shed more light on the behavior of ρ , ω and ϕ mesons in a high-temperature and low-baryon-density environment.

Next, we compare the hadronic many-body calculations to the chiral reduction formalism put forward in its application to electromagnetic emission rates in Refs. [99, 100]. As far as low-mass dilepton production at the CERN-SPS is concerned, the latter seems to give a factor of 2–3 less enhancement in the relevant region around $M_{\eta} \simeq 0.4 \text{ GeV}$ than the results obtained with in-medium ρ spectral functions [47, 102, 49, 123, 50], see Figs. 4.15, 4.19. Although both approaches have been constrained by photoabsorption spectra on nucleons and nuclei the differences in the dilepton excess do mainly emerge from finite density effects. This is *not* due to a deviation at large densities (i.e., through collective effects), but due to a different assignment of “background” and resonance contributions in the photoabsorption data. When moving into the time-like dilepton regime (at small three-momentum), the resonance contributions (which are larger in the spectral function approach, most importantly the $N(1520)$) are relatively much more enhanced than the structureless background (which is larger in the chiral reduction approach), being essentially a kinematic effect. This is further supported

by the fact that in both approaches the direct photon spectra actually agree quite well when integrated over the temperature and density history of central S + Au collisions. Thus a careful separation of background and resonance contributions in the experimental photoabsorption data should provide the key for a more quantitative discrimination of the effects in the time-like regime.

From a theoretical point of view, the most distinctive feature between the many-body and the chiral reduction treatment lies in the fate of the ρ resonance peak: in the master formula framework in-medium corrections are obtained through additive terms in a temperature and density expansion, which have almost no impact on the free ρ peak, whereas the resummation of large imaginary parts in the many-body treatment of the ρ propagator induces a marked depletion. Model-independent results for the in-medium vector and axialvector correlators indeed require that, due to their mixing, strength should be removed from both the ρ and the a_1 poles, at least to lowest order in temperature and in the chiral limit [88] (cf. Sect. 2.6). The phenomenological many-body calculations seem to comply with this feature, although their theoretical relation to chiral symmetry is not always obvious.

In finite-temperature calculations based on chiral $\pi\rho a_1$ Lagrangians the mixing theorem has been shown to be satisfied [110], being mainly realized through a reduction of the $\gamma\rho$ vector dominance coupling $g_{\rho\gamma}(T)$ due to a finite-temperature pion tadpole loop. However, corresponding results for dilepton production rates cannot account for the low-mass enhancement observed at the CERN-SPS [36]. One may raise the question whether phenomenological calculations at finite temperature *and* density are still compatible with the data when including a suppression of the VDM coupling. Since $[g_{\rho\gamma}(T)/g_{\rho\gamma}(0)]^2$ decreases to only about 80% at the relevant temperatures of $T \approx 150\text{ MeV}$ (using the physical pion mass rather than the chiral limit), the answer is that it will only mildly affect the many-body results (in fact, a more complete calculation should also include a (moderate) finite-temperature softening of the single-pion dispersion relation, which re-generates a small enhancement below the free ρ mass).

Another, more practical, issue concerns the role of a finite pion chemical potential in the evolution of (ultra-) relativistic heavy-ion collisions. Although it should have only moderate influence on the *shape* of the dilepton spectra, it certainly has a severe impact on the *total yield* of dilepton pairs originating from $\pi\pi$ annihilation in the interacting fireball (being proportional to the square of the pion density). Both microscopic transport and hydrodynamical calculations correctly reproduce the total

number of pions at freezeout, but the former seem to imply a finite μ_π (not present in current hydrodynamical analyses), resulting in a larger dilepton signal by a factor of 2–3. The introduction of a $\mu_\pi > 0$ in a thermal fireball calculation has been shown to essentially resolve this discrepancy [50]. This needs to be confirmed in a full hydrodynamic treatment.

Finally we repeat that there is currently no theoretical explanation available for the strong enhancement in the low-mass dilepton spectra measured by the DLS collaboration [34] in heavy-ion collisions at relativistic projectile energies (1–2 AGeV). Both the dropping-mass scenario [233] and the broadening of the in-medium ρ spectral function [237] fall short of the data by a factor of 2–3 at invariant masses around 0.4 GeV. Hopes to resolve this puzzle reside on the upcoming precision measurements to be performed with the HADES detector at SIS (GSI) at similar bombarding energies.

5. CONCLUSIONS

The investigation of hadron properties in a hot and dense environment as produced in energetic collisions of heavy nuclei represents one of the main frontiers in modern nuclear physics. In particular, it is directly related to the approach towards the QCD phase transition, which constitutes the “Holy Grail” of the ultrarelativistic heavy-ion initiative. In the present article we have tried to review a very active subfield of this research program, namely the major theoretical accomplishments that have been achieved in connection with low-mass dilepton production over the past five years or so. Of course, the strong interest in this rapidly developing field is largely fueled by the exciting data that our experimental colleagues have obtained despite the notorious difficulties in extracting these observables.

The nature of dilepton final states mediated by electromagnetic currents immediately attaches to the vector mesons as the key objects for gaining direct non-trivial information on in-medium effects. In the low-mass region which we have focused on, these are the ρ , ω and ϕ mesons, with the ρ meson playing the dominant role since it has the shortest lifetime and the largest dilepton decay width. The now widely accepted viewpoint is that the main nonperturbative feature of low-energy strong interactions—the spontaneous breakdown of the global chiral symmetry in the fundamental QCD Lagrangian—is not only responsible for the build-up of the “constituent” quark masses but

governs the appearance of the low-energy hadron spectrum altogether. Hence the approach to chiral restoration in hot/dense matter is intimately related to changing in-medium properties of light hadrons. Here the only strict prediction from QCD is that the spectral distributions of “chiral partners” have to become identical (or “degenerate”). This is encoded in “Weinberg sum rules” which (in the chiral limit) relate the energy-integrated difference of the vector and axialvector correlators to the weak pion-decay constant, f_π , one of the order parameters for chiral symmetry restoration. Medium effects of the ρ meson therefore necessarily have to be put into context with those of its chiral partner, the a_1 meson, as well as the pion. How the “degeneration” is realized in nature is far from obvious and marks the central question to be answered in our context. For the ω meson the problem is further complicated by the fact that it couples to three-pion (**or** $\pi\text{-}\rho$) states through the Wess-Zumino term and hence the anomaly structure of QCD. Also the assessment of in-medium properties of the ϕ meson is hampered by the fact that the current mass of the s -quark is quite large so that arguments based on the chiral limit are not as stringent as in the $u\text{-}d$ sector.

Based on general properties of QCD we have started our discussion with a focus on model-independent approaches. To lowest order in temperature (and in the chiral limit), soft pion theorems imply the leading temperature effect to be a mere mixing between vector and axialvector correlators with no medium effects in the correlators themselves. QCD sum rules relate physical vacuum correlators to the various condensates thus providing a direct link between physically observed hadrons and the underlying QCD vacuum structure. It has now become clear that, when applied within a hadronic medium, they have limited predictive power for in-medium spectral distributions since they only provide a band of allowed combinations of large/small masses with corresponding large/small widths of the light vector mesons.

More specific predictions can be obtained from hadronic model Lagrangians which have been applied at various levels of approximations. Mean-field treatments typically focus on the in-medium behavior of the masses, and here results from chiral Lagrangians including vector mesons as gauge bosons (when applied at finite temperature) seem to allow for both an increasing **ρ -meson** mass—becoming degenerate with the a_1 —as well as a decreasing mass as conjectured in the famous Brown-Rho paper based on scale invariance arguments. On the other hand, several independent many-body calculations of in-medium vector meson spectral functions come to the consensus that multiple interactions in hadronic matter inevitably induce a broadening of the spectral distribu-

tions. Nevertheless, certain S -wave scattering processes—most importantly resonant $\rho N \rightarrow N(1520)$ excitations—can be associated with a reduction of the ρ/ω mass. Towards higher densities, however, the widths of the spectral functions (most prominently for the ρ meson) increase to such an extent that the entire resonance structures are “melted” into an essentially structureless continuum. At the same time the real parts in the propagators also become very flat so that the concept of a single mass ceases to be meaningful.

We have argued that a scenario of melting resonances has in fact the very appealing feature to establish a continuous link (“duality”) between hadron- and quark-gluon-based calculations of the vector correlator, in the following sense: in vacuum the “duality-threshold”, i.e., the invariant mass where the total cross section $\sigma(e^+e^- \rightarrow \text{hadrons})$ empirically starts to follow the perturbative QCD prediction for $q\bar{q}$ production is located at about $M \approx 1.5 \text{ GeV}$. Resonance formation at lower invariant masses is an inherently nonperturbative effect associated with spontaneous chiral symmetry breaking which is a “large distance phenomenon”. It should not play any role at the small space-time distances probed beyond 15 GeV. Consequently, above this mass also the axialvector correlator, being identical to the vector one, ought to be given by perturbative QCD (which is unfortunately not well-established experimentally). Medium modifications can be studied through dilepton production, the reverse process of e^+e^- annihilation. We have pointed out that the finite-temperature mixing of vector and axialvector channels, which to lowest order arises from the coupling to pions of the heat bath, suffices to equalize the hadronic and quark-antiquark description down to the ϕ meson mass when extrapolated to temperatures where chiral symmetry is restored. This feature is corroborated by model-independent approaches, such as the chiral reduction formalism, as well as detailed model calculations in the region above the ϕ meson peak. It can thus be stated that “duality” of hadronic and quark descriptions for the in-medium rates down to 1 GeV is well established for the case of vanishing baryon density and is likely to also hold for the latter case. The appealing physical interpretation is that, as electromagnetic probes couple to charges, in the vicinity of the phase boundary it becomes immaterial whether they reside in free quarks or in a large number of strongly interacting hadrons.

The continuation of the “duality” argument to even lower invariant masses is not rigorously established at present, although suggestive indications have emerged. It is clear that the lowest-order mixing does not affect dynamically generated (low-mass) resonance structures in the

correlators. This is precisely where the many-body effects enter through a flattening of the resonance peaks, which now requires arbitrary orders in density introduced through resummations. Hadronic model calculations near the phase boundary show that the resulting dilepton rates in the ρ region and somewhat below continue to match rather well the perturbative quark-antiquark rates. Deviations set in for $M \leq 0.5 \text{ GeV}$. At such low invariant masses it is, however, conceivable that “soft” processes could significantly alter the quark rates. From a more practical point of view, the melting of especially the ρ resonance directly entails an enhanced dilepton production *below* the free mass which has turned out to be compatible with current data from the SpS. At the same time, to verify the associated depletion of the in-medium signal in the free ρ/ω mass region of the spectra, it will be crucial to discriminate free ω decays, occurring after freezeout, which is anticipated to be feasible with improved mass resolution measurements at the CERN-SpS. Clearly, this applies equally to *both* the commissioned low-energy run at 40 AGeV and additional future ones at the full SpS energy.

There remain a number of further problems which have to be resolved. First, it will be important to establish a more profound theoretical connection between the processes that reshape the vector (ρ) and axialvector (a_1) spectral distributions. In particular one has to find reliable ways to perform a similarly advanced calculation for the in-medium properties of the a_1 as has been achieved for the ρ . Also, since (at comparable densities) the medium effects from baryonic matter seem to be more pronounced than at finite temperature, the fate of the (light) vector mesons in purely mesonic matter near the phase boundary is not really settled. Here, the upcoming collider experiments at RHIC and LHC, where the meson-to-baryon ratios at midrapidity are expected to increase by another substantial factor ($\sim 5\text{--}10$ at RHIC) as compared to current SpS conditions, will provide answers.

ACKNOWLEDGMENTS

Many of our experimental and theoretical colleagues have integrally contributed to the progress reported in this article. We especially thank our collaborators G. E. Brown, M. Buballa, M. Urban, G. Chanfray, W. Cassing, E. L. Bratkovskaya and C. Gale for the fruitful joined efforts. We are also grateful for many productive conversations with P. Braun-Munzinger, A. Drees, J. W. Durso, M. Ericson, J. Friese, B. Friman, F. Karsch, F. Klingl, C. M. Ko, V. Koch, G. Q. Li, C. Lourenço, V. Metag,

U. Mosel, W. Nörenberg, M. Prakash, K. Redlich, M. Rho, A. Richter, P. Schuck, E. V. Shuryak, H. Sorge, H. J. Specht, J. Stachel, I. Tserruya, W. Weise, A. Wirzba and I. Zahed. We furthermore thank G. E. Brown, W. Cassing, C. Lourenço and B. J. Schaefer for useful comments and a careful reading of the manuscript. We apologize to our colleagues whose work we did not appropriately discuss. One of us (RR) acknowledges support from the Alexander-von-Humboldt foundation through a 3-year Feodor-Lynen fellowship at Stony Brook during which most of his work on the presented topics has been performed. This work is supported in part by the National Science Foundation under Grant No. NSF PHY98-00978, the U.S. Department of Energy under Grant No. DE-FG02-88ER40388, the BMBF and GSI Darmstadt.

REFERENCES

1. See, for example, the proceedings of the recent International Conferences on Ultra-relativistic Nucleus-Nucleus Collisions:
 Quark Matter '95, Nucl. Phys. **A590** (1995);
 Quark Matter '96, Nucl. Phys. **A610** (1996);
 Quark Matter '97, Nucl. Phys. **A638** (1998);
 Quark Matter '99, Nucl. Phys. **A661** (1999).
2. C.-Y. Wong, *Introduction to High-Energy Heavy-Ion Collisions*, World Scientific, Singapore 1994.
3. P. Braun-Munzinger and J. Stachel, Nucl. Phys. **A638** (1998) 3c.
4. J. Stachel, Proc. of the International Nuclear Physics Conference, Paris, Aug. 1998, Nucl. Phys. **A654** (1999) 119.
5. P. Braun-Munzinger, J. Stachel, J. Wessels and N. Xu, Phys. Lett. **B365** (1996) 1.
6. W. Cassing and E. L. Bratkovskaya, Phys. Rep. **308** (1999) 65.
7. C. M. Ko, V. Koch and G. Q. Li, Annu. Rev. Nucl. Part. Sci. **47** (1997) 505.
8. E. L. Feinberg, Nuovo Cim. **A34** (1976) 391.
9. E. V. Shuryak, Phys. Lett. **B78** (1978) 150.
10. E. V. Shuryak, Phys. Rep. **61** (1980) 71.
11. K. Kajantie, J. Kapusta, L. McLerran and A. Mekjian, Phys. Rev. **D34** (1986) 2746.
12. I. Tserruya, Nucl. Phys. **A590** (1995) 127c.
13. R. Rueckel, Phys. Lett. **B64** (1976) 39.
14. J. Jalilian-Marian and V. Koch, Phys. Rev. **C58** (1998) 3763.
15. K. Geiger, Phys. Rep. **258** (1995) 237.
16. A. Drees, private communication.
17. T. Matsui and H. Satz, Phys. Lett. **B178** (1986) 416.
18. See, e.g.,
 R. Vogt, Phys. Rep. **310** (1999) 197;
 D. Kharzeev, Nucl. Phys. **A638** (1998) 279c;
 C. Y. Wong, Nucl. Phys. **A610** (1996) 434c.
19. L. McLerran and T. Toimela, Phys. Rev. **D31** (1985) 545.

20. G. Agakichiev *et al.*, CERES collaboration, Phys. Rev. Lett. **75** (1995) 1272;
P. Wurm for the CERES collaboration, Nucl. Phys. **A590** (1995) 103c;
A. Drees and T. Ullrich, CERES Memorandum (1995), unpublished.
21. Th. Ullrich for the CERES/NA45 collaboration, Nucl. Phys. **A610** (1996) 317c.
22. A. Drees, Nucl. Phys. **A610** (1996) 536c.
23. G. Agakichiev *et al.*, CERES collaboration, Phys. Lett. **B422** (1998) 405.
24. M. Masera for the HELIOS-3 collaboration, Nucl. Phys. **A590** (1995) 93c;
I. Kralik for the HELIOS-3 collaboration, Proc. of the International Workshop XXIII
on "Gross Properties of Nuclei and Nuclear Excitations", Hirschegg 1995, eds. H.
Feldmeier and W. Nörenberg, (GSI-Darmstadt 1995), p. 143;
A. L. S. Angelis *et al.* (HELIOS-3 Collaboration), Eur. Phys. J. **C5** (1998) 63.
25. M. C. Abreu *et al.* (NA38 collaboration), Phys. Lett. **B368** (1996) 230; *ibid.* 239.
26. M. Gonin *et al.* (NA50 collaboration), Nucl. Phys. **A610** (1996) 404c.
27. E. Scomparin *et al.* (NA50 collaboration), Nucl. Phys. **A610** (1996) 331c;
E. Scomparin *et al.* (NA50 collaboration), Proc. of the International Conference on
"Strangeness in Quark Matter '98" (Padova, Italy, 20.-24.07.98), J. Phys. **G25** (1999)
235;
P. Bordalo *et al.* (NA50 collaboration), Proc. of Quark Matter '99 (Torino, Italy, 10.-
15.05.99), Nucl. Phys. **A661** (1999) 538c.
28. A. de Falco *et al.* (NA38/NA50 collaboration), Nucl. Phys. **A638** (1998) 487c;
M. C. Abreu *et al.* (NA38/NA50 collaboration), *Low mass dimuon production in
proton and ion induced interactions at the SPS*, preprint CERN-EP/99-112, submitted
to Eur. Phys. J. C.
29. A. Drees, Nucl. Phys. **A630** (1998) 449c.
30. I. Tserruya, Nucl. Phys. **A638** (1998) 365c.
31. P. Wurm, Proc. of APCTP Workshop on "Hadron Properties in Medium" (World
Scientific, Singapore, 1998).
32. T. J. Hallman and J. Thomas, Nucl. Phys. **A590** (1995) 399c;
D. P. Morrison *et al.*, Nucl. Phys. **A638** (1998) 565c.
33. G. Roche *et al.* (DLS collaboration), Phys. Rev. Lett. **61** (1988) 1069;
C. Naudet *et al.* (DLS collaboration), Phys. Rev. Lett. **62** (1989) 2652;
G. Roche *et al.* (DLS collaboration), Phys. Lett. **B226** (1989) 228;
S. Beedoe *et al.* (DLS collaboration), Phys. Rev. **C47** (1993) 2840.
34. R. J. Porter *et al.* (DLS collaboration), Phys. Rev. Lett. **79** (1997) 1229;
W. K. Wilson *et al.* (DLS collaboration), Phys. Rev. **C57** (1997) 1865.
35. W. Koenig, Proc. of the Workshop on "Dilepton Production in Relativistic Heavy-Ion
Collisions", ed. H. Bokemeyer (GSI, Darmstadt, 1994).
36. V. Koch and C. Song, Phys. Rev. **C54** (1996) 1903.
37. G. Q. Li, C. M. Ko and G. E. Brown, Phys. Rev. Lett. **75** (1995) 4007; Nucl. Phys. **A606**
(1996) 568.
38. W. Cassing, W. Ehehalt and C. M. Ko, Phys. Lett. **B363** (1995) 35.
39. W. Cassing, W. Ehehalt and I. Kralik, Phys. Lett. **B377** (1996) 5.
40. D. K. Srivastava, B. Sinha and C. Gale, Phys. Rev. **C53** (1996) R567.
41. R. Baier, M. Dirks and K. Redlich, Phys. Rev. **D55** (1997) 4344; Proc. of the 28th Int.
Conf. on High Energy Physics, Warszawa, Poland (July 1996), hep-ph/9612448.
42. L. A. Winckelmann *et al.*, Nucl. Phys. **A610** (1996) 116c.
43. C. M. Hung and E. V. Shuryak, Phys. Rev. **C56** (1997) 453.
44. J. Murray, W. Bauer and K. Haglin, Phys. Rev. **C57** (1998) 882.
45. G. E. Brown and M. Rho, Phys. Rev. Lett. **66** (1991) 2720.

46. T. Hatsuda and S. H. Lee, Phys. Rev **C46** (1992) R34.
47. R. Rapp, G. Chanfray and J. Wambach, Nucl. Phys. **A617** (1997) 472.
48. W. Cassing, E. L. Bratkovskaya, R. Rapp and J. Wambach, Phys. Rev. **C57** (1998) 916.
49. R. Rapp, Proc. of the 33rd Rencontres de Moriond on “QCD and High Energy Hadronic Interactions”, Les Arcs (France), March 21–28, 1998, J. Tran Thanh Van (Edt.), Editions Frontieres (Paris, France 1998) 553–558, and nucl-th/9804065.
50. R. Rapp and J. Wambach, Eur. Phys. J. **A6** (1999) 415.
51. For theoretical introductions, see, e.g.,
 - F. J. Yndurain, *Quantum Chromodynamics: an Introduction to the Theory of Quarks and Gluons*, Springer, Heidelberg/New York (1983);
 - T. D. Lee, *Particle Physics and Introduction to Field Theory*, Harwood Academic, London (1981);
 - F. E. Close, *An Introduction to Quarks and Partons*, Academic Press, New York (1979).
52. M. Schmelling, Proc. of the XXVIII. International Conference on “High Energy Physics”, Warsaw, July 25–31, 1996, and hep-ex/9701002.
53. For overviews, see, e.g.,
 - B. W. Lee, *Chiral Dynamics*, Gordon & Breach, London (1972);
 - S. Weinberg, in “Lectures on Elementary Particles and Quantum Field Theory”, Vol. I, E. Deser, M. Grisaru and H. Pendleton (Eds.), MIT Press, Cambridge (Massachusetts) (1970) 283;
 - V. de Alfaro, S. Fubini, G. Furlan and C. Rossetti, *Currents in Hadronic Physics*, North-Holland, Amsterdam (1973).
54. T. Schäfer and E. V. Shuryak, Rev. Mod. Phys. **70** (1998) 323.
55. M. C. Chu, J. M. Grandy, S. Huang and J. W. Negele, Phys. Rev. **D49** (1994) 6039; J. W. Negele, Proc. of LATTICE 98, and hep-lat/9810053.
56. E. G. Drukarev and E. M. Levin, Prog. Part. Nucl. Phys. **27** (1991) 77.
57. Y. Nambu and G. Jona-Lasinio, Phys. Rev. **122** (1961) 345; *ibid.* **124** (1961) 246; Y. Nambu and D. Lurie, Phys. Rev. **125** (1962) 1429.
58. M. Gell-Mann, R. J. Oakes and B. Renner, Phys. Rev. **175** (1968) 2195.
59. M. A. Shifman, A. I. Vainshtein and V. I. Zakharov, Nucl. Phys. **B147** (1979) 385.
60. G. Chanfray, private communication.
61. J. Gasser, H. Leutwyler and M. E. Saino, Phys. Lett. **B253** (1991) 252.
62. I. Jameson, A. W. Thomas and G. Chanfray, J. Phys. **G18** (1992) L159.
63. M. Birse and J. McGovern, Phys. Lett. **B292** (1992) 242.
64. J. Gasser and H. Leutwyler, Phys. Lett. **B184** (1987) 83.
65. P. Gerber and H. Leutwyler, Nucl. Phys. **B321** (1989) 327.
66. H. Leutwyler, *Deconfinement and Chiral Symmetry*, in “QCD 20 years later”, Vol. 2, P. M. Zervas and H. A. Kastrup (Eds.), World Scientific, Singapore, (1993) 693.
67. R. Brockmann and W. Weise, Phys. Lett. **B267** (1996) 40.
68. Z. Aouissat, G. Chanfray, P. Schuck and J. Wambach, Nucl. Phys. **A603** (1996) 458.
69. B.-J. Schaefer and H. Pirner, nucl-th/9903003.
70. J. Kapusta, *Finite Temperature Field Theory*, Cambridge University Press, 1989.
71. K. G. Wilson, Phys. Rev. **D10** (1974) 2445.
72. J. Kogut and L. Susskind, Phys. Rev. **D11** (1975) 395.
73. D. Kaplan, Phys. Lett. **B288** (1992) 342;
 - Y. Shamir, Nucl. Phys. **B406** (1993) 90;
 - for a recent review, see also T. Blum, Nucl. Phys. Proc. Suppl. **73** (1999) 167.
74. C. Bernard *et al.*, Phys. Rev. **D55** (1997) 6861.
75. G. Boyd and D. E. Miller, hep-ph/9608482.

76. H. Satz, private communication (1999).
77. F. Karsch, Nucl. Phys. **A590** (1995) 367c.
78. S. Gottlieb *et al.*, Phys. Rev. **D55** (1997) 6852.
79. Z. Huang, Phys. Lett. **B361** (1995) 131.
80. C. Bacci *et al.* ($\gamma\gamma$ collaboration), Phys. Lett. **B86** (1979) 234.
81. B. Wiik and G. Wolf, *Electron-Positron Interactions* (Springer Verlag, Berlin 1979).
82. L. M. Barkov *et al.* (OLYA collaboration), Nucl. Phys. **B256**, 365 (1985).
83. A. Cordier *et al.* (DM1 collaboration), Nucl. Phys. **B172** (1980) 13.
84. V. Siderov, Proc. of the International Symposium on "Lepton and Photon Interactions" (1979) (Fermilab, Batavia 1980).
85. S. Weinberg, Phys. Rev. Lett. **18** (1967) 507.
86. K. Kawarabayashi and M. Suzuki, Phys. Rev. Lett. **16** (1966) 255;
Riazuddin and Fayyazuddin, Phys. Rev. **147** (1966) 1071.
87. J. Kapusta and E. V. Shuryak, Phys. Rev. **D49** (1994) 4694.
88. M. Dey, V. L. Eletsky and B. L. Ioffe, Phys. Lett. **B252** (1990) 620;
V. L. Eletsky, Phys. Lett. **B245** (1990) 229.
89. B. Krippa, Phys. Lett. **B427** (1998) 13.
90. M. C. Birse, Phys. Rev. **C53** (1996) R2048.
91. F. Klingl, N. Kaiser and W. Weise, Nucl. Phys. **A624** (1997) 527.
92. D. B. Leinweber, Ann. Phys. **254** (1997) 328.
93. B. Borasoy and U.-G. Meißner, Phys. Lett. **B365** (1996) 285.
94. M. Asakawa and C. M. Ko, Phys. Rev. **C48** (1993) R526; Nucl. Phys. **A560** (1993) 399.
95. S. Leupold, W. Peters and U. Mosel, Nucl. Phys. **A628** (1998) 311.
96. H. Yamagishi and I. Zahed, Ann. Phys. **247** (1996) 292.
97. M. Veltmann, Phys. Rev. Lett. **17** (1966) 553;
J. S. Bell, Nuovo Cim. **50 A** (1967) 129.
98. R. E. Peierls, Proc. Roy. Soc. (London) **A214** (1952) 143.
99. J. V. Steele, H. Yamagishi and I. Zahed, Phys. Lett. **B384** (1996) 255.
100. J. V. Steele, H. Yamagishi and I. Zahed, Phys. Rev. **D56** (1997) 5605.
101. W. Peters, M. Post, H. Lenske, S. Leupold and U. Mosel, Nucl. Phys. **A632** (1998) 109.
102. R. Rapp, M. Urban, M. Buballa and J. Wambach, Phys. Lett. **B417** (1998) 1.
103. G. E. Brown, G. Q. Li, R. Rapp, M. Rho and J. Wambach, Acta Phys. Polon. **B29** (1998) 2309.
104. J. V. Steele and I. Zahed, Phys. Rev. **D60** (1999) 037502.
105. R. D. Pisarski, Phys. Rev. **D52** (1995) R3773; hep-ph/9503330 (unpublished);
hep-ph/9505257 (unpublished).
106. T. Hatsuda and T. Kunihiro, Phys. Lett. **B185** (1987) 304.
107. J. J. Sakurai, *Currents and Mesons* (University of Chicago, Chicago 1969).
108. V. L. Eletsky and B. L. Ioffe, Phys. Rev. **D51** (1995) 2371.
109. U.-G. Meißner, Phys. Rep. **161** (1988) 213.
110. S. H. Lee, C. Song and H. Yabu, Phys. Lett. **B341** (1995) 407.
111. C. Song, Phys. Rev. **C47** (1993) 3338; Phys. Rev. **D48** (1993) 1375; Phys. Rev. **D53** (1996) 3962.
112. M. Bando, T. Kugo, S. Uehara, K. Yamawaki and T. Yanagida, Phys. Rev. Lett. **54** (1985) 1215;
M. Bando, T. Kugo and K. Yamawaki, Phys. Rep. **164** (1988) 217.
113. C. Song and V. Koch, Phys. Rev. **C54** (1996) 3218.
114. G. Chanfray and P. Schuck, Nucl. Phys. **A545** (1992) 271c; Nucl. Phys. **A555** (1993) 329.

115. C. A. Dominguez and M. Loewe, Nucl. Phys. **B** (Proc. Suppl.) **16** (1990) 403; Zeit. Phys. **C49** (1991) 423.
116. V. L. Eletsky and B. L. Ioffe, Phys. Rev. **D47** (1993) 3083.
117. C. A. Dominguez and M. Loewe, Phys. Lett. **B233** (1989) 201.
118. C. Gale and J. Kapusta, Nucl. Phys. **B357** (1991) 65.
119. C. Gale and P. Lichard, Phys. Rev. **D49** (1994) 3338.
120. K. Haglin, Nucl. Phys. **A584** (1995) 719.
121. V. L. Eletsky, B. L. Ioffe and J. I. Kapusta, Eur. Phys. J. **A3** (1998) 381; V. L. Eletsky and J. I. Kapusta, nucl-th/9810052.
122. S. Gao, C. Gale, C. Ernst, H. Stöcker and W. Greiner, nucl-th/9812059.
123. R. Rapp and C. Gale, Phys. Rev. **C60** (1999) 24903.
124. S. Gao and C. Gale, Phys. Rev. **C57** (1998) 254.
125. J. J. Sakurai, Ann. Phys. **11** (1960) 1.
126. M. Urban, M. Buballa, R. Rapp and J. Wambach, Nucl. Phys. **A641** (1998) 433.
127. E. V. Shuryak, Nucl. Phys. **A533** (1991) 761.
128. R. Rapp and J. Wambach, Phys. Lett. **B315** (1993) 220; *ibid.* **B351** (1995) 50.
129. R. Rapp, PhD thesis Bonn 1996, in *Berichte des Forschungszentrum Jülich* vol. 3195 (Jülich, 1996) p. 1-141.
130. R. Rapp, J. W. Durso and J. Wambach, Nucl. Phys. **A596** (1996) 436.
131. T. Hatsuda and T. Kunihiro, Prog. Theo. Phys. **91** (1987) 284.
132. N. Kaiser and U.-G. Meißner, Nucl. Phys. **A519** (1990) 671.
133. C. Itzykson and J. B. Zuber, *Quantum Field Theory* (McGraw Hill, New York, 1980).
134. T. E. O. Ericson and W. Weise, *Pions and Nuclei* (Clarendon, Oxford, 1988).
135. J. Ellis, Nucl. Phys. **B22** (1970) 478;
B. A. Campbell, J. Ellis and K. A. Olive, Nucl. Phys. **B345** (1990) 57.
136. G. E. Brown and M. Rho, Phys. Rep. **269** (1996) 333.
137. A. B. Migdal, E. E. Saperstein, M. A. Troitsky and D. N. Voskresensky, Phys. Rep. **192** (1990) 179.
138. R. Rapp and J. Wambach, Nucl. Phys. **A573** (1994) 626.
139. J. C. Ward, Phys. Rev. **78** (1950) 182;
Y. Takahasi, Nuovo Cim. **6** (1957) 371.
140. M. Herrmann, B. Friman and W. Nörenberg, Nucl. Phys. **A545** (1992) 267c; Nucl. Phys. **A560** (1993) 411.
141. M. Asakawa, C. M. Ko, P. Lévai and X. J. Qiu, Phys. Rev. **C46** (1992) R1159.
142. G. Chanfray, R. Rapp and J. Wambach, Phys. Rev. Lett. **76** (1996) 368.
143. R. Machleidt, K. Holinde and C. Elster, Phys. Rep. **149** (1987) 1.
144. G. Chanfray, J. Delorme, M. Ericson and M. Rosa-Clot, nucl-th/9809007.
145. N. Kaiser, P. B. Siegel and W. Weise, Nucl. Phys. **A594** (1995) 325.
146. Particle Data Group, R. M. Barnett *et al.*, Phys. Rev. **D54** (1996) 1.
147. B. Friman, Nucl. Phys. **A610** (1996) 358c;
B. Friman and H. J. Pirner, Nucl. Phys. **A617** (1997) 496.
148. B. Friman, M. Lutz and G. Wolf, Proc. of *BARYONS 98*, Bonn (Germany), Sept. 98, and nucl-th/9811040; Proc. of the 28th International Workshop on Gross Properties of Nuclei and Nuclear Excitations, Hirschegg (Austria), 16-22 Jan. 2000, and nucl-th/0003012.
149. V. L. Eletsky and B. L. Ioffe, Phys. Rev. Lett. **78** (1997) 1010.
150. T. H. Bauer, R. D. Spital, D. R. Yennie and F. M. Pipkin, Rev. Mod. Phys. **50** (1978) 261.

151. L. A. Kondratyuk, A. Sibirtsev, W. Cassing, Ye. S. Golubeva and M. Effenberger, Phys. Rev. **C58** (1998) 1078.
152. F. Klingl, N. Kaiser and W. Weise, Zeit. Phys. **A356** (1996) 193.
153. B. Friman, Proc. of the ACTP Workshop on "Hadron Properties in Medium", Seoul, Korea, Oct. 27–31, 1997, to be published, and nucl-th/9801053; Acta Phys. Polon. **B29** (1998) 3195, and nucl-th/9808071.
154. W. M. Layson, Nuovo Cim. **20** (1961) 1207.
155. J. H. Koch and E. J. Moniz, Phys. Rev. **C27** (1983) 751.
156. F. Bonnuttii *et al.*, Phys. Rev. Lett. **77** (1996) 603.
157. C. Gaarde *et al.*, SATURNE proposal (1996).
158. TAGX Collaboration, G. J. Lolos *et al.*, Phys. Rev. Lett. **80** (1998) 241; G. M. Huber, G. J. Lolos and Z. Papandreou, Phys. Rev. Lett. **80** (1998) 5285.
159. G. Freedom, International Workshop on "Soft Dilepton Production", LBNL, August 20–22, 1997.
160. W. Schön, H. Bokemeyer, W. Koenig and W. Metag, Acta Phys. Polon. **B27** (1996) 2959.
161. R. S. Hayano *et al.*, GSI-SIS proposal #214 (1997).
162. F. Klingl and W. Weise, Nucl. Phys. **A606** (1996) 329.
163. M. Effenberger, A. Hombach, S. Teis and U. Mosel, Nucl. Phys. **A613** (1997) 353; M. Effenberger and U. Mosel, Proc. of the "Conference on Perspectives in Hadronic Physics", Trieste, May 12–16, 1997, and nucl-th/9707010.
164. Particle Data Group, Phys. Rev. **D50** (1994) 1173.
165. A. Lepretre *et al.*, Phys. Lett. **79B** (1978) 43.
166. J. Ahrens, Nucl. Phys. **A446** (1985) 229c; J. Ahrens *et al.*, Phys. Lett. **146B** (1984) 303.
167. Th. Frommhold *et al.*, Phys. Lett. **B295** (1992) 28; Zeit. Phys. **A350** (1994) 249.
168. N. Bianchi *et al.*, Phys. Lett. **B299** (1993) 219; Phys. Rev. **C54** (1996) 1688.
169. R. L. Walker, Phys. Rev. **182** (1969) 1729.
170. B. Krusche *et al.*, Phys. Rev. Lett. **74** (1995) 3736.
171. A. Braghieri *et al.*, Phys. Lett. **B363** (1995) 46.
172. W. M. Alberico, G. Gervino, and A. Lavagno, Phys. Lett. **B321** (1994) 177.
173. L. A. Kondratyuk, M. I. Krivoruchenko, N. Bianchi, E. De Sanctis and V. Muccifora, Nucl. Phys. **A579** (1994) 453.
174. N. M. Kroll, T. D. Lee and B. Zumino, Phys. Rev. **157** (1967) 1376.
175. T. A. Armstrong *et al.*, Phys. Rev. **D5** (1972) 1640.
176. T. A. Armstrong *et al.*, Nucl. Phys. **B41** (1972) 445.
177. J. Cleymans, J. Fingberg and K. Redlich, Phys. Rev. **D35** (1987) 2153.
178. H.-J. Schulze and D. Blaschke, Phys. Lett. **B386** (1996) 429.
179. E. Braaten, R. D. Pisarski and T. C. Wang, Phys. Rev. Lett. **64** (1990) 2242.
180. L. Chatterjee and C.-Y. Wong, Phys. Rev. **C51** (1995) 2125.
181. M. G.-H. Mostafa, C.-Y. Wong, L. Chatterjee and Z.-Q. Wang, Int. J. Mod. Phys. **E5** (1996) 631.
182. C. H. Lee, J. Wirstam, I. Zahed and T. H. Hansson, Phys. Lett. **B448** (1999) 168.
183. T. Schäfer, E. V. Shuryak and J. J. M. Verbaarschot, Phys. Rev. **D51** (1995) 1267.
184. M. Velkovsky and E. V. Shuryak, Phys. Rev. **D56** (1997) 2766.
185. R. Rapp, T. Schäfer, E. V. Shuryak and M. Velkovsky, Ann. Phys. **280** (2000) 35.
186. H. A. Weldon, Phys. Rev. **D61** (2000) 036003.
187. A. Peshier and M. Thoma, Phys. Rev. Lett. **84** (2000) 841.
188. S. M. H. Wong, Zeit. Phys. **C53** (1992) 465.

189. J. Cleymans, V. V. Goloviznin and K. Redlich, Phys. Rev. **D47** (1993) 989.
190. J. D. Bjorken, K. L. Kowalski and C. C. Taylor, Proc. of Les Rencontres de la Vallee D'Aoste, La Thuile, Italy, 1993, ed. by M. Greco (Edition Frontiers, Gif-sur-Yvette, 1993), p. 507.
191. K. Rajagopal and F. Wilczek, Nucl. Phys. **B404** (1993) 577.
192. Z. Huang and X.-N. Wang, Phys. Lett. **B383** (1996) 457.
193. Y. Kluver, V. Koch, J. Randrup and X.-N. Wang, Phys. Rev. **C57** (1998) 280.
194. S. Gavin, Nucl. Phys. **B351** (1991) 561.
195. W. Ehehalt and W. Cassing, Nucl. Phys. **A602** (1996) 449.
196. X.-N. Wang and M. Gyulassy, Phys. Rev. **D44** (1991) 3501.
197. H. Bebie, P. Gerber, J. L. Goity and H. Leutwyler, Nucl. Phys. **B378** (1992) 95.
198. B. Nilsson-Almquist and E. Stenlund, Comput. Phys. Commun. **43** (1987) 387.
199. R. Baier, M. Dirks and C. Redlich, Acta Phys. Polon. **B28** (1997) 2873.
200. R. Rapp, Proc. of Quark Matter '99 (Torino, Italy, 10-15.05.99), Nucl. Phys. **A661** (1999) 33c.
201. A. V. Leonidov and P. V. Ruuskanen, Heavy Ion Phys. **1** (1995) 61; Eur. Phys. J. **C4** (1998) 519.
202. C. Song, C. M. Ko, and C. Gale, Phys. Rev. **D50**, R1827 (1994).
203. J. K. Kim, P. Ko, K. Y. Lee and S. Rudaz, Phys. Rev. **D53** (1996) 4787.
204. G. Q. Li and C. Gale, Phys. Rev. Lett. **81** (1998) 1572; Phys. Rev. **C58** (1998) 2914.
205. C.-H. Lee, H. Yamagishi and I. Zahed, Phys. Rev. **C58** (1998) 2899.
206. J. Kapusta, P. Lichard and D. Seibert, Phys. Rev. **D44** (1991) 2774; and *Erratum, ibid. D47* (1993) 4171.
207. L. D. Landau, Izv. Akad. Nauk. SSSR Ser. Fiz. **17** (1953) 51.
208. E. V. Shuryak, Yad. Fiz. **20** (1974) 549.
209. F. Cooper, G. Frye and E. Schonberg, Phys. Rev. **D11** (1975) 292.
210. H. von Gersdorff, L. McLerran, M. Kataja and P. V. Ruuskanen, Phys. Rev. **D34** (1986) 794.
211. E. Schnedermann and U. Heinz, Phys. Rev. Lett. **69** (1992) 2908.
212. U. Katscher, D. H. Rischke, J. A. Maruhn, W. Greiner, I. N. Mishustin and L. M. Saratov, Zeit. Phys. **A346** (1993) 209.
213. C. M. Hung and E. V. Shuryak, Phys. Rev. Lett. **75** (1995) 4003.
214. J. Sollfrank, P. Huovinen, M. Kataja, P. V. Ruuskanen, M. Prakash and R. Venugopalan, Phys. Rev. **C55** (1997) 392.
215. D. H. Rischke, Y. Pürsün and J. A. Maruhn, Nucl. Phys. **A595** (1995) 383; and *Erratum, ibid. A596* (1996) 717.
216. B. R. Schlei, Heavy Ion Phys. **5** (1997) 403.
217. D. K. Srivastava, J. Pan, V. Emel'yanov and C. Gale, Phys. Lett. **B329** (1994) 157.
218. J. D. Bjorken, Phys. Rev. **D27** (1983) 140.
219. R. Hwa and K. Kajantie, Phys. Rev. **D32** (1985) 1109.
220. B. Kämpfer, O. P. Pavlenko, A. Peshier and G. Soff, Phys. Rev. **C52** (1995) 2704.
221. K. Haglin, Phys. Rev. **C53** (1996) R2606.
222. G. F. Bertsch and S. Das Gupta, Phys. Rep. **160** (1988) 189.
223. C. M. Ko and Q. Li, Phys. Rev. **C37** (1988) R2270.
224. B. Blättel, V. Koch, W. Cassing and U. Mosel, Phys. Rev. **C38** (1988) 1767; for a review, see e.g., B. Blättel, V. Koch and U. Mosel, Rep. Prog. Phys. **56** (1993) 1.
225. J. Aichelin, Phys. Rep. **202** (1991) 233.
226. H. Sorge, H. Stöcker and W. Greiner, Ann. Phys. **192** (1989) 266.
227. S. A. Bass *et al.*, Prog. Part. Nucl. Phys. **41** (1998) 225.

228. K. Weber, B. Blättel, W. Cassing, H.-C. Dönges, V. Koch, A. Lang and U. Mosel, Nucl. Phys. **A539** (1992) 713.
229. B. D. Serot and J. D. Walecka, Adv. Nucl. Phys. **16** (1986) 1.
230. E. L. Bratkovskaya and W. Cassing, Nucl. Phys. **A619** (1997) 413.
231. G. Q. Li and C. M. Ko, Nucl. Phys. **A582** (1995) 731.
232. G. Q. Li, C. M. Ko, G. E. Brown and H. Sorge, Nucl. Phys. **A611** (1996) 539.
233. E. L. Bratkovskaya and C. M. Ko, Phys. Lett. **B445** (1999) 265.
234. W. Cassing and S. Juchem, nucl-th/9903070.
235. J. Knoll, nucl-th/9811099.
236. V. Koch and G. F. Bertsch, Nucl. Phys. **A552** (1993) 591.
237. E. L. Bratkovskaya, W. Cassing, R. Rapp and J. Wambach, Nucl. Phys. **A634** (1998) 168.
238. P. Koch, Zeit. Phys. **C57** (1993) 283.
239. B. Kämpfer, P. Koch and O. P. Pavlenko, Phys. Rev. **C49** (1994) 1132.
240. P. Braun-Munzinger and J. Stachel, Nucl. Phys. **A606** (1996) 320.
241. J. Stachel, Nucl. Phys. **A610** (1996) 509c.
242. U.A. Wiedemann, Proc. of Quark Matter '99, Torino (Italy), May 10–15, 1999, Nucl. Phys. **A661** (1999) 65c.
243. H. Sorge, Phys. Lett. **B373** (1996) 16.
244. K. Gallmeister, B. Kämpfer and O. P. Pavlenko, Phys. Lett. **B473** (2000) 20.
245. L. Xiong, Z. G. Wu, C. M. Ko and J. Q. Wu, Nucl. Phys. **A512** (1990) 772.
246. Gy. Wolf, G. Batko, W. Cassing, U. Mosel, K. Niita and M. Schäfer, Nucl. Phys. **A517** (1990) 615;
Gy. Wolf, W. Cassing and U. Mosel, Nucl. Phys. **A552** (1993) 549.
247. C. Ernst, S. A. Bass, M. Belkacem, H. Stöcker and W. Greiner, Phys. Rev. **C58** (1998) 447.
248. E. L. Bratkovskaya, W. Cassing, M. Effenberger and U. Mosel, Nucl. Phys. **A653** (1999) 301.
249. R. Averbeck *et al.* (TAPS collaboration), Zeit. Phys. **A359** (1997) 65.
250. J. Zhang and C. Gale, Phys. Rev. **C50** (1994) 1617.
251. B. Lenkeit, Doctoral Thesis, University of Heidelberg, 1998;
B. Lenkeit *et al.*, CERES collaboration, Proc. of Quark Matter '99, Torino (Italy), May 10–15, 1999, Nucl. Phys. **A661** (1999) 23c.
252. P. Huovinen and M. Prakash, Phys. Lett. **B450** (1999) 15.
253. J. Kapusta, D. Kharzeev and L. McLerran, Phys. Rev. **D53** (1996) 5028;
Z. Huang and X.-N. Wang, *ibid.* 5034.
254. A. Drees, Phys. Lett. **B388** (1996) 380.
255. G. Q. Li, G. E. Brown and C. M. Ko, Nucl. Phys. **A630** (1998) 563.
256. D. Irmscher, Doctoral Dissertation, Univ. Heidelberg 1993; T. Ullrich, Doctoral Dissertation, Univ. Heidelberg 1994; G. Agakichiev *et al.*, CERES collaboration, Eur. Phys. J. **C4** (1998) 231; and A. Drees, private communication.
257. V. Koch, Proc. of the XXXVII. International "Winter Meeting on Nuclear Physics", Bormio (Italy) Jan. 1999, and nucl-th/9903008.
258. P. Braun-Munzinger, D. Miskowiec, A. Drees and C. Lourenço, Eur. Phys. J. **C1** (1998) 123.
259. Z. Lin and X. N. Wang, Phys. Lett. **B444** (1998) 245.
260. R. Rapp and E. V. Shuryak, Phys. Lett. **B473** (2000) 13.
261. I. Tserruya, Prog. Theor. Phys. Suppl. **129** (1997) 145.
262. T. Akesson *et al.*, HELIOS-2 collaboration, Zeit. Phys. **C46** (1990) 369.

263. R. Baur *et al.*, CERES collaboration, *Zeit. Phys.* **C71** (1996) 571.
264. R. Albrecht *et al.*, WA80 collaboration, *Phys. Rev. Lett.* **76** (1996) 3506.
265. B. Wyslouch for the WA98 collaboration, *Nucl. Phys.* **A638** (1998) 147c.
266. D. K. Srivastava and B. Sinha, *Phys. Rev. Lett.* **73** (1994) 2421.
267. A. Dumitru *et al.*, *Phys. Rev.* **C51** (1995) 2166.
268. G. Q. Li and G. E. Brown, *Nucl. Phys.* **A632** (1998) 153.
269. S. Sarkar *et al.*, *Nucl. Phys.* **A634** (1998) 206.
270. M.-A. Halasz, J. V. Steele, G. Q. Li and G. E. Brown, *Phys. Rev.* **C58** (1998) 365.

Chapter 2

FUNDAMENTAL SYMMETRY VIOLATION IN NUCLEI

H. Feshbach

Center for Theoretical Physics

Laboratory for Nuclear Science and Department of Physics

Massachusetts Institute of Technology

Cambridge, MA 02139-4307

M. S. Hussein

Instituto de Fisica,

Universidade de Sao Paulo,

Caixa Postal 66318, 5315-970

Sao Paulo, SP, Brasil

A. K. Kerman

Center for Theoretical Physics

Laboratory for Nuclear Science and Department of Physics

Massachusetts Institute of Technology

Cambridge, MA 02139-4307

O. K. Vorov

Instituto de Fisica,

Universidade de Sao Paulo,

Caixa Postal 66318, 5315-970

Sao Paulo, SP, Brasil

1. Introduction	208
2. Summary of the experimental results From the TRIPLE collaboration	210
3. Symmetry Violation within Reaction Theory	218
4. Parity Nonconservation (PNC) in the Compound Nucleus	222
5. The Sign Correlation Problem and the Role of $2p - 1h$ Doorway States	224
6. Optical Model Description of PNC	230
7. Strength of PNC Interaction in Exotic (Halo) Nuclei	248
8. Time Reversal Symmetry Breaking	260
9. Conclusions	267

1. INTRODUCTION

The electron-neutrino, i.e. the leptonic, manifestations of the standard model have been much studied. No deviation from theory has been found. The standard model also predicts a weak interaction between nucleons and more generally between hyperons and nucleons. It is the hadronic aspect of the standard model with which we shall be concerned in this paper.

The observation of parity non conserving processes is the tool with which one probes the weak interaction between hadrons. Parity conservation has been directly studied in nucleon-nucleon scattering. It has been studied by the observation of the mixing of a small magnetic dipole component of the opposite parity. In an electromagnetic decay, say of the electric dipole variety, the recipient level will have a parity opposite to the decaying level. The small component can also be responsible for a decay. However its radiation will be that of a magnetic dipole so that the limited gamma ray will be a coherent mixture of electric and magnetic dipole radiation. This fact can be observed by determining the circular polarization of the emitted radiation. If it exists, parity is not conserved. This effect is a consequence of the interference between the electric and magnetic dipole components and is thus linear in the weak interaction strength. From the experiment one can obtain the magnitude of the matrix element of the weak interaction. At a pion Compton

wavelength the ratio of the weak to strong nucleon-nucleon interaction is of the order of 10^{-7} . If the strong force has the magnitude of 10 MeV, the weak force has the magnitude of 1 eV. This is an extremely small force. Amplification is essential if it is to be brought within reach of observation [1].

Amplification is obtained if two levels of differing parity are approximately degenerate for then the mixing of those two levels will be especially strong. Such near degeneracy can be found in several nuclei and as a consequence the ratio of weak to strong matrix elements can be raised from 10^{-7} to roughly (it varies with nuclei) 10^{-4} . This effect has been observed in a wide variety of nuclei.

The recently discovered symmetry breaking exhibited in the formation of compound nuclear levels by epithermal neutrons provides new insights into the nature of the weak interaction and the structure of the compound nucleus. When very slow neutrons bombard a heavy target nucleus a compound nucleus with excitation energy of about 6–7 MeV is formed. Generally a high density of resonances is seen. Because of the low neutron kinetic energy only *s* and *p*waves are involved and the compound nuclear levels which are excited are correspondingly constrained. We shall refer to these levels as *s* and *p* levels. They have opposite parity. Parity nonconservation occurs when, because of the weak interactions, the *s* and *p* levels mix. Such mixing is enhanced in the compound nucleus because of the close spacing of the *s* and *p*levels. An additional enhancement occurs if several levels belonging to the same doorway states are involved.

Similar remarks may be made about time reversal. There will be levels of differing time reversal properties, odd or even. Mixing these will lead to time reversal symmetry breaking. Needless to say the weak force stands on its own as an important vehicle with whose help several properties of the strongly interacting system can be studied.

The very close spacing of the *s* and *p* levels, together with the huge complexity of the compound nuclear wave function introduces an enhancement factor that would amplify the signature of parity or time reversal nonconservation. This makes the use of the compound nucleus to study fundamental symmetry violation a natural undertaking.

Further, owing to the complexity of the compound nuclear wave function, it is expected that the measured quantity, the longitudinal asymmetry at a given resonance, should be random in sign. The large value of the asymmetry and its randomness have been nicely verified in a number of nuclei. Only one exception, ^{232}Th , has presented a challenge. Here the randomness is not complete. Instead, the average value of the

asymmetry was found to be large and positive. This has become known as the sign correlation problem. Several reviews on parity violation in the compound nucleus have been published [2, 3, 4, 5, 6]. A most recent review by Mitchell, Bowman and Weidenmuller [5] concentrates on the statistical features of the TRIPLE data.

In so far as parity nonconservation (PNC) is used to further test the compound nucleus model, and more importantly, to set measurement standards for the future investigation of time reversal symmetry breaking (TRSB) tests, it is important to have at hand a unified reaction theory which can address the statistical and nonstatistical aspects of symmetry violation. The purpose of this paper is to supply this theory.

Of course, besides PNC and TRSB, there is another discrete symmetry that is also broken in the nucleus, namely isospin. The force that is responsible for the breakdown in the EM one, several orders of magnitude larger than the weak force which is our main interest. Though some of the reaction theory techniques used here are similar to the one developed in this review, we shall not dwell upon this issue in the following.

The paper is organized as follows: In Section 2, a summary of the experimental results of the TRIPLE group is given. In Section 3, a full development of the reaction theory needed to study symmetry violation is presented. Here, the hierarchy of complexities (optical potential, 2 particle-1 hole doorways, 3 particle-2 hole hallways, etc.) is exhibited in the formulation. In Section 4 the data on PNC in the compound nucleus are analyzed using the result of Section 3. The sign correlation effect in ^{232}Th is traced to the 2p-1h doorway states which are taken to be responsible for the PNC. This is discussed in Section 5. The rms value of weak matrix element extracted from the data is also discussed in Section 5. In Section 6 the optical model description of PNC is developed and applied to the TRIPLE data. In Section 7 the strength of the PNC matrix element is calculated for neutron-rich (exotic) nuclei, and compared with that of stable nuclei. In Section 8, the TRSB is considered both in the isolated resonance and the overlapping resonances, statistical, cases. Finally, in Section 9, concluding remarks are made.

2. SUMMARY OF THE EXPERIMENTAL RESULTS FROM THE TRIPLE COLLABORATION

In this section we give a brief review of the experimental result of the TRIPLE collaboration [7, 8, 9, 10, 11, 12, 13, 14, 15, 16]. The under-

taking of the TRIPLE group followed the earlier discovery [17] at Dubna of the very large parity violation in the scattering of slow polarized neutrons from heavy target nuclei.

Measurements of the PNC longitudinal asymmetries were done for the following targets: ^{81}Br , ^{93}Nb , ^{103}Rh , $^{107+109}\text{Ag}$, $^{104-106,108}\text{Pd}$, ^{113}Cd , ^{115}In , ^{117}Sn , $^{121,123}\text{Sb}$, ^{127}I , ^{131}Xe , ^{133}Cs , ^{232}Th and ^{238}U (see Table 2.1). For the epithermal energies considered here the dominant partial wave is $l = 0$ (s -wave). Several p -wave resonances are populated as well with much smaller cross section. It is the mixing of these $p - waves$ with nearby s -waves owing to PNC that is extracted from the longitudinal asymmetry

$$P_i = \frac{\sigma_i^{(+)} - \sigma_i^{(-)}}{\sigma_i^{(+)} + \sigma_i^{(-)}}, \quad (2.1)$$

where the index i refers to the p -wave resonance being probed and $\sigma^{(+/-)}$ refers to the total p -wave cross-section with positive (negative) helicities. If one uses the usual sum-over-resonances form for the scattering amplitude and with the use of the optical theorem, one may write for P_i the following expression, assuming the p -resonance is mixed with one s -resonance

$$P_i = 2 \frac{\langle i|V_{PNC}|j\rangle}{E_{s_j} - E_{p_i}} \sqrt{\frac{\Gamma_{s_j}}{\Gamma_{p_i}}} \equiv 2 \frac{V_{ij}}{\Delta E_{ij}} \sqrt{\frac{\Gamma_{s_j}}{\Gamma_{p_i}}} \quad (2.2)$$

where Γ_{p_i} and Γ_{s_j} are the neutron decay amplitudes of $p - wave$ and $s - wave$ resonances respectively. Since the compound states $|i\rangle$ and $|j\rangle$ are very complicated, one expects the matrix element $\langle i|V_{PNC}|j\rangle$ to involve a much reduced overlap and then a smaller value when compared to single particle matrix element. The reduction factor is roughly \sqrt{D} where D is the average spacing between resonances in dimensionless units [17, 18], see also [3] for review. On the other hand, the energy difference $E_{s_j} - E_{p_i}$ becomes smaller as the excitation energy is increased and it goes as D . Writing $E_{s_j} - E_{p_i} \approx \Delta D$, where Δ is a measure of the single particle energy difference, and $V_{ij} \equiv \langle i|V_{PNC}|j\rangle \approx \sqrt{D} (V_{PNC})$, where (V_{PNC}) designates average single particle value of the PNC matrix element, we find [17]b

$$P_i = 2 \frac{1}{\sqrt{D}} \frac{(V_{PNC})}{\Delta} \sqrt{\frac{\Gamma_{s_j}}{\Gamma_{p_i}}}. \quad (2.3)$$

Further, expressing Γ_{s_j} and Γ_{p_i} in terms of their respective reduced widths, $\Gamma_{s_j} = \dot{\gamma}_{s_j}^2$, $\Gamma_{p_i} = \dot{\gamma}_{p_i}^2 (kR)^2$, where the factor $(kR)^2$ accounts for the effect of the $\ell = 1$ centrifugal barrier, we have finally

TABLE 2.1

Relative signs of parity violations observed by the TRIPLE Collaboration. "Total number" is the number of parity-violating asymmetries observed in each nuclide; only asymmetries with statistical significance greater than three standard deviations are included. The columns labeled "positive" and "negative" are the number of asymmetries with + or - sign relative to the sign of the effect at 0.74 eV in ^{139}La [7, 8, 9, 10, 11, 12, 13, 14, 15, 16].

Target	Total number	Positive	Negative
^{81}Br	1	1	0
^{93}Nb	0	0	0
^{103}Rh	4	3	1
^{107}Ag	8	5	3
^{109}Ag	4	2	2
^{104}Pd	1	1	0
^{105}Pd	7	4	3
^{106}Pd	1	0	1
^{108}Pd	0	0	0
^{113}Cd	3	2	1
^{115}In	9	5	4
^{117}Sn	6	3	3
^{121}Sb	5	3	2
^{123}Sb	1	0	1
^{127}I	7	5	2
^{131}Xe	1	0	1
^{133}Cs	1	1	0
^{139}La	1	1	0
^{232}Th	10	10	0
^{238}U	5	3	2

Br C. M. Frankle *et al.*, Physical Review, C46, 1542 (1992).

Nb E. I. Sharapov *et al.*, Physical Review, C46, 1542 (1992).

Rh D. A. Smith *et al.*, Physical Review, to be published.

Ag L. Y. Lowie *et al.*, Physical Review, C59, 1119 (1999).

$^{104,105}\text{Pd}$ D. A. Smith *et al.*, unpublished.

$^{106,108}\text{Pd}$ B. E. Crawford *et al.*, Physical Review, submitted.

^{113}Cd S. J. Seestrom *et al.*, Physical Review, C58, 2977 (1998).

^{115}In L. Y. Lowie *et al.*, PhD Thesis, NCSU 1996; (in progress).

^{117}Sn D. A. Smith *et al.*, unpublished.

Sb I. Y. Matsuda *et al.*, PhD Thesis, Kyoto 1998.

Xe J. J. Szymanski *et al.*, Physical Review, C53, R2576 (1996).

Cs E. I. Sharapov *et al.*, Physical Review, C59, 1772 (1999).

La Yuan *et al.*, Physical Review, C44, 2187 (1991).

Th S. L. Stephenson *et al.*, Physical Review, C58, 1236 (1998).

U B. E. Crawford *et al.*, Physical Review, C58, 1225 (1998).

$$P_i = \left[\frac{1}{\sqrt{D}} \right] \left[\frac{1}{kR} \right] \left[2 \frac{(V_{PNC})}{\Delta} \frac{\dot{\gamma}_{s_j}}{\dot{\gamma}_{p_i}} \right]. \quad (2.4)$$

The first factor in Eq. (2.4) is the dynamical enhancement factor which can be as large as 10^2 . The second factor is roughly 10^3 for epithermal neutrons scattered off heavy targets. The first factor grows with excitation energy while the second decreases. Further, there is an important oscillatory behavior of the reduced resonance amplitudes with the mass

number. This is exemplified by the strength function, $\left\langle \frac{\dot{\gamma}^2}{D} \right\rangle$ as a function of A , shown in Figs. 2.1 and 2.2 for s - and p -waves. The factor $\frac{\dot{\gamma}_{s_j}}{\dot{\gamma}_{p_i}}$ in Eq.

(2.4) is equal to $\sqrt{\frac{S_o}{S_1}}$ and accordingly, one would expect a good target choice would be such as to have a minimum in S_1 and a maximum in S_o ($A \sim 160$). However, a minimum in p -wave scattering implies a smaller cross-section thus making the measurement more difficult. Thus a more judicious choice has be made such that S_1 is large enough

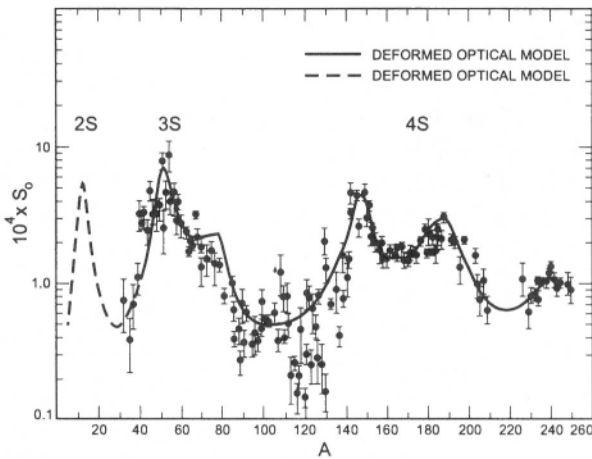


Fig. 2.1. The s -wave neutron strength function plotted against mass number (A) [2].

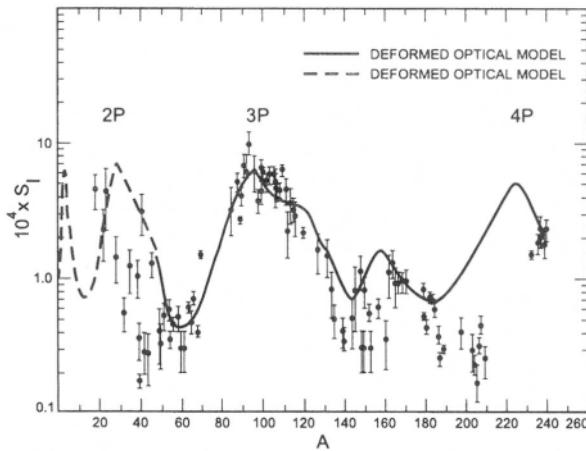


Fig. 2.2. The p -wave neutron strength function plotted against mass number (A) [2].

to make the p -wave cross-section easy measurable and yet maintaining $\sqrt{\frac{S_o}{S_1}}$ as large as possible.

Having dwelt upon the physical parameters in the longitudinal asymmetry which would help make the optimal choice of neutron energy and target mass we turn now to the experimental results, obtained using an experimental set up as shown in Fig. 2.3 (for details see, e.g., Ref. [5]). A typical measurement of the helicity dependence of the neutron cross section at a p -resonance is shown in Fig. 2.4 for ^{238}U .

It has been shown by the TRIPLE group [7, 8, 9, 10, 11, 12, 13, 14, 15, 16] that the P_i data for all targets except ^{232}Th are consistent with an average value of P_i equal to zero (see Table 2.1), in accordance with the statistical nature of the compound nucleus. As an example we show in Fig. 2.5 P_i vs. E_n for $n + ^{238}\text{U}$ for $0 < E_n < 300\text{eV}$.

The analyses were performed using a generalized form Eq. (2.2),

$$P_i = \sum_j \left(\frac{2}{E_j - E_i} \sqrt{\frac{\Gamma_j}{\Gamma_i}} \right) V_{ij} \equiv \sum_j A_{ij} V_{ij}. \quad (2.5)$$

Thus since $\bar{V}_{ij} = 0$, $\bar{P} = 0$. This is confirmed for $^{107+109}\text{Ag}$, ^{113}Cd , ^{115}In , ^{127}I and ^{238}U . The *rms* value of V_{ij} , defined by

$$M^2 \equiv \langle |V_{ij}|^2 \rangle, \quad (2.6)$$

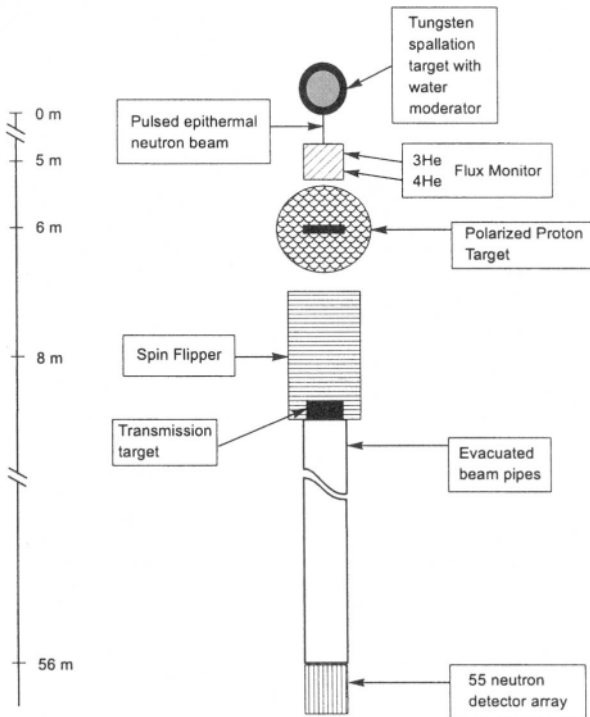


Fig. 2.3. The TRIPLE experimental system [7–16].

was found to be $M \approx 1 \text{ meV}$, which corresponds to a PNC spreading width $\Gamma_{PNC}^\downarrow = 2\pi \frac{M^2}{D}$ of the order of $1.35 \times 10^{-7} \text{ eV}$. Table 2.2 summarizes the results for several targets.

The ^{232}Th case warrants special care. In Fig. 2.6 we show the p -wave asymmetries for $n + ^{232}\text{Th}$ at $0 < E_n < 300 \text{ eV}$. Here the average value of P_i is large and positive, in the resonance region, $\bar{P}_i \approx 0.04$. The contribution of the background here is almost three orders of magnitude smaller [8], consistent with zero value for $\langle P_{nonres} \rangle$. Statistical analysis done in this case yielded value for the *rms* value of the PNC matrix element M , and the corresponding PNC spreading width Γ_{PNC}^\downarrow which is of the same order of magnitude as in the other cases that have been already mentioned. More recent data on this system indicated that $\langle P \rangle$ dips into negative values at $E_n \geq 300 \text{ eV}$ [19]. So far only one

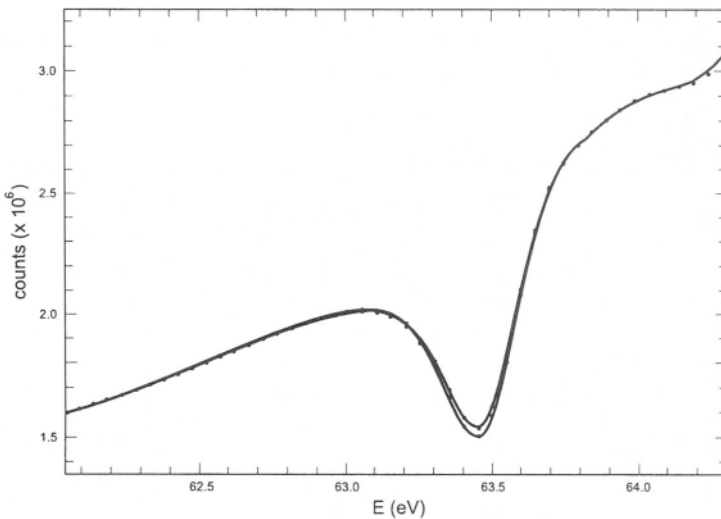


Fig. 2.4. Transmission spectra for the two helicity states near the 63-eV resonance in ^{238}U .
The resonance appears as a dip in the transmission curve. Since the transmission at the resonance is significantly different for the two helicity states, the parity violation is apparent by inspection [2].

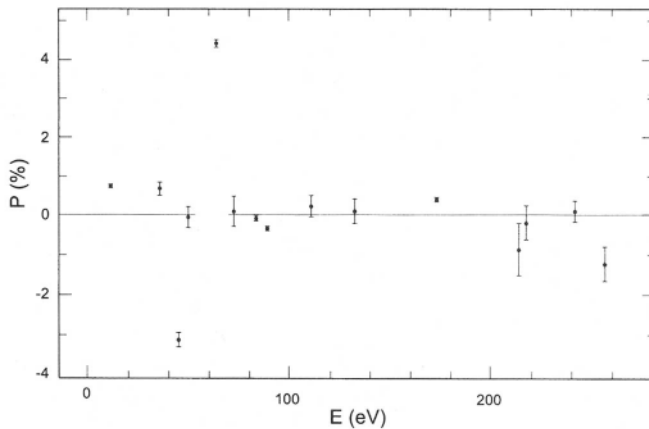


Fig. 2.5. Parity violating asymmetries P versus neutron energy E_n for ^{238}U [10].

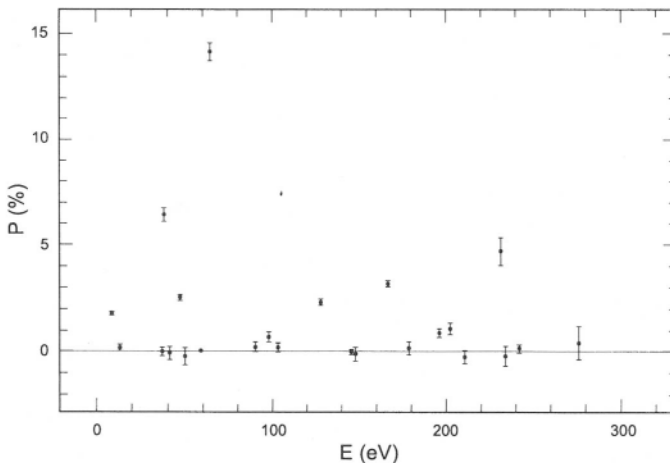


Fig. 2.6. Parity violating asymmetries P versus neutron energy E_n for ^{232}Th [9].

point was measured in this region. It would be of great importance to extend the measurement to higher energies to verify the average trend of \bar{P} .

In order to understand the origin of the non-zero value of $\langle P_i \rangle$ for Thorium, we shall apply in the following sections the hierarchy-of-complexity description of section 3. We shall show that the origin of the non-statistical behavior in P_i can be traced to simple p -wave $2p - 1h$ doorway states which are parity mixed with nearby s -wave $2p - 1h$ doorways.

Further, we shall demonstrate that a more appropriate quantity to analyze is the cross-section difference, $\Delta\sigma_i \equiv \sigma_i^{(+)} - \sigma_i^{(-)} \approx 2\sigma_i P_i$. The reason being that the average $\langle \Delta\sigma_i \rangle$ can be directly compared to optical model calculation. Further, in cases where the σ 's are small and difficult to measure, as is the case at higher neutron energies, one would be bound to be content with the analysis of $\Delta\sigma$.

To conclude, the experimental findings of the TRIPLE Collaboration can be summarized as follows

1. The longitudinal asymmetries, P_p , for p -wave resonance scattering of epithermal neutrons from several targets are large.
2. The average longitudinal asymmetry, $\langle P \rangle$, is roughly zero for all cases studied except in ^{232}Th where it is found to be positive and significant (~ 0.04).

TABLE 2.2
 Weak spreading widths $\Gamma^{\downarrow} = 2\pi v^2/D$ obtained by the
 TRIPLE Collaboration [7, 8, 9, 10, 11, 12, 13, 14, 15, 16].

NUCLEUS	$\Gamma^{\downarrow}(10^{-7} \text{ eV unless noted})$		
⁹³ Nb		<1.0	
¹⁰³ Rh	1.42	+1.4	
		-0.59	
¹⁰⁷ Ag	2.67	+2.65	
		-1.21	
¹⁰⁹ Ag	1.30	+2.44	
¹⁰⁴ Pd	2.53	+10.4*	
		-1.7	
¹⁰⁶ Pd	3.6	+5.1 $\times 10^{-6}$	
		-2.4	
¹⁰⁸ Pd		<1.2 $\times 10^{-6}$	
¹¹³ Cd	16.4	+18.0	
		-8.4	
¹¹⁵ In	0.91	+0.54	
		-0.30	
¹¹⁷ Sn	0.86	+1.94*	
		-0.54	
¹²¹ Sb	6.45	+9.72*	
		-3.66	
¹²³ Sb	1.2	+15.0*	
		-0.96	
¹²⁷ I	2.05	+1.91*	
		-0.43	
¹³³ Cs	0.006	+0.154*	
²³² Th	9.7	+2.7	
²³⁸ U	1.35	+0.97	

3. The average longitudinal asymmetries of all cases studied in the off-resonance region are practically zero.
4. The PNC spreading width is found to be weakly dependent on the mass number of the compound nucleus involved ($\Gamma^{\downarrow} \sim A^{1/3}$) with average value of $\sim 10^{-7}$ eV [20].

3. SYMMETRY VIOLATION WITHIN REACTION THEORY

At very low energies one expects the population of widely spaced, isolated, resonances in the compound nucleus. To describe the scattering

problem, we use the unified theory of nuclear reactions of Feshbach [21] together with the optical background representation (OBR) method developed by Kawai, Kerman and McVoy [22]. We also allow for the existence of a single doorway to test its influence. Further, we allow the Hamiltonian of the system to be a general one, containing both PNC and TRSB terms.

The many-body Schrödinger equation describing the n + Target system can be written as usual, within the Feshbach formalism:

$$\begin{aligned} (E - PHP)P\Psi &= PHQQ\Psi \\ (E - QHQ)Q\Psi &= QHPP\Psi, \end{aligned} \quad (3.1)$$

where P projects onto the elastic channel, as well as the 2p-1h doorway state, and Q onto the compound states. We consider all the subspace Hamiltonians to contain a symmetry conserving part H_s , and symmetry violating part, H_y . The second equation in (3.1) can be formally solved for $Q\Psi$, and when the solution is inserted into Eq. (3.1), we obtain:

$$\begin{aligned} (E - PHP - PHQH_QQHP)P\Psi &= 0 \\ G_Q &= \frac{1}{E - QHQ}. \end{aligned} \quad (3.2)$$

We now perform the OBR on Eq. (3.2). We do this by writing:

$$G_Q = \bar{G}_Q + (G_Q - \bar{G}_Q) \quad (3.3)$$

where \bar{G}_Q is the energy-averaged compound propagator which is given by

$$\bar{G}_Q = \frac{1}{E - QHQ + iI/2} \quad (3.4)$$

with I denoting the energy interval that contains many compound resonances but still smaller than the width of the doorway.

Equation (3.2) can be written as:

$$G_Q = \bar{G}_Q + \bar{G}_Q^{1/2}(iI/2)G_Q\bar{G}_Q^{1/2} \quad (3.5)$$

and thus we can write formally:

$$\begin{aligned}
& (E - PHP - PHQ\bar{G}_Q QHP)P\Psi \\
&= PHQ\bar{G}_Q^{1/2} \left(\frac{iI}{2}\right)^{1/2} G_Q \left(\frac{iI}{2}\right)^{1/2} \bar{G}_Q^{1/2} QHP P\Psi \\
&\equiv PVQG_Q QVP P\Psi, \\
PVQ &\equiv PHQ\bar{G}_Q^{1/2} \left(\frac{iI}{2}\right)^{1/2} \tag{3.6}
\end{aligned}$$

We then obtain the desired solution:

$$\begin{aligned}
P\Psi &= \overline{P\Psi} + G_{Opt}^{(+)} PVQ \frac{1}{E - QHQ - QVPG_{Opt}^{(+)} PVQ} QVP P\Psi \\
&\equiv \overline{P\Psi} + P\Psi^{\dagger} \tag{3.7}
\end{aligned}$$

The energy average of the second term on the RHS of Eq. (3.7) is identically zero by construction. The solution $P\Psi$ is the optical model wave function and $G_{Opt}^{(+)}$ is:

$$G_{Opt}^{(+)} = (E - PHP - PHQ\bar{G}_Q QHP + i\varepsilon)^{-1} \tag{3.8}$$

The S-matrix element for the transition $a \rightarrow b$ is directly obtained from the asymptotic form of $P\Psi$:

$$S_{ab} = \bar{S}_{ab} - i \sum_q \frac{\tilde{\gamma}_{qa}\gamma_{qb}}{E - \varepsilon_q} \tag{3.9}$$

where \bar{S}_{ab} is the optical + doorway S-matrix while the γ 's are given by:

$$\gamma_{qa} = \sqrt{2\pi} \langle \tilde{q} | H_{QP} | \Psi_a^{(+)} \rangle \tag{3.10}$$

$$\tilde{\gamma}_{qa} = \sqrt{2\pi} \langle \Psi_a^{(-)} | H_{PQ} | q \rangle \tag{3.11}$$

In the above equations $|\Psi_a^{(+)}\rangle$ is the optical + doorway solution ($P\Psi^{(+)}$) and the complex energies, ε and vectors $|q\rangle$ and $\langle\tilde{q}|$ are the solutions of the equations:

$$(QHQ + QVPG_{Opt}^{(+)} PVQ) |q\rangle = \varepsilon_q |q\rangle \tag{3.12}$$

$$(QHQ^+ + (QVPG_{Opt}^{(+)} PVQ)^+) |\tilde{q}\rangle = \varepsilon_q^* |\tilde{q}\rangle \tag{3.13}$$

We set $\varepsilon_q = E_q - i\Gamma_q/2$.

Equation (3.9) is the starting point for discussing symmetry violation in nuclei. For PNC, $\tilde{\gamma} = \gamma$. However, γ depends on the helicity of the impinging neutron. Here one attaches to γ the helicity label, $\gamma^{(\pm)}$. For TRSB, $\tilde{\gamma} \neq \gamma$ and one has to define and calculate the observables sensitive to the difference $(\tilde{\gamma} - \gamma)$. This is left out to Section 8.

In discussing Eq. (3.9) one has assumed that all the compound nucleus states can be treated on the same footing. However, if simple $2p - 1h$ doorway states are present and should be considered explicitly, the formalism above can be easily generalized. For this purpose a further splitting of the projection operator Q is required $Q = D + q$, where D is the doorway projectors. If P is assumed to be coupled to the genuine compound states projected off by q , only through D , one can obtain easily the necessary modifications in the physical observables [21, 23]. Depending on convenience, one may take D to be part of a new P projector, namely $P' = P + D$ and q .

Assuming that the doorway state is contained in P' , allows the γ_{qa} 's to have the following structure:

$$\gamma_{qa} = \gamma_{qD} C_{Da} \quad (3.14)$$

where the coefficients C_{Da} are random in sign and average to zero over many resonances. Further, the same doorway state would cause correlation among channels to which it is coupled to. A full account of the formalism with ideas of intermediate structure and doorways has been given long time ago [24] and has been reviewed recently by Feshbach [21]. Thus we shall not repeat this formalism here, but point out in the next section the qualitative effect the doorway state has on the scattering observables.

In the following, we discuss the application of the reaction theory to PNC and TRSB. For this purpose, it is useful to write the scattering amplitude that is obtained from S_{ab} , Eq. (3.9), for a given partial wave

$$f_{ab} = \bar{f}_{ab} - \frac{1}{2k} \sum_q \frac{\tilde{\gamma}_{qa} \gamma_{qb}}{E - E_q - i\Gamma_q/2}. \quad (3.15)$$

The total cross-section, $\sigma_T^{(a)}$ is directly obtained from f_{aa} through the optical theorem. For very low energy neutrons, $l = 0$ dominates, and we can write

$$\sigma_T^{(a)} = \frac{4\pi}{k} Im f_{aa} = \frac{4\pi}{k} Im \bar{f}_{aa} - \frac{\pi}{k^2} \sum_q \frac{\Gamma_q \tilde{\gamma}_{qa} \gamma_{qa}}{(E - E_q)^2 + \Gamma_q^2/4}. \quad (3.16)$$

4. PARITY NONCONSERVATION (PNC) IN THE COMPOUND NUCLEUS

From the previous section, The cross-section for positive helicity, $\sigma^{(+)}$, and negative helicity, $\sigma^{(-)}$, for p -wave resonances can be generally written as

$$\sigma_p^{(\pm)} = \frac{4\pi}{k} \text{Im}f_p^{(\pm)}(0) \quad (4.1)$$

where $f^{(\pm)}$ is given by

$$f_p^{(\pm)} = \bar{f}_p^{(\pm)} - \frac{\xi}{2k} \frac{\gamma_p^{(\pm)} \gamma_p^{(\pm)} e^{2i\delta(\pm)}}{E - E_p + i\Gamma_p/2} \quad (4.2)$$

Above, ξ is the factor $2l + 1$ for p -waves, $\gamma_p^{(\pm)} = \gamma_p^S + \gamma_p^W$, $\Gamma_p = (\gamma_p^S)^2$ with $S(W)$ standing for the strong (weak) resonance amplitude. Since $\gamma_p^S \gg \gamma_p^W$, we can write

$$f_p^{(\pm)} = \bar{f}_p^{(\pm)} - \frac{1}{2k} \frac{(\gamma_p^S)^2 \pm 2\gamma_p^W \gamma_p^S}{E - E_p + i\Gamma_p/2} \quad (4.3)$$

Thus, at a p -wave resonance, $E = E_p$, and taking γ_p^S, γ_p^W to be real,

$$\sigma_p^{(\pm)} \simeq \bar{\sigma}_p^{(\pm)} + \frac{4\pi}{k^2} \frac{(\Gamma_p^2 \pm 2\gamma_p^W \gamma_p^S)}{\Gamma_p}, \quad (4.4)$$

Eq. (4.4) is the basic formula used to analize PNC in the compound nucleus. If we ignore the contribution of $(\bar{\sigma}_p^{(+)} - \bar{\sigma}_p^{(-)})$ [8] then we get

$$P_p = \frac{\sigma_p^{(+)} - \sigma_p^{(-)}}{\sigma_p^{(+)} + \sigma_p^{(-)}} = 2 \frac{\gamma_p^W}{\gamma_p^S}. \quad (4.5)$$

for each resonance.

Using first order perturbation theory for the treatment of the PNC interaction, we use the following form for the p -state wave function

$$|p'_{1/2}\rangle = |p_{1/2}\rangle + \sum_s \frac{|s_{1/2}\rangle}{E_s - E_p} \langle s_{1/2}|V_{PNC}|p_{1/2}\rangle \quad (4.6)$$

The state $|p'_{1/2}\rangle$ is what we called $|q\rangle$ in Eq. (3.15). With (4.6), we have for $\gamma_{p_{1/2}}^W$, the following (see Eq. (3.11) for the definition of $\tilde{\gamma}_{qa}$, which is equal to $\gamma_{q,a}$ when time reversal symmetry is not violated)

$$\gamma_{p_{1/2}}^W \equiv \sqrt{2\pi} \sum_s \langle \psi_q^{(-)} | H_{pq} | s_{1/2} \rangle \frac{1}{E_s - E_p} \langle s_{1/2} | V_{PNC} | p_{1/2} \rangle \quad (4.7)$$

$$= \sum_s \gamma_{s_{1/2}}^s \frac{1}{E_s - E_p} V_{sp}^{PNC} \quad (4.8)$$

Notice that $|s_{1/2}\rangle$ and $|p_{1/2}\rangle$ are complicated compound nucleus states. We shall use the labels v and μ to designate $|s_{1/2}\rangle$ and $|p_{1/2}\rangle$, respectively.

With (4.8), we obtain the well-known formula for P_μ

$$P_\mu = 2 \sum_v \frac{1}{E_v - E_\mu} \frac{\gamma_v^s}{\gamma_\mu^s} V_{\mu,v}^{PNC} \quad (4.9)$$

or

$$P_\mu = 2 \sum_v \frac{1}{D_{\mu,v}} \left(\frac{\Gamma_v^s}{\Gamma_\mu^s} \right)^{1/2} V_{\mu,v}^{PNC} \quad (4.10)$$

where $D_{\mu,v} \equiv E_v - E_\mu$ and Γ_q is the neutron width of level q .

The statistical theory of the compound nucleus tells us that the Γ_q 's obey the Porter-Thomas distribution, the energy spacing of levels with mixed parities the Poisson distribution and the weak matrix element $V_{\mu,v}^{PNC}$ is Gaussian distributed with a zero mean value, $\langle V_{\mu,v}^{PNC} \rangle = 0$. Accordingly, $\langle P_\mu \rangle = 0$. The average value of P_μ^2 can be related to the second moment of the $V_{\mu,v}^{PNC}$ distribution, $M^2 = \langle (V_{\mu,v}^{PNC})^2 \rangle$

$$\begin{aligned} \langle P_\mu^2 \rangle &= \left\langle \sum_v \frac{1}{D_{\mu,v}} \left(\frac{\Gamma_v}{\Gamma_\mu} \right)^{1/2} \frac{1}{D_{\mu',v}} \left(\frac{\Gamma_{\mu'}}{\Gamma_\mu} \right)^{1/2} V_{\mu,v}^{PNC} V_{\mu',v}^{PNC} \right\rangle \\ &= \left\langle \sum_\mu \frac{1}{D_{\mu,v}^2} \left(\frac{\Gamma_\mu}{\Gamma_\mu} \right) \right\rangle M^2 \\ &\equiv A_\mu^2 M^2 \end{aligned} \quad (4.11)$$

The quantity A_μ^2 can be calculated for each $p_{1/2}$ resonance. From the experimental data one determines the ensemble average of P_μ^2 and thus from Eq. (4.11), the important quantity M^2 is found. This quantity is directly related to the average weak spreading width of a given p -wave nuclear level

$$\Gamma^\downarrow = \left\langle \frac{2\pi |\langle \mu | V^{PNC} | v \rangle|^2}{D_v} \right\rangle \quad (4.12)$$

$$\Gamma^\downarrow \simeq 2\pi \frac{M^2}{D} = 2\pi M^2 \rho \quad (4.13)$$

with ρ being the density of states of the $s_{1/2}$ levels. Since M goes roughly as $\frac{1}{\rho^{1/2}}$, we expect Γ^\downarrow to be weakly dependent on excitation energy and as a consequence on the mass number of the nucleus [20]a. The results of the TRIPLE data [7, 8, 9, 10, 11, 12, 13, 14, 15, 16] summarized in Section 2 seems to bear out all of the above properties of the PNC in the compound nucleus except for ^{232}Th , where $\langle P_\mu \rangle$ was found to be large and positive ($\langle P_\mu \rangle \sim 0.038 \pm 0.013$ [9]b).

5. THE SIGN CORRELATION PROBLEM AND THE ROLE OF $2P - 1H$ DOORWAY STATES

We discuss in what follows a possible cause of the large and positive value of $\langle P \rangle$ in ^{232}Th . Several theories have been proposed in the recent literature. These range from distant doorways [25], to parity doublets owing to octupole deformation [26, 27]. A very good account of the theoretical literature can be found in Ref. [28]. In the following we describe the model of Ref. [29].

A very natural mechanism that could account for this sign correlation is to assume that the compound nuclear process occurs through a *single* dominantly p-wave *local* doorway which contains a small parity violation. For simplicity we start with this extreme hypothesis. Below we will consider the more general case including more doorways. This doorway is relatively simple but statistical combination of two particle-one hole ($2p - 1h$) states in ^{233}Th . In passing we note that it is the dominance of local doorways which may give rise to intermediate structure in the energy dependence of nuclear cross-sections and their statistical nature which gives rise to fluctuations in strength functions from nucleus to nucleus over and above the general optical model trend [23, 24]. We stress that our local doorway states [29] are statistical in nature, in contrast to the collective 0^- doorway (giant monopole) states considered by Auerbach and others [25] as responsible for the sign correlation. We assume that parity violation occurs through the coupling of our p-wave doorway to an s-wave doorway, located nearby. Then:

$$\gamma_q = C_{qD} \gamma_{Dp}, \quad \gamma_q^w = C_{qD} \gamma_{Ds}^w \quad (5.1)$$

where C_{qD} are taken to be random. Taking D to be in the vicinity of the compound resonances in question, we obtain with the aid of perturbation theory:

$$P = 2 \frac{\gamma_{Ds}^w}{\gamma_{Dp}} \quad (5.2)$$

which represents the average value of P , being independent of q . In Eq. (5.2) M^w is a characteristic weak matrix element between p- and s-doorways and ΔE is the corresponding characteristic energy distance between these doorway states given by, e.g.,

$$\begin{aligned} \Delta E &\approx \left| \left(E_{D2} - \frac{i\Gamma_{D2}}{2} \right) - \left(E_{D1} - \frac{i\Gamma_{D1}}{2} \right) \right| \\ &= \left[(E_{D2} - E_{D1})^2 + \frac{(\Gamma_{D1} + \Gamma_{D2})^2}{4} \right]^{1/2} \end{aligned} \quad (5.3)$$

In order to estimate the size of (5.2) we take the smooth energy dependence out of the partial width amplitude in the usual fashion, i.e. we define $(1/kR)$ ($\gamma^{(0)} / \gamma_{Dp}^{(0)}$), where $\gamma^{(0)}$ are the reduced widths. Thus:

$$\langle P \rangle = 2 \frac{M^w}{\Delta E} \frac{\gamma_{Ds}^{(0)}}{\gamma_{Dp}^{(0)}} \frac{1}{kR} \quad (5.4)$$

which will have a definite sign for a given nucleus as seen in the data.

Properties of simple two particle-one hole states can be deduced from the exciton model, usually employed in pre-equilibrium studies [30]. The density of 2p – 1h doorway states coupled to total angular momentum J at an excitation energy E^* in the compound nucleus is given by [31]

$$\rho_{2p-1h}(E^*, J) = \frac{g^3 E^{*2}}{4} \frac{(2J+1) \exp[-(j+1/2)/3\sigma^2]}{(27\pi)^{1/2} \sigma^3} \quad (5.5)$$

where g is the average spacing of single particle levels, and σ is the spin cut-off parameter. For the deformed nucleus ^{233}Th , $g \approx 10 \text{ MeV}^{-1}$, $\sigma \approx 4.0$, and taking $E^* = 6 \text{ MeV}$, $J = 1/2$, we find $\rho_{2p-1h} \approx 34 \text{ MeV}^{-1}$. Thus the average spacing, $D_{2p-1h} = (\rho_{2p-1h})^{-1} \approx 30 \text{ keV}$. For a simple local doorway to dominate the 2p – 1h doorways must not be overlapping. Thus we take

$\Gamma \approx D \approx 30 \text{ keV}$. Then ΔE of Eq. (5.4) becomes roughly $\Delta E \approx \sqrt{2} \Gamma_D \approx 50 \text{ keV}$.

Taking for $M^w \approx 1.0 \text{ eV}$ [1] and $kR \approx 10^{-3}$ for $E_n \approx 1 \text{ eV}$, we find that the data ($\langle P \rangle = 0.04$) require:

$$\left| \frac{\gamma_{Ds}^{(0)}}{\gamma_{Dp}^{(0)}} \right| \approx 2$$

which seems to contradict the fact that p-waves are resonant while s-waves are off resonance. This requires an enhancement which may come about if the particular statistical doorway involved in M^w couples strongly to s and less so to p or if the particular matrix element M^w is larger than average. This will be a statistical phenomenon associated with random properties of the local doorways.

The fluctuation part of P can also be analyzed within the local doorway model. If we consider nearby local doorways which for simplicity we collectively call D' , then:

$$\gamma_q = C_{qD}\gamma_{Dp} + C_{qD'}\gamma_{D'p}, \quad \gamma_q^w = C_{qD}\gamma_{Ds}^w + C_{qD'}\gamma_{D's}^w \quad (5.6)$$

where:

$$C_{qD} < C_{qD'} \quad (5.7)$$

on average. Then:

$$P = \frac{\gamma_{Ds}^w}{\gamma_{Dp}} + \frac{C_{qD'}}{C_{qD}} \left[\frac{\gamma_{D's}^w}{\gamma_{Ds}^w} - \frac{\gamma_{D'p}}{\gamma_{Dp}} \right] \quad (5.8)$$

The variance of P is then given by

$$v \equiv \sqrt{\langle P^2 \rangle - \langle P \rangle^2} \approx \sqrt{\left\langle \left| \frac{C_{qD'}}{C_{qD}} \right|^2 \right\rangle} \left| \frac{\gamma_{D's}^w}{\gamma_{Ds}^w} - \frac{\gamma_{D'p}}{\gamma_{Dp}} \right| \quad (5.9)$$

From Ref. [2] we find v to be about unity. Because of (5.7), we find

$$\left| \frac{\gamma_{D's}^w}{\gamma_{Ds}^w} - \frac{\gamma_{D'p}}{\gamma_{Dp}} \right| > 1 \quad (5.10)$$

which is entirely reasonable. Thus the fine structure analysis furnishes us with constraining relations involving the weak and strong decay amplitudes of D and D' .

In the above discussion we presented qualitative considerations concerning the role of the simple $2p - 1h$ doorway states in the sign cor-

relations seen in the longitudinal asymmetry of epithermal neutrons scattered from ^{232}Th . We emphasised the statistical nature of these simple nuclear states. Further, a typical nucleus which does not show the sign correlation phenomenon, and belong to the same actinide family, ^{238}U , is used to elucidate better the phenomenon. An important physical quantity that enters in the analysis is the density of states of these doorways. In the following we present a detailed quantitative calculation of ρ_{2p-1h} in both ^{233}Th and ^{239}U , using a deformed mean field description of these nuclei. The details of the calculation can be found in a recent preprint [32]. The method used is the microscopic combinatorial approach of [33]. The numerical results for ρ_{2p-1h} are compared with analytical, equidistant model, formula of Ericson (Williams's formula) [31]. Effects of deformation on the level density has been first studied by Bjornholm, Bohr and Mottelson [34] within the Bethe-Fermi theory. Here we have extended their studies to the calculations of the density of states within the exiton model.

In Ref. [32], a microscopic combinatorial approach is used to calculate the level densities for a given number of excitons (# of excitons = # of particles + # of holes) using a deformed Saxon-Wood shell model. The details of this model are given in Ref. [33]. A part of the residual interaction, namely pairing, was taken into account by applying the BCS theory to each configuration. Both the spin and parity distributions were obtained and the effect of deformations is assessed. Quadrupole and octupole deformations are taken into account.

The result for ρ_{2p-1h} for ^{233}Th and ^{239}U are shown in Fig. 5.1 for the $j = 1/2$ positive parity levels. The density of negative parity $j = 1/2$ states is in principle the same (see, however, below). In the same figure the results obtained from the Ericson formula for ρ_{2p-1h} of Eq. (5.5) is also shown for comparison. It is clear from the figure that Eq. (5.5) underestimates ρ_{2p-1h} at $E^* = 6.0\text{ MeV}$ in ^{233}Th and ^{239}U (corresponding to $E_n \sim 1\text{ eV}$ on ^{232}Th and ^{238}U) by a factor of 3. This stems not so much from the equidistant single particle level approximation of the Ericson formula but rather almost exclusively from deformation [32]. This is clearly seen when a spherical S-W potential is used, Fig. 5.2. With the above, the average spacing, D , at the above excitation energy is roughly the same for both ^{233}Th and ^{239}U and is about $D \approx 10\text{ keV}$. This is, as expected, three times smaller than the value employed in Ref. [29] and used in the previous section.

An interesting feature of the result concerns the number of positive and negative parity states for a given value of j . In Fig. 5.3 we show

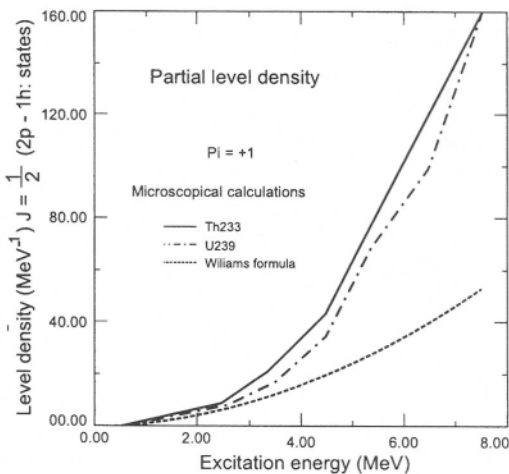


Fig. 5.1. The $2p - 1h$ level density for ^{239}U and ^{233}Th . The Microscopic Combinatorial Method results are compared with the equidistant Ericson formula. See text and Ref. [32] for details.

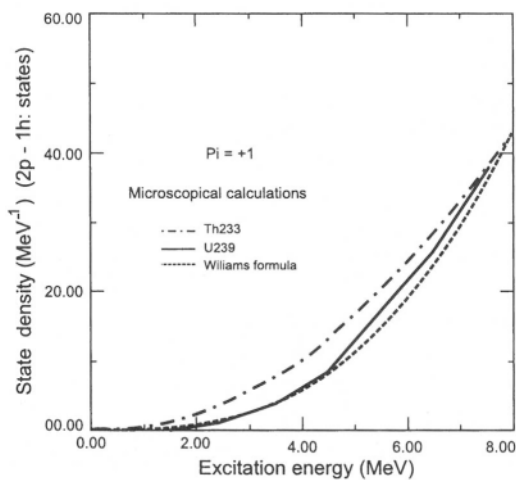


Fig. 5.2. Same as Fig. 5.1 but with no deformation.

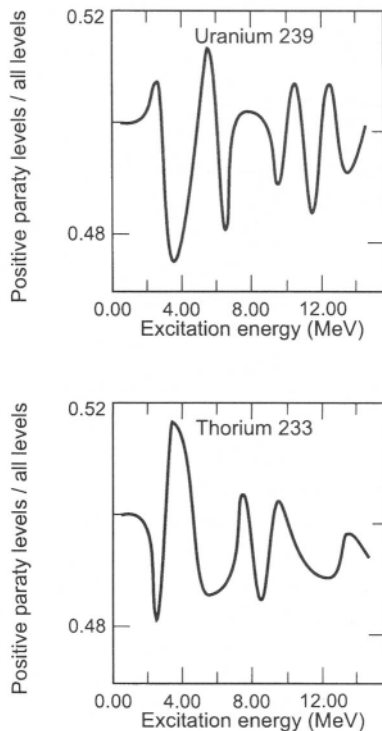


Fig. 5.3. The parity distribution of levels obtained using the Microscopic Combinatorial Method [32].

the fraction, $\frac{(+)}{(+)+(-)}$ of positive parity levels (with respect to all levels) for $j = 1/2$ in ^{239}U (a) and ^{233}Th (b) vs. excitation energy. The sharp, albeit small magnitude, oscillation around the value 0.5 is very clear. Clearly the fraction of negative parity levels, $\frac{(-)}{(+)+(-)}$, is given by the value in Figure (8) subtracted from unity. At $E^* \sim 6\text{ MeV}$, the negative parity fraction for ^{239}U is ~ 0.49 , while it is 0.51 in ^{233}Th . This translates into $D_{2p-1h}^{(-)}(^{233}\text{Th}) \approx 11\text{ keV}$ and $D_{2p-1h}^{(-)}(^{238}\text{U}) \approx 13\text{ keV}$. This fact encouraged several authors [26, 27] to suggest that the pear-like shape associated with octupole deformation results in parity doublets which when taken explicitly into account can, in principle, lead to positive longitudinal asymmetry. This suggestion, however, was shown to be inconsistent with actual doublet spacings seen in ^{233}Th [35]. Further, and more importantly, recent measurement on ^{238}U [36] has unambiguously demonstrated that this

nucleus also has significant octupole deformation. Thus from the collective point of view ^{233}Th and ^{239}U are very similar.

The presence of a dominant local doorway that gives rise to a large value of $\langle P \rangle$ is certainly possible in some nuclei. The probability P that $|\gamma_{Ds}^{(0)}/\gamma_{Dp}^{(0)}|$ is, say f , can be calculated as follows. Since the local doorways are statistical in nature, the γ_{Ds}^0 and γ_{Dp}^0 are the Gaussian distributed with about the same width. We thus have:

$$P\left(\left|\frac{\gamma_{Ds}^{(0)}}{\gamma_{Dp}^{(0)}}\right|=f\right)=\frac{1}{\pi} \int_{-\infty}^{+\infty} dx \int_{-\infty}^{+\infty} dy e^{-(x^2+y^2)} \delta\left(\left|\frac{x}{y}-f\right|\right)=\frac{2}{\pi} \frac{1}{1+f^2} \quad (5.11)$$

Thus, within our model, the probability for the occurrence of the phenomenon of large parity violation *with* sign correlation goes as $(1+f^2)^{-1}$, which is small for $f \approx 2$ which we found in $\text{n} + ^{232}\text{Th}$. Therefore such a phenomenon is not a global one that is exhibited by nuclei over the periodic table. It happens in ^{232}Th due to a statistical fluctuation among the properties of local doorways. In fact, in all other systems studied by the TRIPLE Group the average value of P was found to be zero and its magnitude smaller so that $f \approx 1$. This implies that a local dominant $2p - 1h$ doorway state, seemingly so conspicuous in ^{233}Th , does not occur in the other nuclei studied. With no single dominant doorway present, e.g. if two closely spaced doorways are relevant in the energy region of interest, the sign correlation disappears.

Our analysis points to the conclusion that the phenomenon of "sign correlation" is purely a conventional nuclear structure problem, and it is not connected to "exotics". Further, the phenomenon occurs in Th by statistical accident. Before ending we mention that in Th the single particle p-wave is resonant whereas the s-wave is not. Even so, $f = |\gamma_{Ds}^{(0)}/\gamma_{Dp}^{(0)}|$ was found to be about 2. It seems to us that a more favorable case would be to have the p-wave off-resonance and the s-wave on ($A \approx 170$). This would give rise to a larger f , with higher probability. Of course, this will be experimentally more difficult because the p-wave resonances in this region may be too narrow.

6. OPTICAL MODEL DESCRIPTION OF PNC

Our doorway picture emphasizes the role of a local $2p - 1h$ doorway state which is responsible for the weak coupling between the p and s waves. In ^{232}Th , this doorway state is reasonably well separated from other doorways, whereas in, e.g., ^{238}U , where no sign correlation is seen,

there are several 2p – 1h doorways present in the energy range of interest. In the following we address another question also relevant to the parity non-conserving (PNC) neutron reaction, namely to what extent is the total cross-section difference $\langle \Delta\sigma_q \rangle$ accounted for by an optical model which contains an appropriate one-body PNC. The quantity $\langle \Delta\sigma_q \rangle$ is just $\sigma_q^{(+)} - \sigma_q^{(-)}$ where σ_q is the cross-section at the q th p -resonance and the superscripts +(-) refer to positive (negative) helicity of neutrons.

Before we start our discussion of the optical model analysis, we give first a derivation of the symmetry violating optical potential, based on the theoretical discussion presented in Section 3.

The optical model operator can be read off from Eq. (3.6), if we write $H = H_0 + V$, with H_0 being diagonal in channel space and V is the interaction:

$$\begin{aligned} V_{opt} &\equiv PVQ\bar{G}_Q QVP + PVP \\ \bar{G}_Q &= (E - QHQ + iI)^{-1} \end{aligned} \quad (6.1)$$

Writing V as a symmetry conserving piece V_s , plus a symmetry violating piece V_v , we may write, to first order in V_v :

$$\begin{aligned} V_{opt} &= PV_s P + PV_v P + PV_s Q \bar{G}_Q^s Q V_s P + P_v Q \bar{G}_Q^s Q V_s P \\ &\quad + PV_s Q \bar{G}_Q^s Q V_v P + PV_s Q \bar{G}_Q^s Q V_v Q \bar{G}_Q^s Q V_s P \end{aligned} \quad (6.2)$$

Thus the symmetry violating part of V_{opt} is:

$$\begin{aligned} V_{opt,v} &= PV_s P + PV_v Q \bar{G}_Q^s Q V_s P + PV_s Q \bar{G}_Q^s Q V_v P \\ &= PV_v P + PV_v^D(E)P \end{aligned} \quad (6.3)$$

where we have denoted by $V_v^D(E)$ the dispersive component of the symmetry violating part of the optical potential. From the general properties of \bar{Q}_Q^s we may write a dispersion relation for $V_v^D(E)$:

$$ReV_v^D(E) = \frac{P}{\pi} \int \frac{ImV_v^D(Z)}{Z - E} dZ, \quad (6.4)$$

where P stands for the principal value.

So far in the application to data analysis of PNC, the dispersion component has been dropped. As for $PV_v P$, it is common to use an expression obtained by Michel [37]:

$$PV_v P = \{\vec{\sigma} \cdot \vec{p}, v(r)\} \quad (6.5)$$

Where the symmetrical form insures Hermiticity and the real nature of V_v guarantees evenness under time reversal.

The calculation described below use the form (6.5). It would be interesting to assess the importance of the dispersion part of the PNC interaction $PV_v^D(E)P$. This we leave for a future work. The optical model approach to the longitudinal asymmetry has been considered in [38, 39, 40, 41].

The interaction of a neutron with a spin zero target of mass number A is taken to be the sum of complex strong (parity conserving, PC) and weak (parity non-conserving, PNC) potentials.

$$V = V_S(r) + V_{PNC} \quad (6.6)$$

$$V_S(r) = U(r) + V_{SO}(r)\vec{I} \cdot \vec{S} \quad (6.7)$$

$$V_{PNC} = PV_vP = \vec{\sigma} \cdot \vec{p} v(r) + v(r) \vec{\sigma} \cdot \vec{p} \quad (6.8)$$

The scattering amplitude which describes the scattering of neutrons from a spin zero target nucleus is generally given by [40]

$$\begin{aligned} F(\theta) &= F_S(\theta) + F_{PNC}(\theta) \\ F_S(\theta) &= f(\theta) + i\vec{\sigma} \cdot (\hat{k} \times \hat{k}') \cdot g(\theta) \end{aligned} \quad (6.9)$$

and

$$F_{PNC}(\theta) = -\vec{\sigma} \cdot (\hat{k} + \hat{k}') \cdot h(\theta) \quad (6.10)$$

Partial wave expansion yields

$$\begin{aligned} f(\hat{k} \cdot \hat{k}') &= \frac{1}{k} \sum_l [(l+1)t_l^{j=l+1/2} + lt_l^{j=l-1/2}] p_l(\hat{k} \cdot \hat{k}') \\ g(\hat{k} \cdot \hat{k}') &= \frac{1}{k} \sum_l [t_l^{j=l+1/2} - t_l^{j=l-1/2}] p'_l(\hat{k} \cdot \hat{k}') \end{aligned} \quad (6.11)$$

and

$$h(\hat{k} \cdot \hat{k}') = \frac{1}{k} \frac{2}{1 + \hat{k} \cdot \hat{k}'} \sum_l \frac{2j+1}{2} t_{l+1,l}^j [P_l(\hat{k} \cdot \hat{k}') + P_{l+1}(\hat{k} \cdot \hat{k}')], \quad (6.12)$$

where t_l are the elements of the T-matrix which is taken to be of the general form

$$t^j = \begin{pmatrix} t_{l,l}^j & t_{l,l+1}^j \\ t_{l+1,l}^j & t_{l+1,l+1}^j \end{pmatrix} \quad (6.13)$$

The diagonal terms $t_{l,l}^j$ and $t_{l+1,l+1}^j$ enter in the definition of F_S while $t_{l,l+1}^j$ defines the PNC amplitude, $F_{PNC}(\theta)$, Eq. (6.10).

For the purpose of evaluating the observables it is useful to remind the reader the relation between the $t_{l,r}^j$'s and the elements of the S-matrix

$$S_{l,r}^j = \delta_{l,r} + 2it_{l,r}^j \quad (6.14)$$

Given the amplitude $F(\theta)$ in spin-space, one may immediately calculate all the spin observables. To do this, we remind that the initial density matrix for an arbitrary polarized beam of spin 1/2 particles incident on a spin-0 target is:

$$\rho_i = \frac{1}{2}(1 + \vec{\sigma} \cdot \vec{P}_i), \quad (6.15)$$

where \vec{P}_i ($|\vec{P}_i| \leq 1$) is the polarization of the incident beam. The density matrix of the scattered beam can then be written in terms of $F(\theta)$ as:

$$\rho_{sc} = F_{\rho} F^+. \quad (6.16)$$

Of course, the total cross-section, σ_T , can be immediately obtained from the optical model theorem, *vis*

$$\sigma_T = \frac{4\pi}{k} \text{Im}F(0), \quad (6.17)$$

which can be written as a sum of the total elastic (shape elastic), σ_E and absorption (compound), σ_{ABS} , cross-sections.

We find

$$\begin{aligned} \sigma_E = & \frac{\pi}{k^2} \sum_j \frac{2j+1}{2} \left[|S_{l,l}^j - 1|^2 + |S_{l,l+1}^j|^2 + |S_{l+1,l+1}^j|^2 + |S_{l,l+1}^j|^2 \right] \\ & - \vec{\sigma} \cdot \hat{k} \frac{\pi}{k^2} \sum_j \frac{2j+1}{2} 2\text{Re}[S_{l,l+1}^j (S_{l,l}^j - 1 + S_{l+1,l+1}^j + 1)] \end{aligned} \quad (6.18)$$

$$\begin{aligned}\sigma_{ABS} &= \frac{\pi}{k^2} \sum_j \frac{2j+1}{2} [1 - |S_{l,l}^j|^2 + 1 - |S_{l+1,l+1}^j|^2] \\ &\quad + \vec{\sigma} \cdot \hat{k} \frac{\pi}{k^2} \sum_j \frac{2j+1}{2} 2\text{Re}[S_{l,l+1}^{j*} (S_{l,l}^j + S_{l+1,l+1}^j)]\end{aligned}\quad (6.19)$$

$$\begin{aligned}\sigma_T &= \sigma_E + \sigma_{ABS} \\ &= \frac{2\pi}{k^2} \sum_j \frac{2j+1}{2} [1 - \text{Re}S_{l,l+1}^j + 1 - \text{Re}S_{l+1,l+1}^j] \\ &\quad + \vec{\sigma} \cdot \hat{k} \frac{2\pi}{k^2} \sum_j \frac{2j+1}{2} 2\text{Re}(S_{l,l+1}^j)\end{aligned}\quad (6.20)$$

The spin-averaged total cross-section is

$$\bar{\sigma}_T = \frac{2\pi}{k^2} \sum_j \frac{2j+1}{2} [1 - \text{Re}S_{l,l}^j + 1 - \text{Re}S_{l+1,l+1}^j]\quad (6.21)$$

Finally, the spin average, optical, longitudinal asymmetry coefficient, P_{opt} , defined as

$$P_{opt} = \frac{\bar{\sigma}_+ - \bar{\sigma}_-}{2(\bar{\sigma}_{ABS})^2}\quad (6.22)$$

is found to be

$$P_{opt} = \frac{\frac{2\pi}{k^2} \sum_j (2j+1) \text{Re}S_{l,l+1}^j}{\bar{\sigma}_{ABS}}\quad (6.23)$$

Secondly, we can evaluate the final spin polarization and rotation. The details are given in Ref. [42].

From Eq. (6.16) we can calculate the polarized cross-sections $\left(\frac{d\sigma}{d\Omega}\right)_{P_i}$, as:

$$\begin{aligned}\left(\frac{d\sigma}{d\Omega}\right)_{P_i} &= \text{tr}(\rho_{sc}) \\ &= \frac{d\sigma}{d\Omega} (1 + \vec{P}(\theta) \cdot \vec{P}_i) + 4(1 + \cos\theta) \text{Re}(gh^*) (\hat{k} - \hat{k}') \cdot \hat{P}_i\end{aligned}\quad (6.24)$$

where we have introduced the **unpolarized** cross-section:

$$\frac{d\sigma}{d\Omega} = |f|^2 + \sin^2 \theta |g|^2 + 2(1 + \cos \theta) |h|^2, \quad (6.25)$$

and the polarization vector $\tilde{\vec{P}}(\theta)$:

$$\begin{aligned} \tilde{\vec{P}}(\theta) = & 2[(\hat{k} \times \hat{k}') Im(fg^*) - (\hat{k} + \hat{k}') Re(fh^*)] \\ & - (\hat{k} - \hat{k}')(1 + \cos \theta) Re(fh^*) \Big/ \left(\frac{d\sigma}{d\Omega} \right) \end{aligned} \quad (6.26)$$

The final polarization of the beam is calculated from:

$$\begin{aligned} \vec{P}(\theta) &= \frac{tr(\bar{\sigma} \rho_{sc})}{tr(\rho_{sc})}, \quad (6.27) \\ \vec{P}_f(\theta) &= \frac{\vec{P}(\theta) + \vec{P}_i - \vec{Q}(\theta) \times \vec{P}_i + \left\{ \frac{[\vec{r}(\vec{r}^* \cdot \vec{P}_i) + \vec{r}^* \cdot (\vec{r} \cdot \vec{P}_i) - 2(\vec{r} \cdot \vec{r}^*) \vec{P}_i]}{d\sigma/d\Omega} \right\}}{1 + \vec{P}(\theta) \cdot \vec{P}_i + 2(\vec{r}^* \times \vec{r}) \cdot \vec{P}_i} \Big/ \left(\frac{d\sigma}{d\Omega} \right), \end{aligned}$$

$$\vec{r} \equiv \hat{n}g + i(\hat{k} + \hat{k}')h. \quad (6.28)$$

In Eq. (6.27) we have introduced the spin rotation vector $\vec{Q}(\theta)$ given by:

$$\vec{Q}(\theta) = \frac{2[(\hat{k} \times \hat{k}') Re(fg^*) + (\hat{k} + \hat{k}') Im(fh^*)]}{\frac{d\sigma}{d\Omega}} \quad (6.29)$$

We find from Eqs. (6.26), (6.27) and (6.28), to leading order in PNC effect that all the PNC spin observables are along the direction of $\hat{k} + \hat{k}'$, i.e., in the scattering plane in contrast to the PC pieces which are in the direction perpendicular to that plane (along $\hat{n} = \hat{k} \times \hat{k}'$)

$$\begin{aligned} \vec{P}_{f,PNC} \cdot \hat{k} &= -\frac{2(1 + \cos \theta) Re(fh^*)}{\frac{d\sigma}{d\Omega}} \\ \vec{Q}_{PNC} \cdot \hat{k} &= \frac{2(1 + \cos \theta) Im(fh^*)}{\frac{d\sigma}{d\Omega}} \end{aligned} \quad (6.30)$$

Whereas the parity conserving counterparts are given, from Eqs. (6.27) and (6.28), by

$$\begin{aligned}\vec{P}_{PC} \cdot \hat{n} &= 2 \sin \theta \frac{\text{Im}(fg^*)}{\frac{d\sigma}{d\Omega}} \\ \vec{Q}_{PC} \cdot \hat{n} &= 2 \sin \theta \frac{\text{Re}(fg^*)}{\frac{d\sigma}{d\Omega}}\end{aligned}\quad (6.31)$$

At sufficiently high energies, the parity conserving amplitudes, $f(\theta)$ and $g(\theta)$ are given by

$$\begin{aligned}f(\theta) &= \frac{1}{2ik} (s_0^{1/2} - 1), \\ g(\theta) &= \frac{1}{2ik} (s_1^{3/2} - s_1^{1/2}),\end{aligned}\quad (6.32)$$

while the PNC amplitude, $h(\theta)$ is given by [42]

$$h(\theta) \simeq \frac{1}{2ik} s_{10}^{1/2}, \quad (6.33)$$

where $s_0^{1/2}$ refers to s_L^J and the non-diagonal amplitude $s_{10}^{1/2}$ is proportional to the PNC interaction.

Using the above expressions, we find

$$\begin{aligned}P_{opt} &= \frac{2 \text{Re} s_{10}^{1/2}}{(1 - |s_{00}|^2) + (1 - |s_{11}|^2)} \\ \vec{P}_{PNC} \cdot \hat{k} &= -2(1 + \cos \theta) \frac{\text{Re} [(s_0^{1/2} - 1)s_{10}^{1/2 *}]}{|s_0^{1/2} - 1|^2} \equiv P_{PNC}^0 \\ \vec{Q}_{PNC} \cdot \hat{k} &= 2(1 + \cos \theta) \frac{\text{Im} [(s_0^{1/2} - 1)s_{10}^{1/2 *}]}{|s_0^{1/2} - 1|^2} \equiv Q_{PNC}^0 \\ \vec{P}_{PC} \cdot \hat{n} &= 2 \sin \theta \frac{\text{Im} [(s_0^{1/2} - 1)(s_1^{3/2} - s_1^{1/2})^*]}{|s_0^{1/2} - 1|^2} \equiv P_{PC}^0 \\ \vec{Q}_{PC} \cdot \hat{n} &= 2 \sin \theta \frac{\text{Re} [(s_0^{1/2} - 1)(s_1^{3/2} - s_1^{1/2})^*]}{|s_0^{1/2} - 1|^2} \equiv Q_{PC}^0\end{aligned}\quad (6.34)$$

In the following we calculate P_{opt} , P_{PC} , Q_{PC} , P_{PNC} and Q_{PNC} for $n + {}^{232}\text{Th}$ in energy region 10^{-5} MeV , using the Madland-Young [43] (MY) strong optical potential given by

$$\begin{aligned}
 U(r) &= -V_0 f_r(r) - iW_0 f'_r(r), \\
 f_l(r) &= \left(1 + \exp\left(\frac{r - R_l}{a_l}\right) \right)^{-1} \\
 V_0 &= 50.378 - 27.0073\left(\frac{N - Z}{A}\right) - 0.354 E_{Lab} (\text{MeV}) \\
 R_r &= 1.264 A^{1/3} \text{ fm}, \quad a_r = 0.612 \text{ fm}, \\
 W_0 &= 9.265 - 12.67\left(\frac{N - Z}{A}\right) - 0.232 E_{Lab} + 0.00332 E_{Lab}^2 (\text{MeV}) \\
 R_l &= 1.256 A^{1/3}, \quad a_l = 0.553 + 0.0144 E_{Lab} (\text{MeV}) \\
 V_{SO}(r) &= \frac{\hbar}{m_\pi c^2} V_{SO}^{(0)} \frac{1}{r} f'_{SO}(r), \\
 V_{SO}^{(0)} &= 6.2 \text{ MeV}, \\
 R_{SO} &= 1.02 A^{1/3} \text{ fm}, \\
 a_{SO} &= 0.75 \text{ fm}. \tag{6.35}
 \end{aligned}$$

This potential is appropriate for treating low energy neutron scattering from actinide nuclei.

As for the Michel-type PNC interaction V_{PNC} , we use the form (6.8) with the following general shape for the formfactor $v(r)$

$$\begin{aligned}
 v(r) &= \frac{1}{2} \varepsilon_7 \hbar c 10^{-7} \left[1 + \exp\left(\frac{r - r_0 A^{1/3}}{a}\right) \right]^{-7}, \\
 r_0 &= 1.25 \text{ fm}, \quad a = 0.6 \text{ fm}, \tag{6.36}
 \end{aligned}$$

and ε_7 is of the order of unity.

6.1 Optical Model Calculation of the Longitudinal Asymmetry

In the following, we use the formalism developed above in conjunction with the Madland-Young optical potential and Eq. (6.36) for $v(r)$ to calculate the longitudinal asymmetry for ${}^{232}\text{Th}$.

The strong potential, Eq. (6.35) gives for the s - and p -wave strength functions S_0 , S_1 in ${}^{232}\text{Th}$ the values (at $E_n = 1 \text{ eV}$):

$$\begin{aligned}
 S_0 &= \frac{T(s1/2)}{2\pi\sqrt{E_{Lab}(eV)}} = 1.2 \times 10^{-4}, \\
 S_1 &= \left[\frac{1}{3} \frac{T(p1/2)}{2\pi\sqrt{E_{Lab}(eV)}} + \frac{2}{3} \frac{T(p3/2)}{2\pi\sqrt{E_{Lab}(eV)}} \right] \Big/ \left(\frac{k^2 R^2}{1+k^2 R^2} \right) \\
 &= 2.0 \times 10^{-4}
 \end{aligned} \tag{6.37}$$

where

$$T(s1/2) = 1 - |S_0^{1/2}|^2, \quad T(p_j) = 1 - |S_1^j|^2. \tag{6.38}$$

In Eq. (6.37) and (6.38) T refers to the transmission coefficient and R in Eq. (6.37) is taken to be $1.25A^{1/3}$ fm. The above values of S_0 and S_1 (both shown vs. A in Figs. 6.1 and 6.2) are in reasonable agreement with the experimental ones given, respectively, by $0.84 \pm 0.07 \times 10^{-4}$ and 1.0×10^{-4} . The value of S_1 in Eq. (6.37) could certainly be improved by a convenient fine adjustment of the parameters of the M-Y potential.

The compound nucleus resonances in the $n + {}^{232}\text{Th}$ system start at a neutron Lab. energy of 8 eV. Therefore we have to know the value $P_{opt}(p1/2)/\epsilon_7$ at this energy. We have calculated $P_{opt}(p1/2)/\epsilon_7$ as a function of E_n and concluded that it exhibits an $E_n^{-1/2}$ dependence as observed by the TRIPLE group [7, 8, 9, 10, 11, 12, 13, 14, 15, 16]. In Fig. 6.3, we show

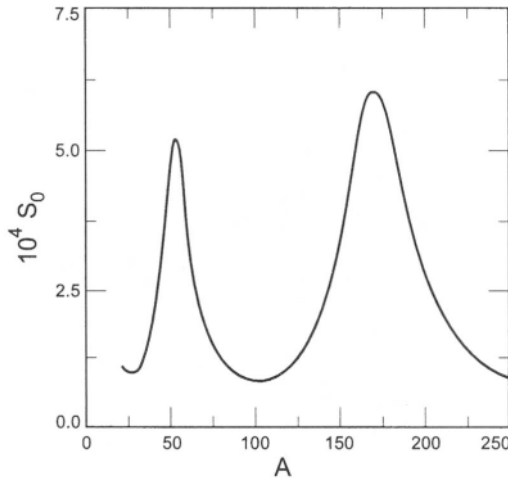


Fig. 6.1. The singlet strength function, S_0 , vs the mass number A , obtained with the Madland-Young optical potential.

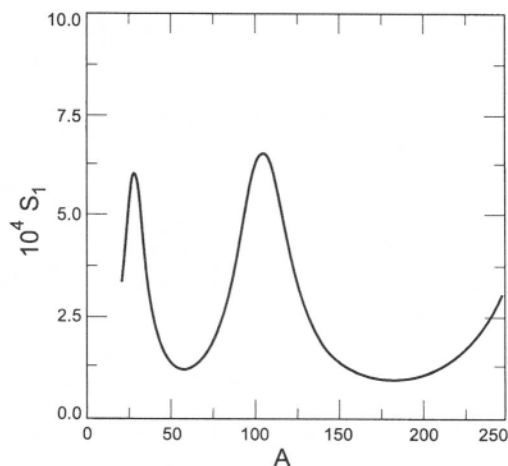


Fig. 6.2. The triplet strength function, S_1 , vs the mass number A , obtained with the Madland–Young optical potential.

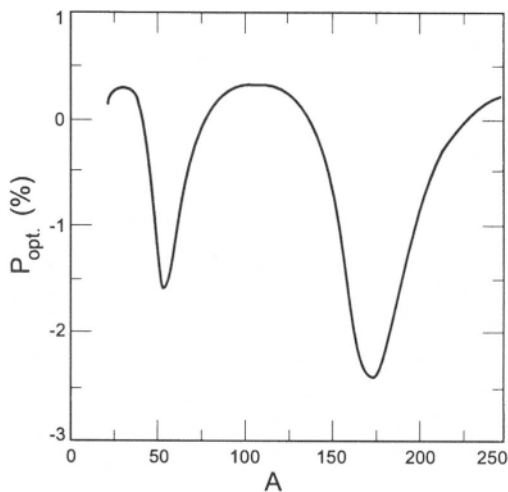


Fig. 6.3. The optical asymmetry calculated with the Madland–Young potential vs. the mass number at $E_n = 1$ eV. The parameter ϵ_7 was set equal to unity. See text for details.

$P_{opt}(p_{1/2})$ vs. A at $E_n = 8\text{ eV}$. At $E_n = 8\text{ eV}$ we get $P_{opt}(p_{1/2}) = 2.37 \times 10^{-4}$ ($E_n = 8\text{ eV}, \epsilon_7 = 1$). Thus to account for the experimental value of $P(p_{1/2})$ in the resonance region ($E_n > 8\text{ eV}$), which is $3.8 \pm 1.3\%$ we have to take for $\epsilon_7 = 54 \pm 40$. Qualitatively similar conclusions were reached in Ref. [38] who use a different optical potential. However, the above conclusion is misleading since the optical P_{opt} is obtained from energy averaged cross-sections, while $\langle P_p \rangle$ is calculated from resonance averaged ratios of resonance parameters. In order to make sensible comparison between the TRIPLE data and the optical model, we have to analyze the cross-section difference $\sigma_p^{(+)} - \sigma_p^{(-)}$.

6.2. Optical Model Analysis of the TRIPLE Data

From the optical model point of view, the quantity $\langle P_q \rangle_q$ is rather cumbersome to analyze. A more natural quantity to discuss is the ratio of energy averages:

$$P_{opt} = \frac{\langle \Delta\sigma \rangle_E}{2\langle \sigma \rangle_E} \equiv \frac{\Delta\sigma_{opt}}{2\sigma_{opt}} \quad (6.39)$$

which will behave differently from $\langle P_q \rangle_E$, where $\langle \dots \rangle_E$ implies energy average. It is simple matter to show that:

$$\sigma_{opt} = \sigma_0 + \frac{\pi\Gamma}{2D}\langle \sigma \rangle_q, \quad (6.40)$$

and therefore:

$$\frac{2D}{\pi\Gamma}\Delta\sigma_{opt} = \langle \Delta\sigma \rangle_q + \frac{2D}{\pi\Gamma}\Delta\sigma_0, \quad (6.41)$$

where $\langle \Delta\sigma \rangle_q$ is the cross-section difference at the peak of the resonance (q), averaged over q , and D and Γ are the average spacing and width of the resonances. From the data of Refs. [9, 10] we constructed $\Delta\sigma_q$ for $n + {}^{232}\text{Th}$ and $n + {}^{238}\text{U}$, shown respectively in Figs. 6.4 and 6.5. The average, $\langle \Delta\sigma_q \rangle_q$, over the resonances in the energy range $1 < E_n < 400\text{ eV}$ is $(690 \pm 300) \text{ mb}$ for $n + {}^{232}\text{Th}$, and $(65 \pm 86) \text{ mb}$ for $n + {}^{238}\text{U}$. In performing these averages, involving experimental points with error bars, we followed the procedure of [35]. The data points were scaled by E_n . It is obvious from this analysis that $\langle \Delta\sigma_q \rangle_q$ for $n + {}^{238}\text{U}$ is consistent with a zero value, whereas for $n + {}^{232}\text{Th}$ it is appreciable. To understand this difference in behavior between the two rather similar systems we performed an optical model calculation following the procedure of Refs. [38] and [40]. The results are previously summarized in [45].

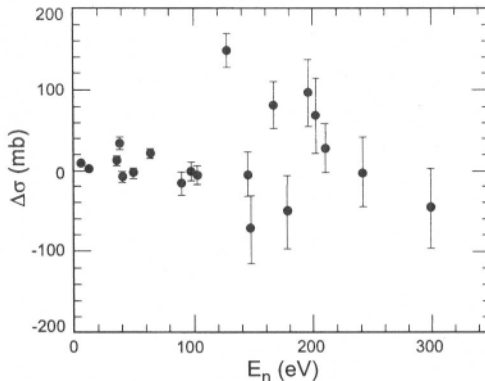


Fig. 6.4. Cross-section difference for ^{232}Th resonances. See text for details.

In view of Eq. (6.41) the optical model cross-section differences must be multiplied by the factor $(2D/\pi\Gamma)$, before comparing with the experimental $\langle \Delta\sigma_q \rangle_q$ given above. The value of $2D/\pi\Gamma$ was found to be 297.1 for $n + ^{232}\text{Th}$ and 197.6 for $n + ^{238}\text{U}$. For ^{232}Th , we used $\Gamma_1 = \Gamma_\gamma = 24\text{ meV}$ and $D_1 = 11.2\text{ eV}$. For ^{238}U , we used $\Gamma_1 = \Gamma_\gamma = 23.2\text{ meV}$ and $D_1 = 7.2\text{ eV}$ (the notation Γ_1, D_1 means width and spacing for the p -wave ($l = 1$) resonances). With the exception of the D_1 value for ^{232}Th , these numbers come from the book of Mughabghab on nuclear resonance parameters and thermal cross sections [46]. We obtained the value for D_1 in ^{232}Th by averaging over the spacings of ^{232}Th p -wave resonances below 100 eV. The value of ϵ_7 , which appears in the PNC piece of the optical model potential was set equal to unity. The parity conserving part

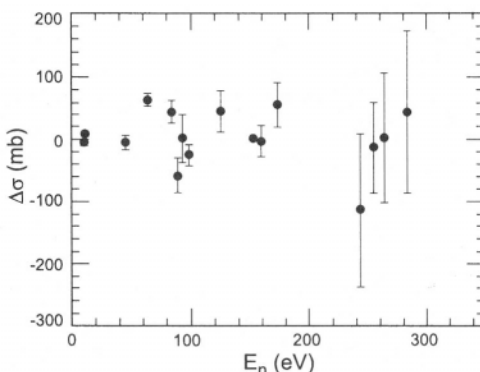


Fig. 6.5. Cross-section difference for ^{238}U resonances. See text for details.

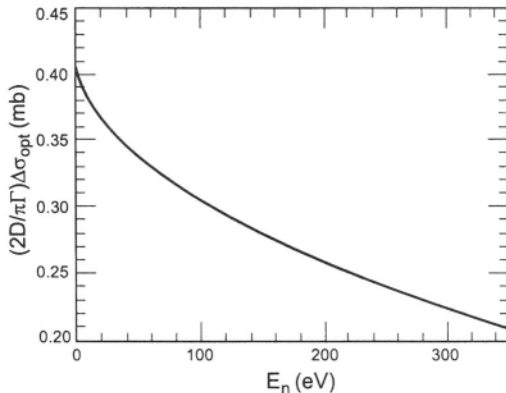


Fig. 6.6 Optical model calculation of $\Delta\sigma$ for $n + {}^{232}\text{Th}$.

of the optical model potential is that of Ref. [43], which is appropriate to the actinides.

The results $\frac{2D}{\pi\Gamma} \Delta\sigma_{opt}$ for are shown in Figs. 6.6 and 6.7 for the two systems under discussion. The values of $\frac{2D}{\pi\Gamma} \Delta\sigma_{opt}$ at $E_n = 1\text{ eV}$ is 0.4mb for $n + {}^{232}\text{Th}$ and 0.68mb for $n + {}^{238}\text{U}$ at $E_n = 1\text{ eV}$. Therefore it is reasonable to conclude that the $n + {}^{238}\text{U}$ system exhibits a “normal” behavior since its $\langle \Delta\sigma_q \rangle_q$ is consistent with the optical value of 0.4mb: namely PNC transitions whose average is zero and whose resonance back-

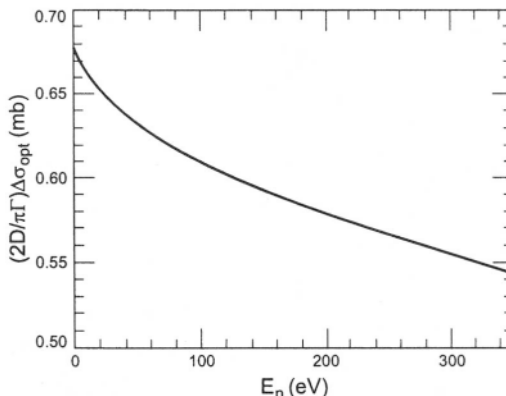


Fig. 6.7. Optical model calculation of $\Delta\sigma$ for $n + {}^{238}\text{U}$.

ground, is basically the low-energy extrapolated optical model result. On the other hand, the $n + {}^{232}\text{Th}$ system is “abnormal” in the sense that $\langle \Delta\sigma_q \rangle_q = 690 \text{ mb}$ (see above) is more than two orders of magnitude larger than the “scaled” optical model result (scaled in the sense of the factor $2D/\pi\Gamma$. This is certainly related to the fact that $\langle P_q \rangle_q$ is zero $n + {}^{238}\text{U}$ and relatively large in $n + {}^{232}\text{Th}$.

We further investigated the behavior of the two systems by examining the p-wave and s-wave optical transmission coefficients and compared them with the corresponding experimental values, namely $2\pi \frac{\Gamma_{0,n}}{D_0}$

and $2\pi \frac{\Gamma_{1n}}{D_1}$ where $\Gamma_{0,n}(\Gamma_{1n})$ is the s-wave (p-wave) neutron width. The values of $\Gamma_{0,n}$ and Γ_{1n} for ${}^{232}\text{Th}$ and ${}^{238}\text{U}$ were taken from Refs. [2] and [46]. Again, the comparison showed the “abnormal” nature of ${}^{232}\text{Th}$ when compared to ${}^{238}\text{U}$. The experimental values of $2\pi \frac{\Gamma_{0,n}}{D_0}$, averaged over the resonances, for $n + {}^{232}\text{Th}$ are slightly lower ($\approx 20\%$) than the optical transmission coefficients whereas $2\pi \frac{\Gamma_{1n}}{D_1}$ shows conspicuously larger values ($\approx 30\%$) than the optical transmission in the energy range, $100 \text{ eV} < E_n < 200 \text{ eV}$. This behavior is not shared by $n + {}^{238}\text{U}$.

The existence of a local doorway that is required to explain the sign correlation has clearly important implications on the energy averaged cross-section. Within the energy range where the averaged cross-section is calculated we are assuming that there is only one doorway present, as we emphasized earlier [29]. The contribution to the optical interaction that arises from the doorways is given by [45]:

$$\Delta U_{Doorway}^{(\pm)} = \frac{V_{Dp}(r)[V_{Dp}(r') \pm V_{Ds}^W(r')]}{E - E_D + i\Gamma_D^\downarrow/2} \quad (6.42)$$

to first order in the weak force, where $V_{Di}(r)$ is an appropriate form factor representing the doorway coupling to channel i . In (6.42) Γ_d^\downarrow is the spreading width of the 2p – 1h doorway, due to its coupling to the compound nuclear states.

It is clear from Eq. (6.42) that if treated as an optical potential, $\Delta U_{doorway}^{(\pm)}$ will contain a PNC part which is complex:

$$\Delta U_{Doorway}^{PNC} = \frac{2V_{Dp}(r)V_{Ds}^W(r')}{-E + i\Gamma_D^\downarrow/2} \quad (6.43)$$

In the optical model calculation of [4], whose results for $\Delta\sigma$ are shown in Figs. 6.6 and 6.7, an empirical local energy-dependent optical potential [43], was used to generate distorted waves that are then employed to evaluate the first-order perturbation matrix element:

$$f_{PNC} \propto I\mu \langle \Psi_s^{(-)} | V^{PNC} | \Psi_p^{(+)} \rangle \quad (6.44)$$

where V^{PNC} is just the Michel-type interaction, Eq. (6.5). It is clear from the discussion above that the reported OM calculation is incomplete, since, to say the least, U must be complex. Further, the imaginary part to be used in a consistent optical model analysis of the TRIPLE data must arise entirely from the doorway (see Eq. (8.23)). It is, however, conventional to use an empirical complex potential to represent the parity conserving interaction since there are other doorways and, when used at higher energies the averaged potential will contain the contribution of many terms, of the type given in Eq. (6.42). Roughly speaking, the parity conserving (PC) imaginary part will then be given by:

$$\text{Im}\Delta U_{\text{Doorway}} = -2\pi \overline{V_{Dp}(R)V_{Dp}(r')\Gamma_D^\downarrow\rho D} \quad (6.45)$$

where ρ_D is the $2p - 1h$ density of states. It is usually assumed that when an equivalent local potential is constructed from Eq. (6.45) and extrapolated to low energies, it can be represented by the empirical imaginary potential. On the other hand the PNC interaction to be used must be complex, on account of the local doorway contribution. We believe that the difference between the optical model $\Delta\sigma$ using the real PNC interaction and the data resides in this fact.

We now use the above argument to further pin-down the nature of the local doorway state. We calculate the contribution of the single local doorway to the energy averaged cross-section. This is straightforward, since is separable. We find, taking for an “optical potential”, a background real piece plus the parity conserving part of (6.42):

$$\langle \Delta\sigma \rangle_E = \Delta\sigma_0 + \frac{2\pi}{k^2} \frac{\gamma_{Ds}^w \gamma_{Dp} \Gamma_D}{(E_D^2 + \Gamma_D^2/4)} \quad (6.46)$$

where Γ_D is the total width of the doorway, $\Gamma_D = \Gamma_D^\downarrow + \Gamma_D^\uparrow$. The escape width Γ_D^\uparrow accounts for the doorway decay to the open channels. We obtain from Eqs. (6.4) and (6.41) the following form for $\langle \Delta\sigma_q \rangle_q$:

$$\langle \Delta\sigma_q \rangle_q = \left(\frac{\gamma_{Ds}^w}{\gamma_{Dp}} \right) \left(\frac{2D}{\pi\Gamma} \right) \left(\frac{1}{k^2} \right) \left[\frac{2\pi\gamma_{Dp}^2 \Gamma_D}{E_D^2 + \Gamma_D^2/4} \right] \quad (6.47)$$

Note that the factor $\frac{2D}{\pi\Gamma}$ refers to the fine structure compound resonances, whose value for $n + {}^{232}\text{Th}$ was found to be ≈ 300 . From Eq. (6.47) we find that $\langle \Delta\sigma_q \rangle_q$ is independent of energy. This is so since $\gamma_{Dp}^2 \propto (KR)^3$, and $\gamma_{Ds}^{\omega}/\gamma_{Dp} \propto k^{-1}$. We choose $E_n = 1\text{ eV}$ to evaluate the RHS of (6.47). In Ref. [29], γ_{Ds}/γ_{Dp} was identified with $\langle P_q \rangle_q$, which, at this energy, ≈ 0.04 . Using for $\langle \Delta\sigma_q \rangle_q$ the value cited earlier, namely 690mb, we find the following numerical value for the doorway factor inside the square brackets,

$$\left[\frac{2\pi\gamma_{Dp}^2\Gamma_D}{E_D^2 + \Gamma_D^2/4} \right] \approx 1.7 \times 10^{-7} \quad (6.48)$$

As in [29] we take $E_D \approx \Gamma_D = 30\text{ keV}$, which then gives for the partial p-wave neutron width of the local 2p – 1h doorway, $2\pi\gamma_{Dp}^2 \approx 6.3\text{ meV}$, several orders of magnitude larger than the average width of the compound p-wave neutron resonances, quite consistent with our doorway picture. At this point it is important to remind the reader of an interesting relation involving the doorway strength function and that of the compound nucleus [21]. This relation reads:

$$2\pi \frac{\Gamma_D^\uparrow}{D_D} = 2\pi \left\langle \frac{\Gamma_q}{D_q} \right\rangle_q \quad (6.49)$$

For p-resonances in Th, $\langle \Gamma_q/D_q \rangle$, in the energy range of interest, is 2.1×10^{-3} . In Ref. [29] we have calculated $D_{Dp} \equiv 1/\rho_{Dp}$, which came out to be about 30keV. Taking half this value for the negative parity states, therefore we get the following value for the average escape width of the p-wave 2p – 1h doorway, $\tilde{\Gamma}_{Dp}^\uparrow \approx 31\text{ eV}$. Within our model, the value of the total width of the doorway is assumed to be $\Gamma = 30\text{ keV}$. Thus, most of this width is spreading.

6.3. Optical Model Calculation of Spin Polarization and Rotation

Though difficult to measure, the final spin polarization and rotation of the ongoing neutrons are interesting quantities to investigate. Here we present the elements of our calculations using the optical potential of Eqs. (6.35) and (6.36) [42].

The results of our calculations are shown in Figs. 6.8 and 6.9 for the angle-independent parity conserving and parity non-conserving spin

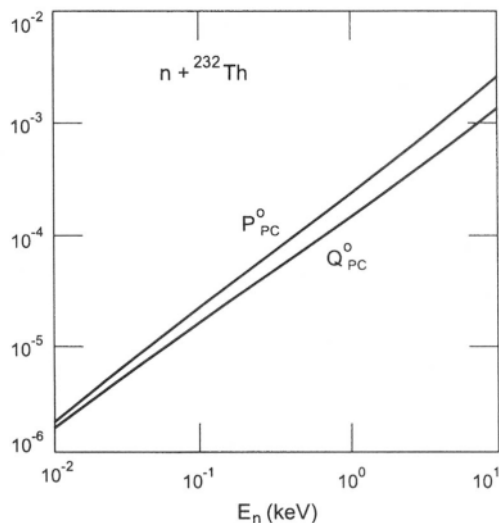


Fig. 6.8. The optical model angle-independent parity conserving spin polarization and spin rotation quantities vs. E_n , for $n + {}^{232}\text{Th}$. See text for details.

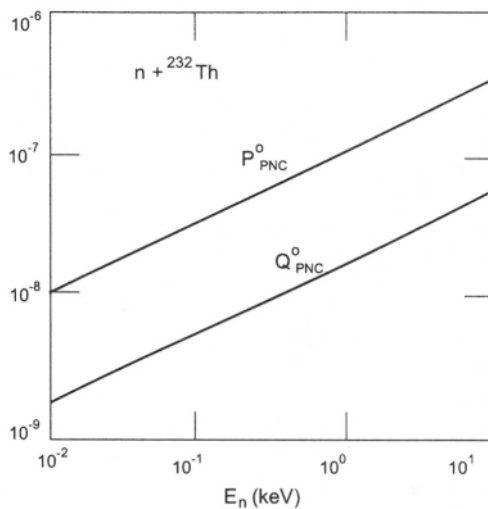


Fig. 6.9. Same as in previous figure, but for parity non-conserving quantities.

polarization and rotation quantities defined above, vs. E_n , in the range $10\text{eV} \leq E_n \leq 10\text{keV}$. At 10keV , the S -matrix elements $s_1^{1/2} - 1$ and $s_1^{3/2} - 1$ are about 1% of the value of the element $s_0^{1/2} - 1$ and are increasing. We thus expect the deviations of the angular dependence of the spin polarization and rotation functions from the forms given in Eq. (6.34) to also

be about 1% and increasing. From the figures we observe that $\frac{P_{PNC}^0}{P_{PC}^0}$ is about 7×10^{-3} at $E_n = 10\text{eV}$ and decreases to 1.3×10^{-4} at $E_n = 10\text{keV}$.

The quantity $\frac{P_{PNC}^0}{P_{PC}^0}$, on the other hand, is 1.5×10^{-3} at $E_n = 10\text{eV}$ and decreasing to 6×10^{-5} at $E_n = 10\text{keV}$. We now have to make contact with the longitudinal asymmetry anomaly discussed extensively in Section 5,

namely the extracted value of resonance-averaged $\frac{\sigma_T^{(+)}(p_{1/2}) - \sigma_T^{(-)}(p_{1/2})}{2\sigma_T(p_{1/2})}$,

where $\sigma_T^{(\pm)}(p_{1/2})$ is the total cross-section for \pm helicity neutron populating a $p_{1/2}$ resonance in ^{233}Th , was found to be positive and large, 0.04. The optical model calculation performed required a value of ϵ_7 of 54 ± 40 .

As emphasized above a more natural quantity to compare the data with is the optical model cross-section difference. Thus

$$\Delta\sigma_{opt} = \frac{8\pi}{k^2} Res_{01}^{1/2}. \quad (6.50)$$

Within the doorway model of Section 5, $s_{10}^{1/2}$ acquires the following structure

$$s_{10}^{1/2} = \frac{-1}{2i} \frac{\gamma_{Dp}\gamma_{Ds}^W}{E - E_D + \frac{i\Gamma_D}{2}}. \quad (6.51)$$

Clearly the same degree of enhancement of $\langle\Delta\sigma_T(P_{1/2})\rangle$ over the optical value, due to the doorway, would manifest itself in Q_{PNC}^0 and P_{PNC}^0 since all the quantities involve the same $s_{01}^{1/2}$, Eq. (6.34). To get an idea, the optical model value of $Res_{01}^{1/2}$ at $E_n = 1\text{eV}$ is 7×10^{-12} , to be compared to the doorway $Res_{01}^{1/2}$ (Eq. (6.51)) = 6×10^{-9} . We expect an enhancement of more than two orders of magnitude in P_{PNC}^0 and Q_{PNC}^0 over the values shown in Fig. 6.8.

7. PARITY VIOLATION IN EXOTIC NUCLEI

In recent years the field of neutron- and proton rich nuclei has flourished into a worldwide experimental and theoretical activity. A natural question to ask is to what extent the r.m.s. value of the PNC matrix element extracted by the TRIPLE Collaboration compares with its value in these exotic nuclei.

The answer to the above question would shed light on the general properties of instability of the nuclear systems subjected to both strong and weak hadronic forces. Needless to say that the instability of drip-line nuclei arises from the diminishing intensity of the strong force at the larger radii where, e.g., halo or skin nucleons reside. The study of the weak force operating in this loose region is therefore very important in elucidating the full nature of the instability of unstable nuclei. To remind the reader, the extracted value of the single particle matrix element MM^w is $\approx 1.0 \text{ eV}$, which compares well with typical structure calculation [47] based on existing theory of the weak interaction or within the Standard Model [48].

In this section, we consider the Parity Nonconserving (PNC) mixing in the ground state of exotic (halo) nuclei caused by the PNC weak interaction between outer neutron and nucleons within nuclear interior. For the nucleus ^{11}Be as an example of typical nucleus with neutron halo, we use analytical model for the external neutron wave functions to estimate the scale of the PNC mixing. The amplitude of the PNC mixing in halo state is found to be an order of magnitude bigger than that of typical PNC mixing between the “normal” nuclear states in nearby nuclei. The enhanced PNC mixing in halo cloud is proportional to the neutron weak PNC potential constant g_n^w only.

So far, the PNC effects have been probed in “normal” nuclei. The physics of “exotic” nuclei studied with unstable nuclear beams [49, 50, 51, 52, 53, 54, 55, 56, 57, 58, 59, 60] appears to be one of the most promising modern nuclear areas. Because of their specific structure, exotic nuclei, e.g., halo nuclei can offer new possibilities to probe those aspects of nuclear interactions which are not accessible with normal nuclei. It is therefore interesting to examine the possibilities of using exotic nuclei to investigate the effects of the violation of fundamental symmetries, i.e., spatial parity and time reversal.

Some aspects of the Weak interactions in exotic nuclei have been discussed in the literature [50], [51] in relation to beta decay and to the possibilities of studying the parameters of the Cabibbo-Kobayashi-Maskawa matrix. To the best of our knowledge, however,

the issue of PNC effects in exotic nuclei has been addressed only recently [61].

The aim of this Section is to give an estimate of the magnitude of the PNC effects in halo nuclei. We confine ourselves to the case of the nucleus ^{11}Be , the most well studied, both experimentally and theoretically [49, 50, 51, 54, 55]. We find that the ground state, the $2s_{1/2}$ halo configuration, acquires an admixture of the closest in energy halo state of opposite parity, $1p_{1/2}$. This effect originates from the weak interaction of the external halo neutron with the core nucleons in the nuclear interior. As a result, the neutron halo cloud surrounding the nucleus acquires the wrong parity admixtures that may be tested in experiments which can probe the halo wave functions in the exterior.

The magnitude of the admixture is found to be $\sim 10^{-6} \times g_n^W$, which is an order of magnitude bigger than the PNC effects in normal spherical nuclei. What is important to notice is that the enhanced effect we have found here is proportional to the *neutron weak constant* g_n^W only. The value of this constant remains as one of the most questionable points in the modern theory of parity violation in nuclear forces [62]. The enhanced PNC mixing in halo found here can be therefore useful in studies of the neutron weak constant.

7.1. Proton and Neutron Weak Potential Strengths

The knowledge about the proton and neutron constants g_p^W and g_n^W accumulated to date can be summarized as follows:

$$g_p^W = 4.5 \pm 2, \quad g_n^W = 1 \pm 2 \quad (7.1)$$

These values correspond to the microscopic parameters of the DDH Hamiltonian [48] described above and they are found to be in reasonable agreement with the bulk experimental data on parity violation. The above relatively small absolute value of the neutron constant that follows from DDH analysis results basically from a cancellation between π - and ρ -meson contribution to g_n^W , while both terms contribute coherently to the proton constant g_p^W . One should mention that due to this difference between the absolute values of the proton and neutron constants, the proton constant tends to dominate most measurable PNC effects, especially when both g_p^W and g_n^W contribute, provided that DDH model gives correct estimates. In this sense, one usually measures the value of g_p^W , and it is difficult to probe g_n^W unless special suppression of the proton contribution occurs, and contribution of g_n^W is highlighted. By contrast, the

case we consider in this work is sensitive to the value of the neutron constant only.

7.2 Halo Structure Effects on the PNC Mixing

The basic specific properties of the halo nuclei are determined by the fact of the existence of the loosely bound nucleon in addition to the core composed of the rest of the nucleons [52] (we will be interested here in the most well studied case of the neutron halo). The matter distribution is shown schematically in Fig. 7.1 (part a).

c) Illustration of the single-particle PNC mixing in the ground state of ^{11}Be .

In a one-body halo nuclei like ^{11}Be , the ground state is particularly simple: it can be represented as a direct product of the single-particle wave function of the external neutron, ψ_{halo} , and the wave function of the core. The residual interaction V_s^{res} can be neglected as the many-body

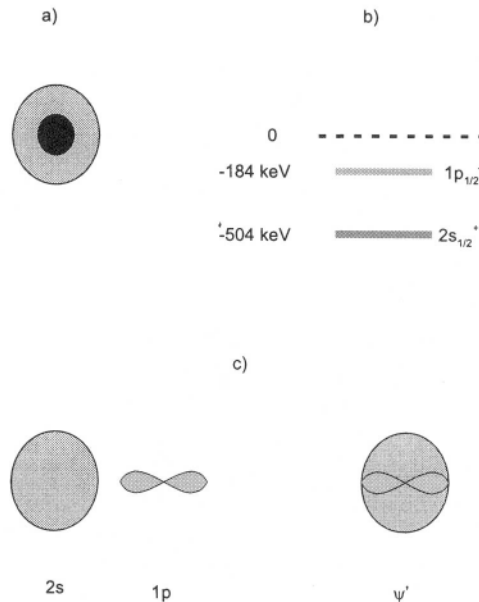


Fig. 7.1. a) Schematic plot of matter distribution in halo nuclei. The dark region corresponds to the nuclear core, the grey region shows the halo neutron cloud, b) The spectrum of the bound states ^{11}Be . c) Illustration of the single-particle PNC mixing in the ground state of ^{11}Be .

effects related to the core excitations are generically weak in such nuclei [63]. The problem is then reduced to a single-particle problem for the external nucleon. The PNC potential matrix element between the ground state of the halo nucleus and a state with opposite parity is

$$\langle \psi_{\text{halo}}^+ | W^{PNC} | \psi_{\text{halo}}^- \rangle = g_n^W \frac{G}{2\sqrt{2}m} \langle \psi_{\text{halo}}^+ | \{(\vec{\sigma}_n \vec{p}_n), \rho c\} | \psi_{\text{halo}}^- \rangle, \quad (7.2)$$

where $\rho_c(r)$ is the core density. As a result of the relatively heavy core for $A \approx 10$, the difference between the center of mass coordinate and the center of core coordinate can also be neglected.

The effective potential that binds the external neutron is a rather shallow yielding small single-neutron separation energy, and one can expect a small energy spacing between the opposite parity states. The PNC effects can therefore be considerably magnified. The spectrum of ^{11}Be is shown in Fig. 7.1 (part b). To evaluate the PNC mixing f^{HALO} in the ground state of this nucleus, it is enough to know the single-particle matrix element between the ground state $2s$ and the nearest opposite parity state $1p$, and use their energy separation which is known experimentally.

The second effect of the halo is that the value of the matrix element of the weak interaction operator between the halo states can be dramatically reduced as compared to its value in the case of “normal” nuclear states. The single-particle weak PNC potential in (7.2) originates from the DDH Hamiltonian [48] which is a two-body operator. This fact is hidden in the nucleon density of the core $\rho_c(r)$. The external neutron spends most of its time away from the core region where only it can experience the PNC potential created by the rest of nucleons. Indeed, the dominant contribution to the matrix element (7.2) must come from the regions where the three functions can overlap coherently: $\psi_{\text{halo}}^+(r)$, $\psi_{\text{halo}}^-(r)$ and the core density $\rho_{\text{core}}(r)$. The latter one is essentially restricted by the region of nuclear interior, $r < r_c$, thus reducing the effective volume of the required interference region to $\frac{4}{3}\pi r_c^3$. The normalization condition implies that the extended wave function of the bound state halo $\psi_{\text{halo}}^+(r)$ must be considerably reduced in the volume of the coherent overlap $\frac{4}{3}\pi r_c^3$. By contrast, in “normal” nuclei the radii of localization of the wave functions with opposite parity that can be mixed by the weak interaction coincide generically with the core radius r_c . The resulting suppression for the PNC halo matrix element $\langle \psi_{\text{halo}}^-(r) | W_{sp} | \psi_{\text{halo}}^+(r) \rangle$ with respect to the matrix element for the normal nuclei can be extracted from the following simple estimate:

$$\frac{\langle \psi_{halo}^- | W_{sp} | \psi_{halo}^+ \rangle}{\langle \psi_{normal}^- | W_{sp} | \psi_{normal}^+ \rangle} \sim \left(\frac{r_c}{r_{halo}} \right)^3 \sim \left(\frac{2 fm}{6 fm} \right)^3 \sim \frac{1}{25} - \frac{1}{30} \quad (7.3)$$

where we have used the mean square radii of halos from Ref. [51]. This suppression factor can cancel out the effect of the small energy separation between opposite parity levels which would suppress the PNC mixing. This simple estimate does not take into account the structure of the halo wave functions which can be quite substantial and may even lead to further suppression in the PNC mixing. In the following, we present a detailed analysis of related effects. In particular, we find that the crude estimate (7.3) turns out to be rather pessimistic.

7.3. Halo Model and Evaluation of the PNC Mixing in the Ground State of ^{11}Be

The form of the single-particle wave functions of halo states can be deduced from their basic properties [55] and their quantum numbers [51]. The results of the Hartree-Fock calculations which reproduce the main halo properties (e.g., mean square radii) are also available [51]. We use the following ansatz for the model wave function of the $2s$ halo state:

$$\psi_{2s} = R_{2s}(r) \Omega_{j=1/2,m}^{l=0}, \quad R_{2s}(r) = C_0 (1 - (r/a)^2) \exp(-r/r_0) \quad (7.4)$$

Here, $R_{2s}(r)$ is the radial part of the halo wave function and $\Omega_{j=1/2,m}^{l=0}$ is the spherical spinor. As we can neglect the center of mass effect for the heavy ($A = 10$) core, the halo neutron coordinate r in $R_{2s}(r) = \frac{1}{r} \chi_{2s}(r)$ is reckoned from the center of the nucleus. The constant C_0 is determined from the normalization condition $\int_0^\infty dr [\chi_{2s}(r)]^2 = 1$ (we choose the radial wave functions to be real). We have

$$C_0 = \frac{2^{3/2} a^2}{r_0^{3/2} \sqrt{45 r_0^4 + 2 a^4 - 12 a^2 r_0^2}}. \quad (7.5)$$

The parameters r_0 and a are the corresponding lengths to fit the density distributions obtained in Ref. [51] and the mean square radius.

The value of a is practically fixed to be $a = 2\text{fm}$ which corresponds to the position of the node. Recently, the node position have been restored from an analysis of the scattering process in work [55].

For the wave function $\psi_{1p} = R_{1p}(r)\Omega_{j=1/2,m}^{l=1}$ of the excited state $1p$, the following simplest form of the radial wave function turns out to be adequate

$$R_{1p}(r) = C_1 r \exp(-r/r_1), \quad (7.6)$$

where C_1 is the normalization constant $C_1 = \frac{2}{\sqrt{3}} r_1^{-5/2}$ and the only tunable parameter r_1 is related to the $1p$ halo radius. The mean square root radii for the halo wave states (7.4) and (7.6) are given by

$$\begin{aligned} \sqrt{\langle r_{2s}^2 \rangle} &= r_0 \left(\frac{6(45r_0^4 + 2a^4 - 12a^2r_0^2)}{105r_0^4 + a^4 - 15a^2r_0^2} \right)^{1/2}, \\ \sqrt{\langle r_{1p}^2 \rangle} &= \left(\frac{15}{2} \right)^{1/2} r_1. \end{aligned} \quad (7.7)$$

The matrix element of the weak interaction (7.2) between the ground state and the first excited state reads

$$\begin{aligned} \langle 2s | W_{sp} | 1p \rangle &= \\ ig_n^w \frac{G}{\sqrt{2m}} \int_0^\infty dr \chi_{2s}(r) &\left(\rho_c(r) \frac{d}{dr} + \frac{\rho_c(r)}{r} + \frac{1}{2} \frac{d\rho_c(r)}{dr} \right) \chi_{1p}(r) \end{aligned} \quad (7.8)$$

The core nucleon density $\rho_c(r)$ has been tuned to reproduce the data obtained from Ref. [51]. We found that their results are excellently reproduced by the Gaussian-shaped ansatz $\rho_c(r)$,

$$\rho_c(r) = \rho_0 e^{-(r/R_c)^2} \quad (7.9)$$

with the values of the parameters $\rho_0 = 0.2\text{fm}^{-3}$ and $R_c = 2\text{fm}$, as shown on Fig. 7.2.

Using the model wave functions (7.4), (7.6) and the core density (7.9), the required integrals can be done analytically, and we arrive with the result

$$\langle 2s | W | 1p \rangle = ig_n^w \frac{G}{\sqrt{2m}} \mathcal{R} \quad (7.10)$$

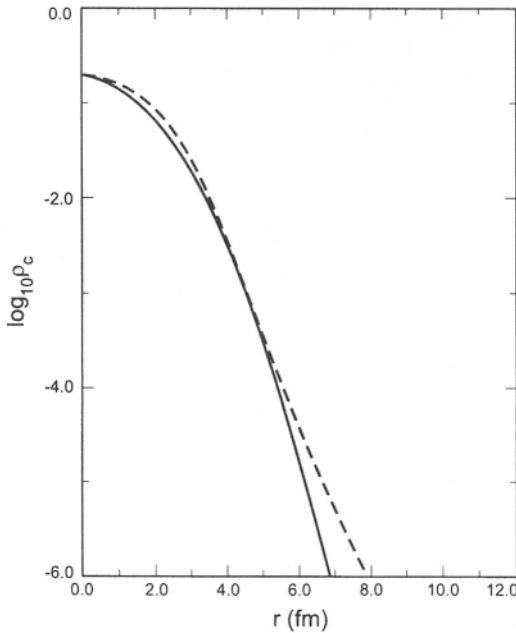


Fig. 7.2. The core density distribution (logarithmic scale). The dashed line corresponds to Ref. [51], the solid line gives parametrization (7.9).

where

$$\mathcal{R} = \rho_0 R_c^3 C_0 C_1 \left\{ 3I_2(y) - \left[3\left(\frac{R_c}{a}\right)^2 + 1 \right] I_4(y) + \left(\frac{R_c}{a} \right)^2 I_6(y) - \frac{R_c}{r_1} \left[I_3(y) - \left(\frac{R_c}{a} \right)^2 I_5(y) \right] \right\} \quad (7.11)$$

where $y = \frac{R_c(r_0 + r_1)}{r_0 r_1}$ and the functions I_n are given by

$$I_n(y) = \int_0^\infty dx x^n e^{-x^2 - yx} = (-1)^n \frac{\sqrt{\pi}}{2} \frac{d^n}{dy^n} e^{y^{2/4}} erfc(y/2)$$

where $erfc(y)$ is the error function

$$erfc(y) = 1 - \frac{2}{\sqrt{\pi}} \int_0^y dt \exp(-t^2/2)$$

To obtain the results for the PNC weak interaction matrix element, we used the parameters r_0 and r_1 in the halo wave functions to fit the radial densities of the halos obtained by Sagawa [51].

The results for the best parameters are shown in Figs. 7.3 and 7.4 for the $2s$ and the $1p$ halos, respectively. One sees that the agreement for the densities is very good. Below, we use the values

$$\begin{aligned} r_0(\text{best value}) &= 1.45 \text{ fm}, \\ r_1(\text{best value}) &= 1.80 \text{ fm}, \end{aligned} \quad (7.12)$$

to calculate the matrix elements in Eqs. (7.8, 7.10, 7.11). The radial wave functions χ are given in Fig. 7.5. We used also deviations of the both r_0 and r_1 from (7.12) to check the robustness of the results with respect to variations in the halo structure details. The values of the halo radii given by (7.7), $\sqrt{\langle r_{2s}^2 \rangle} = 5.9 \text{ fm}$ and $\sqrt{\langle r_p^2 \rangle} = 4.9 \text{ fm}$ are close to the values of Ref. [51] 6.5 fm and 5.9 fm which agree with experimental matter radii.

Substituting the values (7.12) into our expressions for the matrix elements we obtain the following value of the matrix element $\langle 2s|W_{sp}|1p \rangle_{HALO}$

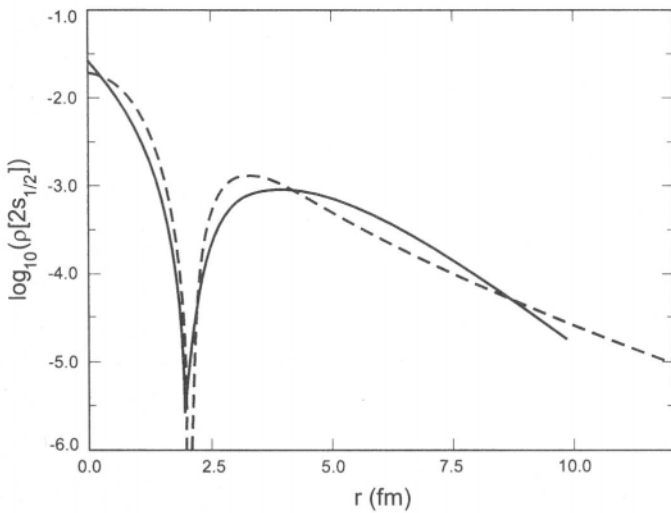


Fig. 7.3. The halo density in the ground state, $\rho_{2s1/2}(r) = \frac{1}{4\pi} (R_{2s1/2}(r))^2$. The dashed line corresponds to the Hartree-Fock calculations of Ref. [51], the solid line gives parametrization (7.4), (7.12).

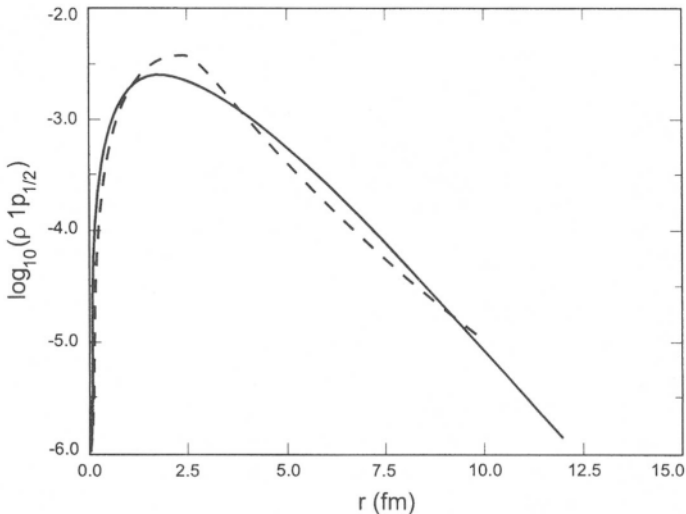


Fig. 7.4. The halo density in the first excited state, $\rho_{1p1/2}(r) = \frac{1}{4\pi}(\mathbf{R}_{1p1/2}(r))^2$. The dashed line corresponds to the Hartree-Fock calculations of Ref. [51], the solid line gives parametrization (7.6), (7.12).

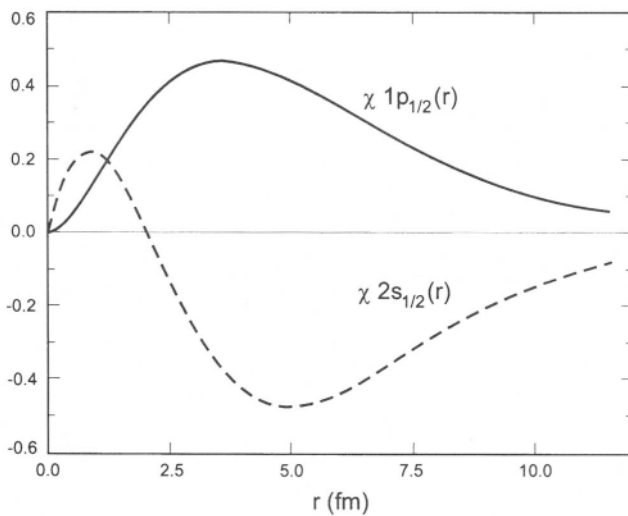


Fig. 7.5. Plot of the radial wave functions of the states $|2s1/2\rangle$ and $|1p1/2\rangle$, $\chi_{2s1/2}(r) = rR_{2s1/2}(r)$ and $\chi_{1p1/2}(r) = rR_{1p1/2}(r)$.

$$\begin{aligned}\langle 1p|W_{sp}|2s \rangle_{HALO} &= -i0.2 \quad g_n^W \quad eV, \\ &= -i0.2 \quad eV \quad (\text{for } g_n^W \approx 1).\end{aligned}\quad (7.13)$$

It is seen that this value is only a few times smaller than the standard value of the matrix element of the weak potential between the opposite parity states in spherical nuclei (see e.g., [1]), which is typically about 1eV. This results the wave function structure and comes basically from the fact that the $2s$ wave function crosses the zero line near the core surface while the $1p$ radial wave function does not have nodes. Thus the functions χ_{1p} and $d\chi_{2s}/dr$ look similar and are folded constructively with $\rho_c(r)$ in the region of interaction (nuclear interior), see Figs. 7.5 and 7.6.

The matrix element of W_{sp} between the “normal” nuclear states can be evaluated for example, in the oscillator model. Taking the typical matrix element between the states $2s$ and $1p$ and using the same formula (7.8), one has

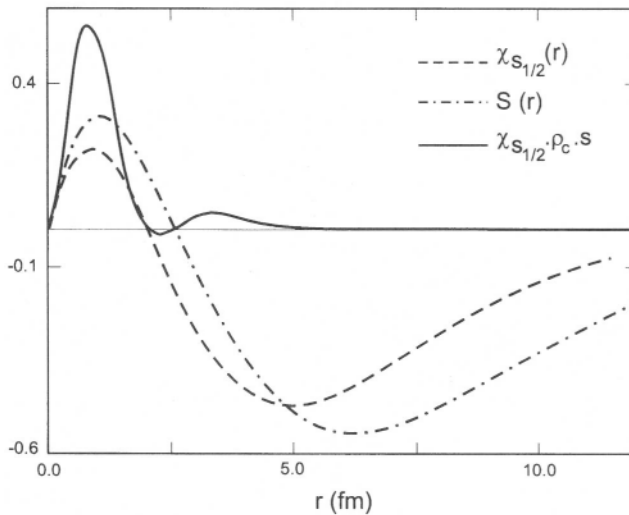


Fig. 7.6. Plot of the functions contributing to the weak PNC matrix element. The function $s(r) = \frac{d}{dr} \chi_{1p1/2}(r) + \frac{\chi_{1p1/2}(r)}{r} + \frac{d\rho_c/dr}{2r_c} c_{1p1/2}(r)$ (dot-dashed line) depends on r in the way similar to $\chi_{2s1/2}(r)$ (dashed line). The combination $\chi_{2s1/2}(r)\rho_c s(r)$ that enters the PNC matrix element in Eq. (7.8) is shown by the solid line. It contributes coherently to $\langle 2s|W_{sp}|1p \rangle$.

$$\langle 1p|W_{sp}|2s\rangle_{osc} = -ig_n^w G_{\rho_0} \left(\frac{\omega}{2m} \right)^{1/2} \quad (7.14)$$

where $\omega \approx 40 A^{-1/3}$ MeV is the oscillator frequency [64], We used here the constant value of core nucleon density, $\rho_0 \approx 0.138 fm^{-3}$. This is a very good approximation for the case of a normal nucleus (see, e.g., [18]).

Recalling the energy difference between the ground state and the first excited state $1p$ which is known experimentally,

$$|\Delta E_{HALO}| = E_{p1/2} - E_{s1/2} = 0.32 MeV \quad (7.15)$$

we obtain, using Eq. (7.13), the coefficient of mixing the opposite parity state ($1p$) to the halo ground state $2s$:

$$\begin{aligned} |f_{sp}^{HALO}| &= \frac{|\langle 1p|W_{sp}|2s\rangle|}{|\Delta E_{HALO}|} = \frac{0.2eV_g^w}{0.32 MeV} \\ &\approx 0.6 \times 10^{-6} g_n^w \\ &\approx 0.6 \times 10^{-6} \quad (\text{for } g_n^w \approx 1) \end{aligned} \quad (7.16)$$

This PNC mixing is about one order of magnitude stronger than the scale of single-particle PNC mixing in “normal” nuclear states that can be extracted from Eq. (7.14). In the case of normal $p - s$ mixing, we have

$$\begin{aligned} |f_{sp}^{normal}| &= \frac{|\langle 1p|W_{sp}|2s\rangle|}{\omega} = \frac{Gg_n^w \rho_0}{\sqrt{2m}} \left(\frac{m}{\omega} \right)^{1/2} \\ &\approx 0.7 \times 10^{-7} g_n^w \\ &\approx 0.7 \times 10^{-7} \quad (\text{for } g_n^w \approx 1) \end{aligned} \quad (7.17)$$

in the same region of nuclei with $A \sim 11$. The above value (7.17) for normal PNC mixing is rather universal and it is practically insensitive to variations of the details of the normal nuclear wave functions and core densities [18]. Comparing Eqs. (7.16) and (7.17), we obtain the halo enhancement factor to be

$$\frac{|f_{sp}^{HALO}|}{|f_{sp}^{normal}|} \approx 9. \quad (7.18)$$

This result is quite remarkable in a number of respects. First, it is seen that in experiments when the halo wave functions in the nuclear exterior are probed, the value of PNC mixing is even stronger than in “normal” nuclei. Second, this PNC mixing is dominated by the neutron

TABLE 7.1

Stability analysis for the matrix element of W_{sp} between the halo states $2s_{1/2}$ and $1p_{1/2}$. The results for the values of the parameters r_0 and r_1 differing from the best values are shown. The central entry in the table corresponds to the best value. It is seen that variations in r_0 and r_1 do not affect $\langle 2s_{1/2}|W_{sp}|1p_{1/2} \rangle$ any considerably [61].

	$r_0 = 1.40$	$r_0 = 1.45$	$r_0 = 1.50$
$r_1 = 1.75$	1.168	1.052	0.950
$r_1 = 1.80$	1.110	1.000	0.903
$r_1 = 1.85$	1.056	0.952	0.860

weak constant g_n^w . Such experiments with neutron halo nuclei would therefore provide a unique opportunity to probe the value of this constant. Usually, the sensitivity of experiments to the value of this constant is “spoiled” by a comparably large value of the proton weak constant g_n^w ; cf. Eqs. (7.1).

In order to assess the reliability of the results, we have studied the stability of the enhancement factor against variations in the parameters of the halo wave functions. As one can see from the results presented in Table 7.1, the matrix element (7.13) is changed by a few per cent only when the wave functions are deformed. The enhancement factor (7.16) is therefore quite stable.

Having in mind to present a first estimate of the PNC effect in halo nuclei, we have chosen here the simplest possible case of a one-body halo where the existing data allow one to rely on a simple analytical model of the halo structure. In this section, we confined ourselves to the case of the exotic nucleus ^{11}Be for which we presented a detailed consideration.

The analysis presented above rests basically on the most reliably known facts: the quantum numbers of the states involved, the halo radii which match the matter radii known from experiment, and the Hartree-Fock wave functions. With these input data, further quantitative analysis is a straightforward analytical exercise which does not require any approximations. The stability of the results has been checked analytically. The PNC enhancement factor of one order of magnitude allows one to speak about the qualitative halo effect that should not be overlooked.

It is a matter of further studies to check the universality of the effect while going along the table of exotic nuclei. One sees that other

exotic nuclei with developed halo structure manifest similar properties (see, e.g., [51]). Indeed, the effect of PNC enhancement found here results basically from the two facts:

- (i) the small energy separation between the mixed opposite parity states and
- (ii) the considerably strong overlap between the mixed wave functions and the core density, which saves part of the suppression in the PNC weak matrix element.

The first of these points is rather common for nuclei with developed neutron halos. The systematics of the separation energies for a single neutron [52] shows that the ground states of halo nuclei can be distanced from the continuum by a typical spacing $\epsilon_{\text{halo}} \sim (2mr_{\text{halo}})^{-1/2} \sim$ few hundreds of keV. Even in cases when no bound states with parity opposite to that of the ground state occur, PNC admixtures to the ground state wave functions must exist. In these cases, the PNC admixtures can be evaluated by means of the Green function method.

The second point (ii) is related to the wave function structure and requires further studies. It would be also interesting to study the PNC effects in proton rich nuclei [52, 53, 54].

One possible experimental manifestation of the discussed effect is related to the anapole moment [65] which is attracting much attention in the current literature [66] in view of new experimental results (detection of anapole moment in nucleus ^{133}Cs [67]). Since the anapole moment is created by the toroidal electromagnetic currents which results from PNC, its value grows as the size of the system is increased [68]. In the case of a halo-type nucleus which we considered here, the value of the anapole moment can therefore be enhanced due to the extended halo cloud.

8. TIME REVERSAL SYMMETRY BREAKING

The breaking of CP symmetry observed for neutral kaons [69] implies, because of CTP invariance, time reversal symmetry breaking (TRSB), which has never been demonstrated experimentally. Because of the results of tests looking for TRSB effects, expectations are that they will be small. We believe, however, that the amplification which occurs in low energy neutron reactions may make them visible—and in any event will provide limits [70, 71]. In this Section we apply the results of section 3. to extract time symmetry breaking from both resonance and

energy averaged experiments. In the following, we will discuss first, isolated resonances and then we turn our attention to the case of overlapping resonances regime.

We consider first the case of isolated resonances. This situation is usually encountered at neutron energies in the electron volt region. The parity nonconservation experiment of the TRIPLE Group was performed under these conditions. The study of TRSB in the isolated resonance regime has been discussed recently [72, 73]. Here we present a different point of view concerning this matter. It is convenient for the discussion to use the K-matrix, which at a given isolated resonance, we write, in the presence of TRSB, as:

$$K_{cc}^q = \frac{1}{2\pi} \frac{\gamma_{qc}\gamma_{qc}^*}{E - E_q} \quad (8.1)$$

K^q is hermitian but neither real, nor is it symmetric (see discussion in section 2.). Note that E_q in (8.1) is the real energy of the compound level, q . The T-matrix is obtained from the K-matrix through

$$T_{cc}^q = \frac{1}{2\pi} \frac{\gamma_{qc}\gamma_{qc}^*}{E - E_q + i\Gamma_q/2} \quad (8.2)$$

with Γ_q^* being the radiative decay width of resonance q , which is the dominant piece of Γ_q . The above form of T_{cc}^q establishes the link with the discussion at the beginning of the paper, i.e., for the present case $\gamma_{qc}^0 = Re\gamma_{qc}$ and $\Delta\gamma_{qc} = iIm\gamma_{qc} \equiv i\gamma_{qc}^w$. Going back to Eq. (8.1), we introduce the eigen-channels that diagonalize K_{cc}^q , by the requirement $\gamma_{qc}\Sigma_{c'}\gamma_{qc}^*f_{c'} = \lambda f_c$, which is solved by $\lambda = \Sigma_{c'} |\gamma_{qc'}|^2$ and $f_c = \gamma_{qc}$. All other solutions have $\lambda = 0$. Thus there is only one physical eigenchannel for each level q . We thus write for K_q in operator form:

$$K^q = \frac{|\gamma_q|^2}{E - \epsilon_q} |\hat{\gamma}_q\rangle\langle\hat{\gamma}_q|$$

where $|\hat{\gamma}_q\rangle$ is a unit vector with components $\frac{\gamma_{qc}}{\sqrt{\sum_c |\gamma_{qc}|^2}}$. Note that this eigenchannel also diagonalizes T^q :

$$T^q = \frac{|\gamma_q|^2}{E - \epsilon_q + i\Gamma_q/2} |\hat{\gamma}_q\rangle\langle\hat{\gamma}_q| \quad (8.3)$$

If we represent the TRSB measurement operator by θ_T , then the difference in total cross-sections with two different neutron helicities and a polarized nuclear target is:

$$\Delta\sigma_q = \frac{2\pi}{k^2} \text{Im} \frac{1}{E - \varepsilon_q + i\Gamma_q/2} \sum_{c,c'} \langle \gamma_{qc} | \theta_T | \gamma_{qc'} \rangle \quad (8.4)$$

where c denotes the entrance channel, and c' the channel that θ_T couples. Since θ_T is by definition Hermitian and antisymmetric, $\langle \gamma_{qc} | \theta_T | \gamma_{qc'} \rangle$ must be purely imaginary. Accordingly, we have at the q -th resonance,

$$\Delta\sigma_q = \frac{2\pi}{k^2} \frac{2}{\Gamma_q} \sum_{c,c'} [\gamma_{qc'}^* \gamma_{qc} - \gamma_{qc}^* \gamma_{qc'}^*] (\theta_T)_{cc'} \quad (8.5)$$

As noted above we have $\gamma_{qc} = \gamma_{qc}^o + i\gamma_{qc}^w$, where γ_{qc}^o is the (real) strong T-even amplitude. Thus to first order in γ^w , and defining $(\theta_T)_{cc'} = i\theta_{cc'}$ where $\theta_{cc'}$ is antisymmetric:

$$\Delta\sigma_q = \frac{2\pi}{k^2} \frac{4}{\Gamma_q} \sum_{c,c'} [\gamma_{qc'}^w \gamma_{qc}^o] \theta_{cc'} \quad (8.6)$$

For the special case of two channels, one (c_1) coupled weakly and the other (c_0) coupled strongly:

$$\Delta\sigma_q = \frac{2\pi}{k^2} \frac{4}{\Gamma_q} \gamma_{qc_1}^w \gamma_{qc_0}^o \quad (8.7)$$

The asymmetry, $P_q \equiv \frac{\Delta\sigma_q}{2\sigma_q}$ is then given by (ignoring the background contribution):

$$P_q = \frac{2\gamma_{qc_1}^w}{\gamma_{qc_0}^o} \quad (8.8)$$

Generally, P_q will have a vanishing average value because of the random nature of γ_{qc}^w , and $\gamma_{qc_0}^o$. This situation changes if a local 2p-1h doorway dominates the TRSB mixing. Just as in the PNC case, discussed extensively in the previous sections, the P_q , Eq. (8.8), will have a definite sign.

We mention here that the detailed nature of the T-violation experiment depends on the T-violating operator θ_T . Several forms may be cited. For parity non-conserving, time reversal violating, these are:

$$\theta_{TP,1} = (\vec{\sigma} \cdot \vec{q}) \quad (8.9)$$

$$\theta_{TP,2} = (\vec{\sigma} \times \vec{I}) \cdot \vec{p} \quad (8.10)$$

The time reversal violating P-even interactions are more complicated. We list these operators in terms of the unit vectors $\hat{q} = \hat{k}' - \hat{k}$, $\hat{p} = \hat{k} + \hat{k}'$ and $\hat{n} = \hat{p} \times \hat{q}$:

$$\theta_{T,1} = i[\vec{\sigma} \times \vec{I} \cdot \hat{n}] \quad (8.11)$$

$$\theta_{T,2} = i[\vec{\sigma} \times \vec{I} \cdot \hat{q}](\vec{I} \cdot \hat{q}) \quad (8.12)$$

$$\theta_{T,3} = i[\vec{\sigma} \times \vec{I} \cdot \hat{p}](\vec{I} \cdot \hat{p}) \quad (8.13)$$

where $\frac{\vec{\sigma}}{2}$ is the spin of the nucleon, \vec{I} the spin of the target nucleus. In a neutron transmission experiment where the total cross sections are measured, only $\theta_{TP,2}$ and $\theta_{T,3}$ survive. It is clear that in order to see time reversal violation both for P-odd and P-even, we must have at least two channel spins coupled by the violating interaction. As examples we mention the transition caused by the T-odd, P-odd interaction and the transition $^1P_1 \rightarrow ^3P_1$ caused by a P-even, T-odd interaction. In particular, the transition $^1P_1 \rightarrow ^3S_1$ mentioned above, which could occur in the neutron scattering from a spin 1/2 nucleus, is particularly interesting as it resembles the P-odd T-even case studied by the TRIPLE Group except for the change in channel spin. We suggest that to get a measurable Pq , Eq. (8.8), one comes in a 1P_1 state in a nucleus where the single particle P-wave strength function exhibits a minimum and comes out in a centrifugal barrier uninhibited 3S_1 -state sitting at a maximum in the corresponding s-wave strength function. In the $A \approx 180$ and 140 region one encounters such a situation [46]. The nucleus ^{139}La considered in Ref. [74] seems to be a good candidate to study TRSB.

We now turn to the case of overlapping (statistical) resonances. For this purpose we use the methods employed by Kawai, Kerman and McVoy (KKM) [22] to obtain the average fluctuation cross-section. Because of time symmetry breaking the S matrix is not symmetric, $S_{ab} \neq S_{ba}$ [Eq. (3.9)]. We write $\tilde{\gamma} = \gamma^0 + \Delta\gamma$, and $\gamma = \gamma^0 - \Delta\gamma$.

The energy averaged fluctuation cross-section is given by:

$$\langle \sigma_{ab}^f \rangle = \langle S_{ab}^f S_{ab}^{f*} \rangle \quad (8.14)$$

which, with the usual random phase assumption, gives:

$$\langle \sigma_{ab}^{fl} \rangle = x_0^2 \langle \gamma_{qa}^* \tilde{\gamma}_{qb}^* \gamma_{qa} \tilde{\gamma}_{qb} \rangle_q \quad (8.15)$$

We now introduce the following quantities obtained by applying the KKM analysis [22]:

$$X = x_0 \langle \gamma \gamma^* \rangle, \quad \overline{\overline{X}} = x_0 \langle \tilde{\gamma} \tilde{\gamma}^* \rangle, \quad \overline{X} = x_0 \langle \gamma \tilde{\gamma}^* \rangle, \quad (8.16)$$

In Eq. (8.16) $x_0 = \sqrt{\frac{2\pi}{\Gamma D}}$, where Γ and D are the average width and spacing of the resonance. This constant will drop out in our final expressions. The average on the RHS of Eqs. (8.15) and (8.16) is carried out over the compound nuclear states as indicated by the subscript q . In terms of these quantities, the energy average fluctuation cross section is given by:

$$\langle \sigma_{ab}^{fl} \rangle = X_{aa} \overline{\overline{X}}_{bb} + \overline{X}_{ab} \overline{X}_{ba}^+ \quad (8.17)$$

and

$$\langle \sigma_{ab}^{fl} \rangle = \overline{\overline{X}}_{aa} X_{bb} + \overline{X}_{ba} \overline{X}_{ab}^+ \quad (8.18)$$

As in the KKM example the above quantities can be related to the transmission coefficients which are given by the optical model:

$$\begin{aligned} T_{ab} &\equiv \delta_{ab} - (\overline{S} \overline{S}^+)_{ab} = \langle (S^{fl} S^{fl})_{ab} \rangle \\ &= X T \overline{\overline{X}} + |\overline{X}|^2 \end{aligned} \quad (8.19)$$

where \overline{S} is the optical model S matrix. In principle three other transmission coefficients can be defined:

$$\overline{\overline{T}} = \overline{\overline{X}} \text{Tr} X + |\overline{X}|^2 \quad (8.20)$$

$$\overline{T} = \overline{X} \text{Tr} \overline{X}^+ + X \overline{\overline{X}} \quad (8.21)$$

$$\tilde{\overline{T}} = \overline{X}^+ \text{Tr} \overline{X} + \overline{\overline{X}} X \quad (8.22)$$

Assuming pair correlations among the γ 's and the random independence of γ^0 and $\Delta\gamma$ we find (it is assumed that the number of levels is large),

$$X = \overline{\overline{X}} = X^o + x \quad (8.23)$$

where

$$X_{ab}^o = x_0 \langle \gamma_{qa}^0 \gamma_{qb}^{0*} \rangle q, \quad x_{ab} \approx x_0 \langle \Delta \gamma_{qa} \Delta \gamma_{qb}^* \rangle q$$

We can now formulate the consequences of the above analysis. First note that according to Eq. (8.23), $\langle \sigma_{ab}^f \rangle = \langle \sigma_{ba}^f \rangle$. Thus it is not possible to detect time reversal symmetry breaking by comparing the energy averaged cross sections for $a \rightarrow b$ with that for $b \rightarrow a$. Detailed balance holds in the presence of symmetry breaking. An early experimental test of this was reported in [75]. Figure 8.1 summarizes this results for $p + {}^{27}Al \rightarrow \alpha_0 + {}^{24}Mg$. To observe symmetry breaking we have to analyze the appropriate cross-section correlation function C_{ab} :

$$C_{ab} = \frac{\langle \sigma_{ab}^f \sigma_{ba}^f \rangle - \langle \sigma_{ab}^f \sigma_{ab}^f \rangle}{\langle \sigma_{ab}^f \sigma_{ab}^f \rangle} \quad (8.24)$$

It can be shown using the pair correlation assumption that to first order in N , where N is the number of open channels,

$$C_{ab} = \frac{\langle \tilde{\sigma}_{ab}^f \rangle^2 - \langle \tilde{\sigma}_{ab}^f \rangle^2}{\langle \tilde{\sigma}_{ba}^f \rangle^2} \quad (8.25)$$

where we have introduced the pseudofluctuation cross-section $\langle \tilde{\sigma}_{ab}^f \rangle$

$$\begin{aligned} \langle \tilde{\sigma}_{ab}^f \rangle &= \langle S_{ab} S_{ba}^* \rangle = \bar{X}_{aq} \bar{X}_{bb} + X_{ab} X_{bq}^+ \\ &= (X^o - x)_{aa} (X^o - x)_{bb} + (X^o + x)_{ab}^2 \end{aligned} \quad (8.26)$$

From Refs. [22], we know that the non-diagonal term in (8.26) is N^{-1} smaller than the first, diagonal one.

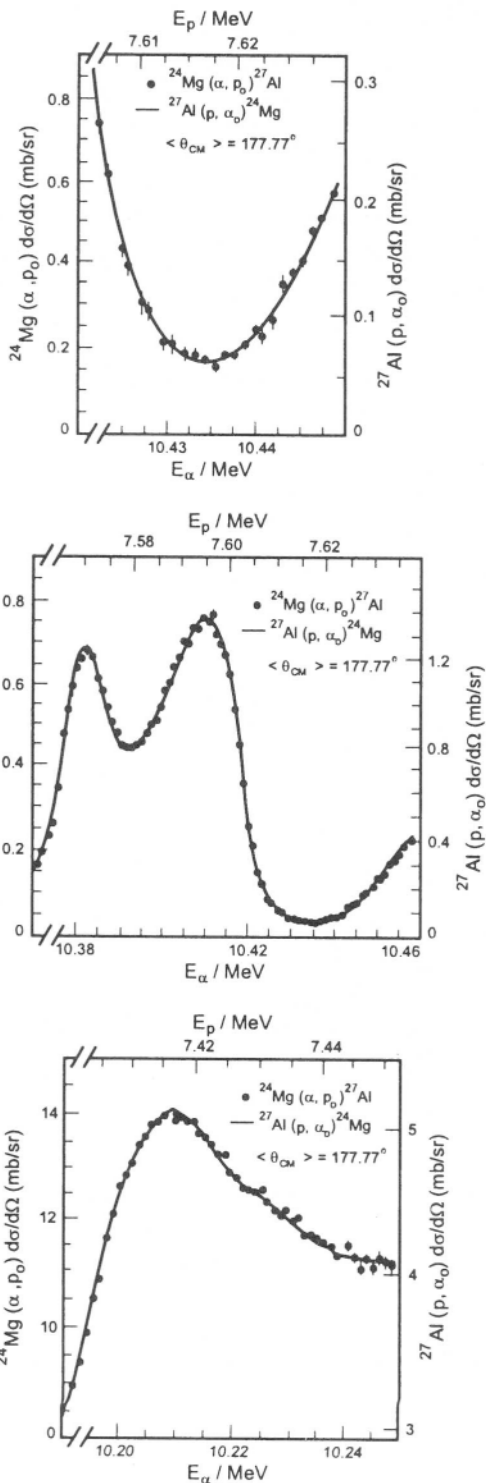
From Eq. (8.17), Eq. (8.23) and Eq. (8.26), and neglecting the non-diagonal terms ($X_{ab} = 0 = x_{ab}$), one finds, to leading order in the TRSB matrix element, the following form for C_{ab} :

$$C_{ab} \simeq -4 \frac{x_{aa} X_{bb} + X_{aa} X_{bb}}{X_{aa} X_{bb}}. \quad (8.27)$$

When written in terms of the transmission coefficient, we find:

$$C_{ab} \simeq -4 \left(\frac{t_{aa}}{T_{aa}^o} + \frac{t_{bb}}{T_{bb}^o} \right) \quad (8.28)$$

where T_{aa} is the optical transmission matrix element in channel a without TRSB, and t_{aa} is just the difference ($T_{aa} - T_{bb}^o$).



Equation (8.28) clearly shows that C_{ab} depends on the channels. This is in contrast to the result of Refs. [75, 76, 77]. In particular Ref. [77]

$$\text{calculated } |C_{ab}|^2 = \frac{\left[\langle \sigma_{ab}^{fl} \sigma_{ba}^{fl} \rangle - \langle \sigma_{ab}^{fl} \rangle^2 \right]}{\langle \sigma_{ab}^{fl} \rangle^2} \text{ using the theory of random matrices}$$

and claimed that it does not depend on a and b . The reason for this is that the authors of [77] consider TRSB to be entirely in H_{qq} and do not consider its effect on H_{pq} . Thus, if treated as purely internal mixing, the TRSB is channel independent (in C_{ab}). In fact to first order C does not depend on the symmetry breaking as contained in H_{qq} .

The use of symmetry breaking one-body potentials to treat energy-averaged observables has already been discussed in Section 7. In the case of parity nonconservation following the procedure suggested by Michel [37]. An optical model description of TRSB has been presented recently [78]. It would be profitable to calculate C_{ab} , Eq. (8.28), using one-body models of TRSB.

9. CONCLUSIONS AND DISCUSSION

In this review we have discussed fundamental symmetry violation in nuclear reactions. The unified theory of nuclear reactions is used for the purpose. The problem of parity nonconservation in epithermal neutron scattering is discussed. The data seem to follow nicely the prediction of the statistical model except for ^{232}Th . The role of simple $2p - 1h$ doorway states is pointed out as a possible cause of the sign correlation in the longitudinal asymmetries of the $n + ^{232}\text{Th}$ system.

The optical model description of the PNC is fully developed and several observables are calculated. The optical cross-section difference

Fig. 8.1. Left-hand side: Excitation function of the reaction $^{27}\text{Al}(p, \alpha_0)^{24}\text{Mg}$ folded with an energy spread of $\Delta E = 2\text{keV}$ and a mean energy loss $t_E = 4\text{keV}$ (solid curve) plotted together with the excitation function of the reaction $^{24}\text{Mg}(\alpha, p_0)^{27}\text{Al}$ (open circles, not all measured points shown normalized to the (p, α_0) excitation function. The quantities ΔE and t_E result from a computer search minimizing χ^2 . These fit parameters can be determined precisely because of the steep slopes left and right of the maximum. Middle part: a comparison of the forward and backward reaction cross-sections near and at a deep minimum with same procedure and normalization factor as at the maximum. Right-hand side: The region around the minimum displayed on an enlarged scale. This figure demonstrates the validity of detailed balance for the cross sections measured [75].

$\sigma^{(+)} - \sigma^{(-)}$, where + and – refer to positive and negative helicity neutrons, is compared to the available data involving several target nuclei. In particular, we found that the data on $n + {}^{238}\text{U}$ can be nicely accounted for by the optical model calculation, while the same is not true for $n + {}^{232}\text{Th}$, where the calculation underestimates the data by about two orders of magnitude. This discrepancy is attributed to shortcoming of the optical potential in this case which should contain explicit reference to the $2p - 1h$ doorways which is needed to explain the sign correlation. It would be important to extend the optical model analysis to other systems and to establish possible general correlation between the average longitudinal asymmetry and the average cross-section difference. Such a study would be useful to further elucidate the reaction dynamics involved in PNC.

Another important conclusion reached in this review concerns Time Reversal Symmetry Breaking (TRSB). It is emphasised that in studies of deviations from detailed balance, the cross-section correlation function is channel-dependent, contrary to the findings of other authors. This conclusion warrants further theoretical scrutiny and eventually should be put to the, understandably very difficult, experimental test. The problem of TRSB is also considered in the case of isolated resonance. Several options for observables are available here. A short account for the fundamental theory of symmetry violation in the nucleon-nucleon system is presented.

Before ending, it is useful to hit the highlights of our conclusions and point out future directions.

1. In the analysis of the longitudinal asymmetry, $P_{\mu\mu}$, one usually uses the expression

$$P_\mu = \sum_v A_{\mu v} \langle \mu | V^{PNC} | v \rangle, \quad (9.1)$$

$$A_{\mu v} = \frac{2}{E_\mu - E_v} \left(\frac{\Gamma_v}{\Gamma_\mu} \right)^{1/2} \equiv \frac{2}{S_{v\mu}} \left(\frac{\Gamma_v}{\Gamma_\mu} \right)^{1/2} \quad (9.2)$$

where μ and v refer to compound nuclear levels with opposite parities. Randomness of the weak matrix element guarantees that the ensemble average of P_μ is zero. The average of P_μ^2 is calculated by considering $A_{\mu v}$ and $\langle \mu | V^{PNC} | v \rangle$ as uncorrelated

$$\langle P_\mu^2 \rangle = \left(\sum_v A_{\mu v}^2 \right) \langle \langle \mu | V^{PNC} | v \rangle^2 \rangle = \sum_v A_{\mu v}^2 M^2. \quad (9.3)$$

Now the average of $\langle P_\mu^2 \rangle$ over all the μ resonances gives

$$\frac{1}{N} \sum_{\mu} \langle P_\mu^2 \rangle = \left\langle \sum_{\nu} A_{\mu\nu}^2 \right\rangle M^2 = A^2 M^2, \quad (9.4)$$

from which M^2 is extracted since A^2 can be calculated from the known energies and widths.

We point out that A^2 can be confronted directly with the assumed random matrix ensemble that represents the compound nucleus. In fact, we can write

$$A^2 = \left\langle \frac{4}{s_{\nu\mu}^2} \frac{\Gamma_\nu}{\Gamma_\mu} \right\rangle \quad (9.5)$$

Statistically, the s and Γ distributions are independent which should allow a detailed statistical analysis of A^2 independent on the system. This should furnish another test of the statistical theory and would allow the extraction of M^2 from the data more directly.

2. The recent extended data of the TRIPLE Collaboration indicated that at about $E_n \sim 300$ eV the asymmetry becomes negative in $n + {}^{232}\text{Th}$. Presently a more careful analysis of these negative asymmetries in Thorium are being performed using our suggestion of looking at $\sigma_{\mu}^{(+)} - \sigma_{\mu}^{(-)}$ rather than P_{μ} . If confirmed, the dip of P_{μ} to predominantly negative values at $E_n > 30$ eV in Th, would supply a very important test of the statistical nature of the $2p - 1h$ doorways: An average of P_{μ} over resonances in a wider energy interval may end up being zero after all even in ${}^{232}\text{Th}$.

3. The weak spreading width deserves more investigation, especially with regards to its mass-dependence. The analysis of the TRIPLE data indicated a rather weak dependence on the mass number of the compound states. However, once A^2 is known a priori, following the proposal above, and if knowledge of $\langle \sigma_{\mu}^{(+)} - \sigma_{\mu}^{(-)} \rangle$ from the global optical model calculation reported in this review can be transformed into knowledge of cross-section variance analysis, $\langle (\sigma_{\mu}^{(+)} - \sigma_{\mu}^{(-)})^2 \rangle$, one would be able to obtain the mass dependence of the PNC spreading width more precisely.

4. At a more fundamental level, we have found in Section 6, that the optical potential appropriate for systems that exhibit the sign correlation effect contains a PNC term which is manifestly complex. Thus we propose that analysis of epithermal neutron scattering data should be

performed with a real Michel-type PNC potential added to it a doorway inspired imaginary part.

5. The r.m.s. value of the PNC matrix element extracted by the TRIPLE Collaboration are consistent with those expected for stable nuclei. There is ongoing great effort in the field of neutron- and proton-rich nuclei. Certainly, important change may be inflicted on the strength of the weak matrix element due to the loose nature of the excess nucleons. We have calculated such a change in the case of the light halo nucleus ^{11}Be . We found that the strength of PNC mixing in the halo nucleus is almost ten times larger than in stable nuclei. A not-so-trivial fact since the instability of halo nuclei stems from the strong force and not the weak one. Our finding shows an enhanced β -decay of these nuclei which contributes further to their instability. Similar effect should be manifested in proton-rich nuclei such as ^{8}B . Further, stronger PNC admixture in the halo wave function combined with its extended range would result in an appreciable enhancement of the anapole moment, an object of great importance in the physics community.

6. The Time Reversal Symmetry Breaking is also investigated. We have found that the deviation from detailed balance symmetry can be quantitatively studied by looking at an appropriate correlation function. We found that in the overlapping resonance region this correlation function is channel-dependent contrary to the findings of other authors. This finding certainly deserves further theoretical scrutiny to understand the differences cited above and warrant a careful, though understandably difficult, experimental test.

We have also looked into TRSB in the case of isolated resonance. We point out that, as in PNC, one may encounter a sign correlation “problem”, not necessarily in ^{232}Th .

ACKNOWLEDGMENT

We thank Gary Mitchell for very useful discussion and for providing Tables 2.1 and 2.2. The work by H. F. and A.K. K. is supported in part by funds provided by the U.S. Department of Energy (D.O.E.) under contract #DE-FC02-94ER40818. The work by M.S.H. is supported in part by the CNPq and FAPESP, O.K.V. acknowledges support from FAPESP.

REFERENCES

1. E. G. Adelberger and W. C. Haxton, Annu. Rev. Nucl. Part. Sci. **35** (1985) 50.
2. J. D. Bowman, G. T. Garvey, M. Johnson and G. E. Mitchell, Annu. Rev. Nucl. Part. Sci. **43** (1993) 829.
3. V. V. Flambaum and G. F. Gribakin, Prog. Part. Nucl. Phys. **35** (1996) 423.
4. B. Desplanques, Phys. Reports **297** (1998) 1.
5. G. E. Mitchell, J. D. Bowman and H. A. Weidenmüller, Rev. Mod. Phys. **71** (1999) 435.
6. G. E. Mitchell *et al.*, "Applications of Accelerators in Research and Industry" edited by J. L. Duggan and I. L. Morgan, AIP (1999) 219.
7. C. M. Frankle *et al.*, Phys. Rev. Lett. **67** (1991) 564; C. M. Frankle *et al.*, Phys. Rev. **C46** (1992) 778; X. Zhu *et al.*, Phys. Rev. **C46** (1992) 768.
8. J. D. Bowman *et al.*, Phys. Rev. **C48** (1993) 116.
9. S. L. Stephenson, Ph.D. Thesis, North Carolina State University, 1996; S. L. Stephenson, Phys. Rev. **C58** (1998) 1236.
10. B. E. Crawford, Ph.D. Thesis, Duke University, 1997; B. E. Crawford *et al.*, Phys. Rev. **C58** (1998) 1225.
11. J. D. Bowman, L. Y. Lowie, G. E. Mitchell, E. I. Sharapov and Yi-Fen Yen, Phys. Rev. **C59** (1996) 285.
12. L. Y. Lowie *et al.*, Phys. Rev. **C59** (1999) 1331.
13. L. Y. Lowie *et al.*, Phys. Rev. **C59** (1999) 119.
14. E. I. Sharapov *et al.*, Phys. Rev. **C59** (1999) 1772.
15. B. E. Crawford *et al.*, Phys. Rev. **C58** (1998) 729; B. E. Crawford *et al.*, TRIPLE preprint (1999).
16. D. A. Smith *et al.*, "Parity Violation in Neutron Resonances of ^{103}Rh ", Phys. Rev. **C**, accepted (1999); D. A. Smith *et al.*, "Neutron resonance spectroscopy of ^{103}Rh from 30eV to 2keV", Phys. Rev. **C**, accepted (1999).
17. V. P. Al'fimenkov *et al.*, Nucl. Phys. **A398** (1983) 93; O. P. Sushkov and V. V. Flambaum, Sov. Phys. Usp. **25** (1982) 1.
18. V. V. Flambaum and O. K. Vorov, Phys. Rev. Lett. **70** (1993) 4051.
19. G. E. Mitchell and S. L. Stephenson, private communications.
20. See, e.g., N. Auerbach and O. K. Vorov, Phys. Lett. **B391** (1997) 249.
21. H. Feshbach, Theoretical Nuclear Physics: Nuclear Reactions (John Wiley and Sons, New York, 1992).
22. M. Kawai, A. K. Kerman and K. M. McVoy, Ann. Phys. (NY) **75** (1973) 156.
23. H. Feshbach, A. K. Kerman and R. M. Lemmer, Ann. Phys. (NY) **41** (1967) 280.
24. B. Block and H. Feshbach, Ann. Phys. **28** (1963) 47; A. K. Kerman, L. S. Rodberg and J. E. Young, Phys. Rev. Lett. **11** (1963) 422.
25. See, e.g., N. Auerbach, Proceedings of the "5th Conference on Intersections of Particle and Nuclear Physics", St. Petersburg, Florida, AIP, 1995, pp. 279-284.
26. V. Spevak and N. Auerbach, Phys. Lett. **B359** (1995) 254; N. Auerbach, J. D. Bowman and V. Spevak, Phys. Rev. Lett. **74** (1995) 2638; V. Spevak, N. Auerbach and V. V. Flambaum, Phys. Rev. **C56** (1997) 1357.
27. V. V. Flambaum and V. Zelevinsky, Phys. Lett. **B350** (1995) 8.
28. Proceedings of "Parity and Time Reversal Violation in Compound Nuclear States and Related Topics", editors: N. Auerbach and J. D. Bowman (World Scientific; Singapore, 1996).
29. M. S. Hussein, A. K. Kerman and C.-Y. Lin, Z. Phys. **A351** (1995) 301.

30. See, e.g., R. Bonetti, M. Chadwick, P. E. Hodgson, B. V. Carlson and M. S. Hussein, Phys. Rep. **202** (1991) 171.
31. T. Ericson, Phil. Mag. Suppl. **9** (1960) 425.
32. F. Garcia, O. Rodriguez, F. Guzman, H. Dias, M. S. Hussein and A. K. Kerman, Nucl-th/9907108. Submitted for publication in Phys. Rev. C.
33. M. Herman and G. Reffo, Phys. Rev. **C36** (1987) 1546; ibid **C37** (1988) 797; F. Garcia *et al.*, J. Phys. **G19** (1993) 2165.
34. S. Bjornholm, A. Bohr and B. R. Mottelson, Proceedings of the "Third IAEA Symposium on the Physics and Chemistry of Fission", IAEA, Vol. I (1973) 367.
35. A. Hayes, private communication.
36. A. Krasznahorkay *et al.*, Phys. Rev. Lett. **80** (1998) 2073.
37. F. C. Michel, Phys. Rev. **133** (1964) B329.
38. S. E. Koonin, C. W. Johnson and P. Vogel, Phys. Rev. Lett. **69** (1992) 1163.
39. C. H. Lewenkopf and H. A. Weidenmüller, Phys. Rev. **C46** (1992) 2601.
40. B. V. Carlson and M. S. Hussein, Phys. Rev. **C47** (1993) 376.
41. B. Desplanques and S. Noguéra, Nucl. Phys. **A598** (1993) 189.
42. B. V. Carlson and M. S. Hussein, Phys. Rev. **C56** (1997) 292.
43. D. G. Madland and P. G. Young, Los Alamos Report n° LA7533-mb (1978) (unpublished).
44. P. R. Bevington, "Data Reduction and Error Analysis for the Physical Sciences" (McGraw-Hill, New York 1969) pp. 66–71.
45. B. V. Carlson, M. S. Hussein, A. K. Kerman and C.-Y. Lin, Phys. Rev. **C52** (1995) R11.
46. S. K. Mughabghab, "Neutron Cross Sections" (Academic Orlando, 1984) Vol. I.
47. See, e.g., A. C. Hayes and I. S. Tower, Phys. Lett. **B302** (1993) 157.
48. B. Desplanques, J. F. Donoghue and B. Holstein, Ann. Phys. (NY) **124** (1980) 449.
49. J. S. Al-Khalili, J. A. Tostevin, Phys. Rev. Lett. **76** (1996) 3903.
50. R. C. Johnson, J. S. al-Khalili, J. A. Tostevin, Phys. Rev. Lett. **79** (1997) 2771.
51. H. Sagawa, Phys. Lett. **B286** (1992) 7.
52. C. A. Bertulani, L. F. Canto and M. S. Hussein, Phys. Rep. **226** (1993) 281.
53. C. A. Bertulani, L. F. Canto and M. S. Hussein, Phys. Lett. **B353** (1995) 413.
54. K. Hencken, G. Bertsch and H. Esbensen, Phys. Rev. **C54** (1996) 3043.
55. A. Mengoni, T. Otsuka, T. Nakamura, M. Ishihara, Contribution to the 4th International Seminar on Interaction of Neutrons with Nuclei, Dubna (Russia), April 1996, Preprint nucl-th/9607023.
56. J. Hardy, talk given at International Workshop on Physics of Unstable Nuclear Beams, Serra Negra, 1996 (unpublished).
57. T. Suzuki, In Physics of Unstable Nuclear Beams. C. A. Bertulani, L. F. Canto and M. S. Hussein ed., World Scientific, Singapore, 1997, p. 157.
58. B. A. Brown and P. G. Hansen, Phys. Lett. **B381** (1996) 391.
59. S. Karataglidis and C. Bennhold, Phys. Rev. Lett. **80** (1998) 1614.
60. Z. Z. Ren, A. Faessler and A. Bobyk, Phys. Rev. **C57** (1998) 2752.
61. M. S. Hussein, A. F. R. de Toledo Piza, O. K. Vorov and A. K. Kerman, "Enhancement of parity violating mixing in halo nuclei and the problem of neutron weak PNC potential", Phys. Rev. **C60**, 064615(1999), in press.
62. O. P. Sushkov and V. B. Telitsin, Phys. Rev. **C48** (1993) 1069.
63. T. T. S. Kuo, F. Krmpotic and Y. Tzeng, Phys. Rev. Lett. **78** (1997) 2708.
64. A. Bohr and B. R. Mottelson, Nuclear Structure (Benjamin, New York, 1969), Vol. I.
65. Ya. B. Zel'dovich, Zh. Exp. Teor. Fiz. **33** (1957) 1531 [Soviet Phys. JETP **6** (1957) 1184].
66. W. C. Haxton, Science **275** (1997) 1753.

67. C. S. Wood, S. C. Bennet, D. Cho, B. P. Masterson, J. L. Roberts, C. E. Tanner and C. E. Wieman, *Science* **275** (1997) 1759.
68. V. V. Flambaum and L. B. Khriplovich, *Zh. Eksp. Teor. Fiz.* **79** (1980) 1656 [*Sov. Phys. JETP* **52** (1980) 835]; V. V. Flambaum and I. B. Khriplovich and O. P. Sushkov, *Phys. Lett.* **B146** (1984) 367.
69. J. H. Christenson, J. W. Cronin, V. L. Fitch and R. Turlay, *Phys. Rev. Lett.* **13** (1964) 138.
70. E. M. Henley and B. A. Jacobson, *Phys. Rev.* **113** (1959) 225.
71. For a recent review, see: W. C. Haxton and A. Höring, *Nucl. Phys.* **A560** (1993) 469; P. Herczeg in *Proceedings on “Parity and Time Reversal Violation in Compound Nuclear States and Related Topics”*, Editors: N. Auerbach and J. D. Bowman (World Scientific, Singapore 1996) pp. 214–230.
72. V. E. Bunakov, *Phys. Rev. Lett.* **60** (1988) 2250.
73. V. E. Bunakov, E. D. Davis and H. A. Weidenmüller, *Phys. Rev.* **C42** (1990) 1718.
74. Y. Takahashi, H. M. Shimizu, T. Maekawa and T. Yabuzaki, *Phys. Lett.* **B326** (1994) 27.
75. E. Blanke, H. Driller, W. Glöckle, H. Genz, A. Richter and G. Schreider, *Phys. Rev. Lett.* **51** (1983) 355.
76. T. E. O. Ericson, *Phys. Lett.* **23** (1966) 97.
77. D. Boosé, H. L. Harney and H. A. Weidenmüller, *Phys. Rev. Lett.* **19** (1986) 2012; E. D. Davis and U. Hartmann, *Ann. Phys. (NY)* **211** (1991) 334.
78. V. Hnizdo and C. R. Gould, *Phys. Rev.* **C49** (1994) R612.

Chapter 3

NUCLEON-NUCLEUS SCATTERING: A MICROSCOPIC NONRELATIVISTIC APPROACH

K. Amos, P. J. Dortmans

*School of Physics
University of Melbourne
Parkville, Victoria
Australia, 3052*

H. V. von Geramb

*Theoretische Kernphysik
Universität Hamburg
Luruper Chaussee 149
D-22761, Hamburg, Germany*

S. Karataglidis

*TRIUMF
4004 Wesbrook Mall
Vancouver, British Columbia
Canada, V6T 2A3
(present address)
Theoretical Division
Los Alamos National Laboratory
Los Alamos
NM 87545, U.S.A.*

J. Raynal
Service de Physique Théorique
C.E.-Saclay
F-91191
Gif-sur-Yvette Cedex, France

1. Introduction	276
2. Formal Theory of the Nucleon–Nucleus Optical Potential	282
3. Momentum Space Optical Models.	285
4. Coordinate Space Optical Model	301
5. The Two-Nucleon t Matrices	328
6. Nuclear Matter and $NN g$ Matrices.	353
7. The Effective NN Interaction.	366
8. Nuclear Structure.	380
9. Electron Scattering: Operators and Observables	403
10. Applications of the Coordinate Space Optical Model	437
11. Equivalent Local Potentials	465
12. Inelastic Scattering	500
Appendix: Projection Operators and HF State Normalizations and Overlaps	527
References	537

1. INTRODUCTION

A review of the nucleon based microscopic theory of nucleon–nucleus (NA) scattering and its applications is due in the first instance because of the developments that have occurred within the last decade. In addition, the microscopic optical model has progressed to a stage where a long held goal may be achieved, namely to predict cross sections and spin observables for NA scattering with confidence that they are correct to a high degree. A review is timely also as scattering of exotic nuclei from hydrogen targets has been measured for energies to $70A$ MeV and new experiments are planned for $200A$ to $500A$ MeV. By inverse kinematics those investigations equate to proton scattering from

the exotic nuclei with energies to 500 MeV, for which suitable analyses can be made with the present microscopic optical potentials. The scattering of radioactive beams from hydrogen is the most promising current means from which one can seek a sensitive assay of the microscopic structure of exotic nuclei.

Elastic scattering is the predominant event in the interactions of nucleons with nuclei. This process has been extensively studied over many decades both experimentally and theoretically and there now exists extensive data on the scattering of nucleons from stable nuclei. All formulations of the nuclear optical model for elastic scattering have in common an allowance of flux loss from the incident beam to non-elastic channels when energies are above inelastic and reaction thresholds. These model formulations range from strong geometric forms to ones based upon complex potential representations. The geometric approaches [1] remain valid and appropriate for high energies, typically above 1 GeV, while use of complex potential models is most appropriate for energies below that. Those complex potential models broadly fall into two classes, the first being phenomenologically formed and the other microscopically based.

The concept of a complex optical potential as a single particle representation of NA interactions dates at least to the study by Bethe [2] of neutron-nucleus cross sections. All early optical potentials were phenomenological. Studies of that phenomenology proceeded apace thereafter, culminating in attempts to prescribe global forms for all target masses and for projectile energies typically to 40 MeV. Tabulations of those potential parameters have been made [3]. Likewise there have been a number of reviews of the topic of which those of Refs. [4, 5, 6] are a selection that we have found useful. Phenomenological and semi-phenomenological optical potentials are used still to interpret elastic scattering data as well as to define the distorted waves required in DWBA analyses of non-elastic processes. Likewise the semi-phenomenological approach has reached a very sophisticated stage. With it data from many nuclei, for energies ranging from keV to GeV, have been analyzed successfully [7].

It has been over 40 years since Chew [8] and Watson and collaborators [9, 10] gave theoretical justification for the NA optical potential built in terms of underlying nucleon–nucleon (NN) scattering amplitudes. For sufficiently high incident energies it was supposed that those NA interactions would be ascertained from free NN scattering. Bethe [11] showed that the cross section and polarization from the scattering of 310 MeV protons from ^{12}C at forward scattering angles were consistent with that conjecture. Then Kerman, McManus, and Thaler (KMT)

[12] developed the Watson multiple scattering approach expressing the NA optical potential by a series expansion in terms of the free NN scattering amplitudes. Those formulations result in the definition of an effective interaction between projectile and the target nucleons. Feshbach [5] and Adhikari and Kowalski [13] give lucid reviews of these theories. They also give many details of the NN scattering amplitudes and t matrices. However, adequate numerical implementation of those theories of NA scattering did not follow for quite some time, in part due to lack of knowledge of the underlying NN scattering amplitudes. To some extent this spurred study of NN phase shift analyses [14, 15] and the development of NN potentials.

About 20 years ago there was a watershed in the studies of NN and NA scattering. First, reliable NN scattering amplitude and phase shift analyses [16] to the pion threshold were made. Second the Nijmegen [17], Paris [18], and later, Bonn [19] NN potentials were developed to fit those NN amplitudes and phase shifts. Then the status of the microscopic NA optical potential theories was reviewed at the seminal topical workshop in Hamburg in 1978 [20]. Finally, experimental programs in those years produced many and varied high quality data sets for energies to 1GeV [21], adding incentive to effect implementations of those theories.

This review encompasses the developments since that period. There have been other reviews in the interim of course, since the optical model for scattering has a central role in almost all studies of nucleon-induced reactions [4, 5, 6]. The most recent comprehensive one on non-relativistic and relativistic optical model formalisms and related topics for energies below 1 GeV is that of Ray, Hoffmann, and Coker [22]. Since then progress has slowed but significant steps have been made nonetheless in understanding the importance of different effects with NN scattering in the presence of other nucleons. The optical potential, as we consider it, uses the non-relativistic multiple scattering theory with the NN scattering amplitudes modified from the free NN values. Such is designated hereafter as an *effective interaction*. Those modifications are caused by the two nucleons interacting within the nuclear medium and are due to *Pauli blocking* and *mean field effects* for both projectile and bound state nucleons. In addition, there are other effects due to the convolution of the NN scattering amplitudes with target structure that require off the energy shell scattering amplitudes. Also of importance is the complete antisymmetrization of the $A + 1$ nucleon scattering system which leads to direct and knock out exchange amplitudes for NA scattering. The effect of such exchange amplitudes is not small at any energy and they are a source of

non-locality. That is also the case with the other medium effects [23].

The underlying principle of non-relativistic multiple scattering theories is that the fundamental dynamics leading to the NN potential is unaltered although medium effects vary the NN amplitudes from what the free NN system define them to be. There are other approaches to ascertain medium effects upon the NN potential. One of these is to use quark-gluon dynamics directly [24]. That approach involves a limited number of open parameters whose values, very often, are constrained by chiral symmetry. With that means, NA scattering has been analyzed allowing medium variation of coupling constants, masses, and form factors of boson exchange interactions. However, that approach is relevant with nuclear densities significantly above nuclear saturation as is the case in some astrophysical problems. It is very different from the *classical* one that is based upon the NN t matrix and which we discuss in this review.

If one assumes that only the free NN t matrix on the energy shell is necessary in calculations of the optical potential, the experimental NN amplitudes can be used. But if both the on- and off-shell properties of the t matrix are important, suitable representations of those properties are required. One of the first of such representations for the effective interaction used a local superposition of Gaussians or Yukawas in coordinate space [25, 26, 27]. At the same time, Love and Franey [28] also defined an effective t matrix comprising a sum of central, spin-orbit, and tensor components. However, their parameter values were chosen to match the then existent NN amplitudes [16] in an energy range between 50MeV and 1 GeV. So their force was controlled solely by the on-shell NN amplitudes. The Yukawa form factors were preferred since such forms were required with the suite of programs then in general use for NA scattering. Those programs were early versions of DWBA91 [29]. The same structural form remains in use today with parameters defined to match both on- and off-shell properties of the NN t - and g matrices as are required to use the code, DWBA98 [30]. With DWBA98 not only can one calculate non-local microscopic NA optical potentials, elastic scattering observables, and distorted waves, but also a consistent evaluation of inelastic and charge exchange reactions can be made with the same effective interaction acting as the transition operator. These calculations include direct and knockout amplitudes for all processes. A discussion of the developments of this coordinate space approach to scattering is an important facet of this review.

In parallel with the coordinate space investigations, there has been an ongoing interest in finding a rigorous treatment of momentum space

multiple scattering theory for NA scattering of which the most recent are presented in Refs. [31, 32]. The momentum space approaches, for both non-relativistic and relativistic optical model formulations, has been reviewed [22] and so we address what has developed since, being concerned particularly with NN potentials and the on- and off-shell attributes of the t - and g matrices they spawn.

To obtain the off-shell properties one relies on NN scattering theory. One such theory involves boson exchange potentials (OBEP), potentials which are termed *realistic* when they reproduce NN phase shifts. The most commonly used realistic potentials are those given by groups from Nijmegen [33], Paris [18], Bonn [34], Argonne [35] and Hamburg [36]. These potentials give very similar results for all phase shifts for energies below pion threshold. The alternative approach is to use fixed angular momentum inverse scattering theory [37, 38]. This mathematical approach, which produces off-shell t matrices from data [39], is also predicated upon a limiting class of interaction potentials. It is a surprise then to find that, in their effects, the off-shell properties of the t matrices from all of these realistic potentials differ little.

Both the direct and inverse approaches can be applied in the energy regime above pion threshold to specify t - and g matrices on- and off-shell. For example, the basic OBEP approaches have been extended seeking to incorporate other channel information [40, 41, 35], and a coupled channel method for NN scattering above threshold has been developed by Ray [42]. Alternatively, the inversion approach can be used to specify complex NN optical potentials for such energies [43].

The nuclear target and its microscopic structure is the other essential element in NA scattering theory. Originally, the structure assumed was that of a simple independent particle model. Today refinements and extensions to the shell model have made it possible to calculate wave functions in a large space allowing all, or a large fraction of, nucleons to be active. Other approaches to structure in NA scattering analyses include projected Hartree-Fock methods and mean-field models. Irrespective of what model of structure is chosen, one-body density matrix elements (OBDME) must be specified to construct an optical potential based on the NN interaction. To validate the wave functions obtained from the assumed structure model, and hence OBDME, it is often necessary to analyse complementary scattering data. Electron scattering form factors provide just such data as they reflect the target charge and current densities that are defined by the same OBDME.

This review comprises 12 Sections. The first is a brief outline of some formal aspects of the nuclear optical potential and the scattering theory by which it is related to NN scattering amplitudes, t matrices, and

g matrices. Then follows a presentation of the momentum space NA optical potential formed by the folding of NN t - and g matrices with nuclear densities. Applications are discussed with the examples taken from the works of Elster *et al.* [44, 45] and of Arellano *et al.* [46]. A folding model denning the optical potential in coordinate space is then considered in Section 4. That model presupposes an effective NN interaction to be comprised of density and energy dependent central, tensor, and two-body spin-orbit terms. Such effective interactions are basic for the computer codes DWBA91 [29] and DWBA98 [30] that are the current technology to calculate and use microscopic non-local coordinate space optical potentials. Thus in Section 4, we present the helicity formalism for the multipole expansion of the effective interaction and the particle-hole matrix elements that underly calculations made with those programs. A key feature of both the momentum and coordinate space formulations of the NA optical potentials are the NN t - and g matrices. Details of those are given in Sections 5 and 6 respectively. Therein the on- and off-shell properties of the t - and g matrices from realistic boson exchange potentials, as well as from potentials determined by inversion of phase shift data, are discussed. To form the coordinate space NA optical potentials requires the effective interaction in coordinate space. Thus a parameterisation scheme is needed to specify such from t - and g matrices. A scheme that has proven useful is discussed in Section 7. In fact, the effective interactions that result, when folded with nuclear structure, give NA potentials from which good fits are found to NA scattering data from targets ranging from ${}^3\text{He}$ to ${}^{238}\text{U}$, for energies from 40 to 300 MeV. The nuclear structure is required in all cases, and so in Section 8, a brief discussion of those used to date in the folding calculations is given. To confirm that the wave functions are appropriate, they have been used in analyses of electron scattering form factors, and the results of those analyses are discussed in Section 9. That validates use of those wave functions in DWBA analyses of inelastic proton scattering and of charge exchange reactions. With effective interactions and structure wave functions set, the folding procedure described in Section 4 has been applied to analyse pA scattering from stable nuclei. Those results are shown and discussed in Section 10. So also are those found by using the folding model to analyse the elastic scattering of radioactive beams of ${}^{6,8}\text{He}$ and ${}^{9,11}\text{Li}$ from hydrogen.

There are many applications in which use of a non-local NA potential is impractical. For such cases, equivalent local potentials and approximate forms for the exact wave functions are sought. There are several means by which these equivalent quantities can be found and they are presented in Section 11. By equivalent it is usually meant that the local

potential gives the same scattering phase shifts as does the non-local one. There are more approximate conditions though which can be made through equating non-local and local Schrödinger equations by transforms on the solutions or by finding equivalent wave number functions. Of more precise nature are the local optical potentials developed from data by use of inverse scattering theories [37].

Finally, in Section 12, we consider the extension of *NA* scattering to inelastic scattering and charge exchange reactions to discrete excited states using the DWBA with the non-local microscopic optical potentials specifying the distorted waves and the effective interactions as the transition operators effecting the excitations.

2. FORMAL THEORY OF THE NUCLEON-NUCLEUS OPTICAL POTENTIAL

The optical potential for *NA* scattering has been reviewed in an elegant way by Feshbach using projection operators [5]. It has also been given in some detail by Taylor [47]. Its formulation in terms of underlying *NN* interactions within a many nucleon theory, as was initiated by Chew and Watson and by Kerman, McManus and Thaler, is reviewed by Ray, Hoffmann, and Coker [22].

However, whatever the choice of formalism used or whatever many nucleon theory is adopted, practical application requires low order approximations to be taken on some facets. In the optical model approach, the many nucleon problem is reduced to one for a single particle with the kinetic energy being that of the projectile and with the potential energy accounting effectively for all of the complexity of the many body system. The *generalised optical model* includes more than the entrance channel and so our use of the term *optical potential* throughout this review is to be taken as the single elastic channel reduction.

The Feshbach formalism [48, 49] divides the Hilbert space using two projection operators P and Q . P projects onto the elastic channel and Q on to all others. Thus $P + Q = 1$, $PQ = QP = 0$ and $Q|\Psi_{gs}\rangle = 0$. With these projection operators, the Schrödinger equation segments as

$$(E - H_{PP})|\Psi^+\rangle = H_{PQ}|\Psi^+\rangle$$

$$(E - H_{QQ})|\Psi^+\rangle = H_{QP}|\Psi^+\rangle.$$

Using the second equation to eliminate $Q|\Psi\rangle$ from the first gives

$$(E - H_{PP} - H_{PQ}[E - H_{QQ} + i\epsilon]^{-1}H_{QP})|\Psi^+\rangle = 0, \quad (2.1)$$

where outgoing wave boundary conditions are assumed. The Feshbach formalism reduces the many nucleon problem to an effective one body one by invoking explicitly the ground state and transitions to other channels from the ground state with

$$(E - H_0 - \langle \Phi_{gs} | V | \Phi_{gs} \rangle - \langle \Phi_{gs} | V G_{QQ}^{(+)} V | \Phi_{gs} \rangle) |\chi^+ \rangle = 0. \quad (2.2)$$

Thereby the single nucleon *distorted wave* $|\chi^+\rangle$ for elastic scattering is defined. The intermediate state propagator is complex due to pole contributions. It contains the whole complex spectrum of many body excitations of the projectile and target nucleons in bound as well as in continuum states, with

$$G_{QQ}^{(+)} = [E - H_{QQ} + i\epsilon]^{-1}. \quad (2.3)$$

Thus the optical potential is identified by

$$U = U_{OM}(E) = \langle \Phi_{gs} | V | \Phi_{gs} \rangle + \langle \Phi_{gs} | V G_{QQ}^{(+)} V | \Phi_{gs} \rangle. \quad (2.4)$$

In general it is non-local, complex, and energy dependent due to the second term. With a local V the leading term is real, local, and energy independent. That is so provided antisymmetrization is ignored. Multiple scattering effects are contained within the second term. This concentration of all multiple scattering effects in the second term is largely ineffective since realistic NN potentials are short ranged and multiple scattering are significant. Treating them explicitly is the leading idea behind the Chew and Watson multiple scattering theory. They replace the potential in Eq. (2.4) by the complex NN t matrix. As a result, the leading term is now complex, non-local, and energy dependent. A more detailed development of its present implementations is given in the next two chapters dealing with the optical potentials in momentum and coordinate space. In the simplest versions it is assumed that only pairwise interactions between the projectile and target nucleons are important. With the projectile tagged 0, and target nucleons tagged i ,

$$V = \sum_{i=1}^A v_{0i} = A v_{0i}. \quad (2.5)$$

Furthermore, the NN t matrices are associated with the Lippmann-Schwinger (LS) equation

$$t_{0i} = v_{0i} + v_{0i} G_0^+(E) t_{0i}, \quad (2.6)$$

while the NN g matrices are associated with the Brueckner–Bethe–Goldstone (BBG) equation

$$\mathbf{g}_{0i} = \mathbf{v}_{0i} + \nu_{0i} \mathbf{G}_Q^+(\omega) \mathbf{g}_{0i}, \quad (2.7)$$

where \mathbf{G}_Q designates that medium effects such as Pauli blocking and a mean field are included and so modifying the free NN scattering propagation. Instead of V , the t and g matrices occur in Eq. (2.4) yielding formulations of the microscopic optical models in the spirit of KMT. In particular we follow the developments given in the book by Adhikari and Kowalski [13]. They use some auxiliary operators

$$\tilde{\mathbf{g}}_{0i} = (\mathbf{A} - 1) \mathbf{g}_{0i}, \quad (2.8)$$

and

$$\tilde{\mathbf{U}}_{\text{OM}}(E) = \frac{(\mathbf{A} - 1)}{\mathbf{A}} \mathbf{U}_{\text{OM}}(E), \quad (2.9)$$

with which a modified pA T matrix is defined by

$$\tilde{\mathbf{T}}_{\text{OM}} = \frac{(\mathbf{A} - 1)}{\mathbf{A}} \mathbf{T}_{\text{OM}} = \tilde{\mathbf{g}}_{0i} + \tilde{\mathbf{g}}_{0i} \mathbf{G}_0^{(+)} \tilde{\mathbf{T}}_{\text{OM}}. \quad (2.10)$$

The Feshbach subtraction technique then yields

$$\tilde{\mathbf{T}}_{\text{OM}} = \mathbf{U}_{\text{KMT}} + \mathbf{U}_{\text{KMT}} \mathbf{G}_0^{(+)} \mathbf{P} \tilde{\mathbf{T}}_{\text{OM}} \quad (2.11)$$

and

$$\mathbf{U}_{\text{KMT}} = \tilde{\mathbf{g}}_{0i} + \tilde{\mathbf{g}}_{0i} \mathbf{Q} \mathbf{G}_{\text{KMT}}^{(+)} \mathbf{Q} \tilde{\mathbf{g}}_{0i}, \quad (2.12)$$

where the resolvent is that of KMT [12],

$$\mathbf{G}_{\text{KMT}}^{(+)} = [\mathbf{E} - \mathbf{Q}(\mathbf{H}_0 + \tilde{\mathbf{g}}_{0i})\mathbf{Q}]^{-1}. \quad (2.13)$$

The optical potential itself then is the expectation value taken with the wave function attributes of the i^{th} nucleon in the target. It is still a many-nucleon problem as evaluation requires knowledge of the excitation spectrum of the target.

Expansion of Eq. (2.13) and truncation of this series at the first term gives the lowest order g matrix approximation which has been used for projectile energies in excess of about 40MeV. However, other studies [7, 15] suggest that the optical model approach has validity at even lower energies.

In a lowest order model, the complexity of the problem is reduced to a weighted sum of one nucleon expectation values. The weights, to first order, are the shell occupancy numbers. The resultant optical potential is still complex but that is now due to the complex nature of the g matrix rather than higher order terms in the expansion of

Eq. (2.12). Neglecting medium effects in the g matrix defines the t matrix approximation. If in addition, the antisymmetrization of the projectile and target nucleon wave function is ignored one has a fully off-shell $t\rho$ approximation.

As will be developed subsequently, the zero angular momentum transfer $I=0$ component of the optical potential will be used in specifying radial Schrödinger equations whose solutions are the distorted waves. There are also $I \neq 0$ amplitudes contributing to elastic scattering from non-zero spin targets. They may yield reorientation amplitudes even though, generally, they are small in comparison to the $I=0$ ones. A practical means of evaluation of the relevant $I \neq 0$ scattering amplitudes uses the distorted wave approximation. This is discussed in a later section.

3. MOMENTUM SPACE OPTICAL MODELS

In the last two decades, there has been considerable progress in implementing a rigorous treatment of k -space multiple scattering approaches for NA elastic scattering. The use of intuitive approximations have been reduced significantly and many have been eliminated [22, 51, 52, 53, 54, 31, 55, 56, 57, 58, 32]. Other degrees of freedom such as intermediate excitation of the Δ , meson production, and short range QCD effects either are effectively subsumed in the underlying NN interaction or have been found not to play any essential role.

The energy domains of investigations can be divided roughly into regions of projectile energies. The first lies below pion threshold and it is possible to identify therein, a low energy sector when $T_{lab} < 100\text{MeV}$ and a medium energy one with $T_{lab} \sim 100\text{--}300\text{MeV}$. The other domain is the conventionally defined medium energy sector with $T_{lab} > 300\text{MeV}$. The review by Ray, Hoffman, and Coker [22] gives an appraisal of non-relativistic and relativistic models mostly suitable and tested in the highest energy domain which they demonstrate is affected by relativistic dynamics and kinematics, relativistic phase space effects, relativistic spin rotations, and boosts of the pair interaction into the proper reference frame. Nevertheless, many analyses of data belonging to this second domain of energy have been analyzed using the simpler non-relativistic treatments of NA scattering since the underlying equation of motion is the Schrödinger or, equivalently, the LS equation. In those studies, relativistic kinematics and two component spinor wave functions have been taken.

There is an advantage in studying NA scattering below meson production threshold. For that energy domain, several high quality NN potentials now exist with which the NN observables and phase shifts are well fit [18, 34, 59, 60, 33, 35]. Additionally, quantum inversion potentials [46, 61] have been developed from the current and extensive phase shifts SAID [15] and Nijmegen [33]. The quantum inversion method is a rigorous mathematical method developed by Gel'fand, Levitan, Marchenko and others for various purposes. The Gel'fand-Levitan-Marchenko integral equations are used to continue on-shell t matrices into the off-shell domain via intermediate NN partial wave potentials which directly enter calculations of t and g matrices [62, 63]. Thus, with this approach, the microscopic NA optical model is based solely upon experimental NN scattering information in combination with a description of the target ground state density.

Whatever NN force is chosen, at all energies it is important to account for the effects of medium modification in evaluations of effective NN interactions. The primary effects are associated with off-shell t matrices, with Pauli blocking, and with the inclusion of mean field propagation of both the projectile and target nucleons. The treatment of anti-symmetrization between projectile and target nucleons also is required as that is a further source of non-locality in the optical models. All of these items are indispensable in the low and medium energy optical potentials in order to achieve quantitative results.

3.1. The Full-Folding t Matrix Approach

The central element of this approach is the spectator expansion of multiple scattering theory. That expansion usually is based upon the Watson multiple scattering theory [9, 10, 64], a paradigm of the early work of Chew and collaborators [8]. Scattering of a projectile from a complex bound system of A identical nucleons is described by the LS equation for the full T matrix

$$T = V + V\mathcal{G}_0(E)T \quad (3.1)$$

where V represents the pairwise interactions between projectile and each and every target nucleon. Taking the $A + 1$ particle Hamiltonian for NA scattering to have the form

$$\mathcal{H} = H_0 + \mathcal{H}_A + \sum_{i=1}^A V_{0i} = \mathcal{H}_0 + \sum_{i=1}^A V_{0i}, \quad (3.2)$$

the Green's function Eq. (3.1) is

$$\mathcal{G}_0(E) = [E - \mathcal{H}_0 + i\epsilon]^{-1}, \quad (3.3)$$

in which the interaction between the distinguishable projectile and target nucleon is ignored.

When it is conjectured that the elastic scattering sub-channel of the complete T matrix can be described by an optical model potential in a LS equation

$$T = U + U\mathcal{G}_0(E)PT, \quad (3.4)$$

that optical potential is defined by an integral equation,

$$U = V + V\mathcal{G}_0(E)QU. \quad (3.5)$$

Therein the projection operators P and Q are used, with the closure being $P + Q = 1$. If P is the projector onto the elastic channel then $[\mathcal{G}_0, P] = 0$. Based upon the ground state equation $\mathcal{H}_A |\Phi_A\rangle = E_A |\Phi_A\rangle$, the projection operator has the form $P = |\Phi_A\rangle\langle\Phi_A|$. With these limitations, the full elastic scattering T matrix is denoted by the integral equation

$$T_{el} = PTP = PUP + PUP\mathcal{G}_0(E)T_{el}. \quad (3.6)$$

The basic idea behind the spectator expansion is to order the scattering process in a sequence of active projectile-target interactions. In first order, the interaction between projectile and target is denoted in terms of *NN quasi scattering amplitudes*,

$$U = \sum_{i=1}^A \tau_{0i}, \quad (3.7)$$

where

$$\tau_{0i} = V_{0i} + V_{0i}\mathcal{G}_0(E)Q\tau_{0i} = \hat{\tau}_{0i} - \hat{\tau}_{0i}\mathcal{G}_0(E)P\tau_{0i}. \quad (3.8)$$

The reduced amplitudes $\hat{\tau}_{0i}$ are solutions of

$$\hat{\tau}_{0i} = V_{0i} + V_{0i}\mathcal{G}_0(E)\hat{\tau}_{0i}. \quad (3.9)$$

For elastic scattering only $P\tau_{0i}P$, or equivalently $\langle\Phi_a|\tau_{0i}|\Phi_A\rangle$, contribute to the optical model potential. If the interactions V_{0i} are the same for all target nucleons and differences between protons and neutrons are neglected then the KMT equation is recovered from the first order Watson expansion [12, 64].

The prime task is to find solutions of Eqs. (3.8) and (3.9). These equations involve many-body effects within the target as they contain

the Green's function $G_0(E)$. The model proceeds by expanding $G_0(E)$ yielding, in first order, the active pair Green's function

$$G_i(E) = [E + E_i - H_0 - H_i - W_i + i\epsilon]^{-1}, \quad (3.10)$$

where H_i is the kinetic energy and W_i is a single particle mean field acting upon the struck bound nucleon due to the other $A - 1$ nucleons present in the target. Here we note a caveat of this expansion approach: Pauli blocking and other medium effects are to be effectively included in W_i . Furthermore, there is no such medium effect present for the projectile. KMT approaches neglect this effect as well [65]. This asymmetry is eliminated in the antisymmetrized version of the optical model expansion [32].

Thus the effective interaction $\hat{\tau}_{0i}$ can be evaluated from the free t matrix

$$\hat{\tau}_{0i} = V_{0i} + V_{0i}G_0(E)\hat{\tau}_{0i} = t_{0i} + t_{0i}G_i(E)\hat{\tau}_{0i}, \quad (3.11)$$

where t_{0i} satisfies the LS equation

$$t_{0i} = V_{0i} + V_{0i}G_{0i}t_{0i}, \quad (3.12)$$

with the free two-particle Green's function

$$G_{0i} = [E + E_i - H_0 - H_i + i\epsilon]^{-1}. \quad (3.13)$$

In lowest order, Eq. (3.11) reduces to $\hat{\tau}_{0i} = t_{0i}$ and the spectator model then is a form of tp approximation which neglects all medium effects. Nevertheless, it has become customary to retain the nomenclature $\hat{\tau}_{0i}$ of the advanced approach already in the lowest order calculations used today.

Convolution of the effective interaction with the target wave function yields a non-local NA optical potential,

$$U(\mathbf{k}', \mathbf{k}; E) = \langle \mathbf{k}' | U | \mathbf{k} \rangle = \left\langle \mathbf{k}' \Phi_A \left| \sum_{\alpha} \hat{\tau}_{\alpha} \right| \mathbf{k} \Phi_A \right\rangle. \quad (3.14)$$

This is the spectator optical model potential. If the C.M. momentum of the active pair does not change in the collision,

$$U(\mathbf{k}', \mathbf{k}; E) = \sum_{\alpha} \int d\mathbf{p}' d\mathbf{p} \langle \mathbf{k}' \mathbf{p}' | \hat{\tau}_{\alpha} | \mathbf{k} \mathbf{p} \rangle \rho_{\alpha} \left(\mathbf{p}' + \frac{\mathbf{k}'}{A}, \mathbf{p} + \frac{\mathbf{k}}{A} \right) \delta(\mathbf{k}' + \mathbf{p}' - \mathbf{k} - \mathbf{p}), \quad (3.15)$$

where \mathbf{k} and \mathbf{k}' are the initial and final momenta of the projectile in the NA rest frame and ρ_{α} are the proton and neutron density matrices respectively. Using the variables

$$\mathbf{q} = \mathbf{k}' - \mathbf{k}, \quad \mathbf{K} = (\mathbf{k} + \mathbf{k}')/2, \quad \mathbf{P} = (\mathbf{p}' + \mathbf{p})/2, \quad (3.16)$$

yields

$$U(\mathbf{q}, \mathbf{K}; E) = \sum_{\alpha} \int d\mathbf{P} \left\langle \mathbf{k}', \mathbf{P} - \frac{1}{2} \mathbf{q} | \hat{\tau}_{\alpha} | \mathbf{k}, \mathbf{P} + \frac{1}{2} \mathbf{q} \right\rangle \\ \times \rho_{\alpha} \left(\mathbf{P} - \frac{A-1}{A} \frac{\mathbf{q}}{2} + \frac{\mathbf{K}}{A}, \mathbf{P} + \frac{A-1}{A} \frac{\mathbf{q}}{2} + \frac{\mathbf{K}}{A} \right). \quad (3.17)$$

With the redefinition $\mathbf{P} + \mathbf{K}/A \rightarrow \mathbf{P}$, which accounts for the recoil of the nucleus differently,

$$U(\mathbf{q}, \mathbf{K}; E) = \sum_{\alpha} \int d\mathbf{P} \left\langle \mathbf{k}', \mathbf{P} - \frac{\mathbf{q}}{2} - \frac{\mathbf{K}}{A} | \hat{\tau}_{\alpha} | \mathbf{k}, \mathbf{P} + \frac{\mathbf{q}}{2} - \frac{\mathbf{K}}{A} \right\rangle \\ \times \rho_{\alpha} \left(\mathbf{P} - \frac{A-1}{A} \frac{\mathbf{q}}{2}, \mathbf{P} + \frac{A-1}{A} \frac{\mathbf{q}}{2} \right) \quad (3.18)$$

The amplitudes $\hat{\tau}_{\alpha}$ are needed in the NA rest system. They relate to matrix elements in the NN rest frame by

$$\left\langle \mathbf{k}', \mathbf{P} - \frac{1}{2} \mathbf{q} - \frac{\mathbf{K}}{A} | \hat{\tau}_{\alpha} | \mathbf{k}, \mathbf{P} + \frac{1}{2} \mathbf{q} - \frac{\mathbf{K}}{A} \right\rangle = \eta(\mathbf{P}, \mathbf{q}, \mathbf{K}) \langle \mathbf{k}' | \hat{\tau}_{\alpha} | \mathbf{k} \rangle, \quad (3.19)$$

where $\mathbf{k} = (\mathbf{k} - \mathbf{P} - \mathbf{q}/2 + \mathbf{K}/A)/2$ and $\mathbf{k}' = (\mathbf{k} - \mathbf{P} + \mathbf{q}/2 + \mathbf{K}/A)/2$ are the initial and final momenta in the NN rest system. The Moeller factor $\eta(\mathbf{P}, \mathbf{q}, \mathbf{K})$ imposes a Lorentz invariant flux in the transformation from the NN to NA frame [66, 50, 67]. It is given by

$$\eta(\mathbf{P}, \mathbf{q}, \mathbf{K}) = \frac{[E(\mathbf{k}')E(\mathbf{k})]^2}{E(\mathbf{k}')E(\mathbf{P} - \mathbf{q}/2 - \mathbf{K}/A)E(\mathbf{k})E(\mathbf{P} + \mathbf{q}/2 - \mathbf{K}/A)} \quad (3.20)$$

where $E(\mathbf{k})$ are relativistic kinetic energies. With these specifications the spectator optical model is

$$U(\mathbf{q}, \mathbf{K}; E) = \sum_{\alpha} \int d\mathbf{P} \eta(\mathbf{P}, \mathbf{q}, \mathbf{K}) \hat{\tau}_{\alpha}(\mathbf{k}', \mathbf{k}; \omega) \\ \times \rho_{\alpha} \left(\mathbf{P} - \frac{A-1}{A} \frac{\mathbf{q}}{2}, \mathbf{P} + \frac{A-1}{A} \frac{\mathbf{q}}{2} \right). \quad (3.21)$$

In the spectator model, the amplitudes of $\hat{\tau}_{\alpha}$ are those of the free t matrix calculated at an appropriate energy ω . This energy should be evaluated from the beam energy and the binding energy of the struck particle so that ω is coupled to the integration variable \mathbf{P} . In spectator model calculations so far made, ω has been decoupled from the integration variable. In contrast, full-folding g matrix calculations include that coupling explicitly [46].

The ground state density matrix is chosen from an independent particle model which may be specified in terms of non-relativistic [22, 51, 68] or relativistic [22, 31] single particle equations. The density matrix is the sum over occupied orbits

$$\rho_\alpha(\mathbf{p}', \mathbf{p}) = \sum_i \Psi_{\alpha,i}^\dagger(\mathbf{p}') \Psi_{\alpha,i}(\mathbf{p}). \quad (3.22)$$

The optical potential, Eq. (3.21), requires its transformation into a function of \mathbf{q} and \mathbf{P} variables. Finally, a connection is made between density matrix and the density profile

$$\rho_\alpha(\mathbf{q}) = \int d\mathbf{P} \rho_\alpha\left(\mathbf{P} - \frac{A-1}{A} \frac{\mathbf{q}}{2}, \mathbf{P} + \frac{A-1}{A} \frac{\mathbf{q}}{2}\right). \quad (3.23)$$

3.2. The Full Folding g Matrix Approach

In this approach, a non-local \mathbf{k} -space optical potential results from a convolution of antisymmetrized effective interaction matrix elements [32]. The potential has the form

$$U(\mathbf{k}', \mathbf{k}; E) = \int d\mathbf{p} d\mathbf{p}' \sum_{\alpha \leq \epsilon_F} \Phi_\alpha^+(\mathbf{p}', \epsilon_\alpha) \langle \mathbf{k}', \mathbf{p}' | g(E + \epsilon_\alpha) | \mathbf{k}, \mathbf{p} \rangle_A \Phi_\alpha(\mathbf{p}, \epsilon_\alpha), \quad (3.24)$$

where E and ϵ_α are projectile and bound nucleon energies. In this model, the effective interaction is fully off-shell as it accounts for multiple scattering and contains medium effects. The latter comprise of Pauli blocking and mean fields acting upon both projectile and target nucleons. Eq. (3.24) contains a factorisation of target structure and effective interaction so that this folding model approach can use infinite nuclear matter g matrices. As with the r matrix approach, it is assumed that only two-nucleon correlations are important and that all other nucleons provide the mean field. The problem then is the construction of an NN propagator. For an energy ω , the BBG equation

$$g(\omega) = V + V G_Q(\omega) g(\omega) \quad (3.25)$$

is the relevant two-nucleon equation. It contains a bare NN interaction V and a medium dependent propagator $G_Q(\omega)$. Using details that are found in Refs. [55, 56, 57, 58, 32, 46] scattering in infinite nuclear matter is specified by

$$\begin{aligned} \langle \mathbf{K}', \mathbf{k}' | g(\omega) | \mathbf{K}, \mathbf{k} \rangle &= \delta(\mathbf{K}' - \mathbf{K}) \langle \mathbf{k}' | V | \mathbf{k} \rangle \\ &+ \int d\mathbf{q}' d\mathbf{Q}' d\mathbf{q} d\mathbf{Q} \langle \mathbf{K}', \mathbf{k}' | V | \mathbf{Q}', \mathbf{q}' \rangle \\ &\langle \mathbf{Q}', \mathbf{q} | G_Q(\omega) | \mathbf{Q}, \mathbf{q} \rangle \langle \mathbf{Q}, \mathbf{q} | g(\omega) | \mathbf{K}, \mathbf{k} \rangle. \end{aligned} \quad (3.26)$$

Conservation of total momentum by V eliminates one integral of the set in Eq. (3.26). Then, by using relative and C.M. momenta, $\mathbf{p} = \mathbf{K} - \mathbf{K}'$ and $\mathbf{P} = \frac{1}{2}(\mathbf{K}' + \mathbf{K})$, Eq. (3.26) becomes

$$\begin{aligned} \left\langle \mathbf{P} - \frac{1}{2}\mathbf{p}, \mathbf{k}' | g(\omega) | \mathbf{P} + \frac{1}{2}\mathbf{p}, \mathbf{k} \right\rangle &= \delta(\mathbf{p}) \langle \mathbf{k}' | V | \mathbf{k} \rangle \\ &+ \int d\mathbf{p}' d\mathbf{q}' d\mathbf{q} \langle \mathbf{k}' | V | \mathbf{q}' \rangle \left\langle \mathbf{P} - \frac{1}{2}\mathbf{p}, \mathbf{q}' | G_Q(\omega) | \mathbf{P} - \frac{1}{2}\mathbf{p} - \mathbf{p}', \mathbf{q} \right\rangle \\ &\times \left\langle \mathbf{P} - \frac{1}{2}\mathbf{p} - \mathbf{p}', \mathbf{q} | g(\omega) | \mathbf{P} + \frac{1}{2}\mathbf{p}, \mathbf{k} \right\rangle. \end{aligned} \quad (3.27)$$

The model proceeds by using Wigner transformations,

$$\begin{aligned} \left\langle \mathbf{P} - \frac{1}{2}\mathbf{p}, \mathbf{k}' | g(\omega) | \mathbf{P} + \frac{1}{2}\mathbf{p}, \mathbf{k} \right\rangle &= \frac{1}{(2\pi)^3} \int d\mathbf{R} e^{i\mathbf{R}\cdot\mathbf{p}} \\ \langle \mathbf{k}' | g(\omega, \mathbf{P}, \mathbf{R}) | \mathbf{k} \rangle \end{aligned} \quad (3.28)$$

to define a reduced effective interaction $g(\omega, \mathbf{P}, \mathbf{R})$ and similarly to get a reduced Green's function $G(\omega)$ from $G_Q(\omega)$. These reduced quantities link via the integral equation

$$\begin{aligned} g(\omega, \mathbf{P}, \mathbf{R}) &= V(\mathbf{P}, \mathbf{R}) + \frac{1}{(2\pi)^6} \int dr dr' d\mathbf{p} d\mathbf{p}' V(\mathbf{P} + \mathbf{p}, \mathbf{R} + \mathbf{r}) \\ &G(\omega, \mathbf{P} + \mathbf{p}, \mathbf{R} + \mathbf{r}) \times e^{i(r'p - r'p')} g\left(\omega, \mathbf{P} - \frac{1}{2}\mathbf{p}', \mathbf{R} - \frac{1}{2}\mathbf{r}'\right). \end{aligned} \quad (3.29)$$

Arellano *et al.* [46] link this to the BBG g matrix so that

$$\begin{aligned} \left\langle \mathbf{P} - \frac{1}{2}\mathbf{p}, \mathbf{k}' | g(\omega) | \mathbf{P} + \frac{1}{2}\mathbf{p}, \mathbf{k} \right\rangle &\sim \frac{1}{(2\pi)^3} \int d\mathbf{R} e^{i\mathbf{R}\cdot\mathbf{p}} \\ \langle \mathbf{k}' | g(\omega, \mathbf{P}, \mathbf{R}) | \mathbf{k} \rangle. \end{aligned} \quad (3.30)$$

The nuclear structure facet is specified using spectral functions such as

$$\langle \mathbf{p}_1, \mathbf{p}_2 | G_Q(\omega) | \mathbf{q}_1, \mathbf{q}_2 \rangle = \int dz_1 dz_2 \frac{A(\mathbf{p}_1, \mathbf{q}_1; z_1) A(\mathbf{p}_2, \mathbf{q}_2; z_2)}{\omega - z_1 - z_2 + i\epsilon}. \quad (3.31)$$

They have been used as a general scheme for practicality. In early approaches, a symmetric interacting Fermi gas model was used to construct the spectral function $A(z)$. That spectral function is characterised by the Fermi momentum k_F and the Fermi energy ϵ_F . In r -space

$$A_p(\mathbf{x}, \mathbf{y}; z) = \frac{1}{(2\pi)^3} \int d\mathbf{k} e^{i\mathbf{k} \cdot (\mathbf{x} - \mathbf{y})} \delta(z - \epsilon(k, k_F)) \Theta(\epsilon(k, k_F) - \epsilon_F). \quad (3.32)$$

Neglecting absorption, the dispersion relation contains a real mean field

$$\epsilon(k, k_F) = \frac{k^2}{2m} + U_{HF}(k, k_F), \quad (3.33)$$

with the Fermi gas relation linking density and Fermi momentum by

$$\rho(R) = \frac{2}{3\pi^2} k_F^3(R). \quad (3.34)$$

There exist several prescriptions to relate R with the projectile and target nucleon coordinates \mathbf{x} and \mathbf{y} respectively, such as $\mathbf{R} = |\mathbf{x} + \mathbf{y}|/2$, $(\mathbf{x} + \mathbf{y})/2$, x , y . The spectral function in \mathbf{k} -space is given by

$$A_p(\mathbf{p}_1, \mathbf{q}_1; z) = \frac{1}{(2\pi)^3} \int d\mathbf{r} d\mathbf{R} e^{i\mathbf{R} \cdot (\mathbf{q}_1 - \mathbf{p}_1)} e^{i\mathbf{r} \cdot (\mathbf{p}_1 + \mathbf{q}_1)/2} \times A_p\left(\mathbf{R} - \frac{1}{2}\mathbf{r}, \mathbf{R} + \frac{1}{2}\mathbf{r}; z\right), \quad (3.35)$$

with $\mathbf{r} = \mathbf{x} - \mathbf{x}'$. Using $\mathbf{P} = (\mathbf{q}_1 + \mathbf{p}_1)/2$ and $\mathbf{p} = \mathbf{q}_1 - \mathbf{p}_1$, upon integration the particle spectral function becomes

$$A_p\left(\mathbf{P} - \frac{1}{2}\mathbf{p}, \mathbf{P} + \frac{1}{2}\mathbf{p}; z\right) = \frac{1}{(2\pi)^3} \int d\mathbf{R} e^{i\mathbf{R} \cdot \mathbf{p}} \times \delta(z - \epsilon(P, k_F(R))) \Theta(\epsilon(P, k_F(R)) - \epsilon_F(R)). \quad (3.36)$$

If the approximation $k_F(|\mathbf{R} \pm \mathbf{r}/2|) \sim k_F(R)$ is used, the propagator becomes

$$\langle \mathbf{Q}', \mathbf{q} | G_Q(\omega) | \mathbf{Q}, \mathbf{q} \rangle = \frac{1}{(2\pi)^3} \int d\mathbf{R} e^{-i\mathbf{R} \cdot (\mathbf{Q}' - \mathbf{Q})} G_Q^{NM} \left(\omega, \frac{1}{2}(\mathbf{Q}' + \mathbf{Q}), \mathbf{q}, k_F(R) \right), \quad (3.37)$$

where

$$G_Q^{NM} = \frac{\mathcal{Q}(P_+, P_-, k_F)}{\omega - \epsilon(P_+, k_F) - \epsilon(P_-, k_F) + i\epsilon} \quad (3.38)$$

with $P_{\pm} = |\frac{1}{2}\mathbf{P} \pm \mathbf{q}|$ and

$$\mathcal{Q}(P_+, P_-, k_F) = \Theta(\epsilon(P_+, k_F) - \epsilon_F)\Theta(\epsilon(P_-, k_F) - \epsilon_F). \quad (3.39)$$

The k -space optical model of Eq. (3.24), with the g matrix approximation of Eq. (3.30), is the sum of antisymmetrized single particle matrix elements of the effective interaction between projectile and target nucleon pairs. Therein, Φ_{α} and ϵ_{α} are single particle wave functions and energies and the optical potential is

$$U(\mathbf{k}', \mathbf{k}; E) = \frac{1}{(2\pi)^3} \sum_{\alpha \in eF} \int d\mathbf{R} d\mathbf{P} d\mathbf{p} e^{i\mathbf{R} \cdot (\mathbf{q} - \mathbf{p})_{\rho_{\alpha}}} \left(\mathbf{P} + \frac{1}{2}\mathbf{p}, \mathbf{P} - \frac{1}{2}\mathbf{p} \right) \\ \times \left\langle \mathbf{k} - \frac{1}{4}(\mathbf{p} - \mathbf{q}) | g(E + \epsilon_{\alpha}, \mathbf{K} + \mathbf{P}, \mathbf{R}) | \mathbf{k} + \frac{1}{4}(\mathbf{p} - \mathbf{q}) \right\rangle_{\mathcal{A}}, \quad (3.40)$$

where

$$\rho_{\alpha} \left(\mathbf{P} + \frac{1}{2}\mathbf{p}, \mathbf{P} - \frac{1}{2}\mathbf{p} \right) = n_{\alpha} \Phi_{\alpha}^{\dagger} \left(\mathbf{P} + \frac{1}{2}\mathbf{p} \right) \Phi_{\alpha} \left(\mathbf{P} - \frac{1}{2}\mathbf{p} \right), \quad (3.41)$$

with n_{α} being shell occupation numbers. This k -space optical potential resembles closely that developed in r -space [25, 69, 70]. But it is a feature of this k -space approach that off-shell effects are treated more explicitly than in those r -space models which use instead a parameterisation of the g matrix. However, in the work of Arellano *et al.* [46], which is arguably the most complete application of the g matrix approach in k -space to date, several simplifying steps were used to effect calculations. First the interaction was assumed to be independent of \mathbf{R} , whence the g matrix elements do not depend on \mathbf{p} , thus $\mathbf{p} = 0$ was used and

$$U(\mathbf{k}', \mathbf{k}; E) = \int d\mathbf{R} e^{i\mathbf{R} \cdot \mathbf{q}} \sum_{\alpha} \int \mathbf{P} W_{\alpha}(\mathbf{R}, \mathbf{P}) \\ \langle \mathbf{k}' | g(E + \epsilon_{\alpha}, \mathbf{P} + \mathbf{K}, \mathbf{R}) | \mathbf{k} \rangle_{\mathcal{A}} \quad (3.42)$$

where

$$W_{\alpha}(\mathbf{R}, \mathbf{P}) = \frac{1}{(2\pi)^3} \int d\mathbf{p} e^{-i\mathbf{R} \cdot \mathbf{p}_{\alpha}} \left(\mathbf{P} + \frac{1}{2}\mathbf{p}, \mathbf{P} - \frac{1}{2}\mathbf{p} \right). \quad (3.43)$$

Next, the single particle energy in the g matrix is approximated by an average value and an expansion of the target density of the form

$$\rho\left(\mathbf{P} + \frac{1}{2}\mathbf{p}, \mathbf{P} - \frac{1}{2}\mathbf{p}\right) = \frac{4}{(2\pi)^3} \int d\mathbf{R}_\rho(\mathbf{R}) e^{i\mathbf{R}\cdot\mathbf{P}} \frac{1}{\hat{\rho}(\mathbf{R})} \Theta(\hat{k}_F(\gamma) - P) \quad (3.44)$$

was used, with the relation between and Fermi momentum in $\hat{\rho}(\mathbf{R})$ taken either with the Slater approximation, Eq. (3.34), or with that of Campi–Bouyssy [71].

With these approximations in k -space, a local coordinate space optical potential can be obtained using

$$U(\mathbf{k}', \mathbf{k}, E) = \frac{1}{(2\pi)^{3/2}} \int d\mathbf{R} e^{i(\mathbf{k}-\mathbf{k}')\cdot\mathbf{R}} \mathcal{U}(\mathbf{R}, E) \quad (3.45)$$

where

$$\begin{aligned} \mathcal{U}(\mathbf{R}, E) &= \frac{4}{(2\pi)^{3/2}} \frac{\rho(\mathbf{R})}{\hat{\rho}(\mathbf{R})} \int d\mathbf{P} \Theta(\hat{k}_F(\mathbf{R}) - P) \\ &\langle \mathbf{k}' | g(E + \bar{\epsilon}, \mathbf{K} + \mathbf{P}, \mathbf{R}) | \mathbf{k} \rangle_{\mathcal{A}}. \end{aligned} \quad (3.46)$$

Note however, that the results of calculations presented in the following were obtained by Arellano *et al.* [46] using the complete momentum space expression, Eq. (3.42), for the g matrix optical potential.

3.3. Results of Calculations

The results of calculations made by Weppner, Elster, and Huber [45] for the elastic scattering of 200MeV protons from ^{40}Ca and from ^{208}Pb are shown in Figs. 3.1 and 3.2. The purpose of that study was to assess the sensitivity of elastic nucleon scattering to the off-shell properties of NN t matrices. The optical potentials were based upon density matrices obtained from Dirac–Hartree (DH) calculations [72]. They used NN t matrices of the Nijmegen potentials [33], the Nijm-I and Nijm-II specifically, and of the charge dependent (CD) Bonn interaction [73]. All three t matrix sets fit the Nijmegen pp and pn scattering data base very well. On-shell, these t matrices are close in the energy range up to

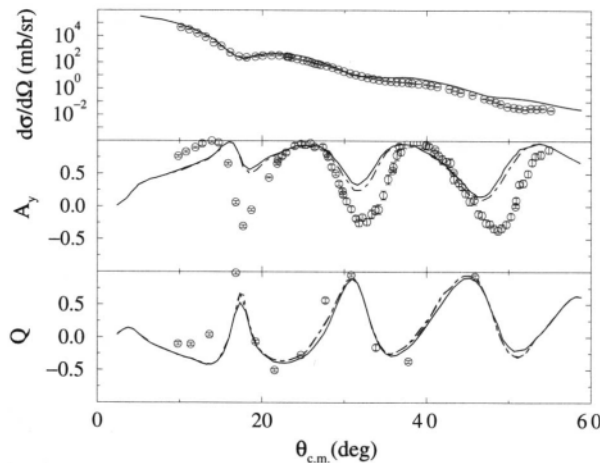


Fig. 3.1. The differential cross section (top), analyzing power (middle), and spin rotation Q (bottom) for the elastic scattering of 200MeV protons from ^{40}Ca . The solid lines represent the results of calculations made using the CD-Bonn t matrix, while the dashed and dot-dashed curves depict those obtained using the Nijm-I and Nijm-II t matrices in the folding respectively.

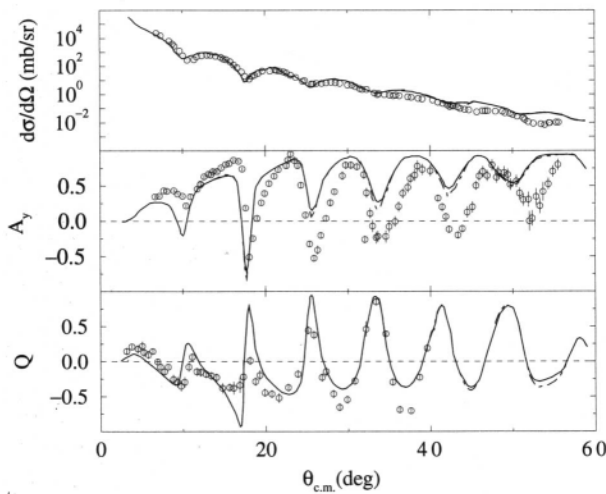


Fig. 3.2. As for Fig. 3.1, but for ^{208}Pb .

300MeV, but they do vary by several percent in the partial waves. The Nijm-I potential includes a momentum dependent non-local term while the Nijm-II is purely local in form. The ^{40}Ca results shown in Fig. 3.1 are compared with data taken by Meyer *et al.* [74,75]. All three calculations give very similar results with good reproduction of the differential cross section. They give too little structure in comparison to observation for the spin observables, and for the analyzing power in particular. The three calculated results for the scattering from ^{208}Pb shown in Fig. 3.2 are in even closer agreement with each other than in the case of ^{40}Ca . They also agree better with the analyzing power data, albeit the differential cross-section data now is less well reproduced than in the case of ^{40}Ca . The NA scattering results therefore do not show much sensitivity to different off-shell properties of the chosen t matrices. However, it has been noted [76] that NN interactions that are on-shell equivalent do have very similar off-shell variations in the region of the on-shell momentum.

The same cases were used previously by Elster, Weppner, and Chinn [44] taking different density matrices for the nuclei. They used the mean fields to vary the free t matrix to account for the effect of the nuclear medium upon the struck bound nucleon. Again many examples have been given in that paper [44] and we only present two. Thus, the results of those off-shell tp calculations are given in Figs. 3.3 and 3.4 for 200MeV proton elastic scattering from ^{40}Ca and ^{208}Pb respectively. Therein the full Bonn interaction [19] was used to specify the NN t matrices which were then folded with the DH density. The solid curves give the full results while those displayed by the dashed curves were found with the optimal factorisation approximation. Essentially the same results were found when a Hartree-Fock-Bogoliubov density matrix was used. The calculated results are very similar and now the spin observables found are in good agreement with the data. But the cross sections are noticeably less well reproduced by these calculations than by those of the later study [45] discussed above.

The prime problem with the off-shell tp approximation is that the medium modification of the projectile properties and the full treatment of exchange scattering amplitudes are very important. In momentum space calculations these have been taken into account in the g matrix folding calculations of Arellano *et al.* [32, 46]. That study [46] sought to identify the scope of the effects of off-shell differences in interactions in NA scattering. To do so they ensured that the (two) different starting NN interactions were, as far as possible numerically, phase

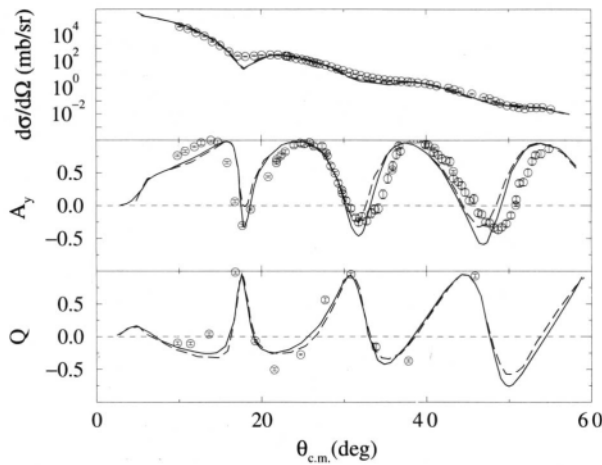


Fig. 3.3. The differential cross section (top), analyzing power (middle), and spin rotation Q (bottom) for the elastic scattering of 200 MeV protons from ^{40}Ca . The solid lines represent the results of full off-shell $t\rho$ calculations made using the full Bonn interaction t matrix, while the dashed curves depict results obtained in the optimal factorisation approximation.

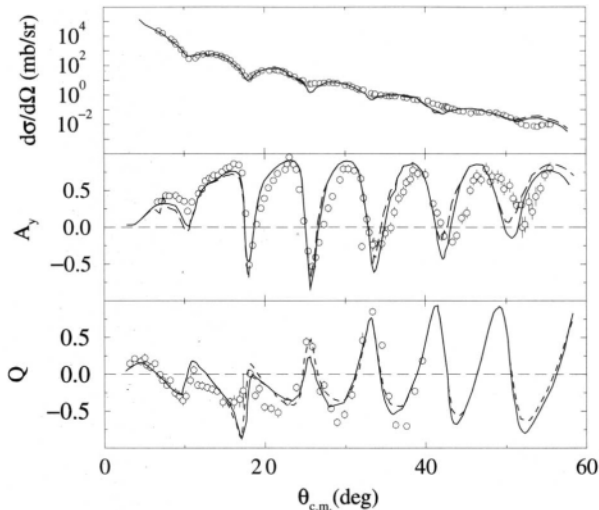


Fig. 3.4. As for Fig. 3.3, but for ^{208}Pb .

equivalent over a wide energy range. They chose the full momentum space Paris interaction [18] to define all NN channel phase shifts to 1 GeV which were then used in the Gel'fand-Levitan-Marchenko inversion to specify local energy independent interactions in all important NN scattering channels [77, 63]. By construction those inversion potentials have the same on-shell t matrices as the Paris interaction between 0 and 1GeV. A few degree differences were allowed with the phase shifts of the 3D_1 channel above 300 MeV to ensure numerical smoothness in the inversion. Thus these two interactions, the Paris and the Paris inversion, are phase equivalent and any differences they provide in calculations should arise from the intrinsic dynamics of the potentials off-shell.

The Paris and Paris inversion g matrices were used to calculate off-shell gp optical potentials for proton scattering from ^{40}Ca and ^{208}Pb with energies between 40 and 500 MeV. The bound state properties and densities were those used in Ref. [32]. All resulting scattering observables found with the two NN interactions are very close. The differences in cross sections and analyzing powers are of the same size as those between the results found later by Weppner *et al.* [45] using the Nijmegen and CD Bonn forces. It is to be concluded that, whatever the origin of interactions, as long their on-shell values are in very good agreement, their off-shell properties are very similar in the region of importance for NA scattering.

The inversion scheme is designed to work with phase shifts given from data analysis and a set of inversion potentials were obtained using the SM94 NN phase shifts [14]. Thus the Gel'fand-Levitan-Marchenko inversion process is a mediating method by which NN and NA scattering can be connected independent of a specific model prescription of NN scattering. Arellano *et al.* [46] used two g matrices in full folding calculations. The first g matrix was specified from the potentials obtained by inversion of the phase shifts of the Paris interaction; values which are not exactly equal to SM94 NN phase shifts. The second g matrix was built from the inversion potentials that were found by using the SM94 data. Results of the g folding calculations made using these two forces are epitomised by those shown in Fig. 3.5 wherein the cross sections and analyzing powers for the elastic scattering of 200 and of 300 MeV protons from ^{40}Ca are presented. The solid curves give the results obtained using the potentials found by inversion of the SM94 phase shifts. The dashed curves are those obtained using the Paris inversion potentials. Again the differences between

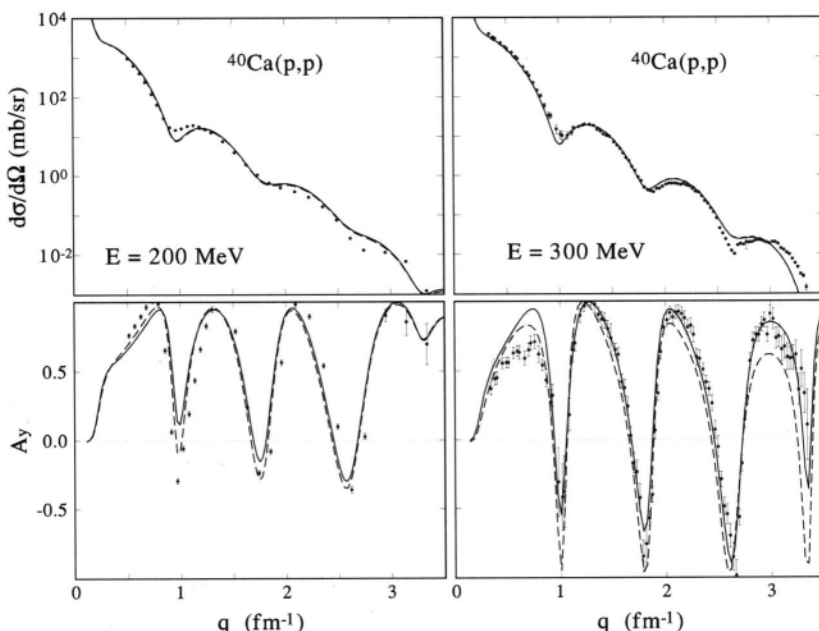


Fig. 3.5. The calculated and measured differential cross sections and analyzing powers for 200 and 300 MeV proton elastic scattering from ^{40}Ca .

the two calculations are not great and the results are in quite good agreement with the data to cross-section values of a few tenths of a mb/sr.

Likewise the results of the two calculations agree to a few percent at lower energies. Typical values are shown in Fig. 3.6 wherein is displayed the elastic scattering cross section and analyzing power from the scattering of 40MeV protons from ^{40}Ca . The level of agreement with actual data is as good as at higher energies for angles to 80° which typically is the range shown for most calculations.

An important point for momentum space folding models made by Arellano *et al.* [46] is that the choice of NN interaction, denned to fit NN scattering data below pion threshold while disregarding the higher energy behavior, is unlikely to be a realistic candidate to describe the NN interaction within the nuclear medium at medium energies.

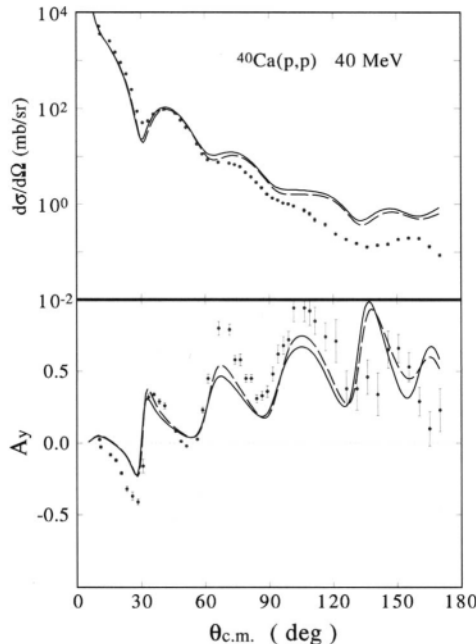


Fig. 3.6. The calculated and measured differential cross sections and analyzing powers for 40MeV proton elastic scattering from ^{40}Ca .

The results of calculations for 400 and 500 MeV protons from ^{40}Ca are shown in Fig. 3.7 where they are compared with the data from Refs. [78, 79]. Again the solid curves give the results obtained using the potentials found by inversion of the SM94 phase shifts, while the dashed curves are those obtained using the Paris inversion interaction. The results obtained using the Paris interaction do not fit the data, neither for NN scattering nor for NA scattering. On the other hand, by construction, the SM94 inversion potential reproduces the experimental NN phase shifts and the NA results obtained using g folding are in agreement with the 400 and 500 MeV cross sections and analyzing powers. This indicates that a quantitative description of NA data is a direct consequence of a quantitative description of NN data given that the microscopic treatment linking the two has been established. This holds for all other realistic potentials, and not just the Paris, as they all break down above 300 MeV. The complexity of the interaction dynamics in boson exchange potentials proves to be less relevant so

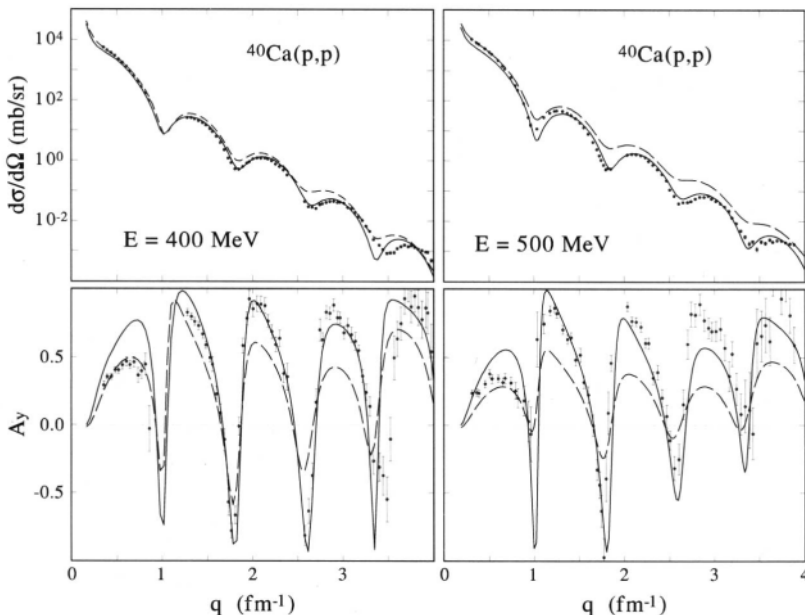


Figure. 3.7. As for Fig.3.5, but for 400 and 500 MeV protons.

far than their failure to reproduce on-shell NN properties. A further benefit of using inverse scattering theory to specify NN potentials is that it can be used to define those potentials at any time from the then best available phase shifts. Such phase shifts analyses extend presently to about 2 GeV for which no realistic boson exchange potential exists.

4. COORDINATE SPACE OPTICAL MODEL

The conventional coordinate space approach to study elastic NA scattering is a phenomenological one in which it is assumed that the scattering wave function satisfies a Schrödinger equation containing a local and energy dependent potential,

$$-\frac{\hbar^2}{2\mu} \nabla^2 \chi^{(+)}(\mathbf{r}; E) + U(\mathbf{r}; E) \chi^{(+)}(\mathbf{r}; E) = E \chi^{(+)}(\mathbf{r}; E). \quad (4.1)$$

But from the foregoing discussion, one can anticipate that the potential $U(r; E)$ should be non-local as well as energy dependent. Indeed, non-local potentials do result from microscopic treatments based upon NN interactions.

Manweiler [25] was one of the first to use a g folding model of the optical potential in coordinate space. He applied that model to analyse pA elastic scattering data for proton energies up to 40 MeV. The non-local character of the potentials were assessed and found to be consistent with the bound state Hartree-Fock (HF) potentials specified by Negele [80], albeit supplemented by an imaginary term. Manweiler found for the continuum systems that Negele's observation on bound systems remained valid, namely that the local equivalent to a strongly non-local but energy independent potential is strongly energy dependent. Further he noted also that the caveat of Negele and Vautherin [81] that the density matrix should not be replaced by the density profile, remained true for scattering. Brieva and Rook [82, 83] follow this approach closely.

4.1. The Folding Model of the Optical Potential

In practical applications, one uses the real and imaginary NA optical potentials calculated to first order in AW t or g matrices as effective interactions. The essential difference in approach to those described in the previous chapter is that an effective NN interaction in coordinate space is parameterised such that its plane wave matrix elements reproduce as best possible the on- and off-shell properties of those t and g matrices.

Historically, there was concern that no such parameterisation scheme could be designed to guarantee sufficient accuracy in reproduction of all the important on- and off-shell properties of the t and g matrices. The first of such parameterisations did not have that specifically in mind as it was designed to be a significant improvement on the then existing transition operators for inelastic scattering processes. Thus, at the time, it was a surprise to find that parameterisation led to folding models of the optical potential that gave very good results for elastic scattering [20, 84].

The original parameterisation [20, 84] used a potential ansatz of superpositions of Gaussian or Yukawa form factors. With that ansatz, the strengths of those form factor terms had to be energy and density dependent. The parameterisation scheme was simple and based directly upon

radial wave functions of the LS and BBG equations. Later the fitting procedure was altered to directly map large sets of values of on- and off-shell t and g matrix elements [85]. A key feature of this scheme is that the form factors remain local and of the form of superpositions of Yukawas as such is required with the programs of import for analysis of elastic, inelastic, and charge exchange reactions, DWBA91 and DWBA98 [29, 30].

With n_i being shell occupancies of the target, the potential in coordinate space can be defined by

$$\begin{aligned} U(\mathbf{r}, \mathbf{r}'; E) &= \delta(\mathbf{r} - \mathbf{r}') \sum_i n_i \int \varphi_i^*(\mathbf{s}) g_D(\mathbf{r}, \mathbf{s}; E) \varphi_i(\mathbf{s}) d\mathbf{s} \\ &\quad + \sum_i n_i \varphi_i^*(\mathbf{r}) g_E(\mathbf{r}, \mathbf{r}'; E) \varphi_i(\mathbf{r}') \\ &= U_D(\mathbf{r}; E) \delta(\mathbf{r} - \mathbf{r}') + U_E(\mathbf{r}, \mathbf{r}'; E), \end{aligned} \quad (4.2)$$

where the subscripts D, E designate the direct and exchange contributions, respectively. The coordinates \mathbf{r} and \mathbf{r}' are projectile coordinates and the summations are taken over the occupied bound single particle states. The basic ingredient in this approach is the choice of the direct and exchange g functions which are mixtures of the NN channel terms of the effective NN interaction. In principle they should be evaluated in the finite system studied using the most detailed structure information of the target available. To date this is impractical. It suffices to assume that they can be defined locally in terms of the parameterised NN interaction for the appropriate energies and at densities related to those from infinite nuclear matter systems, i.e.

$$g_{D/E} = g_{D/E} \left[\mathbf{r} - \mathbf{r}'; k_f \left(\frac{\mathbf{r} + \mathbf{r}'}{2} \right); E \left(\frac{\mathbf{r} + \mathbf{r}'}{2} \right) \right]. \quad (4.3)$$

Ignoring spin attributes temporarily, with this form of an optical potential the Schrödinger equation for elastic scattering is

$$\begin{aligned} \frac{\hbar^2}{2\mu} \nabla^2 \chi^{(+)}(\mathbf{r}, \mathbf{k}) + [E - U_D(\mathbf{r}; E)] \chi^{(+)}(\mathbf{r}, \mathbf{k}) \\ = \int U_E(\mathbf{r}, \mathbf{s}; E) \chi^{(+)}(\mathbf{s}, \mathbf{k}) d\mathbf{s}, \end{aligned} \quad (4.4)$$

where the Coulomb potential, usually that of a uniformly charged sphere, is included in the direct term. Using standard partial wave expansions, the radial Schrödinger equations have second order integro-differential form,

$$\frac{\hbar^2}{2\mu} \left[\frac{d^2}{dr^2} - \frac{l(l+1)}{r^2} + k^2 \right] f_{lj}(kr) = \sum_{l'j'} U_{lj'l'j'}^{D,(J)}(r) f_{l'j'}(kr) + \sum_{l'j'} \int_0^\infty U_{lj'l'j'}^{E,(J)}(r, r') f_{l'j'}(kr') dr'. \quad (4.5)$$

This reduces to an uncoupled system of equations for a target with angular momentum $J = 0$, for which $I = 0$ only. Likewise for nuclei with $J \neq 0$, by considering only the $I = 0$ contributions, one obtains a similar uncoupled set of equations. Collectively they are

$$\frac{\hbar^2}{2\mu} \left[\frac{d^2}{dr^2} - \frac{l(l+1)}{r^2} + k^2 \right] f_{lj}(kr) = U_{lj,lj}^{D,(J0)}(r) f_{lj}(kr) + \int_0^\infty U_{lj,lj}^{E,(J0)}(r, r') f_{lj}(kr') dr'. \quad (4.6)$$

The program suite, DWBA91 and DWBA98 [29, 30] evaluate the 5 matrix elements from solutions of those uncoupled integro-differential equations. For nuclei with $J \neq 0$, $I \neq 0$ contributions evidenced in Eq. (4.5) are also evaluated in those programs using a distorted wave Born approximation (DWBA). Technical details of these suite of programs are given next.

4.2. The Helicity Formalisms

The distorted wave for relative motion of a nucleon on a nucleus expanded in partial wave form is

$$\chi_v^{(+)}(\mathbf{k}, \mathbf{r}) = \frac{4\pi}{kr} \sum_{l,j,m,\mu,j',v'} i^l f_{lj}(kr) \left\langle l\mu \frac{1}{2} v | jm \right\rangle \left\langle l\mu' \frac{1}{2} v' | jm \right\rangle \times Y_{\mu}^*(\theta_k, \phi_k) Y_{\mu'}(\theta_r, \phi_r) \left| \frac{1}{2} v' \right\rangle, \quad (4.7)$$

where v is the spin projection of the in-going nucleon taken for an arbitrary axis and v' is its projection on the same axis at the point \mathbf{r} . Choosing this quantisation axis to be in the direction of \mathbf{k} leads to an equivalent expansion in terms of the two helicities λ where the two helicity functions $\left| \frac{1}{2} \lambda \right\rangle$ have projections $\lambda = \pm \frac{1}{2}$ along an axis parallel to \mathbf{r} [86]. The two spin representations link by the rotation matrix relationship,

$$\left| \frac{1}{2} v \right\rangle = \sum_{\lambda} R_{v,\lambda}^{*(\frac{1}{2})}(\phi_r, \theta_r, \psi_r) \left| \frac{1}{2} \lambda \right\rangle \quad (4.8)$$

where $(\phi_r, \theta_r, \psi_r)$ are the Euler angles between the $[\mathbf{k}]$ and $[\mathbf{r}]$ frames. The relationships between spherical harmonics and rotation matrices then give

$$\chi_{\lambda}^{(+)}(\mathbf{k}, \mathbf{r}) = \frac{1}{kr} \frac{1}{\sqrt{2\pi}} \sum_{j, \lambda'} (2j+1) X_{\lambda\lambda'}^{(j)}(kr) R_{\lambda, \lambda'}^{(j)*}(\phi_r, \theta_r, \psi_r) \left\langle \frac{1}{2} \lambda' \right\rangle \quad (4.9)$$

and the radial helicity functions are given by

$$X_{\lambda\lambda'}^{(j)}(kr) = i^{\left(\frac{j-1}{2}\right)} \frac{1}{r} [f_{l=j-1/2, j}(kr) + i(-1)^{(\lambda-\lambda')} f_{l=j+1/2, j}(kr)]. \quad (4.10)$$

These functions depend explicitly upon the helicity and so do not have a well defined parity. Thus one must define the outgoing wave by using the same transformations as well. This gives

$$\chi_{\lambda}^{(-)*}(\kappa, \rho) = \frac{1}{kr} \frac{1}{\sqrt{2\pi}} \sum_{j, \lambda'} (2j+1) \tilde{X}_{\lambda\lambda'}^{(j)}(kr) R_{\lambda, \lambda'}^{(j)*}(\phi_r, \theta_r, \psi_r) \left\langle \frac{1}{2} \lambda \right\rangle, \quad (4.11)$$

where

$$\tilde{X}_{\lambda\lambda'}^{(j)}(kr) = i^{\left(\frac{1}{2}-j\right)} \frac{1}{r} [f_{l=j-1/2, j}(kr) - i(-1)^{(\lambda-\lambda')} f_{l=j+1/2, j}(kr)]. \quad (4.12)$$

At this point it is convenient to develop the DWBA matrix elements for scattering. In the DWBA, scattering properties from a process in which the target nuclear states change from $\Phi_{J_f M_f}$ to $\Phi_{J_i M_i}$ are determined from scattering amplitudes

$$F_{v_f M_f; v_i M_i}(\mathbf{k}_f, \mathbf{k}_i) = -\frac{\mu}{2\pi\hbar^2} \sqrt{\frac{v_f}{v_i}} \mathcal{M}_{v_f M_f; v_i M_i}(\mathbf{k}_f, \mathbf{k}_i), \quad (4.13)$$

where

$$\begin{aligned} \mathcal{M}_{v_f M_f; v_i M_i}(\mathbf{k}_f, \mathbf{k}_i) = \\ \langle \chi_{v_f}^{(-)}(0) | \langle \Phi_{J_f M_f} (1, 2, \dots, A) | g_{trans} | \Phi_{J_i M_i} (1, 2, \dots, A) \rangle | \chi_{v_i}^{(+)}(0) \rangle, \end{aligned} \quad (4.14)$$

with g_{trans} in the pairwise interaction approximation being of the form

$$g_{trans} = \sum_{i=1}^A g_{trans}(0i) \mathcal{A}_{0i}; \quad (4.15)$$

\mathcal{A} being the antisymmetrization operator. These amplitudes may be defined for nucleons having helicities v_i, v_f quantize in the directions of the incident and emergent particle momenta $\mathbf{K}_i, \mathbf{K}_f$ and the differential cross section is given by

$$\frac{d\sigma}{d\Omega} = \frac{1}{2(2J_i+1)} \sum_{v_f, M_f; v_i M_i} |F_{v_f M_f; v_i M_i}(\mathbf{k}_f, \mathbf{k}_i)|^2. \quad (4.16)$$

As the NN transition operator \mathbf{g}_{trans} involves the projectile (emergent) nucleon, it is effectively a one-body operator in the space of the A -nucleon target states. Therefore with a cofactor expansion the nuclear states,

$$|\Phi_{JM}(1, 2, \dots, A)\rangle = \frac{1}{\sqrt{A}} \sum_{\alpha} a_{\alpha} |\Phi_{JM}(1, 2, \dots, A)\rangle |\phi_{\alpha}(1)\rangle, \quad (4.17)$$

which lead to one body density matrix elements (OBDME),

$$S_{j_1 j_2 J} = \left\langle J_f \left| \left[a_{j_2}^+ \times \tilde{a}_{j_1} \right] \right|^J \right| J_i \right\rangle = \sqrt{(2J_i + 1)(2J + 1)} Z_{j_1 j_2}^J, \quad (4.18)$$

being present in scattering amplitudes. These quantities will be discussed later in the chapters on nuclear structure and electron scattering. The equivalence of all target nucleons allows $\mathbf{g}_{trans} = \mathbf{A}_g(01)$ so that for protons scattering from target nucleons given with isospin projection ζ , the scattering amplitudes, Eq. (4.14), become

$$F_{v_f M_f, v_i M_i} = -\frac{\mu}{2\pi\hbar^2} \sqrt{\frac{v_f}{v_i}} \sum_{j_1, j_2, I, (N), \zeta} \frac{1}{\sqrt{2J_f + 1}} \langle J_i M_i | N | J_f M_f \rangle \\ S_{j_1 j_2 I}^{(J_i J_f)} \times \sum_{m_1 m_2} (-1)^{j_1 - m_1} \langle j_1 m_1 j_2 - m_2 | I - N \rangle f_{v_f j_2 m_2; v_i j_1 m_1}^{(\zeta)}(\mathbf{k}_f, \mathbf{k}_i), \quad (4.19)$$

where $f_{v_f j_2 m_2; v_i j_1 m_1}^{(\zeta)}(\mathbf{k}_f, \mathbf{k}_i)$ are NN direct plus exchange scattering amplitudes,

$$f_{scat} = f_{v_f j_2 m_2; v_i j_1 m_1}^{(\zeta)}(\mathbf{k}_f, \mathbf{k}_i) \\ = \langle \chi_{v_f}^{(-)}(0) \langle \phi_{j_2 m_2}(1) | g_{trans}(01) \mathcal{A}_{01} [\chi_{v_i}^{(+)}(0) \langle \phi_{j_1 m_1}(1) \rangle] \rangle_{\zeta}. \quad (4.20)$$

Adapting the initial and final scattering states to have helicities defined with respect to the direction of the incident particle for the initial state and to the direction of the outgoing particle for the final state, specifies the Jacob and Wick formalism. A similar formalism can be used for the target and hence the reaction may be described by a matrix with different frames for the initial and final states. Time reversal invariance is expressed with a minimal number of different matrix elements and the observables defined by tensor notations in these two frames can be obtained quite simply [87].

The bound state of a spin- $\frac{1}{2}$ particle with orbital angular momentum l , total angular momentum j , and projection m on the quantisation axis, is defined in the helicity formalism [88, 89] by,

$$|nljm\rangle = \sqrt{\frac{2j+1}{4\pi}} \sum_{\lambda} \varphi_{\lambda}^j(r) R_{m,\lambda}^{(j)}(\phi, \theta, \psi) |\lambda\rangle \quad (4.21)$$

with

$$\begin{aligned} \varphi_{1/2}^j(r) &= (-1)^{1+j-1/2} f_{nlj}(r) \\ \varphi_{-1/2}^j(r) &= f_{nlj}(r). \end{aligned} \quad (4.22)$$

There $|\lambda\rangle$ is the spin eigenfunction projected along the direction (ϕ, θ, ψ) and $f_{nlj}(r)$ is the radial function normalised according to

$$\int_0^\infty r^2 f_{nlj}^2(r) dr = 1 \quad (4.23)$$

All references to the orbital angular momentum have disappeared in this description of the bound state, but now there are two radial functions $\varphi_{\pm 1/2}^j$ which are equal to within a sign for any state of well-defined parity.

Thus the NN scattering amplitudes involve expectation values of an effective NN interaction (g_{trans}) with bound and scattering wave functions. Further development must allow for antisymmetrization of the NN product states and for tensor characteristics of the effective interactions. The prescription of DWBA matrix elements required in this approach to specify elastic scattering is also that required in analyses of inelastic scattering and charge exchange reactions. Development of those matrix elements proceed by using multipole expansions of the effective interactions.

4.3. Multipole Expansion of the Effective Interaction

If no spins are involved or their presence is ignored, an NN interaction can be expanded around the origin as

$$V(|\mathbf{r}_1 - \mathbf{r}_2|) = \sum_L (2L + 1) V_L(\mathbf{r}_1, \mathbf{r}_2) P_L(\cos \theta). \quad (4.24)$$

There are relationships between multipoles that are linked to the Fourier transform of $V(r)$, namely

$$\begin{aligned} W(q) &= \int e^{i\mathbf{q} \cdot \mathbf{r}} V(r) dr \\ V_L(\mathbf{r}_1, \mathbf{r}_2) &= \frac{2}{\pi} \int_0^\infty W(q) j_L(q\mathbf{r}_1) j_L(q\mathbf{r}_2) q^2 dq \end{aligned} \quad (4.25)$$

For spin- $\frac{1}{2}$ particles, the above generalizes to

$$V(1, 2) = \sum_{J, \lambda_1, \lambda_2, \lambda'_1, \lambda'_2} (2J+1) \left\langle \frac{1}{2} \lambda'_1 \right| \left\langle \frac{1}{2} \lambda'_2 \right| V^J_{\lambda'_1 \lambda'_2, \lambda_1 \lambda_2}(1, 2) \\ \left\langle \frac{1}{2} \lambda_1 \right| \left\langle \frac{1}{2} \lambda_2 \right| \times \sum_{\mu} (-1)^{\mu} R^{(J)}_{\mu, \lambda_1 - \lambda'_1}(\phi_1, \theta_1, \psi_1) R^{(J)}_{-\mu, \lambda_2 - \lambda'_2}(\phi_2, \theta_2, \psi_2), \quad (4.26)$$

where $(\phi_1, \theta_1, \psi_1)$ describes a co-ordinate system with z -axis in the direction of \mathbf{r}_1 and $(\phi_2, \theta_2, \psi_2)$ a second system having its z -axis in the direction of \mathbf{r}_2 . Note that the summed result is independent of the angles ψ_1 and ψ_2 .

Some symmetry properties of the two-body force hold in this development. To study their consequences, it is simplest to choose the axis of quantisation in the direction of \mathbf{r}_1 together with a frame of reference for particle 2 given by the Euler angles $(0, \theta, 0)$. As a result,

$$V^J_{\lambda'_1 \lambda'_2, \lambda_1 \lambda_2}(1, 2) = \sum_J V^J_{\lambda'_1 \lambda'_2, \lambda_1 \lambda_2}(1, 2) (-1)^{\lambda'_1 - \lambda_1} r^{(J)}_{\lambda'_1 - \lambda_1, \lambda_2 - \lambda'_2}(\theta). \quad (4.27)$$

The action of the parity operator P gives the symmetry

$$V^J_{\lambda'_1 \lambda'_2, \lambda_1 \lambda_2}(1, 2) = V^J_{-\lambda'_1 - \lambda_2, -\lambda_1 - \lambda'_2}(1, 2), \quad (4.28)$$

but time reversal invariance depends on the nature of the operators and is fulfilled if

$$V^J_{\lambda'_1 \lambda'_2, \lambda_1 \lambda_2}(1, 2) = \eta V^J_{-\lambda_1 - \lambda_2, -\lambda'_1 - \lambda'_2}(1, 2), \quad (4.29)$$

where $\eta = -1$ for any element involving a derivative operator or with any element that is odd under permutation of λ and λ' . It is $+1$ otherwise.

For an AW interaction, there are *a priori* 16 helicity amplitudes for each value of J and a two-body form factor could be associated with them. Conservation of parity reduces that to an independent set of just 8 while under time reversal invariance 10 of the 16 are even; six of those 10 are parity invariant. Finally one needs to ensure invariance under particle exchange, and with all three symmetries invoked, the properties can be represented by Kronecker products of 2×2 matrices in the space of the helicity for each particle, i.e.,

$$\begin{vmatrix} 1 & 0 \\ 0 & 1 \end{vmatrix}; \begin{vmatrix} 0 & 1 \\ 1 & 0 \end{vmatrix}; \begin{vmatrix} -1 & 0 \\ 0 & 1 \end{vmatrix}; \begin{vmatrix} 0 & 1 \\ -1 & 0 \end{vmatrix}. \quad (4.30)$$

The first two of these four innately satisfy the parity condition of Eq. (4.27), while the two other have odd parity. Thus, if parity conservation applies, these two kinds of elementary matrices cannot be mixed and the two-body interaction can be separated into even and odd parity parts. The even parity part has the structural form

$$a'(1, 2) \begin{vmatrix} 1 & 0 \\ 0 & 1 \end{vmatrix} \otimes \begin{vmatrix} 1 & 0 \\ 0 & 1 \end{vmatrix} + b'(1, 2) \begin{vmatrix} 1 & 0 \\ 0 & 1 \end{vmatrix} \otimes \begin{vmatrix} 0 & 1 \\ 1 & 0 \end{vmatrix} \\ + b''(1, 2) \begin{vmatrix} 0 & 1 \\ 1 & 0 \end{vmatrix} \otimes \begin{vmatrix} 1 & 0 \\ 0 & 1 \end{vmatrix} + c'(1, 2) \begin{vmatrix} 0 & 1 \\ 1 & 0 \end{vmatrix} \otimes \begin{vmatrix} 0 & 1 \\ 1 & 0 \end{vmatrix}, \quad (4.31)$$

and the odd part has the form

$$d'(1, 2) \begin{vmatrix} -1 & 0 \\ 0 & 1 \end{vmatrix} \otimes \begin{vmatrix} -1 & 0 \\ 0 & 1 \end{vmatrix} + e'(1, 2) \begin{vmatrix} -1 & 0 \\ 0 & 1 \end{vmatrix} \otimes \begin{vmatrix} 0 & -1 \\ 1 & 0 \end{vmatrix} \\ + e''(1, 2) \begin{vmatrix} 0 & -1 \\ 1 & 0 \end{vmatrix} \otimes \begin{vmatrix} -1 & 0 \\ 0 & 1 \end{vmatrix} + f'(1, 2) \begin{vmatrix} 0 & -1 \\ 1 & 0 \end{vmatrix} \otimes \begin{vmatrix} 0 & -1 \\ 1 & 0 \end{vmatrix}. \quad (4.32)$$

Under time-reversal invariance, a , c , d , e , and f must be expressed in terms of time-reversal invariant operators, and b must change sign. Consequently b vanishes for a local interaction.

As the absolute value of the magnetic quantum numbers of the reduced matrix element must be less or equal to J some two-body form factors vanish for $J = 0$, notably

$$a^0(1, 2) \neq 0, \quad b^0(1, 2) = b'^0(1, 2) = c^0(1, 2) = 0, \\ d^0(1, 2) \neq 0, \quad e^0(1, 2) = e'^0(1, 2) = f^0(1, 2) = 0. \quad (4.33)$$

For a spin-independent central interaction as in Eq. (4.24), the multipoles are given in the helicity notation by

$$a' = V_J(\mathbf{r}_1, \mathbf{r}_2), \quad b' = c' = 0, \quad d' = e' = f' = 0. \quad (4.34)$$

A consequence is that the odd parity terms vanish. On the other hand, for a central interaction component such as $V(|\mathbf{r}_1 - \mathbf{r}_2|) \{\boldsymbol{\sigma}_1 \cdot \boldsymbol{\sigma}_2\}$ one finds

$$a' = b' = 0, \quad c' = -V_J(\mathbf{r}_1, \mathbf{r}_2) \\ d' = \frac{1}{2J+1} [JV_{J-1}(\mathbf{r}_1, \mathbf{r}_2) + (J+1)V_{J+1}(\mathbf{r}_1, \mathbf{r}_2)] \\ e' = \frac{\sqrt{J(J+1)}}{2J+1} [V_{J-1}(\mathbf{r}_1, \mathbf{r}_2) - V_{J+1}(\mathbf{r}_1, \mathbf{r}_2)] \\ f' = \frac{1}{2J+1} [(J+1)V_{J-1}(\mathbf{r}_1, \mathbf{r}_2) + JV_{J+1}(\mathbf{r}_1, \mathbf{r}_2)]. \quad (4.35)$$

Thus as the central element in any NN interaction involves just the unit and $\{\boldsymbol{\sigma}_1 \cdot \boldsymbol{\sigma}_2\}$ operators, in the helicity formalism for this one need consider just four basic operators. They are $(I, \boldsymbol{\sigma})$ for the even part and $(-\boldsymbol{\sigma}, -i\boldsymbol{\sigma}^y)$ for the odd part of the force. The magnetic quantum numbers of the rotationally reduced matrix element in Eq. (4.27) are $(0, 0)$ for

σ^i and σ^j , $(0, \pm 1)$ for b^j and e^j , and $(\pm 1, \pm 1)$ for c^j and f^j . To compute the expression of $V(|\mathbf{r}_1 - \mathbf{r}_2|)\{\sigma_1 \cdot \sigma_2\}$ it is necessary to express $\sigma_1 \cdot \sigma_2$ in terms of these matrices, taking into account that σ_1 must be expressed with an axis of quantisation along \mathbf{r}_1 and σ_2 with quantisation along \mathbf{r}_2 . Using the components σ^1 , σ^0 , and σ^{-1} gives

$$\sigma_1 \cdot \sigma_2 = \sum_{i,j} (-1)^i \sigma_1^{-i} \sigma_2^j r_{i,j}^{(1)}(\theta), \quad (4.36)$$

which when multiplied by $V(|\mathbf{r}_1 - \mathbf{r}_2|)$ as specified in Eq. (4.24), gives

$$V(|\mathbf{r}_1 - \mathbf{r}_2|)\{\sigma_1 \cdot \sigma_2\} = \sum_J V_J (2J+1) (-1)^{\lambda_1 - \lambda_2} r_{\lambda_1 - \lambda_2, \lambda_2 - \lambda_1}^{(J)}(\theta), \quad (4.37)$$

in which the strength is

$$V^J = \frac{1}{2J+1} \sum_{ijL} (2L+1) V_L(\mathbf{r}_1, \mathbf{r}_2) \langle L01i | J_i \rangle \langle L01j | J_j \rangle \sigma_1^{-i} \sigma_2^j. \quad (4.38)$$

The symmetry relations of the Clebsch-Gordan coefficients mean that the $L = J$ terms reduce to

$$V_{L=J}^J = -V_J(\mathbf{r}_1, \mathbf{r}_2) \left(\frac{1}{2} \right) (\sigma_1^{-1} - \sigma_1^1)(\sigma_2^{-1} - \sigma_2^1), \quad (4.39)$$

where the Kronecker product of two-dimension matrices is twice that used in the definition of the coefficient c^J in Eq. (4.35). The factor of $\frac{1}{2}$ is simply the square of a Clebsch-Gordan coefficient, $\langle J011 | J1 \rangle^2$ specifically. For terms with $L \neq J$ the Clebsch-Gordan coefficients with opposite magnetic quantum numbers are equal and they can be expressed with σ^0 and $\sigma^1 \pm \sigma^{-1}$ to obtain d^J , e^J , and f^J of Eq. (4.35). Note that the matrices in Eqs. (4.31) and (4.32) are not the spin- $\frac{1}{2}$ Pauli matrices but simply a convenient way to span the helicity space. However, for a spin dependent interaction which does not involve the identity matrix, there is no identity matrix in the helicity representation and $a' = b' = 0$.

The two-body scalar interaction is expressed conveniently in two-body spin and isospin channels. The interaction is cast in terms of $V_{(S=0, T=0)}$, $V_{(S=0, T=0)}$, and $V_{(S=0, T=1)}$. The isospin will be considered later. However the foregoing formalism remains in force as with $S = \frac{1}{2}(\sigma_1 + \sigma_2)$ the eigenvalue of $\{\sigma_1 \cdot \sigma_2\}$ is -3 for $S = 0$ and 1 for $S = 1$. Therefore, the interaction in this form can be identified by

$$\begin{aligned} V_{(S=0)} &= V \frac{1 - \boldsymbol{\sigma}_1 \cdot \boldsymbol{\sigma}_2}{4}, \\ V_{(S=1)} &= V \frac{3 + \boldsymbol{\sigma}_1 \cdot \boldsymbol{\sigma}_2}{4}, \end{aligned} \quad (4.40)$$

with a similar prescription for the isospin.

In the helicity formalism, the multipole expansion of a tensor interaction follows by using the form

$$V_{\text{tens}} = V(|\mathbf{r}_1 - \mathbf{r}_2|) \{ 3[\boldsymbol{\sigma}_1 \cdot (\mathbf{r}_1 - \mathbf{r}_2)][\boldsymbol{\sigma}_2 \cdot (\mathbf{r}_1 - \mathbf{r}_2)] - (\mathbf{r}_1 - \mathbf{r}_2)^2 [\boldsymbol{\sigma}_1 \cdot \boldsymbol{\sigma}_2] \}. \quad (4.41)$$

This is the usual form of the tensor interaction multiplied by $(\mathbf{r}_1 - \mathbf{r}_2)^2$. This interaction has even and odd parity parts, with the even part identified by

$$\begin{aligned} a'(1, 2) &= b'(1, 2) = 0 \\ c'(1, 2) &= (r_1^2 + r_2^2) V_J(r_1, r_2) \\ &\quad - r_1 r_2 \left[\frac{2J+3}{2J+1} V_{J-1}(r_1, r_2) + \frac{2J-1}{2J+1} V_{J+1}(r_1, r_2) \right]. \end{aligned} \quad (4.42)$$

The odd part of the tensor interaction has

$$\begin{aligned} d'(1, 2) &= 2(r_1^2 + r_2^2) \left\{ \frac{J}{2J+1} V_{J-1}(r_1, r_2) + \frac{J+1}{2J+1} V_{J+1}(r_1, r_2) \right\} \\ &\quad - r_1 r_2 \left\{ \frac{J(J-1)}{(2J-1)(2J+1)} V_{J-2}(r_1, r_2) + \frac{14J^2 + 14J - 10}{(2J-1)(2J+3)} \right. \\ &\quad \left. V_J(r_1, r_2) + \frac{(J+1)(J+2)}{(2J+1)(2J+3)} V_{J+2}(r_1, r_2) \right\} \\ e'(1, 2) &= (2r_1^2 - r_2^2) \frac{\sqrt{J(J+1)}}{2J+1} \{ V_{J-1}(r_1, r_2) - V_{J+1}(r_1, r_2) \} \\ &\quad + r_1 r_2 \sqrt{J(J+1)} \left\{ \frac{J-1}{(2J-1)(2J+1)} V_{J-2}(r_1, r_2) \right. \\ &\quad \left. + \frac{1}{(2J-1)(2J+3)} V_J(r_1, r_2) - \frac{J+2}{(2J+1)(2J+3)} V_{J+2}(r_1, r_2) \right\} \\ f'(1, 2) &= -(r_1^2 + r_2^2) \left\{ \frac{J+1}{2J+1} V_{J-1}(r_1, r_2) + \frac{J}{2J+1} V_{J+1}(r_1, r_2) \right\} \\ &\quad - r_1 r_2 \left\{ \frac{(J-1)(J+1)}{(2J-1)(2J+1)} V_{J-2}(r_1, r_2) - \frac{10J^2 + 10J - 9}{(2J-1)(2J+3)} V_J(r_1, r_2) \right. \\ &\quad \left. + \frac{J(J+2)}{(2J+1)(2J+3)} V_{J+2}(r_1, r_2) \right\}. \end{aligned} \quad (4.43)$$

Next we consider the relative spin-orbit interaction in the form

$$\begin{aligned}
 V(r_{12})(\mathbf{L} \cdot \mathbf{S}) &= V(|\mathbf{r}_1 - \mathbf{r}_2|)(\mathbf{L} \cdot \mathbf{S}) \\
 &= \frac{1}{4} V(|\mathbf{r}_1 - \mathbf{r}_2|)[(\mathbf{r}_1 - \mathbf{r}_2) \times i(\nabla_1 - \nabla_2)] \cdot (\boldsymbol{\sigma}_1 + \boldsymbol{\sigma}_2) \\
 &= \frac{1}{4} (|\mathbf{r}_1 - \mathbf{r}_2|) \left[\mathbf{L}_1 + \mathbf{L}_2 + i(\mathbf{r}_1 \times \mathbf{r}_2) \left(\frac{1}{r_2} \frac{d}{dr_2} - \frac{1}{r_1} \frac{d}{dr_1} \right) \right. \\
 &\quad \left. + \frac{1}{r_2^2} \mathbf{r}_1 \times (\mathbf{r}_2 \times \mathbf{L}_2) + \frac{1}{r_1^2} \mathbf{r}_2 \times (\mathbf{r}_1 \times \mathbf{L}_1) \right] \cdot (\boldsymbol{\sigma}_1 + \boldsymbol{\sigma}_2). \quad (4.44)
 \end{aligned}$$

This specification differs from that given previously [88] and [90] which omitted the factor of $\frac{1}{4}$. Following the above procedure, the helicity multipoles for the odd parity part of this interaction are given by

$$\begin{aligned}
 d^J(1, 2) &= -\frac{1}{2(2J+1)} \left[2J(J+1) - (\alpha'_{j_1 j_1})^2 \right] (V_{J-1} - V_{J+1}) \\
 e^J(1, 2) &= -\frac{\sqrt{J(J+1)}}{8(2J+1)} \left\{ \left[(J+2)V_{J-1} - (2J+1) \left(\frac{r_2}{r_1} \right) V_J + (J-1)V_{J+1} \right] \right. \\
 &\quad \left. - \frac{1}{J(J+1)} (\alpha'_{j_1 j_1})^2 \left[(J+1)V_{J-1} - (2J+1) \left(\frac{r_2}{r_1} \right) V_J + JV_{J+1} \right] \right\} \\
 f^J(1, 2) &= -\frac{1}{4(2J+1)} [(J+1)V_{J-1} + JV_{J+1}] + \frac{1}{8} \left(\frac{r_1}{r_2} + \frac{r_2}{r_1} \right) V_J. \quad (4.45)
 \end{aligned}$$

The coefficients $\alpha'_{jj'}$ will be defined later in the specification of particle-hole matrix elements. For the even part of this spin-orbit interaction however, the multipoles are given by

$$\begin{aligned}
 a'(1, 2) &= -\frac{1}{2} V_J - \frac{1}{8} \left(\frac{r_1}{r_2} + \frac{r_2}{r_1} \right) \left[\frac{J(J-1)}{2J+1} V_{J-1} - \frac{(J+1)(J+2)}{2J+1} V_{J+1} \right] \\
 &\quad + \frac{1}{8(2J+1)} \left[\frac{r_1}{r_2} (\alpha'_{j_2 j'_2})^2 + \frac{r_2}{r_1} (\alpha'_{j_1 j'_1})^2 \right] (V_{J-1} - V_{J+1}) \\
 b'(1, 2) &= b'_1(1, 2) + b'_2(1, 2) \\
 c'(1, 2) &= \frac{1}{4} V_J - \frac{1}{2(2J+1)} \left(\frac{r_1}{r_2} + \frac{r_2}{r_1} \right) [(J+1)V_{J-1} + JV_{J+1}]. \quad (4.46)
 \end{aligned}$$

The multipole $b'(1, 2)$ is the sum of a derivative term,

$$b_1^J(1, 2) = \frac{\sqrt{J(J+1)}}{4(2J+1)} \left[(V_{J-1} - V_{J+1}) \left(r_2 \frac{d}{dr_1} - \kappa_1 \frac{d}{dr_2} \right) + \frac{1}{2} \left(\frac{r_2}{\kappa_1} - \frac{\kappa_1}{r_2} \right) (c_1 V_{J-1} + c_2 V_{J+1}) \right], \quad (4.47)$$

and a term that is odd under permutation of j_1 and j_2 with j'_1 and j'_2 ,

$$b_2^J(1, 2) = \frac{1}{8} \frac{k_{j_1}^2 - k_{j_2}^2}{\sqrt{J(J+1)}} \left\{ -V_J + \left(\frac{r_2}{\kappa_1} \right) \left[\frac{J+1}{2J+1} V_{J-1} + \frac{J}{2J+1} V_{J+1} \right] \right\} + \frac{1}{4} \left(\frac{k_{j_2} + k_{j_2}}{k_{j_2} - k_{j_2}} \right) \left\{ V_J - \left(\frac{\kappa_1}{r_2} \right) \left[\frac{J}{2J+1} V_{J-1} + \frac{J+1}{2J+1} V_{J+1} \right] \right\}. \quad (4.48)$$

The coefficients κ_j are also specified later in the development of particle-hole matrix elements. Note that the weight coefficients $c_1 = J + 1$ and $c_2 = J$ become $c_1 = J - 1$ and $c_2 = J + 2$ if the form of the radial functions are r times the ones taken here.

As a consequence, for a natural parity excitation effected by the two-body spin-orbit force, the multipole operator has the general form

$$F_{LS}(r) = A(r) + B(r) \frac{1}{\sqrt{J(J+1)}} (k_i - k_f) + A_1(r) \frac{1}{J(J+1)} (k_i - k_f)^2 + B_2(r) (k_i + k_f) + A_2(r) \frac{1}{J(J+1)} (k_i - k_f)(k_i + k_f) + \left[A_3(r) + B_3(r) \frac{1}{\sqrt{J(J+1)}} (k_i - k_f) \right] \frac{d}{dr}, \quad (4.49)$$

while for unnatural parity excitations, they take the form

$$F_{LS}(r) = C(r) + D(r) \frac{1}{\sqrt{J(J+1)}} (k_i + k_f) + C_1(r) \frac{1}{J(J+1)} (k_i + k_f)^2. \quad (4.50)$$

The spin-orbit interaction only contributes to $S = 1$ channels.

It may be appropriate in nuclear transitions to allow the effective NN interaction to have a form that includes quadratic spin-orbit $(\mathbf{L} \cdot \mathbf{S})^2$ and \mathbf{L}^2 components to more accurately reflect the energy and channel variations of the underlying NN g matrix in the scattering theory. As with the tensor and spin-orbit interactions, the quadratic spin-orbit interaction is effective only in $S = 1$ channels. The \mathbf{L}^2 interaction, on the other hand, influences results in both $S = 0$ or $S = 1$ channels. Also one need consider two terms with this \mathbf{L}^2 force, namely $\mathbf{L}^2 \mathbf{1}$ and $\mathbf{L}^2 (\boldsymbol{\sigma}_1 \cdot \boldsymbol{\sigma}_2)$. From these two terms, equivalent interactions in the form $\mathbf{L}^2_{(S=0)}$ and

$L^2_{(S=1)}$ may be obtained using the developments with the central force given above.

The multipole expansions of all of these interactions, generically denoted by the superscript (x) , can be expressed in the form,

$$\begin{aligned} F^{(x)} = & \sum_L C_1^L V_L \left(r_1^2 \frac{d^2}{dr_2^2} - 2r_1 r_2 \frac{d^2}{dr_1 dr_2} + r_2^2 \frac{d^2}{dr_1^2} \right) \\ & + \sum_L C_2^L V_L \left(\frac{r_1^2}{r_2} \right) \frac{d}{dr_2} + \sum_L C_3^L V_L \left(\frac{r_2^2}{r_1} \right) \frac{d}{dr_1} + \sum_{L'} C_4^{L'} V_{L'} r_1 \frac{d}{dr_2} \\ & + \sum_L D_2^L V_L r_1 \frac{d}{dr_1} + \sum_L D_3^L V_L r_2 \frac{d}{dr_2} + \sum_{L'} D_4^{L'} V_{L'} r_2 \frac{d}{dr_1} \\ & + \sum_L C_5^L V_L \left(\frac{r_1^2}{r_2^2} \right) + \sum_L C_6^L V_L + \sum_L C_7^L V_L \left(\frac{r_2^2}{r_1^2} \right) + \sum_{L'} C_8^{L'} V_{L'} \left(\frac{r_1}{r_2} \right) \\ & + \sum_{L'} C_9^{L'} V_{L'} \left(\frac{r_2}{r_1} \right), \end{aligned} \quad (4.51)$$

with the constraints,

$$D_2^L = -C_2^L - C_1^L, \quad D_3^L = -C_3^L - C_1^L, \quad D_4^L = -C_4^{L'}. \quad (4.52)$$

These interactions do not act in relative $NN S$ -states and so they vanish in the zero range limit. However, using the zero range property that all multipoles are equal infers a number of relations. Specifically,

$$\begin{aligned} \sum_L C_1^L &= \sum_L [C_2^L - C_3^L] \\ &= \sum_{L'} C_4^{L'} \\ &= \sum [C_5^L + C_6^L + C_7^L] + \sum [C_8^{L'} + C_9^{L'}] \end{aligned} \quad (4.53)$$

and there are symmetries under permutation of the two particles, from which

$$\begin{aligned} C_1^L &\rightarrow C_1^L, \quad C_2^L \rightarrow C_3^L, \quad C_4^{L'} \rightarrow -C_4^{L'}, \\ C_5^L &\rightarrow C_7^L, \quad C_6^L \rightarrow C_8^L, \quad C_8^{L'} \rightarrow C_9^{L'}. \end{aligned} \quad (4.54)$$

Note also that there is a symmetry between the multipole for $L = J + n$ and that for $L = J - n$, namely if $C_i^{J+n} = f_{n,i}(J)$, then $C_i^{J-n} = -f_{n,i}(-J - 1)$.

In addition, in the natural parity case, the summations over L and L' are constrained to involve

$$L = J - 2, J, J + 2, L \geq 0, \quad \text{and} \quad L' = J - 1, J + 1, L' \geq 0. \quad (4.55)$$

In the unnatural parity case, there is a simple useful expression for the operator \mathbf{L}^2 , namely

$$\begin{aligned}\mathbf{L}^2 = & \frac{1}{8 J(J+1)} \left[V_{J-1} + V_{J+1} - \left(\frac{\mathbf{r}_1}{\mathbf{r}_2} + \frac{\mathbf{r}_2}{\mathbf{r}_1} \right) V_J \right] \\ & \times [J(J+1) + \alpha_{j_1 j_1}^J (1 - \alpha_{j_1 j_1}^J)] [J(J+1) + \alpha_{j_2 j_2}^J (1 - \alpha_{j_2 j_2}^J)]\end{aligned}\quad (4.56)$$

and the sums are restricted (with $L, L' \geq 0$) in the $(\mathbf{L} \cdot \mathbf{S})^2$ case, by

$$L = J - 1, J + 1, \quad \text{and} \quad L' = J - 2, J, J + 2, \quad (4.57)$$

while in the $\mathbf{L}^2(\boldsymbol{\sigma}_1 \cdot \boldsymbol{\sigma}_2)$ case they are

$$L = J - 3, J - 1, J + 1, J + 3, \quad \text{and} \quad L' = J - 2, J, J + 2. \quad (4.58)$$

Then with

$$\beta_{j_1 j_1}^J = k_{j_1} - \eta_{j_1} k_{j_1}, \quad (4.59)$$

the interaction generates very complex forms of particle-hole matrix elements. Therein two form factors involve double derivatives, the second of which is scaled by an α coefficient. There are also six form factors which involve single derivatives with the last five scaled by factors α , α^2 , $\alpha\beta$, and $(\alpha^2 - 1)\beta$. Finally one finds twelve form factors for natural parity cases, and ten for unnatural parity ones, that do not involve derivatives. The first six of those terms contain the coefficients specified above while the others contain terms with β^2 , α^3 , $\alpha\beta^2$, $\alpha^2\beta^2$, $\alpha^2\beta^3$, and $\alpha^3\beta$.

Thus with the multipoles of these special forms of interaction, computation of particle-hole matrix elements f involve operators characterised by

$$U_{L,int} = r_1^m r_2^n V_L(\mathbf{r}_1, \mathbf{r}_2) \frac{d^{p+q}}{dr_1^p dr_2^q}, \quad (4.60)$$

with the condition $m + n - p - q = 0$. Note that the parity of every term in the form Eq. (4.60), defined by the change $\mathbf{r}_1 \rightarrow -\mathbf{r}_1$, is

$$\eta_J = (-1)^{m-p+L} = (-1)^{n-q+L}. \quad (4.61)$$

Also, in particle-hole matrix elements, the geometric coefficient for every such term exists only if $L \geq 0$ and involves

$$\frac{P_{L,int}(J, \alpha_{j_1 j_1}^J, \beta_{j_1 j_1}^J, \alpha_{j_2 j_2}^J, \beta_{j_2 j_2}^J)}{Q_{L,int}(J)}, \quad (4.62)$$

where $P_{L,int}$ and $Q_{L,int}$ are polynomials. For the interactions discussed, the denominator polynomial $Q_{L,int}(J)$ is a product of simple terms like $(2J + n)$ and/or $(J + n)$. On the other hand, the numerator polynomial $P_{L,int}(J, \alpha'_{j_1 j'_1}, \beta'_{j_1 j'_1}, \alpha'_{j_2 j'_2}, \beta'_{j_2 j'_2})$ according to the selected interaction, is one of any degree in J and up to the sixth degree in the α and the β . But it is limited to the fifth degree for each particle. It is limited as well to the third degree for each coefficient listed above for the non-derivative form factors. This complex dependence can be rewritten in terms of the 11 coefficients X_i to facilitate evaluations.

There is a useful procedure by which computation of the helicity multipoles of such complicated interactions can be achieved in terms of simpler ones. Suppose the task is to compute the particle-hole matrix elements of an interaction of the form $V(|\mathbf{r}_1 - \mathbf{r}_2|) V_x(1, 2) V_y(1, 2)$ where $V_x(1, 2)$ and $V_y(1, 2)$ are two interactions with which one can associate known elements

$$g'_{h_1 h_2, h_1 h_2} = \sum_{m'_1 m'_2 m_1 m_2} (-1)^{h-m_1+h-m_2} \langle j'_1 m'_1 j_1 - m_1 | JM \rangle \langle j_2 m_2 j'_2 - m'_2 | JM \rangle \\ \times \langle j'_1 m'_1 j'_2 m'_2 | V(|\mathbf{r}_1 - \mathbf{r}_2|) V_x(1, 2) | j_1 m_1 j_2 m_2 \rangle, \quad (4.63)$$

which has a radial dependence through $V(|\mathbf{r}_1 - \mathbf{r}_2|)$, and

$$h'_{h_1 h_2, h_1 h_2} = \sum_{m'_1 m'_2 m_1 m_2} (-1)^{h-m_1+h-m_2} \langle j'_1 m'_1 j_1 - m_1 | JM \rangle \langle j_2 m_2 j'_2 - m'_2 | JM \rangle \\ \times \langle j'_1 m'_1 j'_2 m'_2 | V_y(1, 2) | j_1 m_1 j_2 m_2 \rangle, \quad (4.64)$$

which has no interaction radial dependence so that it is purely an $L = 0$ particle-hole matrix element. Therefore, for chosen states $|j_1 m_1\rangle$ and $|j_2 m_2\rangle$, the possible $|j'_1 m'_1\rangle$ and $|j'_2 m'_2\rangle$ are very limited. The complete particle-hole matrix elements then can be expanded as

$$\langle j'_1 m'_1 j'_2 m'_2 | V(|\mathbf{r}_1 - \mathbf{r}_2|) V_x(1, 2) V(1, 2) | j_1 m_1 j_2 m_2 \rangle = \\ \sum_{j''_1 m''_1 j''_2 m''_2} \langle j'_1 m'_1 j'_2 m'_2 | V(|\mathbf{r}_1 - \mathbf{r}_2|) V_x(1, 2) | j''_1 m''_1 j''_2 m''_2 \rangle \\ \times \langle j''_1 m''_1 j''_2 m''_2 | V_y(1, 2) | j_1 m_1 j_2 m_2 \rangle \quad (4.65)$$

from which one has

$$f_{j_1' j_2' j_1 j_2}^J = \sum_{J' J'' j_1' j_2'} (-1)^{j_2 + j_2' + j_1 + j_1' + J + J' + J''} (2J'+1)(2J''+1) \\ \times \left\{ \begin{matrix} J'' & J' & J \\ j_1' & j_1 & j_1' \end{matrix} \right\} \left\{ \begin{matrix} J'' & J' & J \\ j_2' & j_1 & j_2'' \end{matrix} \right\} g_{j_1' j_2' j_1' j_2''}^{J'} h_{j_1' j_2' j_1 j_2}^{J''}. \quad (4.66)$$

The values of (j_1'', j_2'') are limited to the values (j_1', j_2') that are compatible with (j_1, j_2) through the constraints embodied in Eq. (4.64).

The expansion of particle-hole matrix elements within the helicity formalism are now discussed. Such matrix elements are involved not only in the specification of the optical potentials but also in the DWBA amplitudes for inelastic and charge exchange scattering calculations.

4.4. Particle-Hole Matrix Elements

Using the helicity formalism for both the interaction and for bound particle and hole states, the antisymmetrized particle-hole matrix element expands as

$$\langle j_1' j_1^{-1}; JM | V(1, 2) | j_2 j_2'; JM \rangle = \\ \sum_{m_1' m_2' m_1 m_2} (-1)^{\hbar - m_1 + \hbar - m_2'} \langle j_1' m_1' j_1 - m_1 | JM \rangle \langle j_2 m_2 j_2' - m_2' | JM \rangle \\ \times \{ \langle j_1' m_1' | \langle j_2' m_2' | V(1, 2) | [j_1 m_1] \rangle | j_2 m_2 \rangle - | j_2 m_2 \rangle | j_1 m_1 \rangle \} \\ = f_{\hbar \hbar, \hbar \hbar}' - \sum_{J'} (-1)^{\hbar + j_2 + J + J'} (2J'+1) \left\{ \begin{matrix} j_1 & j_1' & J \\ j_2 & j_2' & J' \end{matrix} \right\} f_{\hbar \hbar, \hbar \hbar}^{J'}, \quad (4.67)$$

where the order of the single particle states gives the designation of the coordinates 1 and 2 and the NN multipole elements are

$$f_{\hbar \hbar, \hbar \hbar}' = \sum_{\lambda_1' \lambda_2' \lambda_1 \lambda_2} \frac{1}{4} \sqrt{(2j_1' + 1)(2j_2' + 1)(2j_1 + 1)(2j_2 + 1)} \\ \times (-1)^{\hbar - \lambda_1 + \hbar - \lambda_2} \left(\begin{matrix} j_1' & J & j_1 \\ \lambda_1' & \lambda_1 - \lambda_1' & -\lambda_1 \end{matrix} \right) \left(\begin{matrix} j_2' & J & j_2 \\ \lambda_2' & \lambda_2 - \lambda_2' & -\lambda_2 \end{matrix} \right) \\ \times \int r_1^2 dr_1 \int r_2^2 dr_2 V_{\lambda_1' \lambda_2', \lambda_1 \lambda_2}^J (1, 2) \varphi_{\lambda_1'}^{j_1*}(r_1) \varphi_{\lambda_2'}^{j_2*}(r_2) \varphi_{\lambda_1}^{j_1*}(r_1) \varphi_{\lambda_2}^{j_2*}(r_2), \quad (4.68)$$

The direct particle-hole elements f' involve only multipoles with the J -value to which the particle and the hole are coupled.

For numerical implementation it is useful to note that the geometrical coefficient in Eq. (4.68) reduces to

$$G_{j_1 j_1}^J = (-1)^{j_1 + \frac{1}{2}} \sqrt{(2j_1 + 1)(2j_1' + 1)} \begin{pmatrix} j_1' & J & j_1 \\ -\frac{1}{2} & 0 & \frac{1}{2} \end{pmatrix}, \quad (4.69)$$

for elements diagonal in the helicity space of particle '1'. This is a simplification of the more general expression

$$G_{j_1 j_1}^J = (-1)^{j_1 + \frac{1}{2}} \sqrt{(2j_1 + 1)(2j_1' + 1)(2l_1 + 1)(2l_1' + 1)} \begin{pmatrix} l_1 & l_1' & J \\ 0 & 0 & 0 \end{pmatrix} \begin{Bmatrix} l_1 & l_1' & J \\ j_1' & j_1 & \frac{1}{2} \end{Bmatrix}. \quad (4.70)$$

At this point it is useful also to define an expansion coefficient

$$\begin{aligned} \alpha_{j_1 j_1}^J &= (-1)^{l_1+1} \sqrt{J(J+1)(2j_1 + 1)(2j_1' + 1)} \begin{pmatrix} j_1' & J & j_1 \\ -\frac{1}{2} & 1 & -\frac{1}{2} \end{pmatrix} \{G_{j_1 j_1}^J\}^{-1} \\ &= (-1)^{l_1+j_1-\frac{1}{2}} \left(j_1 + \frac{1}{2} \right) - \eta_J (-1)^{l_1'+j_1'-\frac{1}{2}} \left(j_1' + \frac{1}{2} \right) \\ &= k_{j_1} - \eta_J k_{j_1'}, \end{aligned} \quad (4.71)$$

where

$$\eta_J = (-1)^{J+l_1+l_1'} = \begin{cases} 1 & \text{if parity} = (-1)^J \\ -1 & \text{if parity} = (-1)^{J+1} \end{cases} \quad (4.72)$$

and k_j is the eigenvalue of $(\mathbf{l} \cdot \boldsymbol{\sigma} + 1)$. It is also the quantum number of the two component radial Dirac equation [91] which may be written as

$$\begin{aligned} \left[-\frac{d}{dr} + \frac{\kappa}{r} \right] G &= (E - m - V) F \\ \left[\frac{d}{dr} + \frac{\kappa}{r} \right] F &= (E + m - V) G. \end{aligned} \quad (4.73)$$

These coefficients were introduced previously in defining the radial multipoles of the spin-orbit and \mathbf{L}^2 forces. With this specification of the elementary matrices, the sum on the helicities of one particle involves two

terms. Taking into account the relative signs of the two components as given by Eq. (4.22), the geometrical coefficient reduces to

$$\frac{1}{2}(-1)^{h-h_1}\left[1+\eta(-1)^{h+h+J}\right]\sqrt{(2j_1+1)(2j'_1+1)}\binom{j'_1}{\lambda'_1}\binom{j}{\lambda_1-\lambda'_1}\binom{h}{-\lambda_1} \quad (4.74)$$

where η in this case is the symmetry of the matrix. Thus there are two kinds of particle-hole matrix elements, those for natural and those for unnatural parity.

In the natural parity matrix elements, for which $l_1 + l'_1 + J$ is even, all contribution comes from the even parts of the interaction multipoles, giving

$$\begin{aligned} A^{Jj_1j'_1} &= G_{j_1j'_1}^J \int \left[a^J(1, 2) + \frac{\alpha_{j_1j'_1}^J}{\sqrt{J(J+1)}} b'^J(2, 1) \right] \rho_{j'_1j_1}(r_1) r_1^2 dr_1 \\ B^{Jj_1j'_1} &= G_{j_1j'_1}^J \int \left[b^J(1, 2) + \frac{\alpha_{j_1j'_1}^J}{\sqrt{J(J+1)}} c^J(1, 2) \right] \rho_{j'_1j_1}(r_1) r_1^2 dr_1, \end{aligned} \quad (4.75)$$

which correspond respectively to macroscopic model transition form factors with $\Delta L = \Delta J$, $\Delta S = 0$ and $\Delta S = 1$.

With the unnatural parity matrix elements, $l_1 + l'_1 + J$ is odd, and all contribution comes from the odd parts of the interaction multipoles, giving

$$\begin{aligned} C^{Jj_1j'_1} &= G_{j_1j'_1}^J \int \left[d^J(1, 2) + \frac{\alpha_{j_1j'_1}^J}{\sqrt{J(J+1)}} e'^J(2, 1) \right] \rho_{j'_1j_1}(r_1) r_1^2 dr_1 \\ D^{Jj_1j'_1} &= G_{j_1j'_1}^J \int \left[e^J(1, 2) + \frac{\alpha_{j_1j'_1}^J}{\sqrt{J(J+1)}} f^J(1, 2) \right] \rho_{j'_1j_1}(r_1) r_1^2 dr_1, \end{aligned} \quad (4.76)$$

which are a mixture of transition form factors with $\Delta S = 1$ and $\Delta L = \Delta J \pm 1$. In Eqs. (4.75) and (4.76), for simplicity the states product

$$\rho_{j_2,j_1}(r) = f_{n_2l_2j_2}^*(r_1) f_{n_1l_1j_1}(r_1), \quad (4.77)$$

has been introduced. With these terms, the particle-hole matrix elements become

$$f_{hh}^J = (-1)^{h-h} G_{hh}^J \int \left[\binom{A}{C} + \frac{\alpha_{hh}^J}{\sqrt{J(J+1)}} \binom{B}{D} \right] \rho_{hh}(r_2) r_2^2 dr_2, \quad (4.78)$$

where A and B are to be used for the natural parity cases and C and D for the unnatural parity cases.

4.5. The Distorted Waves

Consider the total wave function of the scattered particle and the target in the form

$$\Psi(\mathbf{r}; 1, 2, \dots, A) = \frac{1}{r} \sum_{l, j, J, J} f_{ljJ}(r) \Delta_{lsjJM}(\hat{\mathbf{r}}; 1, 2, \dots, A) \quad (4.79)$$

where

$$\Delta_{lsjJM}(\hat{\mathbf{r}}; 1, 2, \dots, A) = i^l \langle jm | m' JM \rangle Y_{lsj}^m(\hat{\mathbf{r}}) \Phi_{JM}(1, 2, \dots, A) \quad (4.80)$$

are the target-spin-angular functions involving a target state $\Phi_{JM}(1, 2, \dots, A)$ and the spin $s(\frac{1}{2})$ of the incident nucleon. The projectile spin-angular functions, are defined by

$$|jm\rangle \equiv Y_{lsj}^m = \sum_{\mu\sigma} \langle l\mu s\sigma | j m \rangle Y_{l\mu}(\hat{\mathbf{r}}) | s\sigma \rangle. \quad (4.81)$$

The radial equations for the distorted waves $f_{ljJ}(r)$ then are obtained by projecting the complete $A + 1$ nucleon Schrödinger equations,

$$[T + V(1, 2) - E] \Psi^{(+)}(\mathbf{r}, 1, 2, \dots, A) = 0, \quad (4.82)$$

on all of the functions $\Delta_{lsjJM}(\hat{\mathbf{r}}, 1, 2, \dots, A)$. In this process, the values of J, M , and the parity are conserved and the number of coupled equations is limited and depends upon the spins of the target states taken into account. For nucleon projectiles, the coupled equations split into two sets, one for positive and the other for negative parity. In each, the total number of coupled equations essentially is $\Sigma_i (2I_i + 1)$ for a sufficiently small value of J . Those equations have the form, with m_i now designating the reduced mass,

$$\begin{aligned} & \frac{\hbar^2}{2m_i} \left[\frac{d^2}{dr^2} - \frac{2\eta_i k_i}{r} - \frac{l_i(l_i+1)}{r^2} + k_i^2 \right] f_{l_i j_i l_i J}^{J_{pp}}(r) \\ &= i^{l_j - l_i} \sum_j f_{l_i j_i l_i J}^{J_{pp}}(r) \left[\sum_{J_{ph}} Z_{ph}^{J_{ph}} (-1)^{J_{pp} + l_i + j_i} (2J_{ph} + 1) \begin{Bmatrix} j_i & j_j & J_{ph} \\ I_j & I_i & J_{pp} \end{Bmatrix} \tilde{f}_{l_i j_i l_j j_i p j_h}^{J_{ph}}(r) \right] \\ & - i^{l_j - l_i} \int_0^\infty dr' \sum_j \left[\sum_{J_{ph}} Z_{ph}^{J_{ph}} (2J_{ph} + 1) \begin{Bmatrix} j_i & j_j & J_{ph} \\ I_i & I_j & J_{pp} \end{Bmatrix} \tilde{f}_{l_i j_i l_j j_i p j_h}^{J_{ph}}(r, r') f_{l_i j_i l_i J}^{J_{pp}}(r) \right] \end{aligned} \quad (4.83)$$

wherein η_i is the relevant Sommerfeld parameter and $Z_{ph}^{J_{ph}}$ are the scaled OBDME as defined in Eq. (4.18). The functions $\tilde{f}_{l_i j_i l_j j_i p j_h}^{J_{ph}}(r)$ and $\tilde{f}_{l_i j_i l_j j_h j_k}^{J_{ph}}(r, r')$ are derived from particle-particle matrix elements by limit-

ing the inferred integrations. To distinguish clearly the angular momenta, the value of the total spin J has been written as J_{ph} . Note that the helicity radial functions described by Eq. (4.10) have not been used in this specification. The direct potential term in the right hand side of Eq. (4.83) takes the form

$$\begin{aligned} \tilde{f}_{l_i l_j l_h j_j j_p j_h}^{J_{ph}}(\mathbf{r}) &= \sum_{m_p, m_h} (-1)^{j_h - m_h + j_j - m_j} \langle j_p \mathbf{m}_p j_h - m_h | J_{ph} M \rangle \\ &\quad \langle j_i \mathbf{m}_i j_i - m_j | J_{ph} M \rangle \times \int d\hat{\mathbf{r}} \int d\mathbf{r}' (j_i \mathbf{m}_i(r)) \langle n_p l_p j_p m_p(r') | V(\mathbf{r}', \mathbf{r}) \\ &\quad | n_h l_h j_h m_h(r') \rangle | j_i \mathbf{m}_i(r) \rangle, \end{aligned} \quad (4.84)$$

where $|nljm\rangle$ represents a complete bound state wave function but $|jm\rangle$ is just the spin angular part of scattering function as specified in Eq. (4.81). In fact, the resulting expression Eq. (4.84) is symbolic because, for $J_{ph} \neq 0$ or odd parity, it represents the operator

$$\tilde{f}_{l_i l_j l_h j_j j_p j_h}^{J_{ph}}(\mathbf{r}) = \tilde{f}_0(\mathbf{r}) + \tilde{f}_1(\mathbf{r}) \frac{d}{dr} + \tilde{f}_2(\mathbf{r}) \frac{d^2}{dr^2}. \quad (4.85)$$

The $\tilde{f}_1(\mathbf{r})$ term exists in the even parity case also if there is a spin-orbit component. So also does $\tilde{f}_2(\mathbf{r})$ if there is an \mathbf{L}^2 or an $(\mathbf{L} \cdot \boldsymbol{\sigma}_1)(\mathbf{L} \cdot \boldsymbol{\sigma}_2)$ component in the interaction. The $\tilde{f}_2(\mathbf{r})$ element exists also for $J_{ph} = 0$ with an \mathbf{L}^2 component in the interaction.

For the exchange term in the second member of Eq. (4.83), the radial dependences of the bound states must be separated from their spin-angular parts using

$$|nljm\rangle = \varphi_{nlj}(\mathbf{r}) |jm\rangle, \quad (4.86)$$

to find

$$\begin{aligned} \tilde{f}_{l_i l_j l_h j_j j_p j_h}^{J_{ph}}(\mathbf{r}, \mathbf{r}') &= \sum_{m_p, m_h} (-1)^{j_h - m_h + j_j - m_j} \{ \varphi_{n_p l_p j_p}(\mathbf{r}') \varphi_{n_h l_h j_h}(\mathbf{r}) \} \\ &\quad \times \langle j_p \mathbf{m}_p j_h - m_h | J_{ph} M \rangle \langle j_i \mathbf{m}_i j_i - m_j | J_{ph} M \rangle \\ &\quad \times \left[\int d\hat{\mathbf{r}} \int d\hat{\mathbf{r}'} (j_i \mathbf{m}_i(r)) (j_p \mathbf{m}_p(r') | V(\hat{\mathbf{r}}, \hat{\mathbf{r}}) | j_h \mathbf{m}_h(r)) | j_i \mathbf{m}_i(r') \right]. \end{aligned} \quad (4.87)$$

As with the direct term, this expression of the exchange term is symbolic in that it may have the operator form

$$\bar{f}_{l_i l_j l_h j_j j_p j_h}^{J_{ph}}(\mathbf{r}, \mathbf{r}') = \bar{f}_0(\mathbf{r}, \mathbf{r}') + \bar{f}_1(\mathbf{r}, \mathbf{r}') \frac{d}{dr'} + \bar{f}_2(\mathbf{r}, \mathbf{r}') \frac{d^2}{dr'^2} \quad (4.88)$$

according to the character of the NN interaction. Therein, $\bar{f}_0(\mathbf{r}, \mathbf{r}')$ can include up to second derivatives and $\bar{f}_i(\mathbf{r}, \mathbf{r}')$ up to first derivatives with respect to \mathbf{r}' on $\phi_{n_h l_h i_h}(\mathbf{r}')$.

With $f_f(\mathbf{r})$ designating solutions to Eqs. (4.83), their asymptotic values cast in terms of regular and irregular Coulomb functions, have the form

$$\begin{aligned} f_f(\mathbf{r}) &\xrightarrow[r \rightarrow \infty]{} \delta_{if} F_{l_f}(\eta_f; k_f r) + C_f^i \sqrt{\frac{k_i m_f}{k_f m_i}} [G_{l_f}(\eta_f; k_f r) + i F_{l_f}(\eta_f; k_f r)] \\ &\Rightarrow \delta_{if} F_{l_f}(\eta_f; k_f r) + \bar{C}_f^i [G_{l_f}(\eta_f; k_f r) + i F_{l_f}(\eta_f; k_f r)], \end{aligned} \quad (4.89)$$

Matching values and first derivatives of the solutions of the radial equations to those of these asymptotic functions at large radius specify the coefficients \bar{C}_f^i . The C_f^i with are symmetric under exchange of i and f as can be shown using Wronskian relations.

Reforming the partial wave equations as

$$\begin{aligned} &\left\{ -\frac{\hbar^2}{2m_i} \left[\frac{d^2}{dr^2} - \frac{2\eta_i k_i}{r} - \frac{l_i(l_i+1)}{r^2} + k_i^2 \right] - \mathcal{U}_i^{\text{OMP}}(r) + V_{ii}^0(r) \right\} f_i(r) \\ &= \int_0^\infty W_{ii}^0(r, r') f_i(r') dr' \\ &= - \sum_j \left[V_{ij}(r) f_j(r) + \int_0^\infty W_{ij}(r, r') f_j(r') dr' \right] \end{aligned} \quad (4.90)$$

enables the scattering matrix elements of $\{C\}$ for the coupled channels to be expressed as

$$\bar{C}_i^0 = C_i^{\text{opt}} \delta_{ii} - \frac{2m_i}{\hbar^2 k_i} \int_0^\infty g_i(r) \sum_j \left[V_{ij}(r) f_j(r) + \int_0^\infty W_{ij}(r, r') f_j(r') dr' \right] dr \quad (4.91)$$

where $g_i(r)$ are solutions of the uncoupled equations

$$\begin{aligned} &\left\{ -\frac{\hbar^2}{2m_i} \left[\frac{d^2}{dr^2} - \frac{2\eta_i k_i}{r} - \frac{l_i(l_i+1)}{r^2} + k_i^2 \right] - \mathcal{U}_i^{\text{OMP}}(r) + V_i^0 i(r) \right\} g_i(r) \\ &= - \int_0^\infty W_{ii}^0(r, r') g_i(r') r'^2 dr' \end{aligned} \quad (4.92)$$

for which C_i^{opt} is the scattering coefficient. These relations hold also when $V_{ij}(\mathbf{r})$ and $W_{ij}(\mathbf{r})$ incorporate derivative terms. Note that an arbitrary optical potential $\mathcal{U}_i^{\text{OMP}}(\mathbf{r})$ has been introduced, and the interactions $V_{ii}(\mathbf{r})$ and $W_{ii}(\mathbf{r})$ have been divided between the two terms in Eq. (4.90). The

arbitrary optical potential enables one to correct the point charge Coulomb potential for that due to a finite charge distribution, for example.

4.6. Amplitudes, Cross Sections and Observables

If the incoming particle is assumed to have a spin projection σ_i on the quantisation axis and the target has angular momentum I_i with projection μ_i on the same axis, the total wave function of Eq. (4.79) should asymptote as

$$\phi_{\mu_i \sigma_i}(r) \xrightarrow[r \rightarrow \infty]{} e^{ikr} \left| I_i \mu_i \right\rangle \left\langle \frac{1}{2} \sigma_i \right| + \sum_{\mu_f \sigma_f} f_{\mu_f \sigma_f \mu_i \sigma_i}(\theta) \frac{e^{ikr}}{r} \left| I_f \mu_f \right\rangle \left\langle \frac{1}{2} \sigma_f \right| \quad (4.93)$$

where σ_f and μ_f are the projections of the spin of the outgoing particle and of the residual target state angular momentum on the same quantisation axis. The scattering amplitudes are given in terms of the scattering coefficients by

$$f_{\mu_i \sigma_f \mu_f \sigma_i}(\theta) = \frac{4\pi}{k_i} \sum e^{i(\sigma_i + \sigma_f)} C_f^i \langle l_i v_i s \sigma_i | j_i m_i \rangle \langle j_i m_i I_i \mu_i | JM \rangle \\ \times \langle l_f v_f s \sigma_f | j_f m_f \rangle \langle j_f m_f I_f \mu_f | JM \rangle Y_{l_f v_f}^*(\hat{k}_i) Y_{l_f v_f}(\hat{k}_f), \quad (4.94)$$

where the σ_i and σ_f are Coulomb phase-shifts.

These amplitudes are specified conveniently by the helicity formalism [86, 87] in which the spin of the particle is projected onto its momentum and the angular momentum of the target is projected onto the reverse direction. For the target, the definition of the helicity as projection of the spin on the impulsion of the target implies a quantisation axis opposite to that of the particle, at least in the center of mass system. Note then that if $\psi_{p,\mu}$ is a particle helicity state, the target helicity state $\chi_{p,\mu}$ of a particle of spin s is defined by

$$\chi_{p,\mu} = (-1)^{s-\mu} e^{i\pi\lambda} \psi_{p,\mu} \quad (4.95)$$

when the phase is chosen so that $\chi_{0,\lambda} = \psi_{0,-\lambda}$. Then with the axes of quantisation along $\mathbf{k}_i(\mathbf{k}_f)$ for the initial (final) scattering particle states, the helicities of the target are the opposites in the initial (final) states of the scattering. Consequently the helicity amplitudes relate to those specified above by simply the action of a reduced rotation matrix element,

$$f_{\mu_f \sigma_f \mu_i \sigma_i}^{hel.}(\theta) = f_{\mu_f \sigma_f \mu_i \sigma_i}^{(Coul)hel.}(\theta) \delta_{if} + \sum_J f_{\mu_f \sigma_f \mu_i \sigma_i}^{(J)hel.}(\theta) r_{\sigma_f - \mu_f, \sigma_i - \mu_i}^{(J)}(\theta) \quad (4.96)$$

with

$$f_{\mu_f \sigma_f \mu_i \sigma_i}^{(J)hel.}(\theta) = \frac{1}{k_i} \sum e^{i(\sigma_{l_i} + \sigma_{l_f})} C_f^i \sqrt{(2l_i + 1)(2l_f + 1)} \langle l_i 0s_i \sigma_i | j_i \sigma_i \rangle \\ \times \langle j_i \sigma_i I_i - \mu_i | JM_i \rangle \langle l_f 0s_f \sigma_f | j_f \sigma_f \rangle \langle j_f \sigma_f I_f - \mu_f | JM_f \rangle, \quad (4.97)$$

wherein the Coulomb helicity amplitude is the usual Coulomb amplitude multiplied by the reduced rotation matrix elements for the spin s_i of the particle and the spin I_i of the target,

$$f_{\mu_f \sigma_f \mu_i \sigma_i}^{(Coul)hel.}(\theta) = -\frac{\eta}{2k \sin^2 \frac{\theta}{2}} e^{2i(\sigma_0 - 2i\eta \ln \sin \frac{\theta}{2})} r_{\sigma_f, \sigma_i}^{(s_i)}(\theta) r_{-\mu_f, -\mu_i}^{(I_i)}(\theta). \quad (4.98)$$

In terms of these amplitudes, the differential cross section has its usual form, i.e.,

$$\frac{d\sigma}{d\Omega} = \frac{1}{2(2I_i + 1)} \sum_{\sigma_f \mu_i \mu_f} |f_{\mu_f \sigma_f \mu_i \sigma_i}^{hel.}(\theta)|^2 \quad (4.99)$$

where the denominator $2(2I_i + 1)$ is the multiplicity of the initial state for a particle of spin $\frac{1}{2}$ and a target of spin I_i . The utility of the helicity formulation is that all observables defined with respect to the outgoing momentum (in the C. of M.) can be defined without further rotations. Without limiting spin values, all observables can be described [92] with simple tensor operators $\tau_{\lambda, \mu}$ whose matrix elements in the spin space of a particle of spin s are

$$\langle sq | \tau_{\lambda, \mu}^s | sq' \rangle = (-1)^{s-q'} \sqrt{2s+1} \langle sqs - q' | \lambda \mu \rangle. \quad (4.100)$$

Similar tensors are given for the target space. These irreducible, hermitian, tensor operators satisfy

$$\tau_{\lambda, \mu} = (-1)^\mu \tau_{\lambda, -\mu}^\dagger \quad (4.101)$$

and are orthonormal because

$$\text{Tr}\{\tau_{\lambda, \mu} \tau_{\lambda', \mu'}^\dagger\} = (2s+1) \delta_{\lambda, \lambda'} \delta_{\mu, \mu'}. \quad (4.102)$$

In terms of these tensors then, a density matrix ρ of trace unity as is apropos of a beam, can be described by

$$\rho = \frac{1}{2s+1} \sum_{\lambda, \mu} (-1)^\mu t_{\lambda, \mu} \tau_{\lambda, -\mu}^\dagger = \frac{1}{2s+1} \sum_{\lambda, \mu} t_{\lambda, \mu} \tau_{\lambda, \mu}^\dagger \quad (4.103)$$

where $t_{\lambda,\mu} = \text{Tr}\{\rho\tau_{\lambda,\mu}\}$ for which $t_{\lambda,\mu}^* = (-1)^\mu t_{\lambda,-\mu}$ when $\tau_{0,0} = I$ and $t_{0,0} = 1$.

Using such tensor operators, all the observables can be defined from the coefficients

$$A_{\lambda_1\mu_1\lambda_2\mu_2}^{\lambda_3\mu_3\lambda_4\mu_4} = \text{Tr}\{f^{hel.}(\theta)[\tau_{\lambda_1\mu_1}^{s_i} \otimes \tau_{\lambda_2\mu_2}^{I_i}]f^{hel.}(\theta)^\dagger[\tau_{\lambda_3\mu_3}^{s_f} \otimes \tau_{\lambda_4\mu_4}^{I_f}]\}, \quad (4.104)$$

when one takes into account that the projection of the spin of the target on the direction of the beam is opposite to its helicity.

In terms of these amplitudes, the differential cross section is defined by

$$\frac{d\sigma}{d\Omega} = \frac{1}{2(2I_i + 1)} A_{0000}^{0000}, \quad (4.105)$$

and other spin observables $\Gamma(\theta)$ are expressed by

$$\Gamma(\theta) A_{0000}^{0000} = \sum_{\lambda_i\mu_i} x_{\lambda_1\mu_1\lambda_2\mu_2}^{\lambda_3\mu_3\lambda_4\mu_4} A_{\lambda_1\mu_1\lambda_2\mu_2}^{\lambda_3\mu_3\lambda_4\mu_4}; \quad (4.106)$$

the weight coefficients $x_{\lambda_1\mu_1\lambda_2\mu_2}^{\lambda_3\mu_3\lambda_4\mu_4}$ specifying each observable.

The expressions for the complete set of observables for scattering of polarized particles from polarized targets leading to polarized particles in the final state are simplified by use of relationships among the amplitudes due to hermiticity and conservation of parity. Hermiticity of the amplitudes requires

$$(A_{\lambda_1\mu_1\lambda_2\mu_2}^{\lambda_3\mu_3\lambda_4\mu_4})^* = (-1)^{\sum \mu} A_{\lambda_1-\mu_1\lambda_2-\mu_2}^{\lambda_3-\mu_3\lambda_4-\mu_4}, \quad (4.107)$$

while parity conservation requires

$$A_{\lambda_1\mu_1\lambda_2\mu_2}^{\lambda_3\mu_3\lambda_4\mu_4} = (-1)^{\sum \lambda + \sum \mu} A_{\lambda_1-\mu_1\lambda_2-\mu_2}^{\lambda_3-\mu_3\lambda_4-\mu_4} \quad (4.108)$$

As a consequence of these constraints, if the sum over the λ values is an even integer, the amplitude A is real. But if the sum over the λ values is an odd integer, the amplitude A is pure imaginary. Also amplitudes that have the same λ values but opposite μ values will differ then by only a phase $(-1)^{\sum \lambda + \sum \mu}$.

When no measurement is made of the outgoing polarizations, the diverse measurable spin correlations from scattering polarized beam particles from a polarized target are

A_{yy} the analyzing power of two parallel vector polarizations that are perpendicular to the reaction plane in the direction of $\mathbf{k}_i \times \mathbf{k}_f$, is given by

$$A_{yy}(\theta)A_{0000}^{0000} = -A_{nn} = -A_{1111}^{0000} - A_{111-1}^{0000}. \quad (4.109)$$

A_{zz} the analyzing power of two vector polarizations that are in the direction of the incident beam, which is given by

$$A_{zz}(\theta)A_{0000}^{0000} = A_{1010}^{0000}. \quad (4.110)$$

A_{xx} the analyzing power of two parallel vector polarizations that are perpendicular to the beam and in the scattering plane, which is given by

$$A_{xx}(\theta)A_{0000}^{0000} = A_{1111}^{0000} - A_{111-1}^{0000}. \quad (4.111)$$

A_{xz} the analyzing power of a vector polarization of the beam perpendicular to its direction but within the scattering plane, and a polarization of the target taken to be along the direction of the beam, which is given by

$$A_{xz}(\theta)A_{0000}^{0000} = -\sqrt{2}A_{1110}^{0000}. \quad (4.112)$$

A_{zx} the analyzing power of a vector polarization of the beam along its direction and a polarization of the target perpendicular to the direction of that beam but in the scattering plane, which is given by

$$A_{zx}(\theta)A_{0000}^{0000} = -\sqrt{2}A_{1011}^{0000}. \quad (4.113)$$

When the polarization of the outgoing particle is measured in the case of scattering of a polarized beam from a polarized target, there are five spin transfer observables [93] that can be found, namely

D or K_{yy} spin observable for the polarizations in the initial and final states being perpendicular to the reaction plane in the direction of $\mathbf{k}_i \times \mathbf{k}_f$, is given by

$$D(\theta)A_{0000}^{0000} = K_{yy}(\theta)A_{0000}^{0000} = -A_{1100}^{1100} - A_{1100}^{1-100}. \quad (4.114)$$

A' or K_{zz} spin observable for the polarizations in the initial and final states being in the direction of the incident beam, is given by

$$A'(\theta)A_{0000}^{0000} = K_{zz}(\theta)A_{0000}^{0000} = A_{4000}^{1000}. \quad (4.115)$$

R or K_{xx} spin observable for the polarizations in the initial and the final state being perpendicular to the beam and on the side of scattering is given by

$$R(\theta)A_{0000}^{0000} = K_{xx}(\theta)A_{0000}^{0000} = A_{1100}^{1100} - A_{1100}^{1-100}. \quad (4.116)$$

R' or **K_{xz}** spin observable for the polarization in the final state being in the beam direction but the polarization in the initial state is perpendicular to that and in the scattering plane, is given by

$$R'(\theta)A_{0000}^{0000} = K_{zx}(\theta)A_{0000}^{0000} = -\sqrt{2}A_{1100}^{1000}. \quad (4.117)$$

A or \mathbf{K}_{zx} spin observable for the polarization in the initial state being in the beam direction but the polarization in the final state is perpendicular to its momentum but within the scattering plane, is given by

$$A(\theta)A_{0000}^{0000} = K_{zx}(\theta)A_{0000}^{0000} = -\sqrt{2}A_{1000}^{1100}. \quad (4.118)$$

In addition, a combination of these gives the spin flip probability, SP , which is the probability that the spin in the final state is opposite that of the initial one. In terms of the helicity amplitudes

$$SP(\theta)A_{0000}^{0000} = \frac{1}{2}(A_{0000}^{0000} + A_{1100}^{1100} + A_{1-100}^{1100}). \quad (4.119)$$

These observables are specified in the center of mass system. In ref. [93], the coefficients A , R , A' , and R' are defined in the laboratory system (the system does not matter for D). The link between the those and the ones given above can be made simply with a rotation of the tensor operators given by Eq. (4.100), or of the scattering matrix given in Eq. (4.96). This last operation is carried out by a program named as DWBB98 which uses the output created from a run of the program DWBA98.

Other specifications of spin observables exist. Of those

$$\begin{aligned} A_{0n} &= -\sqrt{2}A_{0011}^{0000}, \\ A_{ll} &= \sin^2\left(\frac{\theta}{2}\right)A_{xx} + \cos^2\left(\frac{\theta}{2}\right)A_{zz} - \frac{1}{2}\sin\theta(A_{xz} + A_{zx}), \\ A_{mm} &= \sin^2\left(\frac{\theta}{2}\right)A_{zz} + \cos^2\left(\frac{\theta}{2}\right)A_{xx} - \frac{1}{2}\sin\theta(A_{xz} + A_{zx}), \\ A_{lm} &= \frac{1}{2}\sin\theta(A_{xx} - A_{zz}) - \sin^2\left(\frac{\theta}{2}\right)A_{xz} + \cos^2\left(\frac{\theta}{2}\right)A_{zx}, \\ A_{ml} &= \frac{1}{2}\sin\theta(A_{xx} - A_{zz}) - \sin^2\left(\frac{\theta}{2}\right)A_{zx} + \cos^2\left(\frac{\theta}{2}\right)A_{xz}, \end{aligned} \quad (4.120)$$

are examples considered later. The directions associated with the labels n, l, m are defined in terms of the momentum vectors of the incident and emergent nucleons, \mathbf{k} and \mathbf{k}' respectively, and are

$$\hat{n} = \frac{\mathbf{k} \times \mathbf{k}'}{|\mathbf{k} \times \mathbf{k}'|}; \quad \hat{l} = \frac{\mathbf{k} - \mathbf{k}'}{|\mathbf{k} - \mathbf{k}'|}; \quad \hat{m} = \frac{\mathbf{k} + \mathbf{k}'}{|\mathbf{k} + \mathbf{k}'|}. \quad (4.121)$$

5. THE TWO-NUCLEON t MATRICES

Off-shell properties of NN t matrices are required for detailed studies of few and many body problems in terms of two-body interactions. Three-body wave functions, nuclear matter calculations, microscopic models of nucleon scattering from nuclei, (p , $2p$) analyses, and photonuclear reactions are examples. In fact off-shell scattering amplitudes are required to analyse all but the simplest nuclear processes.

Srivastava and Sprung [94] have given a review of pre-1975 studies of on- and off-shell properties of NN t matrices. They discuss diverse approximations to the fully-off-shell t matrices, and their influence in NN bremsstrahlung and in nuclear matter calculations. However, even the best three-body, nuclear matter, and bremsstrahlung calculations [95] show that, while the off-shell t matrix must be treated exactly the results could not discriminate between off-shell properties determined from different on-shell equivalent NN interactions. This is a crucial finding as many studies claim effects exist that can be attributed to off-shell sensitivity. In fact such effects result from on-shell differences of the chosen interactions. Thus in this we present section a discussion of free NN scattering and consider both the on- and off-energy shell properties of NNt matrices as given by various interactions that accurately reproduce experimental phase shifts.

The usual approach to evaluate the NN t matrices is to start with a well determined NN potential. The potential may be purely phenomenological such as the Nijmegen Reid-like interaction [33], based upon boson exchanges such as the Paris [18], the Bonn set [19, 34], other Nijmegen interactions [33], and the one solitary boson exchange potential (OSBEP) [60, 36]) or obtained by inverse scattering theory [77] from specified phase shift sets [15]. All must be realistic in that they reproduce NN observables for a wide energy range, $0 < E < 300$ MeV for example, and deuteron properties. With this in mind, both the on- and off-shell properties of the NN t matrices are calculated from the LS equation. Effectively the same on-shell properties are determined from the so-called *realistic* interactions.

5.1. The NN Interactions

NN potentials have evolved considerably since the first attempts to describe the NN force. However it has only been in the last twenty years that successful fits to scattering data have been achieved. By the end of the 70's, several groups, notably those of Nijmegen, Paris, and Bonn, had

developed realistic meson exchange potentials built on the one boson exchange (OBE) model. Of these the Paris potential has been used extensively in the first developments of the microscopic NA optical potentials. That potential is based on πN and $\pi\pi$ interactions including the π -, ω -, and 2π -exchange contributions. The 2π -exchange contribution was obtained from dispersion relations which included correlated and uncorrelated processes. It was cut off below $r \sim 1.2$ fm and the short range behavior described by a constant soft core. Later, the interaction was parameterised in the form of an OBE potential (sum of Yukawa terms) for convenient use in either coordinate or momentum space [18]. Likewise there is a set of Nijmegen potentials all designed to fit the phase shifts from their analysis of NN data extremely well. They range in form from a totally phenomenological Reid-like potential through one that is energy independent to one that is both energy and momentum dependent. Closely related is the latest Argonne potential [35]. Other boson exchange potentials based on field theory now have been developed for NN [34, 33, 60, 36], πN [96, 97, 98], and $\pi\pi$ [99] interactions which also provide a simple parameterisation of the force. The field theoretic approach of the full Bonn interaction [19, 34] gives a well defined behavior for many aspects of the NN potential. All relevant 2π -exchange Feynman diagrams have been included in the three dimensional Blankenbecler-Sugar reduction [100] of the Bethe-Salpeter equation [101]. Also, relevant 3π - and 4π -exchanges were included. They have about the same range effects as the ω -exchange contributions. Form factors are used to handle the short-range part of the interaction, again in contrast to the cut-off method of the Paris interaction. Retardation effects are considered in the full model of the Bonn interaction. Although these are of no consequence on-shell, they tend to suppress high momenta off-shell. This more complete treatment also defines the off-shell behavior of the potential unambiguously, unlike the common approximation of using static propagators. The low D -state probability of the deuteron for the Bonn potential has been attributed to the reduction of the OPE tensor interaction strength by meson retardation effects.

The Bonn interaction also has been parameterised as an OBE potential in both configuration and momentum space [19] for convenient application to nuclear reaction and structure calculations. The momentum space version, Bonn-B, has been used most commonly. The Bonn-B interaction results by neglecting the minor 3π - and 4π -exchange effects and replacing the 2π and $\pi\rho$ contributions by the σ -exchange. The resulting OBE terms were applied to the Blankenbecler-Sugar reduction of

the Bethe-Salpeter equation to eliminate the energy dependence and the η meson exchange was added before the meson parameters were adjusted to maintain the quality of the fit to data. But it should be noted that the absence of meson retardation effects and of higher order diagrams in the Bonn-B model results in off-shell differences in some partial wave channels as compared to the full Bonn potential, particularly for the S -waves.

In contrast, the Nijmegen potential (Nijm93) [33] is a non-relativistic coordinate space OBE potential. Besides invoking exchanges of the six mesons used by other interactions [$\pi, \eta, \rho, \omega, \delta$ and σ], the Nijm93 interaction also allowed exchanges of the the $\eta'(958)$, $\phi(1020)$, and $S^*(993)$ mesons. The dominant $J = 0$ parts of the pomeron (or multi-gluon exchange) and tensor (f, f', A_2) Regge trajectories are included as well. It was intended that the Nijm93 potential stay in contact with QCD, by the parameterisation of the short range interaction. The Paris and Bonn potentials imposed no such constraints upon phenomenological parameterisations for this short ranged part of the interaction.

Finally we comment further on the newest development, the OSBEP potential [60, 36, 96]. The technical difficulties and limitations associated with QCD-inspired approaches and the unpleasant situation of the inconsistencies in, and the large numbers of, parameters in the standard phenomenological models, set a challenge to develop the OSBEP model so that it gave a quantitative description of experimental data using a minimum number of parameters in a unified, consistent framework for NN and πN scattering. A link to QCD-inspired models also is established as OSBEP uses a phenomenological nonlinear meson Lagrangian. The key feature of the OSBEP approach is a novel concept for the regularization of the scattering amplitudes by means of a proper normalisation of the meson fields.

As indicated above, modern boson exchange potentials use phenomenological parameterisation for the short range part of the potential, i.e., form factors of different shape are introduced to cure the divergent behavior of the scattering amplitudes when integrating over intermediate states. These form factors, however, differ in application to NN and πN scattering if quantitative agreement with scattering data is to be found. It is not possible to describe both systems within one unified framework using the standard models. One of the successes of the OSBEP model is that by regularising the scattering amplitudes in a different way, it provides a consistent description of both NN and πN scattering results. The ansatz of the OSBEP model is to regularize all self-scattering diagrams *a priori* at the level of the meson dynamics. That process is in stark contrast to approaches of the conventional models

where regularization is done *a posteriori* by attaching empirical form factors to the scattering amplitudes. With the OSBEP model, all amplitudes remain finite independent of whether NN or πN scattering is considered. That is achieved by using meson field operators that are associated with an energy dependent normalisation designed to regularize all self-energy amplitudes. Since all Feynman diagrams in the boson exchange picture involve meson fields by definition, this procedure suffices to ensure that all scattering amplitudes for NN and πN scattering can be regularized. The shape of this normalisation is constrained by physical boundary conditions and, to avoid the introduction of new parameters, its strength is determined by the coupling constant of the meson self-interaction. This coupling constant enters the normalisation of the asymptotic in- and out-fields only if the self-interaction acts for all times. As a consequence, nonlinear terms of the meson Lagrangian enter the field equation for the meson fields, and to be feasible, analytic solutions must be found. That is possible as Burt [102] demonstrated with his model of solitary mesons. He found classical wave like solutions, the *solitary mesons*, which can be quantized to calculate a propagator function and scattering amplitudes. Such analytic classical solutions that can be quantized have been used for the NN and πN system [60, 36].

There is an additional, advantageous property within the OSBEP. The values of the parameters of the self-interaction of the various mesons follow an empirical scaling relation that is similar to the symmetry constraints of QCD-inspired models. More importantly, this scaling law significantly reduces the number of free parameters in the model without sacrificing the accuracy of the description of data. Thus with OSBEP, there are no adjustable cutoff masses and, as many parameters of meson nonlinearities are interrelated by a simple scaling relation, only the pion self-interaction coupling constant remains as an adjustable parameter involved with the meson self-interaction. With OSBEP, one then has only the meson-meson and meson-baryon coupling constants not fixed by experiment or symmetry relations.

5.2. The Free NNt Matrices

It is generally accepted that a valid covariant description of NN scattering formally is given by the Bethe-Salpeter equation

$$\mathcal{M} = \mathcal{V} + \mathcal{V}\mathcal{G}\mathcal{M}, \quad (5.1)$$

where \mathcal{M} are invariant amplitudes that are based upon irreducible diagrams as contained in \mathcal{V} and \mathcal{G} is a relativistic propagator. This equation serves generally as an ansatz for approximations. Of those, the three

dimensional reductions are of great use and, of those, the Blankenbecler-Sugar [100] reduction gives an equation that has received the most attention for applications with NN scattering [34, 103]. In the Blankenbecler-Sugar approach, an effective potential operator is introduced which one identifies as the NN interaction potential. This reduction is obtained from the integral equation (5.1), which in terms of four-momenta is [104]

$$\mathcal{M}(q', q; \omega) = \mathcal{V}(q', q; \omega) + \int d^4 k \mathcal{V}(q', k; \omega) \mathcal{G}(k; \omega) \mathcal{M}(k, q; \omega) \quad (5.2)$$

with the propagator, taken in the limit $\epsilon \rightarrow 0^+$,

$$\mathcal{G}(k; \omega) = \frac{i}{(2\pi)^4} \left[\frac{\frac{1}{2}\phi + \mathbf{k} + M}{\left(\frac{1}{2}\omega + k\right)^2 - M^2 + i\epsilon} \right]^{(1)} \left[\frac{\frac{1}{2}\phi + \mathbf{k} + M}{\left(\frac{1}{2}\omega + k\right)^2 - M^2 + i\epsilon} \right]^{(2)} \quad (5.3)$$

The superscripts refer to the nucleon (1) and (2) respectively, and in the C.M. system $\omega = (\sqrt{s}, 0)$ with total energy \sqrt{s} . The Blankenbecler-Sugar reduction of the propagator \mathcal{G} is to use the covariant form

$$\mathcal{G}_{BBS}(k, s) = -\frac{\delta(k_0)}{(2\pi)^3} \frac{M^2}{E_k} \frac{\Lambda_{+}^{(1)}(\mathbf{k}) \Lambda_{+}^{(2)}(-\mathbf{k})}{\left[\frac{1}{4}s - E_k^2 + i\epsilon\right]}, \quad (5.4)$$

where the positive energy projector is given as

$$\Lambda_{+}^{(i)}(\mathbf{k}) = \left(\frac{\gamma^0 E_k - \gamma \cdot \mathbf{k} + M}{2M} \right)^{(i)}. \quad (5.5)$$

Then the three-dimensional equation,

$$\begin{aligned} \mathcal{M}(\mathbf{q}', \mathbf{q}; \omega) &= \mathcal{V}(\mathbf{q}', \mathbf{q}; \omega) + \int \frac{d\mathbf{k}}{(2\pi)^3} \mathcal{V}(\mathbf{q}', \mathbf{k}; \omega) \frac{M^2}{E_k} \frac{\Lambda_{+}^{(1)}(\mathbf{k}) \Lambda_{+}^{(2)}(-\mathbf{k})}{[\mathbf{k}_0^2 - \mathbf{k}^2 + i\epsilon]} \\ &\quad \mathcal{M}(\mathbf{k}, \mathbf{q}; \omega), \end{aligned} \quad (5.6)$$

results with $\omega \propto k_0^2$. Taking matrix elements with only positive energy spinors, an equation with minimum relativity is obtained for the NNT matrix, namely

$$\begin{aligned} \mathcal{T}(\mathbf{q}', \mathbf{q}; \omega) &= \mathcal{V}(\mathbf{q}', \mathbf{q}; \omega) + \int \frac{d\mathbf{k}}{(2\pi)^3} \mathcal{V}(\mathbf{q}', \mathbf{k}; \omega) \frac{M^2}{E_k} \frac{1}{[\mathbf{k}_0^2 - \mathbf{k}^2 + i\varepsilon]} \\ &\quad \mathcal{T}(\mathbf{k}, \mathbf{q}; \omega). \end{aligned} \quad (5.7)$$

With the substitutions

$$\mathcal{T}(\mathbf{q}', \mathbf{q}; \omega) = \left(\frac{M}{E_{q'}} \right)^{\frac{1}{2}} \mathcal{T}(\mathbf{q}', \mathbf{q}; \omega) \left(\frac{M}{E_q} \right)^{\frac{1}{2}}, \quad (5.8)$$

and

$$V(\mathbf{q}', \mathbf{q}; \omega) = \left(\frac{M}{E'_q} \right)^{\frac{1}{2}} \mathcal{V}(\mathbf{q}', \mathbf{q}; \omega) \left(\frac{M}{E_q} \right)^{\frac{1}{2}}, \quad (5.9)$$

one obtains the expression

$$T(\mathbf{q}', \mathbf{q}; \omega) = V(\mathbf{q}', \mathbf{q}; \omega) + \int \frac{d\mathbf{k}}{(2\pi)^3} V(\mathbf{q}', \mathbf{k}; \omega) \frac{M}{[\mathbf{k}_0^2 - \mathbf{k}^2 + i\varepsilon]} T(\mathbf{k}, \mathbf{q}; \omega). \quad (5.10)$$

This is equivalent to the non-relativistic LS equation as $\{E_q, E_{q'}\} \rightarrow M$.

For energies to a few hundred MeV, $\{E_q, E_{q'}\} \rightarrow M$ is a good approximation and the potentials essentially can be taken as energy independent, i.e., $V(\mathbf{q}', \mathbf{q}; \omega) \rightarrow V(\mathbf{q}', \mathbf{q})$.

5.2.1. The Partial Wave t Matrices

The NN scattering phase shifts are defined from the on-shell values of the free NNt matrices in the diverse allowed NN channels so that partial wave expansions,

$$X(\mathbf{q}', \mathbf{q}; \omega) = \frac{2}{\pi k} \sum_{\substack{JST \\ LL'N}} \mathcal{Y}_{JLS}^N(\hat{\mathbf{q}'}) x_{LL'}^{JST}(q q; \omega) \mathcal{Y}_{JLS}^{N\dagger}(\hat{\mathbf{q}}) \hat{P}_T, \quad (5.11)$$

are made where J , L , S , and T are the NN total angular momentum, orbital angular momentum, spin, and isospin respectively, \hat{P}_T is the NN isospin projection operator, and $\mathcal{Y}_{JLS}^N(\hat{\mathbf{q}})$ are tensor spherical harmonics. Using partial wave expansions of both $V(\mathbf{q}', \mathbf{q}; \omega)$ and $T(\mathbf{q}', \mathbf{q}; \omega)$ in Eq. (5.10), coupled Fredholm integral equations of the second kind are found, namely

$$t_{L'L}^{JST\pm}(q', q; \omega) = v_{L'L}^{JST}(q', q; \omega) + \frac{2}{\pi} \sum_l \lim_{\epsilon \rightarrow 0} \int_0^\infty dk k^2 v_{L'l}^{JST}(q', k; \omega) [k_0^2 - k^2 + i\epsilon]^{-1} t_{lL}^{JST\pm}(k, q; \omega). \quad (5.12)$$

These amplitudes satisfy time reversal invariance if

$$t_{L'L}^{JST\pm}(q', q; \omega) = t_{LL'}^{JST\pm}(q, q'; \omega), \quad (5.13)$$

and the property,

$$t_{L'L}^{JST\pm}(q', q; \omega) = [t_{L'L}^{JST\pm}(q', q; \omega)]^*, \quad (5.14)$$

ensures that the solutions with incoming and outgoing wave boundary conditions relate by complex conjugation. The solutions with outgoing wave boundary conditions are chosen for further study and so the \pm superscript will be omitted unless required.

The integral equations, Eqs. (5.12) are solved numerically. Real K matrix equations also may be defined having the solutions which relate back to the t matrices by the Heitler equation [38]. This intermediate step is based on unitarity and on the Dirac relation

$$\lim_{\epsilon \rightarrow 0} \frac{1}{[k_0^2 - k^2 \pm i\epsilon]} = P \frac{1}{[k_0^2 - k^2]} \mp i\pi\delta(k_0^2 - k^2), \quad (5.15)$$

for the propagator to be used in Eq. (5.12). P signifies that the principal value of the integral is to be taken. The relation between the t - and K matrices then is given by the Heitler equation,

$$t_{L'L}^{JST}(q', q; \omega) = K_{L'L}^{JST}(q', q; \omega) - ik_0 \sum_l K_{L'l}^{JST}(q', k_0; \omega) t_{lL}^{JST}(k_0, q; \omega). \quad (5.16)$$

The K matrices satisfy the Fredholm integral equation of the second kind

$$K_{L'L}^{JST}(q', q; \omega) = v_{L'L}^{JST}(q', q; \omega) + \frac{2}{\pi} \sum_l P \int_0^\infty dk k^2 v_{L'l}^{JST}(q', k) \frac{1}{[k_0^2 - k^2]} K_{lL}^{JST}(k, q; \omega), \quad (5.17)$$

whose solutions imply standing wave boundary conditions.

There are many methods by which the t - and K matrices may be generated. They are discussed in the review of Srivastava and Sprung [94]. One of particular use is that of matrix inversion since there is an easy technique to extract the pole at $k = k_0$. The integrand becomes smooth by subtracting a zero term since

$$P \int_0^\infty dk \frac{1}{[k_0^2 - k^2]} = 0. \quad (5.18)$$

The resultant Fredholm integral equation of the second kind is then

$$\begin{aligned} K_{L'L}^{JST}(q', q; \omega) = & v_{L'L}^{JST}(q', q; \omega) + \frac{2}{\pi} \sum_l \int_0^\infty dk \frac{1}{k_0^2 - k^2} \\ & \times [k^2 v_{L'l}^{JST}(q', k; \omega) K_{lL}^{JST}(k, q; \omega) - k_0^2 v_{L'l}^{JST}(q', k_0; \omega) K_{lL}^{JST}(k_0, q; \omega)], \end{aligned} \quad (5.19)$$

which is numerically well posed.

Finally, a remark about the deuteron wave function is appropriate. In momentum space, the bound state S and D wave functions of the deuteron are solutions of the coupled Fredholm integral equation of the first kind,

$$\psi_{L'}(q; \omega) = -\frac{2}{\pi} \sum_L \int_0^\infty dk k^2 v_{L'L}^{JST}(q, k) \frac{1}{[q_D^2 + k^2]} \psi_L(k; \omega), \quad (5.20)$$

The matrix method of solution of this is ill posed, however procedures of solution exist in numerical analysis.

5.3. Solution of the Lippmann-Schwinger Equation

First, the on-shell properties of the NN t matrices and the solutions to the bound state equations, i.e., the scattering phase shifts and deuteron properties are discussed. Then the off-shell features of the NN t matrices are considered. In the latter use is made of the Noyes-Kowalski functions [105, 106, 107] since they suppress on-shell differences that arise with different input interactions.

5.3.1. Phase Shifts and Deuteron Properties

In Figs. 5.1–5.4, np phase shifts that have been calculated from various potentials are compared with the SM97 phase shifts of Arndt *et al.* [15]. In Figs. 5.1 and 5.2 the results to 300 MeV are given for the OSBEP (solid curves), the Bonn-B (dashed curves), the Nijm93 (dotted curves), and Paris (dash-dotted curves) interactions. It is evident that all of these potential models lead to phase shifts that are in good agreement with the SM97 analysis in most partial waves. Differences that exist are only a few degrees. The forces were designed for the energy regime below pion threshold and so their use at energies above 300 MeV are

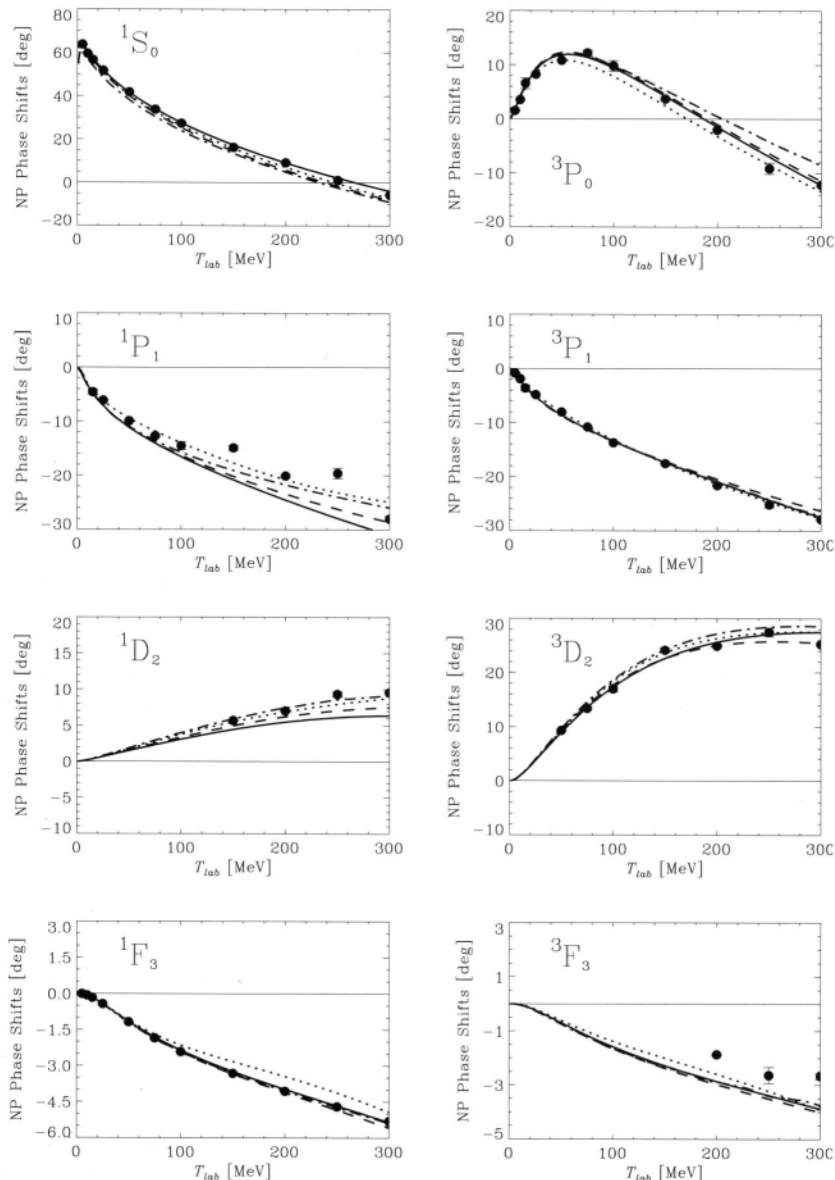


Fig. 5.1. The single channel SM97 phase shift analysis, single energy fits (filled circles), compared with the results found using the OSBEP (solid curves), Bonn-B (dashed curves), Nijm93 (dotted curves), and Paris (dash-dotted curves) potentials.

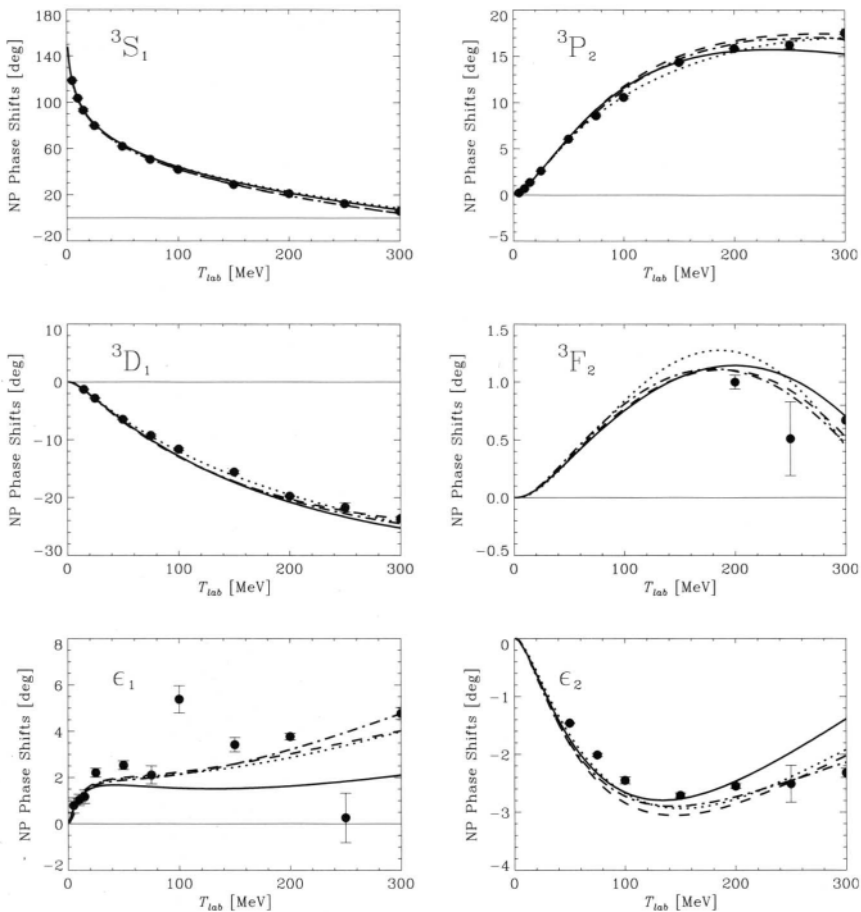


Fig. 5.2. As for Fig. 5.1, but for the np coupled channels.

extrapolations. The phase shifts found using the potentials are shown to 1600 MeV in Figs. 5.3 and 5.4. The filled circles are the real phase shifts of the SM97 single energy, and the solid lines are those of the SM97 continuous energy, solutions. These are compared with the results of potential models, namely OSBEP (dash-dotted curves), the Argonne AV18 (long dashed curves), and the Bonn-B (dotted curves). In addition the results found using inversion potentials based upon the SM94 phase shifts are displayed by the dashed curves. All these potential model results extrapolate smoothly and remain in qualitative agreement with the data.

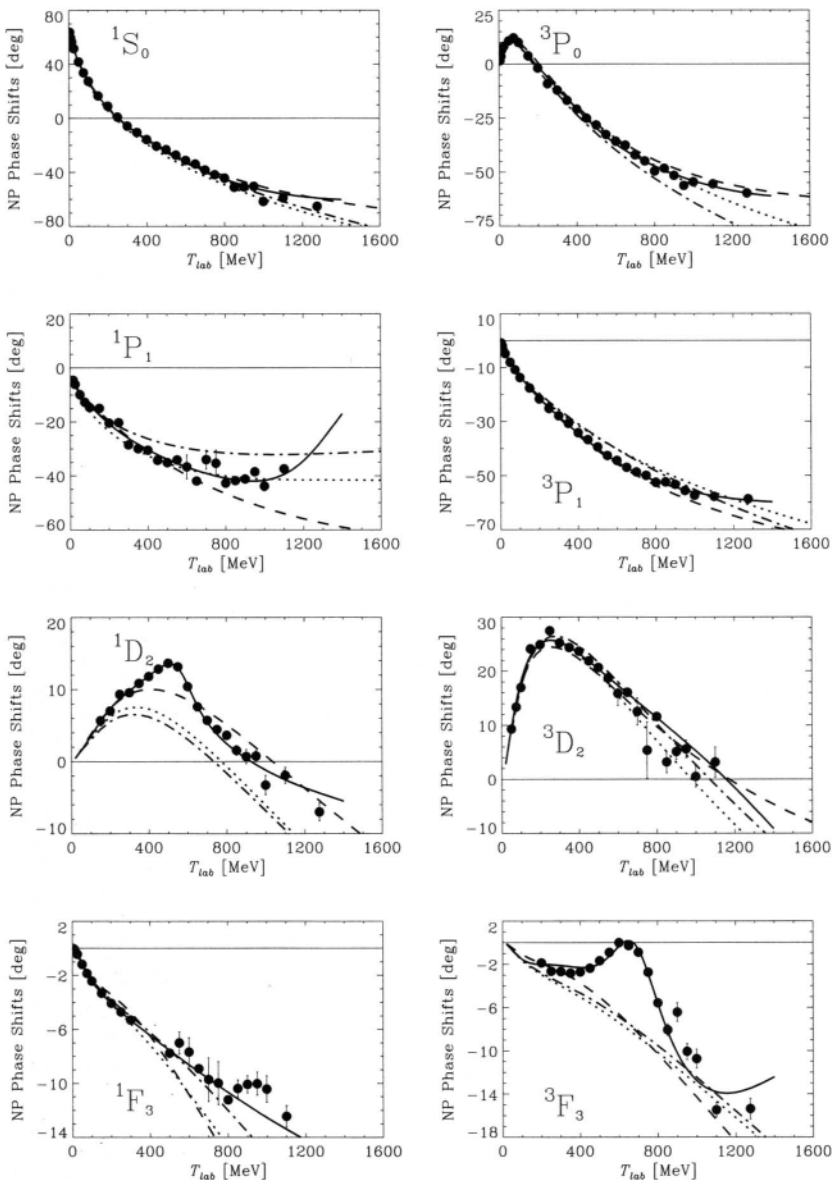


Fig. 5.3. The real phase shifts for np scattering in uncoupled channels. The full dots are SM97 single energy solutions while the solid curves represent the SM97 continuous solutions. The results from potential models are designated by OSBEP (dash-dotted curves), Bonn-B (dotted curves), and AV18 (long dashed curves). The dashed curves give the results of SM94 inversion potentials.

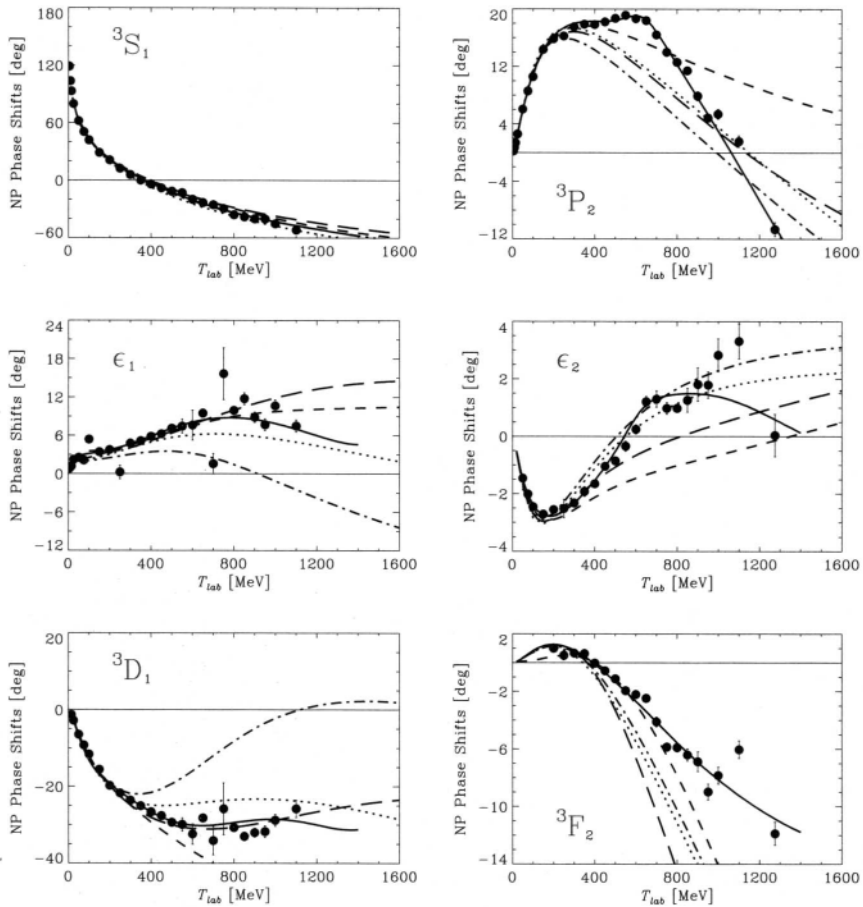


Fig. 5.4. As for Fig. 5.3, but for the np coupled channels.

In Table 5.1, the low energy np parameters and deuteron properties are compared with experimental values. All of the model predictions compare well with the experimental scattering length and effective range values, although the Paris and OSBEP interactions are fitted to small values for the singlet scattering length. The deuteron properties, other than the D state probability, do not distinguish between any of them. The Bessel transforms of the momentum space S and D state wave functions for all the interactions are given in Fig. 5.5. They are quite similar save in the region to 2 fm. The smaller D state probability of the Bonn-B in

TABLE 5.1
Low-Energy np scattering and deuteron properties for three interactions.

Property	Bonn-B	Paris	OSBEP	Experiment
a_s (fm)	-23.7	-17.6	-17.4	-23.748 (10)
a_t (fm)	5.42	5.43	6.50	5.424 (4)
r_s (fm)	2.70	2.88	2.58	2.75 (5)
r_t (fm)	1.76	1.77	1.69	1.759 (5)
E_D (MeV)	2.2246	2.2246	2.2246	2.22458900 (22)
μ_D (nm)	0.8514*	—	0.8456*	0.857406 (1)
Q_D (fm 2)	0.2783*	0.279*	0.2728*	0.2859 (3)
P_D (%)	4.99	5.77	6.00	—
A_S	0.8862	—	0.8788	0.8802 (20)
D/S	0.0264	0.0261	0.0256	0.0256 (4)
r_{rms} (fm)	1.9688	—	1.9554	1.9627 (38)

*Meson exchange current contributions are not included.

comparison to that of the Paris interaction is reflected by the smaller peak in the associated D state function.

5.3.2. Off-Energy-Shell t Matrices

The t matrices are said to be off-shell when the variables q and q' differ from the on-shell momentum value k_0 . Of particular interest are the half-off-shell K - and t matrices $q' = k_0$ or $q = k_0$ as these elements appear explicitly in calculations of few body photonuclear reactions such as pp bremsstrahlung and deuteron photo-disintegration. Furthermore, for energy independent potentials, the fully-off-shell t matrix elements may be expressed in terms of half-off-shell elements [108]. Then all relevant physical information is contained in the half-off-shell t - or K matrices. Nevertheless, pictures of fully off-shell t matrices have been published [109] for many NN channels and a set of energies. From this it was also found that it suffices to look at the half-off-shell properties to understand essential features.

To study the half-off-shell properties of the t matrices, it is instructive to introduce the Noyes-Kowalski functions [105, 106, 107], or f -ratios. Such ratios abrogate any on-shell differences between potential models by scaling so that the relative behavior off the energy shell are stressed. For uncoupled channels $J = L' = L$, these are purely real functions,

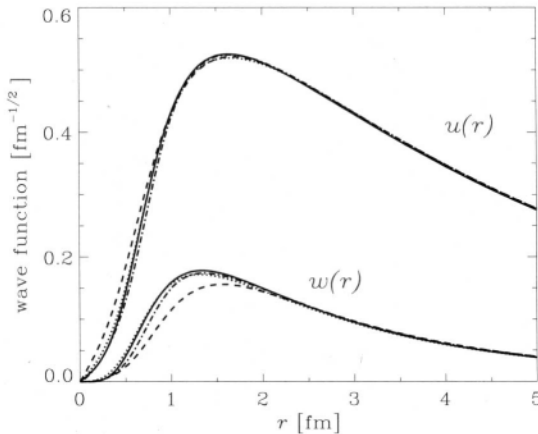


Fig. 5.5. Coordinate space S ($u(r)$) and D ($w(r)$) state deuteron wave functions. The nomenclature is as for Fig. 5.1.

$$f_L^{JST}(q', k_0; \omega) = \frac{t_{LL}^{JST}(q', k_0; \omega)}{t_{LL}^{JST}(k_0, k_0; \omega)} = \frac{K_{LL}^{JST}(q', k_0; \omega)}{K_{LL}^{JST}(k_0, k_0; \omega)}, \quad (5.21)$$

where Eq. (5.16) has been used. Consequently for channel α one has

$$f_\alpha(q', k_0; \omega) = \frac{K_\alpha(q', k_0; \omega)}{|t_\alpha(k_0, k_0; \omega)|^2} \operatorname{Re}\{t_\alpha(k_0, k_0; \omega)\} \quad (5.22)$$

with the use of unitarity,

$$\operatorname{Im}\{t_\alpha(q, q'; \omega)\} = -k_0 t_\alpha^*(q', k_0; \omega) t_\alpha(k_0, q; \omega). \quad (5.23)$$

This condition generalizes for coupled states to

$$\operatorname{Im}\{t_{L'L}^{JST*}(q, q'; \omega)\} = -k_0 \sum_l t_{L'l}^{JST*}(q', k_0; \omega) t_{lL}^{JST}(k_0, q; \omega) \quad (5.24)$$

and as a result, the f -ratios are complex since they cannot be cast in the form of Eq. (5.22). An alternative definition of the f -ratio in such cases is to use K matrix elements,

$$f_{L'L}^{JST}(q', k_0; \omega) = \frac{K_{L'L}^{JST}(q', k_0; \omega)}{K_{L'L}^{JST}(k_0, k_0; \omega)} \quad (5.25)$$

as these functions then are real in all channels. For most states, and especially for the weak ones, the half-off-shell K matrices behave similarly to

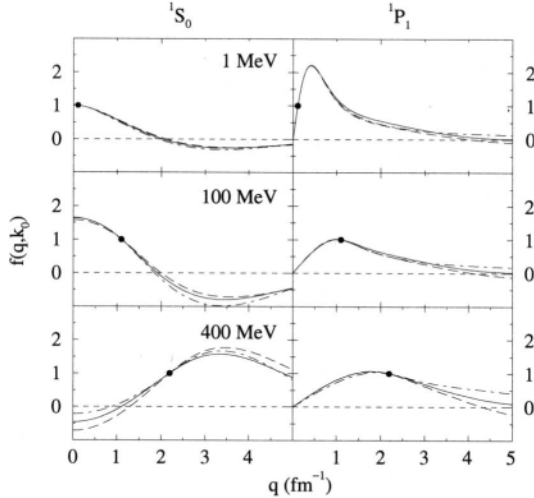


Fig. 5.6. The f -ratios for the 1S_0 (left panels) and 1P_1 (right panels) partial wave channels. The laboratory energies are 1 MeV ($k_0 = 0.11 \text{ fm}^{-1}$, top panels), 100 MeV ($k_0 = 1.1 \text{ fm}^{-1}$, middle panels), and 400 MeV ($k_0 = 2.2 \text{ fm}^{-1}$, bottom panels). The solid, dashed, and dot-dashed curves represent the results found using the Bonn-B, OSBEP, and Paris interactions respectively. The dot represents the on-shell point.

the real parts of the half-off-shell t matrices and thus there is little loss of generality.

The f -ratios for states to $J = 1$ and for the $J = 2$ coupled states are displayed in Figs. 5.6–5.11. Laboratory energies of 1, 100 and 400 MeV are shown in the upper, middle and lower segments of those figures. At 1 and 100 MeV, all forces used have been designed to give a good fit to the phase shifts and so essentially they are equivalent on-shell. At 400 MeV, the scattering is just above the pion threshold, so that the on- and off-shell properties of the interactions are extrapolations from the regime of their determination. It is of interest to see how these extrapolations vary as the base models have been used as reference in various studies seeking interpretation of the NN scattering data at higher energies. Indeed a most relevant one [43] for this review has found a scheme that fits the SM97 data to 2.5 GeV. In these figures, the filled circle in each segment indicates the on-shell point of the f -ratio. Results derived from three momentum space NN interactions are displayed. The dot-dashed curve represents the Paris interaction [18], the solid curve

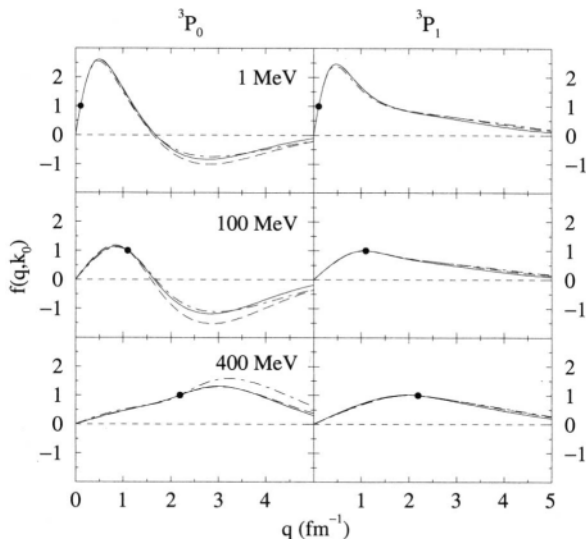


Fig. 5.7. The f -ratios for the 3P_0 (left panels) and 3P_1 (right panels) channels. The energies and curves are as designated in Fig. 5.6.

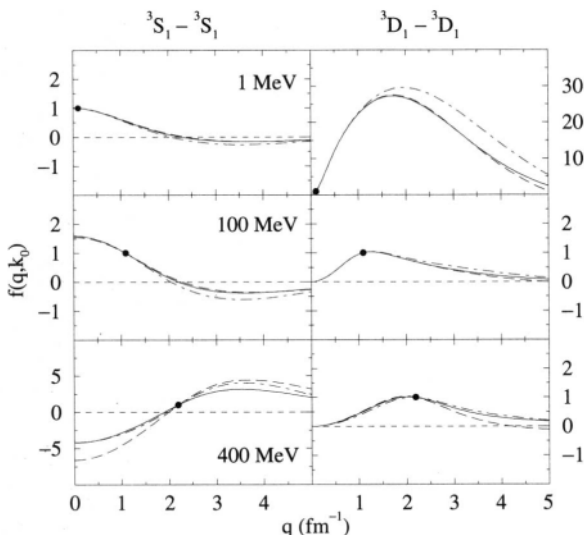


Fig. 5.8. The f -ratios for the 3S_1 (left panels) and 3D_1 (right panels) diagonal partial waves. The energies and curves are as designated in Fig. 5.6.

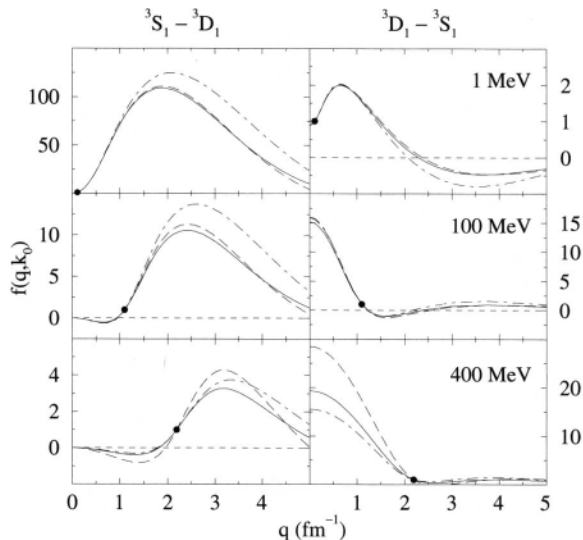


Fig. 5.9. The f -ratios for the coupled off-diagonal $J = 1$ K matrix elements $^3S_1 \rightarrow ^3D_1$ (left panels) and $^3D_1 \rightarrow ^3S_1$ (right panels). The energies and curves are as designated in Fig. 5.6.

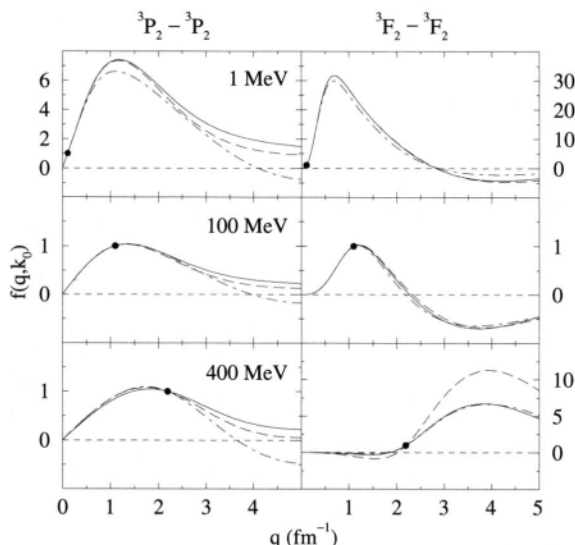


Fig. 5.10. The f -ratios for the 3P_2 (left panels) and 3F_2 (right panels) diagonal partial wave channels. The energies and curves are as designated in Fig. 5.6.

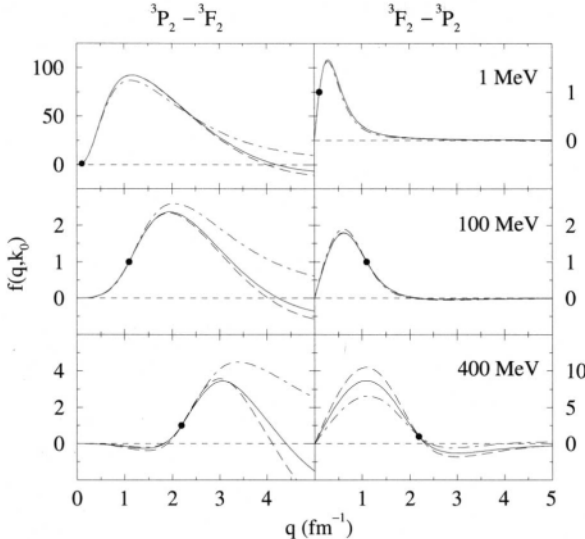


Fig. 5.11. The f -ratios for the coupled off-diagonal $J = 2$ K matrix elements $^3P_2 \rightarrow ^3F_2$ (left panels) and $^3F_2 \rightarrow ^3P_2$ (right panels). The energies and curves are as designated in Fig. 5.6.

represents the Bonn-B interaction [19, 34], and the dashed one represents the OSBEP interaction [60, 36].

The 1S_0 and 1P_1 channel f -ratios displayed in Fig. 5.6 present both the similarities of, and the differences between, the model calculations. For the 1S_0 channel, the potentials give qualitative agreement although some quantitative agreement is lost at higher energies. The curves extrapolate away from the on-shell point in a similar manner. The same observations can be made for the 1P_1 channel. The similarities between these curves below pion production threshold ~ 300 MeV and the phase shifts suggests that little difference would be seen in calculations made with any of these interactions, at least in the surround of the on-shell points. However at 400 MeV, a distinction can be made between the interactions. This is especially so for the Paris interaction; a result that is not surprising since the Paris interaction was designed to fit phase shifts below pion threshold and has a particularly strong repulsion. These phenomena then seem to reflect the character of the on-shell properties of the interactions. But qualitative differences occur between the Paris and Bonn-B potentials at high momenta in contrast to similarity of their phase shifts.

The excellent phase shift fits of the 3P_0 and 3P_1 channels across the whole range of laboratory energies to 400 MeV correspond to the

remarkably similar behavior of the f -ratios for all the interaction models at those energies. That is displayed in Fig. 5.7. The exception is the Paris interaction at 400 MeV for the 3P_0 channel. While the f -ratios for all interactions are virtually identical below the on-shell momentum, above this the magnitude of the Paris K - and t matrices are significantly different from those of the other interactions.

The $J = 1$ coupled channel f -ratios are in good agreement for most of the potentials in the diagonal channels as is seen from Fig. 5.8. The 3S_1 and 3D_1 phase shifts fit data up to 400 MeV very well. Half-off-shell there are only slight variations between the results beyond the on-shell point and in both channels, except for the OSBEP interaction f -ratio at 400 MeV. However, the 3S_1 phase shift passes through zero close to 400 MeV and as that implies small values for the denominators of Eqs. (5.21) and (5.25), the f -ratios at this energy can be quite large. The $J = 1$ off-diagonal f -ratio results for the set of potentials are displayed in Fig. 5.9. In the ${}^3S_1 \rightarrow {}^3D_1$ channel there are large differences between the Paris f -ratios and those of the other interactions for momenta well above the on-shell values. However, the scale of these f -ratios indicate that the on-shell values are very small so that any small variation between on-shell K matrix values would lead to large differences as the off-shell values of the K matrices increase. At 400 MeV, the ${}^3S_1 \rightarrow {}^3D_1$ channel results for the OSBEP interaction are different noticeably from those of the other two interactions. That is associated with the on-shell values of the OSBEP being different from those of the Bonn-B and Paris interactions above threshold. Below threshold, there is little to distinguish between any of the ${}^3D_1 \rightarrow {}^3S_1$ f -ratios. Surprisingly, these f -ratios are very similar for all interactions for large momenta, even at high energies. It is in this and the diagonal 3D_1 channels that the effects of the tensor force are expected to be most important. The major contributions in the 3S_1 phase shift come from the very strong central terms. Due to the S -component, the 1S_0 , 3S_1 and ${}^3D_1 \rightarrow {}^3S_1$ channel contributions essentially are the only non-zero ones at very low momenta.

The $J = 2$ coupled channels f -ratios are displayed in Figs. 5.10 and 5.11. For all energies and at high momenta, the 3P_2 f -ratios determined from the Paris interaction are significantly different to those of the Bonn-B and OSBEP interactions. This is also the case for the 1 MeV results for the 3F_2 channel. However, the fact that the on-shell K matrix values at this energy are so small means that any difference in off-shell properties would be magnified significantly. This can also explain the significant divergence with the OSBEP interaction from the others at 400 MeV. However the structure for all potentials is virtually independent of

energy beyond 100 MeV. While agreement between the interaction results is not necessarily confirmation of correct model behavior, it does indicate that similar constraints result in similar extrapolations away from the on-shell point. The $J = 2$ off-diagonal f -ratios shown in Fig. 5.11 are similar in character to the half-off-shell $J = 1$ channel amplitudes. The results are virtually the same at and below the on-shell point for ${}^3P_2 \rightarrow {}^3F_2$ but diverge beyond the on-shell value. Most notable is the marked differences of the Paris f -ratios from the others at high momenta. The Paris f -ratios are always repulsive. Both the Bonn-B and OSBEP interactions become attractive beyond $\sim 4 \text{ fm}^{-1}$. The structures of the various interaction f -ratios in the ${}^3F_2 \rightarrow {}^3P_2$ channel is very like those observed in the ${}^3D_1 \rightarrow {}^3S_1$ at all energies except for the region below the on-shell value at high energies. As seen in the 3F_2 channel at 400 MeV, the ${}^3F_2 \rightarrow {}^3P_2$ f -ratios of the three interactions are noticeably different at low momenta. In all cases, the f -ratios of the OSBEP interaction are the largest and those of the Paris interaction are the smallest.

The f -ratios are clear representations of the variations between the half-off-shell attributes of the various NN interactions. However there are cautions to be remembered. First, the proximity of the on-shell energy to that for which the phase shift of a given interaction is zero may distort the result by markedly enhancing the f -ratio. Second, because of the division by the on-shell t matrix value involved, the f -ratios do not reflect the relative importance of the NN channels to scattering at each energy. For on-shell energies near zero only the S states contribute sensibly to the scattering and these are an order of magnitude larger than contributions from higher partial waves. By 100 MeV however, the $J = 1$ and $J = 2$ states generally contribute in the same order of magnitude as do the S states.

There is little to distinguish between the on-shell properties of the NN t matrices given by the diverse OBE potential models of Nijmegen, Paris, Bonn-B, OSBEP. Phase shifts calculated from these potentials agree very well below pion threshold with the latest empirical analyses SM97 and with the properties of the deuteron. Slight differences do exist, e.g., in the 1S_0 phase shifts. Deviations also are observed in the calculated values of NN scattering observables. In part those are probably due to the use of different data bases in determining the values of parameters in each of the potentials. Using the SAID data base [15] for scattering below 300 MeV yields a total χ^2/datum of 4.1 (OSBEP), 4.5 (Nijmegen), 9.2 (Paris) and 10.1 (Bonn-B). These numbers reflect that the Paris and Bonn-B potential models were constructed to fit the data base available in the 1980's and need to be updated using today's data base as reference.

An important observation of the f -ratios is the energy dependence of the channels. They are not simply predictable with a trivial function form. All of the states considered display a repulsive f -ratio for small momenta and at low energies. However the 1S_0 state f -ratio becomes quite strongly attractive by 400 MeV. In contrast the 1P_1 structure remains largely unchanged across the whole energy range. Similarly the first zero of the half-off-shell 3P_0 channel K matrices shifts from $\sim 2\text{ fm}^{-1}$ at 1 MeV to $\sim 6\text{ fm}^{-1}$ at 400 MeV but there is little change in this range for 3P_1 values. The similarities between the f -ratios for three quite distinct NN interactions at energies below the pion threshold explains why there is little sensitivity to calculations of other reactions, e.g., of pp bremsstrahlung, made with any of these interactions. Above pion production threshold, the phase shifts, f -ratios, and consequentially calculations dependent upon these t matrices, are interaction dependent. Hence the NN interaction should only be used in the regime for which it has been defined. One should not expect the Paris, Bonn-B or OSBEP interactions to be appropriate with folding model calculations of the pA optical potentials for energies above that for which they give adequate fits to the free NN scattering. Thus one may expect the Paris, Bonn-B, and OSBEP interactions to be appropriate for scattering below pion threshold, but that modified forms will be required if one seeks results at higher energies.

5.4. Quantum Inversion and the NN t Matrix

An alternative to the direct approach of specifying NN t matrix elements by starting with a boson exchange interaction, is to seek them by solutions of the quantum inverse scattering problem [37]. For the NN scattering problem, the inverse scattering theory of relevance is that for fixed angular momentum and with the energy being the spectral variable. In that case, two fundamental inversion equations have been studied with some effect. Specifically they are the Gel'fand-Levitan and the Marchenko equations [37]. The first incorporates the experimental spectral data by means of the Jost function $L_t(k)$ whereas the second involves the S matrix $S_t(k) = \exp\{2i\delta(k)\}$. Both equations define output kernels from Fredholm integral equations whose input kernels are defined by the data. Those output kernels relate to Schrödinger local potentials that are phase equivalent to the input data.

The relevant equations are

$$A(r, s) + G(r, s) + \int_0^r A(r, t)G(t, s)dt = 0, \quad (5.26)$$

for the Gel'fand-Levitman approach where $A(r, s)$ and $G(r, s)$ are the output and input kernels respectively, and

$$K(r, s) + F(r, s) + \int_0^\infty K(r, t)F(t, s)dt = 0, \quad (5.27)$$

for the Marchenko approach where $K(r, s)$ and $F(r, s)$ are the output and input kernels respectively. The input kernels for the two approaches are

$$G(r, s) = \frac{2}{\pi} \int_0^\infty j_l(kr) [\mathcal{L}_l(k)^{-2} - 1] j_l(ks) dk, \quad (5.28)$$

where $j_l(kr)$ are Riccati-Bessel functions, and

$$F(r, s) = \frac{1}{2\pi} \int_{-\infty}^\infty h_l^+(kr) [1 - S_l(k)] h_l^+(ks) dk, \quad (5.29)$$

where $h_l^+(kr)$ are Riccati-Hankel functions. Inversion potentials are then obtained by

$$V^{GL}(r) = 2 \frac{d}{dr} A(r, r), \quad (5.30)$$

with Gel'fand-Levitman inversion and by

$$V^M(r) = -2 \frac{d}{dr} K(r, r), \quad (5.31)$$

in the Marchenko case.

The input kernels to the two equations are quite different and so, therefore, are the output ones. Also the validity domains of the two fundamental integral equations differ. But for the class of potentials dictated by use of rational functions to represent the data, those domains overlap. Using rational function representations of the S matrix then the two inversion potentials coincide for each angular momentum channel,

$$V^{GL}(r) = V^M(r) = V_l(r), \quad (5.32)$$

when it is assumed

$$S_l(k) = e^{2i\delta_l(k)} = \frac{\mathcal{L}_l(-k)}{\mathcal{L}_l(k)} = \frac{1+iK(k)}{1-iK(k)} = \prod_{n=1}^{\infty} \frac{k+a_n}{k-a_n}. \quad (5.33)$$

With either approach to extract potentials from a phase shift set, such as the SM94 tabulation of Arndt *et al.* [58], extrapolation towards infinite energy is required. Above 1 GeV it has been presumed that the limit conditions are to be reached smoothly,

$$\lim_{k \rightarrow \infty} S_l(k) = 1 + \mathcal{O}(k^{-1}). \quad (5.34)$$

Also various phase shift sets taken as input to the inversion procedures have been generated from model NN potentials, e.g., the Paris interaction. From them one gets associated inversion potentials and which will be identified with the starting potential name, e.g., the Paris inversion potential. Full details of the inversion calculations are given in Refs. [39, 77].

By their construction, the potentials determined with fixed angular momentum quantum inverse scattering calculations are phase equivalent to the input scattering information, and thus relate to the exact on-shell t matrices. So forming an inversion potential can be viewed simply as an intermediate step, by way of the LS equation, of relating actual data to the off-shell properties of the t matrix. In this way quantum inverse scattering theory defines the off-shell properties of the t matrix from measured on-shell values.

5.4.1. Case Studies

The Paris interaction has been used to generate a set of phase shifts which then have been taken as input to calculate the corresponding Paris inversion potentials. The method used ensured that the original Paris and the inversion potentials were equivalent on-shell within the accuracy inherent to the numerics used for implementing the quantum inversion method. To be assured of the off-shell continuation with the inversion potentials to be determined from data and not from the extrapolation, the range of on-shell energies should be somewhat higher than the highest energy value used in applications. Therefore, to ensure that properties of the inversion potential depend solely on the dynamical equations and not on the range of energies considered for the phase shifts, it was verified [46] that t matrices that fit phase shifts up to 1.3 GeV are required to construct optical potentials up to 500 MeV.

Phase shifts for selected NN channels with $L \leq 2$ and in the 0–1.2 GeV energy range are shown in Fig. 5.12. Therein the Paris phase shifts are portrayed by the crosses while those obtained by using the inversion potentials are represented by the solid curves. While some differences are observed in the (coupled) 3D_1 state above 400 MeV, the agreement between initial and reproduced sets is generally very good so that the determined inversion potential can be considered as phase equivalent to the Paris potential. The inversion potential, being static and

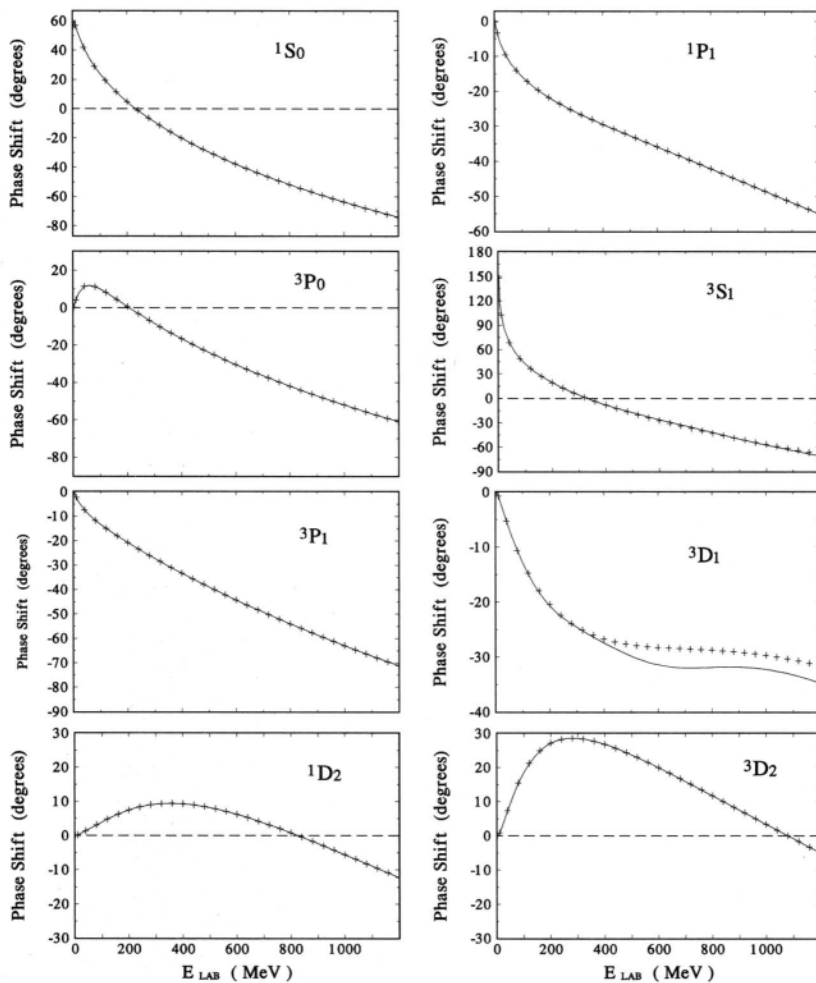


Fig. 5.12. The Paris NN interaction phase shifts compared with the results from the potentials found upon their inversion.

local, will differ in off-shell content from the original Paris potential which is momentum dependent.

Using the Gel'fand-Levitman and Marchenko formulations of the fixed energy quantum inverse scattering theory, NN inversion potentials have been found also from the SM94 data for all NN channels with $J \leq 2$. For selected channels and as a function of the energy, those phase shifts

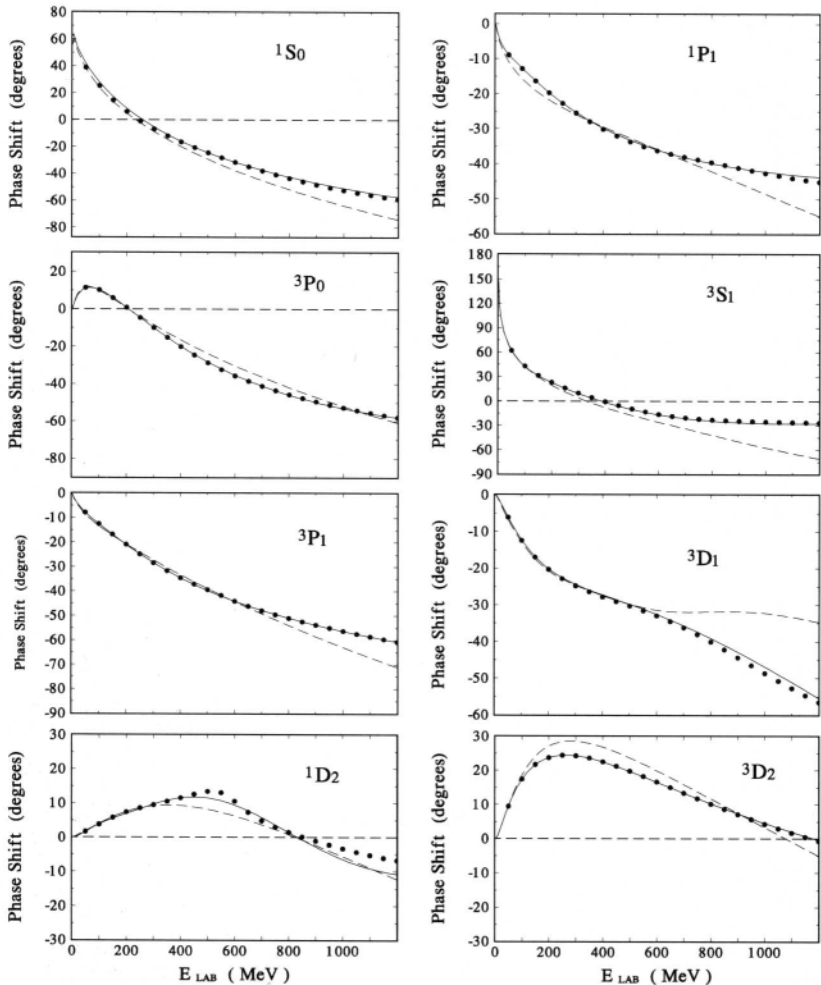


Fig. 5.13. The SM94 phase shifts (filled circles) compared with the results from the potentials found upon their inversion (solid curves). The Paris potential phase shifts are shown by the dashed curves.

are shown in Fig. 5.13. Therein the filled circles designate the SM94 data and the continuous curves are the phase shifts obtained from the inversion potentials constructed from that SM94 data. The phase shifts obtained from the Paris inversion potentials are displayed as well (dashed curves) for reference. Note first the ability of the inversion method to reproduce the input data. The level of accuracy obtained is

excellent with whatever phase shift set is used; SM94 and Paris here. Second, note that there is a clear difference between the Paris phase shifts and the SM94 ones above pion production threshold. It is precisely the presence of these differences which should affect the overall behavior of the inversion potential and, in particular, the optical model potentials above 300 MeV.

6. NUCLEAR MATTER AND $NN g$ MATRICES

It has been many years since Brueckner and his collaborators [110, 111] established a particularly useful perturbation theory of nuclear many-body systems based upon the NN interaction. With the apparent success of the shell model and thus the implication that nucleons within a nucleus move independently, short ranged particle correlations [110] did not complicate that theory. Essentially, their effect was to create an average field [111] in which the nucleons move. In this section the Brueckner theory by which that average field can be obtained from $NN g$ matrices [112] is given. In the context of infinite nuclear matter, the average field modifies the average kinetic energies in the intermediate propagators [113], which, when antisymmetrization is included, defines the BBG integral equations. Solutions of those BBG equations are called the g matrices. The Pauli principle affects those integral equations by restricting intermediate scattering states to be excited states of a fermionic many-body system. That is defined as *Pauli blocking*.

In the development of a Thomas-Fermi theory of large nuclei, Bethe [114] established that the local density approximation (LDA) is a convenient connection between the infinite matter and finite nuclear systems. He found the LDA to be valid for densities in excess of $\sim 17\%$ of the central value. In that paper, Bethe also noted the importance of damping effects due to the auxiliary potentials in the propagators of the Brueckner theory. This importance was revealed also by the study of Yuan *et al.* [115] on the mean free path of nucleons in infinite nuclear matter. Allowing for Pauli blocking effects at normal central densities ($k_f = 1.4 \text{ fm}^{-1}$) they found the nucleon mean free path to be almost double that specified by using the on-shell $t\rho$ approximation. Even so the calculated mean free paths fell short of the empirical value, due in part to the neglect of the auxiliary potentials in the calculations. Cheon [116] allowed for that by using the effective mass approximation to obtain good estimates of the nucleon mean free path. Other studies [117] confirmed that effects of the medium can vary predictions of nuclear matter

absorption potential strengths by as much as a factor of five from values obtained using free NN t matrices. In any event, a primary requirement of microscopic theories of nuclei and their interactions is to know how free NN interactions are influenced by the presence of a nuclear medium.

All nuclear medium calculations require evaluation of the BBG g matrices off-shell. For example, in an analysis of knock-out reactions [118, 119], it was found that extraction of nuclear properties becomes tenuous if conventional on-shell approximations are made. Intriguingly, realistic one boson exchange potentials, as well as those obtained by inversion of the NN phase shifts [120, 39], have very similar off-shell characteristics. Problems therefore lie with the specific medium correction effects to the on-shell values of the free t matrices to be used in defining optical potentials with the tp and gp approximations [121, 55, 51, 32, 31].

6.1. Nuclear Matter g Matrices

Consider a fast nucleon of momentum \mathbf{p}_0 in collision with another of momentum \mathbf{p}_1 which is embedded in infinite nuclear matter. The Fermi sea is defined by a momentum \mathbf{k}_f . This collision involves a relative momentum $\mathbf{k} = (\mathbf{p}_0 - \mathbf{p}_1)/2$ and a center of momentum $\mathbf{K} = (\mathbf{p}_0 + \mathbf{p}_1)/2$. In these coordinates and with separate particle energies $\epsilon_0 = \hbar^2 p_0^2/2m$ and $\epsilon_1 = \hbar^2 p_1^2/2m$, the total energy of the two particles becomes

$$E(\mathbf{k}, \mathbf{K}) = \frac{\hbar^2}{m} (k^2 + K^2). \quad (6.1)$$

After the scattering there is an equivalent set of momenta $\mathbf{p}'_0, \mathbf{p}'_1, \mathbf{k}'$ and $\mathbf{K}' = \mathbf{K}$. The scattering g matrix is a solution of the BBG equation,

$$g(\mathbf{q}', \mathbf{q}; \mathbf{K}) = V(\mathbf{q}', \mathbf{q}) + \int V(\mathbf{q}', \mathbf{k}') \frac{Q(\mathbf{k}', \mathbf{K}; k_f)}{[E(\mathbf{k}, \mathbf{K}) - E(\mathbf{k}', \mathbf{K})]} g(\mathbf{k}', \mathbf{q}; \mathbf{K}) d\mathbf{k}', \quad (6.2)$$

where $Q(\mathbf{k}', \mathbf{K}; k_f)$ is a Pauli blocking operator. A simple realisation of that operator is

$$Q(\mathbf{k}', \mathbf{K}; k_f) = \begin{cases} 1 & \text{if } |\mathbf{k}' \pm \mathbf{K}| > k_f \\ 0 & \text{otherwise.} \end{cases} \quad (6.3)$$

Other medium effects are subsumed in an auxiliary potential $U(|\mathbf{k} + \mathbf{K}|)$ in terms of which the energy denominator is defined [122, 123] by

$$\begin{aligned}[E(\mathbf{k}, \mathbf{K}) - E(\mathbf{k}', \mathbf{K})] = & \frac{\hbar^2}{m} (k^2 - k'^2) + U(|\mathbf{k} + \mathbf{K}|) \\ & + U(|\mathbf{k} - \mathbf{K}|) - U(|\mathbf{k}' + \mathbf{K}|) - U(|\mathbf{k}' - \mathbf{K}|).\end{aligned}\quad (6.4)$$

Both Pauli blocking and the energy denominator are functions of the integrating momentum \mathbf{k}' . It is customary to approximate these by their monopole, or angle averaged, values. This is justified since the g matrices are weakly dependent upon the momentum \mathbf{K} [123]. Standard partial wave expansions yield well behaved Fredholm integral equations of the second kind,

$$\begin{aligned}g_{LL'}^{(\alpha)}(q', q; K) = & V_{LL'}^{(\alpha)}(q', q) \\ & + \frac{2}{\pi} \sum_l \int_0^\infty V_{Ll}^{(\alpha)}(q', k') \left\{ \frac{\bar{Q}(k', K; k_f)}{[\bar{E}(k, K) - \bar{E}(k', K)]} \right\} g_{ll'}^{(\alpha)}(k', q; K) k'^2 dk',\end{aligned}\quad (6.5)$$

with $\{(\alpha) \equiv JLL'ST\}$ and bars designating angle averaged values. Specifically, the angle averaged Pauli operator is

$$\bar{Q}(k, K; k_f) = \begin{cases} 1 & \text{if } k \geq k_f + K \\ 0 & \text{if } k \leq \sqrt{k_f^2 - k^2} \\ \frac{k^2 + k^2 - k_f^2}{2kK} & \text{otherwise.} \end{cases}\quad (6.6)$$

In the context of nuclear matter, Legindgaard [124] has shown this angle averaging to be a good approximation. Subsequently Cheon and Redish [125] demonstrated that this remains valid when positive energies of 300 MeV and normal nuclear matter densities are considered. No such detailed calculation of the accuracy of angle averaging of the energy denominator exists but a sensible approximation to use is

$$\bar{E}(k, K) = \frac{\hbar^2}{m} (k^2 + K^2) + U(|\mathbf{k} + \mathbf{K}|) + U(|\mathbf{k} - \mathbf{K}|).\quad (6.7)$$

$U(p)$ are auxiliary potentials.

Another simplification of the energy denominator is the effective mass approximation in which the individual single particle energies are approximated by

$$\epsilon(p_i) = \left(\frac{\hbar^2 p_i^2}{2m^*} \right) + U_i,\quad (6.8)$$

where m^* and U_i are constants. Since the total energy is the sum of the incoming and struck nucleon energies, one then gets

$$\bar{E}(k, K) = \frac{\hbar^2}{m^*} (k^2 + K^2) + U_0 + U_1, \quad (6.9)$$

It is natural to seek a better prescription of the auxiliary potentials. One way is to consider the arguments of the potential in Eq. (6.4) with the Brueckner angle averaged prescription [126, 127],

$$|\mathbf{k} \pm \mathbf{K}|^2 \approx K^2 + k^2 \pm \left(\frac{2}{\sqrt{3}} \right) k K \bar{Q}^{\frac{3}{2}}(k, K; k_f), \quad (6.10)$$

and an average value for $K \rightarrow \bar{K}$ when determining the single particle potential,

$$\bar{K} = \begin{cases} \sqrt{k^2 + p^2 - \frac{1}{4} [(2k+p)^2 - k_f^2]} & \text{if } k_f - p \leq 2k \leq k_f + p \\ \sqrt{k^2 + p^2} & \text{if } 0 \leq 2k \leq k_f - p. \end{cases} \quad (6.11)$$

The interplay between $U(p)$ and the g matrices is given by the sum over two-body channels,

$$U(p) = \frac{8\hbar^2}{\pi m} \sum_{JT} (2J+1)(2T+1) \int_0^{\frac{1}{2}(k_f+p)} X(k) \operatorname{Re}\{g_{LL}^{(\alpha)}(k, k; \bar{K})\} k^2 dk. \quad (6.12)$$

The integration weight $X(k)$ is

$$X(k) = \{1 | k \in [0, (k_f - p)/2]\} \quad (6.13)$$

and

$$X(k) = \begin{cases} \frac{1}{2pk} [(k_f^2 - p^2)/4 - k(k - p)]; & |k| \in [(k_f - p)/2, (k_f + p)/2] \\ 0 & \text{otherwise} \end{cases} \quad (6.14)$$

The momentum k is an on-shell relative momentum value which, with the chosen values of k_f and p , specify \bar{K} . The energy $\hbar^2 \bar{K}^2/m$ is that at which one evaluates the g matrices. To facilitate calculation, the principal value of the integral is taken [123, 109, 122].

$$K_{LL'}^{(\alpha)}(q', q; \bar{K}) = V_{LL'}^{(\alpha)}(q', q) + \frac{2}{\pi} \sum_l P \int_0^\infty V_{Ll}^{(\alpha)}(q', k') \frac{\bar{Q}(k', \bar{K}; k_f)}{[\bar{E}(k, \bar{K}) - \bar{E}(k', \bar{K})]} K_{lL'}^{(\alpha)}(k', q; \bar{K}) k'^2 dk', \quad (6.15)$$

defining the reactance matrix $K^{(\alpha)}$ which is related to the g matrix by

$$g_{LL'}^{(\alpha)}(q', q; \bar{K}) = K_{LL'}^{(\alpha)}(q', q; \bar{K}) - iB(k) \sum_l K_{Ll}^{(\alpha)}(q', k; \bar{K}) g_{lL'}^{(\alpha)}(k, q; \bar{K}), \quad (6.16)$$

where [122]

$$B(k) = \frac{2k^2 \bar{Q}(k, \bar{K}; k_f)}{[2k + 2mU'(k)/\hbar]} \quad (6.17)$$

involves

$$U'(k) \equiv \frac{d}{dk} [U(|\mathbf{k} + \bar{\mathbf{K}}|) + U(|\mathbf{k} - \bar{\mathbf{K}}|)]. \quad (6.18)$$

Since the average momentum \bar{K} is dependent upon the energy of the incoming nucleon and upon the Fermi momentum, both the g and $K^{(\alpha)}$ matrices are functions of these. Note that if the Fermi momentum is zero, Eq. (6.16) simplifies to the Heitler equation [109]. It is customary [50, 122] to use the real parts of the on-shell g matrices in the summations to define a real auxiliary potential for the BBG equation.

The range of momentum for which Eq. (6.12) is used to define the auxiliary potentials has been a point of discussion. A standard choice has been to set $U(p_0)$ to zero if p_0 is greater than k_f . This is not truly self-consistent as outside the Fermi surface a zero set potential on iteration does not give convergent g matrices. It has also been argued that a continuous choice of the auxiliary potential is more realistic as that allows for appropriate cancellation of some higher order terms [128]. Also, with the continuous choice, the appropriate behavior of the imaginary component of the optical model potential in the vicinity of the Fermi surface can be estimated [128, 129].

The utility of the $K^{(\alpha)}$ matrices at positive energies is that they reflect the off-shell character of the complete g matrices and that character can be displayed for any channel by Noyes-Kowalski f -ratios [105, 106, 107], which now are medium dependent, as

$$f_{LL'}^{(\alpha)}(q, k; \bar{K}) = \frac{K_{LL'}^{(\alpha)}(q, k; \bar{K})}{K_{LL'}^{(\alpha)}(k, k; \bar{K})} \quad (6.19)$$

with $\bar{K}(k; k_f, p)$. Note again that this ratio emphasises off-shell behavior by scaling against the on-shell value so that one must always bear in mind the actual size of the denominator when considering any significance of f -ratios.

Solution of the BBG equations may also be obtained for negative energies. In this case the g matrices are purely real and the infinite matter calculation leads to the Brueckner-Hartree-Fock (BHF) approximation of the binding energy per particle via

$$\begin{aligned} \frac{E_B}{A} &= T(\epsilon_f) + \frac{1}{2} W_o(k_f) \\ &= \frac{3}{5} \epsilon_f + \frac{4\hbar^2}{\pi m} \sum_{JT} (2J+1)(2T+1) \int_0^{k_f} \left[1 - \frac{3k}{2k_f} + \frac{k^2}{2k_f^2} \right] g_{LL}^{(\alpha)}(k, k; \bar{K}) k^2 dk, \end{aligned} \quad (6.20)$$

wherein ϵ_f is the Fermi energy, k again represents the relative momentum and the average center of mass momentum is now redefined [123] as

$$\bar{K}^2 \equiv \bar{K}^2(k_f, k) = \frac{3}{5} (k_f - k) \left[k_f + \frac{k^2}{3(2k_f + k)} \right]. \quad (6.21)$$

Note that here $T(\epsilon_f)$ represents the kinetic term and $W_o(k_f)$ the first order excitation. The choice of NN interaction, as well as the auxiliary potential, markedly affects predictions of the binding energy per particle as will be shown. Day [130] and others [128, 131] have further extended the BHF approximation to take into consideration the so-called renormalised excitation, leading to the renormalised Brueckner-Hartree-Fock approximation.

6.2. *g* Matrices from Realistic Interactions

For nucleon projectile energies such that the inherent NN collisions are below pion threshold, the BBG equations have been solved using various realistic interactions. Herein results found using the Paris [18], Bonn-B [19], and OSBEP [36] NN interactions are shown. In Fig. 6.1 the auxiliary potentials as specified in Eq. (6.12) are displayed for a range of Fermi momenta from 0.6 to 1.8 fm^{-1} . An iterative method of solution was

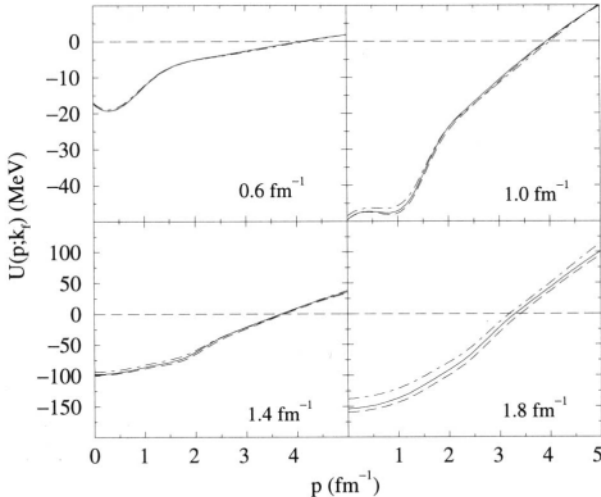


Fig. 6.1. The auxiliary potential obtained using the Bonn-B (solid), OSBEP (dashed), and Paris (dot-dashed) interactions at various Fermi momentum.

employed starting with values for the auxiliary potential per Eq. (6.12), and using them in the energy denominator of Eq. (6.5) until convergence was obtained. As evident in Fig. 6.1, at low densities the auxiliary potentials from all interactions are small in size and almost indistinguishable from each other. However when $k_f = 1.8 \text{ fm}^{-1}$ the auxiliary potentials are not only very strong but those determined from each interaction are slightly different. With increasing density the auxiliary potentials become more strongly attractive at low incident momenta $p < 3 \text{ fm}^{-1}$ and more strongly repulsive at high incident momenta. The auxiliary potentials at densities less than central nuclear values display a distinct shoulder-like structure in their momentum dependence in the vicinity of the Fermi surface (k_f). With increasing density that structure dissipates.

The interactions give different values for the binding energy per particle as defined by Eq. (6.20). Those differences are displayed in Fig. 6.2 wherein the solid, dashed, and dash-dotted lines again are the results obtained using the Bonn-B, the OSBEP, and the Paris interaction respectively. The three interactions all give nuclear saturation, albeit at densities higher than the empirical one for which $k_f = 1.36 \text{ fm}^{-1}$. The binding energy per particle at saturation for each interaction differs as well. Empirically one expects the binding energy per particle at saturation to be in the range -15 to -17 MeV [34]. A value of that amount has been

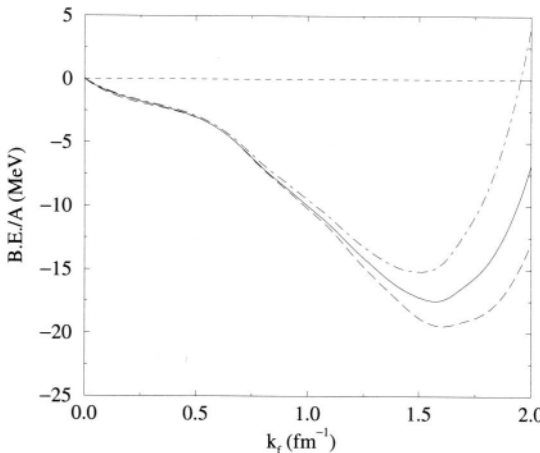


Fig. 6.2. The binding energy per particle determined from infinite matter calculations and as a function of the Fermi momentum.

obtained by using the Bonn-B interaction, but at too high a density. With the Paris interaction, under-binding occurs while with the OSBEP there is over-binding. Again, those saturation results occur at too high a density. However, Machleidt [34] argues in favour of relativistic effects to be important in fine tuning results of such calculations. When relativistic corrections are made, the saturation density and binding energy per particle both decrease, k_f by about 0.2 fm^{-1} and E_B/A by 3 to 4 MeV. Their effect is significant on the plots shown in Fig. 6.2, and would move the OSBEP result into quite good agreement with the experimental values. This shift of Coester lines is well known and hence the expectation of the final OSBEP result. It is important to appreciate that these relativistic effects are 5–10% corrections. The binding energies depicted in Fig. 6.2 are the result of subtraction of the kinetic from potential energies typically of 40 MeV at central densities. The changes wrought on the non-relativistic results therefore are more impressive in the diagrams because of that subtraction.

It is instructive to note the contributions to the binding energy with each interaction channel by channel. The values are given in Table 6.1 for Fermi momenta 0.6 and 1.0 fm^{-1} , and in Table 6.2 for Fermi momenta of 1.4 and 1.8 fm^{-1} . From these tables it is clear that, to saturation density, the S -channel contributions dominate. But the P -wave contributions increase in value with density to the extent that, by $k_f = 1.8\text{ fm}^{-1}$, the 3P_1 -

TABLE 6.1

Contributions to the binding energy per particle by NN channels for Fermi momenta of 0.6 and 1.0fm^{-1} and for the Paris, Bonn-B, and OSBEP interactions.

State	$kf = 0.6$			$kf = 1.0$		
	Paris	Bonn-B	OSBEP	Paris	Bonn-B	OSBEP
1S_0	-2.85	-2.97	-2.96	-8.77	-9.14	-9.15
3S_1	-5.54	-5.58	-5.56	-13.14	-13.52	-13.56
1P_1	0.22	0.22	0.21	1.49	1.53	1.40
3P_0	-0.23	-0.23	-0.22	-1.45	-1.46	-1.37
3P_1	0.45	0.45	0.43	3.29	3.33	3.14
3P_2	-0.21	-0.20	-0.20	-2.14	-2.14	-2.12
1D_2	-0.06	-0.05	-0.05	-0.72	-0.64	-0.60
3D_1	0.03	0.03	0.03	0.38	0.39	0.38
3D_2	-0.09	-0.09	-0.09	-1.13	-1.10	-1.06
3D_3	0.00	0.00	0.00	0.00	0.04	0.04
1F_3	0.01	0.01	0.01	0.20	0.20	0.19
3F_2	-0.01	-0.01	0.00	-0.12	-0.12	-0.11
3F_3	0.02	0.02	0.02	0.36	0.35	0.33
3F_4	0.00	0.00	0.00	-0.07	-0.05	-0.04
1G_4	0.00	0.00	0.00	-0.09	-0.08	-0.08
3G_3	0.00	0.00	0.00	0.03	0.03	0.03
3G_4	0.00	0.00	0.00	-0.13	-0.13	-0.12
3H_4	0.00	0.00	0.00	-0.01	-0.01	-0.01
$J \geq 5$	0.00	0.00	0.00	0.06	0.07	0.07
KE	4.48	4.48	4.48	12.44	12.44	12.44
E_B/A	-3.79	-3.92	-3.91	-9.49	-10.00	-10.20

channel value is comparable with those of the S -waves. This table also reveals how the total binding energy is constructed with each interaction. The Paris interaction contributions are similar to those of the Bonn-B in all but the S -channels. At $k_f = 1.4\text{fm}^{-1}$ with the Paris interaction, S -waves elements contribute just over 2.5 MeV less to the binding than do the corresponding ones with the Bonn-B interaction. On the other hand, the S - and D -wave contributions for the OSBEP and Bonn-B interactions are quite similar at all densities. However significant differences do occur with those interactions in the calculated binding energies for the P -waves. In fact, it is the reduced repulsive P -wave contributions in the channels 1P_1 and 3P_1 , found with the OSBEP interaction, that makes the resultant binding energy per particle significantly larger and saturation occur at a higher density than found with the Bonn-B.

TABLE 6.2

Contributions to the binding energy per particle by NN channels for Fermi momenta 1.4 and 1.8 fm^{-1} and for the Paris, Bonn-B, and OSBEP interactions.

State	$kf = 1.4$			$kf = 1.8$		
	Paris	Bonn-B	OSBEP	Paris	Bonn-B	OSBEP
1S_0	-16.96	-17.84	-17.97	-24.20	-26.37	-27.08
3S_1	-20.66	-22.41	-22.71	-21.83	-29.02	-30.32
1P_1	4.77	4.99	4.39	11.06	12.06	10.01
3P_0	-3.83	-3.87	-3.55	-6.25	-6.18	-5.19
3P_1	11.35	11.38	10.75	28.78	28.25	26.85
3P_2	-8.43	-8.57	-8.49	-21.34	-21.82	-21.58
1D_2	-3.18	-2.77	-2.59	-9.01	-7.75	-7.19
3D_1	1.67	1.73	1.66	4.39	4.60	4.39
3D_2	-4.74	-4.59	-4.44	-12.38	-11.88	-11.56
3D_3	0.04	0.25	0.27	0.28	0.85	0.98
1F_3	0.97	0.98	0.94	2.76	2.79	2.64
3F_2	-0.69	-0.66	-0.63	-2.10	-2.02	-1.97
3F_3	1.84	1.82	1.73	5.43	5.47	5.20
3F_4	-0.52	-0.39	-0.38	-2.01	-1.67	-1.65
1G_4	-0.55	-0.50	-0.48	-1.89	-1.68	-1.60
3G_3	0.25	0.25	0.24	0.93	0.93	0.89
3G_4	-0.88	-0.85	-0.81	-3.09	-2.96	-2.84
3H_4	-0.11	-0.11	-0.10	-0.49	-0.46	-0.44
$J \geq 5$	0.52	0.53	0.49	1.72	1.87	1.79
KE	24.38	24.38	24.38	40.31	40.31	40.31
E_B/A	-14.78	-16.24	-17.30	-9.04	-14.68	-18.35

To ascertain the effects of the nuclear matter properties in the positive energy domain, consider the $\mathbf{K}^{(\alpha)}$ matrices generated from the three interactions at various energies and with Pauli and average field influences isolated. Solutions of Eq. (6.15) have been obtained for many energies to 800 MeV but just the results at 65 and 200 MeV are discussed herein. The on-shell values are presented in Table 6.3. Therein, the results found using Pauli blocking but with no self consistent potential taken in the propagators are identified with the label “PB”. The results of full solutions of the BBG equations are denoted by “PB + SCP”, indicating by the label that both Pauli blocking and the auxiliary potential determined in a self consistent fashion have been included. The other entry is designated by FREE and those results are obtained from solution of LS equations. While 33 channels have been used in all studies, to note the

TABLE 6.3

Table of on-shell $K^{(\alpha)}$ matrices at 65 and 200 MeV for the Bonn-B, Paris, and OSBEP interactions, and for various NN channels. FREE denotes solution of the LS equations, "PB" denotes solution of BBG equations but with the auxiliary potential set to zero, and "PB + SCP" denotes full solution of the BBG equations.

Channel		65 MeV			200 MeV		
		Bonn-B	Paris	OSBEP	Bonn-B	Paris	OSBEP
1S_0	FREE	-0.789	-0.735	-0.830	-0.064	-0.053	-0.090
	PB	-0.799	-0.757	-0.817	-0.073	-0.058	-0.103
	PB + SCP	-0.741	-0.685	-0.761	-0.042	-0.018	-0.076
1P_1	FREE	0.259	0.253	0.231	0.280	0.257	0.221
	PB	0.296	0.285	0.255	0.282	0.257	0.221
	PB + SCP	0.308	0.293	0.261	0.312	0.279	0.236
3P_0	FREE	-0.244	-0.238	-0.224	0.011	-0.006	0.030
	PB	-0.237	-0.231	-0.219	0.017	-0.003	0.038
	PB + SCP	-0.228	-0.223	-0.206	0.034	0.013	0.063
3P_1	FREE	0.207	0.204	0.195	0.240	0.245	0.229
	PB	0.234	0.232	0.220	0.246	0.252	0.235
	PB + SCP	0.243	0.242	0.229	0.271	0.281	0.261
3S_1	FREE	-1.605	-1.622	-1.676	-0.222	-0.225	-0.245
	PB	-1.257	-1.288	-1.274	-0.260	-0.261	-0.289
	PB + SCP	-1.020	-0.915	-1.048	-0.209	-0.150	-0.243
3D_1	FREE	0.175	0.173	0.168	0.237	0.238	0.225
	PB	0.128	0.123	0.123	0.206	0.205	0.195
	PB + SCP	0.129	0.124	0.123	0.201	0.200	0.188
$^3S_1 \leftrightarrow ^3D_1$	FREE	-0.072	-0.067	-0.070	-0.038	-0.041	-0.032
	PB	-0.341	-0.347	-0.332	-0.100	-0.111	-0.093
	PB + SCP	-0.346	-0.349	-0.335	-0.136	-0.155	-0.125
3P_2	FREE	-0.160	-0.155	-0.156	-0.193	-0.190	-0.180
	PB	-0.133	-0.129	-0.131	-0.187	-0.184	-0.176
	PB + SCP	-0.126	-0.123	-0.125	-0.173	-0.171	-0.165
3F_2	FREE	-0.010	-0.010	-0.009	-0.013	-0.013	-0.013
	PB	-0.011	-0.011	-0.010	-0.015	-0.015	-0.015
	PB + SCP	-0.011	-0.011	-0.010	-0.015	-0.015	-0.016
$^3P_2 \leftrightarrow ^3F_2$	FREE	0.045	0.044	0.043	0.034	0.032	0.031
	PB	0.043	0.043	0.041	0.037	0.036	0.035
	PB + SCP	0.043	0.043	0.041	0.038	0.037	0.035

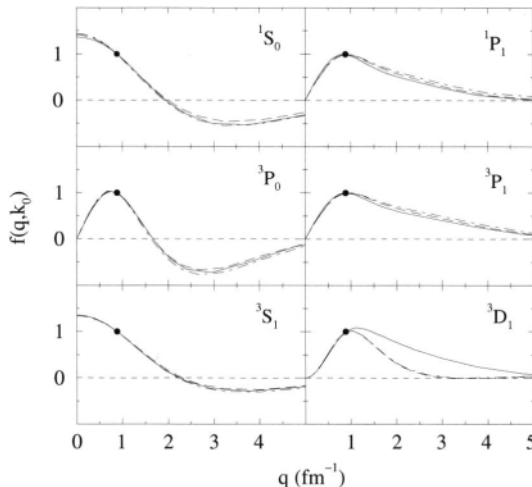


Fig. 6.3. The Noyes-Kowalski f -ratios for the set of NN channels indicated and at 65 MeV for the Bonn-B interaction. The solid, dashed and dot-dashed lines refer to the FREE, PB, and PB + SCP calculations respectively.

effects of medium changes it suffices to display results only for the dominant ones. Clearly, at all energies the effects of the medium are quite large. With the odd channels, Pauli blocking increases the strength of the real parts by some 10 to 20%. That is most strongly seen at 65 MeV. In those odd channels, inclusion of the auxiliary potentials in the calculations enhance the changes. But the effects of Pauli blocking and of the auxiliary potentials are not as coherent in the S channels.

Application of Eq. (6.16) with these $K^{(\omega)}$ matrices produces the complex t and g matrices. In that way, g matrices have been obtained for values of k_f ranging from 0 to 2 fm⁻¹. The properties of those half-off-shell g matrix elements for $k_f = 0$ and 1.4 fm⁻¹ will be discussed below. Note also that those elements have been evaluated using the full BBG equations as well as by using the reduced forms in which only Pauli blocking and no auxiliary potential has been used. The off-shell properties of the t and g matrices are displayed in Figs. 6.3 and 6.4, wherein the Noyes-Kowalski f -ratios are plotted for the energies 65 and 200 MeV respectively. For the most important channels, the results displayed in Figs. 6.3 and 6.4 were obtained with the free case $k_f = 0$, with the $k_f = 1.4$ fm⁻¹ runs with only Pauli blocking involved, and from the full solutions of the BBG equations at $k_f = 1.4$ fm⁻¹. Those results are portrayed

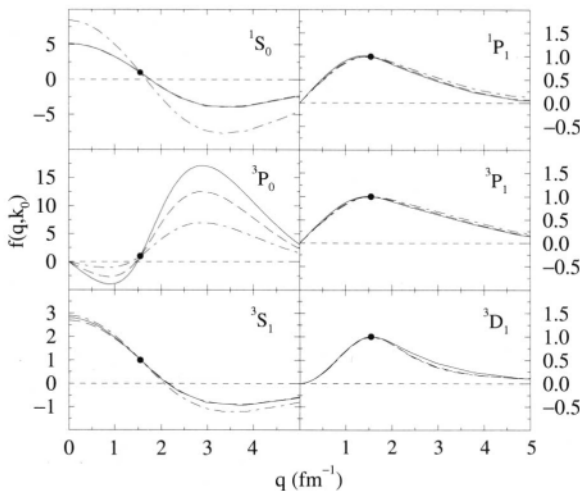


Fig. 6.4. As for Fig. 6.3, but at 200 MeV.

by the solid, dashed, and dot-dashed curves respectively. The Bonn-B interaction was used as the starting interaction in all cases. At 65 MeV, and as seen in Fig. 6.3, the medium has little effect on the f -ratios, save for the 3D_1 channel. In that channel, the values given in Table 6.3 demonstrate that nuclear medium effects are significant. Indeed, the free f -ratio peaks at a slightly higher momentum than do the medium modified ones. All in all, despite there being significant differences between the various free and medium modified $K^{(\alpha)}$ matrices on-shell, medium effects in the off-shell variations are slight.

Differences between the f -ratios are more noticeable at the higher energies. From Fig. 6.4, it is obvious that at 200 MeV the 1S_0 channel off-shell variations are quite affected by inclusion of the auxiliary potentials. But the on-shell values in this channel are very small, a reflection of the fact that the NN phase shift for the 1S_0 passes through zero in this energy regime. This is also the case for the 3P_0 channel when one notes in Table 6.3 that the on-shell $K^{(\alpha)}$ matrix elements are almost zero. Indeed, large variations in f -ratios are due to the denominators being very small. In both cases, the shape of the f -ratios are similar, showing that again the nuclear medium does not significantly alter the shape of the off-shell $K^{(\alpha)}$ matrices, and hence of the t - and g matrices as well. In all cases when the on-shell magnitudes are of order or greater than 0.1, the f -ratios are little affected by either the Pauli blocking or the energy denominators. Thus

the prime effects of the nuclear medium upon the effective interactions are to alter the on-shell values in the diverse scattering channels. The off-shell variations essentially are unchanged.

7. THE EFFECTIVE NN INTERACTION

Coordinate space effective NN interactions, between protons with energies to over 300 MeV incident upon nuclei and each bound nucleon in the target, have been defined by optimal fits to the on- and half-off-shell t and nuclear matter g matrices that have been determined from solutions of the LS and BBG equations respectively. Realistic NN potentials, such as Paris [18], Bonn-B [19], and OSBEP [59] have been used as input. Folding these medium modified effective interactions with appropriate density matrices give nonlocal optical potentials for the elastic scattering of protons from nuclei. As will be shown, good reproduction of the differential cross-section data and diverse spin observables with scattering from all nuclei in the range ${}^3\text{He}$ to ${}^{238}\text{U}$ has been obtained [132, 133] by solving the associated non-local Schrödinger equations.

Herein, a specific form of the effective interaction in coordinate space that is useful in making a folding optical potential is investigated. That form of the effective interaction is dictated by the structure used in the programs DWBA91 and DWBA98 [29, 30]. Not only do those programs evaluate the nonlocal optical potentials from a full folding prescription but also they solve the associated integro-differential Schrödinger equations for pA scattering. In the main we discuss the effective interaction form in reference to the free t matrices. The same techniques are used to find the coordinate space forms of the effective interactions defined from nuclear matter g matrices.

7.1. Coordinate Space Representations

Momentum space studies of NN scattering below pion threshold involve solution of partial wave LS equations starting with one of the realistic interactions. The result is a tabulation of arrays $t_{LL}^{IST}(q', q; \omega)$ for each on-shell energy ω . But the spin structure of the t matrix is very important, so classification in terms of central, tensor, and two-body spin-orbit characteristics has proven useful [85]. Also, meson exchange concepts, when used to define the NN interactions, often are more conveniently described in coordinate space with Yukawa form factors. A number of the interactions such as the Reid [134], the Paris [18], and the

Bonn-R [19] forces were determined in this way. Further, if one wishes to consider more complicated NA systems and their reactions, such a representation has been used for most studies that go beyond the simplest of microscopic calculations [28, 135]. Indeed, to obtain sensible optical model potentials medium corrections must be considered. Only by so doing can one obtain reasonable predictions of differential cross sections and spin observables from proton-nucleus elastic scattering for energies to 300 MeV and above.

There are circumstances in which interactions do not have convenient structure. Interactions which necessarily have been obtained solely from the NN scattering data [39] are examples. In such cases, an effective parameterisation scheme facilitates a recasting of the t matrices into utilitarian nuclear operator structure. One such effective interaction scheme consists of central (C), tensor (S_{12}), and two-body spin-orbit ($L \cdot S$) components each of which has a form factor that is a set of Yukawas of various ranges. Each of those Yukawas has a complex strength which is dependent upon the energy and the spin/isospin state.

7.2. The Parameterisation Scheme

The form of an effective interaction in coordinate space that is now used is

$$t_{\text{eff}}^{ST}(r, \omega) = \sum_i \langle \theta_i \rangle t_{\text{eff}}^{(i)ST}(r, \omega), \quad (7.1)$$

with radial functions that have the form,

$$t_{\text{eff}}^{(i)ST}(r, \omega) = \sum_{j=1}^n S_j^{(i)}(\omega) \frac{e^{-\mu_j^{(i)} r}}{r}, \quad (7.2)$$

for each operator of the set $(i) = \{C, S_{12}\text{ and }L \cdot S\} . (L \cdot S)^2\text{ and }L^2$ components have been considered in some cases as well. $S_j^{(i)}(\omega)$ are complex energy dependent strengths, $\mu_j^{(i)}$ are the inverse ranges of the interaction, and j represents the set of the inverse ranges chosen. In principle, the number of strengths and ranges chosen can be as large as one likes, though experience shows that four suffice.

To match data in $\{JSTLL'\}$ channel form to the effective interaction elements in ST channel form, the angular momentum state expectation values of the operators in the effective interactions are needed. Explicitly, those expectation values are given by the set

$$\begin{aligned}\langle \theta_C \rangle &= \delta_{LL'} \\ \langle \theta_{LS} \rangle &= \frac{1}{2}[J(J+1) - L(L+1) - S(S+1)]\delta_{LL'} \\ \langle \theta_{S_{12}} \rangle &= \begin{cases} 2\delta_{S1} & \text{if } L = J \\ -\frac{2(J-1)}{2J+1} & \text{if } L = L' = J-1 \\ -\frac{2(J+2)}{2J+1} & \text{if } L = L' = J+1 \\ \frac{6}{2J+1}\sqrt{J(J+1)} & \text{if } L = J \pm 1, L' = J \mp 1. \end{cases}\end{aligned}$$

Originally [39], it was thought additional elements would be needed in analyses. Those extra operator terms are

$$\langle \theta_{(LS)^2} \rangle = (\langle \theta_{LS} \rangle)^2 \quad \text{and} \quad \langle \theta_{L^2} \rangle = L(L+1)\delta_{LL'}. \quad (7.3)$$

Those terms have not proved necessary for application to find optical potentials to describe elastic pA scattering. However, they may be required as elements of the transition operator in assessments of some inelastic and charge exchange processes.

With the selected form of $t_{\text{eff}}^{ST}(r, \omega)$, a double Bessel transform determines the equivalent momentum space representation [85, 123],

$$\begin{aligned}t_{\text{eff}LL'}^{IST}(q', q; \omega) &= \sum_i \langle \theta_i \rangle \int_0^\infty r^{2+\lambda} j_L(q'r) t_{\text{eff}}^{(i)ST}(r, \omega) j_{L'}(qr) dr \\ &= \sum_{ij} \langle \theta_i \rangle S_j^{(i)}(\omega) \int_0^\infty r^{2+\lambda} j_L(q'r) \frac{e^{-\mu_j^{(i)}r}}{r} j_{L'}(qr) dr \\ &= \sum_{ij} \langle \theta_i \rangle S_j^{(i)}(\omega) \tau^\alpha(q', q; \mu_j^{(i)}),\end{aligned} \quad (7.4)$$

where $\lambda = 2$ for tensor states and 0 otherwise, and α designates the two-body channel set of quantum numbers $\{JSTLL'\}$.

Assuming the ranges to be independent of energy and momenta and the strengths to depend only on the energy, the effective representation may be separated into individual sets. Later it can be assumed that the strengths also depend on the density. The optimal set of ranges and strengths then are those which satisfy

$$\min := \|t_{LL'}^{IST}(q', q; \omega) - t_{\text{eff}LL'}^{IST}(q', q; \omega)\|. \quad (7.5)$$

This optimization of the effective interaction is facilitated using by a two-step process. First the ranges, assumed independent of both energy and

density, are determined optimally. Then the strengths at the desired energies are determined for each spin/isospin state and energy. The assumptions about the range values are justified from the properties of the Noyes-Kowalski f -ratios of the t and g matrices. Those f -ratios for both free and medium modified quantities off-shell are very similar in all channels. In those circumstances where considerable variation exists, that variation can be traced to the denominators of the f -ratios being very small. Such occur at energies where phase shift values cross the real axis. The dominant effect of the nuclear medium then is to vary the on-shell values of the g matrices from those of the NN t matrices.

For every two-body channel and momentum pair q and q' , one can obtain the effective t matrices by summing over the appropriate number of strengths and ranges. Since this parameterisation is sought to be accurate for all momenta, it is possible to rewrite Eq. (7.4) as a linear system of equations,

$$T_\gamma(\omega) = \tau_{\gamma\beta}(\mu)S_\beta, \quad (7.6)$$

in which γ has the dimension m due the combination of the number of channels taken for the set of input t matrices and the momenta and energies considered. The dimension of β is n , equal to the number of ranges considered for the operators.

The minimization required is that of the Euclidean norm

$$\min := \|\tau_{\gamma\beta}(\mu)S_\beta(\omega) - T_\gamma(\omega)\|, \quad (7.7)$$

where τ is an $[m \times n]$ matrix with $m >> n$. Hence the system is over determined and an optimal set of strengths and ranges must be found. Inversion of Eq. (7.6),

$$S_\beta(\omega) = \tau_{\beta\gamma}^+(\mu)T_\gamma(\omega), \quad (7.8)$$

allows replacement of the strength in Eq. (7.7) giving the requirement

$$\min := \|\tau_{\gamma\beta}(\mu)\tau_{\beta\delta}^+(\mu)T_\delta(\omega) - T_\gamma(\omega)\|, \quad (7.9)$$

which can be found by using singular value decomposition (SVD) upon the matrix τ . Tikhonov regularization [136] is also useful in that process [85]. Once the optimal set of ranges is found, their values can be used in Eq. (7.8) to obtain the set of complex strengths for any given energy.

7.3. Effective g Matrices in Coordinate Space

Microscopic theories of NA interactions necessarily involve medium corrections to many body matrix elements if they are to best

describe scattering. Diverse applications have shown that such medium modifications in g matrices play an important role [80, 84, 69, 70, 137, 138, 139, 132]. But practical considerations mean that approximations to those matrix elements are required; one such approximation is to use a parameterisation scheme for those g matrices. Given that is so, one is free to choose the structure of the interactions. Though some such studies have been made using optimization strictly through Landau parameters [140, 141, 142, 27] or other structures [143, 144, 145], most have involved the use of Gaussian [146, 147, 148, 149, 150] or Yukawa [85, 28, 135, 151, 84, 70, 137, 152, 153, 154, 155] form factors.

In the case of Gaussian form factors, the general structure of the interaction has been chosen [146, 156, 157] as either

$$g_{\text{eff}}^{ST}(\mathbf{r}; \mathbf{k}_f, \omega) = \sum_{ij} \langle \theta_i \rangle \alpha_j^{(i)ST} [1 + \alpha_i(\omega)k_f + \beta_i(\omega)k_f^2] e^{-(\lambda_j^{(i)} r)^2}, \quad (7.10)$$

or [147, 148, 149, 150]

$$g_{\text{eff}}^{ST}(\mathbf{r}; \mathbf{k}_f, \omega) = \sum_{ij} \langle \theta_i \rangle \alpha_j^{(i)ST} [1 + \alpha_i(\omega)k_f^\gamma] e^{-(\lambda_j^{(i)} r)^2}, \quad (7.11)$$

for various inverse ranges in the region $\lambda = 0.5$ to 2.0 fm^{-1} . Again $\langle \theta_i \rangle$ represent the expectation values of the nuclear operator set identified by i , while j indicates the choice of ranges. Within the prescription determined by Sprung and Banerjee [147] whereby the shortest range only was varied to improve the fit, the optimal value for description of density dependence was found [148] with $\gamma = \frac{1}{2}$. With that effective interaction, polarization and differential cross-section results for the elastic scattering from closed shell nuclei were described quite well [148, 149].

Many detailed calculations have also been made with Yukawa form factors in the effective interactions. Early ones were based upon the free t matrix premise of Love and Franey [28, 135], namely to vary the set of on-shell values of the t matrices for various channels to produce an effective interaction that gives good results for inelastic scattering. But it was shown [69, 153] that the inclusion of density dependencies of the NN interactions by ascertaining the NN g matrices from infinite nuclear matter systems better described many elastic and inelastic scattering properties. That was the case for calculations wherein density effects were included by using the Hamburg g matrices [84, 153]. Nakayama *et al.* [27], confirmed that the effects of Pauli blocking and of the auxiliary

potential are very significant. The Hamburg g matrices were used to specify microscopic optical model potentials [26, 70] and then to analyse both elastic and inelastic scattering [158]. The sensitivity of the isovector contributions to nuclear scattering were seen clearly therein. Studies [137, 155] have shown the sensitivity in $^{14}\text{C}(p, n)$ reactions to the isoscalar and isovector density dependent character of the transition interaction in the intermediate energy regime. For all of those studies, representation of the nuclear medium corrected matrices was chosen using Yukawa form factors and the standard operator set $\langle \theta_i \rangle$ in the form specified in Eqs. (7.1) and (7.2), so that

$$g_{\text{eff}}^{(i)ST}(r, k_f, \omega) = \sum_{j=1}^{n_i} A_j^{(i),ST}(k_f, \omega) \frac{e^{-\mu_j^{(i)} r}}{r}. \quad (7.12)$$

The success in application for high energy scattering with t matrices modified by a density dependent scaling parameter [28, 135, 159], and of more complicated g folding schemes [14, 55, 32, 46] for medium energy studies, suggests that use of the g matrices will give better descriptions of NA scattering. It is a problem that most effective interactions employed in the past did not represent the off-shell properties of the original g matrices [137] well. When that was realized, half-off-shell g matrix elements were taken as the input to the mapping process to specify the effective interaction. With that a number of studies were made. In the nuclear medium, the bound nucleon is moving within the Fermi sea prior to being struck by the incoming particle. Assuming that the strengths are not only energy but also density dependent, one has the problem of variation with the initial momentum of the struck particle. More precisely, since one transforms the incoming and struck momenta into relative and center of mass coordinates, the g matrices required will be functions of the center of mass momenta K . However, specification of an average center of mass momentum [123, 153, 155] simplifies the problem. Defining the root mean square (rms) average for the center of mass momentum by

$$\bar{p}_b^2 = \langle p_b^2 \rangle = \frac{\int_{p_{\min}}^{p_{\max}} p^2 dp}{\int_{p_{\min}}^{p_{\max}} dp} \quad (7.13)$$

gives to $\bar{p}_b = 0.85773 k_f$ and the momentum of the incoming nucleon for a given relative momentum is $p_0 = 2k + \sqrt{2p_b^2 - k_f^2}$ if $p_b < \sqrt{(k_f - 2k)^2 + 4k^2}$ and $\sqrt{p_b^2 - 4k^2}$ otherwise. The rms average center of mass momentum is then determined in the usual way [123, 122].

TABLE 7.1

The inverse ranges $\mu_i(i)$ in fm⁻¹ of the interaction components.

Component	Central	Spin-Orbit and Tensor
1	0.71	1.25
2	1.758	2.184
3	2.949	3.141
4	4.0	4.0

7.3.1. Optimal Effective g Matrices

In applying the parameterisation scheme to represent g matrices and because of the nature of the nuclear medium, one has to allow the struck nucleon to have a range of momenta. That variation is treated using average values. The parameterisation scheme applied under that constraint yields excellent fits to the tabled g -matrix values. The fits are as good as those achieved in the analyses of the t matrices. Although there is great variation in the strength parameters, there is no density dependence required with the ranges of Yukawa form factors. Thus the parameterisation scheme has been applied to g -matrix elements with the set of ranges listed in Table 7.1, being the optimised values for incident energies to 300MeV [151]. One needs also bear in mind that not all partial waves contribute to the different aspects of the the interaction. The linkages for channels with $J \leq 4$ are displayed in Table 7.2.

TABLE 7.2

Contributions in components of the effective interaction.

State	S	T	Central	Spin-Orbit	Tensor
¹ S ₀ ; ¹ D ₂	0	1	X		
³ S ₁	1	0	X		
¹ P ₁ ; ¹ F ₃	0	0	X		
³ P _{0,1,2} ; ³ F _{2,3,4} ; ³ H ₄	1	1	X	X	X
³ D _{1,2,3} ; ³ G _{3,4}	1	0	X	X	X
³ S ₁ \leftrightarrow ³ D ₁ ; ³ D ₃ \leftrightarrow ³ G ₃	1	0			X
³ P ₂ \leftrightarrow ³ F ₂ ; ³ F ₄ \leftrightarrow ³ H ₄	1	1			X

7.3.2. Integral and Moments of the Effective Interaction

The first measure of the energy and medium variations to the effective interaction are the volume integrals and the radial moments. With the effective interaction in the form specified by Eq. (7.2), volume integrals are given by

$${}^0V_i^{S,T}(k_f; \omega) = \sum_{j=1}^4 \frac{1}{\mu_j^2} A_j^{(i),S,T}(k_f; \omega), \quad (7.14)$$

for the central and spin-orbit components. For the tensor force an additional factor of r^2 enters, thus

$${}^2V_i^{S,T}(k_f; \omega) = 6 \sum_{j=1}^4 \frac{1}{\mu_j^4} A_j^{(i),S,T}(k_f; \omega). \quad (7.15)$$

However, the values so found from Eqs. (7.14) and (7.15) do not reflect the relative importance of these components when they are used in calculations of matrix elements as antisymmetrization effects have not been considered explicitly. Values of matrix elements are dependent upon the interference between direct and exchange terms and the extent of that interference is dependent upon the range of each term.

The effective interaction is short ranged and it is useful to consider properties of the extreme limit that the interaction component form factors have zero range. In that limit, each form factor is a **δ -function** and the interaction acts only on relative S -states. Then direct and exchange matrix elements are equal in magnitude and either constructive or destructive for the central force components as the spin and isospin sum $S + T + 1$ is an even or an odd integer. For spin-orbit and tensor forces, higher order terms need be considered to infer their relative importance. However, the spin-orbit interactions yield direct and exchange ($S = 1$) matrix elements that are equal and constructive in the isovector case but destructive for the isoscalar terms.

Thus, while it is still appropriate to compare the volume integrals as functions of the density of the central even channel forces higher moments are more relevant for the other elements. For the central odd channels, the isovector spin-orbit, and the tensor interactions, it is more appropriate to consider the r^2 moment, while for the isoscalar spin-orbit it is the r^4 moment. Note that the tensor force, as defined by Eq. (7.2), involves the extra factor of r^2 so that their r^2 moments are also of the form

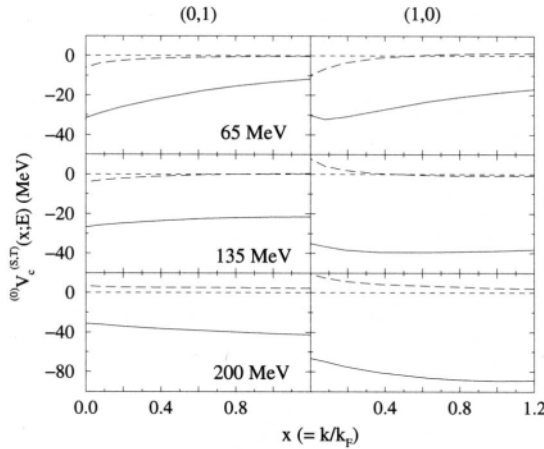


Fig. 7.1. The volume integrals of the central-even state effective interactions determined from the Paris potential. The 65, 135, and 200 MeV results are displayed in the top, middle and bottom segments with the real and imaginary components depicted by the solid and long dashed curves respectively.

$$^4V_i^{S,T}(k_f; \omega) = 120 \sum_{j=1}^4 \frac{1}{\mu_j^6} A_j^{(i),S,T}(k_f; \omega). \quad (7.16)$$

The volume integrals and moments have been evaluated for the effective interaction built upon the Paris potential and with 65, 135, and 200 MeV. The values for each energy and at a set of densities for $0 \leq k_f \leq 1.4 \text{ fm}^{-1}$ are displayed in four figures. This is achieved by displaying results as functions of the momentum ratio $x = k/k_F$ where k_F is the central nuclear density value. The S and T components of the real and imaginary parts of the integrals are depicted by the solid and long dashed curves in each panel.

In Fig. 7.1, the volume integrals of the central-even $S = 0, T = 1$ and $S = 1, T = 0$ states are shown. The singlet and triplet spin effective interaction results are shown in the left and right panels respectively. These volume integrals all vary smoothly and slowly with density. With increasing energy, the real parts of the effective interactions change from slowly decreasing with density at 65 MeV to slightly increasing with density at 200 MeV. The actual strengths of the real parts of these volume integrals increase overall by a factor of 3 to 4 between the two energy extremes. The imaginary parts of the volume integrals are small in general and

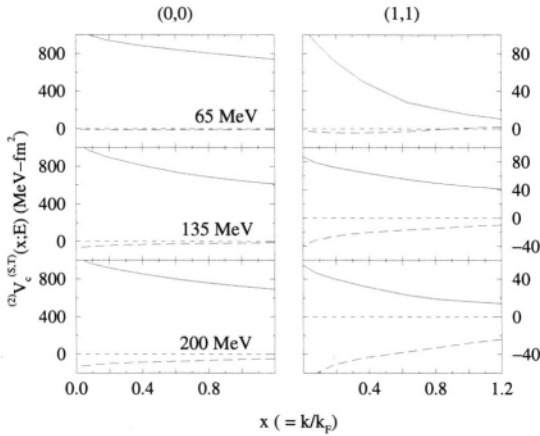


Fig. 7.2. The r^2 moment integrals of the central-odd state effective interactions. The notations are as defined in Fig. 7.1.

decrease in importance with density. Such gives surface peaked absorption which will change noticeably with energy.

The second moment r^2 integrals of the central-odd interactions, for which $S = 0$, $T = 0$ and $S = 1$, $T = 1$, are given in Fig. 7.2 with the singlet-odd and triplet-odd channel values given in the left and right panels respectively. The singlet-odd results are very large and their sizes over-emphasise the importance the channel has in defining the optical potential. Both channel results decrease with density and extremely so for the 65MeV triplet-odd channel. The imaginary parts are relatively small in comparison to the real parts save for the triplet-odd channel with increasing energy.

Thus the central interaction integrals are quite diverse in behavior with both energy and density. They range from being negligible in strength to being of the order of 1000 MeV-fm^3 . The variations are not the same in different spin-isospin channels nor are they linear either in energy or density. Certainly no simple functional form linear or quadratic in energy and/or linear with density as given in Eqs. (7.10) and (7.11) can approximate well these results.

The spin-orbit interaction moment integrals are shown in Fig. 7.3. The isospin singlet and triplet channel results are shown on the left and right sections respectively. The r^4 and r^2 moments for the isoscalar and isovector channels are displayed in the right and left panels respectively and with the energies of 65, 135, and 200MeV shown from top to bottom.

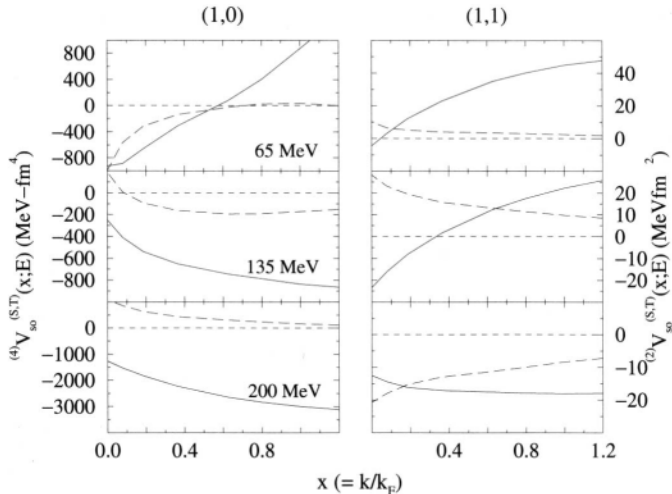


Fig. 7.3. The moment integrals of the spin-orbit components of the effective interactions; r^4 and r^2 moments for the isoscalar and isovector channels respectively. The notations are as defined in Fig. 7.1.

The density and energy variations of these components are large for both the real and imaginary terms. The isoscalar component (r^4) moments vary most strongly with both energy and density. At 65 MeV the real part changes sign at about 40% central density ($k \sim 0.6k_F$) but at the higher energies it is increasing and negative with density. The imaginary part of these moment integrals varies very markedly as well, even changing character at each energy. The isovector r^2 moment is as variable. Both real and imaginary parts change with energy and density in non-trivial ways.

The moment integrals of the tensor force components are shown in Fig. 7.4. Note that, as the tensor form factor is r^2 times Yukawas, the r^2 moments are given by Eq. (7.16). The isoscalar and isovector component results are shown in the left and right hand panels again with the 65, 135, and 200 MeV cases shown from top to bottom. The isoscalar results generally decrease with increasing density. That decrease becomes quite appreciable with the real part as the energy increases. The imaginary part of that isoscalar result is weakly positive to energies above 135 MeV and at 200 MeV is noticeable and absorptive.

The isovector result is more varying with density changing sign at 65 MeV and being positive but decreasing by a factor of two from free scattering results at higher energies. The imaginary parts also decrease

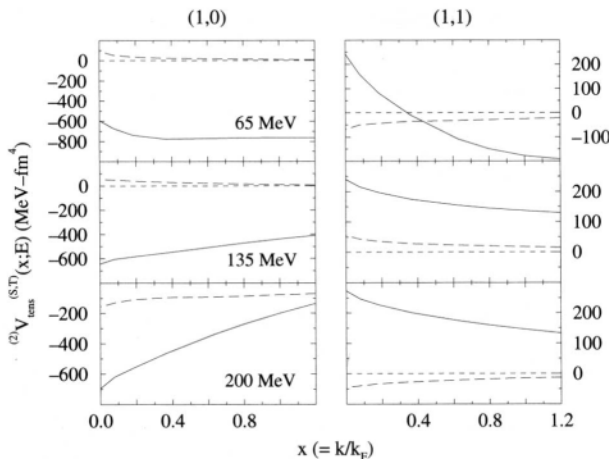


Fig. 7.4. The r^2 moment integrals of the tensor components of the effective interactions. The notations are as defined in Fig. 7.1.

with density but now change from absorptive to repulsive and then back at the three energies displayed.

7.3.3. Radial Variations of the Effective Interactions

The radial variations of the effective interactions based upon the Paris interaction are displayed in four figures. In each, the radial variations of the 65, 135, and 200 MeV effective interactions are shown again from top to bottom and each panel contains the real and imaginary parts of the interactions for zero and central nuclear densities. The real and imaginary parts of the free interactions are depicted by the long dashed and dot-dashed curves while those of the interaction at central nuclear density are portrayed by the solid and dotted curves respectively.

The radial variation of the central singlet components are shown in Fig. 7.5. With the notable exception at 200 MeV, the real and imaginary parts decrease with density and the imaginary components become more negative with energy. The medium also increases the attractive real potential at 200 MeV. The properties of the central interactions in the triplet channels are presented in Fig. 7.6. The variations with energy and density are even more marked and diverse than with the central singlet potentials. The spin-orbit and tensor force results are displayed in Figs. 7.7 and 7.8 respectively. In the spin-orbit cases, the triplet-even channel

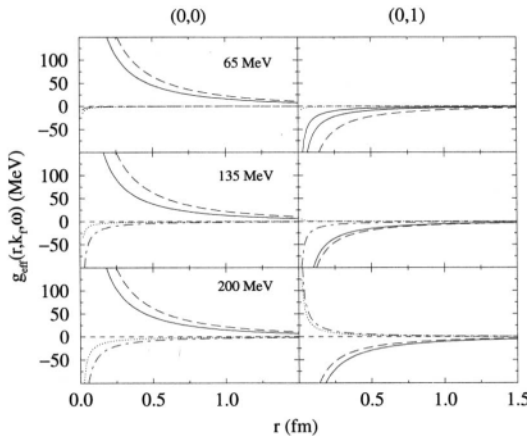


Fig. 7.5. The radial variations of the effective interactions in the central singlet channels determined from the Paris potential. The 65, 135, and 200MeV results are displayed in the top, middle, and bottom segments with the real and imaginary parts of the interactions at central nuclear density ($k_f = 1.4$) depicted by the solid and dotted curves respectively. The matching results for the free NN interaction are shown by the long dashed and dot-dashed curves respectively.

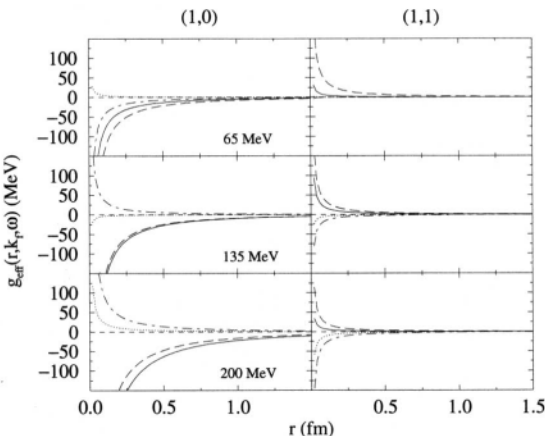


Fig. 7.6. The radial variations of the effective interactions in the central triplet channels. The notation is as given in Fig. 7.5.

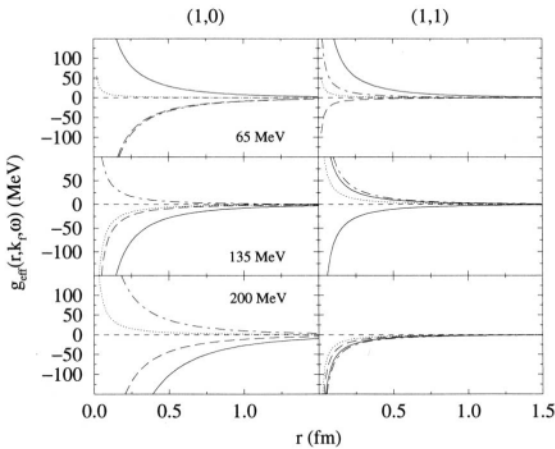


Fig. 7.7. The radial variations of the effective interactions with the spin-orbit forces. The notation is as given in Fig. 7.5.

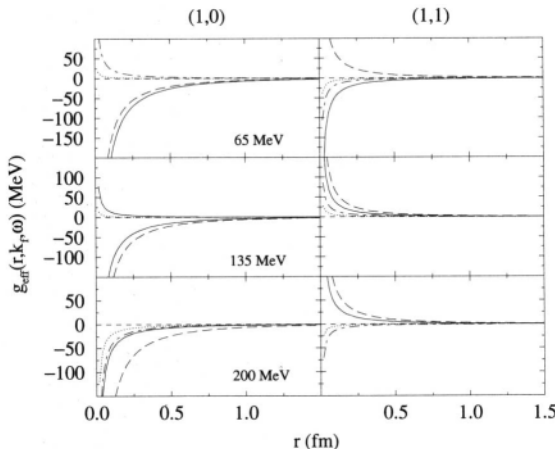


Fig. 7.8. The radial variations of the effective interactions with the tensor force. The notation is as given in Fig. 7.5.

variations are large. The medium effects show a marked increase in size and sometimes a change of sign of the potentials. Such is also the case in the triplet-odd channel interactions for 65 and 135 MeV, while at 200 MeV medium effects are slight. At 200 MeV, the spin-orbit triplet-odd interactions are rather small as well. The variations with energy and density of the tensor force interactions are even more disparate with energy and density than are those of the spin-orbit cases.

8. NUCLEAR STRUCTURE

To describe the scattering of particles from nuclei in a predictive way that reveals details of the structure of the target, one requires as best a description as possible of the target states from a suitable many-nucleon theory. At the microscopic level considered herein, the scattering of nucleons from nuclei proceeds via the interactions between the projectile and each and every nucleon in the target. Hence a theory of structure encompassing nucleon degrees of freedom is required. An approach most suited to this task is to use the shell model, especially for light nuclei. But a detailed description of the shell model itself is beyond the scope of this review and so we present only a brief outline of the model. Also we highlight the results of recent calculations that are relevant to the development of the microscopic optical potential as specified in Chapters 2 and 3. We refer the reader to Refs. [160, 161, 162] for a more comprehensive study of the shell model and nuclear structure. Of particular interest with these shell model studies are the helium isotopes ($^{3,4,6,8}\text{He}$), the lithium isotopes ($^{6,7,9,11}\text{Li}$), ^{12}C , ^{14}N , and ^{16}O . For these nuclei, wave functions have been calculated using multi- $\hbar\omega$ shell model spaces. In each case, all particles are assumed active to give *no-core* results for spectra and the OBDME that are required both in the folding that gives the non-local optical potentials and in DWBA calculations of inelastic scattering and charge exchange reactions.

For specific states of some nuclei, other methods are of use. We note that mean field theories are being studied in depth seeking quite detailed specification of nuclear ground states. Also the Hartree-Fock (HF) method [163], or the more modern version of the Brueckner-Hartree-Fock (BHF) approach, is a very convenient scheme by which select states in nuclei can be defined in quite a large basis. Ground state bands of $N = Z$ nuclei are examples. A consequence of structure generated with large space models is that enhancement of electromagnetic and hadronic

transitions above simple structure model estimates, result naturally from macroscopic deformations that are inherent with deformed self-consistent field. The HF procedure extracts an average field that each of the nucleons feels due to its interactions with every other bound nucleon. The minimal energy Slater determinant that is formed by filling the most bound deformed single particle states associated with that average field is then the optimal independent particle model structure within the chosen model space. Physical states of the nucleus can be represented therefrom by projection. The study of Bassichis, Kerman, and Svenne [164] give details for a number of nuclei.

Finally we discuss an extension of the HF method, defined as the particle hole model (PHM) [165]. This model extends the HF prescription by considering not only the minimal energy HF Slater determinant but also all such determinants formed by one particle—one hole ($1p - 1h$) excitations upon it within the chosen single particle basis. Multi-particle—multi-hole excitations are ignored under the assumption that the HF method obtains the best possible reference field and minimises the residual interactions, at least for the ground state of the nucleus. A consequence of the PHM is that states of both parities are generated.

8.1. The Shell Model

In second quantised form, the conventional Hamiltonian describing a bound many-nucleon system has the form

$$H = \sum_{ik} T_{ik} a_i^\dagger a_k + \frac{1}{4} \sum_{ijkl} V_{ijkl} a_i^\dagger a_j^\dagger a_l a_k, \quad (8.1)$$

where a_i^\dagger and a_i are nucleon creation and annihilation operators. Those operators are spherical in that they are associated with good angular momentum quantum numbers ($i \equiv l, s, j, m$), and they satisfy anti-commutation relations,

$$\begin{aligned} \{a_i, a_j\} &= \{a_i^\dagger, a_j^\dagger\} = 0 \\ \{a_i^\dagger, a_j\} &= \delta_{ij}. \end{aligned} \quad (8.2)$$

For nuclear systems, T_{ik} are the matrix elements of the kinetic energy operator and V_{ijkl} are those of the NN interaction. To solve the eigenvalue problem with such a Hamiltonian for a many-nucleon system, it is convenient to introduce a modulating single particle potential U_k so that the shell model Hamiltonian is

$$\begin{aligned}
 H_{SM} &= \sum_{ik} (T_{ik} + U_{ik}) a_i^\dagger a_k + \sum_{ijkl} \left(\frac{1}{4} V'_{ijkl} - U_{ik} \delta_{jl} \right) a_i^\dagger a_j^\dagger a_l a_k \\
 &= \sum_i \epsilon_i a_i^\dagger a_i + \sum_{ijkl} V'_{ijkl} a_i^\dagger a_j^\dagger a_l a_k.
 \end{aligned} \tag{8.3}$$

Therein ϵ_i are the single nucleon energies and V'_{ijkl} are the matrix elements of the two-nucleon residual interaction.

In a shell model approach, there are two basic methods by which the residual interaction may be specified. The first is to adopt a model space that is believed to be applicable to a series of nuclei. Then the potential matrix elements V'_{ijkl} defined in the model space are chosen to fit some energy levels of those nuclei. Cohen and Kurath (CK) [166] pioneered that approach with a study of the $0p$ -shell nuclei. It has been extended since to more complicated model spaces by including higher shells. The alternative approach takes advantage of the observation that the strength of the modulating potential may be considered weak so that the residual interaction may be obtained directly from the NN interaction. Such an approach, first developed by Lee and Suzuki [167], involves evaluation of NN G matrices for realistic interactions. This approach culminated recently in the work of Zheng *et al.* [168]. They solved the BBG equations for bound states with multi- $\hbar\omega$ model spaces to study properties of light mass nuclei. Their calculations required the G -matrix to be multi-valued, an acknowledgement that the mean field of the nucleus changes with the rearrangements of the nucleons for each state. Calculation of G -matrices becomes prohibitive as the mass number increases however, and rapidly so.

Besides the standard approach, spectra have been obtained from variational Monte Carlo (VMC) calculations of light nuclei performed by the Argonne group [169]. Their approach goes beyond the standard shell model, however, as they consider three-nucleon interactions in the many-uncleon Hamiltonian and solve the Schrödinger equation directly. In that scheme, the wave functions so obtained are exact. To date however, and due to the complexities in computation, application has been limited to just the lightest of nuclei.

8.2. Projected HF Theory and the PHM Model

The Projected Hartree-Fock (PHF) theory of spectroscopy assumes that the nucleus may be described using a basis of deformed orbitals (as opposed to the shell model in which spherical orbitals are assumed). As such, it is structured to describe collective effects in nuclear spectra. For light nuclei, as the nucleon number is small, there is no need

to assume a closed core and, with the PHF, low excitation modes of deformed nuclei are described in terms of rotating intrinsic states of nucleons moving in a deformed field. Usually a number of simplifying assumptions are made. It is customary to assume that parity and isospin are good quantum numbers and that the deformed field is axially symmetric with respect to some body-fixed axis. Then the ground state rotational band of a deformed (even-even) nucleus is assumed to be described by states of good angular momentum projected from the minimal energy solution of the axially symmetric HF equations. Frequently also only $N = Z$ nuclei are studied. If K is the angular momentum projection quantum number along the symmetry axis, the minimal energy HF solution may be expressed as [170]

$$|\Phi_K\rangle = \frac{1}{\sqrt{A!}} \det \{ |\psi_{\lambda_i}\rangle \}, \quad (8.4)$$

where $|\psi_{\lambda_i}\rangle$ are the single-particle deformed orbits. As K is good quantum number,

$$K = \sum_{i=1}^A \lambda_i. \quad (8.5)$$

The single particle deformed states may be expanded in a spherical basis as,

$$|\psi_{\lambda}(i)\rangle = \sum_{jm} C_{jm}^{\lambda} |\varphi_{jm}(i)\rangle, \quad (8.6)$$

in which, when axial symmetry is imposed, the summation over m reduces to a single term having the λ value of the particular deformed orbit. The expansion coefficients, $C_{jm=\lambda}^{\lambda}$, are real and satisfy time-reversal, i.e.,

$$C_{j-m} = (-1)^{j-m} C_{jm}. \quad (8.7)$$

More than one deformed orbit can have the same symmetry axis quantum number k .

The intrinsic wave function $|\Phi_K\rangle$ is not an eigenstate of J^2 or J_z . However, physical states may be obtained from the intrinsic one by the projection method of Peierls and Yoccoz, [171], and be written as

$$|\Psi_{JM}^K\rangle = N_{JK} P_{MK}^J |\Phi_K\rangle. \quad (8.8)$$

where the projectors P_{MK}^J project from the HF wave function physical states of good angular momentum J . N_{JK} is the normalisation. A method

for calculating these normalised PHF states is described in Ref. [170], and is based upon the Hill-Wheeler integral [172]. Details are given in the Appendix.

The PHM of Schmid [165] was introduced primarily to study the spectra and transition probabilities of giant multipole resonances. Nevertheless it also provides the spectrum and wave functions for the ground and excited states of light deformed nuclei. The PHM approach uses the standard HF minimal energy state given by Eq. (8.4) as reference determinant in creating a complete set of particle-hole states. Those states are specified within the selected oscillator basis underlying the HF deformed single particle states of Eq. (8.6) but now allowing for the deformed orbits that lie above the Fermi level. Angular momentum projection on the intrinsic PHM basis states so formed gives a suitably truncated space of good angular momentum states in which to diagonalise the nuclear Hamiltonian, albeit that they are non-orthogonal. The procedure also gives nuclear states by limiting spurious components in the resulting spectrum.

Great simplifications exist under the approximations that axial symmetry is in force, that we consider only $N = Z$ nuclei, and that there is no parity mixing. These are assumed hence as they were in the foregoing discussion of the PHF model. With β^\dagger designating a nucleon creation operator for the HF single particle orbits for light $N = Z$ nuclei, the physical state vectors in the PHM model then have the form,

$$|\Psi_{JM};(i)\rangle_{(T)}^{\pi} = x_{(0)}^{J\pi 0}(i)\{P_{M0}^J|\Phi^0\rangle\}_{(0)} + \sum_{\eta n} x_{(\eta n)}^{J\pi T}(i)\{P_{MK(\eta n)}^J b_\eta^\dagger b_n |\Phi^{K(n)}\rangle\}_{(T)} \quad (8.9)$$

where “ i ” delineates multiple entries for a given spin-parity and isospin, J^π , T . The sums over η and n are limited to be above and below the Fermi level respectively. The eigenstates are obtained by solving the non-orthogonal eigenvalue problem,

$$\left[\{H^{J\pi T}\}_{KK'} - E^{J\pi T} \{N^{J\pi T}\}_{KK'} \right] x_{K'}^{J\pi T} = 0. \quad (8.10)$$

The matrix $\{N\}$ is the overlap matrix that measures the lack of orthogonality of the projected intrinsic states vectors. In studies [165, 173] of light nuclei, the nuclear Hamiltonian was defined by the Barrett-Hewitt-McCarthy two-nucleon G -matrices [174] and the $0s_{\frac{1}{2}}$ to $0g_{\frac{3}{2}}$ inclusive spherical single particle basis was used.

As an example, consider the reference HF determinant for ^{12}C as defined by the Bassichis, Kerman, and Svenne calculations [164]. They is

TABLE 8.1
HF single particle energies and wave functions for ^{12}C .

λ^π	ϵ (MeV)	$0s_{\frac{1}{2}}$	$1s_{\frac{1}{2}}$	$0d_{\frac{3}{2}}$	$0d_{\frac{5}{2}}$	$0g_{\frac{9}{2}}$
$\frac{1}{2}^+$	-36.76	0.9751	0.1349	0.1206	-0.1279	0.0107
$\frac{3}{2}^+$	-3.65				0.9977	-0.0681
$\frac{1}{2}^+$	-1.98	-0.0534	0.8831	-0.0657	0.4584	-0.0545
$\frac{3}{2}^+$	-1.31			0.6733	0.7355	-0.0755
$\frac{1}{2}^+$	4.60	0.0907	-0.3643	0.5024	0.7722	-0.1020
$\frac{3}{2}^+$	4.78			0.7394	-0.6687	0.0784
$\frac{1}{2}^+$	7.71	-0.1952	0.2632	0.8537	-0.4008	0.0569
$\frac{3}{2}^+$	21.53					1.0000
$\frac{7}{2}^+$	23.24					1.0000
$\frac{5}{2}^+$	24.46				0.0681	0.9977
$\frac{3}{2}^+$	25.24			-0.0073	0.1086	0.9941
$\frac{1}{2}^+$	25.62	0.0071	-0.0055	-0.0022	0.1290	0.9916
		$0p_{\frac{1}{2}}$	$0p_{\frac{3}{2}}$	$1p_{\frac{1}{2}}$	$1p_{\frac{3}{2}}$	$0f_{\frac{7}{2}}$
$\frac{3}{2}^-$	-17.64		0.9845		0.1128	0.0801
$\frac{1}{2}^-$	-16.48	0.7222	0.6701	0.0796	0.1061	-0.0599
$\frac{1}{2}^-$	-3.57	0.6710	-0.7189	-0.0040	0.0243	-0.1182
$\frac{7}{2}^-$	7.75					1.0000
$\frac{5}{2}^-$	9.85				0.4592	0.8883
$\frac{3}{2}^-$	10.21		0.0709		-0.8532	-0.7537
$\frac{1}{2}^-$	10.57	0.0978	0.0233	-0.6233	-0.6988	-0.0980
$\frac{7}{2}^-$	12.83		0.1160		-0.5067	0.3056
$\frac{5}{2}^-$	13.65					0.8883
$\frac{3}{2}^-$	13.74	0.0214	0.1685	-0.3919	-0.0937	0.1143
$\frac{1}{2}^-$	15.62		0.1105		-0.0148	-0.9363
$\frac{7}{2}^-$	15.67	-0.0100	0.0498	0.6534	-0.6730	-0.2461
$\frac{5}{2}^-$	16.36	-0.1341	0.0522	-0.1569	0.2250	-0.9483
						0.0695

based upon HF single particle energies and wave functions specified by the expansion coefficients of Eq. (8.6) that are listed in Table 8.1. Note that while the $0s_{\frac{1}{2}}$ and $0p_{\frac{3}{2}}$ basis states dominate the expansions of the $\lambda^\pi = \frac{1}{2}^+$ and $\frac{3}{2}^-$ states of the HF spectrum, the $\frac{1}{2}^-$ states are very strongly mixed. This equates to a spreading of occupancies within the spherical basis space from what one would anticipate with standard shell model calculations. That is shown in Table 8.2, where the CK, $0\hbar\omega$ shell model [166] values for ^{12}C are compared with those from the HF and also the PHM [173] calculations. The HF and PHM give similar ground states as one might expect, but they are quite distinct from that of the CK shell model [166]. Notably the $0p_{\frac{3}{2}}$ shell occupancy has been

TABLE 8.2
Single nucleon (shell) occupancies in ^{12}C .

nl_j	CK	HF	PHM	nl_j	HF	PHM
$0s_{\frac{1}{2}}$	2.00	1.94	1.90	$0d_{\frac{5}{2}}$	0.03	0.04
$0p_{\frac{1}{2}}$	0.74	0.96	1.04	$1p_{\frac{1}{2}}$	0.00	0.01
$0p_{\frac{3}{2}}$	3.27	2.99	2.84	$1p_{\frac{3}{2}}$	0.01	0.05
$1s_{\frac{1}{2}}$		0.01	0.04	$0f_{\frac{5}{2}}$	0.01	0.02
$0d_{\frac{3}{2}}$		0.02	0.03	$0f_{\frac{7}{2}}$	0.03	0.04

reduced and the probability redistributed notably into the $0p_{\frac{1}{2}}$ shell but also with small values in all of the basis states.

8.3. Matrix Elements of Nuclear Structure Observables

The matrix elements required for the calculation of γ -decays, and of electron and proton scattering observables, are the OBDME. For isoscalar transitions they are simply the singly reduced amplitudes,

$$S_{hhJ} = \left\langle J_f \left| \left[\mathbf{a}_h^\dagger \times \tilde{\mathbf{a}}_h \right] \right|^J \right| J_i \rangle, \quad (8.11)$$

where the Wigner-Eckart theorem used to define the reduced matrix elements is

$$\langle J_f M_f | \hat{O}_{JM} | J_i M_i \rangle = \frac{1}{\sqrt{2J_f + 1}} \langle J_i M_i JM | J_f M_f \rangle \langle J_f | \hat{O}_J | J_i \rangle \quad (8.12)$$

They may be obtained directly from the shell model wave functions or from the PHF calculations as we describe next. They have been tabulated elsewhere for several of the case considered herein [68, 139].

To Obtain the OBDME from the PHF models is a little more complex. First the HF intrinsic state is expressed in second quantised form,

$$|\Phi_K\rangle = \prod_{i=1}^A \alpha_{\lambda_i}^\dagger |0\rangle, \quad (8.13)$$

where $\alpha_{\lambda_i}^\dagger$ creates a particle in the deformed orbit λ_i , and obeys the normal fermion operator anti-commutation rules. The deformed

operators may also be expanded in terms of the spherical ones using the coefficients defined in Eq. (8.6), [170],

$$\alpha_{\lambda_i}^{\dagger} = \sum_j C_{j\lambda_i} \alpha_{jlm_i}^{\dagger} = \lambda_i \rho_i. \quad (8.14)$$

The calculation proceeds by making a deformed state cofactor expansion,

$$|\Phi_K(1 \dots p \dots A)\rangle = \frac{1}{\sqrt{A}} \sum_k |\psi_k(p)\rangle \alpha_k |\Phi_k\rangle, \quad (8.15)$$

from which the physical state vectors may be expressed as

$$|\Psi_{JM}^K\rangle = \frac{1}{\sqrt{A}} N_{JK} \sum_{J_1 M_1} \sum_{J_2 M_2} \sum_{K_1 K_2} \langle J_1 M_1 J_2 M_2 | JM \rangle \\ \times \langle J_1 K_1 J_2 K_2 | JK \rangle C_{J_1 K_1} |\varphi_{J_1 M_1 P_1}\rangle P_{M_2 K_2}^{J_2} \alpha_{K_1} |\Phi_K\rangle, \quad (8.16)$$

where $|\varphi_{J_1 M_1 P_1}\rangle$ is a spherical state.

From this, the OBDME may be obtained [170] by using

$$S_{\hbar p J} = \left\langle J_f \left| \left[\alpha_{\hbar}^{\dagger} \times \alpha_{\hbar} \right] \right|^f \right| J_i \rangle \\ = N_{J_i K_i} N_{J_f K_f} \sqrt{(2J_f + 1)(2J_i + 1)(2J + 1)} \sum_{J_c} (-1)^{\hbar + J_c + J + J_i} \begin{Bmatrix} J & \hbar & j_2 \\ J_c & J_f & J_i \end{Bmatrix} \\ \times C_{\hbar k_f}^* C_{\hbar k_i} \langle j_1 k_i J_c K_i - k_i | J_i K_i \rangle \langle j_2 k_f J_c K_f - k_f | J_f K_f \rangle \\ \times \langle \varphi_{K_f} | \alpha_{k_f}^{\dagger} P_{K_f - k_f, K_i - k_i}^c \alpha_{k_i} | \varphi_{K_i} \rangle. \quad (8.17)$$

The use of Eq. (8.14) together with the integral form of the projection operator [172] allows the overlap function $\langle \varphi_{K_f} | \alpha_{k_f}^{\dagger} P_{K_f - k_f, K_i - k_i}^c \alpha_{k_i} | \varphi_{K_i} \rangle$ to be calculated [170]. Details are given in the Appendix. As a result, the transition densities can be calculated for a large spherical basis from wave functions calculated in the much smaller deformed single particle basis.

8.4. Spectra and Properties from the Models

Wave functions for the isotopes $^{3,4,6,8}\text{He}$, the lithium isotopes $^{6,7,9,11}\text{Li}$, ^{12}C , ^{14}N , and ^{16}O , have been calculated using the shell model with multi- $\hbar\omega$ shell model spaces. In most of the calculations all particles were active so that no-core results were found.

8.4.1. Helium Isotopes

The He isotopes are a special set within themselves. ^3He and ^4He have been solved exactly using the Faddeev and Faddeev-Yakubovsky schemes, in which the three- and four-nucleon problems are transformed to ones involving summations over effective two-nucleon interactions. This is achieved by a transformation of the nucleon coordinates into hyperspherical ones of the nucleus. A goal of the more traditional shell model then is to obtain wave functions that converge to the exact few-body ones. Navrátil and Barrett have calculated the ground state wave functions for ^3He [175] and ^4He [176] with a view to understanding that convergence.

The wave functions of ^4He were obtained in a complete $8\hbar\omega$ model space, while those for ^3He in model spaces up to the complete $32\hbar\omega$ model space. Note that, for simplicity, the nomenclature $n\hbar\omega$ model space has been used to identify the complete $(0 + 2 + \dots + n)\hbar\omega$ model space. For ^3He , convergence of the shell model binding energy to within 10% of the Faddeev solution can be found with a calculation in the $8\hbar\omega$ space. With increasing basis size, further convergence is very slow. A slight variance remains even if the calculation is made within the $32\hbar\omega$ model space.

The other He isotopes, ^6He and ^8He , lie near the neutron drip line. They are weakly bound with two-neutron separations energies of 0.975 MeV and 2.137 MeV, for ^6He and ^8He , respectively [177]. Further, they are examples of Borromean nuclei as the $(A - 1)$ isotope in each case is unbound, as is any two-body subsystem of ^6He and ^8He . The weaker binding of ^6He is manifest in a halo of the two valence neutrons surrounding the ^4He core; a condition that strongly suggests a three-body model of its structure would be appropriate. However, the results of the $4\hbar\omega$ model calculation of ^6He by Navrátil and Barrett [176] infer that no additional information beyond the standard shell model in this model space is required to adequately describe some ground state properties and spectra. This should not be interpreted necessarily that ^6He does not have a halo.

Spectra for ^6He and ^8He are given in Figs. 8.1 and 8.2 respectively. In Fig. 8.1 the results for ^6He from the traditional shell models, as calculated in either $4\hbar\omega$ or $6\hbar\omega$ model spaces are compared with the results from the VMC calculation [169] and with experimentally determined values [178]. The two calculations made using the traditional shell model approach ascribe $J^\pi; T = 2^+; 1$ to the first two excited states, in agreement with experiment. While the energy of the $2^+_1; 1$ state is similar in the $4\hbar\omega$

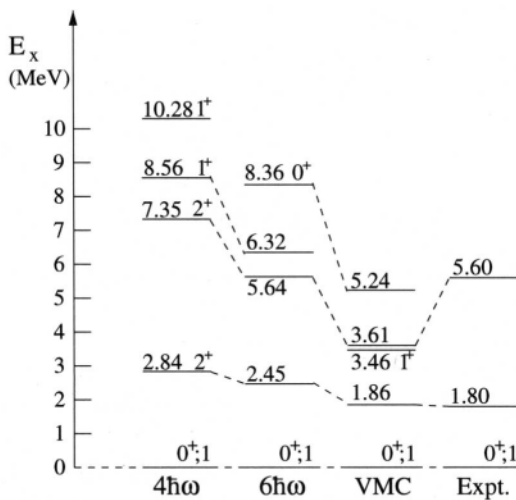


Fig. 8.1. The spectrum of ${}^4\text{He}$. The result of the $4\hbar\omega$ shell model calculation is compared with that of the $6\hbar\omega$ calculation [176], with that of the VMC calculation [169], and with experiment [178].

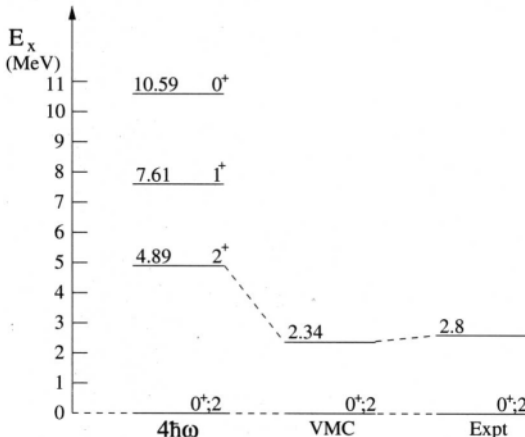


Fig. 8.2. The spectrum of ${}^8\text{He}$. The result of the $4\hbar\omega$ shell model calculation is compared with that of the VMC calculation [179]. The data are from Ref. [177].

and $6\hbar\omega$ models, the energy of the $2\frac{1}{2}$ state in the $6\hbar\omega$ model is in much better agreement with the data. This may be due to the modification of the auxiliary potential in the Hamiltonian made in the calculation [176] from what was used with the smaller basis. The modification does not affect the spectrum significantly as the increase in energy of each state is less than 1 MeV. But without it, over-binding of the order of 4 MeV occurs. This over-binding will influence any calculation that uses the same interaction, but it is not expected to affect wave functions significantly. The results of the VMC calculation place the $2\frac{1}{2}$ state in very close agreement with experiment. However, that calculation places a 1^+ state in the spectrum. Not only has that state not been observed in experiment, but also it has not been found with other calculations.

There is very little experimental information on the spectrum of ${}^8\text{He}$. The first excited state is listed at 2.8 ± 0.4 MeV and has $J^\pi, T = (2^+); 2$ [177]. Other states, at 1.3, 2.6, and 4.0 MeV [177], have been suggested from a heavy ion transfer experiment, but as yet no other data support the existence of those states. The spectrum obtained by Navráil and Barrett in the $4\hbar\omega$ model space and using their updated G -matrix interaction [175], is so similar to that shown that they have not been included in the figure. The first excited state is predicted (correctly) by all calculations to be the $2\frac{1}{2}; 2$ state, although only the VMC calculation gives a good value for its excitation energy. The disagreement between the shell model results for that excitation energy and experiment may reflect the failing of the shell model to reproduce the correct neutron density distribution within the $4\hbar\omega$ model space.

One feature of halo nuclei is a large r.m.s. radius. The r.m.s. radii for ${}^6\text{He}$ and ${}^8\text{He}$ are listed in Table 8.3. Therein, the r.m.s. radii shown in the first two columns were calculated using two sets of WS wave functions. First, a set of WS wave functions which reproduced the elastic scattering form factors of ${}^6\text{Li}$ were used for ${}^{6,8}\text{He}$, and those which reproduced the elastic scattering form factors for ${}^9\text{Be}$ were used for ${}^{9,11}\text{Li}$. That set of results obtained with those wave functions are designated as no-halo. Note that this specification simply indicates that the neutron density is not extensive. The results obtained using wave functions when the valence neutron orbits are weakly bound are designated as halo. The binding energy of the valence nucleon influences the extension of the tail of the wave function. While ${}^6\text{He}$ and ${}^8\text{He}$ are Borromean nuclei, the shape of the single particle wave function of each valence neutron is influenced by the binding of that neutron to the $(A - 1)$ system. For ${}^{6,8}\text{He}$, the single neutron separation energies to the lowest resonances in the

TABLE 8.3

Root-mean-square radii for ${}^6\text{He}$, ${}^8\text{He}$, ${}^9\text{Li}$, and ${}^{11}\text{Li}$, as calculated using single particle wave functions specifying *halo* and *no-halo* as given in the text. The Glauber model results were extracted from data [180, 181, 182].

Nucleus	$r_{r.m.s}$		
	no-halo	halo	Glauber model
${}^6\text{He}$	2.301	2.586	2.54 ± 0.04
${}^8\text{He}$	2.627	2.946	2.60
${}^9\text{Li}$	2.238	2.579	2.30 ± 0.02
${}^{11}\text{Li}$	2.447	2.964	3.53 ± 0.10

unbound ($A = 1$) systems are 1.87 MeV and 2.584 MeV for ${}^6\text{He}$ and ${}^8\text{He}$ respectively [177].

The r.m.s. radii found using the halo and no-halo shell model descriptions differ by only 0.2 fm but comparison with the Glauber model value [180] indicates that ${}^6\text{He}$ has an extensive neutron density, as dictated by the loose binding. However, the shell model calculations indicate that ${}^8\text{He}$ does not have an extensive neutron distribution, when compared with the value obtained from a few-body analysis of high-energy ${}^8\text{He}$ - p scattering data [182].

8.4.2. Lithium Isotopes

There are distinct similarities between the He and Li isotopes. The stable isotopes ${}^6\text{Li}$ and ${}^7\text{Li}$ lend themselves to few-body descriptions as suggested by the ordering of the low-lying states and a *natural* approximation to consider an α particle component. There have been numerous studies of cluster model specifications for these nuclei seeking to explain their properties, especially the very low quadrupole moment of ${}^6\text{Li}$ and the substantially greater one of ${}^7\text{Li}$ [183, 184]. However, such two- and three-body descriptions innately are approximations. The two nuclei are 6 and 7 nucleon systems respectively and models able to describe them in that fashion are required eventually.

The other bound isotopes, ${}^9\text{Li}$ and ${}^{11}\text{Li}$, are Borromean nuclei. ${}^{11}\text{Li}$ has been the subject of intense study since Tanihata *et al.* [185] experimentally established the presence of a halo in that nucleus. While ${}^9\text{Li}$ is

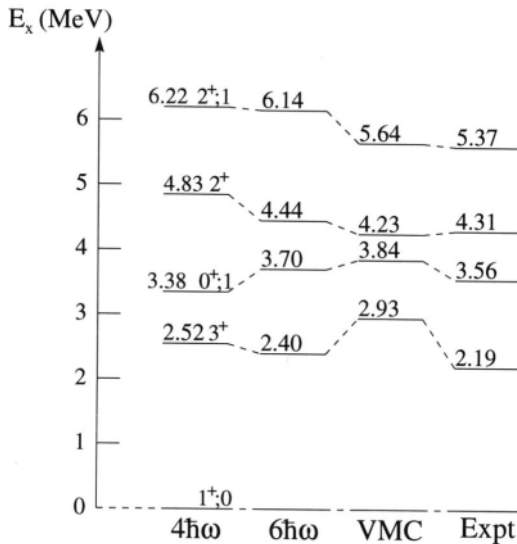


Fig. 8.3. The low-lying spectrum of ${}^6\text{Li}$. The results of the traditional shell-model approaches, as calculated in the $4\hbar\omega$ [186] and $6\hbar\omega$ [175] model spaces, and the result of VMC model calculation [169], are compared with the measured spectrum [177].

also a Borromean nucleus, the momentum distributions of its neutrons in the breakup reactions are too wide to suggest a halo.

Navrátil and Barrett [175, 176] have made no-core shell model calculations of ${}^6\text{Li}$ and ${}^7\text{Li}$ using the $6\hbar\omega$ model space and their G matrix interaction. The results compare very well with calculations of the mass-6 and 7 systems that were made by the Argonne group using the VMC approach [169]. The spectrum of the low-lying states in ${}^6\text{Li}$ is presented in Fig. 8.3, wherein the results of the traditional shell model calculations and the VMC model are compared with experimental values [177]. The spectra obtained in the $4\hbar\omega$ and $6\hbar\omega$ model spaces are similar. There is a degree of over-binding in the $4\hbar\omega$ shell model case (as was evident in the spectra for ${}^6,8\text{He}$), so that the energies of the ${}^6\text{Li}$ excited states are slightly too high. All calculations reproduce the states in the low-lying spectrum, although the VMC result also places the 3^+ state even higher in excitation than does the traditional shell model.

The spectrum for the low-lying states in ${}^7\text{Li}$ is presented in Fig. 8.4. As for ${}^6\text{Li}$, all model results reproduce the observed spectrum, although the VMC result now places the $\frac{1}{2}^-$ state too low in energy. Again, the

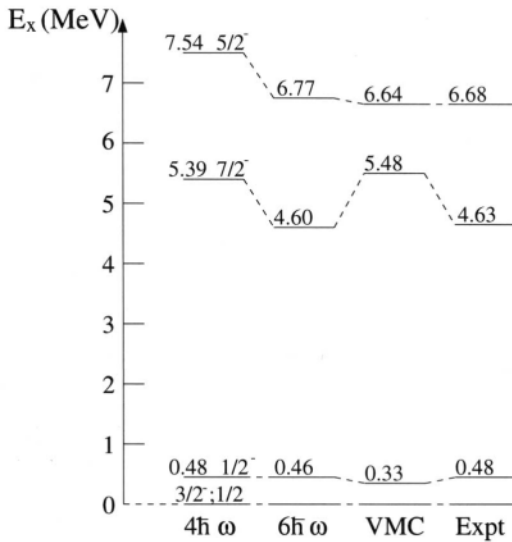


Fig. 8.4. The low-lying spectrum of ${}^7\text{Li}$. The results are as for Fig. 8.3.

over-binding inherent in the $4\hbar\omega$ model space calculations noted with the ${}^6\text{Li}$ results is evident.

One can assess the cluster behaviour of the wave functions of ${}^6\text{Li}$ and ${}^7\text{Li}$ by examining the ground state properties predicted with each model. It must be remembered that there is a correspondence between the shell and cluster models. Clusters arise naturally as correlations out of the shell model Hamiltonian [187], but for such clusters to become evident in the shell model wave functions, multi- $\hbar\omega$ model spaces are required [188]. It should be noted, however, that even the simple $0\hbar\omega$ shell model suggests clusters as the $0s$ core forms the α particle while the nucleons in the $0p$ shell form the other elements. The ground state properties are zero momentum transfer information however. To investigate the behaviour at higher momentum transfers, analyses of scattering data are required, and such are presented in later chapters.

Diverse ground state properties of ${}^{6,7}\text{Li}$ have been obtained from wave functions found from the $0\hbar\omega$, the $2\hbar\omega$, the $4\hbar\omega$, and the $6\hbar\omega$ shell models. All calculations used the Zheng interaction. The results of these calculations, in which HO wave functions were used with $\hbar\omega = 14 \text{ MeV}$, are compared with data [177, 186, 189] in Table 8.4. For both

TABLE 8.4

The r.m.s. radii, magnetic moments, and quadrupole moments of ${}^6\text{Li}$ and ${}^7\text{Li}$ as calculated in the $0\hbar\omega$, $2\hbar\omega$, $4\hbar\omega$, and $6\hbar\omega$ model spaces [186]. All calculations used the Zheng interaction [168].

Nucleus	Model space	$r_{r.m.s}$ (fm)	$\mu (\mu_N)$	$Q (efm^2)$
${}^6\text{Li}$	$0\hbar\omega$	2.32	0.869	-0.264
	$2\hbar\omega$	2.27	0.848	-0.208
	$4\hbar\omega$	2.33	0.845	-0.012
	$6\hbar\omega$	2.36	0.840	0.017
	Expt.	2.57	0.822	-0.083
${}^7\text{Li}$	$0\hbar\omega$	2.33	3.024	-1.68
	$2\hbar\omega$	2.26	3.057	-2.43
	$4\hbar\omega$	2.30	3.039	-2.63
	$6\hbar\omega$	2.32	3.006	-2.85
	Expt.	2.41	3.256	-4.06

nuclei, the r.m.s. radius is predicted adequately by all model calculations and is generally insensitive to the addition of **higher- $\hbar\omega$** excitations to the $0\hbar\omega$ model space. The effect of increasing the size of the model space is more noticeable in the magnetic and quadrupole moments. In the case of ${}^6\text{Li}$, the increase in the size of the model space serves to reduce the magnetic moment but with little change in proceeding from the $2\hbar\omega$ to the $6\hbar\omega$ space. The most significant effect is noticed in the quadrupole moment, in which the greatest change is evident in the $4\hbar\omega$ model space calculation. In this observable, the effect of increasing the model space to $4\hbar\omega$ is to overcompensate and that is exacerbated by also including $6\hbar\omega$ components. For ${}^7\text{Li}$, there is also a significant change in both the magnetic and quadrupole moments when one includes **higher- $\hbar\omega$** excitations. While the extreme deformation of ${}^7\text{Li}$ as evidenced by its large quadrupole moment is not reproduced, inclusion of **higher- $\hbar\omega$** components brings the calculated results in the direction of the data.

The ground state properties have also been calculated using the $0\hbar\omega$, $2\hbar\omega$, and $4\hbar\omega$ model spaces but with other interactions [186]. The results are displayed in Table 8.5. Therein, the r.m.s. radius for ${}^6\text{Li}$ calculated using the CK interaction ($\hbar\omega = 14.53 \text{ MeV}$) in the $0\hbar\omega$ model space is comparable to that obtained using the Zheng interaction in the $4\hbar\omega$ space. However, the results for the magnetic and quadrupole moments differ significantly. The magnetic moment predicted using the wave functions obtained from the CK interaction is closer in agreement

TABLE 8.5

As for Table 8.4, but using the CK, MK3W, and Zheng interactions in the complete $0\hbar\omega$, $2\hbar\omega$, and $4\hbar\omega$ model space, respectively [186].

Nucleus	Interaction			
	CK	MK3W	Zheng	Expt.
^6Li	$r_{r.m.s}$ (fm)	2.33	2.51	2.33
	$\mu (\mu_N)$	0.834	0.770	0.845
	$Q (e\text{-fm}^2)$	-0.78	-1.98	-0.012
^7Li	$r_{r.m.s}$ (fm)	2.33	2.46	2.30
	$\mu (\mu_N)$	3.171	3.192	3.039
	$Q (e\text{-fm}^2)$	-1.84	-3.21	-2.63
				-4.06

to the measured value than that obtained from the wave functions calculated using the Zheng interaction. However the predicted quadrupole moment is much worse. Likewise, the values for all quantities predicted using the wave functions obtained from the MK3W interaction ($\hbar\omega = 15.06$ MeV) all differ markedly from those obtained using the Zheng interaction. A similar pattern is observed for ^7Li (with oscillator energies of 15.06 and 16.02 MeV for the CK and MK3W interactions respectively), and for both nuclei the best and consistent results are obtained in the largest space.

The spectrum of ^9Li is shown in Fig. 8.5. Therein, the results of a $0\hbar\omega$ model space calculation [186] are compared with those obtained within the $4\hbar\omega$ model space [175]. The spectrum obtained in the $0\hbar\omega$ model space is in general agreement with that obtained in the $4\hbar\omega$ model space, although the first excited state comes much lower in the latter. There are no spin assignments in the experimental spectrum other than of the ground and first excited states and which all models correctly predict.

The ^{11}Li spectrum is displayed in Fig. 8.6, wherein the experimental results of Gornov *et al.* [190] are compared with the results of a $2\hbar\omega$ model space calculation [186]. The experimental excitations were obtained from a $^{14}\text{C}(\pi, pd)^{11}\text{Li}$ experiment which did not provide any spin-parity assignments, so the comparison between experiment and theory at this stage must be tentative. Even so, there is some agreement between the result of the shell model calculation and the data.

The r.m.s. radii for ^9Li and ^{11}Li calculated using the shell model wave functions for both the halo and no-halo representations, are listed

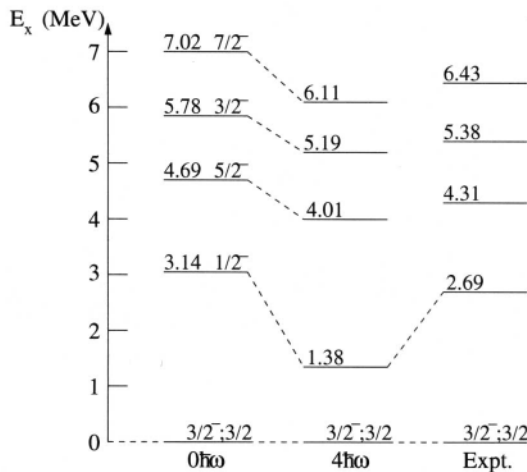


Fig. 8.5. The spectrum of ${}^9\text{Li}$. The result of the $0\hbar\omega$ calculation [186] is compared with that obtained in the $4\hbar\omega$ model space [175]. The data are from Ref. [177].

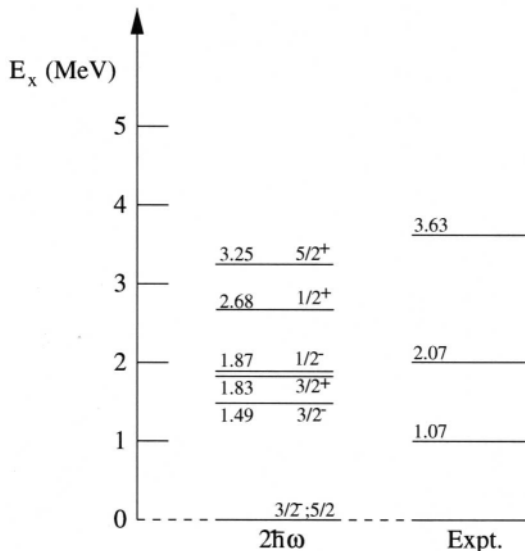


Fig. 8.6. The spectrum of ${}^{11}\text{Li}$. The result of the $2\hbar\omega$ model space calculation [186] is compared with the data of Gornov *et al.* [190].

TABLE 8.6
Nucleon occupation numbers for the ground state of
 ^{11}Li calculated in the $2\hbar\omega$ model space.

Orbit	Protons	Neutrons	Total
$0s_{\frac{1}{2}}$	1.9874	1.9988	3.9862
$0p_{\frac{3}{2}}$	0.9352	3.7738	4.7090
$0p_{\frac{1}{2}}$	0.0343	1.5446	1.5789
$0d_{\frac{5}{2}}$	0.0162	0.3568	0.3730
$0d_{\frac{3}{2}}$	0.0196	0.0617	0.0813
$0s_{\frac{1}{2}}$	0.0057	0.2597	0.2654
$0f_{\frac{7}{2}}$	0.0000	0.0001	0.0001
$0f_{\frac{5}{2}}$	0.0000	0.0002	0.0002
$1p_{\frac{3}{2}}$	0.0016	0.0031	0.0046
$1p_{\frac{1}{2}}$	0.0000	0.0012	0.0012

in Table 8.3. The single particle wave functions were those used in the proton scattering analyses [191, 192] to specify the nuclei as halo or no-halo like. Comparison with the experimental values, obtained from a Glauber model analysis of the scattering of $^{9,11}\text{Li}$ from ^{12}C that are given in Table 8.3 [181], indicates that ^{11}Li should be halo-like while ^9Li is not. However, while the value from the shell model for ^{11}Li as a halo is consistent within the errors of the quoted Glauber model estimate, the lower value may indicate that the shell model wave functions require either higher- $\hbar\omega$ excitations or smaller binding of the valence neutrons to account for a more extensive neutron density.

The ground state wave function of ^{11}Li in the $2\hbar\omega$ model is,

$$|^{11}\text{Li}\rangle = 62.71\%|0\hbar\omega\rangle + 37.29\%|2\hbar\omega\rangle. \quad (8.18)$$

This has a substantial admixture of $2\hbar\omega$ components, of which 19.62% comes from pure $(0d)^2$ configurations and a further 10.02% arise from pure $(1s)^2$ configurations. From this wave function, the proton and neutron occupancies can be specified. Those calculated using the $2\hbar\omega$ wave function are presented in Table 8.6. In this model, the ground state is predominantly $0p$ -shell with sd -shell admixtures mostly being of neutrons in the $0d_{\frac{5}{2}}$ and $1s_{\frac{1}{2}}$ sub-shells. Such a distinction is important as the halo neutrons are s -wave in nature [193].

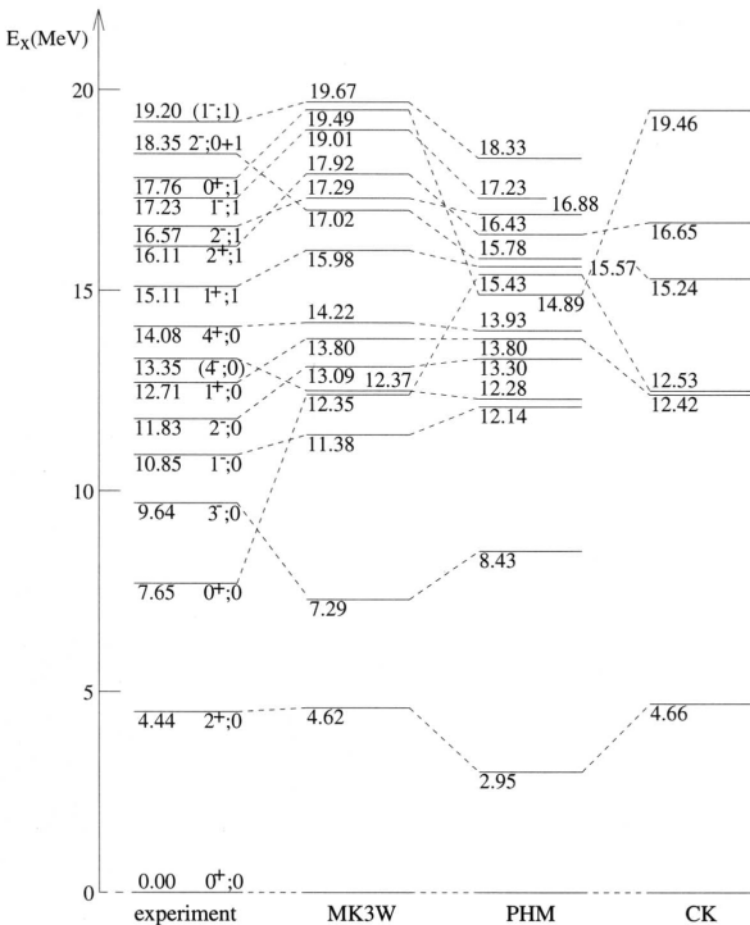


Fig. 8.7. Energy level diagram for the low-lying states in ^{12}C . The spectrum calculated with the MK3W interaction [139] is compared with experiment [194], as well as with the results of the PHM model of Amos *et al.* [173], and the 0p-shell model of Cohen and Kurath [166].

8.4.3. The Spectrum of ^{12}C

The spectrum of ^{12}C calculated using a $2\hbar\omega$ shell model [139] is displayed in Fig. 8.7 where it is compared not only with the experimental values [194] but also with the PHM [173] and the CK model [166] spectra. The 0p-shell basis of the CK model means that only positive parity states are obtained. With exceptions, most notably the $3^-;0$ state

at 9.64 MeV and the super-deformed 0^+ state at 7.65 MeV, the calculated $2\hbar\omega$ spectrum is in agreement with observation to within 2 MeV, and is a marked improvement on the other models, particularly as the PHM calculation places the $2^+;0$ (4.44 MeV) state far from the values predicted by the other models and experiment.

Spuriousity in the wave functions is a problem with large basis shell model calculations caused by whatever restrictions are imposed to facilitate evaluations. In the studies of ^{12}C discussed hereein, spuriousity is a problem only for the negative parity states. The positive parity spectra were evaluated using complete spaces in all cases. The negative parity spectra were generated with the $3\hbar\omega$ space restricted to take into account nothing more than the $0f1p$ shell. The use of such a large but restricted $3\hbar\omega$ model space is necessary as a smaller space shell model calculation, such as the MK3W interaction in a complete $1\hbar\omega$ space, places the $3^-;0$ (9.64 MeV) and $1^-;0$ (10.85 MeV) states at 19.25 MeV and 22.29 MeV respectively. The inclusion of $3\hbar\omega$ components brings those predicted energies down to 7.29 MeV and 11.38 MeV respectively, in far better agreement with experiment. Any spuriousity associated with centre of mass motion could be a major problem with the $1^-;0$ state. But this was found to be not the case in that particular calculation [139].

8.4.4. The Spectrum of ^{14}N

The states in ^{14}N of particular interest are the ground and first two excited states. There is inherent interest with these states as the anomalously long β -decay of the ground state of ^{14}C places a severe restriction on the structure of the mass-14 systems. Two approaches given in the current literature have been used to obtain wave functions for ^{14}N . The first, as used by Karataglidis *et al.* [68], is to adopt a model space for the structure and to diagonalise a suitable Hamiltonian within this model space, i.e., to construct standard shell model wave functions. The alternative is to assume that the wave functions for ^{14}N are completely specified by two holes coupled to a closed $0p$ -shell with amplitudes for the components determined from static properties and analyses of electron scattering data. The wave functions of Ensslin *et al.* [195] and of Huffman *et al.* [196] belong to the second category. However, there is a serious problem with this second approach in that the Hamiltonian underlying the wave functions is unphysical. It implies a much too large value for the symmetry violating matrix element $\langle ^3P_0 | v | ^1S_0 \rangle$ [197, 198]. The use of the associated wave functions

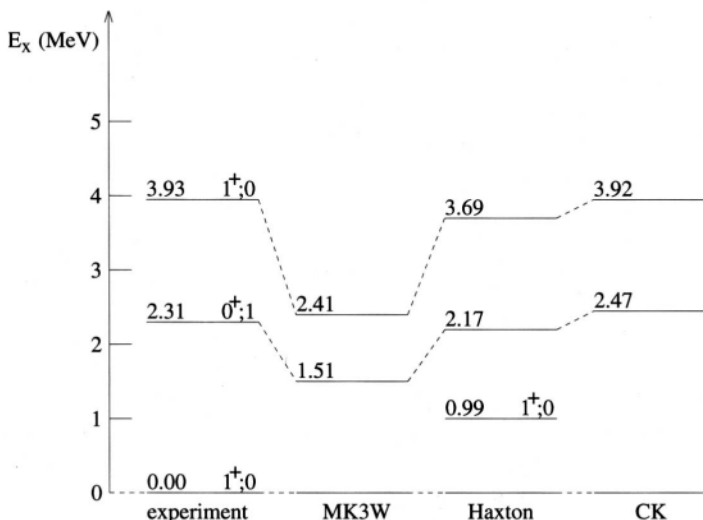


Fig. 8.8. The low-lying spectrum of ^{14}N . The results of the $2\hbar\omega$ (MK3W) and $4\hbar\omega$ calculations (Haxton) [68] are compared with the results of the $0\hbar\omega$ calculation of Cohen and Kurath [166], and with experiment [199].

in analyses of inelastic scattering data or of (γ, π^+) reactions then is questionable.

The low-lying spectrum of ^{14}N is presented in Fig. 8.8. As well as from the $2\hbar\omega$ calculation using the MK3W interaction, wave functions have been obtained in a complete $4\hbar\omega$ space using the Haxton and Johnson interaction [200]. That interaction was used to obtain the spectrum of ^{16}O also. All the elements are defined within the $0p1s0d$ -shells. The single particle energies were set as those used for the calculation of the ^{16}O spectrum. All relevant shells, from the $0s$ -shell up to and including the $0h1f2p$ -shell were included as that allows for the exact projection of spurious centre-of-mass excitations. The undefined matrix elements in that space were set to zero. This specification also omitted all $1p - 1h$ excitations which violate the HF condition. While the $2\hbar\omega$ wave functions are within 1 MeV of the experimental values, the $0\hbar\omega$ and $4\hbar\omega$ calculations are in much closer agreement with the observed excitation energies. Also, results of calculations of the Gamow-Teller matrix element for the β^- -decay of the ^{14}C ground state obtained from the $4\hbar\omega$ wave functions [201] were consistent with those obtained from $0p$ -shell models.

However, the $4\hbar\omega$ calculation using the Haxton and Johnson interaction predicts an extra $1^+; 0^-$ state at 0.99 MeV. The wave functions for the ground and this 0.99 MeV states in the $4\hbar\omega$ model are

$$\begin{aligned} |gs\rangle &= 61.15\% |0\hbar\omega\rangle + 29.78\% |2\hbar\omega\rangle + 9.07\% |4\hbar\omega\rangle, \\ |0.99\rangle &= 25.10\% |0\hbar\omega\rangle + 64.77\% |2\hbar\omega\rangle + 10.13\% |4\hbar\omega\rangle. \end{aligned}$$

Such a highly deformed state at this low excitation energy cannot be considered realistic. The lowest $2\hbar\omega$ $1^+; 0^-$ state is at 6.20 MeV [199]. This discrepancy may be caused either by the choice of the $2\hbar\omega$ interaction in the calculation, given the strength of the $2\hbar\omega$ component in the wave function, or, as is more likely, by use of interactions which have been optimised for results of structure calculations made with much smaller bases.

8.4.5. The Spectrum of ^{16}O

Haxton and Johnson [200] made a $4\hbar\omega$ calculation to obtain the spectrum of ^{16}O using an interaction based on the G -matrices of a realistic NN interaction. That same interaction was used in the $4\hbar\omega$ shell model calculation of the states of ^{14}N ; the results of which were discussed above. With their study, Haxton and Johnson sought to determine whether or not the Brown and Green model [202] for ^{16}O could be reproduced with a traditional shell model calculation. The Brown and Green model places great importance on the inclusion of $4\hbar\omega$ components in the wave functions of ^{16}O , and especially in the case of the $0^+_2; 0^-$ (6.05 MeV) state. The states of ^{16}O up to 10 MeV determined from the Haxton and Johnson study are shown in Fig. 8.9. Later calculations [68] of ^{16}O have been made using a model in which the positive parity states were calculated in a complete $4\hbar\omega$ space, while the negative parity states were obtained in a restricted $5\hbar\omega$ space. The Haxton and Johnson interaction was used therein. Those results [68] are distinct from the one found by Haxton and Johnson [200] who used a complete $3\hbar\omega$ space. Both sets of calculations took the single particle basis as the $0s$ -shell up to and including the $0hf2p$ -shell. All particles were active. The only restriction placed on the $5\hbar\omega$ space was that single particle excitations from the $0p$ -shell to the $0i1g2d3s$ -shell were excluded. Again, this restriction does not guarantee complete removal of the spuriousness associated with the centre of mass motion. However, for all the calculated states, the centre-of-mass energy eigenvalue was 19.19 MeV, ensuring that there is little or no spuriousness in the wave functions of most low excitation states. The exception

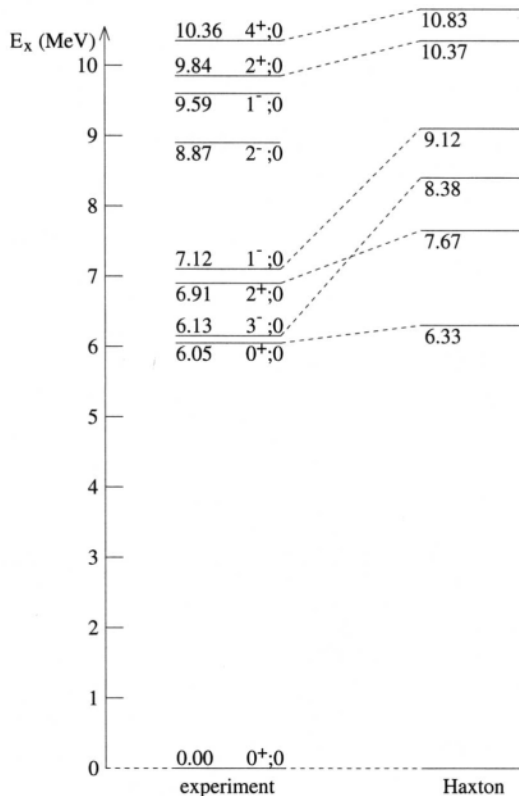


Fig. 8.9. The low-lying spectrum of ^{16}O . The experimental energy spectrum [203] is compared with the results of the calculation using the Haxton and Johnson interaction [200, 68].

is the isoscalar electric dipole state at 7.12 MeV excitation, but for that also the problem is not severe [68].

All positive parity states displayed in Fig. 8.9 are well reproduced by the calculation save for the $3^-;0$ (6.13 MeV) and $1^-;0$ (7.12 MeV) states which lie about 2 MeV from the experimental values. Also, and as found by Haxton and Johnson [200] in their $3\hbar\omega$ calculation of the negative parity states, the predictions for the $1^-;0$ (9.59 MeV) and the $2^-;0$ (8.87 MeV) states are very poor. The predicted energies are 15.97 MeV and 12.67 MeV respectively, and hence they are not shown in Fig. 8.9.

A complete $2\hbar\omega$ calculation, using the MK3W interaction was performed for the positive parity spectrum of ^{16}O also. This calculation placed

all the excited states above 20 MeV, indicating that $4\hbar\omega$ components are essential to give the correct mixing of $2\hbar\omega$ and $4\hbar\omega$ components even when solely a $2\hbar\omega$ interaction is involved. Indeed, such mixing brings down the energy of the states to give agreement with experiment [200].

9. ELECTRON SCATTERING: OPERATORS AND OBSERVABLES

9.1. Introduction

While NA scattering is a probe of the matter density of the target nucleus, electron-nucleus scattering gives information about the nuclear charge and current densities. Hence the two processes are complementary. With nucleonic models of structure, analyses of electron and of nucleon scattering from a nucleus involve the same OBDME. However, the interaction between the electron and the nucleus is known exactly. Therefore an analysis of electron scattering can provide a stringent test of nuclear wave functions prior to their use in NA scattering analyses. Indeed to show that is the objective of this chapter. Thus we concentrate on select results and select structure models that have been used in generation of NA optical potentials. This is not a review of the very extensive literature on the topic.

The differential cross section for electron-nucleus scattering may be expressed in terms of longitudinal and transverse form factors. The longitudinal form factor is related primarily to the charge density of the nucleus, and hence their analyses probe the proton density. There is a small dependence therein on the neutron density through relativistic corrections. Analyses of the transverse form factors, on the other hand, probe both the proton and neutron current densities. Hence, analysis of a complete set of form factors for a given nucleus gives an indication of the propriety of the matter density description of that nucleus as obtained from a structure model.

9.2. Form Factors

In the Born approximation, the differential cross section for an electron of energy ϵ_1 scattering from a nucleus is given by [204]

$$\frac{d\sigma}{d\Omega} = \frac{Z^2 \sigma_M}{[1 + 2\epsilon_1 \sin^2(\theta/2)/M_T]} \left\{ \left[\frac{q_\mu^2}{q^2} \right]^2 |F^L(q)|^2 + \left[\frac{q_\mu^2}{2q^2} + \tan^2 \frac{\theta}{2} \right] |F^T(q)|^2 \right\} \quad (9.1)$$

where with σ_M = being the Mott cross section, $q_\mu = (\mathbf{q}, \omega)$ being the four-momentum transfer to the nucleus, and $q = |\mathbf{q}|$, $|F^L(q)|^2$ and $|F^T(q)|^2$ are the longitudinal and transverse form factors that may be expressed as [204],

$$|F^L(q)|^2 = \frac{1}{2J_i + 1} \left(\frac{4\pi}{Z^2} \right) \sum_{J_f=0}^{\infty} |\langle J_f | \hat{M}_J(q) | J_i \rangle|^2, \quad (9.2)$$

and

$$|F^T(q)|^2 = \frac{1}{2J_i + 1} \left(\frac{4\pi}{Z^2} \right) \sum_{J_f=1}^{\infty} \{ |\langle J_f | \hat{T}_J^{el}(q) | J_i \rangle|^2 + |\langle J_f | \hat{T}_J^{mag} | J_i \rangle|^2 \}. \quad (9.3)$$

The scale $4\pi/Z^2$ is included to ensure that the elastic scattering form factor equals unity at zero momentum transfer. For transitions with a unique angular momentum transfer the sums in Eqs. (9.2) and (9.3) reduce to a single term whence

$$|F^L(q)|^2 = \frac{1}{2J_i + 1} \left(\frac{4\pi}{Z^2} \right) |\langle J_f | \hat{M}_J(q) | J_i \rangle|^2, \quad (9.4)$$

and

$$|F^T(q)|^2 = \frac{1}{2J_i + 1} \left(\frac{4\pi}{Z^2} \right) \{ |\langle J_f | \hat{T}_J^{el}(q) | J_i \rangle|^2 + |\langle J_f | \hat{T}_J^{mag} | J_i \rangle|^2 \}. \quad (9.5)$$

For $J = 0$ only the longitudinal form factor is non-zero.

The operators are one body in character. If a cofactor expansion is taken of the nuclear states, then the reduced matrix elements separate as

$$\langle \Psi_{J_f} | \hat{T}_J^\eta(q) | \Psi_{J_i} \rangle = \frac{1}{\sqrt{2J+1}} \text{Tr}(SM) \quad (9.6)$$

where $\eta = 1, 2, 3$ labels the longitudinal, transverse electric, and transverse magnetic operators respectively, while S and M are the matrices containing the OBDME and the one-body transition matrix elements respectively. Formally, the one-body transition matrix elements are defined as

$$M_{J_f J_i} = \langle \varphi_{j_2} | \hat{T}_J^\eta(q) | \varphi_{j_1} \rangle, \quad (9.7)$$

in which the operators are

$$\hat{M}_{JM}(q) = \int d^3r M_{JM}(qr) \rho(r), \quad (9.8)$$

$$\hat{T}_{JM}^{el}(q) = \frac{1}{q} \int d^3r \{\nabla \times M_{jj}^M(qr)\} \cdot j(r), \quad (9.9)$$

and

$$\hat{T}_{JM}^{mag}(q) = \int d^3r M_{jj}^M(qr) \cdot j(r) \quad (9.10)$$

wherein the functions $M_{JM}(qr)$ and $M_{jL}^M(qr)$ are defined by

$$\begin{aligned} M_{JM}(qr) &= j_J(qr) Y_{JM}(\Omega_r) \\ M_{jL}^M(qr) &= j_L(qr) Y_{jL}^M(\Omega_r). \end{aligned} \quad (9.11)$$

The operators defined by Eqs. (9.8), (9.9), and (9.10) depend on the nuclear charge density $\rho(r)$ and the nuclear three-current density $j(r)$.

Usually, the one-body approximation is taken for the charge and current densities as the inclusion of higher order terms is not straightforward. At the two-body level, for example, a description of all meson exchange currents (MEC) is required with specific calculations necessary in the case of the transverse magnetic form factor. Their inclusion in the calculation of form factors requires two-body density matrix elements from the model of structure. A review of MEC is beyond the scope of this article but a comprehensive one has been made by Riska [205].

In the case of the transverse electric form factor, there is an alternative which does not require a specific description for the two-body current. Siegert [206] proposed replacing, in the long wavelength limit, the transverse electric current multipoles with the time derivatives of the electric charge multipoles. This scheme makes use of the continuity equation,

$$\nabla \cdot j(r) = -i[H, \rho(r)], \quad (9.12)$$

where H is the nuclear Hamiltonian. The two-body components of the current are included when the Siegert hypothesis is used as the nuclear Hamiltonian contains the necessary meson-exchange-current terms through the NN interaction [207].

9.2.1. Alternative Forms of the Operator \hat{T}_{JM}^{el}

In the long wavelength limit, the matrix elements of the electric operators can be rewritten in terms of the matrix elements of the charge operator,

$$\begin{aligned}\hat{T}_{JM}^{el}(q) &\xrightarrow[q \rightarrow 0]{} \frac{i}{q} \sqrt{\frac{J+1}{J}} \int d^3r [\nabla M_{JM}(qr)] \cdot j(r) \\ &= -\frac{i}{q} \sqrt{\frac{J+1}{J}} \int d^3r M_{JM}(qr) \nabla \cdot j(r).\end{aligned}$$

Using current conservation, to leading order in q ,

$$\langle f | \hat{T}_J^{el}(q) | i \rangle = \frac{E_i - E_f}{q} \sqrt{\frac{J+1}{J}} \langle f | \hat{M}_J(q) | i \rangle. \quad (9.13)$$

Thus, in the long wavelength limit, the matrix elements of the transverse electric operator can be replaced with the matrix elements of the charge operator. However, this only works for low energy real photon processes. It does not apply to higher momentum transfers. But it is possible to obtain an alternative form to $\hat{T}_J^{el}(q)$ that not only has the long wavelength behavior of Eq. (9.13) but also retains the high- q behavior of the original expression, Eq. (9.9). Using the identity,

$$\frac{1}{q} \nabla \times \mathbf{M}_{JJ}^M(qr) = i \sqrt{\frac{J+1}{J}} \frac{1}{q} \nabla M_{JM}(qr) - i \sqrt{\frac{2J+1}{J}} \mathbf{M}_{JJ+1}^M(qr), \quad (9.14)$$

and current conservation, gives

$$\begin{aligned}\langle f | T_J^{el'}(q) | i \rangle &= \frac{E_i - E_f}{q} \sqrt{\frac{J+1}{J}} \langle f | \hat{M}_J(q) | i \rangle \\ &\quad - i \sqrt{\frac{2J+1}{J}} \int d^3r \langle f | \mathbf{M}_{JJ+1}^M(qr) \cdot \mathbf{j}(r) | i \rangle.\end{aligned} \quad (9.15)$$

An effective operator then can be written [208] as

$$I_{JM}^{el'}(q) = \frac{E_i - E_f}{q} \sqrt{\frac{J+1}{J}} \hat{M}_J(q) - i \sqrt{\frac{2J+1}{J}} \int d^3r \mathbf{M}_{JJ+1}^M(qr) \cdot \mathbf{j}(r), \quad (9.16)$$

with the understanding that this equation is valid when matrix elements are taken. This new form for the transverse electric operator is exactly equivalent to the first form, Eq. (9.9), if matrix elements are evaluated between exact many-body wave functions for which the current is conserved [208].

The question of extending the Siegert hypothesis to arbitrary wavelength has been addressed by Friar and Fallieros [209]. Considering the case of the retarded electric field and performing a multipole analysis of the operators, they obtained [208].

$$\begin{aligned}\hat{T}_{JM}^{el}(q) = & \sqrt{\frac{J+1}{J}} \frac{E_i - E_f}{q} \int d^3r \frac{(qr)^J}{(2J+1)!!} Y_{JM}(\Omega_r) \rho(r) g_J(qr) \\ & + \frac{2q}{2J+2} \int d^3r \frac{(qr)^J}{(2J+1)!!} Y_{J_1 M}^*(\Omega_r) \cdot \mu(\rho) h_J(qr),\end{aligned}\quad (9.17)$$

with

$$\begin{aligned}g_J(z) = & \frac{J(2J+1)!!}{z^J} \int_0^z \frac{j_J(y)}{y} dy = 1 - \frac{Jz^2}{2(J+2)(2J+3)} + \dots, \\ h_J(z) = & -\frac{J+2}{J} \frac{1}{z} \frac{d}{dz} \frac{1}{z^{2J}} \frac{d}{dz} [z^{2J+1} g_J(z)] = 1 - \frac{(J+2)z^2}{2(J+4)(2J+3)} + \dots,\end{aligned}$$

and

$$\mu(\mathbf{r}) \equiv \frac{1}{2} \mathbf{r} \times \mathbf{j}(\mathbf{r}).$$

Again, the equations are valid when matrix elements are taken. This prescription is fully equivalent to the other forms, Eqs. (9.9) and (9.16), when exact many-body wave functions and exact eigenvalues are used. In this case, the nuclear three-current enters explicitly only through the magnetic moment density. Also, the form given is unique. All components of the electric operator that are constrained by current conservation have been identified and expressed in terms of multipoles of the charge density [208]. Friar and Fallieros [209] and Friar and Haxton [208] suggest that $\hat{T}_{JM}^{el''}(q)$ be used in favor of the other two operators as the current is constrained for all momentum transfer.

9.2.2. One-Body Operators

In principle, the charge and the current densities $\rho(\mathbf{r})$ and $\mathbf{j}(\mathbf{r})$ contain 1-, 2-, up to A -body components. However, even at the two-body level, there is difficulty in defining the operators. To do so requires a complete specification of all two-body meson-exchange currents contributing to the total current. As an aside, the inclusion of such currents does not necessarily guarantee that current conservation will be satisfied [208]. The approximations involved in obtaining model-dependent nuclear wave functions means that such wave functions are not eigenfunctions of the actual nuclear Hamiltonian. Hence current conservation will not be satisfied when they are used to form the matrix elements of Eq. (9.12).

To make computation of form factors practical, issues of violation of conservation of the total nuclear current notwithstanding, the one-

body approximations to the charge and current operators are taken [204],

$$\rho(\mathbf{r}) = \sum_{k=1}^A \delta(\mathbf{r} - \mathbf{r}_k) \frac{1}{2} [F_1^{(0)} + F_1^{(1)} \tau_3(k)], \quad (9.18)$$

and

$$\begin{aligned} j(\mathbf{r}) = & \sum_{k=1}^A \left\{ \left[\frac{1}{i} \frac{\nabla(k)}{M} \delta(\mathbf{r} - \mathbf{r}_k) \right]_{\text{sym}} \frac{1}{2} [F_1^{(0)} + F_1^{(1)} \tau_3(k)] \right. \\ & \left. + \frac{\nabla}{2M} \times [\boldsymbol{\sigma}(k) \delta(\mathbf{r} - \mathbf{r}_k)] \frac{1}{2} [\mu^{(0)} + \mu^{(1)} \tau_3(k)] \right\}. \end{aligned} \quad (9.19)$$

For low momentum transfers $q < 5 \text{ fm}^{-1}$, the single nucleon form factors $F_1^{(0,1)}$ and $\mu^{(0,1)}$ are given by

$$F_1^{(T)} = F_1^{(T)}(0) f_{SN}(q_\mu^2), \quad T = 0, 1,$$

and

$$\mu^{(T)} = \mu^{(T)}(0) f_{SN}(q_\mu^2), \quad T = 0, 1$$

with

$$\begin{aligned} F_1^{(T)}(0) &= 1 \\ \mu^{(0)}(0) &= \mu^s = \mu_p + \mu_n \\ \mu^{(1)}(0) &= \mu^v = \mu_p - \mu_n \end{aligned}$$

and

$$f_{SN}(q_\mu^2) = \left[1 + q_\mu^2 / (855 \text{ MeV})^2 \right]^{-2}.$$

Therein $\mu_p = 2.709 \mu_N$ and $\mu_n = -1.98 \mu_N$ are the proton and neutron magnetic moments respectively. Their substitution in Eqs. (9.9), (9.16), and (9.17) gives the corresponding one-body operators. The bare result is

$$T_{JM}^{(0,1)}(q) = f_{SN}(q_\mu^2) \frac{q}{2M} \sum_{k=1}^A \left\{ \Delta'_{JM}(k) [1 + \tau_3(k)] + \sum_{JM}(k) \frac{1}{2} [\mu^s + \mu^v \tau_3(k)] \right\}, \quad (9.20)$$

where

$$\Delta'_{JM}(k) = \left[-\sqrt{\frac{J}{2J+1}} \mathbf{M}_{J+1}^M(q\mathbf{r}_k) + \sqrt{\frac{J+1}{2J+1}} \mathbf{M}_{J-1}^M(q\mathbf{r}_k) \right] \cdot \frac{1}{q} \nabla(k), \quad (9.21)$$

and

$$\sum_{JM}(k) = \mathbf{M}_{JJ}^M(qr_k) \cdot \boldsymbol{\sigma}(k). \quad (9.22)$$

The Friar and Haxton form is

$$\begin{aligned} T_{JM}^{el(1)}(q) = f_{SN}(q_\mu^2) & \left\{ \sqrt{\frac{J+1}{J}} \left[\frac{q}{2M} + \frac{E_i - E_f}{q} \right] \sum_{k=1}^A M_{JM}(k) \frac{1}{2} [1 + \tau_3(k)] \right. \\ & + \frac{q}{2M} \sum_{k=1}^A \left\{ \frac{2J+1}{J} \Delta''_{JM}(k) [1 + \tau_3(k)] \right. \\ & \left. \left. + \sum_{JM}(k) \frac{1}{2} [\mu^s + \mu^v \tau_3(k)] \right\} \right\}, \end{aligned} \quad (9.23)$$

where

$$\Delta''_{JM}(k) = -\sqrt{\frac{J}{2J+1}} \mathbf{M}_{JJ+1}^M(qr_k) \cdot \frac{1}{q} \nabla(k), \quad (9.24)$$

while the Friar and Fallieros result is

$$\begin{aligned} T_{JM}^{el(1)}(q) = f_{SN}(q_\mu^2) & \left\{ \sqrt{\frac{J+1}{J}} \frac{E_i - E_f}{q} \sum_{k=1}^A M_{JM}^g(k) \frac{1}{2} [1 + \tau_3(k)] \right. \\ & + \sqrt{\frac{J(J+1)}{J+2}} \frac{q}{2M} \sum_{k=1}^A M_{JM}^h(k) \frac{1}{2} [1 + \tau_3(k)] \\ & + \frac{2J+3}{J+2} \frac{q}{M} \sum_{k=1}^A \Delta''_{JM}(k) \frac{1}{2} [1 + \tau_3(k)] \\ & \left. + \frac{q}{2M} \sum_{k=1}^A \sum_{JM}(k) \frac{1}{2} [\mu^s + \mu^v \tau_3(k)] \right\}, \end{aligned} \quad (9.25)$$

where

$$M_{JM}^g(k) = \frac{(qr_k)^J}{(2J+1)!!} g_J(qr_k) Y_{JM}(\Omega_k),$$

$$M_{JM}^h(k) = \frac{(qr_k)^J}{(2J+1)!!} h_J(qr_k) Y_{JM}(\Omega_k),$$

and

$$\Delta''_{JM}(k) = -\frac{(qr_k)^{J+1}}{(2J+3)!!} h_J(qr_k) \frac{1}{\sqrt{2J+1}} \\ [\sqrt{J} Y_{J+11}^M(\Omega_k) + \sqrt{J+1} Y_{J-11}^M(\Omega_k)] \cdot \frac{\nabla(k)}{q}.$$

For simplicity hereafter, the multipole subscripts, mark (1) superscript, and momentum transfer variable will be omitted in references to the *one-body forms* of the transverse electric operators, leaving them as T^{el} , $T^{e\prime l}$, and $T^{e\prime\prime l}$ respectively.

From the definitions of T^{el} , $T^{e\prime l}$, and $T^{e\prime\prime l}$, it is clear that only those wave functions which are eigenfunctions of a Hamiltonian describing a system of particles in which there are no interactions will conserve current. Whatever one of the three one-body operators is used, the same transverse electric form factor will result because the T^{el} contain only one-body components of the nuclear current operator.

While it has been suggested that $\hat{T}_{JM}^{el}(q)$ be used for calculations of form factors, there is a problem in application of the corresponding one-body form T^{el} . Friar and Haxton [208] in an analysis of the isoscalar $E2$ (4.44 MeV) and isovector $E2$ (16.11 MeV) transitions in ^{12}C found that a non-physical singularity was introduced into the calculation at high momentum transfer, manifesting as an anomalously high form factor. By integrating the continuity equation, the convection current becomes

$$\mathbf{j}_c = i[H, \mathbf{d}(\mathbf{r})], \quad (9.26)$$

where

$$\mathbf{d}(\mathbf{r}) = \frac{\hat{r}}{r^2} \int_r^\infty z^2 dz \rho(\hat{r}z). \quad (9.27)$$

Thus a singularity is introduced at $r = 0$ in the Siegert-like part of the current operator \mathbf{j}_c . If wave functions which satisfy current conservation are used, this singularity is canceled by a corresponding term in the magnetic moment current density. Only in that case do Friar and Haxton suggest use of T^{el} . With the modified operator forms, the influence of remaining MEC corrections required is not large. That was shown explicitly in calculations of the forward photo-disintegration of the deuteron [210].

It is usual to apply a relativistic correction, the Darwin term, in calculations of the longitudinal form factor. That term normally is applied by modifying the one-body charge density [211] in the longitudinal multipole operator to

$$\rho(\mathbf{r}) = \left[1 + \frac{q^2}{8m^2} \right] \sum_{i=1}^A \frac{1}{2} [1 + \tau_3^i] \delta(\mathbf{r} - \mathbf{r}_i) - 2 \left(\frac{q^2}{8m^2} \right) \sum_{i=1}^A \left\{ \mu_p \frac{1}{2} [1 + \tau_3^i] \delta(\mathbf{r} - \mathbf{r}_i) + \mu_n \frac{1}{2} [1 - \tau_3^i] \delta(\mathbf{r} - \mathbf{r}_i) \right\}, \quad (9.28)$$

where m is the nucleon mass. With this modification, the longitudinal multipole operator then contains the magnetic moments of the nucleons and so is no longer simply formed from the charge operator. The results we display hereafter were obtained from calculations of the longitudinal form factor made using this modified form.

9.3. Results

Longitudinal and transverse electric form factors from electron scattering to select states in $^{3,4}\text{He}$, the $0p$ shell nuclei $^{6,7}\text{Li}$ and ^{12}C , and to the $2_1^+; 0^-$ states in ^{20}Ne , ^{24}Mg , and ^{28}Si are reported. A particular role of the form factor analyses discussed is to validate models of structure that have been proposed for the $0p$ -shell nuclei and of their wave functions. However, and as described above, there is a question about the proper interaction operator one should use in analyses of the transverse electric form factors. Thus first the $E2$ excitations of $2_1^+; 0^-$ states in the $N = Z$ sd -shell nuclei are considered. Subsequently the results of analyses of diverse form factors of the He isotopes and $0p$ -shell nuclei are discussed.

9.3.1. $E2$ Form Factors with sd -Shell Nuclei

Calculations of the longitudinal and transverse electric multipoles for the $0^+ \rightarrow 2_1^+; 0^-$ states in ^{20}Ne , ^{24}Mg , and ^{28}Si are discussed. The structure of these nuclei have been specified using the complete $0\hbar\omega$ sd -shell model space. The spectra, wave functions, and OBDME were calculated using the OXBASH program with the USD interaction of Brown and Wildenthal [212]. They have also been found by using the PHF wave functions of Ford *et al.* [213].

The results of calculations [214] of the longitudinal $E2$ form factor to the 1.37 MeV state in ^{24}Mg made using both the sd -shell model and PHF wave functions are compared in Fig. 9.1 with the data of Hotta *et al.* [215]. The difference between the results found using the two model prescriptions is noticeable. Both the magnitude and the shape of the form factor is reproduced by the calculation made using the PHF OBDME. In contrast, the sd -shell model calculation underestimates the data by a

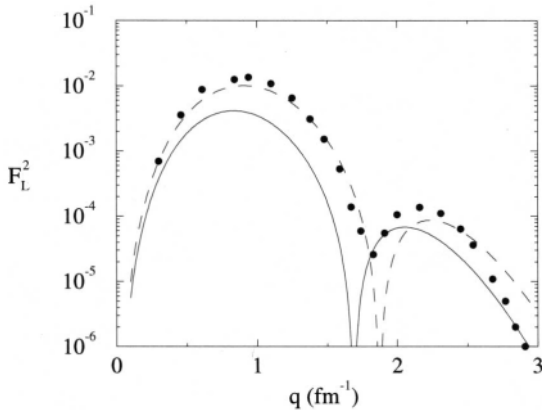


Fig. 9.1. The longitudinal $E2$ form factor for the $0^+ \rightarrow 2^+; 0$ (1.37 MeV) transition in ^{24}Mg . The data of Hotta *et al.* [215] are compared with the results of calculations made using sd -shell model and PHF wave functions that are shown by the solid and dotted curves respectively.

factor of 3, and does not give the minimum at the correct momentum transfer value.

The situation with the transverse electric form factor for this excitation in ^{24}Mg is even more dramatic. In Fig. 9.2(a) the transverse form factors calculated using the sd -shell model wave functions are shown while in Fig. 9.2(b) those found using the PHF OBDME are displayed. In each case, form factors have been calculated using the T^{el} , $T^{el''}$, and $T^{el'''}$ operators and the results are displayed by the solid, dotted, and dashed lines respectively. The effect of using the different operator forms with the sd -shell model wave functions is very marked. Good comparison with data at low q is obtained only by using the modified operator forms, either $T^{el''}$ or $T^{el'''}$. Agreement between the calculations using these two operators at low q is to be expected as both explicitly constrain the current via conservation in this regime. However, the calculation using the $T^{el'''}$ operator overestimates the data and is in severe disagreement with the other calculations above $q = 1.5 \text{ fm}^{-1}$. This is attributable to the singularity and is an effect noted [208] also in analyses of the transverse $E2$ form factors ^{12}C .

With the large basis PHF wave functions however, all three operators give essentially the same form factor at low q . The result at low q when using the bare T^{el} operator is similar to those obtained when the modified operator forms are used with the sd -shell model wave

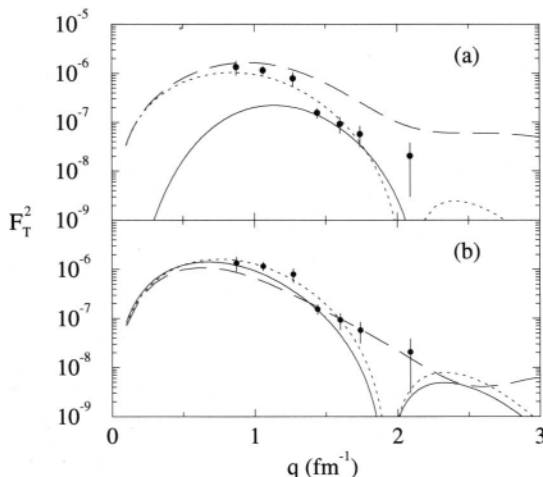


Fig. 9.2. The transverse $E2$ form factor for the $0^+ \rightarrow 2^+; 0$ (1.37 MeV) transition in ^{24}Mg . The data of Hotta *et al.* [215] are compared with results of calculations made using the $T^{el'}$ operator (solid line), $T^{el''}$ operator (dotted line) and $T^{el'''}\text{operator}$ (dashed line). (a) Results found using sd -shell model wave functions. (b) Results found using PHF wave functions.

functions. It seems that one-body current conservation is satisfied quite well by the PHF functions. The low- q agreement with these and the sd -shell model calculations made using $T^{el''}$ indicate that the currents accommodated by $T^{el''}$ are almost entirely from excitations between major shells. Note also that the results found using the PHF OBDME in the calculation with $T^{el''}$ are in very good agreement with the data. The role of the singularity is lessened therein as could be expected. However, the PHF wave functions still describe a system of interacting particles and so the one-body current is not conserved. The results indicate that the violation is not large.

The three transverse electric operators were used in calculations of isoscalar $E2$ form factors for excitation of the $2^+; 0$ (1.63 MeV) state in ^{20}Ne . The results of those calculations are shown in Fig. 9.3. The solid curves therein are the sd -shell model calculations and the dashed curves are those found using the PHF wave functions [214]. As was the case of ^{24}Mg , in comparison to the results obtained with the sd -shell model functions, use of the PHF OBDME for ^{20}Ne effects a redistribute of some strength within the sd -shell. But core polarization effects are very important and they are represented here by single nucleon excitations not constrained to the sd -shell model space.

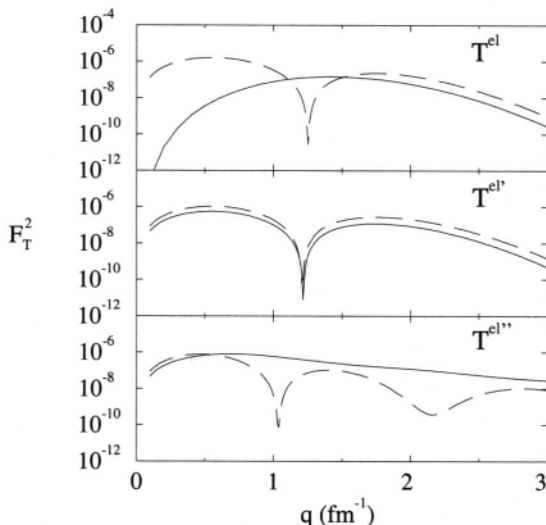


Fig. 9.3. Calculated results for the transverse $E2$ form factor for the $0^+ \rightarrow 2^+$; $0(1.63\text{ MeV})$ transition in ${}^{20}\text{Ne}$. The solid and dashed curves are for the sd -shell model and PHF wave functions [214] respectively. The operators used are as indicated.

Using the bare T^{el} operator gives a dramatic difference between the sd -shell model and the PHF model results. The effect of core polarization is to introduce a minimum in the form factor at $q = 1.25\text{ fm}^{-1}$. Such is not present in the result found using the sd -shell model wave functions. This minimum is present in the results of both calculations when the $T^{el'}$ operator is used however. In this case the discerning effect of core polarization is small. The similarity between these results and that found using the T^{el} operator with PHF wave functions indicates that the $T^{el'}$ operator compensates for deficiencies in the sd -shell model wave functions. Again, it is evident that the sd -shell model wave functions do not conserve the one-body nuclear current. But the similarities between all three calculations at low q using the PHF wave functions suggest that current conservation is nearly satisfied. However, unlike the calculations using T^{el} and $T^{el'}$, there is a second minimum at $q = 2.2\text{ fm}^{-1}$ in the form factor calculated using $T^{el''}$. This is due to cancellation occurring between contributions from the diverse terms in Eq. (9.25) at this value of momentum transfer. The small differences between the calculations in this region are again due to the fact that wave functions describing a system of interacting nucleons are being used.

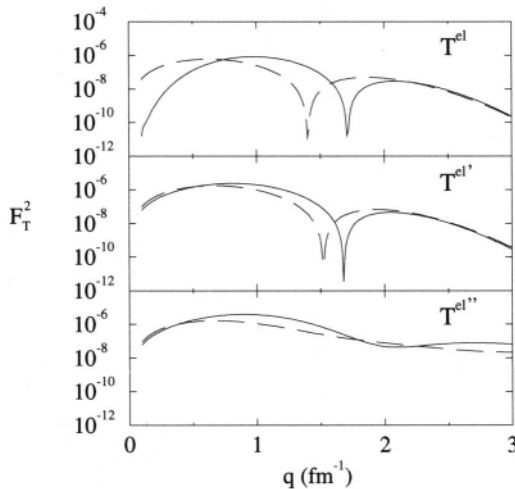


Fig. 9.4. Calculated results for the transverse $E2$ form factor for the $0^+ \rightarrow 2^+; 0$ (**1.78 MeV**) transition in ^{28}Si . The curves presented are as for Fig. 9.3, and the operators used are as indicated.

Because of the major differences between the standard calculation using the T^{el} operator and the sd -shell wave functions and those calculations using the other operators or the PHF wave functions, a measurement of this form factor would help in determining the validity of the various forms of the transverse electric operator available for practical calculations.

The results of the calculations of the transverse $E2$ form factor for ^{28}Si are displayed in Fig. 9.4 wherein the solid curves are those results obtained using the sd -shell model wave functions [214]. The dashed curves are the results obtained using the PHF wave functions [139]. A minimum is present in this transverse $E2$ form factor for ^{28}Si , when calculated using either the T^{el} or $T^{el''}$ operators and irrespective of which model structure is used. There are sharp differences however when $T^{el'}$ is used. The minimum is no longer present, apart from a slight dip in the results of the calculation made using the sd -shell model wave functions. This would indicate that the PHF wave functions for ^{28}Si are not as good in conservation of the one-body current as they are for ^{20}Ne and ^{24}Mg . A measurement of this form factor would also be desirable in determining the relative merits of the one-body transverse electric operators. The differences here are mainly in the position of the minimum and the

orders of magnitude difference at low- q between the results found using sd -shell model and the PHF wave functions with the $T^{\ell\ell}$ operator.

9.3.2. Few-Body Systems: $^{3,4}\text{He}$

The best description so far possible of these highly correlated systems come from the solutions of the Faddeev and Faddeev-Yakubovsky equations. Within the context of the shell model, these correlations arise as one admits **higher- $\hbar\omega$** excitations into the **$0\hbar\omega$** shell model space [188]. The convenience of shell model wave functions in scattering analyses makes it useful therefore to investigate how well the shell model does for both nuclei in **multi- $\hbar\omega$** model spaces. Electron scattering form factors serve that purpose.

The shell model approach to the structure of $^{3,4}\text{He}$ has been actively pursued recently and the results have been summarized in Chapter 8. Analyses of the electron scattering form factors have been made using the shell model wave functions from $4\hbar\omega$ and $8\hbar\omega$ model spaces [216]. Those results are presented in Fig. 9.5. It is evident from these results that, with the one-body impulse approximation (IA), the form factors are well reproduced up to 3 fm^{-1} . Beyond that the shell model fails to

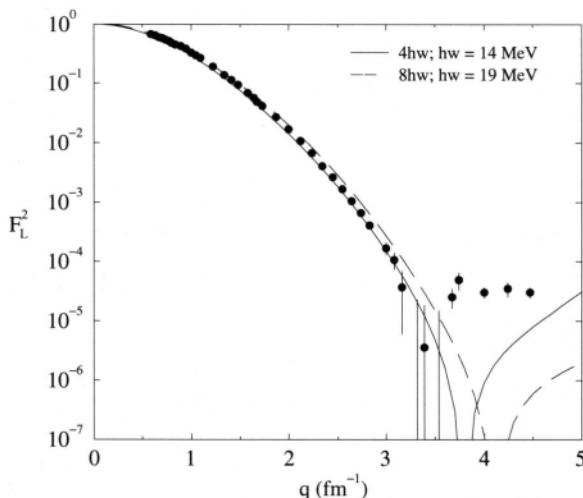


Fig. 9.5. Longitudinal elastic form factor for the scattering of electrons from ^3He . The data of Arnold *et al.* [217], Collard *et al.* [218], and McCarthy *et al.* [219, 220] are compared with the results obtained using the $4\hbar\omega$ and $8\hbar\omega$ model space wave functions.

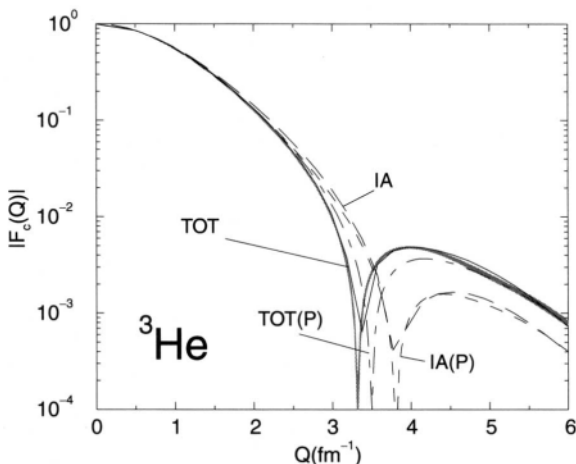


Fig. 9.6. As for Fig. 9.5, but showing the results of Carlson and Schiavilla [221] (reproduced with the kind permission of the authors). The shaded region indicates the data.

account for the magnitude of the form factor. MEC corrections then are needed. That is evident from the analyses of the form factors using Faddeev wave functions [221]. The results are presented in Fig. 9.6. Therein, the results obtained using MEC corrections are denoted by TOT.

The magnetic form factor of the ground state is related to the transverse form factor by [222]

$$F_M(q) = \sqrt{2} \frac{\mu_N}{\mu} \frac{F_T(q)}{q}, \quad (9.29)$$

where μ is the magnetic moment of the nucleus in units of μ_N . That magnetic form factor is displayed in Fig. 9.7 wherein the data [223, 224, 225] are compared with the results found using the $4\hbar\omega$ and $8\hbar\omega$ shell model wave functions. It is clear that the $8\hbar\omega$ model predicts the form factor better than does the $4\hbar\omega$ one. That is a consequence of the additional correlations taken in the $8\hbar\omega$ calculation. However, both models fail at low q where large scale correlations are expected to be most important. Still higher $\hbar\omega$ excitations need be included to explain that low- q data.

Those results using the traditional shell model are to be compared with those obtained using the Faddeev wave functions [221]. The latter

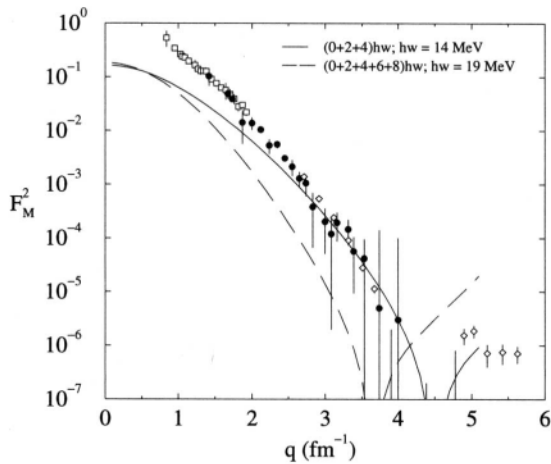


Fig. 9.7. Magnetic form factor for the scattering of electrons from ${}^3\text{He}$. The data of Refs. [223, 224, 225] are compared with the calculations using the $4\hbar\omega$ and $8\hbar\omega$ wave functions as portrayed by the dashed and solid lines respectively.

are shown in Fig. 9.8. Therein all curves converge to the value one at $q = 0$ as they should given the definition of the magnetic form factor. That this behavior is not apparent in the results of calculations made using the shell models indicates that there is not enough correlations in those models. However, the Faddeev (IA) result falls below the data above 1 fm^{-1} and explicit MEC are required with that model to repro-

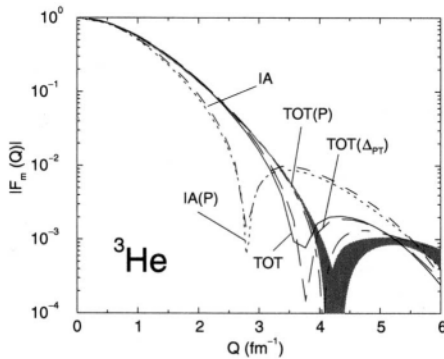


Fig. 9.8. As for Fig. 9.7, but showing the results of Carlson and Schiavilla [221]. The shaded area indicates the data. (Reproduced with the kind permission of the authors.)

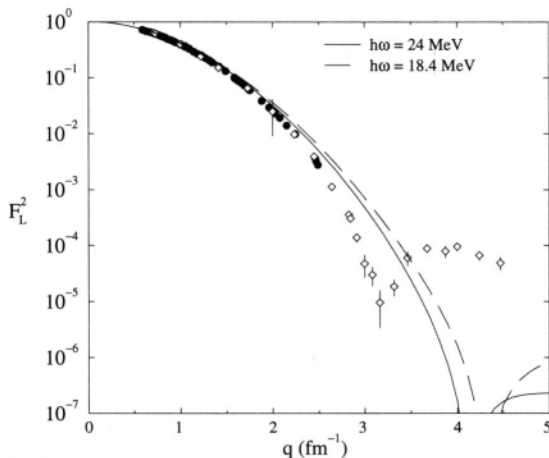


Fig. 9.9. Elastic electron scattering form factor for ${}^4\text{He}$. The data of Arnold *et al.* [217] and Frosch *et al.* [226] are compared with the results of the calculations in the IA made using the $4\hbar\omega$ and $8\hbar\omega$ shell model wave functions.

duce the data. Also shown therein is the result obtained by adding within first-order perturbation theory the contribution of the Δ resonance to the calculation. It has a minor effect.

The longitudinal form factor for the scattering of electrons from ${}^4\text{He}$ is shown in Fig. 9.9 wherein the data of Arnold *et al.* [217] and of Frosch *et al.* [226] are compared with the results found in the IA using the shell model wave functions obtained in the $8\hbar\omega$ model space. Two sets of HO single particle (SP) wave functions as specified by the G matrix interaction with $\hbar\omega=18$ and 24 MeV [176, 216] were used. In both cases, the IA calculations overestimate the data. However, the calculations are to be compared with those made using the VMC wave functions [221] and such is shown in Fig. 9.10. Clearly the result obtained using the VMC wave functions also overestimates the data, and the MEC corrections in this case are significant.

9.3.3. ${}^6\text{Li}$ and ${}^7\text{Li}$

Evidence that clusters in the many-body wave functions of ${}^6\text{Li}$ and ${}^7\text{Li}$ can be found with the shell model was presented in Section 8.4.2 and it was determined that the wave functions obtained within the $4\hbar\omega$ model space calculation did not reproduce the observed radii and moments. In

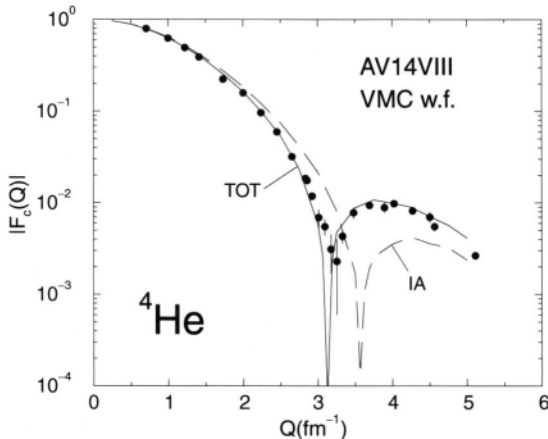


Fig. 9.10. As for Fig. 9.9, but showing the results of Carlson and Schiavilla [221] found from the VMC calculations. (Reproduced with the kind permission of the authors.)

this section, we consider further evidence for clustering obtained from analyses of scattering data. Unless otherwise stated, the results obtained using the $4\hbar\omega$, $2\hbar\omega$, and $0\hbar\omega$ model spaces are given by the solid, dashed, and dot-dashed lines respectively.

The elastic longitudinal electron scattering form factor for ${}^6\text{Li}$ [186] is displayed in Fig. 9.11. Concomitant with the small quadrupole moment of ${}^6\text{Li}$, and as displayed in Fig. 9.11(b), the $C2$ form factor is orders of magnitude smaller than the $C0$ one. The transverse $M1$ form factor is displayed in Fig. 9.11(c). All model results were found using the same SP wave functions that were used in the calculations of the longitudinal form factor. While the magnitudes in all cases are reproduced well, the CK model does not reproduce the position of the minimum. Both the MK3W and Zheng models reproduce that minimum, but only with the Zheng model is the shape of the form factor reproduced at high momentum transfers.

The elastic scattering form factors for ${}^6\text{Li}$ and ${}^7\text{Li}$ were calculated also using the VMC wave functions [231]. The elastic scattering form factor prediction that results for ${}^6\text{Li}$ is displayed in Fig. 9.12. The error bars in those results indicate the statistical uncertainty associated with the Monte Carlo integrations. The calculations reproduce both the longitudinal and transverse form factor data very well, and indicate that the MEC corrections to both form factors are only significant above 3 fm^{-1} .

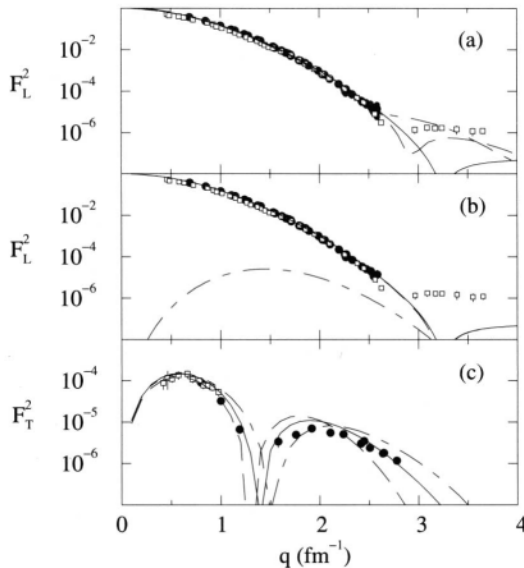


Fig. 9.11. The results of the calculations made for the elastic electron scattering form factors for ${}^6\text{Li}$ [186]. (a) The longitudinal form factor data of Suelzle *et al.* [227] (circles) and Li *et al.* [228] are compared with the results of the calculations made using the Zheng (solid line), MK3W (dashed line), and CK (dot-dashed line) spectroscopies. (b) C_0 (dashed line) and C_2 (dot-dashed line) components contributing to the longitudinal form factor (solid line), (c) The transverse $M1$ form factor data of Bergstrom *et al.* [229] (circles) and Lapikás [230] (squares) are compared with the results of calculations.

The longitudinal inelastic scattering form factor to the $3^+; 0$ (2.185 MeV) state in ${}^6\text{Li}$ [186] is displayed in Fig. 9.13. The form factor, as calculated using all shell models, is dominated by the C_2 component. The C_4 component is negligible. The $2\hbar\omega$ and $4\hbar\omega$ calculations both reproduce the form factor above 1 fm^{-1} as both contain transitions outside of the $0p$ -shell. Such transitions enhance the C_2 strength. However the $B(E2)$ value for the associated γ -decay of this state is $9.31 \pm 2.1 e^2\text{fm}^4$ [177, 233] and the values obtained by all calculations are significantly smaller. This is evidenced in Fig. 9.13(b) wherein the data and calculation results were transformed to display the $B(E2)$ as a function of momentum transfer. That transformation was effected by the prescription of Brown, Radhi, and Wildenthal [236]. Clearly the shell model wave functions including up to $4\hbar\omega$ excitations do not have the correct long range behaviour and it is that region in which clustering effects are

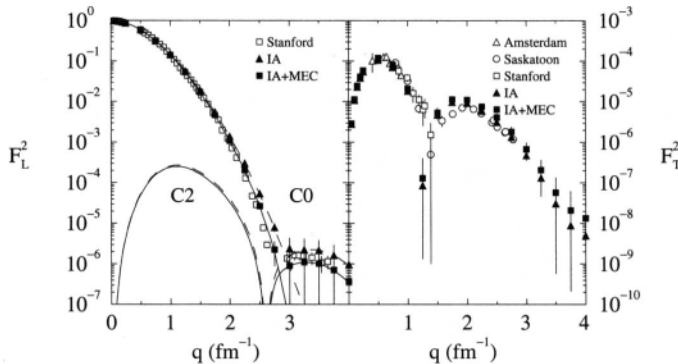


Fig. 9.12. The elastic scattering form factor for ${}^6\text{Li}$ calculated using the VMC wave functions compared with data [231]. The results of calculations made using the IA and IA + MEC are as indicated. (Reproduced with the kind permission of the authors.)

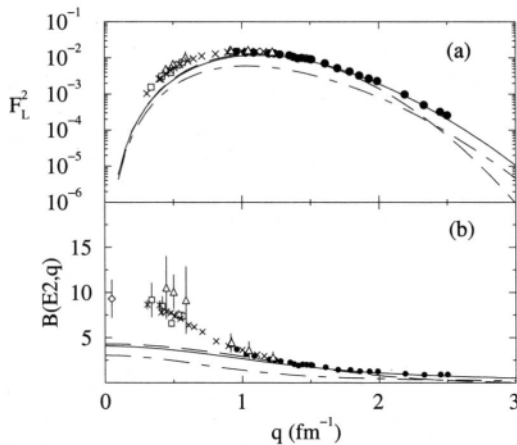


Fig. 9.13. (a) Longitudinal inelastic electron scattering form factor to the 3^+_0 (2.186 MeV) state in ${}^6\text{Li}$, and (b) the $B(E2 \downarrow, q)$ value, in units of $e^2 \text{fm}^4$, as obtained from the form factor [186]. The data of Bergstrom *et al.* [232] (circles), of Yen *et al.* [233] (squares), of Bergstrom and Tomusiak [234] (crosses), and of Hutcheon and Caplan [235] (triangles) are compared with the results of the calculations. The notation is as for Fig. 9.11(a). The $B(E2 \downarrow)$ value from the associated γ decay rate [177] is displayed by the diamond data point in (b).

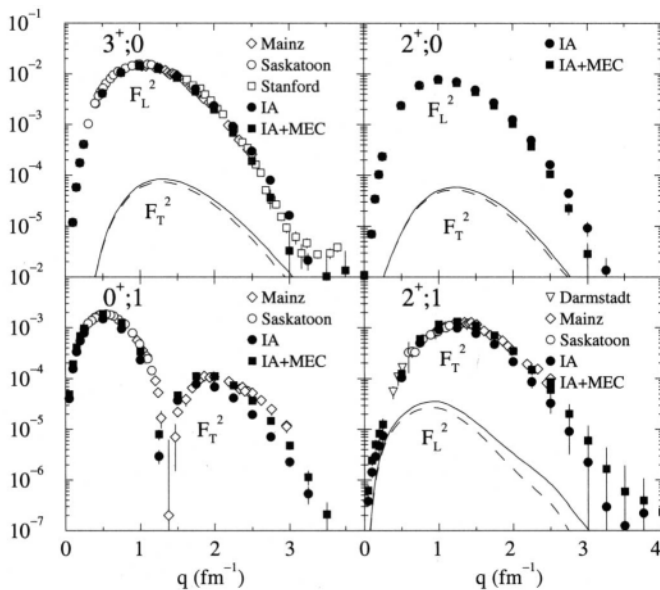


Fig. 9.14. Longitudinal and transverse inelastic electron scattering form factors to the first four excited states of ${}^6\text{Li}$. The data are compared with the IA and IA + MEC results as indicated [231]. (Reproduced with the kind permission of the authors.)

expected to dominate. By comparison, the inelastic scattering form factor to this state is well reproduced for all momentum transfer by results using the VMC wave functions [231] which is displayed in Fig. 9.14. In that respect, the VMC wave functions contain the necessary correlations which give rise to the clustering in ${}^6\text{Li}$.

The transverse $M1$ inelastic electron scattering to the $0^+; 1$ (3.56 MeV) state in ${}^6\text{Li}$ is displayed in Fig. 9.15. Therein the data of Bergstrom *et al.* [232,237] are compared with the results of calculations made using the shell model wave functions [186]. Both the $2\hbar\omega$ and $4\hbar\omega$ model results reproduce the form factor at low momentum transfer and also they give the minimum at 1.4 fm^{-1} . The $0\hbar\omega$ model result, on the other hand, overpredicts the data at low- q and places the minimum at too high a value of momentum transfer. This is to be compared with the results found using the VMC wave functions [231] which are displayed in Fig. 9.14. The IA $4\hbar\omega$ shell model result best compares to that found using the VMC wave functions.

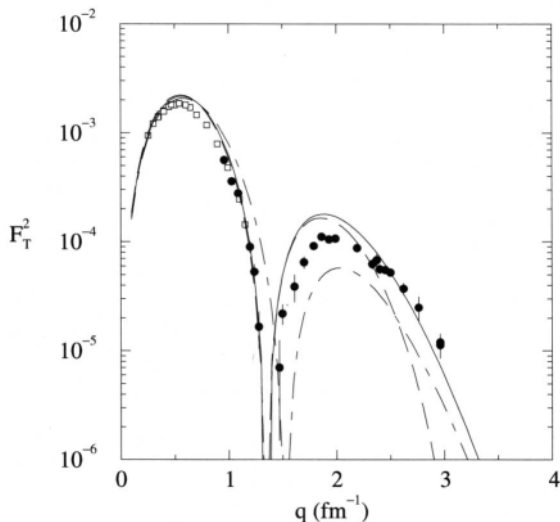


Fig. 9.15. Transverse $M1$ inelastic electron scattering form factor to the $0^+;1$ state in ${}^6\text{Li}$. The data of Bergstrom *et al.* (circles [232] and squares [237]) are compared with the results of the calculations [186] as the notation as for Fig. 9.11(a).

The elastic scattering form factors for ${}^7\text{Li}$ are displayed in Fig. 9.16. Therein, the data of Suelzle *et al.* [227] and of Lichtenstadt *et al.* [238] are compared with the results of calculations made using WS SP wave functions [186]. All the calculations reproduce the form factor, although the data above 3 fm^{-1} allow for some appreciable variation between the models. Unlike the case with ${}^6\text{Li}$, there is a substantial contribution now from the $C2$ component, consistent with the much larger quadrupole moment for ${}^7\text{Li}$. The $C2$ component is displayed in Fig. 9.16(b) from which it is clear that the $C2$ component is necessary to reproduce the data between 2 and 3 fm^{-1} .

The transverse elastic form factor for ${}^7\text{Li}$ is displayed in Fig. 9.16(c). Therein, the data of Lichtenstadt *et al.* [238] and of van Niftrik *et al.* [239] are compared with the results of shell model calculations [186]. All the models predict the form factor up to 2.5 fm^{-1} . At high momentum transfers, the $2\hbar\omega$ model underpredicts the data. However the $0\hbar\omega$ and $4\hbar\omega$ model results are more consistent with that data. The components in the form factor are shown in Fig. 9.16(d). Therein the total, $M1$, and $E2$ components are displayed by the solid, dashed, and dot-dashed lines respectively. The low momentum transfer part of the form factor is

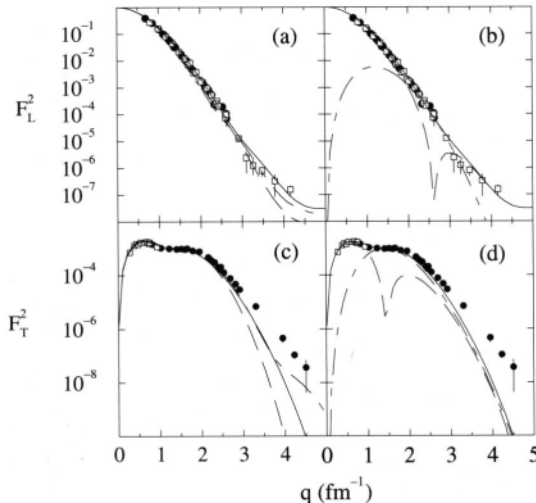


Fig. 9.16. The results of the calculations made for the elastic electron scattering form factors for ${}^7\text{Li}$. (a) The longitudinal form factor data of Suelzle *et al.* [227] (circles) and of Lichtenstadt *et al.* [238] (squares) are compared with the results obtained within the $4\hbar\omega$ (solid line), $2\hbar\omega$ (dashed line), and $0\hbar\omega$ (dot-dashed line) model spaces, (b) C_0 (dashed line) and C_2 (dot-dashed line) components contributing the longitudinal form factor (solid line), as calculated in the $4\hbar\omega$ model, (c) The transverse form factor data of Lichtenstadt *et al.* [238] (circles) and of van Niftrik [239] (squares) are compared with the results obtained as defined in (a). (d) M_1 (dashed line) and E_2 (dot-dashed line) contributions to the total transverse form factor (solid line) as calculated in the $4\hbar\omega$ model.

dominated by the M_1 component while the E_2 is most important between 1 and 3 fm^{-1} . At higher momentum transfer the M_1 and E_2 terms are comparable.

The inelastic scattering form factors to the $\frac{1}{2}^-$ (0.478 MeV) state in ${}^7\text{Li}$ are displayed in Fig. 9.17. In Fig. 9.17(a), the longitudinal form factor data of Lichtenstadt *et al.* [238] and of van Niftrik *et al.* [239] are compared with the results of shell model calculations [186]. The $0\hbar\omega$ shell model result does not reproduce the data. Inclusion of higher $\hbar\omega$ components in the model space yields the necessary strength to do so. But, for $q > 3\text{ fm}^{-1}$, MEC corrections to the charge density operator are required. The $B(E2)$ value for this transition is $16.4\text{ e}^2\text{ fm}^4$ [177]. All models fail to reproduce the measured value [186], again indicating a problem in the long-range behaviour in the shell model wave functions.

This anomaly is in sharp contrast to the analysis of the transverse inelastic form factor transverse data to this state. The results of those

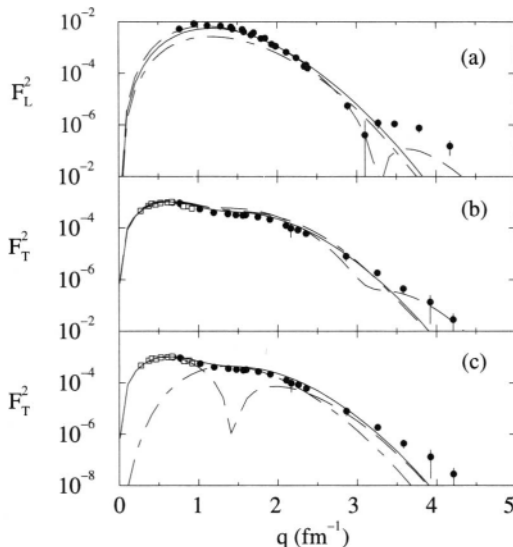


Fig. 9.17. The inelastic electron scattering form factors to the $\frac{1}{2}^-(0.478 \text{ MeV})$ state in ${}^7\text{Li}$. The data of Lichtenstadt *et al.* [238] and of van Niftrik *et al.* [239] (squares) are compared in (a) to the results of the model calculations of the longitudinal form factor, and in (b) to the results of the model calculations of the transverse form factor [186], both defined as in Fig. 9.16(a). The $M1$ (dashed line) and $E2$ (dot-dashed line) components of the total transverse form factor (solid line) [186] are displayed in (c) as calculated in the $4\hbar\omega$ model.

model calculations are compared with the data of Lichtenstadt *et al.* [238] and of van Niftrik [239] in Fig. 9.17(b). All of the model results reproduce the magnitude and shape of this form factor up to 3 fm^{-1} , but with a slight overestimation above 1 fm^{-1} . The relative contributions from the $M1$ and $E2$ components from the $4\hbar\omega$ model calculation are shown in Fig. 9.17(c). The $M1$ component dominates except of the region between 1 and 2 fm^{-1} where it has a minimum. There the $E2$ component gives the important contribution.

The inelastic scattering form factors to the $\frac{1}{2}^-(4.63 \text{ MeV})$ state in ${}^7\text{Li}$ are displayed in Fig. 9.18. The longitudinal inelastic form factor data to this state [235,240,241] are compared with the results of the calculations [186] made using the wave functions in the $0\hbar\omega$, $2\hbar\omega$, and $4\hbar\omega$ model spaces. As with the other calculations of the inelastic scattering form factors, the $0\hbar\omega$ model fails to match the magnitude of the observations. But in this case, inclusion of $2\hbar\omega$ excitations is enough to ensure

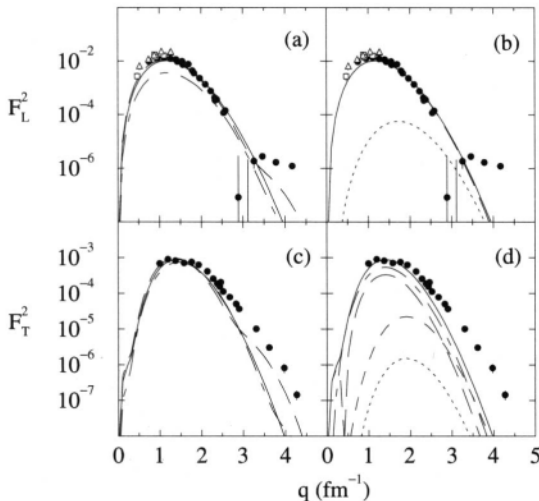


Fig. 9.18. The inelastic electron scattering form factors to the $\frac{7}{2}^{-}$ (4.63 MeV) state in ${}^7\text{Li}$. The longitudinal form factor data of Lichtenstadt *et al.* [240] (circles), Hutcheon and Caplan [235] (squares), and Bernheim and Bishop [241] (triangles) are compared in (a) to the results of the calculations defined in Fig. 9.16(a). The $C2$ (dashed line) and $C4$ (dot-dashed line) components leading the longitudinal form factor (solid line) are displayed in (b) as calculated in the $4\hbar\omega$ model. The transverse form factor data of Lichtenstadt *et al.* [240] are compared in (c) to the results of [186], while in (d) the $E2$, $M3$, $E4$, and $M5$ components, calculated within the $4\hbar\omega$ model, are displayed by the long-dashed, dot-dashed, dotted, and short-dashed lines respectively. The total form factor is given by the solid line.

agreement with the data. Adding $4\hbar\omega$ excitations does not further enhance the form factor prediction as is illustrated in Fig. 9.18(b). The dominance of the $C2$ component of the form factor in the $4\hbar\omega$ model is very evident.

The transverse inelastic scattering form factor to the $\frac{7}{2}^{-}$ state is displayed in Fig. 9.18(c). In this case, all of the calculations reproduce the peak magnitude and position of the form factor data. However all of the results underpredict the data above 2 fm^{-1} . The form factor is dominated by the $M3$ component with the $E2$ component being a factor of two less. That is illustrated in Fig. 9.18(d). The $M5$ form factor is orders of magnitude smaller and, with the $E4$ contribution, may be neglected at low momentum transfer. Above 3 fm^{-1} however, that $M5$ contribution becomes more important than the $E2$ one. MEC effects are then expected to be important.

9.3.4. ^{12}C

Using the PHF wave functions, the calculated $E2$ form factors of ^{24}Mg are in excellent agreement with data. The form factors for all three sd shell nuclei considered also are in agreement whichever form of transition operator is used. The question then is whether such agreement may be obtained also with the wave functions given by multi- $\hbar\omega$ shell model calculations for lighter mass nuclei. To this end, the OBDME for select states in ^{12}C [242] were used in calculations of longitudinal and transverse electric form factors. The elastic scattering was considered first to define the appropriate set of SP wave functions [214]. Two sets of SP wave functions were used, harmonic oscillators (HO) with oscillator length of 1.6 fm and Woods-Saxon (WS) states from a potential of the form

$$V = V_0 \left[1 + \lambda \boldsymbol{\sigma} \cdot \mathbf{l} \left(\frac{\hbar}{m_\pi c} \right)^2 \frac{1}{r} \frac{d}{dr} \right] f(r, R, a), \quad (9.30)$$

where,

$$f(r, R, a) = \frac{1}{1 + \exp\left(\frac{r-R}{a}\right)}, \quad (9.31)$$

with $R = rA^{1/3}$ and parameter values that are listed in Table 9.1. The deeper potential for the $0f1p$ shell was used to ensure that the calculations of the bound state wave functions for these orbitals converged. By so doing, the $0f1p$ orbits are loosely bound, as is evident from the binding energies listed in Table 9.2, but a degree of non-orthogonality is introduced. But orthogonality is guaranteed between states of different angular momenta and the overlap between the $0p$ and $1p$ radial wave functions is zero to within 1 part in 10^{-3} . However, the results studied do not depend strongly on the choice of bound state wave functions. The

TABLE 9.1
Wood, Saxon parameters used for the single particle states in ^{12}C .

	V_0 (MeV)	r_0 (fm)	a_0 (fm)	λ
$0s \rightarrow 1s0d$	-62.5	1.35	0.65	7.0
$0f1p$	-90.0	1.35	0.65	0.0

TABLE 9.2
Binding energies for the single particle states in ^{12}C as calculated from the WS potentials in Table 9.1.

State	E_B (MeV)	State	E_B (MeV)
$0s_{\frac{1}{2}}$	-38.75	$1s_{\frac{1}{2}}$	-5.87
$0p_{\frac{3}{2}}$	-22.37	$0f_{\frac{7}{2}}$	-1.04
$0p_{\frac{1}{2}}$	-20.65	$0f_{\frac{5}{2}}$	-1.07
$0d_{\frac{5}{2}}$	-6.28	$1p_{\frac{3}{2}}$	-3.53
$0d_{\frac{3}{2}}$	-3.58	$1p_{\frac{1}{2}}$	-3.53

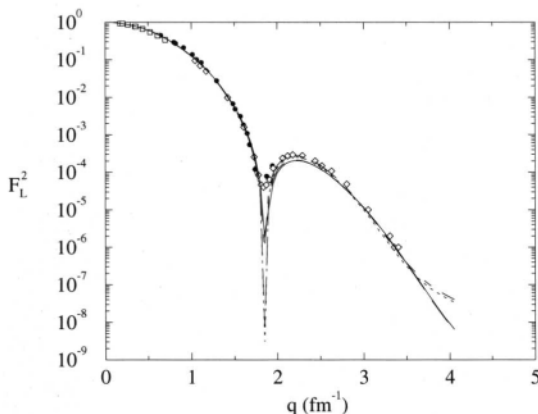


Fig. 9.19. Elastic electron scattering form factor for ^{12}C . The data are those of Jansen *et al.* (squares), of Sick and McCarthy (diamonds) and of Nakada *et al.* (circles). Calculations are with Op-shell wave functions and HO SP functions (solid line) and WS SP functions (dotted line), and with $2\hbar\omega$ wave functions and HO (dashed line) and with WS SP functions (dot-dashed line).

specifics will be important later in studies of scattering of light mass halo nuclei.

The elastic electron scattering form factor for ^{12}C is presented in Fig. 9.19. The data are those of Jansen *et al.* [243] (squares), of Sick and McCarthy [244] (diamonds) and of Nakada *et al.* [245] (circles). Both the $0p$ -shell model wave functions and the $2\hbar\omega$ shell model wave functions have been used in the calculations of the form factors. With both models,

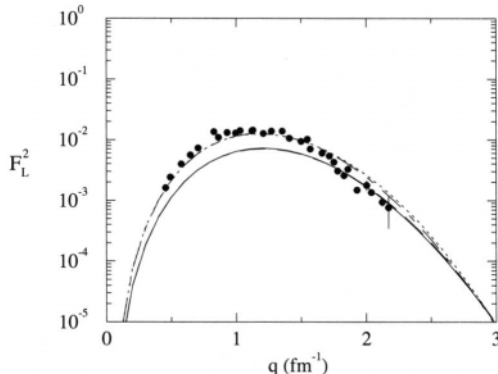


Fig. 9.20. The longitudinal form factor from the isoscalar 2^+ (4.44 MeV) transition in ^{12}C . The data of Flanz *et al.* [246] are compared with the result of the p -shell model calculation, with HO (solid curve) and WS wave functions (dashed curve), and to the result of the calculation made using the full $2\hbar\omega$ shell model wave functions, with HO (dot-dashed curve) and with WS wave functions (dotted curve).

excellent agreement with the data results irrespective of the choice (HO or WS) for the bound states.

The longitudinal $E2$ form factor from electron scattering to the $2^+; 0$ (4.44 MeV) is displayed in Fig. 9.20. Therein the measured longitudinal form factor [246] is compared to the results found from Op-shell model and $2\hbar\omega$ calculations [214]. With the $2\hbar\omega$ structure, it is the inclusion of transitions out of the $0p$ -shell that makes that result be nearly in exact agreement with experiment. The transverse electric form factor from electron scattering to this 2^+ state has also been measured [246] and those data are compared with the results of calculations in Fig. 9.21. Clearly there is a significant improvement in the fit to the data when the T^{el} operator form is used in calculations, irrespective of the assumed nuclear structure. The effect is particularly significant at low q . Then meson exchange effects are not expected to be important so that the T^{el} operator corrects the lack of cross-shell nucleon currents within the Op-shell model. The results found with bigger basis structure input in the calculation are displayed in Fig. 9.21(b). They show that the effect of using the T^{el} operator is not as dramatic now as some of those cross-shell currents have been included explicitly. The variation with operator form is essentially just a scale shift and both calculations reproduce the observed q -dependence. But this shift is not sufficient to fit the measured

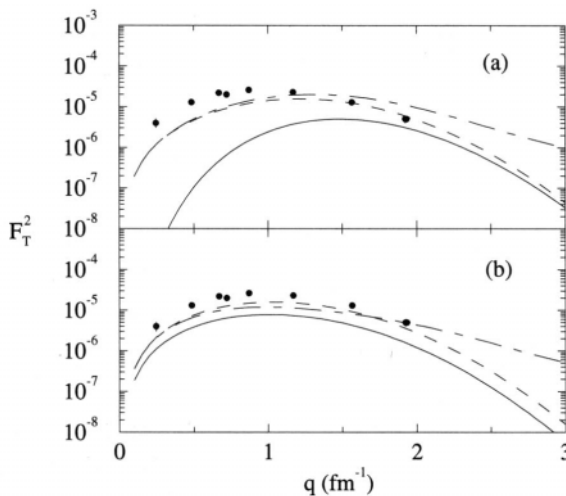


Fig. 9.21. The transverse isoscalar E form factor for the 4.44 MeV transition in ^{12}C . The data are those of Flanz *et al.* [246]. (a): Comparison with p -shell calculations; the solid, dashed and dot-dashed lines depicting the results of using T^{el} , $T^{el''}$, and $T^{el'''}$ operators, (b): Comparison with form factors calculated using the $2\hbar\omega$ shell model wave functions.

data and an enhancement of 1.6 in the result using $T^{el''}$ is required for that.

Using $T^{el'''}$ as the transition operator give form factors that have the anomalous behavior at high q as observed in the results for the sd -shell nuclei. Again, there is agreement between the low q results of calculations made using $T^{el''}$ and the $T^{el'''}$ forms of the excitation operator. These results indicate that higher $\hbar\omega$ components are required in the description of ^{12}C .

A problem in explaining the isoscalar transverse $E2$ form factor of the 4.44 MeV state excitation is revealed by considering the separate contributions from the protons and neutrons. They are displayed in Fig. 9.22. These contributions were calculated using the $T^{el''}$ operator. First, the form factor itself is weak, of the order of 10^{-5} . Second, the total form factor is the result of destructive interference between the proton and neutron amplitudes. Thus small differences in the calculation can lead to large changes in the results.

The isovector $E2$ form factor from inelastic electron scattering to the 16.11 MeV $2^+;1$ state in ^{12}C has also been measured by Flanz *et al.* [246]. This is of interest as past studies suggest that the CK wave

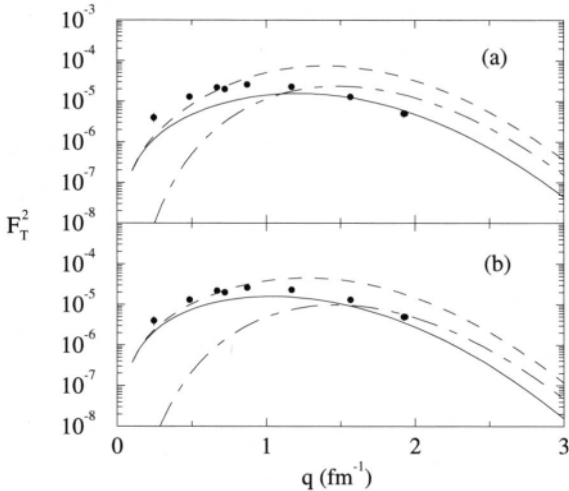


Fig. 9.22. Contributions from the protons (dashed line) and neutrons (dot-dashed line) to the transverse isoscalar $E2$ form factor to the 4.44 MeV state in ^{12}C calculated using the $T^{el''}$ operator (solid line). The data are those of Flanz *et al.* [246]. The $0p$ -shell model wave functions were used in (a), while (b) presents those calculations using the $2\hbar\omega$ wave functions.

functions give a good specification of the transition [246, 208]. Core polarization effects are not as dramatic for this transition as they are with the isoscalar (4.44 MeV) excitation. However they are destructive in nature as is evident from the results displayed in Fig. 9.23. The line types identify results obtained with each of the three operator forms. The notation is that used with Fig. 9.21. With the CK $0p$ -shell wave functions, the results found using the T^{el} operator is in best agreement with data. But when the $2\hbar\omega$ wave functions were used, the best results were found using either the $T^{el''}$ or the $T^{el'''}$ form.

A similar reduction in strength is observed with the isoscalar magnetic dipole form factors. Further there is evidence of isospin mixing between the $1\frac{1}{2};0$ (12.71 MeV) and $1\frac{1}{2};1$ (15.11 MeV) states [247]. The transverse $M1$ electron scattering form factors to these states in ^{12}C are displayed in Fig. 9.24. Therein, the data of Flanz *et al.* [247] are compared with the results of the calculations made using the $2\hbar\omega$ (solid line) and CK wave functions (dotted line) [214]. Those results do not contain any contributions from MEC. But as they are isovector in nature, MEC are expected only to contribute to the isovector $M1$ form factor and then at high momentum transfer. On the other hand isospin mixing can have a

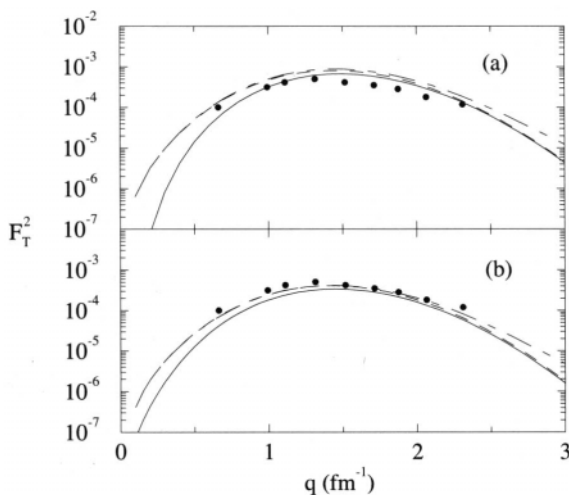


Fig. 9.23. The transverse $E2$ form factor for the isovector $0^+ \rightarrow 2^+$ (16.11 MeV) transition in ^{12}C . The data of Flanz *et al.* [246] are compared with the calculations using T^{el} , $T^{el'}$, and $T^{el''}$ as given for Fig. 9.21.

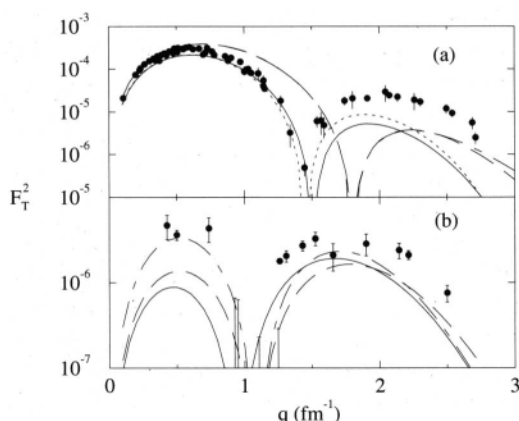


Fig. 9.24. Transverse $M1$ electron scattering form factors to (a) the $1^+_1;1^-(15.11 \text{ MeV})$ state and (b) the $1^+_1;0^-$ (12.71 MeV) state in ^{12}C . The data of Flanz *et al.* [247] are compared with the results of the calculation using the $2\hbar\omega$ wave functions (solid line) and the CK wave functions (dotted line). The dot-dashed line is the results of assuming two-level isospin mixing [247, 214].

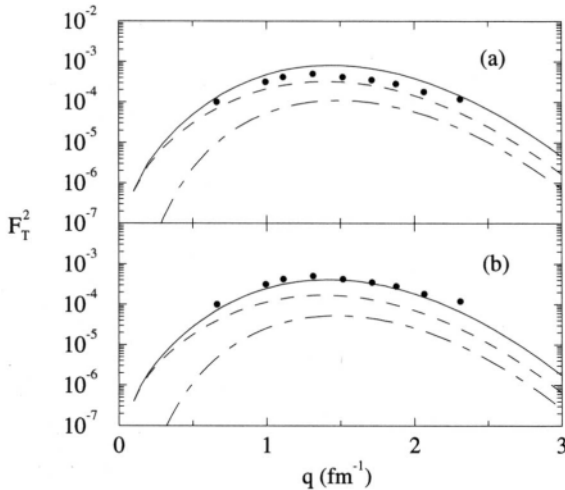


Fig. 9.25. Contributions to the total isovector $E2$ form factor to the 16.11 MeV state in ^{12}C from the proton and neutron amplitudes. The calculations are as for Fig. 9.22. The data are those of Flanz *et al.* [246].

dramatic effect. That is evident in the calculations of Flanz *et al.* [247]. The dot-dashed line in each case is the result obtained when a small degree (7% [247]) of isospin mixing is admitted between the two states. As is evident, there is significant improvement in the prediction of the isoscalar form factor but there is very little change in the isovector form factor caused by this mixing. The reason for this improvement is that a small change in the transition densities induced by the isospin mixing produces a large change in the destructive interference between the individual proton and neutron amplitudes [214].

The success of both the $0p$ -shell model calculations and the $2\hbar\omega$ shell model calculations for the 2^+ (16.11 MeV) isovector transition is due to the constructive interference between the proton and neutron amplitudes. That is illustrated in Fig. 9.25 in which the contributions to the total form factor calculated using the T^{el} operator are displayed.

The longitudinal form factor for the $0^+ \rightarrow 4^+$ (14.08 MeV) transition is displayed in Fig. 9.26. The $0p$ -shell model cannot predict any state with $J > 3$. Hence, the data of Nakada *et al.* [245] are compared with the results of calculations made using the $2\hbar\omega$ shell and the PHF models of spectroscopy. While the PHM model form factor is in close agreement with the data, the $2\hbar\omega$ calculation underestimates it by a factor of three.

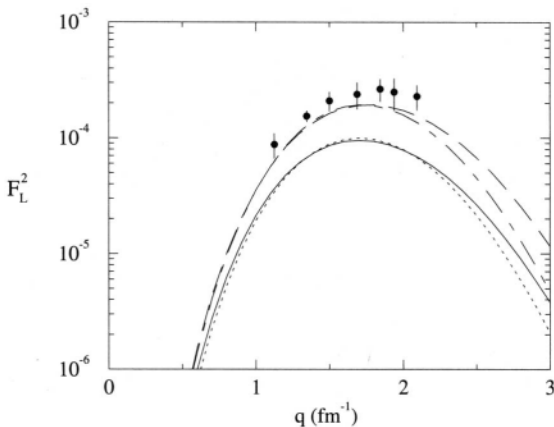


Fig. 9.26. Longitudinal $E4$ electron scattering form factor for the $0^+ \rightarrow 4^+$ (14.08 MeV) transition in ^{12}C . The data of Nakada *et al.* [245] are compared with the calculation using the $2\hbar\omega$ wave functions (using WS wave functions, solid line, and HO wave functions, dotted line), and that using the PHF wave functions (using WS wave functions, dashed line, and HO wavefunctions, dot-dashedline).

Apparently $> 2\hbar\omega$ components are required for an adequate description of the 4^+ state wave function. Two results are shown for each spectroscopic model used. The dotted and dot-dashed curves were obtained using HO functions while those portrayed with the solid and dashed curves result with WS functions. The differences caused by the choice of SP wave functions are not large and occur at momentum transfer values where higher order scattering processes may be important.

The longitudinal form factors for the excitation of the $3^-;0$ (9.64 MeV) and $1^-;0$ (10.85 MeV) states in ^{12}C are displayed in Fig. 9.27. The results found using the $3\hbar\omega$ shell model OBDME are displayed by the solid curves while the dashed curves portray the results obtained using the PHM spectroscopy. Both sets of calculations used WS SP wave functions. In Fig. 9.27(a) and (b) comparisons are made with the data of Crannell [248] and of Torizuka *et al.* [249] respectively. For both form factors, the $3\hbar\omega$ wave functions give better agreement with the data and notably so for the small q .

There is doubt about the spin-isospin assignments of some of the states in ^{12}C that lie between 10 and 20 MeV in excitation. Principally, the state at 18.35 MeV is listed as having the assignments $3^-;1$ and $2^-;0 + 1$. Another 3^- state is listed in the compilation [194] at 18.60 MeV. In Fig. 9.28 the results of a calculation of the $E3$ form factor [201] are

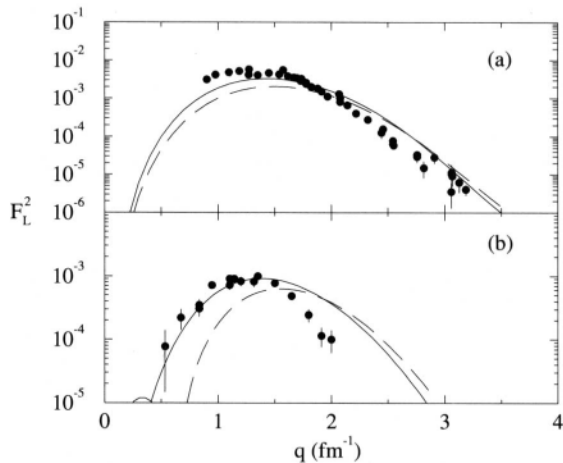


Fig. 9.27. The longitudinal form factors for the excitation of the $3^+; 0$ (9.64 MeV) state (a) and of the $1^-; 0$ (10.85 MeV) state (b) in ^{12}C . The data are those of Crannell [248] and of Torizuka *et al.* [249] for the 3^+ and 1^- excitations respectively. The results of calculations made using the $3\hbar\omega$ and the PHM model wave functions are displayed by the solid and dashed lines respectively.

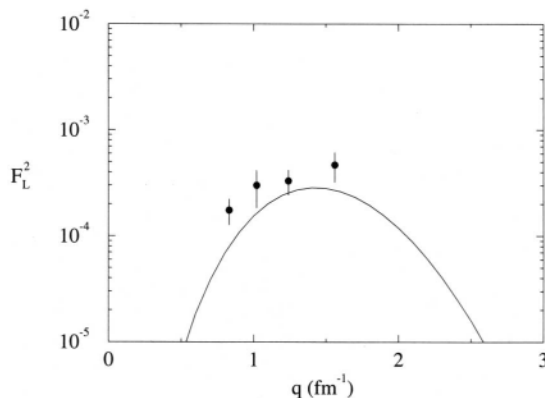


Fig. 9.28. Longitudinal electron scattering form factor for the $0^- \rightarrow 3^+; 1$ (18.60 MeV) transition in ^{12}C . The data of Yamaguchi *et al.* [250] are compared with the results of the calculation using the $2\hbar\omega$ wavefunctions.

displayed. Those results compare very well with the data of Yamaguchi *et al.* [250]. This indicates that the predicted $3^-;1$ (18.77MeV) state corresponds to the observed state at 18.60 MeV and not that at 18.35 MeV.

10. APPLICATIONS OF THE COORDINATE SPACE OPTICAL MODEL

Non-local coordinate space optical potentials for the scattering of 65 and 200 MeV protons from nuclei in the mass range ^3He to ^{238}U have been calculated by folding the complex, medium dependent effective NN interaction with the density matrix elements of each target [132, 251]. For select targets, those optical potentials have been calculated with proton energies in the range 40 to 800 MeV. As described in detail in the foregoing chapters, the effective NN interaction is based upon solutions of the LS and BBG equations having a realistic NN potential as input. The nuclear structure information required in this folding model are the OBDME for the target and single particle (SP) bound state wave functions. The OBDME have been obtained from various models of nuclear structure as discussed in Chapter 8. Where possible, the propriety of those OBDME have been assessed by their use in analyses of electron scattering form factors. Such was illustrated in Chapter 9. For $A \leq 16$, the no-core shell model evaluated in a multi- $\hbar\omega$ space has been used while, for heavier nuclei, calculations in the complete $0\hbar\omega$ space at best are possible due to computational limitations. The bound state SP wave functions that complete specification of the nuclear density matrices are either WS or HO functions. The former are employed when large basis structure is available with the WS potential parameters determined from fits to electron scattering form factors. For heavier nuclei, HO functions have been used in calculations to date, and the oscillator lengths for them are set customarily by an $A^{1/6}$ mass law.

Using the above specifications in the folding process, optical potentials result from which differential cross sections, analyzing powers, and spin rotations can be calculated. In general the results so obtained compare well with data when the effective interactions are built on mapping on- and half-off-shell properties of $NN g$ matrices. That is not the case with effective interactions built solely from mapping properties of $NN t$ matrices. This will be demonstrated by comparing results obtained using optical potentials obtained from folding the effective interactions found from the t and g matrices separately. For simplicity

the two results are designated hereafter as being obtained from g-folding and *t*-folding calculations respectively.

Whatever the choice of structure input, the folding process in coordinate space leads to non-local optical potentials because of knock-out exchange amplitudes. In the model now used, and from which the ensuing results shown have been made, antisymmetrised projectile target nucleon pair wave functions are used. Three and four particle exchanges have not been included. In the past, the resultant non-locality of the optical potential either was ignored or non-local potentials were transformed into equivalent local ones. Today there exists some support for claims that excellent results are found only if the fully non-local optical potential is used in integro-differential forms of the Schrodinger equations.

10.1. Energy and Mass Variations

In this section, the results of calculations of the differential cross sections and analyzing powers made using the non-local optical potentials defined for each target and for proton energies in the range 40 to 300 MeV are compared with data. As the data sets from 52 and 24 targets at the respective energies of 65 and 200 MeV have been presented in the literature [132, 251], only a representative sample is given. The targets range from ^3He to ^{238}U . In addition, for a few of these, the spin rotations, $R(\theta)$, have been measured. Note that some of the data displayed were taken with 185 MeV incident protons and those calculations were made using the appropriate 185 MeV effective interaction. Consideration is limited to no more than 60° and 40° in the center of mass for the energies of 65 and 200 MeV, respectively, by which, typically, the cross-section magnitudes are 1 mb/sr or less. This limitation has been taken as the approximations inherent in the theoretical model may not be appropriate in making calculations of scattering with smaller magnitude at larger scattering angles. Unless stated to the contrary, the results to be shown were obtained from g-folding calculations.

With the light nuclei, ^3He to ^{16}O , those g-folding calculations were made with OBDME obtained from large space shell model studies of the nuclei. Also the SP wave functions have been specified either from the shell model calculations themselves [168] or from the use of those OBDME to find good fits to the longitudinal elastic electron scattering form factors [186]. With medium mass nuclei, from ^{20}Ne to ^{64}Ni , shell model calculations were performed in $0\hbar\omega$ spaces except for those in the middle of the *fp* shell where the dimension of the basis becomes

prohibitively large for matrix diagonalization techniques. In those cases, a restriction on the minimum number of nucleons in the $0f_{\frac{5}{2}}$ orbit was placed in the model. The oscillator length for the SP wave functions was set as $A^{1/6}$ fm. The results for the scattering from heavy nuclei used simple spectroscopy in which the nucleon occupancies are given by a simple packing scheme, with SP functions set by an oscillator length again given by an $A^{1/6}$ law. In so far as all input details to specify the non-local optical potentials for any target are predetermined, one run of the programs, DWBA91 or DWBA98, sufficed to give the results displayed in most of the figures. As such the calculated results are predictions of the observables.

10.1.1. *The Mass Variation with 65 and 200 MeV Protons*

The differential cross sections for a subset of targets considered in the study [251] of 65MeV proton scattering, are displayed in Figs. 10.1 and 10.2. There is a smooth mass trend in the structure of the cross-section data which is reproduced excellently by the optical potential calculations that are displayed by the curves. Small variations are evident and such are due, it is believed, to limitations in the nuclear structure assumed for each target. The analyzing powers from each of those same targets are compared with the calculations in Figs. 10.3 and 10.4. As with the differential cross sections, there is a very definite and smooth trend in structure in the data as the target mass increases; a trend that is again well reproduced by the potential model calculations. The analyzing powers have a number of features in their structure that can be quite difficult to obtain from calculation. With the very light nuclei, the data are very small before rising monotonically and positively to the first peak that indicates the emergent proton to be almost completely polarised. As the target mass increases, that primary maximum is preceded by a small minimum of negative values but the maximum remains almost 100% with its onset becoming sharper. As target mass increases from 90 to 160 that first minimum becomes deeper and the first maximum weakens with the subsequent peaks also becoming more sharply defined. Finally with the heaviest targets, the first minimum and first maximum markedly diminish in value. There is also a trend for the structure of subsequent maxima and minima to be more positive than negative with increasing scattering angle.

The 200 MeV data are shown in Figs. 10.5 and 10.6 for the differential cross sections and analyzing powers respectively. A more complete

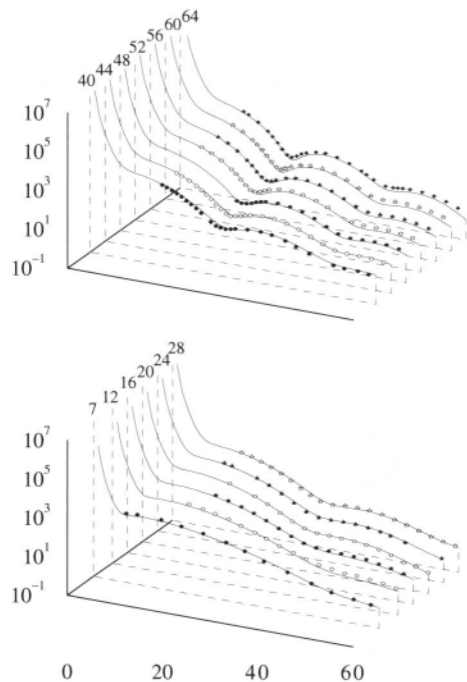


Fig. 10.1. The 65MeV elastic proton scattering differential cross-section data compared with the optical model calculations for targets to mass 64. The target mass identifies each result.

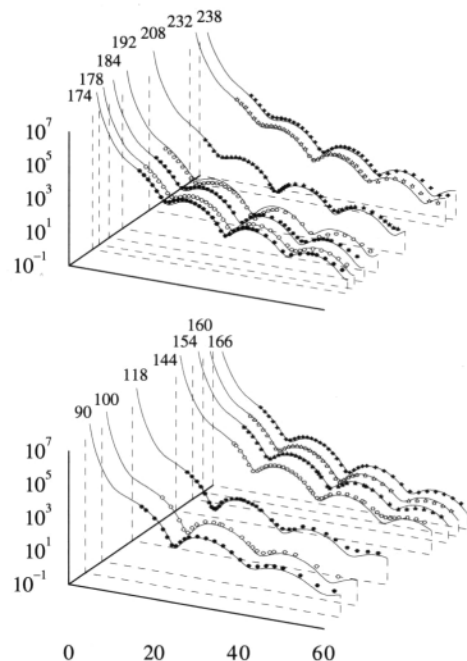


Fig. 10.2. The 65MeV elastic proton scattering differential cross-section data compared with the optical model calculations for targets above mass 90. The target mass identifies each result.

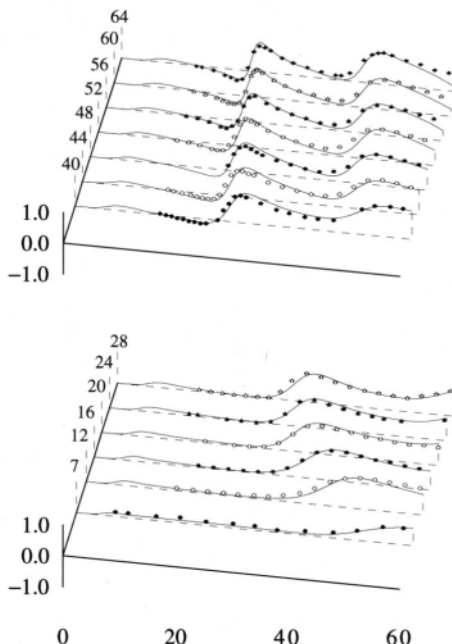


Fig. 10.3. The 65MeV elastic proton scattering analyzing power data compared with the optical model calculations for targets to mass 64. The target mass identities each result.

presentation showing results for 22 nuclei with data is given in Ref. [132]. Herein the results for 14 of those nuclei over the range from ${}^4\text{He}$ to ${}^{208}\text{Pb}$ are shown. The asterisks on some mass numbers in this figure signify that those data and results are for 185MeV proton scattering. As at 65MeV, the data show trends with increasing target mass although now such are not as pronounced or as smoothly varying. Nevertheless the g-folding model results remain in very good agreement with observation and especially with the analyzing power data.

In Figs. 10.7 and 10.8 the analyzing powers and spin rotations R for 65 MeV polarised protons from 8 nuclei, ranging from ${}^{12}\text{C}$ to ${}^{208}\text{Pb}$, are shown. The solid and long dashed curves in these diagrams portray the results obtained by using the g - and t -folding potentials. The comparisons between the results from both calculations with the data are good although in detail the g -folding results are preferred. But those differences do not warrant display. There are discrepancies between the results of both models and the data in some nuclei, e.g., for ${}^{58}\text{Ni}$ and ${}^{208}\text{Pb}$, which

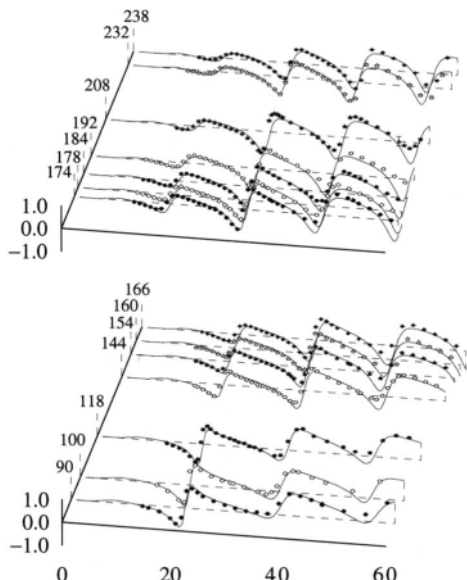


Fig. 10.4. The 65MeV elastic proton scattering analyzing power data compared with the optical model calculations for targets above mass 90. The target mass identifies each result.

will be discussed later. But the preference for g rather than t -folding is most evident with the spin observables. From Fig. 10.7 it can be seen that the structure of the measured analyzing power changes in a consistent way as the mass of the target increases. Indeed, the depth of the first minimum and the sharp rise between this and the next maximum become more pronounced with target masses to ^{118}Sn . As the target mass increases further, the magnitudes of this minimum and of the following maximum are greatly suppressed. The absolute value of those minima and subsequent maxima approaches unity even for the heaviest nuclei. There is a limited set of spin rotation $R(\theta)$ data for 65 MeV polarised protons [252]. These are displayed in Fig. 10.8. For the lightest four nuclei presented, the comparison between the g -folding potential results and data is quite good. Those results found by using the t -folding potential do not match data as well. The differences between the g - and t -folding models are far more pronounced with the scattering from the heavier targets. While g -folding again gives reasonable agreement with the data, t -folding fails to reproduce both shape and magnitude. Indeed, that

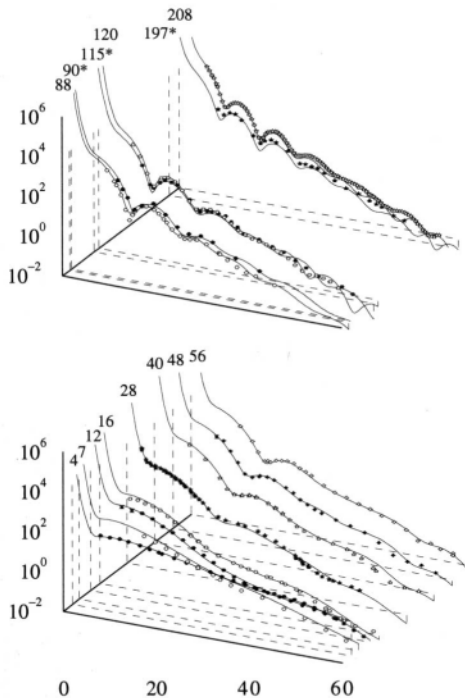


Fig. 10.5. The 200 MeV elastic proton scattering differential cross-section data compared with the optical model calculations for diverse targets as identified.

model predicts a maximum at $\sim 20^\circ$ in the spin rotation for the scattering from ^{90}Zr and ^{118}Sn whereas the data indicate a minimum at that angle. Such is predicted with g folding however. While there are no data for scattering from ^{152}Sm , the difference between the model results is apparent. In the case of scattering from ^{208}Pb , the result obtained with g folding follows the shape of the data although it overestimates the data above 30° .

10.1.2. Variation with Single Particle Wave Functions

In the folding to give optical potentials for all nuclei up to and including ^{20}Ne , the SP wave functions were set either by the shell model

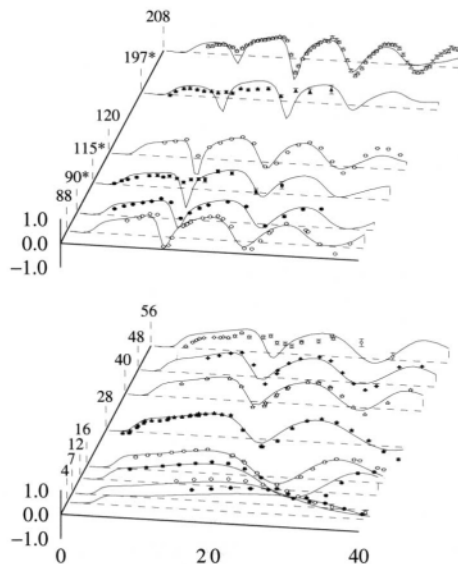


Fig. 10.6. The 200 MeV elastic proton scattering analysing power data compared with the optical model calculations for targets of diverse mass as indicated.

structure calculations themselves or by fitting electron scattering data. For most cases involving heavier targets, HO wave functions with $b = A^{1/6}$ fm have been used. In general, this choice has produced results that compare well with data, but there are discrepancies. In part they are due to the simple prescription for SP wave functions. The effect of variations to the SP descriptions are displayed in Fig 10.9. Therein the results of two g -folding calculations are compared with the scattering data from ^{58}Ni and ^{208}Pb . Therein, the solid line shows the g -folding results of calculations made using HO wave functions with lengths $b = 1.97$ and 2.43 fm for ^{58}Ni and ^{208}Pb respectively. The long dashed lines display results obtained with oscillator lengths $b = 1.87$ and 2.35 fm for ^{58}Ni and ^{208}Pb respectively. The improvement in the results with the altered wave functions is evident. There is also better agreement between the calculation and data for both nuclei, although the angles of the minima in the cross section for the scattering from ^{58}Ni are greater than observed. Using these new sets of wave functions there is much better agreement with the data for both spin observables. In the case of ^{208}Pb , the significant improvement in the

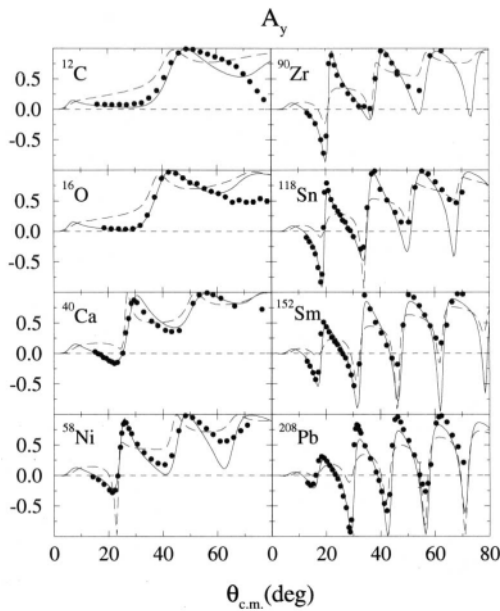


Fig. 10.7. The 65MeV elastic proton scattering analyzing power data from a select set of nuclei compared with the optical model calculations.

spin rotation has been achieved with only a 3% decrease in the oscillator length. Elastic scattering data from medium to heavy nuclei seem to reflect details of both bulk and surface attributes of mass distributions.

10.1.3. Results for 40MeV Proton Scattering

Effective interactions have been defined for a proton energy as low as 40MeV. At this energy, unique structures in the response function of a nucleus, the giant resonances for example, might vitiate any microscopic description of the optical potential that does not take such specifics into account. Two effective interactions have been defined for use. The first was based upon the g matrix obtained starting with the Bonn-B interaction [34] while the second was based upon that found using the Paris interaction [18] as the input. There are slight differences between the two.

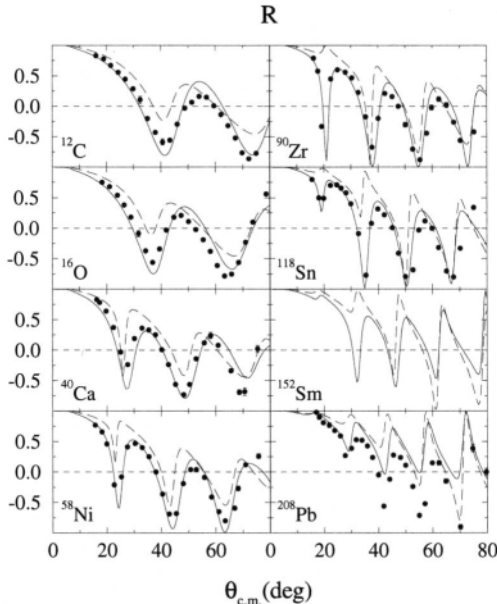


Fig. 10.8. The 65 MeV elastic proton scattering spin rotation data from a select set of nuclei compared with the optical model calculations.

To assay these effective interactions, each has been folded with the same structures used in the analyses of 65 and 200 MeV scattering from ^{12}C , ^{40}Ca , ^{58}Ni , ^{90}Zr , and ^{208}Pb to specify optical potentials for 40 MeV protons. Use of those optical potentials gives the calculations shown in the next two figures. Therein the result of folding to obtain an optical potential for the exotic nucleus ^6He is also given. In this case, very large space calculations ($4\hbar\omega$ and $8\hbar\omega$ [175]) provided the OBDME as well as the HO bound states to be used in the folding. The optical potentials were fixed therefore and single runs of the scattering programs gave the results that are compared with data obtained from Ref. [253] for the stable nuclei and from Ref. [254] with a radioactive beam of 40A MeV ^6He .

In Fig. 10.10, the cross-section calculations are compared with data from the set of nuclei ranging in mass from the exotic ^6He to ^{208}Pb . The solid and long dashed curves in each segment identify the g-

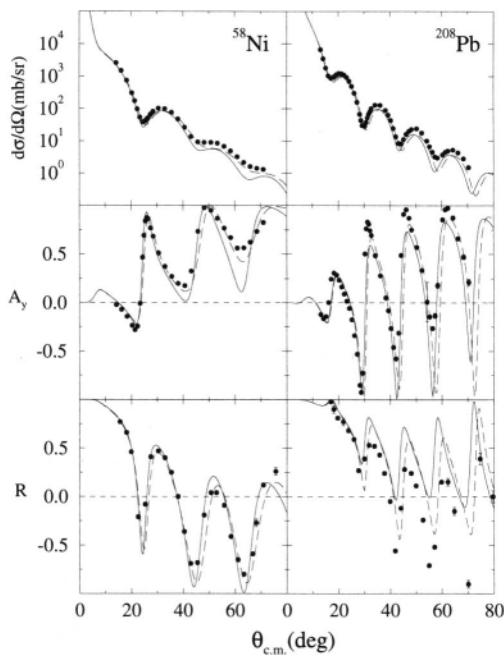


Fig. 10.9. The 65MeV elastic proton scattering data from ^{58}Ni and ^{208}Pb compared with the optical model calculations.

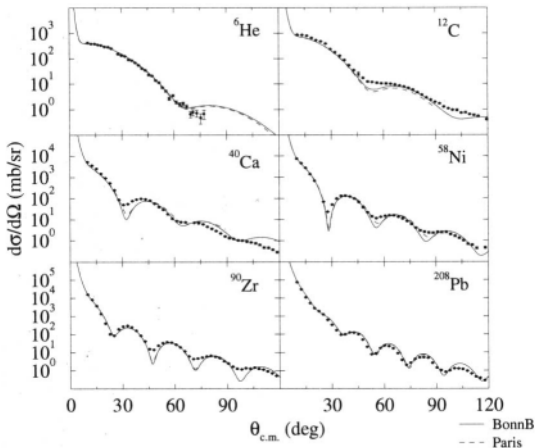


Fig. 10.10. The 40MeV elastic proton scattering cross-section data [253, 254] from a select set of nuclei compared with the optical model calculations.

folding results obtained by using the effective interactions found from the Bonn-B and Paris potentials respectively. The differences in these calculated cross sections are slight. These 40MeV calculations agree with data almost as well as at the higher energies, although they have more sharply defined minima than is evident in the data. By and large though, the calculations are in good agreement with the shapes and magnitudes of the cross-section data and now to 120° scattering.

In Fig. 10.11, the analysing powers associated with 40MeV proton scattering from the same set of nuclei discussed above are compared with data. Again, the solid and long dashed curves portray the g -folding results found with the Bonn-B and Paris interactions as input. The two forces give very similar results, and ones that reflect the structure of the data quite well. But the degree of replication of the data by these calculations is not as high as at 65 and 200 MeV. It would appear, however, that the folded optical potentials are a very good first approximation, sufficiently so that the results may still select between different structure inputs. Also the associated distorted wave functions and effective interactions should still be the most appropriate for use in other reaction calculations [255].

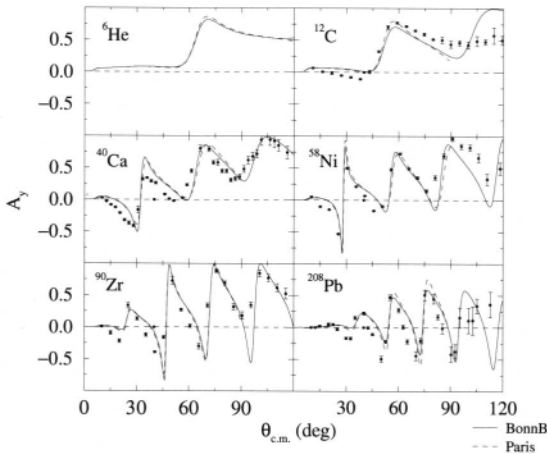


Fig. 10.11. The 40MeV elastic proton scattering analyzing power data from a select set of nuclei compared with the optical model calculations.

10.2. Elastic Scattering from $^{3,4}\text{He}$, $^{6,7}\text{Li}$, and ^{12}C

Application of the folding optical model potential to these light mass nuclei is of interest for many reasons which are epitomised by the basic questions:

- (i) Can shell model calculations adequately specify the properties of systems that, till now, have been the province of few nucleon methods and studies?
- (ii) Can the known collectivity of the Lithium isotopes be reproduced adequately with a central field model structure, given that such have been touted heretofore as the study area of cluster model approaches?
- (iii) Does the folding model method of defining optical potentials apply to such light systems, and if so, for what energies? and
- (iv) At what mass can simple structure models furnish descriptions for the nuclear ground states?

The answers to the structure questions have been dealt with in part in previous chapters and so here we dwell largely on the possibility of optical potentials to describe the scattering from the light mass systems.

10.2.1. Proton Scattering from $^{3,4}\text{He}$

The scattering of polarised protons from polarised ^3He and from ^4He targets has been measured recently at energies that should be appropriate for use of the g -folding prescription of proton-HeIIum optical potentials. Specifically, data which have been taken at 200 and 300 MeV by Hasell *et al.* [256] are displayed by filled triangles in the figures to be discussed. Data taken at 200 and 290 MeV by Häusser *et al.* [257] are shown therein by open diamonds, and data taken at 200 MeV by Brash *et al.* [258] are portrayed by filled circles. These data have been analyzed with optical potentials defined in other ways. Notably a non-relativistic factorized form of the optical potential in momentum space [259] built upon NN t matrices, and a Schrödinger potential equivalent to a phenomenological Dirac optical potential [260], were used by Brash *et al.* [258]. Häusser *et al.* [257] mapped the data to a structured form of p - ^3He T matrices which link to the optical potentials by the relativistic LS equation. Both of those studies do not find good agreement with the 200 MeV data, but their fits to data taken at 500 MeV are better. They use very simple spectroscopy for the target. The first analyses of these data with

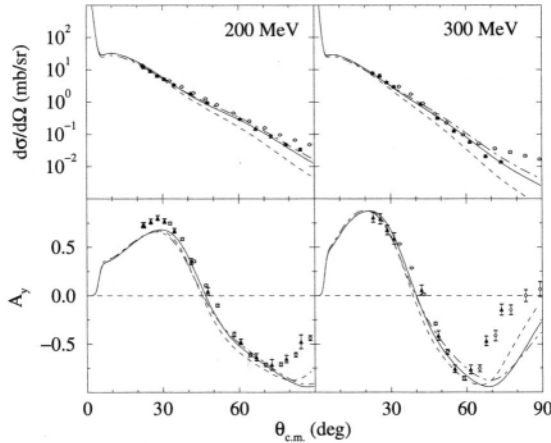


Fig. 10.12. The differential cross sections and analysing powers from the scattering of 200 and 300 MeV polarised protons from polarised ${}^3\text{He}$.

the g -folding approach used OBDME taken from a $4\hbar\omega$ study [133]. In the figures to be shown, those results are compared with the calculations obtained using the structure information from $8\hbar\omega$ shell model calculations. Note that in all the calculations leading to the results displayed, the SP wave functions were taken as HO functions with the values of $b = 1.7$ and 1.5 fm that were used in the $4\hbar\omega$ and the $8\hbar\omega$ shell model calculations respectively. Three results are compared with data in Figs. 10.12, 10.13, and 10.14. Those obtained using the $4\hbar\omega$ spectroscopy are displayed by the long dashed curves while the solid and dash-dotted curves are associated with the $8\hbar\omega$ specifications. The two $8\hbar\omega$ model curves are the results obtained by using the g matrices of the Paris and Bonn-B potentials respectively. The Paris interaction g matrix was used with the $4\hbar\omega$ structure calculations.

In Fig. 10.12 calculations are compared with the experimental data [256, 257] of the differential cross sections and analysing powers from the scattering of 200 and 300 MeV polarised protons from polarised ${}^3\text{He}$. Clearly, the calculations made using the larger basis structure predict cross sections in good agreement with the data. The smaller basis structure results decrease more rapidly. Predominantly this effect is due to the specific SP bound states used in each calculation. The large basis model calculations reproduce the cross-section data to at least 60° scattering angle, where the magnitude is of order 0.1 mb/sr, with either the

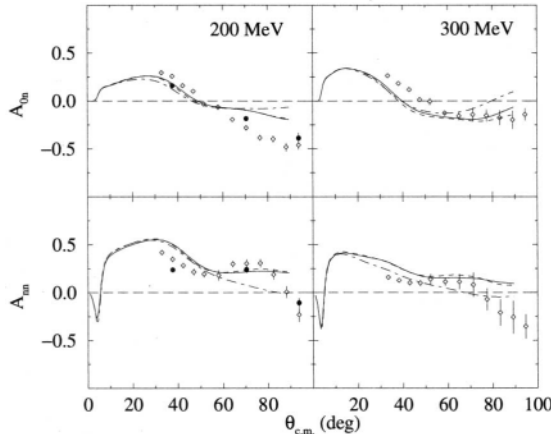


Fig. 10.13. The spin correlations A_{0n} and A_{nn} from the scattering of 200 and 300 MeV polarised protons from polarised ${}^3\text{He}$.

Paris or Bonn-B interaction. All results are similar for the analysing powers, and calculations reproduce the data to 60° very well, save at forward scattering angles in the case of 200 MeV proton scattering. The data at even higher scattering angles are not reproduced at all. In that case details of the folding model approach may no longer be appropriate.

The data shown in the next two figures are those of Refs. [257, 258] and are the single and double spin correlation observables. In Fig. 10.13, the calculations made using the results of the two structure calculations and the two effective interactions are compared with data for spin observables A_{0n} and A_{nn} . The left and right panels display the 200 and 300 MeV results respectively. These calculations have the general trends of the data without the quality of fit that has been found for cross sections and analysing powers. There is little to choose between any of the calculations of A_{0n} . The calculations of A_{nn} show little sensitivity to the effective interaction used.

At 200 MeV, other spin observables have been measured. Those data and calculations of them are shown in Fig. 10.14. There is again little to choose between any of the calculations found using Paris or Bonn-B effective interactions and $4\hbar\omega$ or $8\hbar\omega$ structures. The match to data is good overall despite notable discrepancies in A_{mm} and A_{lm} . However, the former of these discrepancies occurs at large scattering angles $>60^\circ$ and

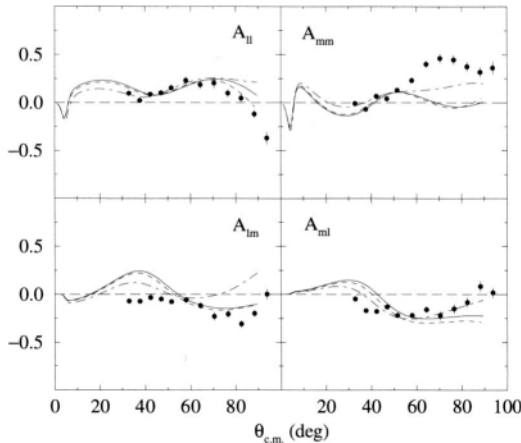


Fig. 10.14. Other spin correlations from the scattering of 200 MeV polarised protons from polarised ^3He .

the latter is small and similar to that noted with the 200 MeV analysing power calculation.

Predictions of the differential cross sections, analysing powers, and spin rotations from the scattering of 200 and 300 MeV polarised protons from ^4He are given in Fig. 10.15 where they are compared with the experimental data of Moss *et al.* [261] and of Yoshimura *et al.* [262], respectively. In this case the results found using the Bonn-B interaction and the $4\hbar\omega$ structure are also displayed by the long dashed curves. Clearly the larger basis structure information leads to a marked improvement in the reproduction of the 200 MeV cross-section data. Indeed the $8\hbar\omega$ results are in good agreement with those data to 80°. This sensitivity to the size of the basis used to determine the OBDME reduces significantly for heavier nuclei. The 300 MeV cross-section data have some structure that is not reproduced but, in general, calculation agrees with observation. The agreement of calculation with analysing power data also is improved with use of the larger basis structure details, although the same kind of discrepancies noted in the analyses of the ^3He scattering are evident. Predictions of the spin rotation data at 300 MeV reflect what is observed at 200 MeV, although there is room for improvement. The choice of NN potential produces differences in this observable at 300 MeV as do the structure bases. But while the Bonn-B and Paris interactions results are different, the quality of reproduction of the data does not show preference.

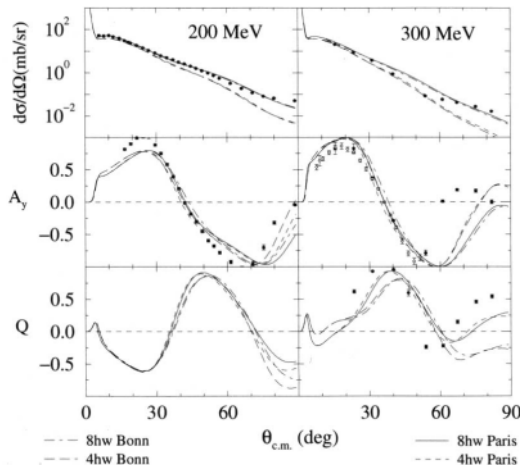


Fig. 10.15. The differential cross sections, analysing powers, and spin rotations from the scattering of 200 and 300 MeV polarised protons from ${}^4\text{He}$.

These analyses of 200 and 300 MeV data, cross sections and spin observables, from polarised proton scattering on a polarised ${}^3\text{He}$ target as well as the cross section and analysing power from 200 MeV polarised protons scattered from ${}^4\text{He}$, confirm that the large basis $8\hbar\omega$ shell model provides the OBDME and single particle bound states necessary to calculate the optical potential.

10.2.2. Proton Scattering from ${}^{6,7}\text{Li}$

The results of g -folding calculations of the elastic scattering for 200 MeV protons from ${}^6\text{Li}$ are compared with the data of Glover *et al.* [263] in Fig. 10.16. The results found using $2\hbar\omega$ and $4\hbar\omega$ space shell model structures are given in the left and right hand panels respectively. The single particle bound states were specified either as WS (solid curves) or HO (long dashed curves) wave functions. The higher $I > 0$ multipoles that are possible in this scattering were calculated in DWBA and in accord with the calculations presented in Ref. [263]. By so doing with OBDME from the $2\hbar\omega$ and $4\hbar\omega$ models, the calculations are in good agreement with both the cross-section and analysing power data. Taken together with the very good agreement achieved with the elastic electron scattering data, this suggests that the ground state wave functions obtained in the multi- $\hbar\omega$ spaces have converged well enough for use in scattering analyses.

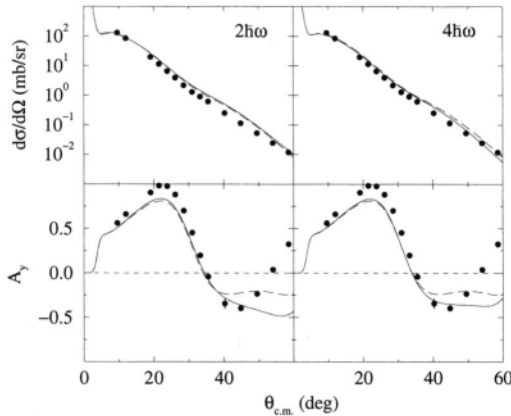


Fig. 10.16. The differential cross sections (top) and analysing powers (bottom) from the scattering of 200 MeV polarised protons from ${}^6\text{Li}$.

The results for the elastic scattering of 200 MeV protons from ${}^7\text{Li}$ are compared with the data of Glover *et al.* [263] in Fig. 10.17. The specification of the results follow that given in the discussion of Fig. 10.16. As with the results for the elastic scattering from ${}^6\text{Li}$, the contributions from the higher multipoles are calculated using DWBA. When such is done, results are in good agreement with the data

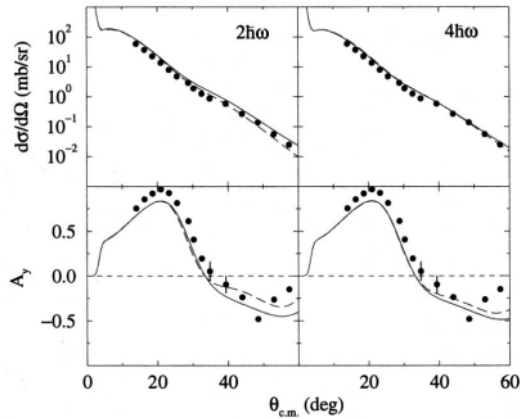


Fig. 10.17. The differential cross sections (top) and analysing powers (bottom) from the scattering of 200 MeV polarised protons from ${}^7\text{Li}$.

suggesting, as with ${}^6\text{Li}$, that the multi- $\hbar\omega$ wave functions for the ground state are appropriate.

10.2.3. Scattering from ${}^{12}\text{C}$

The cross section and analysing power for 200 MeV protons elastically scattered from ${}^{12}\text{C}$ have been calculated using OBDME obtained from a $2\hbar\omega$ basis shell model calculation. Both WS and HO functions have been used with those OBDME to calculate the ${}^{12}\text{C}$ optical potentials [139]. The non-local nature of these optical potentials can be inconvenient and in the past the exchange terms, from which those non-localities arise either have been ignored or transformed into a local potential. By using just the leading, direct, term a $g\rho$ approximation is obtained. In Fig. 10.18, those direct potentials are shown for the effective interaction and density profiles to different maximum densities. The real and imaginary parts of the central and spin-orbit components of the direct potentials that result from t - and g -folding calculations are displayed by the long dashed and solid curves respectively. The dot-dashed and small dashed curves show the direct potentials that result if one uses g -folding with a density profile limited to $\frac{1}{3}$ and $\frac{2}{3}$ of the target

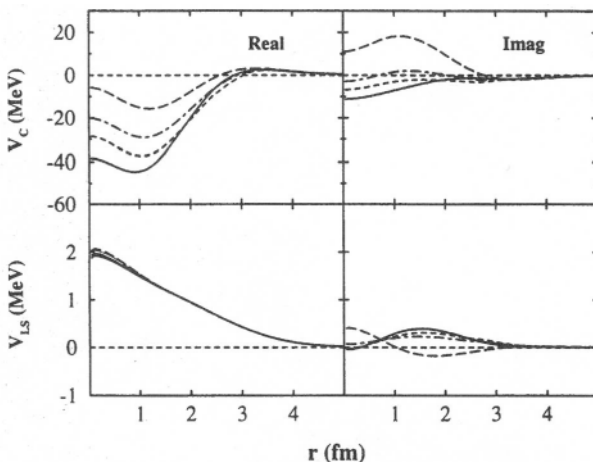


Fig. 10.18. The direct components of the 200 MeV $p\text{-}{}^{12}\text{C}$ optical potentials. The t - and g -folding results are displayed by solid and long dashed curves respectively. Intermediate results are shown by the other curves.

central density respectively, i.e., in those two cases, for radii at which the nuclear density would normally exceed the limits, the limit value of the g matrix was used. The direct spin-orbit interaction is quite weak and essentially real with little variation due to medium effects in the g matrix. However, there is a clear progressive and marked enhancement of the calculated central real interaction strength as one moves from using t - to g -folding. Likewise the imaginary part of the central interaction changes from strongly productive to weakly absorptive with inclusion of the medium modifications. In particular one finds that the differences are not simply equivalent to a choice of SP wave functions or the specific realistic NN interaction chosen.

The cross sections and analysing powers that result on using the full non-local optical potentials are compared with data [264] in Figs. 10.19 and 10.20. Those calculations were made using a $2 \hbar\omega$ shell model results as input [139]. Consistent with the results found with the elastic electron scattering form factors, using the CK $0p$ -shell structure values makes little or no change to the proton elastic scattering calculations from those displayed. In Fig. 10.19 the solid and long dashed curves display the results obtained by using WS and HO bound state wave functions. The results of calculations made using t - and g folding are shown

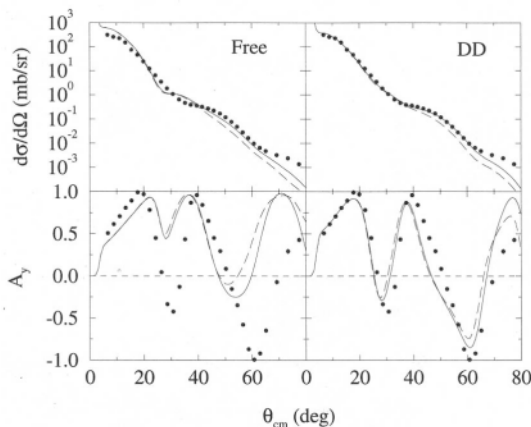


Fig. 10.19. The 200 MeV proton elastic scattering cross section and analysing power data [264] compared with the results found using the t - and g -folding optical potentials and displayed in the left and right sections respectively. The solid and long dashed curves display the results found using WS and HO single particle bound state functions respectively in the calculations.

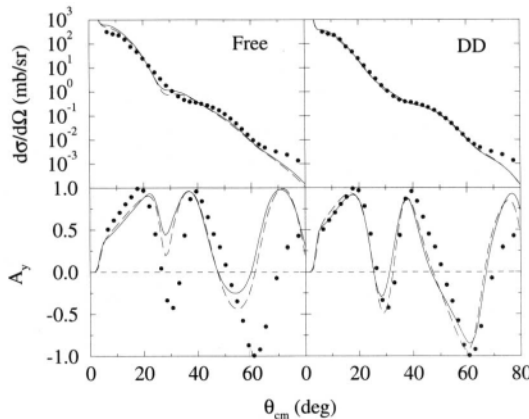


Fig. 10.20. The 200 MeV proton elastic scattering data [264] compared with the results found using the t - and g -folding optical potentials. The solid and long dashed curves give the results found when the Paris [18] and Bonn-B [34] NN forces were used to specify the input t and g matrices respectively.

in the left and right side panels respectively. It is evident that g -folding with WS bound states gives an optical potential from which a cross-section is obtained that match the data best although the choice of bound state wave functions is not too serious. That is even more obvious with the analysing power. The g -folding results are in better agreement with data than are the t -folding ones. Again there is little to choose between the results obtained using HO and WS bound states in the folding.

In Fig. 10.20, the cross sections and analysing powers shown were obtained from t - and g -folding with WS bound state functions and the Paris and Bonn-B potentials as the primary interaction. The Paris and Bonn-B results are shown by the solid and long dashed curves respectively in this figure. Again the g -folding results, whether obtained from the Paris or Bonn-B input, are in better agreement with the data, and especially the analysing power. There is little to choose between the results found with the two differing realistic starting interactions however.

The next set of figures reveal just how important the exchange amplitudes are for the energy range 40 to 250 MeV. In Fig. 10.21, the 200 MeV differential cross section and analysing power data are compared with the results of calculations made with and without the exchange amplitudes in the optical potential. The complete non-local

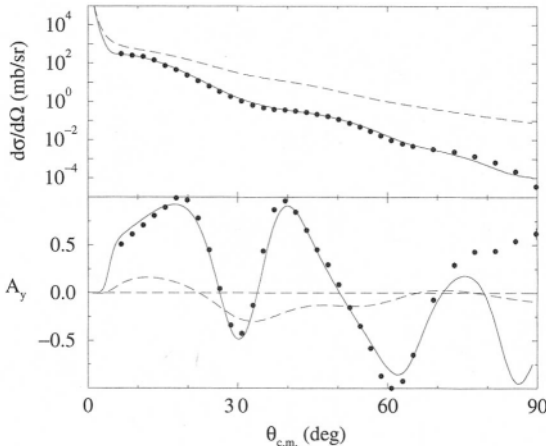


Fig. 10.21. The 200 MeV cross-section and analysing power data compared with the results of calculations made using the non-local optical potential (solid curves) and using local direct ($g\rho$) potential (long dashed curves).

calculation gave the results displayed by the solid curves; those found under the $g\rho$ restriction are displayed by the long dashed curves. The variation between the two sets of results are as noteworthy as is the quality of agreement between the full calculation results and the data.

In the next four figures, the differential cross section and analysing power data from the scattering of 40, 65, 120, 135, 160, 200, and 250 MeV polarised protons from ^{12}C are compared with the results of calculations made using g -folding, with and without exchange terms included [265]. In Figs. 10.22 and 10.23, the Bonn-B g -folding results are shown. The folding was made with the OBDME given by a $2\hbar\omega$ shell model calculation [139]. Cross sections above a few tenths of a mb/sr are presented and clearly the results match the data well. That quality of match to data is almost as good for the analysing powers. In Figs. 10.24 and 10.25, the $g\rho$ -folding results are compared against the same data. Clearly the cross sections are quite disparate from those displayed in the preceding figures. The essential difference between these results arises from the destructive interference between the direct and exchange amplitudes.

Equivalent local potential representations of the non-local components can be formed with which equally good reproduction of the

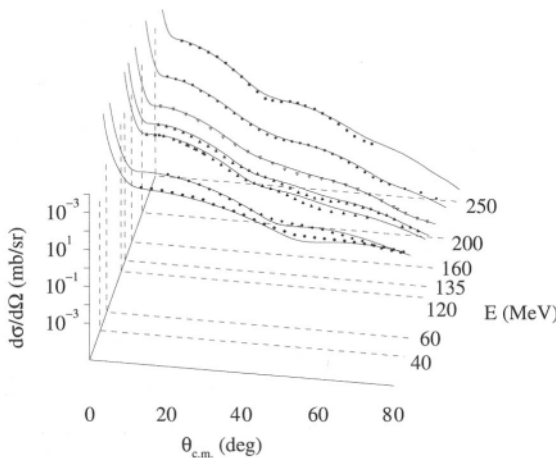


Fig. 10.22. The 40 to 250 MeV cross section data compared with the results of calculations made using the full non-local optical potentials.

cross-section data is obtained. These schemes are discussed in the next chapter. But quality of reproduction of data by use of some of them is not guaranteed at the outset. As a caveat, given the current technology of the programs DWBA91 and DWBA98 [29, 30], and of the computer speed and storage available, there is little gained by using local equivalent potentials to analyse elastic scattering data.

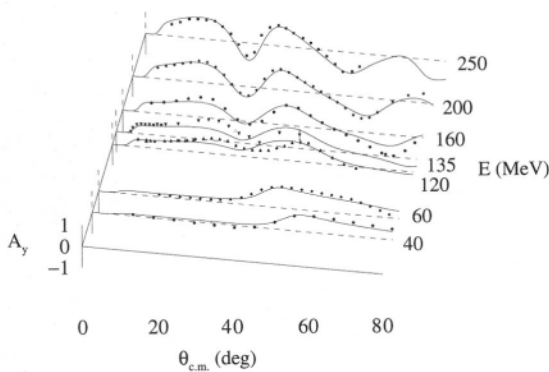


Fig. 10.23. The 40 to 250 MeV analysing power data compared with the results of calculations made using the full non-local optical potentials.

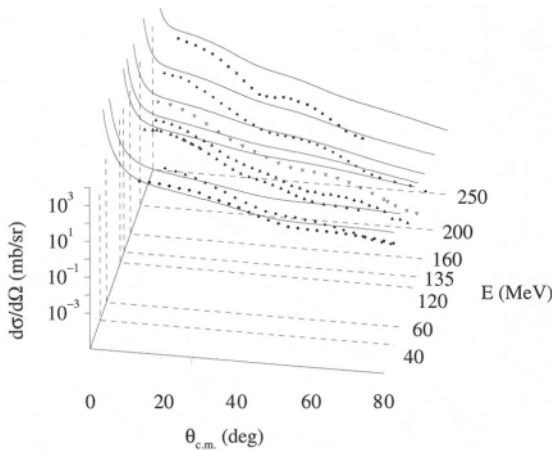


Fig. 10.24. The 40 to 250 MeV cross section data compared with the results of calculations made using only direct $g\varphi$ optical potentials.

10.3. Scattering of $^{6,8}\text{He}$ and $^{9,11}\text{Li}$ from Hydrogen

While interest in these exotic, radioactive beam, systems exists for many and diverse reasons [266], a primary theoretical one is to find their matter distributions. The stable nuclei have spatial distributions of protons and neutrons that are roughly the same. In contrast, exotic systems such as neutron-rich ^{11}Li seem to have a halo formed by some of the valence neutrons, two for ^{11}Li , concomitant with the separation energies of those neutrons being small. Studies of neutron skins in isotopes

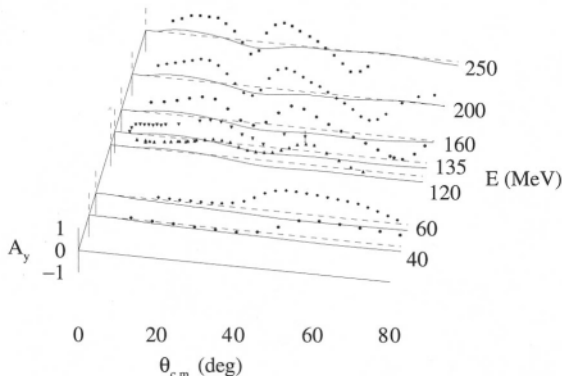


Fig. 10.25. The 40 to 250 MeV analysing power data compared with the results of calculations made using only direct $g\varphi$ optical potentials.

[266] of ${}^8\text{He}$ and the Na isotopes in particular based upon the mass variation of interaction cross sections indicate that the proton rms radii are fixed while the neutron ones vary with mass. But the models used were very simple and give information on the matter profiles only indirectly, as do analyses of most other characteristics of the exotic nuclei [266].

The light mass systems are of interest since their structures have been studied by Navrátil and Barrett [176, 175]. They have made large-space shell model calculations for nuclei up to and including mass 11. In those calculations all nucleons were active and the NN potential energies were generated from a realistic NN interaction, the Nijmegen Reid93 interaction usually. Space size decreases with mass, being $8\hbar\omega$ (and larger) for ${}^4\text{He}$, $6\hbar\omega$ for mass 5, 6, and 7 isobars, and $4\hbar\omega$ thereafter to and including the mass 11 isobars, ${}^{11}\text{Li}$ and ${}^{11}\text{Be}$. These structure calculations give good low excitation spectra for the stable isotopes and for many radioactive ones as well. The calculations also give good results for the binding energies, ground state static moments, and rms radii. With regard to the exotic nuclei of particular interest herein, the large-space shell model calculations indicate that, with a $6\hbar\omega$ space structure, there is no need of any *halo* characteristic to specify ${}^8\text{He}$ properties. The spectra of ${}^8\text{He}$ and ${}^{9,11}\text{Li}$ have been calculated using a shell model and $4\hbar\omega$ space. In those cases, and for ${}^{9,11}\text{Li}$ particularly, the spectra, binding energies, and ground state moments are reproduced well although the calculated proton rms radii are small in comparison to the expected values. The cause of discrepancies may be a halo-like distribution of the excess neutrons, as the Arizona group [168] note that the $4\hbar\omega$ model space is not large enough to encompass any such halo characteristic for these nuclei. Use of these structure details, the OBDME and nucleon bound state wave functions, from the shell model specifications in folding model calculations of proton-nucleus optical potentials lead to the results designated in this discussion as *no-halo* scattering.

To estimate the effects of any halo attribute in the nuclei then requires variation of the SP functions from the HO set defined by the large-space shell model calculations. One choice is to use WS functions instead, with the WS potential parameters chosen to give wave functions from which good fits to electron scattering form factors of stable isobars are found. In particular, those for ${}^6\text{Li}$ [186] to deal with ${}^{6,8}\text{He}$ and those for ${}^9\text{Be}$ [132] to deal with ${}^{9,11}\text{Li}$ have been used. Using those WS wave functions in the g -folding, cross sections result for proton scattering from the exotic nuclei that are almost identical to the ones obtained with the HO forms and which have been identified as no-halo.

To ensure a halo structure with any of the nuclei, the single particle bound state WS potentials were adjusted to reproduce the separation

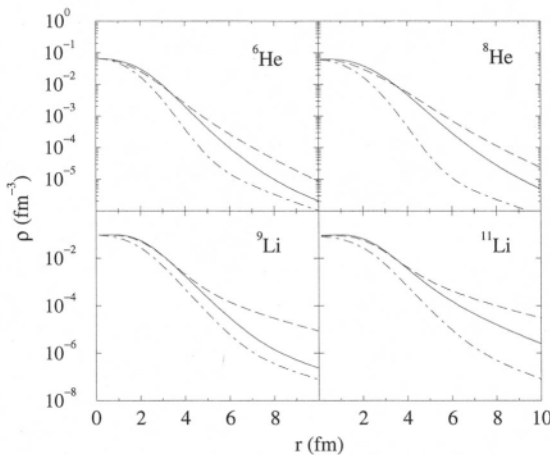


Fig. 10.26. Shell model neutron density profiles for the nuclei $^{6,8}\text{He}$ and $^{9,11}\text{Li}$. The long dashed and solid curves represent, respectively, the profiles when a halo is and is not contained in those structures. The dot-dashed lines represent the proton density for each nucleus.

energies of the weakly bound nucleons in the given shell model state. A halo structure is given to $^{6,8}\text{He}$ by setting the $0p$ shell binding at 2 MeV and the sd shell and higher states at 0.5 MeV. For $^{9,11}\text{Li}$, the halo prescription results by adjusting the WS potentials to bind $0p_{\frac{1}{2}}$ and $1s_{\frac{1}{2}}$ states by just 0.5 MeV. With this approach, ^8He and ^9Li act as controls since ^8He is believed to be an example of a neutron skin and ^9Li an example of a simple core nucleus given that the single neutron separation energies for these nuclei are 2.584 [177] and 4.063 [194] MeV, respectively. Then, by artificially ascribing a halo to these two nuclei, the question is to ascertain whether or not the optical potential calculations and existing data are sensitive enough to detect the enforced property. Such has been found to be the case recently [192].

The neutron density profiles for the exotic nuclei $^{6,8}\text{He}$ and $^{9,11}\text{Li}$ as given by large space shell model calculations described above, are shown in Fig. 10.26. Therein the long dashed and solid lines portray respectively the profiles found with and without halo conditions being implemented. Note, however, that a primary role of halo conditions is to reduce the neutron densities for radii less than the rms radius. With the folding process to define the optical potentials, the short range details, $r < r_{\text{rms}}$, have significant effects and so influence calculations of differential cross sections notably at momentum transfers where scattering is influenced

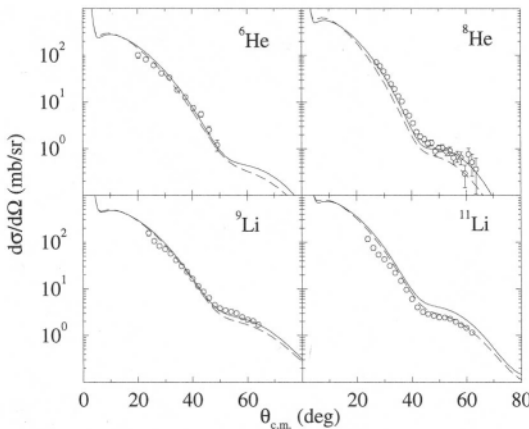


Fig. 10.27. Predictions of the differential cross sections from the scattering of 72A MeV $^{6,8}\text{He}$ and of 62A MeV $^{9,11}\text{Li}$ from hydrogen compared with experimental data. The data are from Refs. [276, 24, 268] and the results, assuming that each nucleus has (does not have) a halo structure, are portrayed by the long dashed (solid) curves.

by the nuclear medium. But the extended nature of the halo shapes also influence the optical potentials with their effects in scattering cross sections being evident in changes to small angle results, typically $\theta < 20^\circ$ for beam energies 60A to 70A MeV.

The predicted differential cross sections for the $^{6,8}\text{He}$ and $^{9,11}\text{Li}$ scattering from hydrogen are presented in Figs. 10.27 and 10.28. In Fig. 10.27, those calculations are compared with data taken by Korsheninnikov *et al.* [267, 24] using 70.5A MeV ^6He and 72A MeV ^8He ions, and by Moon *et al.* [268] using 60A ^9Li and 62A MeV ^{11}Li ions. In Fig. 10.28, the forward angle results, at which there are no data, are displayed to emphasise the effects upon calculations of the halo structure outside of the rms radius, i.e., the neutron tail effects. In both figures, the solid curves portray no-halo calculations while the long dashed curves give the halo differential cross sections. As is evident in Fig. 10.27, the ^8He and ^9Li data extend to momentum transfer values sufficient to discriminate between the results of halo and non-halo calculations. The data are consistent with a no-halo prescription for those nuclei. Those nuclei are controls and so the results indicate that elastic scattering data analyses can distinguish halo from non-halo effects. Indeed with ^{11}Li , the data concur with the calculations only when a halo specification for this nucleus is used. Other studies also suggest that ^{11}Li does have a halo structure.

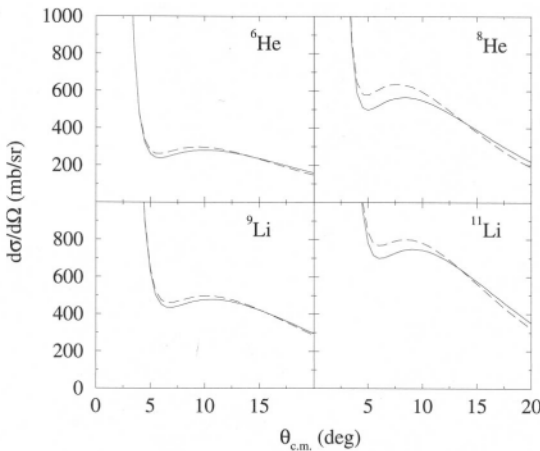


Fig. 10.28. Differential cross sections as shown in Fig. 10.27, but for small angles only.

As noted above, the data cover a range of momentum transfer values at which calculations are most influenced by the character of the optical potentials within the rms radius. The halo influence upon neutron matter distributions at radii greater than the rms value influence the optical potentials in a way that affects scattering at small angles prevalently. The possible influence such features may have upon calculations of the differential cross sections are shown in Fig. 10.28. The definition of the curves is as given for Fig. 10.27. In all cases the effects are not large, and in that of ^{11}Li for which it is believed a halo exists, the effect is about 10% at 6° to 8° scattering.

The case of ^6He is interesting. The data at 70.5A MeV range only to 50° center of mass scattering angle and proves to be insufficient to discriminate the halo from the no-halo specifications. A little more data have been taken at 40A MeV [254], however, and the results of optical model calculations at this energy are shown along with the 70.5AMeV ones again in Fig. 10.29. The results were generated by folding a 40 MeV effective interaction built from the Bonn-B g matrix with $4\hbar\omega$ and $8\hbar\omega$ shell model structures for the ground state. The results found using simple spectroscopy are compared with those found by invoking a halo characteristic in the manner described above. There is slight preference for the halo density at the largest of the scattering angles in the 40A MeV data. But more data is needed for a conclusive result. Clearly the size of the basis space is not a crucial factor as the distinctions between halo

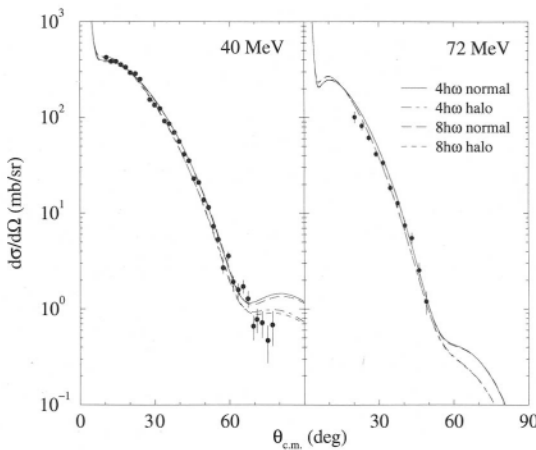


Fig. 10.29. Differential cross sections for $40A$ and $70.5A$ MeV ${}^3\text{He}$ scattering from proton targets compared with calculations.

and non-halo cross-section calculations are far greater than the variations due to an increased basis space in the structure model.

11. EQUIVALENT LOCAL POTENTIALS

The complex optical potentials calculated by t - or g -folding with the OBDME of the target are non-local in character and the associated Schrödinger equations are of integro-differential form. Those equations are solved numerically with the DWBA91 or DWBA98 programs [29, 30] which also generate therefrom the distorted waves for use in DWBA analyses of inelastic scattering and charge exchange reactions. Use of non-local optical potentials is not new. Over thirty years ago, Perey and Buck [269] used the Frahn-Lemmer form [270] to analyse low energy neutron-nucleus scattering. But over the years local nuclear optical potentials have been assumed predominantly. Phenomenological WS potentials have been taken commensurate with known attributes of nuclear densities and consistent with the character of Hartree fields. Most importantly, fits to scattering data were obtained with those local potentials. Finally, Perey and Buck identified the energy dependence of those local potentials as caused by non-locality.

The transition from non-local potentials to equivalent local ones has been effected under various approximations and analytic expressions

[271, 272]. All of those methods rely upon the range of the non-locality being ~ 1 fm which is small in comparison to the size of nuclei. If such is also the case with regard to the de Broglie wavelength of the projectile, a semi-classical WKB approximation may be valid. However, Peierls and Vinh-Mau [272] note that, while the localisation approximations should be well met within the medium of a large nucleus, corrections could be important in the nuclear surface region and for light mass nuclei. In any circumstance that the non-locality range exceeds the characteristic length of the system, they note that the non-local potential cannot be approximated by their algorithm of localisation [272]. Equivalent local potentials can also be used to account for the effects of coupled channels [273]. The resulting form is equivalent to that found by treating just the exchange effects and so we consider just the single channel problems hereafter.

11.1. The Basic Problem and Solutions

The problem is to find a local form of complex potential $V_{\text{LEQ}}(\mathbf{r}; E) = V(\mathbf{r}; E)$ which when used in the Schrödinger equation,

$$\frac{\hbar^2}{2\mu} \nabla^2 \phi(\mathbf{k}, \mathbf{r}) + [E - V(\mathbf{r}; E)] \phi(\mathbf{k}, \mathbf{r}) = 0, \quad (11.1)$$

or its partial wave radial differential equations

$$\left[\frac{d^2}{dr^2} - \frac{l(l+1)}{r^2} + k^2 - V_{lj}(r; E) \right] \phi_{lj}(kr) = 0, \quad (11.2)$$

give phase shifts equal to those found by solution of the non-local ones,

$$\frac{\hbar^2}{2\mu} \nabla^2 \chi^{(+)}(\mathbf{k}, \mathbf{r}) + E \chi^{(+)}(\mathbf{k}, \mathbf{r}) - \int U(\mathbf{r}, \mathbf{r}'; E) \chi^{(+)}(\mathbf{k}, \mathbf{r}') d\mathbf{r}' = 0, \quad (11.3)$$

or

$$\left[\frac{d^2}{dr^2} - \frac{l(l+1)}{r^2} + k^2 \right] f_{lj}(kr) = \int_0^\infty U_{lj}(r, r') f_{lj}(kr') dr', \quad (11.4)$$

respectively.

A weaker condition implies that the local potentials $V(\mathbf{r}; E)$ and $V_{lj}(\mathbf{r}; E)$ are equivalent to the non-local kernels $U(\mathbf{r}, \mathbf{r}'; E)$ and $U_{lj}(\mathbf{r}, \mathbf{r}')$ respectively if all observables are reproduced. Some methods of specifying the local equivalent potential are given next.

In a local density approximation (LDA) [66] the optical model potential is linked to properties given from nuclear matter calculations.

The radial position within the nucleus is related to the density of nuclear matter through the Fermi momentum k_f . Physical justification of the LDA is linked to the short range of the underlying NN interaction and the resultant non-locality in the stationary form of the Schrödinger equation, Eq. (11.3). Then, to evaluate the integral term in the general form of the Schrödinger equation, it is not necessary to know the solution function $\chi^{(+)}(\mathbf{k}, \mathbf{r})$ at all positions. One only needs to know how $\chi^{(+)}(\mathbf{k}, \mathbf{r})$ varies in a volume element characterised by a small distance s about the point \mathbf{r} . In that volume element, $\chi^{(+)}(\mathbf{k}, \mathbf{r})$ oscillates with a wave number $K(\mathbf{r})$ so that integration over s will select only those momentum components of any kernel that are in the neighbourhood of $K(\mathbf{r})$. This justifies expansion of the Fourier transform of a kernel $G(s)$ about the local wave number,

$$G(s) = \frac{1}{(2\pi)^3} \int \tilde{G}(p) e^{-ip \cdot s} dp \quad (11.5)$$

and

$$\tilde{G}(p) = \tilde{G}(p^2) = \tilde{G}(K^2) + (p^2 - K^2) \frac{d}{d(K^2)} \tilde{G}(K^2) + \dots \quad (11.6)$$

The usual LDA uses the first two terms of the expansion. In a simple manner then a local equivalent potential to the exchange term in Eq. (11.3) can be obtained by a Taylor series expansion,

$$\begin{aligned} \int U(\mathbf{r}, \mathbf{r}'; E) \chi^{(+)}(\mathbf{k}, \mathbf{r}') d\mathbf{r}' &\approx \int U(\mathbf{r}, \mathbf{r}'; E) e^{(\mathbf{r}' - \mathbf{r}) \cdot \nabla} \chi^{(+)}(\mathbf{k}, \mathbf{r}') d\mathbf{r}' \\ &= \left[\int U(\mathbf{r}, \mathbf{r}'; E) e^{i(\mathbf{r}' - \mathbf{r}) \cdot \kappa} d\mathbf{r}' \right] \chi^{(+)}(\mathbf{k}, \mathbf{r}) \end{aligned} \quad (11.7)$$

where a local wave number,

$$\kappa(\mathbf{r}) = \sqrt{2\mu[E - V(\mathbf{r}; E)]}, \quad (11.8)$$

has replaced the gradient operator.

Frahn and Lemmer [270] assumed that the non-local kernels of the full Schrödinger equation, Eq. (11.3), have a separable form,

$$U(\mathbf{r}, \mathbf{r}'; E) \rightarrow F(\mathbf{R}) v(\boldsymbol{\rho}), \quad (11.9)$$

where

$$\mathbf{R} = \frac{1}{2}(\mathbf{r} + \mathbf{r}'); \quad \boldsymbol{\rho} = \mathbf{r} - \mathbf{r}'. \quad (11.10)$$

This is also known in the literature as the Perey-Buck [269] prescription. Furthermore, they assume that $F(\mathbf{R}) = F(R)$ with $F(R)$ a slowly varying function about $\mathbf{R} = \mathbf{r}$, and that

$$\nu(\rho) = v(\rho) = (\pi\sigma^2)^{-\frac{3}{2}} \exp\left(-\frac{\rho^2}{\sigma^2}\right), \quad (11.11)$$

where σ is the non-locality range. A Taylor expansion about \mathbf{r} gives to second order

$$\begin{aligned} F(R)\chi^{(+)}(\mathbf{k}, \mathbf{r}') \approx \\ F(R)\chi^{(+)}(\mathbf{k}, \mathbf{r}) + \frac{1}{6}\rho^2 \left\{ \frac{d}{dr}F(r)\frac{d}{dr} + F(r)\nabla^2 + \frac{1}{4r}\frac{d^2}{dr^2}[rF(r)] \right\} \chi^{(+)}(\mathbf{k}, \mathbf{r}) \end{aligned} \quad (11.12)$$

and this gives

$$\begin{aligned} \int U(\mathbf{r}, \mathbf{r}'; E)\chi^{(+)}(\mathbf{k}, \mathbf{r}') d\mathbf{r}' \approx \\ \left\{ v_0 F(r) + \frac{1}{8}v_2 \frac{1}{r} \frac{d^2}{dr^2}[rF(r)] + \frac{1}{2}v_2 \frac{d}{dr}F(r)\frac{d}{dr} + \frac{1}{2}v_2 F(r) \right\} \chi^{(+)}(\mathbf{k}, \mathbf{r}), \end{aligned} \quad (11.13)$$

where v_n are the moments of the non-locality

$$v_n = \frac{4\pi}{(2n-1)} \int_0^\infty \nu(\rho)\rho^{(2+n)} d\rho. \quad (11.14)$$

Under this approximation, the non-local Schrödinger equation reduces to

$$\begin{aligned} \left[\left[-\frac{\hbar^2}{2\mu} + \frac{1}{4}\sigma^2 F(r) \right] \nabla^2 + \frac{1}{4}\sigma^2 \frac{d}{dr}F(r)\frac{d}{dr} \right. \\ \left. - E + F(r) + \sigma^2 \frac{1}{r} \frac{d^2}{dr^2}[rF(r)] \right] \chi^{(+)}(\mathbf{k}, \mathbf{r}) = 0. \end{aligned} \quad (11.15)$$

This equation maps to an equivalent local and energy dependent form

$$\left[-\frac{\hbar^2}{2\mu} \nabla^2 + V(r, E) - E \right] \phi(\mathbf{k}, \mathbf{r}) = 0, \quad (11.16)$$

upon using a point transformation defined by

$$\phi(\mathbf{k}, \mathbf{r}) = T(r)\chi^{(+)}(\mathbf{k}, \mathbf{r}). \quad (11.17)$$

Multiplication of Eq. (11.15) by $T(r)$ gives

$$T(r) \left\{ -\frac{\hbar^2}{2\mu} \nabla^2 - \left[\frac{J_1(r)}{X(r)} \right] \frac{d}{dr} \left[\frac{J_0(r)+E}{X(r)} \right] \right\} T^{-1}(r) \varphi(\mathbf{k}, \mathbf{r}) = 0, \quad (11.18)$$

with

$$J_0(r) = F(r) + \frac{\sigma^2}{16r} \frac{d^2}{dr^2} [rF(r)], \quad J_1(r) = \frac{\sigma^2}{4} \frac{d}{dr} F(r), \quad (11.19)$$

and

$$X(r) = 1 - \frac{\mu\sigma^2}{2\hbar^2} F(r). \quad (11.20)$$

The first derivative term is eliminated by choosing $T(r) = \sqrt{X(r)}$ as then Eq. (11.18) becomes

$$\left[-\frac{\hbar^2}{2\mu} \nabla^2 + \frac{k(r)-E}{X(r)} \right] \varphi(\mathbf{k}, \mathbf{r}) = 0, \quad (11.21)$$

thus identifying

$$V(r, E) = E + \frac{k(r)-E}{X(r)} \quad (11.22)$$

when

$$\begin{aligned} k(r) &= J_0(r) - \frac{1}{r} J_1(r) - \frac{1}{2} \frac{d}{dr} J_1(r) - \frac{3}{2} \frac{1}{X(r)} J_1^2(r) \\ &= F(r) - \frac{\sigma^2}{8r} \frac{d}{dr} F(r) - \frac{\sigma^2}{16r} \frac{d^2}{dr^2} F(r) \\ &\quad - \frac{3\mu\sigma^4}{32\hbar^2} \frac{1}{[1-\mu\sigma^2/(2\hbar^2)]F(r)} \left[\frac{d}{dr} F(r) \right]^2 \end{aligned} \quad (11.23)$$

To illustrate this approximation, consider the Perey-Buck non-local potential used by Bauhoff, von Geramb, and Pálá [274] with which $\sigma = 0.8$ fm and for the form factor a WS function,

$$F(r) = -72 [1 + e^{(r-4.1)/0.65}]^{-1}. \quad (11.24)$$

With this non-local interaction, the local equivalent form is as shown in Fig. 11.1. The form factor $F(r)$ shown (dashed curve) has a central value tending to -72 MeV and the local equivalent $V(r, E)$ (solid curve) tends

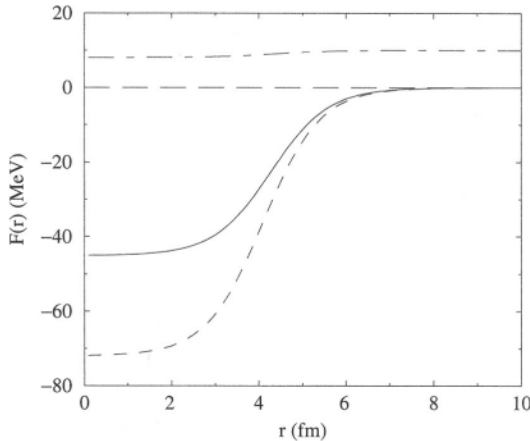


Fig. 11.1. The Frahn-Lemmer (Perey-Buck) form factor $F(r)$ shown by the dashed line compared with the local equivalent as evaluated using Eq. (11.22) (solid curve). The damping factor (times 10) is the dot-dashed curve.

to -45MeV at the origin. The damping factor $T^{-1}(r)$ shown by the solid curve in the upper section of this figure, has been multiplied by a factor of 10 to facilitate display. The constant value (10) is plotted as the dashed curve. The damping factor is a noticeable effect, numerically tending to 0.8057.

The method of equivalent wave numbers was developed for nuclear scattering first by Perey and Saxon [271] and formulated later in detail by Peierls and Vinh-Mau [272]. They presume that the local wave function satisfies a wave equation with an effective wave number that varies with both position and energy, namely

$$[\nabla^2 + q^2(\mathbf{r}, E)]\phi(\mathbf{r}, \mathbf{k}) = 0, \quad (11.25)$$

where, by comparison with Eq. (11.1),

$$q^2(\mathbf{r}, E) = q^2 = \frac{2\mu}{\hbar^2} [E - V(\mathbf{r}, E)]. \quad (11.26)$$

Again it suits to consider the basic interaction to have short range non-locality and to use the Frahn-Lemmer form given by Eqs. (11.9)–(11.11). A Wigner transformation gives the local equivalent potentials as

$$V(r, E) = \frac{4\pi}{q} F(r) \int_0^\infty v(\rho) \sin(q\rho) \rho d\rho = F(r) e^{-\frac{1}{4}\sigma^2 q^2}. \quad (11.27)$$

Expanding the exponential one finds

$$V(r, E) = F(r) - \frac{1}{4} \sigma^2 F(r) q^2(r, E) + \frac{1}{32} \sigma^4 F(r) q^4(r, E) + \dots, \quad (11.28)$$

so defining the energy dependence of the equivalent local potential. As a power series in energy with

$$V(r, E) = \sum_{n=0}^{\infty} W_n(r) E^n, \quad (11.29)$$

to second order, using

$$q^2(r, E) \approx -\frac{2\mu}{\hbar^2} W_0(r) - \frac{2\mu}{\hbar^2} [W_1(r) - 1]E - \frac{2\mu}{\hbar^2} W_2(r) E^2, \quad (11.30)$$

algebraic manipulation gives for small values of $\gamma = 2\mu\sigma^2/(4\hbar^2)$,

$$\begin{aligned} W_0(r) &= F(r) + \gamma F(r) W_0(r) + \frac{1}{2} \gamma^2 F(r) W_0^2(r) \\ W_1(r) &= \gamma F(r) [W_1(r) - 1] + \gamma^2 F(r) W_0(r) [W_1(r) - 1] \\ W_2(r) &= \gamma F(r) W_2(r) + \gamma^2 F(r) \left\{ W_0(r) W_2(r) + \frac{1}{2} [W_1(r) - 1]^2 \right\}. \end{aligned} \quad (11.31)$$

With some rearrangement and using $\zeta(r) = \gamma F(r) [1 + \gamma W_0(r)]$, the expansion functions to second order in γ are

$$W_1(r) = \frac{\zeta(r)}{\zeta(r) - 1}, \quad (11.32)$$

and

$$W_2(r) = \frac{1}{2} \gamma^2 F(r) [1 - \zeta(r)]^{-3}. \quad (11.33)$$

For $W_0(r)$ one finds

$$W_0(r) = -\frac{1}{\gamma^2 F(r)} [1 - \gamma F(r) - \sqrt{1 - 2\gamma F(r) - \gamma^2 F^2(r)}], \quad (11.34)$$

so that

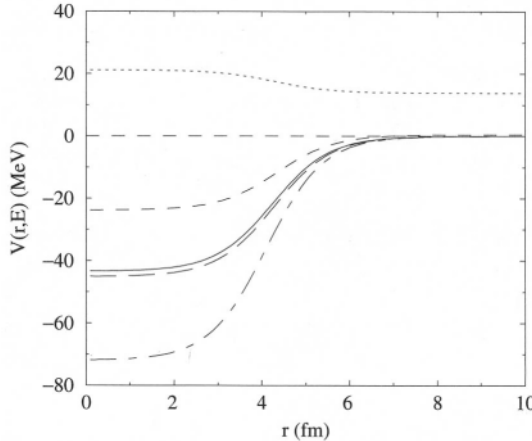


Fig. 11.2. The expansion terms, and the local equivalent potential found by the equivalent wave number method for the case of 30 MeV proton- ^{40}Ca scattering. The curves are as defined in the text.

$$\zeta(r) = 2\gamma F(r) - 1 + \sqrt{1 - 2\gamma F(r) - \gamma^2 F^2(r)}. \quad (11.35)$$

Calculations of the expansion terms, and thus of the $V(r, E)$, have been made for the purely non-local interaction used in the study of Bauhoff, von Geramb, and Pália [274]. An energy of 30 MeV for proton- ^{40}Ca scattering gave the results displayed in Fig. 11.2. The local equivalent potential given by Eq. (11.28) is displayed by the solid curve and it is compared with the Taylor expansion result (long dashed curve). Also shown is the dominant expansion term $W_0(r)$, the non-local form factor $F(r)$, and the equivalent momentum function $[10 \times q^2(r, 30)]$. They are represented by the short dashed, dot-dashed, and dotted curves respectively. Clearly the two local equivalent schemes give quite similar results.

11.2. Local Equivalent Partial Wave Potentials

An alternative to the above is to expand the kernels of the radial Schrödinger equations. Various methods exist to specify the local equivalent potentials by recasting the non-local equations, Eq. (11.4).

The Taylor expansion method is again the simplest to define the equivalent partial wave potentials [275]. It is implemented by invoking a shift operator

$$Z(r') = S(r', r)Z(r). \quad (11.36)$$

Expanded in a Taylor series as

$$S(r', r) = \sum_{n=0}^{\infty} \frac{1}{n!} (r' - r)^n \frac{d^n}{dr^n}, \quad (11.37)$$

action of this shift operator on the non-local potential gives

$$\begin{aligned} \int_0^{\infty} U_{lj}(r, r') f_{lj}(kr') dr' &= \sum_{n=0}^{\infty} W_n^{lj}(r) f_{lj}(kr) \\ W_n^{lj}(r) &= \frac{1}{n!} U_n^{lj}(r) \frac{d^n}{dr^n}, \end{aligned} \quad (11.38)$$

wherein the moments of the radial kernels are

$$U_n^{lj}(r) = \int_0^{\infty} U_{lj}(r, r') (r' - r)^n dr'. \quad (11.39)$$

The replacement of non-local behavior by the action series of derivative operators is practical only if the summations can be limited to relatively few terms. Apagyi and Scheid [275] limit study to second order $n \leq 2$,

$$W^{lj}(r) = U_0^{lj}(r) + U_1^{lj}(r) \frac{d}{dr} + \frac{1}{2} U_2^{lj}(r) \frac{d^2}{dr^2}. \quad (11.40)$$

However, truncation vitiates the hermiticity of the complete series which Apagyi and Scheid [275] restore by taking Hermitian combinations of each term, finding

$$\begin{aligned} W^{lj}(r) &= \frac{1}{2} [U_0^{lj}(r) + U_0^{lj*}(r)] + \frac{1}{2} [U_1^{lj}(r) + U_1^{lj*}(r)] \frac{d}{dr} \\ &\quad - \frac{1}{2r^2} \frac{d}{dr} [r^2 U_1^{lj*}(r)] + \frac{1}{4} [U_2^{lj}(r) + U_2^{lj*}(r)] \frac{d^2}{dr^2} \\ &\quad + \frac{1}{2r^2} \frac{d}{dr} [r^2 U_2^{lj*}(r)] \frac{d}{dr} + \frac{1}{4r^2} \frac{d^2}{dr^2} [r^2 U_2^{lj*}(r)]. \end{aligned} \quad (11.41)$$

The partial wave equations take the form

$$\left\{ A_{lj}(r) \frac{d^2}{dr^2} + B_{lj}(r) \frac{d}{dr} + \left[k^2 - \frac{l(l+1)}{r^2} + C_{lj}(r) \right] \right\} f_{lj}(kr) = 0, \quad (11.42)$$

where

$$A_{lj}(r) = 1 - \frac{1}{2} U_2^{lj}(r), \quad B_{lj}(r) = -\frac{1}{2} U_1^{lj}(r), \quad C_{lj}(r) = -U_0^{lj}(r). \quad (11.43)$$

The limitation to order n^2 ensures that we deal only with second order differential equations and Eqs. (11.42) and (11.43) define the effective mass approximation for the non-local potential [270, 271]. Equivalent local potentials then result by transforming the wave functions using

$$\phi_{lj}(kr) = T_{lj}^{-1}(r)f_{lj}(kr), \quad (11.44)$$

where $\phi_{lj}(kr)$ are solutions of Eq. (11.2) with the boundary condition that

$$T_{lj}(r) \xrightarrow[r \rightarrow \infty]{} 1, \quad (11.45)$$

and the condition that $T_{lj}(r)$ is a solution of

$$\frac{dT_{lj}(r)}{dr} = -\frac{1}{2} \frac{B_{lj}(r)}{A_{lj}(r)} T_{lj}(r). \quad (11.46)$$

Then the first derivative terms vanish, and the local equivalent potential is

$$V^{lj}(r; E) = -\left[k^2 - \frac{l(l+1)}{r^2} \left[\frac{1-A_{lj}(r)}{A_{lj}(r)} \right] \right. \\ \left. - \frac{C_{lj}(r)}{A_{lj}(r)} - \frac{1}{4} \frac{B_{lj}^2(r)}{A_{lj}^2(r)} - \frac{1}{2} \frac{d}{dr} \left[\frac{B_{lj}(r)}{A_{lj}(r)} \right] \right]. \quad (11.47)$$

With the non-local interaction used by Bauhoff, von Geramb, and Pália [274] for 30 MeV proton- ^{40}Ca scattering, the moments of the radial kernels specified by Eq. (11.39) are as displayed in Fig. 11.3. The solid, long dashed, small dashed, and dotted curves in each segment portray the results for angular momenta values $l = 0, 1, 2$, and 3 respectively. The top, middle, and bottom segments show the results for rank $n = 0, 1$, and 2 . Clearly the contributions decrease rapidly with angular momentum but the decrease with rank is not so strong. Indeed, the effects of higher rank terms, and so of higher derivative components in the equivalent local equations, are not assured of being small. Nevertheless, the local equivalent potentials associated with these moments to rank 2 and as defined by Eq. (11.47) are presented in Fig. 11.4. The $l = 0, 1, 2$ and 3 contributions are displayed by the solid, long dashed, small dashed, and dotted curves respectively. Clearly they decrease in effect quite markedly with angular momentum. Unfortunately they do not give phase shifts in sufficiently good agreement with the actual non-local potential results.

A different prescription for finding the partial wave local equivalent potentials uses Wronskians of specific solutions [274, 276] and moment expansions. This method, first proposed by Austern [276]

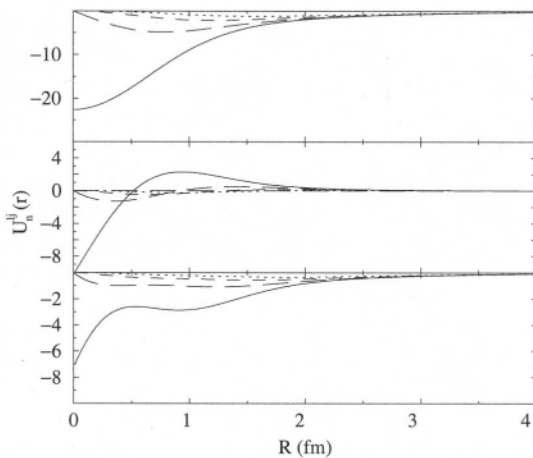


Fig. 11.3. The moments of the nonlocal kernels for rank $n = 0, 1$, and 2 (top, middle, and bottom segments) and for angular momenta $l = 0, 1, 2$, and 3 . The curves are identified in the text.

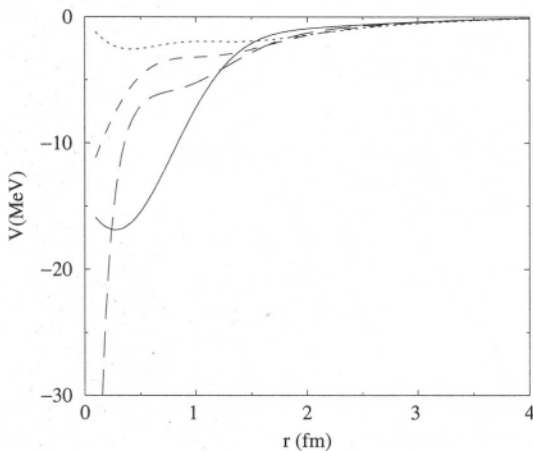


Fig. 11.4. The equivalent local potentials derived from the moments for angular momenta 0 (solid), 1 (long dashed), 2 (small dashed), and 3 (dotted).

and applied later [274], involves transformation of the non-local radial Schrödinger equation, Eq. (11.4), to a local equivalent form by using the Wronskian of solutions of the non-local Schrödinger equation. The transformation is effected by knowing two linearly independent solutions with the boundary conditions for incoming and outgoing waves respectively. Consider those solutions as $f_i^{(i)}(kr) = f^{(i)}(kr)$ with $i = 1, 2$. The local equivalent potential yields two solutions $F_i^{(i)}(kr) = F^{(i)}(kr)$ that are equivalent to the non-local ones in so far as they are asymptotically equal,

$$\lim_{r \rightarrow \infty} [f^{(i)}(kr) - F^{(i)}(kr)] = 0. \quad (11.48)$$

At other radii, it is supposed that the pairs of solutions relate via

$$f^{(i)}(kr) = A(kr)F^{(i)}(kr), \quad (11.49)$$

where the transformation does not shift zeros and has a limit,

$$\lim_{r \rightarrow \infty} A(kr) = 1. \quad (11.50)$$

The essential difference between the two sets of solutions is epitomised by their respective Wronskians,

$$W_{(f^{(1)}, f^{(2)})}(kr) = f^{(1)}(kr) \frac{df^{(2)}(kr)}{dr} - f^{(2)}(kr) \frac{df^{(1)}(kr)}{dr}, \quad (11.51)$$

and $W_{(F^{(1)}, F^{(2)})}(kr)$ defined similarly. The ansatz, Eq. (11.49), relates these Wronskians by

$$W_{(f^{(1)}, f^{(2)})}(kr) = \mathcal{A}^2(kr)W_{(F^{(1)}, F^{(2)})}(kr) \quad (11.52)$$

so that the transformation is

$$\mathcal{A}(kr) = \sqrt{\frac{W_{(f^{(1)}, f^{(2)})}(kr)}{W_{(f^{(1)}, f^{(2)})}(kr)_{r \rightarrow \infty}}}. \quad (11.53)$$

This transformation, named by Austern as the Perey effect, is a damping factor so that the non-local wave functions are smaller than the equivalent local potential solutions, the scale of which was illustrated in Fig. 11.1. This damping seems important for distorted wave calculations of non-elastic processes. As there are two distorted waves involved in calculations of such scattering amplitudes and as the moduli squared of those amplitudes are taken, allowing an average reduction of the wave functions through the interaction range of 10% can equate to a 40% reduction in the transition probability.

The local equivalent potentials are constructed [277, 278] by combining the non-local and local equivalent Schrödinger equations to eliminate any reference to a particular pair of solutions. Pure algebraic manipulations yield

$$\begin{aligned}
 V^{lj}(r; E) &= -\frac{1}{2} \frac{1}{W_{(f^{(1)}, f^{(2)})}(kr)} \frac{d^2 W_{(f^{(1)}, f^{(2)})}(kr)}{dr^2} \\
 &\quad + \frac{3}{4} \left[\frac{1}{W_{(f^{(1)}, f^{(2)})}(kr)} \frac{dW_{(f^{(1)}, f^{(2)})}(kr)}{dr} \right]^2 \\
 &\quad + \frac{1}{W_{(f^{(1)}, f^{(2)})}(kr)} \int_0^\infty U_{lj}(r, r') W_{lj}^{(1,2)}(r, r') dr' \\
 &= -\frac{1}{\mathcal{A}(kr)} \frac{d^2 \mathcal{A}(kr)}{dr^2} + \frac{2}{\mathcal{A}^2(kr)} \left[\frac{d\mathcal{A}(kr)}{dr} \right]^2 \\
 &\quad + \frac{1}{\mathcal{A}^2(kr)} \int_0^\infty U_{lj}(r, r') W_{lj}^{(1,2)}(r, r') dr'. \tag{11.54}
 \end{aligned}$$

where

$$W_{lj}^{(1,2)}(r, r') = \left[f^{(1)}(kr') \frac{df^{(2)}(kr)}{dr} - f^{(2)}(kr') \frac{df^{(1)}(kr)}{dr} \right]. \tag{11.55}$$

Clearly the equivalent local potentials are lj dependent and, given knowledge of the damping functions, those local potentials are defined over the complete radial range. The expression for the local equivalent potentials, Eq. (11.54), is cumbersome to use in practice. A utilitarian approximation is as follows. For a symmetric kernel, the equality involving derivatives of the δ function,

$$U_{lj}(r, r') = \sum_{n=0}^{\infty} \frac{(-1)^n}{n!} e^{ik_0 s} \delta^{(n)}(s) Z_{lj}^{(n)}(R; k_0(s)), \tag{11.56}$$

holds. Therein, $s = r - r'$ and $R = \frac{1}{2}(r + r')$. The wave number k_0 is a function of R whose form can be chosen in a self-consistent fashion [272, 279]. This is discussed later. The expansion functions $Z_{lj}^{(n)}$ are the n^{th} moments of the integral kernel which are defined by

$$Z_{lj}^{(n)}(R; k_0) = Z_{lj}^{(n)}(R) = \int_{-2R}^{2R} e^{-ik_0 s} s^n U_{lj}\left(R + \frac{1}{2}s, R - \frac{1}{2}s\right) ds. \tag{11.57}$$

The consistency of this representation follows simply by inserting the expansion, Eq. (11.56), obtaining

$$Z_{ij}^{(n)}(R; k_0) = \int_{-2R}^{2R} ds s^n \sum_{m=0}^{\infty} \frac{(-1)^m}{m!} \delta^{(m)}(s) Z_{ij}^{(m)}(R; k_0). \quad (11.58)$$

After partial integration, only the $m = n$ term is non-vanishing.

The kernels U_{ij} are peaked about $s = r - r' = 0$ and so appreciable contributions in the integrals only come from the region of small s . Hence the moments $Z^{(n)}$ decrease rapidly with n . Introducing a parameter λ to characterise the scale of magnitudes, the kernel can be recast as

$$U_{ij}(r, r') = \sum_{n=0}^{\infty} \lambda^n V_{ij}^{(n)}(r, r'; k_0), \quad (11.59)$$

with

$$V_{ij}^{(n)}(r, r'; k_0) = \frac{(-1)^n}{n!} e^{ik_0(r-r')} \delta^{(n)}(r-r') Z_{ij}^{(n)}\left(\frac{1}{2}(r+r'); k_0(r-r')\right). \quad (11.60)$$

With a corresponding expansion of the distorted waves of the non-local Schrödinger equation,

$$f_{ij}^{(i)}(r) = \sum_{n=0}^{\infty} \lambda^n Q_{ij}^{(i,n)}(r), \quad (11.61)$$

the non-local equations expand in terms of powers of λ to second order to the set,

$$\begin{aligned} \left[\frac{d^2}{dr^2} - \frac{l(l+1)}{r^2} + k^2 - Z_{ij}^{(0)}(r) \right] Q_{ij}^{(i,0)}(r) &= 0, \\ \left[\frac{d^2}{dr^2} - \frac{l(l+1)}{r^2} + k^2 - Z_{ij}^{(0)}(r) \right] Q_{ij}^{(i,1)}(r) &= \int V^{(1)}(r, r'; k_0) Q_{ij}^{(i,1)}(r') dr', \\ \left[\frac{d^2}{dr^2} - \frac{l(l+1)}{r^2} + k^2 - Z_{ij}^{(0)}(r) \right] Q_{ij}^{(i,2)}(r) &= \int V_{ij}^{(1)}(r, r'; k_0) Q_{ij}^{(i,1)}(r') dr' \\ &\quad + \int V_{ij}^{(2)}(r, r'; k_0) Q_{ij}^{(i,0)}(r') dr'. \end{aligned} \quad (11.62)$$

To develop the expansion of the local equivalent potentials however, one need look also at the expansion of the Wronskians. That expansion with powers of λ is

$$W_{(f^{(1)}, f^{(2)})}(kr) = W_{(f^{(1)}, f^{(2)})}^{(0)}(kr) + \sum_{n=1}^{\infty} \lambda^n W_{(f^{(1)}, f^{(2)})}^{(n)}(kr) \quad (11.63)$$

where for $n = 0$

$$W_{(f^{(1)}, f^{(2)})}^{(0)}(kr) = [\mathcal{Q}_{ij}^{(2,0)}(kr)f_{ij}^{(1)}(kr)\delta(r) - f_{ij}^{(2)}(kr)\delta(r)\mathcal{Q}_{ij}^{(1,0)}(kr)], \quad (11.64)$$

and for $n > 0$

$$\begin{aligned} W_{(f^{(n)}, f^{(2)})}^{(n)}(kr) = & \left[\mathcal{Q}_{ij}^{(2,n-1)}(kr) \frac{d\mathcal{Q}_{ij}^{(1,n)}(kr)}{dr} + \mathcal{Q}_{ij}^{(2,n)}(kr) \frac{d\mathcal{Q}_{ij}^{(1,n-1)}(kr)}{dr} \right. \\ & \left. - \mathcal{Q}_{ij}^{(1,n)}(kr) \frac{d\mathcal{Q}_{ij}^{(2,n-1)}(kr)}{dr} - \mathcal{Q}_{ij}^{(1,n-1)}(kr) \frac{d\mathcal{Q}_{ij}^{(2,n)}(kr)}{dr} \right]. \end{aligned} \quad (11.65)$$

From the set of equations, Eq. (11.64), it is evident that $W_{(f^{(0)}, f^{(2)})}^{(0)}(kr)$ are Wronskians corresponding to solutions of the local Schrödinger equations for which it is known that

$$W_{(f^{(1)}, f^{(2)})}^{(0)}(kr) = \lim_{r \rightarrow \infty} W_{(f^{(1)}, f^{(2)})}^{(0)}(kr) = \text{constant}. \quad (11.66)$$

With the above expansions it is now possible to develop $V_{ij}^l(r)$ in powers of λ . The full calculation is lengthy and it suffices here to consider the process with just a single term. Specifically consider the second term in Eq. (11.54), and to order λ in the expansion of the Wronskians

$$\frac{1}{W_{(f^{(1)}, f^{(2)})}(kr)} \frac{dW_{(f^{(1)}, f^{(2)})}(kr)}{dr} = \frac{1}{W_{(f^{(1)}, f^{(2)})}^{(0)}(kr) \Big|_{r \rightarrow \infty}} \frac{dW_{(f^{(1)}, f^{(2)})}^{(1)}(kr)}{dr}. \quad (11.67)$$

From the definition of $W^{(1)}$, and using the Schrödinger equations to replace second derivatives, gives to order λ ,

$$\begin{aligned} \frac{dW_{(f^{(1)}, f^{(2)})}(kr)}{dr} = & [\mathcal{Q}_{ij}^{(2,0)}(r) \int V_{ij}^{(1)}(r, r'; k_0) \mathcal{Q}_{ij}^{(1,0)}(r') dr' \\ & - \mathcal{Q}_{ij}^{(1,0)}(r) \int V_{ij}^{(1)}(r, r'; k_0) \mathcal{Q}_{ij}^{(2,0)}(r') dr']. \end{aligned} \quad (11.68)$$

Use of the expansion Eq. (11.60), then gives

$$\begin{aligned}
& \left[\mathcal{Q}_{lj}^{(2,0)}(r) \int \mathcal{V}_{lj}^{(1)}(r, r'; k_0) \mathcal{Q}_{lj}^{(1,0)}(r') dr' - \mathcal{Q}_{lj}^{(1,0)}(r) \int \mathcal{V}_{lj}^{(1)}(r, r'; k_0) \mathcal{Q}_{lj}^{(2,0)}(r') dr' \right] \\
& = Z_{lj}^{(1)}(r; k_0) \left[\mathcal{Q}_{lj}^{(2,0)}(kr) \frac{d\mathcal{Q}_{lj}^{(1,0)}(kr)}{dr} - \mathcal{Q}_{lj}^{(1,0)}(kr) \frac{d\mathcal{Q}_{lj}^{(2,0)}(kr)}{dr} \right] \\
& = Z_{lj}^{(1)}(r; k_0) \mathcal{W}_{(f^{(1)}, f^{(2)})}^{(0)}(kr) \Big|_{r \rightarrow \infty}
\end{aligned} \tag{11.69}$$

for the bracket term in Eq. (11.68), so that to order λ ,

$$\frac{1}{\mathcal{W}_{(f^{(1)}, f^{(2)})}(kr)} \frac{d\mathcal{W}_{(f^{(1)}, f^{(2)})}(kr)}{dr} = Z_{lj}^{(1)}(r; k_0). \tag{11.70}$$

The other terms in Eq. (11.54) for the local equivalent potential likewise expand to be given in terms of the moments and, to order λ^2 , one finds

$$\begin{aligned}
V^{lj}(r) &= Z_{lj}^{(0)}(r; k_0) + \lambda \left[-ik_0 Z_{lj}^{(1)}(r; k_0) \right] \\
&\quad + \lambda^2 \left\{ \frac{1}{4} \left[Z_{lj}^{(1)}(r; k_0) \right]^2 - \frac{1}{4} \frac{d^2}{dr^2} Z_{lj}^{(2)}(r; k_0) \right. \\
&\quad \left. + Z_{lj}^{(2)}(r; k_0) \left[\frac{l(l+1)}{r^2} - k^2 - k_0^2 + Z_{lj}^{(0)}(r; k_0) \right] \right\},
\end{aligned} \tag{11.71}$$

where $\lambda \rightarrow 1$ is finally to be taken.

With symmetric kernels the odd order moments are eliminated. In that case, upon using the expansion about $s = 0$, $\sin(k_0 s) = (k_0 s + \frac{1}{3} k_0^3 s^3 + \dots) \cos(k_0 s)$, one finds

$$\begin{aligned}
Z_{lj}^{(1)}(R; k_0) &= i \int_{-2R}^{2R} \sin(k_0 s) s U_{lj} \left(R + \frac{1}{2}s, R - \frac{1}{2}s \right) ds \\
&= ik_0 \int_{-2R}^{2R} \cos(k_0 s) s^2 U_{lj} \left(R + \frac{1}{2}s, R - \frac{1}{2}s \right) ds + \dots, \\
&= 2ik_0 Z_{lj}^{(2)}(R; k_0) + 8ik_0^3 Z_{lj}^{(4)}(R; k_0) + \dots.
\end{aligned} \tag{11.72}$$

All odd moments can be similarly replaced and to order λ^2 with $\lambda \rightarrow 1$,

$$\begin{aligned}
V^{lj}(r) &= Z_{lj}^{(0)}(r; k_0) - \frac{1}{4} \frac{d^2}{dr^2} Z_{lj}^{(2)}(r; k_0) \\
&\quad + Z_{lj}^{(2)}(r; k_0) \left[\frac{l(l+1)}{r^2} - k^2 - k_0^2 + Z_{lj}^{(0)}(r; k_0) \right].
\end{aligned} \tag{11.73}$$

If the entire series is summed there is no dependence upon the choice made for $k_0(\mathbf{r})$. That is not the case if any truncation is taken. In such cases, the best choice seems to be the local momentum of the projectile [279]

$$k_0^2(\mathbf{r}) = k^2 - \frac{l(l+1)}{r^2} - Z_{lj}^{(0)}(\mathbf{r}; k_0). \quad (11.74)$$

With that choice, the last term in Eq. (11.73) vanishes and the only correction to $Z_{lj}^{(0)}(\mathbf{r}; k_0)$ is the small second derivative term. Within a large nucleus the potential is not expected to vary much with r so that, in lowest order, the phase equivalent local potential can be taken as

$$V^{lj}(\mathbf{r}) = Z_{lj}^{(0)}(\mathbf{r}; k_0) = \int_{-2r}^{2r} e^{ik_0(\mathbf{r})s} U_{lj}\left(\mathbf{r} + \frac{1}{2}s, \mathbf{r} - \frac{1}{2}s\right) ds, \quad (11.75)$$

with $k_0(\mathbf{r})$ given by Eq. (11.74). Other choices for k_0 have been found to be less than satisfactory [274].

The first term of the moment expansion given above is similar to that proposed by Perey and Saxon [271] when their kernel was expressed in multipoles. But in higher orders the two are quite different. The moment expansion leads to corrections to the lower order potential and does not involve higher order differential operators.

Bauhoff, von Geramb, and Pália [274] used both the Wronskian and moment expansion approximation methods to find local equivalent potentials from the energy independent, non-local form given by Eqs. (11.9)–(11.11) with the form factor of Eq. (11.24). They obtained results at various energies and those for 30 and 200 MeV for some low partial waves are displayed in Fig. 11.5. The agreement between the Wronskian and the moment expansion results is very good. Only at quite small radii do the two forms of equivalent local potentials differ. Those variations are not significant as such will only affect scattering at the highest momentum transfer values if at all in any sensible way. These results also indicate that the equivalent local potentials are both angular momentum and energy dependent with the original non-local one being neither. The energy dependence is illustrated more strikingly in Fig. 11.6. Therein the s -wave equivalent local potentials are presented at various energies to 180 MeV. These potentials were obtained using the moment expansion approach. At very small radii, the potentials essentially are identical. For radii above 0.5 fm however, they vary quite markedly, almost linearly with energy; this feature justifies the energy expansion approach favoured by Apagyi [280]. The angular momentum dependence of these

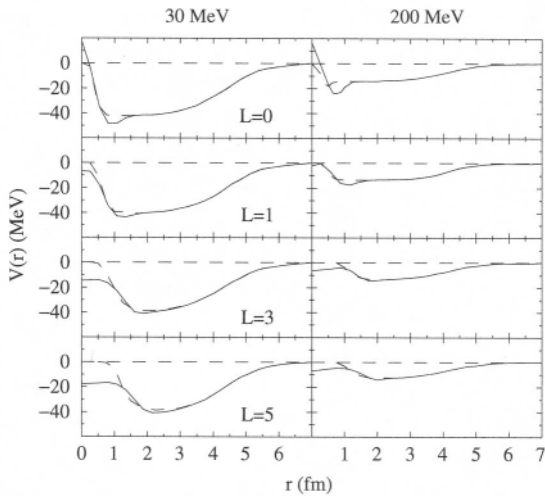


Fig. 11.5. The local equivalent potentials for various angular momentum values as shown as obtained by using the Wronskian and moment expansion methods at 30 and 200 MeV.

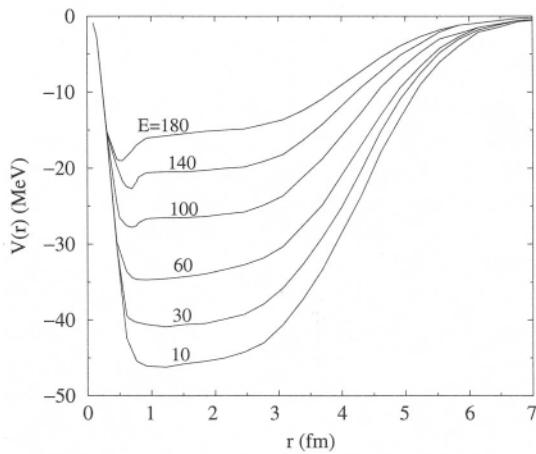


Fig. 11.6. The s -wave local equivalent potentials found by using the moment expansion for various energies to 180 MeV.

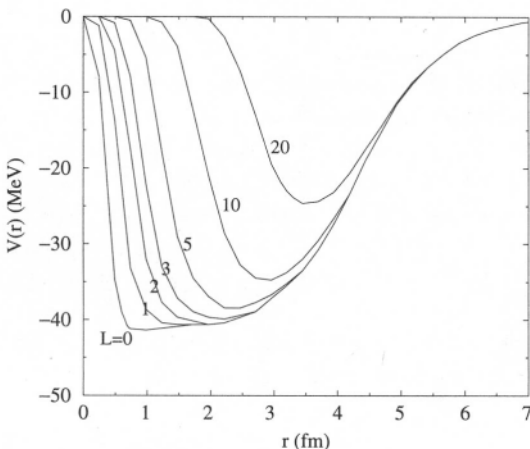


Fig. 11.7. The moment expansion local equivalent potentials for 30 MeV scattering and for various partial waves.

equivalent local potentials is shown in Fig. 11.7, in which the 30 MeV results of the moment expansion method are plotted for diverse partial waves. At large radii these potentials essentially are all the same. Within the nuclear volume however, they vary quite markedly. At very small radii they behave as $r^{(2l+3)}$. This strong variation does not reflect as much in calculations of the scattering phase shifts, and therefore of cross sections. The centrifugal barriers screen the inner features strongly for the high partial waves shown so that only the outer radii aspects are influential in calculations. With the small partial waves and less potent centrifugal barriers, the variations of the local equivalent potentials are not as great so that again the effects in calculations of phase shifts are not as large as might have been anticipated from these plots of the equivalent local potentials.

11.3. Inverse Scattering

Most analyses of physical problems use direct methods of solution such as have been described in the preceding sections. In direct schemes one starts with known or postulated forces and solves the equations of motion to specify the S matrix. On the other hand, scattering problems can be framed in an inverse manner where the S matrix is given *ab initio*

to define the forces acting. The inverse scattering problems (ISP) of interest are based upon scattering being defined by solutions of the local potential Schrödinger equation whose S matrix is known. In contrast to the direct problem which is to evaluate that S matrix for particular choices of $V(\mathbf{r}; E)$, the ISP transcribes to extracting $V(\mathbf{r}; E)$ from phase shifts or, if more ambitious, from differential cross sections.

Inversion procedures have been developed to effect the process

$$\text{Data} \Rightarrow \{S_{lj}(k)\} \Rightarrow \begin{cases} V(r; E) & \text{1 independent} \\ V_{lj}(r) & \text{E independent} \end{cases} \quad (11.76)$$

For fixed energy scattering, as is discussed here, the phase shifts arise from the differential cross section as

$$\frac{d\sigma}{d\Omega}(\theta) = |f(k, \cos\theta)|^2, \quad (11.77)$$

with the scattering amplitude for spinless particles

$$\begin{aligned} f(k, \cos\theta) &= \frac{1}{2ik} \sum_{l=0}^{\infty} (2l+1)[S_l(k) - 1]P_l(\cos\theta) \\ &= \frac{1}{k} \sum_{l=0}^{\infty} (2l+1)e^{i\delta_l(k)} \sin[\delta_l(k)]P_l(\cos\theta). \end{aligned} \quad (11.78)$$

The S matrix relates to the phase shift by

$$S_l(k) = e^{2i\delta_l(k)} = \eta_l(k) e^{2iR_c\{\delta_l(k)\}}. \quad (11.79)$$

Therein $\eta_l = |S_l(k)| \leq 1$ accounts for flux loss in scattering. Ignoring Coulomb effects those phase shifts relate to the asymptotic form of solutions of the radial Schrödinger equations by

$$\chi_l(k, r) \xrightarrow[r \rightarrow \infty]{} e^{i\delta_l(k)} \sin\left[kr - \frac{1}{2}l\pi + \delta_l(k)\right]. \quad (11.80)$$

The ISP for nuclear scattering depends upon the system being studied and the data used to initiate the study. With NN scattering one seeks interactions in each angular momentum channel from phase shifts such as the SM97 set [15]. Thus the fixed l ISP involves inversion of $\delta_l(k)$ with the energy $E(k)$ as the spectral variable. In applications of the fixed l ISP theories to NN scattering [77], $S_l(k)$ was expressed as the rational functions of k ,

$$S_l(k) = \prod_{m=1}^M \frac{k - \sigma_m}{k - \sigma_m^*}. \quad (11.81)$$

The general solution of that inversion problem can be found either from Marchenko's or from Gel'fand and Levitan's integral equations [37, 281]. The potentials in these cases may support bound states whence the spectral properties of those bound states must be given also to obtain unique solutions.

Most *NA* scattering data are taken usually at a fixed energy. Using differential cross sections and other observables as functions of momentum transfer, the ISP then is one in which the energy is fixed and the angular momentum is to be used as a spectral variable. There are many approaches to deal with fixed energy ISP. Often chosen are Newton and Sabatier (NS) formalisms [37] which use the Gel'fand—Levitan theory for fixed energy. The NS approaches require interpolations of the experimental set of $\delta(k)$ as input. Unfortunately one then does not find a complete solution of the ISP but instead solutions that are linked to a particular class of phase shift functions.

Another approach to the fixed energy ISP is to use a Bargmann scheme. In such schemes, the inversion potential is presumed to be a superposition of Bargmann potentials. Associated with Bargmann potentials are phase shifts that can be specified by rational functions of complex angular momentum λ as then can the *S* matrices [282] which have the form

$$S(\lambda, E) = \prod_{n=1}^N \frac{\lambda^2 - \beta_n^2}{\lambda^2 - \alpha_n^2}. \quad (11.82)$$

Physical *S* matrix values are those for which $\lambda = 1 + \frac{1}{2}$.

Sometimes it is convenient to work in Born approximation as by so doing the algebra is more transparent. The lowest order scattering amplitude is defined from the scattering potential by

$$f(k, \theta) = -\frac{1}{2k \sin\left(\frac{\theta}{2}\right)} \int_0^\infty \sin(tr) V(r) r dr, \quad \text{where } t = 2k \sin\left(\frac{\theta}{2}\right). \quad (11.83)$$

The direct problem $V(r) \rightarrow f(k, \theta)$ is well posed, but the inverse one $f(k, \theta) \rightarrow V(r)$ is not. The latter is under-determined since the scattering amplitude is known at best for $\theta \in [0, \pi]$. To facilitate Fourier transformation, an extrapolation into the unphysical θ region is necessary and so the limited physical domain is a source of ill-posedness for all fixed energy ISP. A simple continuation for $t > 2k$ is to use $g(t) = 0$ for $t > 2k$. With that inversion is straightforward and yields the oscillatory potential

$$V(r) = \frac{1}{r} \int_0^{2k} g(t) \sin(rt) dt. \quad (11.84)$$

However the Born approximation is not adequate for many applications and better schemes exist. Of those fixed energy ISP schemes, three will be discussed in more detail. They are the semi-classical WKB, the Lipperheide-Fiedeldey, and the Newton-Sabatier approaches.

11.3.1. The WKB Method

Scattering by a local potential $V(r)$ is characterised by a phase shift function which, in the WKB approximation, is given by [37]

$$\delta(\lambda, E) = ka \int_{z_0}^{\infty} \frac{1}{z} \sqrt{z^2 \left(1 - \frac{V(z)}{E}\right) - \frac{\lambda^2}{(ka)^2}} dz - \int_{\lambda/ka}^{\infty} \frac{1}{z} \sqrt{z^2 - \frac{\lambda^2}{(ka)^2}} dz, \quad (11.85)$$

where $z = r/a$ is a dimensionless variable.

This expression simplifies by using the Sabatier transformation [37],

$$t(z) = z \sqrt{1 - \frac{V(z)}{E}}, \quad (11.86)$$

taken under conditions that $t(z)$ has an inverse, $z(t)$. Defining the turning point condition by $t_0 = \lambda/ka$, the leading term in the phase shift expression becomes

$$\delta^{(1)} = ka \int_{t_0}^{\infty} \sqrt{t^2 - t_0^2} \frac{1}{2} \frac{dz}{dt} dt. \quad (11.87)$$

Redefining the integration variable in the second term as t , the complete result then is

$$\delta(\lambda, E) = ka \int_{t_0}^{\infty} \sqrt{t^2 - t_0^2} \left[\frac{1}{z(t)} \frac{dz(t)}{dt} - \frac{1}{t} \right] dt. \quad (11.88)$$

Integration by parts, gives

$$\delta(\lambda, E) = \ln \left[\frac{z(t)}{t} \right] ka \sqrt{t^2 - t_0^2} \Big|_{t_0}^{\infty} - ka \int_{t_0}^{\infty} \ln \left[\frac{z(t)}{t} \right] \frac{t}{\sqrt{t^2 - t_0^2}} dt. \quad (11.89)$$

Then with the quasi-potential defined by

$$Q(t) = Q(t, E) = 2E \ln \left[\frac{z(t)}{t} \right], \quad (11.90)$$

as the leading term vanishes at both limits,

$$\delta(\lambda, E) = -\frac{ka}{2E} \int_{t_0}^{\infty} \frac{Q(t)}{\sqrt{t^2 - t_0^2}} t dt. \quad (11.91)$$

With $E = \hbar^2 k^2 / 2\mu$ taking $a = 1$, this becomes

$$\delta(\lambda, E) = -\frac{\mu}{\hbar^2 k^2} \int_{\lambda}^{\infty} \frac{Q(t)}{\sqrt{t^2 - \lambda^2}} t dt. \quad (11.92)$$

These are Abel integral equations, and so can be inverted to give

$$Q(t) = \left(\frac{4E}{ka} \right) \frac{1}{\pi i} \frac{d}{dt} \int_t^{\infty} \frac{\lambda(\lambda, E)}{\sqrt{\lambda^2 - \lambda^2}} \lambda d\lambda. \quad (11.93)$$

The potential then arises from the Sabatier transform as

$$V(z) = E \left[1 - \frac{t^2(z)}{z^2} \right], \quad (11.94)$$

and in terms of the quasi-potential,

$$V(z) = E \left[1 - e^{-\frac{Q(t)}{E}} \right]. \quad (11.95)$$

The variables z and t are related by the transcendental equation $z(t) = t \exp [Q(t)/2E]$, and the approach is valid as long as there is a 1:1 correspondence between z and t from that relationship, and provided the energy exceeds that at which orbiting occurs,

$$E > V(r) + \frac{1}{2} r \frac{dV(r)}{dr} \quad (11.96)$$

The quasi-potentials also have limits. For large t , the quasi-potentials decrease so that with $t \rightarrow kr$, $V(r) \rightarrow Q(t)$. As $t \rightarrow 0$ however, the quasi-potentials diverge and the transforms then lead to the limits

$$t \rightarrow kr_0; \quad V(r) \rightarrow E. \quad (11.97)$$

where r_0 is the turning point. However, practical cases may break at larger radii if solution of the transcendental relationship is not unique. The Abel equation, Eq. (11.93), can be solved analytically for specific phase shift functions and a tabulation of cases of particular use in atomic physics applications exists in the literature [283].

Of interest are rational function forms for the S function,

$$S(\lambda) = \prod_{n=1}^N \frac{\lambda^2 - \beta_n^2}{\lambda^2 - \alpha_n^2}. \quad (11.98)$$

With this the WKB method gives a quasi-potential,

$$Q(t) = 2iE \sum_{n=1}^N \left(\frac{1}{\sqrt{t^2 - \alpha_n^2}} - \frac{1}{\sqrt{t^2 - \beta_n^2}} \right). \quad (11.99)$$

Given that a rational form of S function is appropriate as a representation of nuclear scattering, then it is solely a matter of finding the pole/zero set $\{\alpha_n, \beta_n\}$ that matches observation. A reference S function can also be added whenever scattering is influenced by known potential characteristics, e.g., the Coulomb interaction. Thus the WKB method has the benefit of simplicity and gives smooth inversion potentials for any pole/zero set whether or not they lie in the physical domain of the right hand complex λ plane.

As an example, consider the elastic scattering of 200 MeV protons from ^{12}C for which excellent high quality data exist [75]. The differential cross section was fit [284] using the rational form of S function, Eq. (11.82), supplemented by a reference S function of the form,

$$S_0(\lambda) = e^{i\eta \ln[\lambda^2 + \lambda_c^2]}. \quad (11.100)$$

With η being the Sommerfeld parameter, the shifted point Coulomb parameter λ_c value was 3η . But equally good fits were found with the two sets of complex parameters $\{\alpha_n, \beta_n\}$ that are listed in Table 11.1. Both S functions were obtained assuming a rational form for them and varying the parameters therein to fit the cross-section data directly. The two results were found by using quite different starting conditions in a search upon the complex values of a set of five pole/zero pairs.

The first set, Set 1, were obtained by starting with pole/zero parameter values that accurately map the S function obtained from using the best available phenomenological optical model potential [75] in the Schrödinger equation. Those pole/zero values were then varied to obtain an improved fit to the scattering data. In the second search, the initial set of parameter values where chosen arbitrarily and the parameter set so found after minimisation is denoted as Set 2.

The calculated results are indistinguishable and, by design, match the data. The measure of fit is that these results have values of 1.006 and 1.018 for the χ^2 per degree of freedom and so can be considered as statistically significant. This is a striking illustration of the ambiguity in the relationship between the differential cross section and the scattering

TABLE 11.1

The rational function parameters that gave the fit to the 200 MeV p-¹²C cross section data with χ^2 per degree of freedom of 1.018 (Set 1) and 1.006 (Set 2).

Set 1			
α_n		β_n	
	Real	Imaginary	Real
1	-0.0548404233	-1.2599738423	-0.1326287045
2	-6.1751408446	-9.0868456370	-3.7452076971
3	-7.7899061381	-4.2929187247	-10.3231568381
4	10.6813616392	-8.0296693873	4.0784716287
5	3.2755483843	-5.1539508135	7.8586850920

Set 2			
α_n		β_n	
	Real	Imaginary	Real
1	10.2446786946	-5.9807367075	1.5796064650
2	26.5439785204	-42.5669791285	0.4686569859
3	2.6881915849	-3.1400601804	-4.4316628648
4	-2.6559990678	-2.7192349896	-12.4204548530
5	-2.8946159284	-16.0423535307	-23.2285401587

function. Those S functions are radically different as is evident from Fig. 11.9 wherein they are displayed by modulus and phase. These S functions are obviously very different as then also are the associated scattering phase shifts. The S function from the Set 2 rational function form is far more structured and have significant values, in terms of effect in fitting the cross-section data, for a much larger range of angular momentum values than found with Set 1. Therefore it is not surprising to find that these two parameter sets yield markedly different complex, local inversion potentials. Those WKB inversion potentials are given in Fig. 11.10. Therein their real and imaginary components are displayed in the top and bottom sections. The potentials associated with the Set 1 S function are displayed by the dashed curves while those for the Set 2 S function are shown by the solid ones. Not surprisingly, given the two quite different S functions that lead to them, the two inversion potentials are radically different. The Set 1 results are shallow with the general shape of an attractive absorptive well, resembling a WS form. On the other hand, the

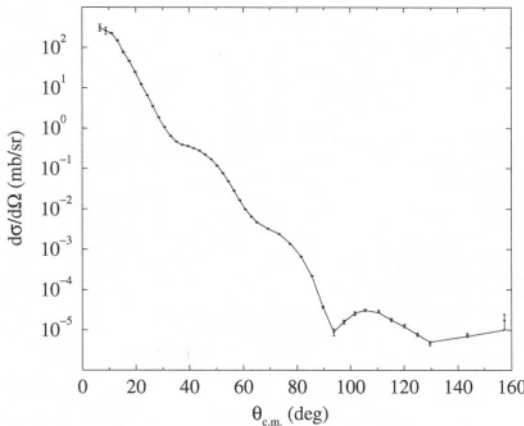


Fig. 11.8. The differential cross section from elastic scattering 200 MeV protons from ^{12}C [75] compared with the fits obtained using the rational form of S function and Table 11.1. The theoretical cross sections were calculated at the data angles and a spline made between them.

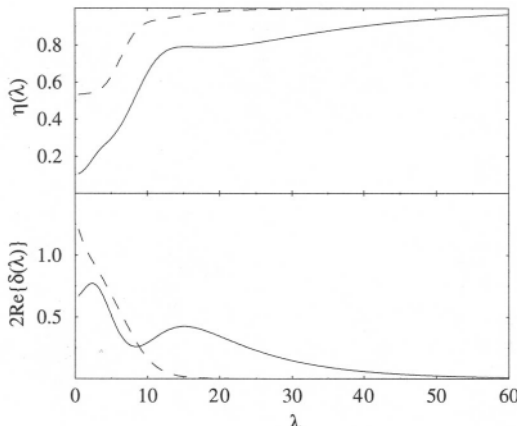


Fig. 11.9. The moduli (top) and phases (bottom) of the rational form S functions of Sets 1 and 2. The dashed and solid curves relate to the Sets 1 and 2 respectively.

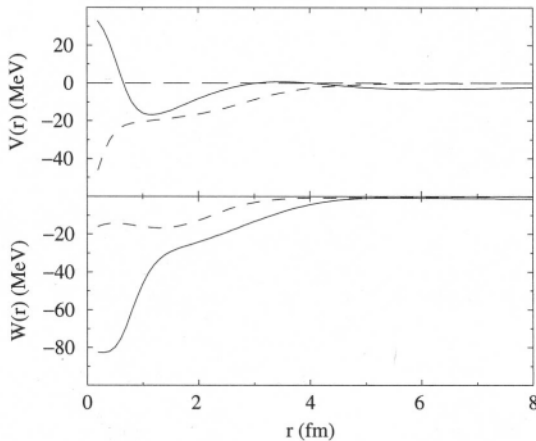


Fig. 11.10. The (complex) inversion potentials found by WKB inversion of the two forms of rational S functions that give equivalent, statistically significant, fits to the cross sections from the elastic scattering of 200 MeV protons from ^{12}C .

inversion potential from the Set 2 S function is very long ranged, has very strong absorption but very shallow refraction.

These potentials are not phase equivalent. The associated S functions are very different. Hence they are not examples of a super-symmetric pair [285] and so do not relate by removal from, or addition to, the bound states of the system [286].

11.3.2. Lipperheide-Fiedeldey Methods

The Lipperheide-Fiedeldey (LF) methods [282] are based upon scattering being associated with Bargmann class potentials. These methods which use angular momentum as the spectral variable, are pertinent with inversion of differential cross-section data. They can be used also to extract spin-orbit potentials by using the approximation of Leeb, Huber, and Fiedeldey [287].

By taking the angular momentum $\lambda = l + \frac{1}{2}$ to be a variable with $\text{Re}\{\lambda\} > 0$, the Schrödinger equation is

$$\left[\frac{d^2}{dr^2} - \frac{\lambda^2 - \frac{1}{4}}{r^2} + k^2 - U(r) \right] \chi(\lambda, k, r) = 0, \quad (11.101)$$

with which there are Jost and regular solutions

$$\begin{aligned} f(\lambda, k, r) &\xrightarrow[r \rightarrow \infty]{} e^{ikr} \\ \phi(\lambda, k, r) &\xrightarrow[r \rightarrow 0]{} r^{\frac{\lambda+1}{2}}. \end{aligned} \quad (11.102)$$

Jost functions are defined as Wronskians,

$$\mathcal{F}(\lambda, k) = W_{(\phi, f)}(\lambda, k, r). \quad (11.103)$$

As the regular solution is given by

$$\phi(\lambda, k; r) = \frac{1}{2ik} [\mathcal{F}(\lambda, -k) f(\lambda, k; r) - \mathcal{F}(\lambda, k) f(\lambda, -k; r)], \quad (11.104)$$

the S function follows as,

$$S(\lambda, k) = \frac{\mathcal{F}(\lambda, -k)}{\mathcal{F}(\lambda, +k)}. \quad (11.105)$$

With the LF approach there are three basic methods in use. The first is termed the rational Bargmann scheme [282] and it uses the S function

$$S(\lambda) = S^{(0)}(\lambda) \prod_{n=1}^N \frac{\lambda^2 - \beta_n^2}{\lambda^2 - \alpha_n^2}. \quad (11.106)$$

With $S^{(0)}(\lambda)$ being a background S function of a potential $V_0(r)$, this method gives an inversion potential $V(r) = V_N(r)$ which is obtained by recursion with

$$V_n(r) = V_{n-1}(r) + \frac{2i}{r} (\beta_n^2 - \alpha_n^2) \frac{d}{dr} \left[\frac{1}{r} \frac{1}{L_{\beta_n}^{(-)(n-1)}(r) + L_{\alpha_n}^{(+)(n-1)}(r)} \right], \quad (11.107)$$

where, with $n = 1, 2, \dots, N$, $L_{\lambda}^{(\pm)(n)}(r)$ are logarithmic derivatives of the Jost functions that satisfy a Riccati equation,

$$\mp \frac{d}{dr} L_{\lambda}^{(\pm)(n)}(r) - [L_{\lambda}^{(\pm)(n)}(r)]^2 + 1 - V_n(r) - \frac{\lambda^2 - \frac{1}{4}}{r^2} = 0. \quad (11.108)$$

To use this inversion method, the rational form for the S matrix, Eq. (11.106), must be found with poles and zeroes that give a fit to scattering data. In so doing the representation may contain poles and zeroes in forbidden quadrants. There should not be either poles lying in the 2nd or 4th quadrants or zeroes lying in the 1st or 3rd quadrants. Hence the rational

form is to be constrained with $\text{Im}\{\alpha^2\} > 0$ and $\text{Im}\{\beta^2\} < 0$. Should the data fitting process lead to rational forms having wrong poles and/or zeroes, inversion results in singularities in the potentials. These singularities may occur not solely at the origin. They may also result at finite radii r_c and take the form of double poles $\sim (r - r_c)^{-2}$. A similar behavior is observed if one inverts non-unitary S functions. Given that most scattering data must be fit with such, the associated rational forms of the S functions may contain wrong poles and zeroes. To offset the resultant problems one can use either a non-rational Bargmann scheme or a mixed one.

The non-rational Bargmann scheme makes use of regular solutions that behave at the origin as

$$\phi_\lambda^{(n)}(r) \xrightarrow[r \rightarrow 0]{} r^{\frac{\lambda+1}{2}}, \quad (11.109)$$

and the logarithmic derivative,

$$L_\lambda^{(n)}(r) = \frac{1}{\phi_\lambda^{(n)}(r)} \frac{d\phi_\lambda^{(n)}(r)}{dr}, \quad (11.110)$$

satisfies a Riccati equation,

$$\frac{d}{dr} L_\lambda^{(n)}(r) + [L_\lambda^{(n)}(r)]^2 + 1 - V_n(r) - \frac{\lambda^2 - \frac{1}{4}}{r^2} = 0. \quad (11.111)$$

In this scheme

$$S(\lambda) = S^{(0)}(\lambda) \frac{\det \left\{ \frac{\sigma_{\beta_n}^{(0)} - \sigma_{\alpha_m}^{(0)}}{\beta_n^2 - \alpha_m^2} - \frac{\sigma_{\beta_n}^{(0)}}{\sigma_\lambda^{(0)}} \frac{\sigma_\lambda^{(0)} - \sigma_{\alpha_m}^{(0)}}{\lambda^2 - \alpha_m^2} \right\}}{\det \left\{ \frac{\sigma_{\beta_n}^{(0)} - \sigma_{\alpha_m}^{(0)}}{\beta_n^2 - \alpha_m^2} - \frac{\sigma_\lambda^{(0)} - \sigma_{\alpha_m}^{(0)}}{\lambda^2 - \alpha_m^2} \right\}}, \quad (11.112)$$

where

$$\sigma_\lambda^{(0)} = S^{(0)}(\lambda) e^{-i\pi\left(\frac{\lambda-1}{2}\right)}. \quad (11.113)$$

The recursive form for the interaction is similar to that given in Eq. (11.107),

$$V_n(r) = V_{n-1}(r) + \frac{2}{r} (\beta_n^2 - \alpha_n^2) \frac{d}{dr} \left[\frac{1}{r} \frac{1}{L_{\beta_n}^{(n-1)}(r) - L_{\alpha_n}^{(n-1)}(r)} \right]. \quad (11.114)$$

Finally a mixed Bargmann scheme is possible. This scheme is a combination of the rational and non-rational schemes requiring no other input than is available for the other two. The rational S function is fitted to experiment with no conditions being placed upon forbidden pole/zeroes. However, any forbidden pole/zeroes that result are grouped into a non-rational S function as

$$S(\lambda) = S_{nr}(\lambda)S_r(\lambda), \quad (11.115)$$

wherein the $S_{nr}(\lambda)$ stems from a reference potential. Then $S_r(\lambda)$ is inverted. This procedure works well if the imaginary parts of forbidden poles/zeroes are not small.

This inversion scheme has been used [284] to analyse proton- ^{12}C elastic scattering cross sections at 200 MeV [75]. As noted earlier, the two sets of pole/zero pairs listed in Table 11.1 give the excellent fits to the differential cross-section data [75] displayed in Fig. 11.8. Those fits are statistically significant as the χ^2/datum of each is of $\mathcal{O}(1)$. Using those rational functions, LF inversion gave the complex inversion potentials shown in Fig. 11.11. The quality of the data fits allowed a meaningful sta-

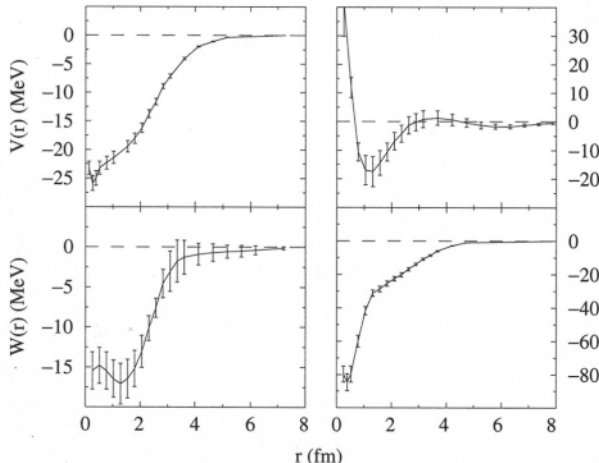


Fig. 11.11. The real (top) and imaginary (bottom) parts of the LF inversion potentials for the rational S functions (Sets 1 and 2) with which high quality fits to the cross-section data from the scattering of 200 MeV protons from ^{12}C were obtained. The inversion potentials are portrayed by the solid curves while the error bars indicate the confidence levels that are described in the text. The results obtained with Sets 1 and 2 are shown in the left and right panels respectively.

tistical error analysis to be applied to these inversion potentials [284] to specify confidence values at each radius. The confidence values which were found under a WKB approximation, are shown in the figures as error bars. The interpretation of these intervals is that, should another potential exist which fits the cross-section data with the same χ^2 per degree of freedom, then there is about a sixty percent probability that it will lie within the confidence band shown by the error bars. Clearly the two results are distinct equivalent solutions. Their confidence bands overlap only where fortuitously the potentials have the same values. Thus a bias built upon the best intuitive knowledge is needed to discriminate between the results of inversion.

11.3.3. Newton-Sabatier Methods

Newton-Sabatier (NS) inversion methods [37] of solution of fixed energy ISP are considered next. In this discussion, initially it is convenient to neglect spin and write the Schrödinger equation in terms of a dimensionless variable $\rho = kr$

$$D^{(U)}(\rho)\chi_l^{(U)}(\rho) = l(l+1)\chi_l^{(U)}(\rho) \quad (11.116)$$

where

$$D^{(U)}(\rho) = \rho^2 \left[\frac{d^2}{d\rho^2} + 1 - U(\rho) \right], \quad (11.117)$$

and with $E = \hbar^2 k^2 / 2\mu$

$$U(\rho) = \frac{V(r) + iW(r)}{E}. \quad (11.118)$$

The solutions are subject to boundary conditions

$$\chi_l^{(U)} \xrightarrow[r \rightarrow \infty]{} B_l \sin \left[\rho - \frac{1}{2} l\pi + \delta_l(k) \right], \quad (11.119)$$

with $\delta_l(k)$ now being complex. The NS method yields

$$U(\rho) = U_0(\rho) - \frac{2}{\rho} \frac{d}{d\rho} \frac{1}{\rho} K(\rho, \rho) \quad (11.120)$$

wherein U_0 is a reference potential and $K(\rho, \rho)$ is the diagonal part of the Jost transformation kernel that is given by the infinite sum

$$K(\rho, \rho') = \sum_l c_l \phi_l^{(U)}(\rho) \phi_l^{(U_0)}(\rho'). \quad (11.121)$$

The solutions are found from the Newton equations

$$\phi_l^{(U)}(\rho) = \phi_l^{(U_0)}(\rho) - \sum_{l'} c_{l'} L_{ll'}(\rho) \phi_{l'}^{(U)}(\rho), \quad (11.122)$$

where

$$L_{ll'}(\rho) = \int_0^\rho \phi_l^{(U_0)}(\rho') \phi_{l'}^{(U_0)}(\rho') \frac{1}{\rho'^2} d\rho'. \quad (11.123)$$

These equations are basic as by matching these solutions asymptotically to the required boundary condition forms, the unknown quantities B_l and $(c_l B_l)$ can be determined. It is assumed that the solutions of the reference potential are known so that the initiating L matrices can be defined. The reference solutions are obtained from

$$D^{(U_0)}(\rho) \phi_l^{(U_0)}(\rho) = l(l+1) \phi_l^{(U_0)}(\rho) \quad (11.124)$$

with

$$\phi_l^{(U_0)} \xrightarrow[r \rightarrow \infty]{} e^{i\delta_l^0(k)} \sin \left[\rho - \frac{1}{2} l\pi + \delta_l^0(k) \right], \quad (11.125)$$

where $\delta_l^0(k)$ are reference input phase shifts. With the normalisation and expansion coefficients so given, the full solutions are determined at all radii.

In practice, the ISP with Coulomb interactions is difficult to handle with the NS method because of convergence problems. Hence a modified NS scheme was developed [288]. Two steps are involved. First one assumes the scattering potential to be a sum of reference and remainder potentials,

$$U(\rho) = U_0(\rho) + \Delta U(\rho) \quad \text{and} \quad \Delta U(\rho) = 0 \quad \text{for } \rho > \rho_0. \quad (11.126)$$

In the asymptotic region $\rho > \rho_0$ then, solution functions have the form

$$\phi_l^{(U)}(\rho) = A_l [\cos(\hat{\delta}_l) F_l(\rho) + \sin(\hat{\delta}_l) G_l(\rho)], \quad (11.127)$$

and

$$\phi_l^{(U_0)}(\rho) = F_l(\rho), \quad (11.128)$$

wherein $F_l(r)$ and $G_l(r)$ are the regular and irregular solutions of Eq. (11.124) with the reference potential, and $\hat{\delta}_l$ are the phase shifts found with the changed asymptotic matching conditions. The second step is to replace the sum with a finite l_{max} . The NS equations then are a finite system of equations,

$$M_x = F \quad (11.129)$$

with N values of ρ , and l_{max} defining the dimension of the matrix. The vector x is $2l_{max}$ in length and contains $\{(A_i), (c_i A_i)\}$. The Newton equations are solved for $\rho < \rho_0$ to define, finally, the Jost kernel of Eq. (11.121). The inversion potential follows from Eq. (11.120).

It is well known that strong spin-orbit interactions contribute in pA scattering and the methods of fixed energy inversion [37] discussed so far do not allow extraction of spin-orbit potentials as the inversion potentials are presumed l - and j -independent. However there are interpolation formulae [289] which provide the connection that, in principle, allows inversion of phase shift sets to extract both central and spin-orbit potentials. Hooshyar [290] has used those Sabatier interpolation formulae to construct an inversion method involving finite differences. Also Huber and Leeb [291] have investigated an approach to the spin-orbit inversion problem in some detail and an approximate scheme of theirs [287] has been used with some success [181] to analyse neutron-alpha scattering data. Recently, a new method based upon the Sabatier interpolation formulae has been developed by which the inversion problem reduces to finding solution of a system of linear-algebraic equations [292, 293].

As test cases of this novel Newton-Sabatier treatment consider 160 and 200 MeV $p-^{12}\text{C}$ scattering and the phase shifts $\delta_{l,j=l\pm\frac{1}{2}}(k)$ predicted with the g folding optical potential as described in the previous chapter. Those phase shifts are displayed in Fig. 11.12 by the filled and open circles for 160 and 200 MeV respectively. The sets for $j = l \pm \frac{1}{2}$ are presented in the top and bottom sections while their real and imaginary parts are displayed in the left and right panels respectively. They have been used recently as input to calculations giving complex central and spin-orbit inversion potentials [294]. Using those inversion potentials in Schrödinger equations gives phase shifts in good agreement with the starting set. The solid curves shown in Fig. 11.12 portray those inversion results. There are small differences between the results however which become more evident in the comparisons of the cross sections and analysing powers which are given in Fig. 11.13. Therein the data as evaluated from calculations made with the g folding optical potentials, shown

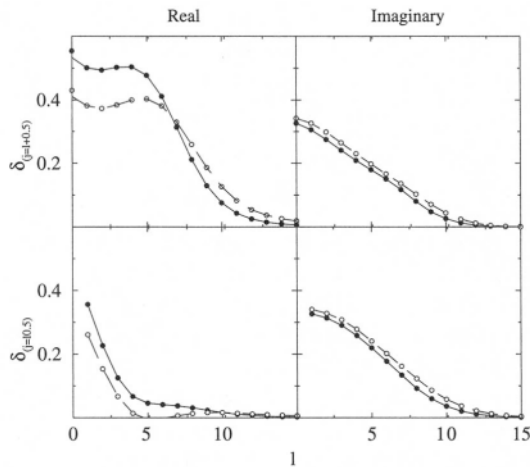


Fig. 11.12. The phase shifts from a fully microscopic optical potential calculation (filled and open circles for 160 and 200 MeV) compared with those found using the local potentials resulting from use of inverse scattering theory.

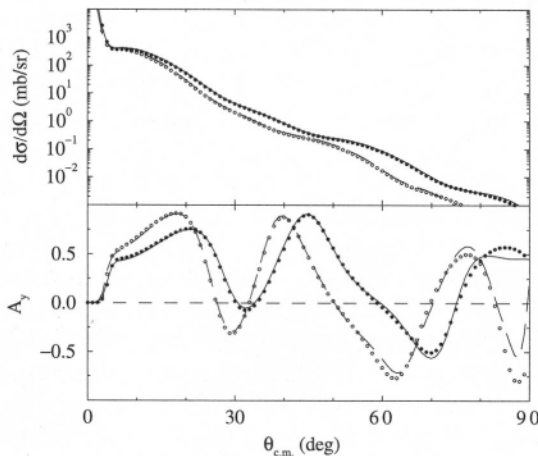


Fig. 11.13. The cross sections and analysing power for 160 MeV $p\text{-}{}^{12}\text{C}$ scattering predicted by the fully microscopic non-local optical potential (filled and open circles for 160 and 200 MeV) compared with those found using the local inversion potentials and shown by the continuous curves.

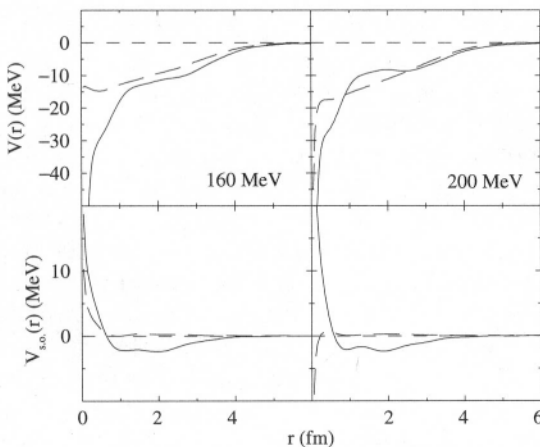


Fig. 11.14. The local central (top segment) and spin-orbit (bottom segment) potentials obtained by inversion of the 160 and 200 MeV $p\text{-}{}^{12}\text{C}$ phase shifts. The real and imaginary parts are shown the continuous and dashed curves respectively.

by the filled and open circles, are compared with the results found using the inversion potentials (solid curves). Only at the larger scattering angles do divergences between the starting data and the inversion results become noticeable.

The 160 and 200 MeV inversion potentials are displayed in Fig. 11.14. The real and imaginary parts of these complex local potentials are displayed by the solid and dashed curves with the central and spin-orbit results shown in the top and bottom sections respectively. The potentials are relatively smooth functions of radius, albeit that there is evident structure in the variations. The absorption is almost a linear function of the radius and so it is not particularly useful to compare these results with phenomenological potentials having WS absorption. The small radius behavior of the inversion potentials is not important as it has little effect in the results of scattering calculations. For the remainder of the potential details however, these inversion results are not visualised by simple WS shapes. The central potential has real and imaginary parts of comparable strength both characterised by a value of 10 MeV save at 200 MeV where the absorption is a bit larger overall. In any event, these inversion potentials are shallow in comparison with the phenomenological ones that have been used to analyse the same data. Also the spin-orbit potentials are relatively weak and predominantly they are real quantities with depths of 2 to 2.5 MeV.

12. INELASTIC SCATTERING

While the microscopic model approach defining the elastic channel optical potentials has been successful, elastic scattering analyses are not as sensitive to details of the effective interaction as are those of inelastic scattering and charge exchange reaction data. The spin-parity changes with such reactions make predictions of the transitions much more sensitive to details of the central, tensor, and two-body spin-orbit components of the transition operator. Using spectroscopy that gives transition OBDME consistent with fits to electron scattering form factors, proton inelastic scattering and charge exchange reactions data can provide more stringent tests of the effective interaction details than formation of the optical potential alone. Conversely if the effective interaction details have been established, inelastic scattering and charge exchange reaction data analyses can be very sensitive tests of the model structure assumed for the nucleus. The basic assumption is that the distorted wave Born approximation (DWBA) is the pertinent theoretical means to specify the inelastic and charge exchange transition amplitudes. As exemplars of this capability, we discuss the results of calculations for transitions in $^{6,7}\text{Li}$, ^{12}C , and for inelastic scattering of the exotic nuclei ^{11}Li and ^6He from hydrogen.

Applications discussed first deal with scattering of protons, typically of 200 MeV, from ^{12}C . For select low excited positive parity states in ^{12}C , no-core $2\hbar\omega$ space shell model wave functions and OBDME are available that reproduce well the electron scattering form factors, as illustrated in Chapter 9. So also are the OBDME from large space projected Hartree-Fock (PHF) [213, 170] calculations and from a particle-hole model (PHM) [165, 173]. Excitations by proton scattering probe the propriety of those structures as well as of the effective interactions. Other transitions to states in ^{12}C for which the spin-parity assignments are not certain are then discussed to show that the analysis of inelastic and charge exchange scattering not only complements those of electron scattering but also can lead to preferred spectral properties. Next, data from inelastic scattering of protons from $^{6,7}\text{Li}$ are considered. Those analyses consider the same aspects of the clustering inherent in the shell model wave functions as indicated by the analyses of the ground state properties and electron scattering discussed previously in Chapters 8 and 9. The same multi- $\hbar\omega$ wave functions are used in DWBA calculations of the inelastic scattering.

The DWBA scattering amplitudes for inelastic and charge exchange scattering of nucleons from nuclei were developed in the

helicity formalism in Chapter 4. Those amplitudes are required also in the specification of the non-zero multipole contributions to elastic scattering and they can be calculated with DWBA91 or DWBA98. In all of the calculations that gave the results to be discussed next, those same programs were used and therein the distorted waves were generated using the optical potential found by g folding. Those foldings involved the same effective interactions used as the inelastic scattering transition operator. Thus the chosen effective interaction specifies consistently the non-local optical potentials used to define the distorted waves and the inelastic scattering transition operator in the two-particle antisymmetrised matrix elements.

12.1. Scattering from ^{12}C

Large space shell model calculations have given the wave functions and OBDME for excitation of many states in ^{12}C . In all, the single particle basis of $0s$ up to and including the $0f1p$ shell was used. That basis was also used for calculations of the negative parity spectrum defining a restricted $3\hbar\omega$ space. The restriction from a full $3\hbar\omega$ study is that the $0g1d2s$ shell was not included. With exceptions, most notably the super-deformed $0_1^+; 0^-$ state at 7.65 MeV, the calculated spectrum to 20 MeV excitation agreed well with data. The OBDME have been used in analyses of data from the inelastic scattering of 200 to 800 MeV protons as well as in analyses of electron scattering form factors [139, 295]. The large basis PHF and PHM structures were used for that as well.

12.1.1. Scattering to Low Excitation States in ^{12}C

The results of DWBA calculations of inelastic scattering cross-sections and analyzing powers of 200 MeV protons from ^{12}C are compared with data in Figs. 12.1–12.7. In those figures the results shown in the left hand panels were obtained using the effective interaction built from the free Paris t matrices. Such results are designated as *Free*. Those in the right hand panels are results found using the medium dependent Paris effective interaction and the results are designated hereafter as *DD*. With one exception, the results for positive parity transitions displayed by the dashed curves were obtained using the $0\hbar\omega$ CK model wave functions [166] while those displayed by the solid curve were calculated using the $2\hbar\omega$ shell model wave functions. The exception is for the $4_1^+; 0^-$ (14.08 MeV) excitation wherein the dashed curves display the results found by using spectroscopic amplitudes from an axially symmetric PHF

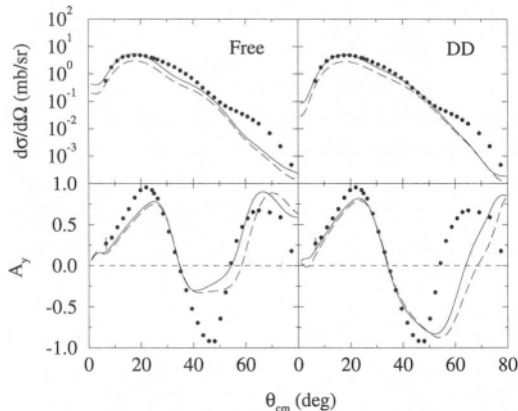


Fig. 12.1. The differential cross-section and analysing power from the inelastic scattering of 200 MeV protons from ^{12}C leading to the $2_1^+; 0$ (4.44 MeV) state.

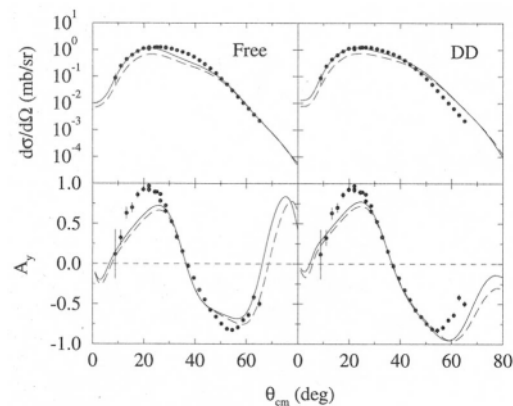


Fig. 12.2. Data [264, 296] from the excitation of the $3_1^+; 0$ (9.64 MeV) state in ^{12}C with 200 MeV protons. The solid and dashed curves portray the results obtained using the restricted $3\hbar\omega$ shell model and PHM structures respectively.

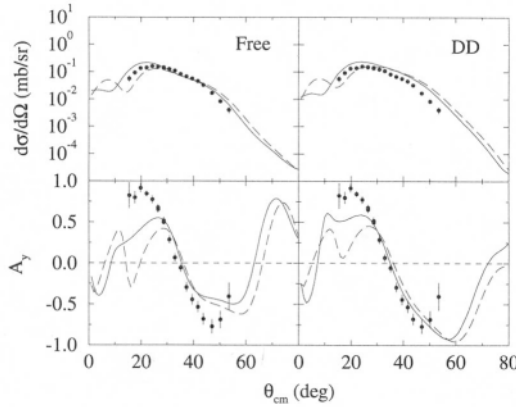


Fig. 12.3. As for Fig. 12.2 but for the excitation of the $1;0$ (10.84 MeV) state.

calculation [139, 295]. The CK (0p-shell) model cannot predict a 4^+ state. With the negative parity excitations, the dashed curves are the results of DWBA calculations made using the spectroscopy of the PHM scheme [173].

The cross-section and analyzing power for 200 MeV protons exciting the $2^+_1; 0$ (4.44 MeV) state in ^{12}C are compared with the data [264, 296] in Fig. 12.1. With both the Free and DD Paris interactions, use of the larger basis structure increase the predicted magnitudes above those

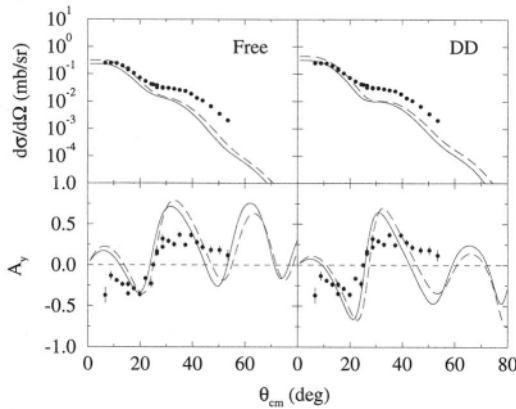


Fig. 12.4. As for Fig. 12.1 but for the excitation of the $1;0$ (12.72 MeV) state.

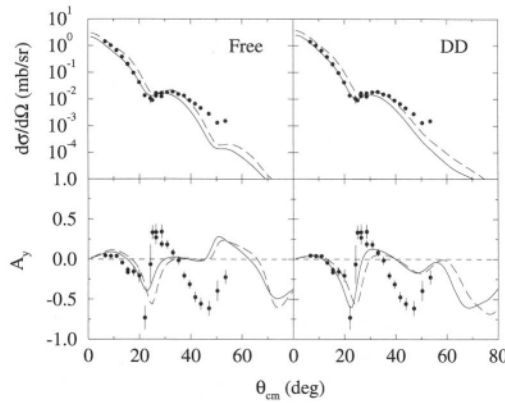


Fig. 12.5. As for Fig. 12.1 but for the excitation of the $1^+_1;1$ (15.11 MeV) state.

given with the CK wave functions bringing the predictions into better agreement with the data. Similar effects were observed when those wave functions were used in calculations of the electron scattering form factors. The cross-sections found using the DD Paris interaction are in better agreement with the data, reproducing the shoulder effect in the 20–40° region in particular. In this transition the central and two body spin-orbit interactions are the most important contributors. Note that no correction was made in the calculations.

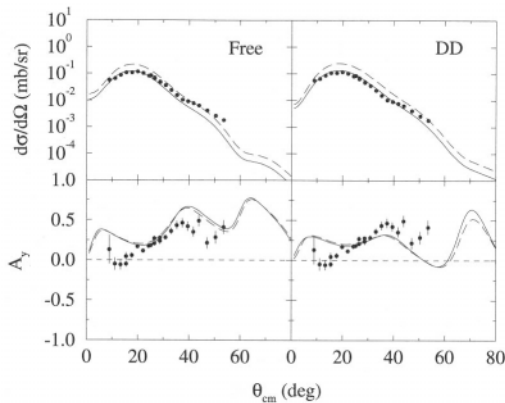


Fig. 12.6. As for Fig. 12.1 but for the excitation of the $2^+_1;1$ (16.11 MeV) state.

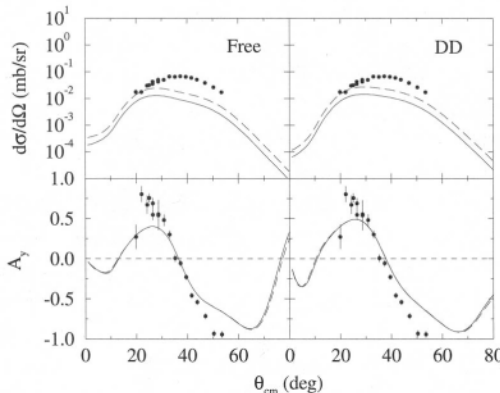


Fig. 12.7. As for Fig. 12.1 but for the excitation of the $4;1$ (14.08 MeV) state.

The results of calculations of 200 MeV proton inelastic scattering to the $3;0$ (9.64 MeV) state are shown in Fig. 12.2. Again the calculations made using Free and DD Paris interactions are shown in the left and right panels respectively. The restricted $3\hbar\omega$ shell model results (solid curves) are compared with those obtained by using the PHM prescription [173]. The two models give similar predictions for the excitation of the $1;0$ (10.85 MeV) state. In that case however, neither prediction yields a satisfactory result as is shown in Fig. 12.3. Note that with an isoscalar dipole transition, the first radial moment of the transition density must vanish otherwise spurious center of mass motion is contained in the wave function. With a restricted basis space defining both the shell and PHM model calculations that cannot be ensured *a priori*. But the shell model does much better [139].

The results and data from magnetic dipole $1;0$ (12.11 MeV) and $1;1$ (15.11 MeV) excitations are shown in Figs. 12.4 and 12.5 respectively. Strength suppression with bigger basis spectroscopy is evident from these calculations, again concurring with the results found for the electron scattering form factors. The results found using the DD Paris interaction are marginally the best of the set. But no calculated result reproduces the large angle cross section or the analysing power. The isovector dipole transition is better reproduced by the results obtained using large basis spectroscopy but all calculated analysing powers are at variance with the data. Unlike the case of the electron scattering form factor, isospin mixing now cannot account for these variations as

the effective NN interactions are charge independent. Note that while the tensor force components of the transition operator are important elements in the calculations of both the isoscalar and iso-vector excitations, the spin-orbit terms are essential for the isoscalar transitions. It is the central terms that are also important for the isovector ones.

The $2^+_1;1$ (16.11 MeV) excitation results are shown in Fig. 12.6. Quenching of transition strength with larger basis calculations is observed with both the Free and DD Paris results. Those obtained using the $2\hbar\omega$ structure are in good agreement with the data. The reduction of the cross-section predictions with the larger basis spectroscopy matches that noted with the transverse form factor from electron excitation of this state. In this case all attributes of the transition operator are important in the calculations, and again no core polarisation corrections have been made to find better agreement with the data.

The results of 200 MeV protons exciting the $4^+_1;0$ (14.08 MeV) state in ^{12}C are compared with the data in Fig. 12.7. As with other normal parity transitions, the central and spin-orbit terms are the most important contributors. In this case, the dashed curves give the results obtained using the PHF spectroscopy [139, 295]. A larger cross-section results with the PHF calculation than that found with the $2\hbar\omega$ shell model one. Both results reflect the general shape of the data but neither gives the correct magnitude of the cross section. That was not so with the longitudinal electron scattering form factors from which it was surmised that the inherent larger basis aspect of the PHF structure was essentially the needed improvement to the $2\hbar\omega$ shell model.

The results found using the Free and DD Paris interactions are little different to those found with effective interactions built upon other realistic potentials. They do vary in comparison to results found using the Love-Franey (LF) [28, 135] medium modified effective interactions however. A comparison of the DD Paris and the LF results are shown next. Differential cross-sections and analysing powers for 200 MeV protons from ^{12}C for the elastic and a select set of inelastic channel, are compared with the data in Figs. 12.8 and 12.9 respectively. The solid lines are the results obtained using the DD Paris interaction while the dashed lines are the equivalent ones found by using the LF force. The data are those of Comfort *et al.* [264, 296]. In all cases, the results of DD calculation are in better agreement with data than are those of the LF calculation.

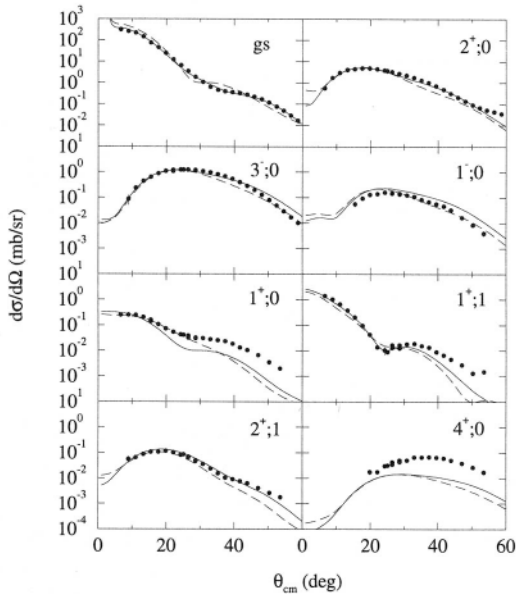


Fig. 12.8. Differential cross section for elastic and inelastic 200 MeV protons scattering from ^{12}C . The solid lines are the results obtained from calculations made using the DD force while the dashed lines are the equivalent ones found by using the LF force.

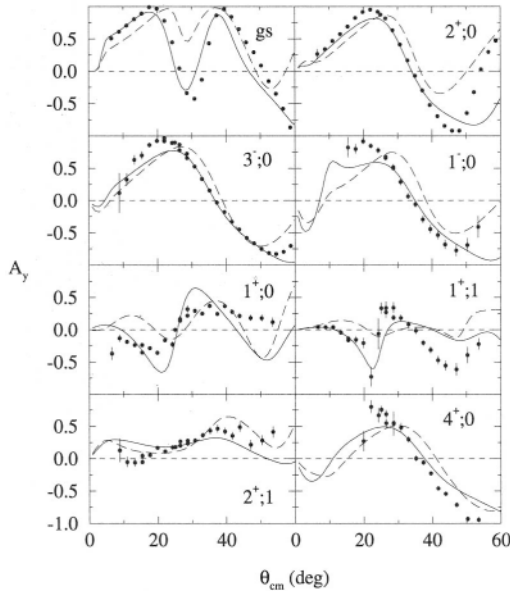


Fig. 12.9. As for Fig. 12.8 but for the analysing powers.

12.1.2. Variations with Energy

As a first example complementing the 200 MeV results discussed above, in Fig. 12.10 calculated differential cross sections are compared with 135 MeV data. The results support the analyses of 135 MeV isovector inelastic scattering and charge exchange (p,n) from ^{12}C that are discussed in the next subsection. The dashed and solid curves display the results of calculations made using the $0\hbar\omega$ and $2\hbar\omega$ models of spectroscopy. Clearly the large space structure and the DD Paris interaction yield excellent results for both cross-sections.

Next, in Fig. 12.11, 160 MeV proton scattering results are shown, both for the elastic and inelastic excitation of the $2^+_1;0$ 4.44 MeV states. *g* folding optical models were used to get the results that are compared with the data of Meyer *et al.* [75] and of Hugi *et al.* [158]. In this case the $2\hbar\omega$ shell model wave functions were used as were both the DD Paris and a medium LF interaction. Those results are portrayed by the solid and dashed curves respectively. Again the results agree very well with the data and there exists a preference for the DD Paris interaction.

Finally, results are compared with the 398 MeV data of Jones *et al.* [297, 298] in Figs. 12.12 and 12.13. The calculations made using the $2\hbar\omega$ structure for positive parity transitions and the restricted $3\hbar\omega$ model for negative parity excitations. The solid and dashed curves are the results found using the DD Paris and LF interactions respectively. As at 200 MeV, the calculations made using the DD Paris interaction are the preferable results. In fact, the DD results for the excitation of the $2^+_1;0$, the $3^-;0$, the $1^-;0$, and now of the $1^+;1$ states are in very good agreement

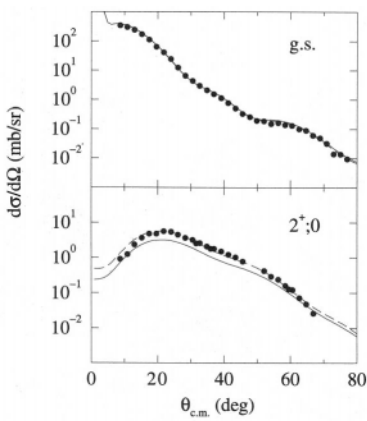


Fig. 12.10. The differential cross section data from the elastic scattering of 135 MeV protons from ^{12}C compared with the result of microscopic optical potential calculations (top) and of DWBA calculations of the excitation of the $2^+_1;0$ (4.43 MeV) state (bottom).

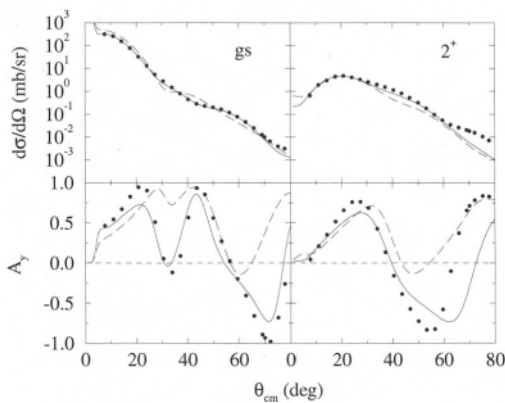


Fig. 12.11. Differential cross sections and analysing powers for the elastic scattering (“gs”) and inelastic scattering (“ 2^+ ”), exciting the $2^+;0$ (4.44 MeV) state of ^{12}C by 160 MeV protons.

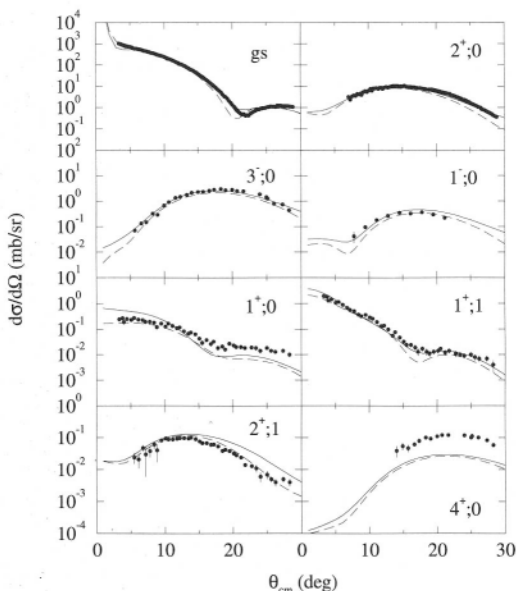


Fig. 12.12. Differential cross sections for 398 MeV protons scattering from ^{12}C and for the elastic and select set of inelastic channels as indicated.

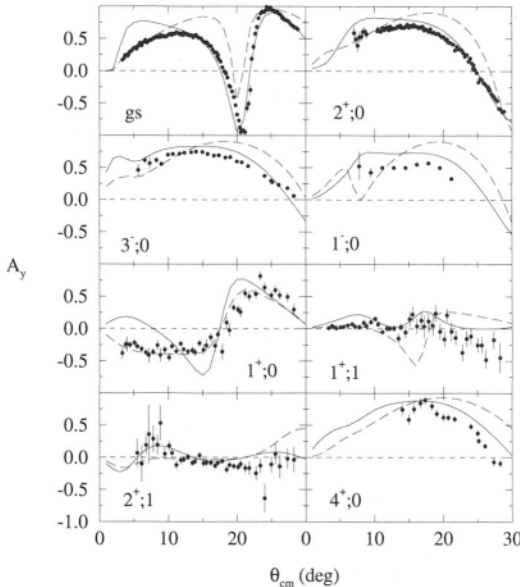


Fig. 12.13. As for Fig. 12.12, but for the analysing powers.

with data, both cross sections and analysing powers. Again a slight reduction to the $1^-; 0$ transition strength would be favoured on the basis of the DD result. The LF result does well with the $1^+; 0$ and the $2^+; 1$ excitations although the analysing power from the latter is better reproduced with the DD calculation. As with the 200 MeV results, both calculations underestimate the strength of excitation of the $4^+; 0$ state. The shape of the $4^+; 0$ cross section is found with the DD result however, and that result also gives an appropriate form for the analysing power.

12.1.3. Isovector Excitations With (p,p') and (p,n) from ^{12}C

The fully microscopic DWBA model of pA inelastic scattering has also been used to analyses cross-section data [299] from excitation of the $1^+; 1$ (15.11 MeV), the $2^+; 1$ (16.11 MeV), and the $2^-; 1$ (16.57 MeV) states of ^{12}C , and from the (p,n) reaction at 135 MeV leading to the ground and to the combined first and second excited states of ^{12}N [300]. The isovector states of ^{12}C are the analogues of those observed in these charge exchange reactions and charge independence of the NN effective interaction dictates that the charge exchange cross sections then should be

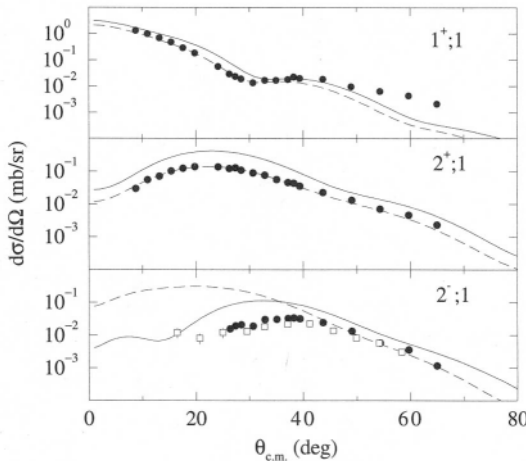


Fig. 12.14. The differential cross section from the inelastic scattering of 135 MeV protons leading to the the $1^+;1$; (15.11MeV) state in ^{12}C , to the $2^+;1$ (16.11MeV) state in ^{12}C (middle), and to the $2^-;1$ (16.57MeV) state in ^{12}C (bottom).

simply a factor of two larger than the appropriate inelastic scattering ones. That has been shown [301] essentially to be the case.

In optical potential calculations, the primary shells as specified by $0\hbar\omega$ model structures so dominate the nucleon occupancies that higher shell contributions to the folding of the effective interaction are not overly significant. But use of larger model space calculations of nuclear structure markedly changes the spectroscopy of most inelastic transitions from the $0\hbar\omega$ model results. While natural parity transitions are enhanced with the use of larger model spaces, for unnatural parity and isovector transitions increasing the size of the model space usually leads to quenching of the cross sections. Such is the case of the isovector excitation of the 15.11 MeV $1^+;1$, of the 16.11 MeV $2^+;1$, and of the 16.57 MeV $2^-;1$ states in ^{12}C . That is shown in Fig. 12.14 wherein the inelastic scattering data [299] are displayed by the solid circles. The calculated results shown by the solid and dashed curves result from use of the $2\hbar\omega$ and the $0\hbar\omega$ models of structure respectively. With the $2^-;1$ state excitation, the respective lines display results found using the restricted $3\hbar\omega$ and the $1\hbar\omega$ models. The inelastic scattering data measured at 122 MeV [301] are shown by the open squares in this figure as well as they further indicate the trend of the $2^-;1$ transition. Clearly the $1^+;1$ and the $2^+;1$ data are reproduced well with the large space calculations but the $2^-;1$ data

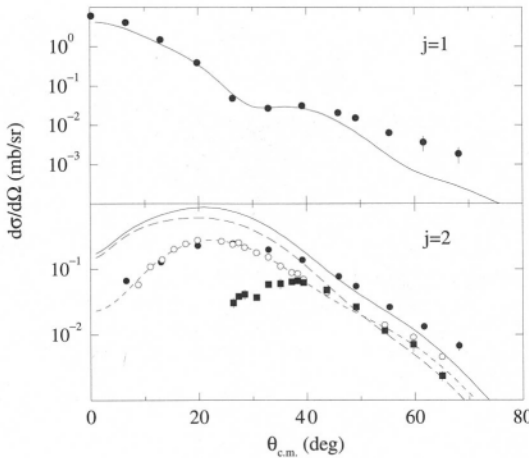


Fig. 12.15. The differential cross sections (solid circles) from the charge exchange scattering of 135 MeV protons leading to the 1^+1 (ground state) of ^{12}N (top and labelled $j = 1$) and to the (summed) $2^+; 1^-$ (0.96 MeV) and $2^-; 1^-$ (1.19 MeV) states in ^{12}N (bottom and labelled $j = 2$).

are not. These results are similar to others found at 200 MeV and higher [139, 295]. For the $2^-; 1^-$ transition, the data essentially indicate just a large angle peak. The forward angle cross section is anticipated to be small given the electron scattering form factor for this state. Calculation thus over-predicts what may be inferred from the cross-section data and that is confirmed by analyses of the charge exchange cross-section data.

The charge exchange cross-section data from the excitation of the ground state in ^{12}N scales very well to the inelastic scattering cross section from the excitation of its analogue, the $1^+; 1^-$ (15.11 MeV) state in ^{12}C . Those data are displayed by the filled circles in the top segment of Fig. 12.15 as are the data from the summed excitation of the 2^+ (0.96 MeV) and 2^- (1.19 MeV) excited states displayed in the bottom segment of Fig. 12.15. In that bottom segment, the appropriately scaled data from the inelastic scattering cross sections to their analogues, the 16.11 MeV $2^+; 1^-$ and the 16.57 MeV $2^-; 1^-$ states in ^{12}C are also shown. Specifically, the scaled data from inelastic scattering to the $2^+; 1^-$ and $2^-; 1^-$ states are given by the open circles and filled squares respectively. The three curves displayed in the bottom section of Fig. 12.15 are the individual scaled inelastic scattering results for the $2^+; 1^-$ (small dashed curve) and $2^-; 1^-$ (large dashed curve) excitations, and the solid curve is their sum. The spectroscopy of the large basis model was used in the calcula-

tions. Clearly the forward angle data, which are dominated by the $2^+;1$ transition, are well reproduced by the calculation of just that transition alone. But the $2^-;1$ transition is in error. This result confirms the expectation that the $2^-;1$ excitation is quite weak at small momentum transfer values. Thus the current structure model for this $2^-;1$ state is inadequate. Millener [302] has noted that the $2^-;1$ transition must be dominated by the $p \rightarrow d$ transition with primarily $L = S = 1$, while $p \rightarrow s$ transitions favour $L = 1$ and $S = 0$. The latter give considerable transition strength at low momentum transfer values.

12.1.4. Inelastic Scattering and Specification of States in ^{12}C

An aim of studies of nuclear scattering is to test the spectroscopy of the target nuclei. That aim seems more decisive now with proton inelastic scattering. As an example consider such scattering to discrete states in ^{12}C for excitations up to 20 MeV. In that excitation region, the assignments of spin, parity, and isospin of the 13.35 MeV, 18.35 MeV, 19.20 MeV, and 19.40 MeV states were in doubt. In the 1990 compilation [194], these states are listed as $13.35 - (2^-);0$, $18.35 -$ both $3^-;1$ and $2^-;0 + 1$, $19.20 - (1^-;1)$, and $19.40 - (2^-;1)$. Millener [302] has suggested, however, that the 13.35 MeV state is a $4^-;0$ state. Its assignment of $2^-;0$ was based on the measurement of the α -decay width of this state being larger than would be consistent with an assignment of 4^- . But Millener noted that the measured α -decay width was reproduced by an α -cluster model calculation of ^{12}C assuming that the assignment was $4^-;0$. Therefore, he surmised that the 13.35 MeV state more rightly should be listed as $4^-;0$.

The 18.35 MeV state is listed both as a $3^-;1$ and a $2^-;0 + 1$ state. The 2^- assignment was supported by analyses of pion and proton inelastic scattering data [297, 303], while the assignment of $3^-;1$ was based on an analysis of inelastic electron scattering data [250]. However, in that analysis of the longitudinal electron scattering form factor, Yamaguchi *et al.* [250] gave the energy of the state they observed as 18.60 MeV. Also, a later measurement [304] of transverse $M2$ electron scattering form factors gave evidence for a $2^-;0$ state at 18.20 MeV. Therefore, the 18.35 MeV state is more likely to have the 2^- assignment.

States that match the number and location to within 2 MeV of the known spectrum of ^{12}C to 20 MeV excitation result from the $2\hbar\omega$ shell model calculation for the positive parity states and from the restricted $3\hbar\omega$ shell model calculation for the negative parity states. The first $2^-;0$ state was predicted to be at 13.09 MeV, for which the measured energy is 11.83 MeV, and the second at 17.02 MeV. Those same shell model

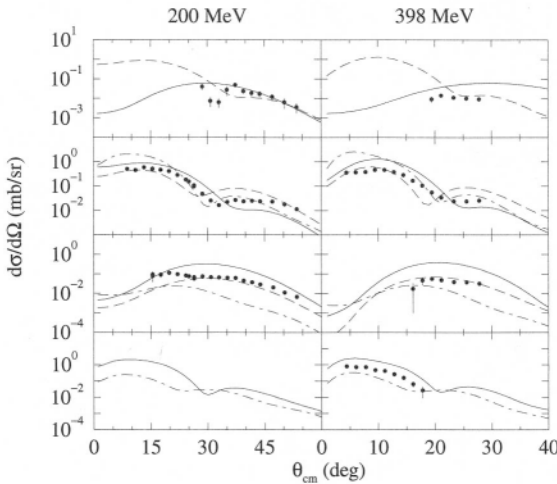


Fig. 12.16. The differential cross section for the inelastic scattering of 200 and 398 MeV protons from ^{12}C . The data from scattering to the 13.35, 18.35, 19.20, and 19.40 MeV states are shown from top to bottom in sequence.

calculations give the energy of the $4_1^-;0$ state as 12.37 MeV, and suggest that the 18.35 MeV state has a 2^- assignment, but both the $T = 0$ and $T = 1$ cases are possible. A $1^-;1$ state is predicted in the vicinity of 19.20 MeV but by no means is that the only candidate assignment for the observed state as a $4_1^-;0$ state is predicted to lie near to this energy too. The shell model also predicts a $2^-;1$ state at 19.28 MeV suggesting another assignment which may be reasonable for the observed 19.40 MeV state.

Results of analyses of inelastic proton scattering data clarify the J^π, T assignments of these four states in question. The 200 MeV cross-section and analysing power data [264, 296] and those for 398 MeV [298] protons have been studied using the microscopic approach. Calculations of the differential cross sections for the inelastic scattering of protons from ^{12}C to these states have been made using the DD Paris interactions and the LF forces [28, 135]. The results found using both the DD and LF forces are shown in Figs. 12.16 and 12.17 for the possible choices of $J\pi, T$. In all four diagrams, the 13.35, 18.35, 19.20, and 19.40 MeV transitions are displayed from top to bottom. The preferred set of assignments, based on the comparison between the measured and the predicted spectra, contains the assignments $4_1^-;0$ (13.35 MeV), $2_2^-;0$ (18.35 MeV), $4_2^-;0$

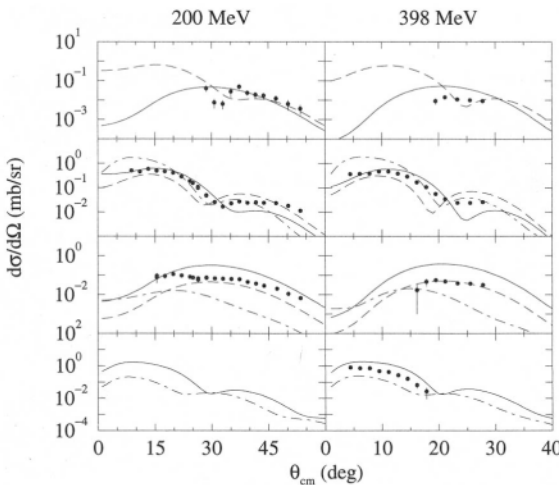


Fig. 12.17. As for Fig. 12.16, but showing the results of calculations made using the LF force.

(19.20 MeV), and $2_{\bar{2}};1$ (19.40 MeV), and is given by the solid curves in these figures.

There are other possibilities. If the 13.35 MeV state were the $2_{\bar{2}};0$ state, then higher excitation assignments could be $2_{\bar{3}};0$ (18.35 MeV) and $4_{\bar{1}};0$ (19.20 MeV). Using that specification in DWBA calculations gave the results displayed in the figures by the dashed curves. A third possibility assigns $2_{\bar{2}};1$ to the 18.35 MeV state and $2_{\bar{3}};1$ to the 19.40 MeV state. The selection of $1_{\bar{2}};1$ for the 19.20 MeV state is independent of all other choices but is included in this third set, the results of which are displayed by the dot-dashed curves.

The results of calculations made using both the DD and LF interactions, exhibit similar features. For the 13.35 MeV excitation by 200 MeV protons, the assignment of $4_{\bar{1}};0$ is preferred, but the data indicate the possibility of there being a minimum at 30° . The presence of such a minimum would favour the $2_{\bar{2}};0$ assignment and so such a choice is not discounted by this analysis. More data at small angles would help to identify the spin of this state, as at small momentum transfers the two calculations differ by up to 3 orders of magnitude. This is so irrespective of the choice of interaction. The results at 398 MeV are less clear. The calculation based on the assignment of 2^- reproduces the magnitude of

the limited data set at large angles but that which is based on the assignment of 4^- reproduces the shape if not the magnitude.

Specification of the 13.35 MeV state affects the choice of assignment for the 18.35 MeV state. The preferred candidate is the $2\bar{2}; 0$ state, a choice supported by both calculations at 200 MeV. Recall that this required the assignment of $4\bar{1}; 0$ for the 13.35 MeV state. However, at 398 MeV the choice is not as definite, for while the results of the calculations of the differential cross section favour the $2\bar{2}; 0$ assignment consistent with the analysis at 200 MeV, the results of the calculations of the analysing power favour other possible assignments.

It is clear from the analysis of the 19.20 MeV differential cross-section data at both 200 and 398 MeV that this excitation is not of a $1^-; 1$ state as the shape of the data at both proton energies favours an assignment of 4^- . If the preferred scheme is correct, then this state would be the $4\bar{2}; 0$ state although calculations based on this assumption consistently overestimate the magnitude of the data. The alternative choice, making this the $4\bar{1}; 0$ state, results in calculations predicting the correct shape and magnitude for both energies. However, such a choice must be questioned on the basis of the calculated energies. The preferred assignments are not discounted as the magnitude of the 19.20 MeV data is higher than that for the 13.35 MeV data suggesting there is more strength required for the excitation of the 19.20 MeV state.

The $J^{\pi}; T$ assignment of the state at 19.40 MeV has been suggested by Jones *et al.* [297] to be $2^-; 1$. However, while confirming the assignment of $2^-; 1$ to this state, the present analysis cannot distinguish between the second or the third $2^-; 1$ state. If it were the second state, this would confirm the choice of the isoscalar transition for the excitation of the 18.35 MeV state. More data at higher momentum transfer may allow an unique conclusion to be drawn.

The analysing powers calculated using the DD and LF forces are displayed in Figs. 12.18 and 12.19, respectively. The notation is consistent with that in Figs. 12.16 and 12.17. As from the analyses of the cross section at 200 MeV, the 13.35 MeV excitation analysing power data are best represented by assuming that it is an excitation of the $4^-; 0$ state. Unfortunately, there are just too few data points at 398 MeV to be instructive. The 18.35 MeV excitation analysing power data is best described by the LF calculation and assuming the $2\bar{3}; 0$ assignment. However, the associated cross sections are not very good and also this would need the 13.35 MeV state to be $2\bar{2}; 0$. The DD cross section assuming the $2\bar{3}; 0$ assignment is good as is the analyzing power at 200 MeV. Finally, the analysing powers from the states at 19.20 and 19.40 MeV are

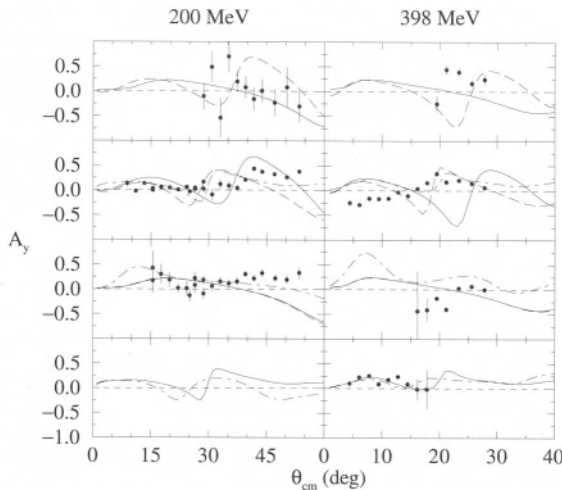


Fig. 12.18. As for Fig. 12.16, but for the analysing powers.

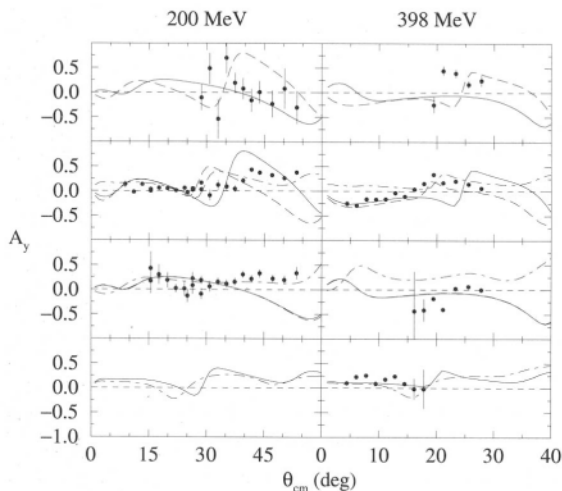


Fig. 12.19. As for Fig. 12.17, but of the analysing powers.

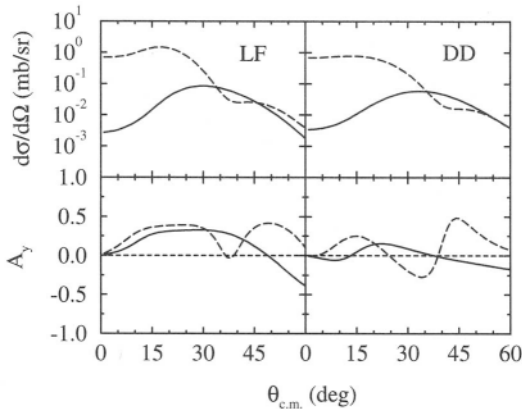


Fig. 12.20. The differential cross sections and analysing powers from excitation of the two candidates for the 13.35 MeV state by 160 MeV protons. The $4\bar{1}; 0$ excitation result is shown by the solid lines while the $2\bar{2}; 0$ excitation is displayed by the dashed curves.

very small but, as with the cross section fits, they discount a $1^-; 1$ assignment.

A key feature in setting a preferred assignment to the levels is the choice of $4\bar{1}; 0$ for the 13.35 MeV state. At 200 and 398 MeV, the inelastic scattering cross sections for that assignment differed by up to 3 orders of magnitude from predictions based upon the alternate $2\bar{2}; 0$ specification; a difference that persists at lower energies. The results of calculations made for 160 MeV protons are shown in Fig. 12.20. In this case the results obtained with the LF and DD forces are shown on the left and right respectively with the calculations made assuming the $4\bar{1}; 0$ and $2\bar{2}; 0$ assignments shown by the solid and dashed curves respectively. The marked differences between the cross sections observed at 200 and 398 MeV persist.

12.2. Inelastic scattering and $^{6,7}\text{Li}$

The nuclei $^{6,7}\text{Li}$ have been studied extensively using cluster model descriptions. That is consistent with the strong correlations evident with their static properties. It has been a challenge therefore to find a large enough basis shell model to encompass such clustering effects. Recently, large space multi- $\hbar\omega$ shell models have been constructed for these nuclei [168]. Shell model wave functions have been obtained also using diverse model spaces, from $0\hbar\omega$ through $4\hbar\omega$. Use of these different model

prescriptions in calculations of the ground state properties and in analyses of complementary elastic and inelastic electron and proton scattering data allows an investigation of how clustering is engendered. Such additions provide the renormalization to the $0\hbar\omega$ model space normally associated with core polarization corrections. Details of the structure models and of the spectral properties that result, as well as of electron scattering form factors they produce, have been discussed in earlier chapters. The use of the OBDME and bound nucleon wave functions in analyses of the electron scattering form factors to each of the states in ${}^{6,7}\text{Li}$ complements their use in calculations of the proton scattering observables thus providing a stringent test of the wave functions from which the OBDME were determined.

In all of the following diagrams, unless otherwise stated, the results obtained using the wave functions of the $4\hbar\omega$, $2\hbar\omega$, and $0\hbar\omega$ model spaces are given by the solid, long dashed and small dashed lines, respectively. These models of spectroscopy were used previously in discussion of the electron scattering form factors for ${}^{6,7}\text{Li}$ as well as in the presentation of the elastic proton scattering results. Excellent results were found, especially with the largest space structure specifications, but only if all angular momentum transfer contributions that are possible in the form factors were included. That was also the case with predictions of elastic proton scattering. Taken together the electron and proton scattering results suggest that the ground state wave functions obtained in the $4\hbar\omega$ space has converged substantially.

In Fig 12.21, the cross sections and analyzing powers obtained from the various shell models for the inelastic scattering of 200 MeV protons to the $3^+; 0$ (2.186 MeV) state in ${}^6\text{Li}$ are compared to the data of Glover *et al.* [263]. Harmonic oscillator (HO) single particle wave functions were used to find the results shown in the left hand panels while those of Woods-Saxon (WS) form were used to obtain the results displayed in the right hand ones. The cross sections displayed are the sum of all possible angular momentum transfers which may contribute. Consistent with the analysis of the inelastic electron scattering form factor, the $I = 2$ component is the most dominant. It is evident from Fig. 12.21 that the result found using the simple $0\hbar\omega$ model is deficient. The larger space structures lead to cross sections almost an order of magnitude greater than that, apart from the region around 20° which is still too weak. This problem at low momentum transfer is consistent with the analyses of the inelastic electron scattering data to this state. Note that even the predicted shape found using the simplest structure changes with increase in the space. The analysing power varies in a similar way with either large

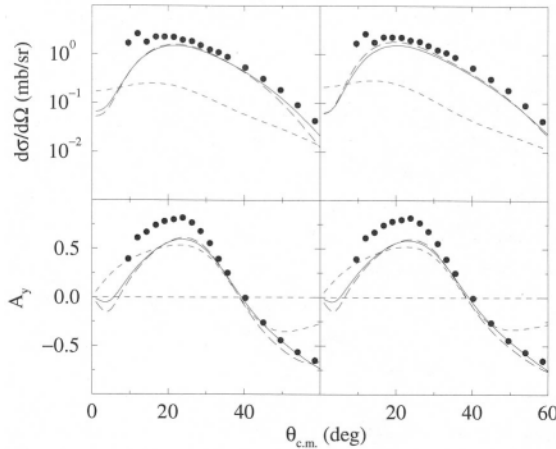


Fig. 12.21. The differential cross section (top) and analyzing power (bottom) from the inelastic scattering of 200 MeV protons from ${}^6\text{Li}$ exciting the $3^-; 0$ (2.186 MeV) state.

basis model calculations well reproducing the data. With the increases to the model space, the $I = 2$ scattering amplitudes are most enhanced to give improved fits to the data. In Fig. 12.22, the cross sections and analysing powers obtained for the excitation of the $0^+; 1$ (3.563 MeV) state in ${}^6\text{Li}$ from the inelastic scattering of 200 MeV protons are compared with the data of Glover *et al.* [263]. Again HO and WS single

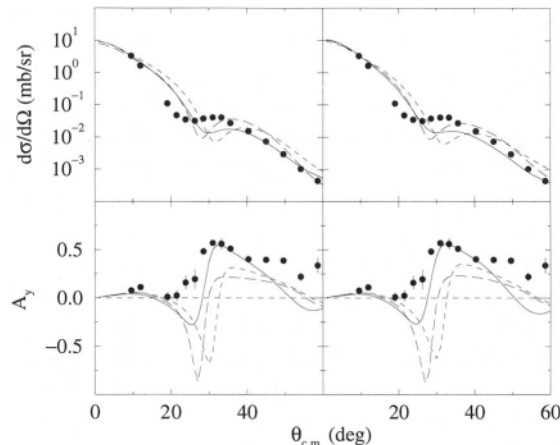


Fig. 12.22. As for Fig. 12.21, but for the excitation of the $0^+; 1$ (3.563 MeV) state in ${}^6\text{Li}$.

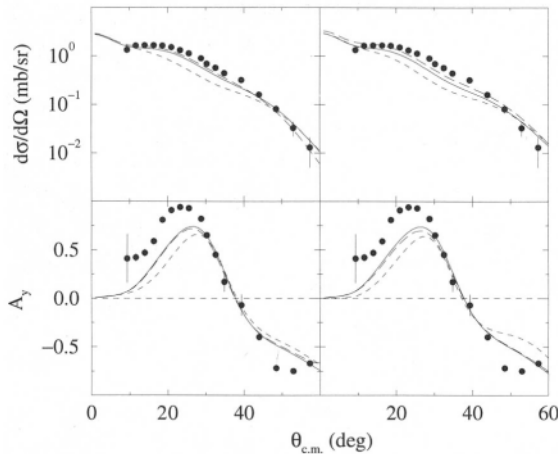


Fig. 12.23. The differential cross section (top) and analyzing power (bottom) from the inelastic scattering of 200 MeV protons exciting the $\frac{1}{2}^-$ (0.478 MeV) state in ${}^7\text{Li}$.

particle wave functions were used to obtain the results presented in the left and right-hand panels respectively. In this case, each result is observably different and clearly the largest space calculations best reproduce the data.

The results of calculations of inelastic proton scattering to low excitation states in ${}^7\text{Li}$ are displayed next. The 200 MeV optical potentials formed by full folding all three model space ground state density matrices with the DD Paris interaction lead to excellent predictions of the elastic scattering cross section and analysing power, when, as with the case for the elastic scattering from ${}^6\text{Li}$, the contributions from all non-zero angular momentum transfer amplitudes are taken into account. They were calculated in the DWBA. The very good agreement observed with the elastic scattering data again suggests that the $4\hbar\omega$ wave function for the ground state has converged substantially. The results of calculations of 200 MeV proton excitation of the $\frac{1}{2}^-$ (0.478 MeV) state in ${}^7\text{Li}$ are compared in Fig. 12.23 with the data of Glover *et al.* [305]. Therein, the cross sections are displayed in the top segments and the analysing powers are shown in the bottom ones. Again the results obtained by using HO wave functions are displayed on the left while those obtained using the WS wave functions are given in the right. For this transition, the $2\hbar\omega$ and $4\hbar\omega$ structures give quite similar results and are in best agreement with data. This is due to the enhancement of the $I = 2$ contributions within the larger space structures and that amplitude

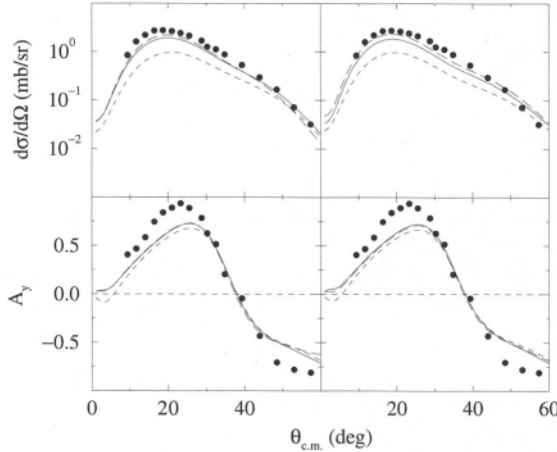


Fig. 12.24. The differential cross section (top) and analyzing power (bottom) from the inelastic scattering of 200 MeV protons exciting the $\frac{7}{2}^-$ (**4.630 MeV**) state in ${}^7\text{Li}$.

dominates all calculated results above 15° . The $I = 1$ amplitudes are changed little by the increase in the size of the model space but note that they are important in the predictions of the data at small scattering angles.

The results for the excitation of the $\frac{7}{2}^-$ in ${}^7\text{Li}$ by the scattering of 200 MeV protons are given in Fig. 12.24. Therein, the cross section and analysing power data of Glover *et al.* [305] are compared (top and bottom sectors) to the curves identified with the same notation used in Fig. 12.23. As for the longitudinal inelastic electron scattering form factor, the cross section is dominated by the $I = 2$ contribution. In the main the contributions from $I > 2$ amplitudes are negligible. Also, the $I = 2$ contribution is enhanced with the addition of higher $\hbar\omega$ admixtures to give good agreement with the data.

Thus, for ${}^{6,7}\text{Li}$, the totality of results show that beyond the simple $0\hbar\omega$ picture of these **0p-shell** nuclei, elements of clustering may be introduced as the larger **multi- $\hbar\omega$** spaces allow for interactions to effect particle exchange between the **0s-shell α -particle** and the clusters formed by the valence shell particles. There is still some degree of renormalization necessary, even in results that have been obtained using $6\hbar\omega$ wave functions, indicating that the shell model wave functions still do not have enough of the correlations defining the clustering. It is clear that the prime effect of increasing the size of the model space has been to

enhance the $I = 2$ contributions to the $3^+; 0^-$ excitation in ${}^6\text{Li}$ and to the $\frac{1}{2}^-$ and $\frac{7}{2}^-$ excitation in ${}^7\text{Li}$. For those transitions, other multipole contributions usually are small and little changed with structure. However, the $0^+; 1^-$ excitation in ${}^6\text{Li}$ is purely $I = 1$ and, for this, the best result is that obtained from the $4\hbar\omega$ model space.

12.3. Scattering of Radioactive Beams from Hydrogen

DWBA analyses suffice to explain inelastic nucleon scattering when the transition structure is well defined and so establish the effective interaction. Therefore, comparison of the results of such calculations with other scattering data gives a measure of the assumed nuclear structure. That is of great import for current studies of the properties of exotic nuclei, whose neutron and/or proton numbers differ from the stability line values. Those nuclei are radioactive and some can be produced as secondary beams in modern heavy ion facilities. The import of scattering of these exotic nuclei from hydrogen targets, which in inverse kinematics equates to proton scattering from those exotic nuclei, is emphasised by the fact that relevant electron scattering form factors for them are not attainable. Herein just the experimental results now available for the inelastic scattering of ${}^6\text{He}$ [254] and of ${}^{11}\text{Li}$ [306] are discussed. Experiments with other exotic nuclei, e.g., with ${}^8\text{B}$, ${}^{18}\text{Ne}$, ${}^{30,32,34,36,38,40}\text{S}$ to list a few, have been made recently with inelastic cross sections tentatively defined. Many other experiments and at energies to 500A MeV or more are planned.

12.3.1. The Scattering of ${}^{11}\text{Li}$

The measurements of ${}^{9,11}\text{Li}$ scattering from hydrogen taken by Moon *et al.* [268] at 60A and 62A MeV and by Korsheninnikov *et al.* [307, 306] at 68A and 75A MeV provide elastic and inelastic scattering data for ${}^{9,11}\text{Li}$ ions from hydrogen. These experiments not only provided energy spectra, by which comparison could be made with model predictions, but also cross-section data with which to test the wave functions. The scattering data at $E_p = 68\text{A MeV}$ of Korsheninnikov *et al.* [306] show a peak in the spectrum at $E_x = 1.3\text{ MeV}$ and a broad distribution which they assumed reflected an inelastic excitation. A coupled-channel optical model analysis of the cross section obtained from this peak suggested that the excitation is dominantly $I = 1$. For the ground state, $J^\pi; T = \frac{3}{2}^-; \frac{5}{2}^-$, and so an assignment of $J^\pi = \frac{3}{2}^+$ was made although the analysis also would allow assignments of $\frac{1}{2}^+$ and of $\frac{5}{2}^+$. But there is a

problem with that conventional model analysis of the data that lies with the specification of the optical potential. Korsheninnikov *et al.* [306] used a phenomenological optical potential of conventional Woods-Saxon form that fitted the elastic scattering cross section found by Moon *et al.* [268] in an analysis of their 62A MeV data. In view of the success of the microscopic, non-local, optical potentials for pA scattering in the energy regime of 65 MeV, local geometric models of the optical potential may be inappropriate for analysis of the scattering of protons from a halo nucleus. It may not take into account adequately the density variation extending as that does to large radii. A Woods-Saxon form also may not be appropriate for densities that reflect halo nucleons and concomitant depletion of neutron strength in the interior. This is reflected in the choice of WS parameters, a shallow real potential depth and large diffuseness in the imaginary potential, in the analysis by Moon *et al.* [268].

Specification of the single particle wave functions was quite important in analyses of the elastic scattering data for $^{6,8}\text{He}$ and $^{9,11}\text{Li}$. That was especially so for the scattering of ^{11}Li as that halo nucleus requires single particle wave functions that result in the density extending to large radii. Thus WS bound state functions were invoked with the $0p_{\frac{1}{2}}$ and $1s_{\frac{1}{2}}$ porbits quite weakly bound. As there are no electron scattering data by which to set the wave functions, the basic WS parameter values first were determined from other data. Those WS parameters were found by making fits to the longitudinal elastic electron scattering form factors for either ^7Li [186], a choice predicated on the similarity of charge, or ^9Be , a choice predicated on a similarity of mass. Then to create a halo, the WS parameter values were adjusted. Specifically WS wave functions with a binding energy of 500 keV for the halo neutron orbits were used. The problem of choosing appropriate radial wave functions for transitions between loosely bound states has been discussed by Millener *et al.* [308] for the case of ^{11}Be . Thus the effective interaction and a consistent set of bound state functions are fixed from the elastic scattering cross-section results and the large space $2\hbar\omega$ shell model gave an excitation spectrum and OBDME for use in predictions of inelastic scattering.

The data for the inelastic scattering of 68A MeV ^{11}Li ions from hydrogen [306] are compared with such predictions [191] in Fig. 12.25(a). Therein the cross sections to possible $\frac{3}{2}^-$ (1.49MeV), $\frac{3}{2}^+$ (1.83MeV), and $\frac{1}{2}^-$ (1.87 MeV) states are displayed by the solid, dashed, and dot-dashed lines respectively. The transitions to the negative parity states are mostly $E2$ in character while the transition to the $\frac{3}{2}^+$ state is

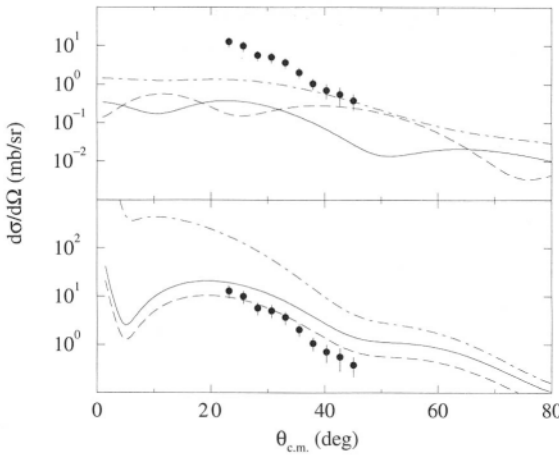


Fig. 12.25. Comparison of the inelastic scattering data from 68A MeV ^{7}Li ions from “hydrogen targets with (a) the results of the calculations made assuming the transition to the $\frac{3}{2}^{-}$ (1.49 MeV) (solid line), the $\frac{3}{2}^{-}$ (1.83 MeV) (dashed line), and the $\frac{1}{2}^{-}$ (1.87 MeV) (dot-dashed line) states and (b) the result of the calculation assuming the shake-off mechanism (solid line). The dashed line in (b) is the solid curve scaled by a factor of 0.5 corresponding to the assumed strength associated with the 1.3 MeV peak in the spectrum. The elastic scattering cross-section of 68A MeV ^{7}Li on hydrogen is displayed by the dot-dashed line for comparison.

dominantly $E1$. However, in all cases, neither the shapes nor the magnitudes agree with the data. This may reflect that the approach does not guarantee proper treatment of excitations in the continuum, and as excited continuum states are broad, the excitation of many higher lying states may contribute to this inelastic cross section. Hence a simple, semi-quantitative, model which incorporates the excitation of the continuum as a whole was suggested [191] as an alternative reaction mechanism. In that alternative, the basic process was assumed to be the elastic scattering of the proton with the ^{7}Li core. The momentum imparted to the halo in the new center-of-mass system entails a certain probability of breakup into the constituents $^{7}\text{Li} + n + n$. Such processes commonly are encountered in atomic physics, where they are referred to as shake-off. Another analogy is the recoil-less absorption of photons in the Mössbauer effect, where the probability that the struck system remains in its ground state is referred to as the Debye-Waller factor. With this shake-off model, the energy spectrum is expected to show an asymmetric peak

with a *tail* extending towards higher energies. Estimating the average excitation energy from the ratio of the energy-weighted to the non-energy-weighted sum rule, Karataglidis *et al.* [191] find a value ≈ 1.3 MeV, in qualitative agreement with the observation assumed [306] to be the energy of an excited state in ^{11}Li .

12.3.2. The Scattering of ^6He

Cross-section data from the excitation of the $2_1^+; 1^-$ state at 1.8 MeV excitation in ^6He have been measured [254] and that data are shown in Fig. 12.26. Therein they are compared with two results. Both results were obtained using a 40 MeV medium modified effective interaction built from the relevant AW g matrices of the Bonn-B interaction. Essentially the same results are found with the Paris potentials. The solid curve portrays the result obtained using a halo specification for ^6He made using adjusted WS bound states, while the dashed line is that obtained using WS functions that do not impart a halo character for the nucleus. The difference between these results is marked with the halo structure very favoured from comparison with the data. This indicates sensitivity to the surface properties of the nucleus given that the radial transition form factor for $E2$ excitations is surface peaked. This is in contrast to the elastic scattering cross-section analyses which are sensitive to the depletion of neutron strength within the body of the nucleus more particularly.

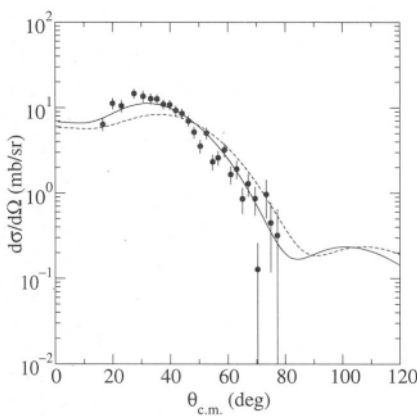


Fig. 12.26. Comparison of the data from the inelastic scattering of 40 AMeV ^6He ions from hydrogen with predictions found assuming that the ground and 2^+ states of ^6He are of halo character (solid curve) or not (dashed curve).

APPENDIX: PROJECTION OPERATORS AND HF STATE NORMALIZATIONS AND OVERLAPS

The projection operators P_{MK}^J when acting upon axially symmetric HF solutions, project out states of good angular momentum J and K and then transform K to M . They can be defined by

$$P_{MK}^J = \sum_{\alpha} |JM\alpha\rangle \langle JK\alpha| \quad (\text{A.1})$$

where α designates any set of labels other than J or K that may be required. Thus P_{MK}^J is a projection operator in the truer sense only if $M = K$. To facilitate evaluations, it is usual to express these projection operators in an integral representation [172] which is given in Euler angles Euler angles $\Omega = (\alpha, \beta, \gamma)$ by

$$P_{MK}^J = \frac{2J+1}{8\pi^2} \int d\Omega D_{MK}^{J*}(\Omega) R(\Omega), \quad (\text{A.2})$$

where

$$R(\Omega) = e^{-i\alpha J_z} e^{-i\beta J_y} e^{-i\gamma J_z} \quad (\text{A.3})$$

which has matrix elements

$$D_{MK}^J(\Omega) = \langle JM|R(\Omega)|JK \rangle. \quad (\text{A.4})$$

On application to an A -nucleon Slater determinant from an axial symmetric HF solution,

$$P_{MK}^J |\Phi_K\rangle = \frac{2J+1}{2} \int_0^\pi d\beta \sin(\beta) D_{MK}^J(\beta) e^{-i\beta J_y} |\Phi_K\rangle. \quad (\text{A.5})$$

These operators have the properties [309],

$$\begin{aligned} P_{MK}^J P_{K'M'}^{J'} &= P_{MM'}^J \delta_{JJ'} \delta_{KK'} \\ (P_{MK}^J)^\dagger &= P_{KM}^J, \end{aligned} \quad (\text{A.6})$$

and they may be partitioned as

$$P_{MK}^J = \sum_{\{1,2\}} \langle J_1 M_1 J_2 M_2 | JM \rangle \langle J_1 K_1 J_2 K_2 | JK \rangle P_{M_2 K_2}^{J_2} P_{M_1 K_1}^{J_1}. \quad (\text{A.7})$$

Application of this partition rule with the action of the A -nucleon projection operator onto a spherical single nucleon state gives

$$\begin{aligned} P_{MK}^J(1, 2, \dots, A) |\phi_{jm}(1)\rangle &= \sum_{m'} |\phi_{jm'}(1)\rangle \\ &\times \sum_{J'M'} \langle J' \mu j m' | JM \rangle \langle J' M' j m | JK \rangle P_{\mu K'}^{J'}(2, \dots, A). \end{aligned} \quad (\text{A.8})$$

A.1. The HF State Normalization

The normalization of the axially symmetric HF state specified in the text is

$$(N_{JK})^{-2} = \langle \Phi_K | (P_{MK}^J)^\dagger P_{MK}^J | \Phi_K \rangle = \langle \Phi_K | P_{KK}^J | \Phi_K \rangle, \quad (\text{A.9})$$

which, by using the integral representation, equates to

$$(N_{JK})^{-2} = \frac{2J+1}{2} \int_0^\pi d\beta \sin \beta \, d_{KK}^J(\beta) \langle \Phi_K | e^{-i\beta J_y} | \Phi_K \rangle \quad (\text{A.10})$$

wherein the matrix elements are given by

$$\langle \Phi_K | e^{-i\beta J_y} | \Phi_K \rangle = \det[\mathcal{N}(\beta)]. \quad (\text{A.11})$$

Therein $\mathcal{N}(\beta)$ is an $A \otimes A$ matrix with elements, for each type of nucleon and under the axial symmetry assumption,

$$\mathcal{N}_{\zeta x} = \langle \zeta | e^{-i\beta J_y} | x \rangle = \sum_j C_{j\zeta}^x C_{ix}^x d_{\zeta x}^j(\beta). \quad (\text{A.12})$$

Since the reduced rotation matrices $d_{mn}^j(\beta)$ are polynomials in β , these matrix elements are easily evaluated. The normalization integrals then reduce to summations over the expansion coefficients.

The matrix elements reduce as shown most easily by considering the action

$$e^{-i\beta J_y} | \Phi_K \rangle = \tilde{\alpha}_{\lambda_1}^\dagger \tilde{\alpha}_{\lambda_2}^\dagger \cdots \tilde{\alpha}_{\lambda_A}^\dagger | 0 \rangle, \quad (\text{A.13})$$

where the $\tilde{\alpha}_\lambda^\dagger$ are rotated, deformed, nucleon creation operators that link to the HF single nucleon state creation operators by,

$$\tilde{\alpha}_\lambda^\dagger = e^{-i\beta J_y} \tilde{\alpha}_\lambda^\dagger e^{i\beta J_y} = \sum_j C_{j\lambda}^\lambda d_{\lambda\lambda}^j(\beta) \alpha_{jm=\lambda}^\dagger. \quad (\text{A.14})$$

The determinant relation, Eq. (A.11), results from the scalar product

$$\langle 0 | \alpha_{\lambda_2} \alpha_{\lambda_1}^\dagger | 0 \rangle = \sum_j C_{j\lambda_1}^{\lambda_1} C_{j\lambda_2}^{\lambda_2} d_{\lambda_1 \lambda_2}^j(\beta). \quad (\text{A.15})$$

A.2. The $A - 1$ Nucleon State Overlaps

The overlap function involved in the OBDME for a transition between states J_i and J_f , effected by an angular momentum transfer of I , with the PHF wave functions is

$$\begin{aligned}\Delta(1, 2, \dots, A - 1) &= \langle \Phi_{K_f} | \alpha_{f\lambda_f}^\dagger P_{K_f - \lambda_f, K_i - \lambda_i}^I \alpha_{j\lambda_i} | \Phi_{K_i} \rangle \\ &= \frac{2I + 1}{2} \int_0^\pi d\beta d_{K_f - \lambda_f, K_i - \lambda_i}^I(\beta) \langle \Xi_{j, K_f - \lambda_f} | e^{-i\beta I_y} | \Xi_{j, K_i - \lambda_i} \rangle,\end{aligned}\quad (\text{A.16})$$

where $|\Xi_{j, K - \lambda}\rangle$ are normalised Slater determinants of $A - 1$ nucleons. The determinant theorem,

$$[\text{cofactor } A]_{ij} = \det[A][A^{-1}]_{ji}, \quad (\text{A.17})$$

permits use of cofactor expansions of the HF ($A - 1$) particle states and so with

$$\langle \phi_{j, K_f - \lambda_f} | e^{-i\beta I_y} | \phi_{j, K_i - \lambda_i} \rangle = \det[\mathcal{N}] [\mathcal{N}^{-1}]_{K_f - \lambda_f, K_i - \lambda_i}, \quad (\text{A.18})$$

evaluation of the OBDME proceeds in a similar fashion as that for the normalization.

REFERENCES

1. M. Kamran, Phys. Rep. **10**, 275 (1984).
2. H. Bethe, Phys. Rev. **57**, 1125 (1940).
3. C. M. Perey and F. Perey, Atom. Data and Nucl. Data Tables **13**, 293 (1974).
4. G. R. Satchler, *Direct Nuclear Reactions, International series of monographs on physics*, 68 ed. (Clarendon, New York, 1983).
5. H. Feshbach, *Theoretical Nuclear Physics: Nuclear Reactions* (Wiley, London, 1992).
6. P. E. Hodgson, *The Nucleon Optical Potential* (World Scientific, Singapore, 1994).
7. E. Bauge, J. P. Delaroche and M. Girod, Phys. Rev. C **58**, 1118 (1998).
8. F. Chew, Phys. Rev. **80**, 196 (1951).
9. K. M. Watson, Phys. Rev. **89**, 575 (1953).
10. N. Francis and K. M. Watson, Phys. Rev. **92**, 291 (1953).
11. H. Bethe, Ann. Phys. **3**, 190 (1958).
12. A. K. Kerman, H. McManus and R. M. Thaler, Ann. Phys. (N.Y.) **8**, 551 (1959).
13. S. K. Adhikari and K. L. Kowalski, in *Dynamical Collision Theory and its Applications* (Academic Press, N.Y., 1991).
14. R. A. Arndt, I. I. Strakovsky and R. L. Workman, Phys. Rev. C **50**, 2731 (1994).
15. R. A. Arndt *et al.*, Phys. Rev. C **56**, 3005 (1997).
16. R. A. Arndt *et al.*, Phys. Rev. D **28**, 97 (1983).
17. M. M. Nagels, T. A. Rijken and J. J. de Swart, Phys. Rev. D **17**, 768 (1978).

18. M. Lacombe *et al.*, Phys. Rev. C **21**, 861 (1980).
19. R. Machleidt, K. Holinde and C. Elster, Phys. Rep. **149**, 1 (1987).
20. *Microscopic Optical Potentials, Proc. of the Hamburg Topical Workshop*, Vol. 89 of *Lecture Notes in Physics*, edited by H. V. von Geramb (Springer-Verlag, Berlin, 1979).
21. P. Schwandt, in *Proc. Int. Workshop on Medium Energy Nucleons in Nuclei*, Vol. 97 of *AIP Conf. Proc.*, edited by H. O. Meyer (AIP, New York, 1983).
22. L. Ray, G. W. Hoffmann and W. R. Coker, Phys. Rep. **212**, 223 (1992).
23. L. Ray, Phys. Rev. C **41**, 2816 (1990).
24. C. M. Ko, V. Koch and G. Li, Ann. Rev. Nucl. Part. Sci. **47**, 505 (1997) and references cited therein.
25. R. W. Manweiler, Nucl. Phys. **A240**, 373 (1975).
26. F. Brieva, H. V. von Geramb and R. Rook, Phys. Lett. **79B**, 177 (1978).
27. K. Nakayama, S. Krewald, J. Speth and W. G. Love, Nucl. Phys. **A431**, 419 (1984).
28. W. G. Love and M. A. Franey, Phys. Rev. C **24**, 1073 (1981).
29. J. Raynal, computer code DWBA91,1991 (NEA 1209/02).
30. J. Raynal, computer code DWBA98, 1999 (NEA 1209/05).
31. C. R. Chinn, C. Elster, R. M. Thaler and S. P. Weppner, Phys. Rev. C **52**, 1992 (1995).
32. H. F. Arellano, F. A. Brieva and W. G. Love, Phys. Rev. C **52**, 301 (1995).
33. V. G. J. Stoks, R. A. M. Klomp, C. P. F. Terheggen and J. J. de Swart, Phys. Rev. C **49**, 2950 (1994).
34. R. Machleidt, Adv. in Nucl. Phys. **19**, 189 (1989).
35. R. B. Wiringa, V. G. J. Stoks and R. Schiavilla, Phys. Rev. C **51**, 38 (1995).
36. L. Jade and H. V. von Geramb, Phys. Rev. C **57**, 496 (1998).
37. K. Chadan and P. C. Sabatier, *Inverse Problems in Quantum Scattering Theory*, 2nd ed. (Springer-Verlag, Berlin, 1989).
38. R. G. Newton, *Scattering Theory of Waves and Particles*, 2nd ed. (Springer-Verlag, New York, 1982).
39. T. Kirst *et al.*, Phys. Rev. C **40**, 912 (1989).
40. C. Elster *et al.*, Phys. Rev. C **37**, 1647 (1988).
41. C. Elster *et al.*, Phys. Rev. C **38**, 1828 (1988).
42. L. Ray, Phys. Rev. C **35**, 1072 (1987).
43. H. V. von Geramb, K. Amos, H. Labes and M. Sander, Phys. Rev. C **58**, 1948 (1998).
44. C. Elster, S. P. Weppner and C. R. Chinn, Phys. Rev. C **56**, 2080 (1997).
45. S. P. Weppner, C. Elster and D. Huber, Phys. Rev. C **57**, 1378 (1998).
46. H. F. Arellano, F. A. Brieva, M. Sander and H. V. von Geramb, Phys. Rev. C **54**, 2570 (1996).
47. J. R. Taylor, *Scattering Theory: The Quantum Theory of Nonrelativistic Collisions* (Wiley, New York, 1972).
48. H. Feshbach, Ann. Phys. (N.Y.) **5**, 357 (1958).
49. H. Feshbach, Ann. Phys. (N.Y.) **19**, 287 (1962).
50. J. P. Jeukenne, A. Lejeunne and C. Mahaux, Phys. Rep. **25**, 83 (1976).
51. C. Elster, T. Cheon, E. F. Redish and P. C. Tandy, Phys. Rev. C **41**, 814 (1990).
52. T. Cheon, C. Elster, E. F. Redish and P. C. Tandy, Phys. Rev. C **41**, 841 (1990).
53. C. R. Chinn, C. Elster and R. M. Thaler, Phys. Rev. C **44**, 1569 (1991).
54. C. R. Chinn, C. Elster and R. M. Thaler, Phys. Rev. C **48**, 2596 (1993).
55. H. F. Arellano, F. A. Brieva and W. G. Love, Phys. Rev. C **41**, 2188 (1990).
56. H. F. Arellano, F. A. Brieva and W. G. Love, Phys. Rev. C **42**, 652 (1990).
57. H. F. Arellano, F. A. Brieva, W. G. Love and K. Nakayama, Phys. Rev. C **43**, 1875 (1991).

58. H. F. Arellano, F. A. Brieva and W. G. Love, Phys. Rev. C **50**, 2480 (1994).
59. L. Jade and H. V. von Geramb, Phys. Rev. C **55**, 57 (1997).
60. L. Jade and H. V. von Geramb, Phys. Rev. C **56**, 1218 (1998).
61. M. Sander and H. V. Geramb, Phys. Rev. C **56**, 1218 (1997).
62. H. V. von Geramb and H. Kohlhoff, in *Lecture Notes in Physics*, edited by H. V. von Geramb (Springer-Verlag, Berlin, 1994), Vol. 427, p. 285.
63. H. Kohlhoff and H. V. von Geramb, in *Lecture Notes in Physics*, edited by H. V. von Geramb (Springer-Verlag, Berlin, 1994), Vol. 427, p. 314.
64. K. M. Watson, Rev. Mod. Phys. **30**, 565 (1958) and references cited therein.
65. R. Crespo, R. C. Johnson and J. A. Tostevin, Phys. Rev. C **41**, 2257 (1990).
66. J. P. Jeukenne, A. Lejeune and C. Mahaux, Phys. Rev. C **10**, 1391 (1974).
67. J. P. Jeukenne, A. Lejeune and C. Mahaux, Phys. Rev. C **16**, 80 (1977).
68. S. Karatagliidis, P. J. Dortmans, K. Amos and R. de Swiniarski, Phys. Rev. C **53**, 838 (1996).
69. L. Rikus and H. V. von Geramb, Nucl. Phys. **A426**, 496 (1984).
70. L. Rikus, K. Nakano and H. V. von Geramb, Nucl. Phys. **A414**, 413 (1984).
71. X. Campi and A. Bouyss, Phys. Lett. **73B**, 263 (1978).
72. C. J. Horowitz and B. D. Serot, Nucl. Phys. **A368**, 503 (1981).
73. R. Machleidt, F. Sammarruca and Y. Song, Phys. Rev. C **53**, R1483 (1996).
74. H. O. Meyer, P. Schwandt, G. L. Mooke and P. P. Singh, Phys. Rev. C **23**, 616 (1981).
75. H. O. Meyer, P. Schwandt, W. W. Jacobs and J. R. Hall, Phys. Rev. C **27**, 459 (1983).
76. H. V. von Geramb and K. Amos, Phys. Rev. C **41**, 1384 (1990).
77. H. V. von Geramb and H. Kohlhoff, in *Lecture Notes in Physics*, edited by H. V. von Geramb (Springer-Verlag, Berlin, 1994), Vol. 427, p. 285.
78. E. Bleszynski *et al.*, Phys. Rev. C **37**, 1527 (1988).
79. D. A. Hutcheon *et al.*, Nucl. Phys. **A483**, 429 (1988).
80. J. W. Negele, Phys. Rev. C **1**, 1260 (1970).
81. J. W. Negele and D. Vautherin, Phys. Rev. C **5**, 1472 (1972).
82. F. A. Brieva and J. R. Rook, Nucl. Phys. **A291**, 299 (1977).
83. F. A. Brieva and J. R. Rook, Nucl. Phys. **A297**, 206 (1978).
84. H. V. von Geramb and K. Nakano, in *Proc. Workshop on the Interaction Between Medium Energy Nucleons in Nuclei*, Vol. 97 of *AIP Conf. Proceedings*, edited by H. O. Meyer (AIP, New York, 1983), p. 44.
85. H. V. von Geramb *et al.*, Phys. Rev. C **44**, 73 (1991).
86. M. Jacob and G. C. Wick, Ann. Phys. (N.Y.) **7**, 404 (1959).
87. J. Raynal, *Aspects Géométriques des Réactions*, Saclay Note CEA-N-1529 (unpublished).
88. J. Raynal, Nucl. Phys. **A97**, 572 (1967).
89. A. Bohr and B. Mottelson, *Nuclear Structure, Vol 1: Single Particle Motion* (W. A. Benjamin, New York, 1969).
90. J. Raynal, Symposium sur les Mécanismes de Réactions Nucléaires et phénomènes de Polarisation, 1969, université Laval, Quebec.
91. A. Messiah, *Quantum Mechanics* (New Holland, Amsterdam, 1961).
92. J. Raynal, *The structure of nuclei*, IAEA, Vienna (unpublished).
93. L. Wolfenstein, Ann. Rev. of Nucl. Sci. **6**, 43 (1956).
94. M. K. Srivastava and D. W. L. Sprung, Adv. in Nuclear Physics **8**, 1 (1975).
95. A. Kievsky *et al.*, Phys. Rev. C **58**, 3085 (1998).
96. L. Jade, Phys. Rev. C **58**, 96 (1998).
97. B. C. Pearce and B. K. Jennings, Nucl. Phys. **A528**, 665 (1991).

98. C. Schütz, J. W. Durso, K. Holinde and J. Speth, Phys. Rev. C **49**, 2671 (1994).
99. D. Lohse, J. W. Durso, K. Holine and J. Speth, Nucl. Phys. **A516**, 513 (1990).
100. R. Blankenbecler and R. Sugar, Phys. Rev. **142**, 1051 (1966).
101. E. E. Salpeter and H. A. Bethe, Phys. Rev. **84**, 1232 (1951).
102. P. B. Burt, Phys. Rev. Lett. **32**, 1080 (1974).
103. M. H. Partovi and E. L. Lomon, Phys. Rev. D **2**, 1999 (1970).
104. C. Itzykson and J. B. Zuber, *Quantum Field Theory* (McGraw-Hill, New York, 1980).
105. H. P. Noyes, Phys. Rev. Lett. **15**, 538 (1965).
106. K. L. Kowalski, Phys. Rev. Lett. **15**, 798 (1965).
107. P. J. Dortmans and K. Amos, Phys. Rev. C **48**, 2112 (1993).
108. E. F. Redish and K. Stricker-Bauer, Phys. Rev. C **36**, 513 (1987).
109. K. Amos *et al.*, Phys. Rev. C **37**, 934 (1988).
110. K. A. Brueckner, C. A. Levinson and H. M. Marmoud, Phys. Rev. **95**, 217 (1954).
111. K. A. Brueckner and C. A. Levinson, Phys. Rev. **97**, 1344 (1955).
112. H. A. Bethe, B. H. Brandow and A. G. Petschek, Phys. Rev. **129**, 225 (1963).
113. B. A. Lippmann and J. Schwinger, Phys. Rev. **79**, 669 (1950).
114. H. Bethe, Phys. Rev. **167**, 879 (1968).
115. H. J. Yuan, H. L. Lin, G. Fai and S. Moszkowski, Phys. Rev. C **40**, 1448 (1989).
116. T. Cheon, Phys. Rev. C **38**, 1516 (1988).
117. K.-H. Müller, Z. Phys. **A295**, 79 (1980).
118. E. F. Redish, J. G. Stephenson and G. M. Lerner, Phys. Rev. C **2**, 1665 (1970).
119. E. F. Redish and K. Stricker-Bauer, Phys. Rev. C **35**, 1183 (1987).
120. K. Amos, L. Berge, H. V. von Geramb and M. Coz, Nucl. Phys. **A499**, 45 (1988).
121. B. Sinha, Phys. Rev. C **20**, 1 (1975).
122. P. J. Dortmans and K. Amos, J. Phys. G **17**, 901 (1991).
123. M. Haftel and F. Tabakin, Nucl. Phys. **A158**, 1 (1970).
124. W. Legindgaard, Nucl. Phys. **A297**, 429 (1978).
125. T. Cheon and E. F. Redish, Phys. Rev. C **39**, 331 (1989).
126. H. A. Bethe, Phys. Rev. **103**, 1353 (1956).
127. K. A. Brueckner and J. L. Gammel, Phys. Rev. **109**, 1023 (1958).
128. C. Mahaux, Nucl. Phys. **A328**, 24 (1979).
129. J. Hüfner and C. Mahaux, Ann. Phys. (N.Y.) **73**, 525 (1972).
130. B. D. Day, Rev. Mod. Phys. **50**, 495 (1978).
131. P. Grange and A. Lejeunne, Nucl. Phys. **A327**, 355 (1979).
132. P. J. Dortmans, K. Amos and S. Karatagliidis, J. Phys. G **23**, 183 (1997).
133. P. J. Dortmans, K. Amos and S. Karatagliidis, Phys. Rev. C **57**, 2433 (1998).
134. R. V. Reid, Ann. Phys. (N.Y.) **50**, 411 (1968).
135. M. A. Franey and W. G. Love, Phys. Rev. C **31**, 488 (1985).
136. A. N. Tikhonov and V. Y. Arsenin, *Solutions of Ill-Posed Problems* (Wiley, New York, 1977).
137. W. G. Love, K. Nakayama and M. A. Franey, Phys. Rev. Lett. **59**, 1401 (1987).
138. T. Cheon and K. Takayangi, Phys. Rev. Lett. **68**, 1291 (1992).
139. S. Karatagliidis, P. J. Dortmans, K. Amos and R. de Swiniarski, Phys. Rev. C **52**, 861 (1995).
140. S. O. Bäckman, Nucl. Phys. **A120**, 593 (1968).
141. W. H. Dickhoff, A. Faessler, J. M. ter Vehn and H. Müther, Phys. Rev. C **23**, 1154 (1981).
142. W. H. Dickhoff, Nucl. Phys. **A405**, 534 (1983).
143. J. P. Elliot, Nucl. Phys. **A121**, 241 (1968).
144. J. J. Kelly *et al.*, Phys. Rev. C **39**, 1222 (1989).

145. J. J. Kelly, Phys. Rev. C **39**, 2120 (1989).
146. N. Yamaguchi, T. Kasahara, S. Nagata and Y. Akaishi, Prog. Theor. Phys. **62**, 1018 (1979).
147. D. W. L. Sprung and P. K. Banerjee, Nucl. Phys. **A168**, 273 (1971).
148. X. Campi and D. W. L. Sprung, Nucl. Phys. **A194**, 401 (1971).
149. M. Kohno and D. W. L. Sprung, Nucl. Phys. **A397**, 1 (1983).
150. S. Nishizaki, T. Takatsuka, N. Yahagi and J. Hiura, Prog. Theor. Phys. **86**, 853 (1991).
151. P. J. Dortmans and K. Amos, Phys. Rev. C **49**, 1309 (1994).
152. W. H. Dickoff, Nucl. Phys. **A399**, 287 (1983).
153. K. Nakano, L. Rikus and H. V. von Geramb, Nucl. Phys. **A414**, 413 (1984).
154. G. Bertsch, J. Borysowicz, H. McManus and W. G. Love, Nucl. Phys. **A284**, 399 (1977).
155. K. Nakayama and W. G. Love, Phys. Rev. C **38**, 51 (1988).
156. N. Yamaguchi, S. Nagata and T. Matsuda, Prog. Theor. Phys. **70**, 459 (1983).
157. N. Yamaguchi, S. Nagata and J. Michiyama, Prog. Theor. Phys. **76**, 1289 (1986).
158. M. Hugi, W. Bauhoff and H. O. Meyer, Phys. Rev. C **28**, 1 (1983).
159. L. Ray *et al.*, Phys. Rev. C **37**, 1169 (1988).
160. P. J. Brussaard and P. W. M. Glaudemans, *Shell model applications in nuclear spectroscopy* (North-Holland Publishing Company, Amsterdam, 1977).
161. I. Talmi, *Simple models of complex nuclei* (Harwood Academic Publishers, Switzerland, 1993).
162. K. Heyde, *The nuclear shell model*, 2nd ed. (Springer-Verlag, New York, 1994).
163. G. Ripka, Adv. Nucl. Phys. **1**, 193 (1971) and references cited therein.
164. W. H. Bassichis, A. K. Kerman and J. P. Svenne, Phys. Rev. **160**, 746 (1967).
165. K. W. Schmid, Phys. Rev. C **24**, 1283 (1981).
166. S. Cohen and D. Kurath, Nucl. Phys. **73**, 1 (1965).
167. S. Y. Lee and K. Suzuki, Phys. Lett. **91B**, 173 (1980).
168. D. C. Zheng *et al.*, Phys. Rev. C **52**, 2488 (1995).
169. B. S. Pudliner *et al.*, Phys. Rev. C **56**, 1720 (1997).
170. P. Nesci, K. Amos and I. Morrison, J. Phys. G **5**, 383 (1978) and references contained therein.
171. R. E. Peierls and J. Yoccoz, Proc. Phys. Soc. **A70**, 81 (1957).
172. D. L. Hill and J. A. Wheeler, Phys. Rev. **89**, 1102 (1953).
173. K. Amos, I. Morrison, R. Smith and K. W. Schmid, Aust. J. Phys. **34**, 493 (1981).
174. B. R. Barrett, R. G. L. Hewitt and R. J. McCarthy, Phys. Rev. C **3**, 1137 (1971).
175. P. Navrátil and B. R. Barrett, Phys. Rev. C **57**, 3119 (1998).
176. P. Navrátil and B. R. Barrett, Phys. Rev. C **54**, 2986 (1996).
177. F. Ajzenberg-Selove, Nucl. Phys. **A490**, 1 (1988).
178. J. Jaenecke *et al.*, Phys. Rev. C **54**, 1070 (1996).
179. R. B. Wiringa, Nucl. Phys. **A631**, 70c (1998).
180. J. A. Tostevin and J. S. Al-Khalili, Nucl. Phys. **A616**, 418c (1997).
181. N. Alexander, K. Amos, B. Apagyi and D. R. Lun, Phys. Rev. C **53**, 88 (1996).
182. J. S. Al-Khalili and J. A. Tostevin, Phys. Rev. C **57**, 1846 (1998).
183. K. Langanke, Adv. in Nucl. Phys. **21**, 85 (1994) and references cited therein.
184. N. W. Schellingerhout, L. P. Kok, S. A. Coon and R. M. Adam, Phys. Rev. C **48**, 2714 (1993).
185. I. Tanihata *et al.*, Phys. Rev. Lett. **55**, 2676 (1985).
186. S. Karatagliidis, B. A. Brown, K. Amos and P. J. Dortmans, Phys. Rev. C **55**, 2826 (1997).
187. K. Wildermuth and Y. C. Tang, *A Unified Theory of the Nucleus* (Academic Press, New York, 1977).

188. A. Arima, H. Horiuchi, K. Kubodera and N. Takigawa, Adv. in Nucl. Phys. **5**, 345 (1972).
189. C. W. de Jager, H. de Vries and C. de Vries, At. Data Nucl. Data Tables **14**, 479 (1974).
190. M. G. Gornow *et al.*, Phys. Rev. Lett. **81**, 4325 (1998).
191. S. Karataglidis *et al.*, Phys. Rev. Lett. **79**, 1447 (1997).
192. S. Karataglidis, P. J. Dortmans, K. Amos and C. Bennhold, nucl-th/9811045 submitted to Phys. Rev. C for publication.
193. O. Häusser, private communication.
194. F. Ajzenberg-Selove, Nucl. Phys. **A506**, 1 (1990).
195. N. Ensslin *et al.*, Phys. Rev. C **9**, 1705 (1974).
196. R. K. Huffman, J. Dubach, R. S. Hicks and M. A. Plum, Phys. Rev. C **35**, 1 (1987).
197. I. Talmi, Phys. Rev. C **39**, 284 (1989).
198. K. Amos, D. Koetsier and D. Kurath, Phys. Rev. C **40**, 374 (1989).
199. F. Ajzenberg-Selove, Nucl. Phys. **A523**, 1 (1991).
200. W. C. Haxton and C. Johnson, Phys. Rev. Lett **65**, 1325 (1990).
201. S. Karataglidis, P. J. Dortmans, K. Amos and R. de Swiniarski, Aust. J. Phys. **49**, 644 (1996).
202. G. E. Brown and A. M. Green, Nucl. Phys. **75**, 401 (1966).
203. D. R. Tilley, H. R. Weller and A. E. S. Green, Nucl. Phys. **A564**, 1 (1993).
204. J. T. deForst and J. D. Walecka, Adv. Phys. **15**, 1 (1966).
205. D. O. Riska, Phys. Rep. **181**, 207 (1989).
206. A. J. F. Siegert, Phys. Rev. **52**, 787 (1937).
207. M. Gari and H. Hebach, Phys. Rep. **72**, 1 (1981).
208. J. L. Friar and W. C. Haxton, Phys. Rev. C **31**, 2027 (1985).
209. J. L. Friar and S. Fallieros, Phys. Rev. C **29**, 1645 (1984).
210. J. L. Friar and S. Fallieros, (unpublished); see also [208].
211. H. Überall, *Electron scattering from complex nuclei* (Academic Press, New York, 1971), Vol. Part A, p. 243.
212. B. A. Brown and B. H. Wildenthal, Ann. Rev. Nucl. Part. Sci. **36**, 29 (1988).
213. W. C. Ford, R. C. Braley and J. Bar-Touv, Phys. Rev. C **4**, 2099 (1971).
214. S. Karataglidis, P. Halse and K. Amos, Phys. Rev. C **51**, 2494 (1995).
215. A. Hotta *et al.*, Phys. Rev. C **36**, 2212 (1987).
216. P. Navrátil, private communication.
217. R. G. Arnold *et al.*, Phys. Rev. Lett. **40**, 1429 (1978).
218. H. Collard *et al.*, Phys. Rev. **138**, 357 (1965).
219. J. S. McCarthy *et al.*, Phys. Rev. Lett. **25**, 884 (1970).
220. J. S. McCarthy *et al.*, Phys. Rev. C **15**, 1396 (1977).
221. J. Carlson and R. Schiavilla, Rev. Mod. Phys. **70**, 743 (1998).
222. R. Schiavilla, V. R. Pandharipande and D. O. Riska, Phys. Rev. C **40**, 2294 (1989).
223. J. M. Cavedon *et al.*, Phys. Rev. Lett. **49**, 986 (1982).
224. P. C. Dunn *et al.*, Phys. Rev. C **27**, 71 (1983).
225. J. P. Juster *et al.*, Phys. Rev. Lett. **55**, 2261 (1985).
226. R. F. Frosch *et al.*, Phys. Rev. **160**, 874 (1968).
227. L. R. Suelzle, M. R. Yearian and H. Crannell, Phys. Rev. **162**, 992 (1967).
228. G. C. Li, I. Sick, R. R. Whitney and M. R. Yearian, Nucl. Phys. **A162**, 582 (1971).
229. J. C. Bergstrom, S. B. Kowalski and R. Neuhausen, Phys. Rev. C **25**, 1156 (1982).
230. L. Lapikás, in *Proceedings of the Conference on Modern Trends in Elastic Electron Scattering, Amsterdam*, edited by C. de Vries (Amsterdam, 1978), p. 49.
231. R. B. Wiringa and R. Schiavilla, Phys. Rev. Lett. **81**, 4317 (1998).
232. J. C. Bergstrom, U. Deutschmann and R. Neuhausen, Nucl. Phys. **A327**, 439 (1979).

233. R. Yen *et al.*, Nucl. Phys. **A235**, 135 (1974).
234. J. C. Bergstrom and E. L. Tomusiak, Nucl. Phys. **A262**, 196 (1976).
235. R. M. Hutcheon and H. S. Caplan, Nucl. Phys. **A127**, 417 (1969).
236. B. A. Brown, R. Radhi and B. H. Wildenthal, Phys. Rep. **101**, 313 (1983).
237. J. C. Bergstrom, I. P. Auer and R. S. Hicks, Nucl. Phys. **A251**, 401 (1975).
238. J. Lichtenstadt *et al.*, Phys. Lett. **219B**, 394 (1989).
239. G. J. C. van Niftrik, L. Lapikás, H. de Vries and G. Box, Nucl. Phys. **A174**, 173 (1971).
240. J. Lichtenstadt *et al.*, Phys. Lett. **244B**, 173 (1990).
241. M. Bernheim and G. R. Bishop, Phys. Lett. **5**, 294 (1963).
242. S. Karataglidis, Technical Report No. UM-P-95/29, University of Melbourne (unpublished).
243. J. A. Jansen, R. T. Peerdeeman and C. de Vries, Nucl. Phys. **A188**, 337 (1972).
244. I. Sick and J. S. McCarthy, Nucl. Phys. **A150**, 631 (1970).
245. A. Nakada, Y. Torizuka and Y. Horikawa, Phys. Rev. Lett. **27**, 745 (1971), *ibid*, **27**, 1102 (1971).
246. J. B. Flanz *et al.*, Phys. Rev. Lett. **41**, 1642 (1978).
247. J. B. Flanz *et al.*, Phys. Rev. Lett. **43**, 1922 (1979).
248. H. Crannell, Phys. Rev. **148**, 1107 (1966).
249. Y. Torizuka *et al.*, Phys. Rev. Lett. **22**, 544 (1969).
250. A. Yamaguchi, T. Terasawa, K. Nakahara and Y. Torizuka, Phys. Rev. C **3**, 1750 (1971).
251. P. J. Dortmans, K. Amos, S. Karataglidis and J. Raynal, Phys. Rev. C **58**, 2249 (1998).
252. M. Yosoi *et al.*, *RCNP Annual Report*, (1995) p. 4 (unpublished).
253. L. N. Blumberg *et al.*, Phys. Rev. **147**, 812 (1966).
254. F. Auger *et al.*, in *Conference on Experimental Nuclear Physics in Europe* (ENPE '99, Seville, Spain, 1999).
255. W. A. Richter *et al.*, Phys. Rev. C **54**, 1756 (1996).
256. D. K. Hasell *et al.*, Phys. Rev. C **34**, 236 (1986).
257. O. Häusser *et al.*, Phys. Lett. **343B**, 36 (1995).
258. E. J. Brash *et al.*, Phys. Rev. C **52**, 807 (1995).
259. M. J. Paes and R. H. Landau, Phys. Rev. C **29**, 2267 (1984).
260. L. Ray and G. W. Hoffmann, Phys. Rev. C **31**, 538 (1985).
261. G. A. Moss *et al.*, Phys. Rev. C **21**, 1932 (1981).
262. M. Yoshimura *et al.*, *RCNP Annual Report*, (1992) p. 48 unpublished).
263. C. W. Glover *et al.*, Phys. Rev. C **41**, 2487 (1990) and J. R. Comfort, private communication.
264. J. R. Comfort *et al.*, Phys. Rev. C **26**, 1800 (1982).
265. P. K. Deb, private communication.
266. I. Tanihata, in *Proceedings of INPC'95*, edited by S. Zuxun and X. Jincheng (Beijing, 1995), p. 611.
267. A. A. Korsheninnikov *et al.*, Phys. Lett. **316B**, 38 (1993).
268. C.-B. Moon *et al.*, Phys. Lett. **297B**, 39 (1992).
269. F. G. Perey and B. Buck, Nucl. Phys. **32**, 353 (1962).
270. W. E. Frahn and R. H. Lemmer, Nuovo Cim. **5**, 523 (1957).
271. F. G. Perey and D. S. Saxon, Phys. Lett. **10**, 107 (1964).
272. R. Peierls and N. V. Mau, Nucl. Phys. **A343**, 1 (1980).
273. H. Fiedeldey, R. Lipperheide, G. H. Rawitscher and S. A. Sofianos, Phys. Rev. C **45**, 2885 (1992).
274. W. Bauhoff, H. V. von Geramb and G. Pálá, Phys. Rev. C **45**, 2466 (1983).
275. B. Apagyi and W. Scheid, J. Phys. G **9**, 73 (1983).

276. N. Austern, Phys. Rev. **137**, B752 (1965).
277. H. Fiedeldey, Nucl. Phys. **77**, 149 (1966).
278. M. Coz, L. G. Arnold and A. D. MacKellar, Ann. Phys. **58**, 504 (1970).
279. W. E. Frahn, Nucl. Phys. **66**, 358 (1965).
280. B. Apagyi, J. Phys. G. **16**, 451 (1990) and references cited therein.
281. B. M. Levitan, *Inverse Sturm Liouville Problems* (VNU Science Press, Utrecht, 1987).
282. R. Lipperheide and H. Fiedeldey, Z. Phys. **A286**, 45 (1978).
283. G. Vollmer, Z. Phys. **226**, 423 (1969).
284. L. Allen, K. Amos and P. J. Dortmans, Phys. Rev. C **49**, 2177 (1994).
285. E. Witten, Nucl. Phys. **B188**, 513 (1981).
286. D. Baye, Phys. Rev. Lett. **58**, 2738 (1987).
287. H. Leeb, H. Huber and H. Fiedeldey, Phys. Lett. **344B**, 18 (1995).
288. M. Münchow and W. Scheid, Phys. Rev. Lett. **44**, 1299 (1980).
289. P. C. Sabatier, J. Math. Phys. **8**, 905 (1967).
290. M. A. Hooshyar, J. Math. Phys. **16**, 257 (1975).
291. H. Huber, *Ph.D. thesis*, TU Wien, 1995 (unpublished).
292. D. R. Lun and S. J. Buckman, Phys. Rev. Lett. **79**, 541 (1997).
293. D. R. Lun *et al.*, Phys. Rev. A **58**, 4993 (1998).
294. A. C. Lovell, private communication.
295. P. J. Dortmans, S. Karataglidis, K. Amos and R. de Swiniarski, Phys. Rev. C **52**, 3224 (1995).
296. P. Schwandt, private communication.
297. K. W. Jones *et al.*, Phys. Lett. **128B**, 281 (1983).
298. K. W. Jones *et al.*, Phys. Rev. C **50**, 1982 (1994).
299. W. Bauhoff *et al.*, Nucl. Phys. **A410**, 180 (1983).
300. P. J. Dortmans, K. Amos and S. Karataglidis, Phys. Rev. C **55**, 2723 (1997).
301. B. D. Anderson *et al.*, Phys. Rev. C **54**, 237 (1996).
302. D. J. Millener, private communication.
303. G. H. Neuschaeffer, M. N. Stephens, S. L. Tabor and K. W. Kemper, Phys. Rev. C **28**, 1594 (1983).
304. R. S. Hicks *et al.*, Phys. Rev. C **30**, 1 (1984).
305. C. W. Glover *et al.*, Phys. Rev. C **43**, 1664 (1991) and J. J. Kelly, private communication.
306. A. A. Korsheninnikov *et al.*, Phys. Rev. Lett. **78**, 2317 (1997).
307. A. A. Korsheninnikov *et al.*, Nucl. Phys. **A616**, 189c (1997).
308. D. J. Millener, J. W. Olness, E. K. Warburton and S. S. Hanna, Phys. Rev. C **28**, 497 (1983).
309. J. O. Corbett, Nucl. Phys. **A169**, 246 (1971).

INDEX

- Abel integral equations, 487
Anapole moment, 260
Asymptotic freedom, 28
- Bargmann potentials, 485, 491–494
Bethe–Salpeter equation, 329, 332
Blankenbecler–Sugar reduction, 329, 331
Big Bang, 2
Bonn potential, 83, 94, 114
Borel transformation, 41
 Borel mass, 41–42
 Borel window, 43
Borromean nuclei, 390–392
Brown–Rho scaling, 77–80, 189, 195
Brueckner–Bethe–Goldstone equation, 283, 353
Brueckner theory, 353, 380
 binding energy, 358–364
- Chiral Lagrangians, 77–80, 90
Chiral master formula framework, 45–49
Chiral perturbation theory, 28
Chiral reduction formalism, 45–49, 165–166, 187, 191
Chiral symmetry, 2, 13, 33, 38, 45
 breaking, 52, 190
 dynamical, 13
 spontaneous, 16, 35
restoration, 5, 7, 8, 32, 50, 53, 89, 189, 195
phase transition, 131
transition temperature, 32, 34, 37
- Cluster models, 393
Cross section fluctuations, 263
Cutkosky rules, 91
- Dalitz decays, 5
Debye screening, 6
Debye–Waller factor, 525
Desplanques, Donoghue, and Holstein (DDH) model, 249
Deuteron wave function, 341
Dilepton
 production, 4, 5, 17, 30–32, 34, 38, 49
 from disoriented chiral condensates, 127–130
 from dropping rho-meson mass, 129, 151, 169, 182, 186, 194
 at finite baryon density, 122
 finite temperature effects, 99–101
 from hot meson gas, 118, 124
 from off-equilibrium pion gas, 130
 from quark–gluon plasma, 125–127
 from thermal annihilation, 30–31
 spectra, 6–11, 37, 101–192
 hadronic cocktail contribution, 138, 155–161, 170
Disoriented chiral condensates, 10, 127–130
Drell–Yan
 annihilation, 4, 180
 production, 6
Dropping mass scenario, 44, 129, 151, 193
Dynamical enhancement factor, 213
Dyson equation, 68, 120

- Effective NN interactions, 278, 281, 307–317, 366–380
- Electron scattering
form factors, 403–411
longitudinal, 412, 416, 417, 430–437
magnetic, 418
transverse, 413–415, 431–433
- inelastic, 426, 427
operators and observables, 403–437
- Energy-weighted sum-rule, 17
- Equation of state, 19, 22, 26, 140
- Exciton model, 225
- Exotic nuclei, 276
- Faddeev method, 388, 417
- Fermi-gas relation, 292
- Feynman–Hellman Theorem, 18
- Fireball, 3–5, 7, 32, 103, 175, 190
hadronic, 160–165
thermal expansion, 146–149
- Freezeout, 5, 102, 173, 193, 196
chemical, 3, 147, 159
hadronic, 138
thermal, 3, 147, 159
- Gel'fand–Levitin–Marchenko
integral equation, 286, 351, 485
inversion, 298, 349
- Gellman–Oakes–Renner relation, 21
- Glueball, 78
- Goldstone bosons, 16, 18, 21, 35, 63, 191
- Hadronic
cocktail, 7, 9
Lagrangians
at finite baryon densities, 10
purely mesonic, 10
- Hadronic matter
phase diagram, 3
- Halo nuclei, 248–260, 390–391, 397, 461–463
and PNC, 250
- Haxton–Johnson interaction, 401
- Heavy-ion reactions, 138–149
Boltzman–Uehling–Uhlenbeck approach, 142, 150
hadron-string dynamics, 142
quantum molecular dynamics, 142
- Helicity formalisms, 304–307
- Hermiticity, 232
- Instantons, 13, 16
- Isospin symmetry breaking, 210
- Jacob–Wick formalism, 306
- KFSR relation, 35, 62, 80
- K-matrix, 261–334
- Kroll–Lee–Zumino coupling, 122
- Lepton tensor, 30
- Lindhard functions, 82, 95, 99
- Linear sigma model, 50–54
- Lipperheide–Fiedeldey method, 491–495
- Local density approximation, 466
- Medium modifications, 18–19, 47
vector mesons, 49–101
- Meson
exchange currents, 405, 417, 423, 427
Lagrangians, 50–76, 330–331
hidden local symmetry, 56–62
leading resonance approximation, 71, 76
linear sigma model, 50–54
massive Yang–Mills (MYM) approach, 54–56, 67
phenomenological, 62–76
open-charm, 6, 155, 180, 183
resonances, 105–107
rho
in-medium width, 45, 49, 65
nucleon resonances, 94–97
pion cloud, 65–66, 108
propagator, 75, 87, 88, 113, 118
rhosobars, 109, 116, 165
self-energy, 74, 76, 86, 94–95, 108
spectral function, 65, 77, 89, 94–97, 101–102, 115, 167, 178, 183, 187
- vector
collision broadening, 64
medium modifications, 77
- Migdal parameters, 82–83, 86, 88
- Neutron stars, 2
restoration, 2
- Neutron strength function, 213, 238–239
- Newton–Sabatier methods, 495–500
- Noether currents, 13–14, 51
- Normalization of HF state, 528–529

- Noyes–Kowalski function, 340, 357, 364–365
Nuclear saturation density, 22
Nucleon–nucleus scattering
 elastic, 437–465
 inelastic, 500–527
Nucleon–nucleon (NN) potentials
 Argonne, 280, 329
 Bonn, 278, 280, 294, 328–353, 358–380, 448–465
 effective, 278, 281, 366–380
 multiple expansion, 307–317
 Hamburg, 280, 370
 Nijmegen, 278, 280, 294, 328–353
 OBEP, 280
 OSBEP, 330–353, 358–380
 Paris, 278, 280, 298, 328–353, 358–380, 448–465, 505, 526
Nucleon weak interaction strengths, 249
- Optical model, 230–248
 coordinate space, 301–328, 437–465
 equivalent local, 465–500
 generalized, 282
 Madland–Young strong potential, 237
 momentum space, 285–301
 and nucleon–nucleus scattering, 276–536
 transmission functions, 243
- Optical theorem, 211, 233
- Parity nonconservation (PNC), 208–271
 matrix element, 215
 Michel type, 237, 244
 optical model description of, 230–248
 spreading width, 215
- Particle-hole matrix elements, 317–320
- Peierls–Yoccoz method, 383
- Perey effect, 476
- Phase transition, 8, 193
- Photon production rates, 137–138
 direct spectra, 184–187, 192
- Pion
 electromagnetic form factor, 60–69, 190
 Goldstone nature, 68
 Lagrangian, 81
 optical potential, 68, 70, 81
 propagator, 82
 spectral function, 85
- Poisson distribution, 223
- Polarized beam observables, 325
- Porter–Thomas distribution, 223
- Projected Hartree–Fock theory, 382–386
- Projection operators, 527–529
- Quantum chromodynamics (QCD)
 anomalies, 13
 axial, 14
 finite temperature phase transition order parameter, 6
 Lagrangian, 10–14, 77, 193
 Euclidean density, 23
 lattice calculations, 13, 22–30
 Grassman integration, 26
 lattice action, 25
 method of domain walls, 25
 method of staggered fermions, 25
 quenched approximation, 26
 screening masses, 28–29
 sum rules, 39–45
 Wilson formulation, 24, 26
 nonperturbative vacuum structure, 40
 partition function, 24
 phase structure, 2
 renormalization, 15, 40
 Wilson coefficients, 40, 43
 scale invariance, 14–15, 28
 strong coupling constant, 11–12, 41
 symmetries, 13
- Quantum hadron dynamics (QHD), 143
- Quark–gluon dynamics, 279
- Quark–gluon phase
 chiral phase transition, 25
 partonic, 4
- Quark–hadron duality, 6, 131–137, 195
- Quarkonium states
 heavy, 5
- Quarks
 confined, 2
 constituent mass, 2
 current mass, 6, 11, 78
 deconfined, 2
 effective mass, 2
 light quark sector, 11
- Radioactive-beam scattering, 523–527
- Reaction theory
 doorway states, 218–221, 224–248

- Reaction theory (*cont.*)
 - doorway states (*cont.*)
 - density of, 227–228
 - giant monopole, 224
 - local, 226
 - statistical, 224
 - Feshbach formalism, 210, 282–300
 - statistical theory, 223
 - and symmetry violation, 218–222
 - Regularization scale, 22
 - Renormalization group, 23, 27
 - Resonance gas, 3
- Sabatier transformation, 486
- Schwinger line integral, 24
- Shell model, 381–382
- Sign correlation problem, 224–230
- Skyrme model, 80
- Skyrme term, 77, 80
- Space-time collision dynamics
 - relativistic hydrodynamics, 10
 - simplistic fireball expansion, 10
 - transport simulations, 10
- Spin polarization and rotation, 245–247
- Time reversal symmetry breaking (TRSB), 209, 221, 260–267, 268
- Vacuum condensates, 15, 28–29
 - gluon, 16, 19–22, 28, 40, 43
 - in-medium, 18–19
 - quark, 16–22, 40, 43, 78
 - medium modification, 18, 194
- Vacuum spectral functions, 35
- Variational Monte Carlo method (VMC), 382, 392, 419–423
- Vector–axialvector
 - correlators, 36–37, 93
 - mixing, 32–36
- Vector dominance model (VDM), 51–76, 77, 89, 97–99, 106, 112–118, 134, 192
- Vector mesons
 - mass scenario, 7
 - medium modifications, 49–101
 - and strong QCD, 11
 - strength function, 42
- Veltman–Bell equations, 46
- Ward–Takahashi identity, 60, 83, 85
- Weinberg relation, 55
- Weinberg sum-rules, 17, 35–37, 39, 90, 194
- Wigner transformations, 291, 470
- Wilson line, 6
- Zheng interaction, 394–395